The Inverse Magneto-electroencephalography Problem for the Spherical Multiple-shell Model

Theoretical Investigations and Numerical Aspects

DISSERTATION
zur Erlangung des Grades eines Doktors
der Naturwissenschaften

vorgelegt von
Sarah Leweke geb. Orzlowski, M. Sc.

eingereicht bei der Naturwissenschaftlich-Technischen Fakultät
der Universität Siegen
Siegen 2018

gedruckt auf alterungsbeständigem holz- und säurefreiem Papier

Betreuer und erster Gutachter

Prof. Dr. Volker Michel

Universität Siegen

Zweiter Gutachter

Univ. Prof. Dr. Ronny Ramlau

Johannes Kepler Universität Linz

Tag der mündlichen Prüfung

26. September 2018

Zusammenfassung

Die Rekonstruktion des menschlichen Hirnstroms aus Messungen der magnetischen Flussdichte (MEG) und des elektrischen Potentials (EEG) ist ein wichtiges Mittel, um die Arbeitsweise des Gehirns zu verstehen und um Krankheiten wie Epilepsie zu diagnostizieren. Die Frage nach der Nichteindeutigkeit des zugehörigen inversen Problems ist nicht vollständig beantwortet, obwohl sie ausgiebig diskutiert wird.

Diese Frage wird im Rahmen des Mehrschalenmodells untersucht, welches aus konzentrisch angeordneten sphärischen Schalen besteht. Wir leiten neue Integralgleichungen für das Modell her, die weniger A-priori-Voraussetzungen benötigen als bisherige Ansätze. Anstatt nur gewisser skalarer Anteile, bilden diese den kompletten vektoriellen Hirnstrom auf die Daten ab. Wir stellen eine neue Entwicklung des Hirnstroms basierend auf einem orthonormalen Basissystem vor, die zu einer Singulärwertzerlegung mit exponentiell schnell abfallenden Singulärwerten führt. Damit kann die Frage der Nichteindeutigkeit wie auch die Frage nach dem messbaren Anteil der Radialkomponente des Stroms vollständig beantwortet werden. Nur der solenoidale und harmonische Anteil des Hirnstroms kann aus MEG- und EEG-Daten rekonstruiert werden.

Um beide exponentiell schlecht gestellten Probleme numerisch zu lösen, sind Regularisierungsverfahren notwendig. Neben dem regularisierten Ritz-Verfahren, einer skalaren Spline Methode und einem speziell für das EEG-Problem auf Basis von reproduzierenden Kernen entwickelten vektoriellen Spline-Verfahren testen wir den in den letzten Jahren von der Arbeitsgruppe Geomathematik der Universität Siegen entwickelten *regularized functional matching pursuit* (RFMP) und seine Weiterentwicklung, den *regularized orthgonal functional matching pursuit* (ROFMP). Wir verbessern die Konvergenzresultate des RFMP und führen neue Sobolevnormen als Strafterm ein. Mittels vektorieller Splines können gute und stabile numerische Ergebnisse erzielt werden, die vom ROFMP sowohl bei unverrauschten als auch bei verrauschten synthetischen Tests übertroffen werden. Abschließend wird der ROFMP für die Inversion realer Datensätze verwendet.

Abstract

The reconstruction of the neuronal current inside the human brain from magnetic flux density (MEG) and electric potential (EEG) measurements is an important tool for understanding the functioning of the brain and for diagnosing brain diseases, such as epilepsy. One partly unanswered question, which is extensively discussed in the literature, is about the non-uniqueness of the related inverse problems.

We investigate this question in the context of the multiple-shell model, which assumes nested spherical geometries. We derive novel integral equations describing the inverse problems, which require less a-priori assumptions on the current than former approaches and map the entire vector-valued current onto the data instead of certain scalar functions. A novel decomposition of the current based on an orthonormal basis system is presented, which yields singular value decompositions of the integral operators with exponentially fast decreasing singular values.

Therewith, we complete the existing non-uniqueness considerations, which includes a characterization of the measurable radial part of the neuronal current: only the harmonic solenoidal part of the current can be measured via the MEG and EEG devices.

For the numerical solution of these severely ill-posed problems, regularization methods are required. We use the regularized Ritz method, scalar splines, novel vector reproducing kernel based splines, and the regularized (orthogonal) functional matching pursuit (ROFMP) algorithm, which was developed by the Geomathematics Group Siegen within the last years. We improve convergence results of the RFMP and introduce novel Sobolev norms as penalty terms. The good and stable numerical results of the vector spline method are outperformed by the ROFMP in non-noisy and noisy synthetic test cases. Finally, we apply the ROFMP to real measurement data.

Contents

Chapter 1.

Introduction

The human brain is one of the most complex organized structures known to exist. Even though it is extensively studied in former and recent research, see, for example, [117, 133, 211], there are still open questions concerning aspects of neuroscience, such as cartography of the brain structures, diagnosis and cause of mental and physical brain diseases, and medical imaging. Different fields of research are concerned with the signal processing and interplay of neuronal cells in the brain. This interplay is responsible for human behaviour and cognition. On the other hand, defects in this interplay or the signal processing cause diseases, such as epilepsy or schizophrenia, see [133].

Today, there are mainly two types of neuroimaging methods available to study the interaction of brain cells, which are either based on measuring blood flow or electrical activity, see [122]. The first type exploits that the cerebral blood flow in a region increases if it is in use. The second type is based on the electrochemical processes that neurons use for signalling. Whereas blood flow only indirectly relates to cerebral activity, bioelectric activity is a direct consequence of this activity. From interactions between neurons and the signal processing occurring therein, an electric current emerges that induces macroscopic electric potentials and magnetic fields, which are transmitted through the conductive brain tissues, see [33, 36, 108, 117, 133]. The potentials and fields can be measured outside the head if the number of simultaneously active neurons is large enough.

In former and recent research, magnetoencephalography and electroencephalography devices, which measure physical quantities related to the currents caused by brain activity, have been used for the non-invasive study of (real time) brain processes. These two measuring methods are of particular interest in neuropsychology since they feature high temporal resolution on the millisecond scale, which is essential for studying responses on external stimuli, see [117, 122]. In contrast, methods based on blood flow only achieve temporal resolutions in the order of seconds, but feature a comparably higher spatial resolution.

For the analysis of the measured data, a relation between the bioelectrical activity and the measured quantity needs to be known. D.B. Geselowitz and J. Sarvas laid out the foundation for such relations in [94, 200]. However, the reconstruction of neuronal currents poses certain challenges. For example, the magnetic field generated by human brain activity is more than hundred million times smaller than the Earth's magnetic field. Thus, the signals are faint and the signal-to-noise ratio may be low. In addition, magnetoencephalographs as well as electroencephalographs only provide few (about 70 to 300) data points per time step on an irregularly distributed sensor grid.

Recent magnetoencephalographs measure components of the magnetic flux density outside the head, which are related to the magnetic potential. Certain devices measure the normal component of the magnetic field with respect to the sensor surface and two tangential directional derivatives of the magnetic flux density. Besides, electroencephalographs detect voltage differences on the scalp, which are differences of two electric potentials. Both

measurement methods can be performed simultaneously. For this purpose, a human subject is wearing an electroencephalograph sensor cap inside a magnetoencephalograph. An extensive survey of magnetoencephalography (MEG) with an insight to electroencephalography (EEG) and further references can be found in the survey of M.S. Hämäläinen et al. [108].

In order to achieve a reconstruction of the brain activity, a model that relates the vector-valued neuronal current to the scalar-valued measurements needs to be known. The quasi-static variant of Maxwell's equations is commonly used in medical electromagnetism to model bioelectric activity. In this context, the changes of the current and the electric and magnetic fields are assumed to be so slow such that they appear to be static. R. Plonsey and D.B. Heppner prove that the errors made by the quasi-static approach, that is the omission of propagation, capacitative and inductive effects, and boundary considerations, are clearly negligible, see [191].

Several approaches, such as LORETA, VARETA, LAURA, FOCUSS, BESA, and MUSIC, see [99, 117], that are used for solving the quasi-static variants of Maxwell's equations are based on a discretize-then-optimize approach. Hence, the neuronal current is discretized by a finite sum of dipoles and, subsequently, the discretized problem is solved. Thus, the problem is cast as a finite-dimensional Tikhonov-regularized normal equation. An advantage of these methods is that they can be combined with real-shaped brain geometries and structures. Although all of these methods include a minimum-norm approach in order to achieve uniqueness, these models cannot characterize the parts of the neuronal current that cannot be detected by magneto-electroencephalographs. Due to the complex geometry, theoretical studies of the inverse problems, such as a singular value decomposition (SVD), are impossible. In the case of an anatomically correctly shaped conductor model, the magnetic field and the electric potential can only be calculated numerically, see [108]. Hence, an approximation of the brain structure is necessary for analytic non-uniqueness considerations.

In contrast to discretize-then-optimize approaches for solving Maxwell's equations, there exist several optimize-then-discretize approaches. In this context, based on modelling the neuronal currents as continuously distributed currents, the partial differential equations are solved analytically, see the seminal papers by G. Dassios, A.S. Fokas, and co-authors [39, 47, 49, 50, 52, 71–75]. For these models, additional knowledge of the structure of the head and properties of its tissues is required. Besides homogeneous head models (i.e. constant conductivity in the entire conductor), more realistic models exist, such as the three-shell model, see [45, 73, 74], the multiple-shell model, see [108, 174], or the ellipsoidal-shell model, see [39, 46, 54]. The multiple-shell model is also used within this thesis. Within this model, the cerebrum is represented by a solid ball $\mathbb{B}_{\varrho_0}$ with radius ϱ_0 and constant conductivity. Around this ball, there is a finite number of spherical shells modelling various head tissues. The conductivity on each shell is assumed to be constant, positive, and known.

These continuous methods have in common that integral equations are derived from Maxwell's equations. For this purpose, the vector-valued neuronal current is decomposed. For example, the Hodge decomposition is used in [47, 52, 71–75] and the Helmholtz decomposition is used in [47, 49, 50, 71, 73, 74]. Both decompositions require additional smoothness or boundary conditions on the neuronal current, which is questionable since the actual smoothness and boundary behaviour of the neuronal current are unknown. These decompositions lead to integral equations containing a scalar-valued density (somehow related to the neuronal current) and a scalar-valued integral kernel, which reduces the numerical effort. However, they only allow an incomplete characterization of the null space of the integral operator in the sense that a representation of the measurable (radial part of the) neuronal current

via an appropriate orthonormal basis on the ball is missing. In addition, in the case of the EEG problem, it is only known that the orthogonal complement of the operator null space is contained in a (too large) particular Hilbert space. This also requires further analysis in order to determine the precise measurable directions. In addition, these decompositions have mostly advantages for either the MEG or the EEG problem such that a joint inversion of the data sets and a joint representation of the neuronal current is difficult to handle.

Even though these integral equations and especially the non-uniqueness of their solutions are discussed extensively in the literature, see the references above, there are still some open questions concerning the ill-posedness of the inverse MEG and EEG problems for the spherical multiple-shell model: which direction, especially in the case of the EEG problem, of the neuronal current is visible for the measurement devices? Can we characterize the radial part of the neuronal current that affects the measurement via orthonormal basis functions in an appropriate (weighted) Lebesgue space? When does a solution of the inverse problem exist?

In order to answer these questions, we derive from the quasi-static Maxwell's equations two novel Fredholm integral equations of the first kind relating the vector-valued neuronal current to the magnetic flux density as well as the electric potential in the case of a continuously distributed neuronal current in the spherical multiple-shell model. The novelty of these integral equations consists of two parts. First, we obtain integral equations that map the entire vector-valued neuronal current to the data instead of mapping only scalar-valued parts of it. Second, we only require that the neuronal current is an $\mathbf{L}_2(\mathbb{B}_{\varrho_0}, \mathbb{R}^3)$-function and, thus, reduce the a-priori assumptions on the neuronal current. We no more require smoothness or boundary assumptions on the current, which are needed, for instance, for the Helmholtz and the Hodge decomposition. Both integral equations consist of a vector-valued integral kernel that is represented by a series of vector Legendre polynomials. Especially in the case of the inverse EEG problem, we are able to add more insight to occurring quantities related to the multiple-shell model.

In order to solve the inverse MEG and EEG problem simultaneously, we define a class of vector-valued integral kernels that covers the MEG as well as the EEG integral kernel. However, this class of integral kernels is not restricted to applications in medical imaging, since it includes, for example, the integral kernel occurring in the inverse Earth's magnetization problem, in which the magnetization inside the Earth's crust is determined from measurements of the Earth's magnetic field, see [15, 93]. Besides the well-definedness of these particular integral kernels, we analyze the well-definedness of the corresponding integral operator $\mathcal{T}$ in the sense that the potential, that is the function $\mathcal{T}\boldsymbol{f}$ for all $\boldsymbol{f} \in \mathbf{L}_2(\mathbb{B}_{\varrho_0}, \mathbb{R}^3)$, exists. The relation between the neuronal current and the gradient field of the potential can also be described by a linear operator $\mathcal{B}\boldsymbol{f} := -\boldsymbol{\nabla}(\mathcal{T}\boldsymbol{f})$ for all $\boldsymbol{f} \in \mathbf{L}_2(\mathbb{B}_{\varrho_0}, \mathbb{R}^3)$, where $\mathcal{B}$ is also well-defined.

Based on an appropriate orthonormal basis for $\mathbf{L}_2(\mathbb{B}_{\varrho_0}, \mathbb{R}^3)$, which consists of orthogonal polynomials in the radial part and Edmonds vector spherical harmonics in the angular part, we can express a function $\boldsymbol{f} \in \mathbf{L}_2(\mathbb{B}_{\varrho_0}, \mathbb{R}^3)$ by a (generalized) Fourier expansion. This novel orthonormal basis is developed based on existing scalar-valued orthonormal basis systems going back to L. Ballani, H.M. Dufour, J. Engels, and E.W. Grafarend, see [13, 59]. The methods used for the constructive approximation on the sphere are mainly based on the extensive survey of W. Freeden, T. Gervens, and M. Schreiner in [81]. Therewith, we compute $\mathcal{T}\boldsymbol{f}$ and $\mathcal{B}\boldsymbol{f}$ and achieve series representations for the potential and its field, which solve the direct problem related to the operators $\mathcal{T}$ and $\mathcal{B}$. This representation allows a

precise characterization of the infinite-dimensional spaces $(\ker \mathcal{T})^{\perp}$ and $(\ker \mathcal{B})^{\perp}$ by means of an orthonormal basis. According to Hadamard, see [106, 107], the corresponding inverse problems are ill-posed since the solution cannot be unique, which is consistent to earlier considerations in the particular application of the inverse MEG and EEG problem.

In the context of ill-posed problems, the SVD of an operator is a major tool, which provides us with a classification of the stability of the problem, Picard's criterion for the existence of a solution, the generalized Moore-Penrose inverse operator, and a best-approximate solution of the problem. This is discussed in detail in the literature, see, for instance, the monographs of H.W. Engl, M. Hanke, and A. Neubauer [63] or A. Rieder [194]. Unfortunately, we are not able to find the SVDs of $\mathcal{T}$ and $\mathcal{B}$ in the general setting, although they exist since $\mathcal{T}$ and $\mathcal{B}$ are compact operators. For this purpose, we further restrict the class of integral kernels and proceed by defining Hilbert spaces with orthonormal basis systems containing either $\overline{\operatorname{ran} \mathcal{T}}$ or $\overline{\operatorname{ran} \mathcal{B}}$. Eventually, this allows us to derive the SVDs of $\mathcal{T}$ and $\mathcal{B}$ in the restricted case. For both operators, the singular values decrease exponentially fast to zero, which makes the corresponding inverse problem severely ill-posed.

After having analyzed the general problem in detail, we come back to the inverse MEG and EEG problem. Since the MEG kernel is covered by the restricted class of integral kernels, the results stated above provide us with an SVD of the operator mapping the neuronal current onto the magnetic field. In contrast, the EEG kernel is not covered by the restricted class. For this reason, another tailor-made Hilbert space containing the closure of the EEG operator range with an appropriate orthonormal basis is constructed. Eventually, this leads to an SVD of the EEG integral operator with exponentially fast decaying singular values. Concluding, we obtain that the inverse MEG and EEG problems are severely ill-posed with an infinite-dimensional null space of the corresponding operators, where we now have a precise characterization of the null spaces by means of an orthonormal basis at hand. The instability of these problems was conjectured earlier in the literature, see [33, 108, 117], and is now verified mathematically. In addition, the information of the neuronal current that can be recovered by MEG and EEG measurements is complementary to each other (in the sense of $\mathbf{L}_2(\mathbb{B}_{\varrho_0}, \mathbb{R}^3)$-orthogonality), see also [47, 71]. Using the structure of the MEG and EEG operator null spaces and properties of the unique minimizer of the Tikhonov-regularized normal equation, we prove that a simultaneous inversion of the MEG and EEG data sets cannot yield more information on the neuronal current than a combination of the single inversions.

We extend and complement existing results concerning the non-uniqueness of this problem, see [47, 50, 71], by using a tailor-made orthonormal basis that leads to an SVD of the operators. We prove that from the simultaneous MEG and EEG inversion only the harmonic solenoidal part of the neuronal current can be reconstructed. Besides this, we state additional uniqueness constraints, for example, the minimum-norm assumption, a harmonicity constraint, and radial uniqueness constraints on the entire vector-valued current instead of on scalar-valued parts. These constraints are stated in the general setting as well as for the particular MEG and EEG problem. Furthermore, we compare our ansatz with existing results in the literature that are obtained via the Hodge and the Helmholtz decomposition and discuss the advantages and disadvantages of each method in detail.

Due to the ill-posedness of the inverse MEG and EEG problem, regularization methods and parameter choice methods are required in order to solve these two problems numerically, see additionally [192] of R. Ramlau and H.W. Engl for a broad overview of this topic. Within the last years, a dictionary based regularization method called the *Regularized Functional*

Matching Pursuit (RFMP) algorithm as well as some enhancements called the *Regularized Orthogonal Functional Matching Pursuit* (ROFMP) and the *Regularized Weak Functional Matching Pursuit* (RWFMP) have been developed, which yield good results in several numerical applications in the geosciences, see the works of D. Fischer, M. Kontak, V. Michel, and R. Telschow in [66, 68, 137, 138, 159, 163, 166, 210]. In addition, we firstly apply these methods to vector-valued problems in medical imaging. We improve existing convergence results for the RFMP and add novel statements concerning the solution produced by the algorithm. The RFMP as well as the ROFMP are used for the inversion of synthetic data sets in the MEG and the EEG problem where we additionally assume that the neuronal current satisfies the minimum-norm condition in order to achieve uniqueness. For their implementation, we construct novel vector-valued Sobolev spaces on the ball for the penalty term and novel vector-valued reproducing kernels as dictionary elements. For each particular problem, the numerical results from the synthetic test case are compared to other established reconstruction methods, namely the regularized Ritz method going back to W. Ritz, see [195], and spline methods. For the MEG, we are able to use a scalar reproducing kernel based spline method based on the work of A. Amirbekyan, V. Michel, and co-authors, see [6, 7, 65, 167], that is also used for the MEG inversion in [73]. In [73], based on the Helmholtz decomposition, a scalar spline method is also employed for the inversion of EEG data. Since this approach cannot be combined with the minimum-norm assumption on the neuronal current, which we also prove in this thesis, we construct novel tensor-valued reproducing kernel based splines on the ball for our numerical investigations.

The considered synthetic test case is constructed via a linear combination of vector-valued analogues of Abel-Poisson kernels used in [73] for scalar synthetic test cases. We calculate the corresponding data analytically and add white Gaussian noise for 1 % to 10 % noise level to it.

Based on the spline method used in [73], we construct scalar splines in order to reconstruct a scalar-valued part of the neuronal current obtained by the Helmholtz decomposition. In contrast to the previous approach, we adapt the radial part of these splines in order to satisfy the minimum-norm condition on the neuronal current. The scalar reconstructions achieved via this method are satisfying even for higher noise levels. However, we are interested in the entire neuronal current. For this purpose, the result of the scalar solution needs to be transferred to the vector-valued current. Due to an additional damping factor, this yields additional blurriness of the reconstruction especially for higher noise levels. The novel vector spline method is applied to the inverse EEG problem and yields adequate numerical results. Only for 10 % noise the solution is fuzzy, which is acceptable since the inverse problem is severely ill-posed. An advantage of both spline methods is a very small relative residual. On the other hand, the Ritz method does not work satisfactorily especially for higher noise levels. The solutions are unstable especially in the inverse MEG problem, where a severe downward continuation comes into play.

The numerical results obtained by the spline and the Ritz method are outperformed by the R(O)FMP reconstructions with respect to the approximation error measured via the normalized root mean square error. More precisely, the results achieved via the ROFMP outperform the results achieved via the RFMP with respect to the quality and smoothness of the reconstruction. However, the relative residual obtained by these methods is higher than for the spline methods. Besides this, we measure the required CPU time for the R(O)FMP and test several parameter choice methods in order to determine the optimal regularization parameter.

This thesis is structured in several parts. In the first part, the magneto-electroencephalography problem for the multiple-shell model is derived. For this purpose, some mathematical foundations are stated in Chapter 2. The modelling of the MEG problem is conducted in Chapter 3 and the modelling of the EEG problem in Chapter 4.

In the second part of the thesis, the related direct problems are considered. This part starts with an introduction to certain orthonormal basis systems and vector-valued special functions on the sphere and on the ball in Chapter 5. Then, the mentioned particular class of vector Legendre-type integral kernels is analyzed in Chapter 6 and the corresponding integral operators in Chapter 7. Limitations on the class of integral kernels and its operator that are required for the construction of a singular system are stated in Chapter 8. This part concludes with the analysis of the direct MEG problem in Chapter 9 and the direct EEG problem in Chapter 10.

The third part is devoted to the inverse problems and starts with an introduction to inverse problems in Chapter 11. Afterwards, the ill-posedness of the general problem is discussed in detail in Chapter 12 and the ill-posedness of the magneto-electroencephalography problem is elaborated in Chapter 13.

In the fourth part, the comparison of our approach with previous scalar approaches from the literature is discussed in Chapter 15. This requires the analysis of a certain class of scalar-valued integral equations in advance, which is realized in Chapter 14.

In the fifth part, regularization methods are treated. This part consists of an introduction to the novel vector-valued Sobolev spaces on the ball as well as basics on regularization and parameter choice methods in Chapter 16. In addition, the RFMP is presented and analyzed in detail in Chapter 17. We also give some details on the ROFMP.

The sixth part is dedicated to the numerical investigations. For this purpose, a synthetic test case is constructed in Chapter 18 and foundations for the implementation are given in Chapter 19. Other reconstruction methods, such as the Ritz method, a scalar spline method, and the novel vector spline method, are presented in Chapter 20 from the theoretical point of view. The numerical results in the synthetic test case as well as in the real data situation obtained by each of the reconstruction methods are presented and discussed in Chapter 21.

In the final part of this thesis, we give a conclusion and an outlook.

Part I.

Basics

Chapter 2.

Preliminaries

In this preliminary chapter, we introduce the used notations and the basic mathematical framework. First, the notation used within this thesis is presented in Section 2.1. For the derivation of an integral equation for the magneto-electroencephalography problem in the context of a ball-shaped conductor, we require some vector calculus in spherical geometries. This is summarized in Section 2.3. An important class of special functions in spherical geometries are (scalar) spherical harmonics. Before we present these particular functions, we briefly introduce some other special functions, namely the Jacobi and Legendre polynomials, in Section 2.2. Via the Legendre polynomials, we are able to give a short overview of spherical harmonics and their properties in Section 2.4. To complete this chapter, we present the basic principles of distribution theory in Section 2.5, which is required for the derivation of the electroencephalography integral equation.

2.1. Notation

As usual, the set of positive integers is denoted by $\mathbb{N}$, where $\mathbb{N}_0 \coloneqq \mathbb{N} \cup \{0\}$. Moreover, $\mathbb{Z}$ is the set of all integers, $\mathbb{R}$ represents the set of real numbers, and the set $\mathbb{C}$ contains all complex numbers.

Furthermore, we use the following nomenclature if not stated otherwise:

- Blackboard letters, for example $\mathbb{G} \subset \mathbb{R}^d$, denote subsets of the $\mathbb{R}^d$ with dimension $d \in \mathbb{N}$. As usual, the exponent is omitted in the case $d = 1$. The token $\mathbb{R}^+$ denotes the set of all positive real numbers and $\mathbb{R}_0^+ \coloneqq \mathbb{R}^+ \cup \{0\}$.
- Capital script-like letters, such as $\mathcal{X}$, denote function spaces.
- Capital calligraphic letters denote functionals and operators, for example $\mathcal{P}_\mathcal{V}$ denotes the projection operator onto $\mathcal{V}$.
- Bold letters, such as $\boldsymbol{x}$, denote vectorial quantities.

In addition, the hat above a bold letter represents a unit vector (e.g. $\hat{\boldsymbol{x}}$), but sometimes, for the sake of readability, they are denoted by a bold Greek letter (e.g. $\boldsymbol{\varepsilon}^1$). We use the corresponding non-bold letters as the absolute value of the vectors (i.e. $\boldsymbol{x} = x\hat{\boldsymbol{x}}$, with $x \in \mathbb{R}_0^+$) if not stated otherwise. The Euclidean standard $\mathbb{R}^3$-inner product (the so-called dot product) is denoted by $\cdot$, the cross product (also called vector product) by $\wedge$, and the tensor product by $\otimes$. They are defined by

$$\boldsymbol{x} \cdot \boldsymbol{y} \coloneqq \sum_{i=1}^{3} x_i y_i, \quad \boldsymbol{x} \wedge \boldsymbol{y} \coloneqq \begin{pmatrix} x_2 y_3 - y_2 x_3 \\ x_3 y_1 - y_3 x_1 \\ x_1 y_2 - y_1 x_2 \end{pmatrix}, \quad \boldsymbol{x} \otimes \boldsymbol{y} \coloneqq \begin{pmatrix} x_1 y_1 & x_1 y_2 & x_1 y_3 \\ x_2 y_1 & x_2 y_2 & x_2 y_3 \\ x_3 y_1 & x_3 y_2 & x_3 y_3 \end{pmatrix}$$

with $\boldsymbol{x} = (x_1, x_2, x_3)^{\mathrm{T}}$, $\boldsymbol{y} = (y_1, y_2, y_3)^{\mathrm{T}} \in \mathbb{R}^3$. The norm induced by the Euclidean dot product is represented by $x = |\boldsymbol{x}| \coloneqq \sqrt{\boldsymbol{x} \cdot \boldsymbol{x}}$. The standard Cartesian basis is given by $\boldsymbol{\varepsilon}^1 \coloneqq (1,0,0)^{\mathrm{T}}$, $\boldsymbol{\varepsilon}^2 \coloneqq (0,1,0)^{\mathrm{T}}$, and $\boldsymbol{\varepsilon}^3 \coloneqq (0,0,1)^{\mathrm{T}}$.

Furthermore, the d-dimensional sphere with radius R is denoted by

$$\mathbb{S}_R^d \coloneqq \left\{ \boldsymbol{x} \in \mathbb{R}^d \;\middle|\; x = R \right\},$$

the corresponding (closed) ball is denoted by

$$\mathbb{B}_R^d \coloneqq \left\{ \boldsymbol{x} \in \mathbb{R}^d \;\middle|\; x \leq R \right\},$$

and the (open) exterior of the ball is denoted by

$$\mathbb{B}_R^{\mathrm{ext}} \coloneqq \left\{ \boldsymbol{x} \in \mathbb{R}^d \;\middle|\; x > R \right\}.$$

For an arbitrary interval $\mathbb{I} \subset \mathbb{R}$, the d-dimensional spherical shell is defined by

$$\mathbb{S}_{\mathbb{I}}^d \coloneqq \left\{ \boldsymbol{x} \in \mathbb{R}^d \;\middle|\; x \in \mathbb{I} \right\}.$$

In this thesis, mostly three-dimensional spheres and balls are considered. Thus, we neglect the dimension for the sake of readability in the case of three-dimensional objects. For the three-dimensional unit sphere and unit ball (i.e. $R = 1$), we also drop the radius, that is $\mathbb{S} \coloneqq \mathbb{S}_1 \coloneqq \mathbb{S}_1^3$, for instance.

Besides this, let $\mathbb{G} \subset \mathbb{R}^d$ with $d \in \mathbb{N}$ be a measurable set. Then the volume integral of the function F over $\mathbb{G}$ is denoted by $\int_{\mathbb{G}} F(\boldsymbol{x}) \, \mathrm{d}\boldsymbol{x}$. If $\mathbb{G}$ is bounded, the surface integral over the surface $\partial\mathbb{G}$ is given by $\int_{\partial\mathbb{G}} F(\boldsymbol{x}) \, \mathrm{d}\omega(\boldsymbol{x})$ with the surface measure ω. A line integral along a piecewise smooth curve γ is given by $\int_\gamma F(\boldsymbol{x}) \, \mathrm{d}\sigma(\boldsymbol{x})$. A standard integral over the real interval $[a, b] \subset \mathbb{R}$ with $a < b$ is denoted by $\int_a^b F(x) \, \mathrm{d}x$.

Now, we introduce some well-known function spaces.

Definition 2.1 (Lebesgue Spaces, [198]). *Let $\mathbb{G} \subset \mathbb{R}^d$ be a region and $s \in \mathbb{N}$. The space $\boldsymbol{\mathcal{L}}_p(\mathbb{G}, \mathbb{R}^s)$ with $1 \leq p < \infty$ includes all measurable (vector-valued) functions $\boldsymbol{f} \colon \mathbb{G} \to \mathbb{R}^s$ that have a finite Lebesgue-integral $\int_{\mathbb{G}} |\boldsymbol{f}(\boldsymbol{x})|^p \, \mathrm{d}\boldsymbol{x} < \infty$. For example, $\boldsymbol{\mathcal{L}}_2(\mathbb{G}, \mathbb{R}^s)$ contains the (vector-valued) square-integrable functions $\boldsymbol{f}$. In order to obtain a properly normed space, we define the quotient space $\mathbf{L}_p(\mathbb{G}, \mathbb{R}^s) \coloneqq \boldsymbol{\mathcal{L}}_p(\mathbb{G}, \mathbb{R}^s) \setminus \boldsymbol{\mathcal{N}}_p(\mathbb{G}, \mathbb{R}^s)$, where*

$$\boldsymbol{\mathcal{N}}_p(\mathbb{G}, \mathbb{R}^s) \coloneqq \left\{ \boldsymbol{f} \in \boldsymbol{\mathcal{L}}_p(\mathbb{G}, \mathbb{R}^s) \;\middle|\; \int_{\mathbb{G}} |\boldsymbol{f}(\boldsymbol{x})|^p \, \mathrm{d}\boldsymbol{x} = 0 \right\}.$$

In the literature, the spaces $\boldsymbol{\mathcal{L}}_p(\mathbb{G}, \mathbb{R}^s)$ and $\mathbf{L}_p(\mathbb{G}, \mathbb{R}^s)$ are distinguished. Thus, we differ from our nomenclature and denote $\mathbf{L}_p(\mathbb{G}, \mathbb{R}^s)$ with non-script-like letters. Note that $\mathbf{L}_p(\mathbb{G}, \mathbb{R}^s)$ is a Banach space with the norm

$$\|\boldsymbol{f}\|_{\mathbf{L}_p(\mathbb{G}, \mathbb{R}^s)} \coloneqq \|[\boldsymbol{f}]\|_{\mathbf{L}_p(\mathbb{G}, \mathbb{R}^s)} \coloneqq \left(\int_{\mathbb{G}} |\boldsymbol{f}(\boldsymbol{x})|^p \, \mathrm{d}\boldsymbol{x} \right)^{1/p},$$

which is independent of the representative $\boldsymbol{f}$ of the equivalence class $[\boldsymbol{f}]$, see, for example, for more details [198].

In the case of $s = 3$, we use the abbreviation $\mathbf{L}_p(\mathbb{G}) \coloneqq \mathbf{L}_p(\mathbb{G}, \mathbb{R}^3)$, and in the case of $s = 1$, we use non-bold letters according to our notation, that is $\mathrm{L}_p(\mathbb{G}) \coloneqq \mathbf{L}_p(\mathbb{G}, \mathbb{R})$. Note that the

same nomenclature is used for all other function spaces. For $p = 2$, the space $\mathbf{L}_2(\mathbb{G}, \mathbb{R}^s)$ is a Hilbert space with the inner product

$$\langle \boldsymbol{f}, \boldsymbol{g} \rangle_{\mathbf{L}_2(\mathbb{G},\mathbb{R}^s)} \coloneqq \int_{\mathbb{G}} \boldsymbol{f}(\boldsymbol{x}) \cdot \boldsymbol{g}(\boldsymbol{x}) \, \mathrm{d}\boldsymbol{x}, \qquad \boldsymbol{f},\, \boldsymbol{g} \in \mathbf{L}_2\left(\mathbb{G}, \mathbb{R}^s\right).$$

Definition 2.2 (Weighted Lebesgue Spaces, [158, Def. 3.1]). *Let $w\colon [a,b] \to \mathbb{R}$ with $a,\, b \in \mathbb{R}$ and $a < b$ be a continuous function on $[a,b]$ that is positive on (a,b). Then for all measurable functions $F\colon [a,b] \to \mathbb{R}$ with $\langle F, wF \rangle_{\mathrm{L}_2([a,b])} < \infty$, we define in analogy to Definition 2.1 a* weighted Lebesgue space *with the norm*

$$\|F\|^2_{\mathrm{L}_2^w([-1,1])} \coloneqq \langle F, wF \rangle_{\mathrm{L}_2([-1,1])}.$$

Definition 2.3 (Space of k Times Continuously Differentiable Functions). *Let $\mathbb{G} \subset \mathbb{R}^d$, where $d \in \mathbb{N}$, be an open set and let $s \in \mathbb{N}$. The set of all $k \in \mathbb{N}$ times continuously differentiable functions $\boldsymbol{f}\colon \mathbb{G} \to \mathbb{R}^s$ is denoted by $\mathbf{C}^k(\mathbb{G}, \mathbb{R}^s)$, for $0 < k < \infty$. In the case $k = 0$, we use the abbreviation $\mathbf{C}(\mathbb{G}, \mathbb{R}^s)$ for the set of all continuous functions. The set of all arbitrarily often differentiable functions is denoted by $\mathbf{C}^\infty(\mathbb{G}, \mathbb{R}^s)$ and they are called smooth functions, see [123].*

In analogy, we define for bounded open sets $\mathbb{G}$ and $k \in \mathbb{N}$ the space $\mathbf{C}^k(\overline{\mathbb{G}}, \mathbb{R}^s)$ as the set containing all functions that are k times continuously differentiable in $\mathbb{G}$ and for which these functions and all derivatives up to degree k can be continuously extended to the boundary $\partial\mathbb{G}$. According to our notation, the set $\mathbf{C}^k(\mathbb{S}, \mathbb{R}^s)$, where $k \in \mathbb{N}_0 \cup \{\infty\}$, denotes the corresponding set of k-times continuously differentiable functions on the sphere $\mathbb{S}$. In this setting, continuity and differentiability are to be understood in the context of functions on manifolds, see [143, Def. 1.52].

If $\mathcal{U} \subset \mathcal{X}$ is a subspace of a Banach space, we denote with $\overline{\mathcal{U}}$ its closure. If the closure is taken with respect to a norm $\|\cdot\|_*$ that is different to $\|\cdot\|_{\mathcal{X}}$, we use the notation $\overline{\mathcal{U}}^{\|\cdot\|_*}$. If $\mathcal{U}$ is a subset of an inner product space $\mathcal{H}$, then we denote the orthogonal complement of $\mathcal{U}$ by $\mathcal{U}^\perp \coloneqq \{y \in \mathcal{H} \mid x \perp y \text{ for all } x \in \mathcal{U}\}$, where $x \perp y \Leftrightarrow \langle x, y \rangle = 0$. Note that $\mathcal{U}^\perp$ is always closed.

2.2. Jacobi and Legendre Polynomials

We will see that spherical harmonics, which are required for the modelling of the magneto-electroencephalography problem in a ball-shaped conductor setting, are closely connected with Legendre polynomials. Legendre polynomials are a particular case of Jacobi polynomials, which are also introduced in this section. For a detailed introduction to orthogonal polynomials and their identities, see [179, 209] or, more recently, [84]. The results relevant for this thesis are recapitulated in the following.

Theorem 2.4 (Jacobi Polynomials, [84, Def. 3.3.1]). *For fixed $\alpha,\, \beta > -1$, there exists one and only one unique system of polynomials $P_m^{(\alpha,\beta)}$ with $m \in \mathbb{N}_0$ that satisfies the following conditions:*

i) Each $P_m^{(\alpha,\beta)}\colon [-1,1] \to \mathbb{R}$ is a polynomial of degree m, that is $\deg P_m^{(\alpha,\beta)} = m$,

ii) for all m, $n \in \mathbb{N}_0$ with $m \neq n$, it holds true that

$$\int_{-1}^{1} (1-x)^\alpha (1+x)^\beta P_m^{(\alpha,\beta)}(x) P_n^{(\alpha,\beta)}(x)\,\mathrm{d}x = 0,$$

iii) and for each $m \in \mathbb{N}_0$, we require $P_m^{(\alpha,\beta)}(1) = \binom{m+\alpha}{m}$.

We call the functions $P_m^{(\alpha,\beta)}$ Jacobi polynomials *of degree m corresponding to the weight function $w(x) \coloneqq (1-x)^\alpha(1+x)^\beta$ with $x \in [-1,1]$.*

The binomial coefficient is given by $\binom{x}{y} \coloneqq \Gamma(x+1)/(\Gamma(y+1)\Gamma(x-y+1))$ for $x,\ y \in \mathbb{R}$ with $x,\ y > -1$ and $x > y-1$. Here, Γ denotes the usual Gamma function, see [2]. Note that this definition coincides with the classical definition via the factorial representation of the binomial coefficient in the case of $x,\ y \in \mathbb{N}_0$.

In this work, there are mainly two particular cases of the Jacobi polynomials of interest. The polynomials corresponding to the first particular case are called the *Legendre polynomials* and are obtained for $\alpha = \beta = 0$.

Definition 2.5 (Legendre Polynomials, [84, Rem. 3.3.4]). *The Legendre polynomials of degree $m \in \mathbb{N}_0$ are defined as $P_m \coloneqq P_m^{(0,0)}$, where $P_m^{(0,0)}$ are the Jacobi polynomials for $\alpha = \beta = 0$ from Theorem 2.4. The corresponding weight function reduces to $w(x) = 1$ with $x \in [-1,1]$.*

The second particular case is detailed in Section 5.1. Now, we sum up some properties and identities of Jacobi and Legendre polynomials that are required for the analysis and the numerics of the inverse magneto-electroencephalography problem later. A representation for the derivatives of Jacobi polynomials is stated in the next theorem.

Theorem 2.6 ([179, Ch. II.5]). *For every $\alpha,\ \beta > -1$ and $m,\ k \in \mathbb{N}_0$ with $k \leq m$, the following holds true:*

$$\frac{\mathrm{d}^k}{\mathrm{d}x^k} P_m^{(\alpha,\beta)}(x) = \frac{\Gamma(\alpha+\beta+m+1+k)}{2^k \Gamma(\alpha+\beta+m+1)} P_{m-k}^{(\alpha+k,\beta+k)}(x), \qquad x \in [-1,1].$$

For the maximal value of the Jacobi polynomials, the following holds true.

Theorem 2.7 ([179, Ch. II.7]). *For all $\alpha,\ \beta > -1$ with $q \coloneqq \max(\alpha,\beta) \geq -1/2$ and every $m \in \mathbb{N}_0$, the Jacobi polynomials fulfil*

$$\max_{x\in[-1,1]} \left|P_m^{(\alpha,\beta)}(x)\right| = \max\left(\left|P_m^{(\alpha,\beta)}(-1)\right|, P_m^{(\alpha,\beta)}(1)\right) = \binom{m+q}{m} \in \mathcal{O}(m^q)$$

as $m \to \infty$, where $\mathcal{O}$ is the usual Landau symbol, see [139]. In the particular case of the Legendre polynomials, we get

$$\max_{x\in[-1,1]} |P_m(x)| = 1 = P_m(1).$$

Combining the result of Theorem 2.6 with the previous theorem, we obtain for the first two derivatives of the Legendre polynomials for all $m \in \mathbb{N}_0$ and all $x \in [-1,1]$ the estimates

$$|P_m'(x)| = \frac{m+1}{2}\left|P_{m-1}^{(1,1)}(x)\right| \leq \frac{m+1}{2}\binom{m}{m-1} = \frac{m(m+1)}{2}, \tag{2.1a}$$

$$|P_m''(x)| = \frac{(m+2)(m+1)}{4}\left|P_{m-2}^{(2,2)}(x)\right| \leq \frac{(m+2)(m+1)m(m-1)}{8}. \tag{2.1b}$$

In general, for Legendre polynomials with $x \in [-1,1]$ and $k \in \mathbb{N}_0$ the result

$$\left| \frac{\mathrm{d}^k}{\mathrm{d}x^k} P_m(x) \right| \leq \left(\frac{\mathrm{d}^k}{\mathrm{d}x^k} P_m(x) \right) \Bigg|_{x=1} \in \mathcal{O}(m^{2k})$$

as $m \to \infty$ holds true. For the construction of complete orthonormal polynomial systems, we need an appropriate Hilbert space. Since the Jacobi polynomials are only orthogonal with respect to the weight function, we need to include the weight function into the Hilbert space. Note that the weighted Hilbert space $\mathrm{L}_2^w([-1,1])$ is defined in Definition 2.2. In addition, we need the corresponding norm of the Jacobi polynomials for its normalization.

Theorem 2.8 ([209, Eq. (4.3.3)]). *For every α, $\beta > -1$, the Jacobi polynomials $P_m^{(\alpha,\beta)}$, where $m \in \mathbb{N}_0$, with the weight function $w(x) = (1-x)^\alpha (1+x)^\beta$ fulfil*

$$\begin{aligned} \left\| P_m^{(\alpha,\beta)} \right\|_{\mathrm{L}_2^w([-1,1])}^2 &= \int_{-1}^{1} (1-x)^\alpha (1+x)^\beta \left(P_m^{(\alpha,\beta)}(x) \right)^2 \mathrm{d}x \\ &= \frac{2^{\alpha+\beta+1}}{2m+\alpha+\beta+1} \frac{\Gamma(m+\alpha+1)\Gamma(m+\beta+1)}{m!\Gamma(m+\alpha+\beta+1)}. \end{aligned}$$

Using this result, we are able to normalize the Jacobi polynomials from Theorem 2.4. These normalized polynomials form an $\mathrm{L}_2^w([-1,1])$-orthonormal basis.

Theorem 2.9 ([209, Thm. 3.1.5]). *Let $w(x) \coloneqq (1-x)^\alpha (1+x)^\beta$ be the weight function, then the normalized Jacobi polynomials form an $\mathrm{L}_2^w([-1,1])$-orthonormal basis.*

A series expansion by means of this basis is often called a *generalized Fourier series*. For the derivation of an integral equation for the magneto-electroencephalography problem, a closed representation of a particular Legendre series is required. It is stated in the next corollary, which completes this section.

Corollary 2.10 ([81, Eq. (3.2.32)]). *For all $\boldsymbol{x}$, $\boldsymbol{y} \in \mathbb{R}^3$ with $x < y$, the following identity holds true pointwise:*

$$\frac{1}{|\boldsymbol{x}-\boldsymbol{y}|} = \sum_{m=0}^{\infty} \frac{x^m}{y^{m+1}} P_m(\hat{\boldsymbol{x}} \cdot \hat{\boldsymbol{y}}). \tag{2.2}$$

2.3. Vector Calculus in Spherical Geometries

Since we consider a ball-shaped conductor in the multiple-shell model, which is introduced in Chapter 3, we need polar coordinates as a local coordinate system. In this section, several properties and identities belonging to the spherical geometry are summed up. They and their Cartesian counterparts can be found in [88], for example.

Definition 2.11 ([81, Ch. 1.2]). *The polar coordinate representation of $\boldsymbol{x} \in \mathbb{R}^3$ is*

$$\boldsymbol{x}(r,\varphi,t) = \begin{pmatrix} r\sqrt{1-t^2}\cos\varphi \\ r\sqrt{1-t^2}\sin\varphi \\ rt \end{pmatrix},$$

where $r \in \mathbb{R}_0^+$ is the distance to the origin, $\varphi \in [0, 2\pi)$ is the longitude, and $t \in [-1,1]$ is the polar distance.

Note that the names 'longitude' and 'polar distance' have their origin in the geosciences. Since the mathematical formulation of the inverse magneto-electroencephalography problem is related to the inverse gravimetric problem, we stick to these names. The relation between these two particular problems is analyzed in more detail in Part IV.

Definition 2.12 ([81, Ch. 1.2]). *Three orthonormal vectors $\boldsymbol{\varepsilon}^r$, $\boldsymbol{\varepsilon}^\varphi$, and $\boldsymbol{\varepsilon}^t$ can be described in local coordinates by*

$$\boldsymbol{\varepsilon}^r(\varphi,t) \coloneqq \begin{pmatrix} \sqrt{1-t^2}\cos\varphi \\ \sqrt{1-t^2}\sin\varphi \\ t \end{pmatrix}, \quad \boldsymbol{\varepsilon}^\varphi(\varphi) \coloneqq \begin{pmatrix} -\sin\varphi \\ \cos\varphi \\ 0 \end{pmatrix}, \quad \boldsymbol{\varepsilon}^t(\varphi,t) \coloneqq \begin{pmatrix} -t\cos\varphi \\ -t\sin\varphi \\ \sqrt{1-t^2} \end{pmatrix}.$$

This representation immediately leads to the next corollary.

Corollary 2.13 ([158, p. 89ff.]). *Let $\boldsymbol{\varepsilon}^r$, $\boldsymbol{\varepsilon}^\varphi$, and $\boldsymbol{\varepsilon}^t$ be defined as in Definition 2.12. Then*

$$\begin{aligned}
\frac{\partial}{\partial\varphi}\boldsymbol{\varepsilon}^r(\varphi,t) &= \sqrt{1-t^2}\boldsymbol{\varepsilon}^\varphi(\varphi,t), & \frac{\partial}{\partial t}\boldsymbol{\varepsilon}^r(\varphi,t) &= \frac{1}{\sqrt{1-t^2}}\boldsymbol{\varepsilon}^t(\varphi,t),\\
\frac{\partial}{\partial\varphi}\boldsymbol{\varepsilon}^t(\varphi,t) &= -t\boldsymbol{\varepsilon}^\varphi(\varphi,t), & \frac{\partial}{\partial t}\boldsymbol{\varepsilon}^t(\varphi,t) &= -\frac{1}{\sqrt{1-t^2}}\boldsymbol{\varepsilon}^r(\varphi,t),\\
\frac{\partial}{\partial\varphi}\boldsymbol{\varepsilon}^\varphi(\varphi,t) &= t\boldsymbol{\varepsilon}^t(\varphi,t) - \sqrt{1-t^2}\boldsymbol{\varepsilon}^r(\varphi,t).
\end{aligned}$$

For the sake of comparability with established literature and for readability, we use the notation $\boldsymbol{x} = r\boldsymbol{\xi}$ with $r = |\boldsymbol{x}|$ and $\boldsymbol{\xi} \coloneqq \boldsymbol{\xi}(\varphi,t) = \boldsymbol{\varepsilon}^r(\varphi,t) \in \mathbb{S}$ in this section and beyond. Usually we neglect the arguments of these three vectors and keep their dependency of φ and t in mind. At every point $\boldsymbol{\xi} \in \mathbb{S}$, the vector $\boldsymbol{\xi}$ is the outer unit normal with respect to the sphere. The remaining two vectors span the tangential plane in this point on the unit sphere. This set of vectors allows a decomposition of vectors and vector-valued functions into their radial and angular parts.

For vector fields $\boldsymbol{f}\colon \mathbb{S} \to \mathbb{R}^3$, we define the corresponding projection operators as follows:

$$(\mathcal{P}_{\mathrm{nor}}\boldsymbol{f})(\boldsymbol{\xi}) \coloneqq (\boldsymbol{\xi}\cdot\boldsymbol{f}(\boldsymbol{\xi}))\boldsymbol{\xi}, \quad (\mathcal{P}_{\tan}\boldsymbol{f})(\boldsymbol{\xi}) \coloneqq \boldsymbol{f}(\boldsymbol{\xi}) - (\mathcal{P}_{\mathrm{nor}}\boldsymbol{f})(\boldsymbol{\xi}) \quad \text{for all } \boldsymbol{\xi} \in \mathbb{S}. \tag{2.3}$$

In addition, the classical vector analysis differential operators, such as the gradient or the Laplacian, can be decomposed into their radial and angular parts. The resulting angular derivative operators are often used within the analysis of functions over the sphere.

Theorem 2.14 ([81, Ch. 1.2]). *The classical three-dimensional gradient $\boldsymbol{\nabla}$ can be decomposed into*

$$\boldsymbol{\nabla}_{\boldsymbol{x}} = \boldsymbol{\varepsilon}^r\frac{\partial}{\partial r} + \frac{1}{r}\boldsymbol{\nabla}^*_{\boldsymbol{\xi}},$$

where

$$\boldsymbol{\nabla}^*_{\boldsymbol{\xi}} \coloneqq \boldsymbol{\varepsilon}^\varphi\frac{1}{\sqrt{1-t^2}}\frac{\partial}{\partial\varphi} + \boldsymbol{\varepsilon}^t\sqrt{1-t^2}\frac{\partial}{\partial t}$$

is called the surface gradient. *The* surface curl gradient $\boldsymbol{L}^*$ *is defined by*

$$\boldsymbol{L}^*_{\boldsymbol{\xi}}F(\boldsymbol{\xi}) \coloneqq \boldsymbol{\xi} \wedge \boldsymbol{\nabla}^*_{\boldsymbol{\xi}}F(\boldsymbol{\xi}) \qquad \text{for all } \boldsymbol{\xi} \in \mathbb{S}$$

and $F \in \mathrm{C}^1(\mathbb{S})$. *Or, in local coordinates,*

$$\boldsymbol{L}_{\boldsymbol{\xi}}^* = -\boldsymbol{\varepsilon}^{\varphi}\sqrt{1-t^2}\frac{\partial}{\partial t} + \boldsymbol{\varepsilon}^{t}\frac{1}{\sqrt{1-t^2}}\frac{\partial}{\partial \varphi}.$$

Finally, the Laplacian has the decomposition

$$\Delta_{\boldsymbol{x}} = \frac{\partial^2}{\partial r^2} + \frac{2}{r}\frac{\partial}{\partial r} + \frac{1}{r^2}\Delta_{\boldsymbol{\xi}}^*,$$

with the (Laplace-)Beltrami *operator*

$$\Delta_{\boldsymbol{\xi}}^* \coloneqq \frac{\partial}{\partial t}\left(1-t^2\right)\frac{\partial}{\partial t} + \frac{1}{1-t^2}\frac{\partial^2}{\partial \varphi^2}.$$

Obviously, $\boldsymbol{L}^*$ defined in the foregoing theorem is an operator. However, we do not stick to our convention and use a non-calligraphic letter for it as it is common in the literature. An immediate consequence for the surface gradient and surface curl operator, see also [88, Ch. 2.6] or [81, Ch. 1.2], is

$$\boldsymbol{\nabla}_{\boldsymbol{\xi}}^* \cdot \boldsymbol{\xi} = 2, \qquad \boldsymbol{L}_{\boldsymbol{\xi}}^* \cdot \boldsymbol{\xi} = 0, \qquad \boldsymbol{\xi} \in \mathbb{S}. \tag{2.4}$$

In addition, $\boldsymbol{\xi} \wedge (\boldsymbol{\xi} F(\boldsymbol{\xi})) = \mathbf{0}$ holds true for all $F \in \mathrm{C}(\mathbb{S})$ and all $\boldsymbol{\xi} \in \mathbb{S}$. The Cartesian counterpart $\boldsymbol{L}$, which is also denoted by a non-calligraphic letter for the same reason, to the surface curl gradient can be defined for all $F \in \mathrm{C}^1(\mathbb{R}^3)$ and all $\boldsymbol{x} \in \mathbb{R}^3$ by

$$\boldsymbol{L}_{\boldsymbol{x}} F(\boldsymbol{x}) \coloneqq \boldsymbol{x} \wedge \boldsymbol{\nabla}_{\boldsymbol{x}} F(\boldsymbol{x}).$$

With $\boldsymbol{x} = r\boldsymbol{\xi}$, we achieve that $\boldsymbol{L}$ coincides with the surface curl operator, that is

$$\boldsymbol{L}_{\boldsymbol{x}} F(\boldsymbol{x}) = r\boldsymbol{\xi} \wedge \left(\boldsymbol{\xi}\frac{\partial}{\partial r} + \frac{1}{r}\boldsymbol{\nabla}^*\right) F(r\boldsymbol{\xi}) = \boldsymbol{L}_{\boldsymbol{\xi}}^* F(r\boldsymbol{\xi}) \qquad \text{for all } F \in \mathrm{C}^1\Big(\mathbb{R}^3\Big). \tag{2.5}$$

This can also be shown by using the local coordinate representation, which results in an easy but lengthy calculation. We also need the following identities for some calculations.

Theorem 2.15 ([88, Eq. (2.151), Eq. (2.152)]). *Let* $F \in \mathrm{C}^1([-1,1])$ *and* $\boldsymbol{\xi}$, $\boldsymbol{\eta} \in \mathbb{S}$. *Then*

$$\begin{aligned}
\boldsymbol{\nabla}_{\boldsymbol{\xi}}^* F(\boldsymbol{\xi} \cdot \boldsymbol{\eta}) &= F'(\boldsymbol{\xi} \cdot \boldsymbol{\eta})\left(\boldsymbol{\eta} - (\boldsymbol{\xi} \cdot \boldsymbol{\eta})\boldsymbol{\xi}\right), \\
\boldsymbol{L}_{\boldsymbol{\xi}}^* F(\boldsymbol{\xi} \cdot \boldsymbol{\eta}) &= F'(\boldsymbol{\xi} \cdot \boldsymbol{\eta})\left(\boldsymbol{\xi} \wedge \boldsymbol{\eta}\right) = -\boldsymbol{L}_{\boldsymbol{\eta}}^* F(\boldsymbol{\xi} \cdot \boldsymbol{\eta}).
\end{aligned}$$

Certain orthogonality results concerning the spherical differential operators are frequently used within this thesis. For all $F \in \mathrm{C}^1(\mathbb{S})$ and all $\boldsymbol{\xi} \in \mathbb{S}$ we get

$$\boldsymbol{\xi} \cdot \left(\boldsymbol{\nabla}_{\boldsymbol{\xi}}^* F(\boldsymbol{\xi})\right) = 0, \qquad \boldsymbol{\xi} \cdot \left(\boldsymbol{L}_{\boldsymbol{\xi}}^* F(\boldsymbol{\xi})\right) = 0, \tag{2.6a}$$

see [88, Eq. (5.28)-(5.29)], and for all $F \in \mathrm{C}^2(\mathbb{S})$ the following useful identities hold true:

$$\boldsymbol{L}_{\boldsymbol{\xi}}^* \cdot \left(\boldsymbol{\nabla}_{\boldsymbol{\xi}}^* F(\boldsymbol{\xi})\right) = 0, \qquad \boldsymbol{\nabla}_{\boldsymbol{\xi}}^* \cdot \left(\boldsymbol{L}_{\boldsymbol{\xi}}^* F(\boldsymbol{\xi})\right) = 0, \tag{2.6b}$$

see [88, Eq. (2.142)-(2.143)]. As a consequence of the local coordinate expressions from Theorem 2.14 and the identities in Corollary 2.13, we obtain

$$\boldsymbol{\nabla}_{\boldsymbol{\xi}}^* \wedge \boldsymbol{\xi} = \mathbf{0} \qquad \text{for all } \boldsymbol{\xi} \in \mathbb{S}. \tag{2.7}$$

Furthermore, for all $\boldsymbol{f} \in \mathbf{C}^1(\mathbb{S})$ and $F \in \mathrm{C}^1(\mathbb{S})$ the following product rule holds true

$$\boldsymbol{\nabla}_{\boldsymbol{\xi}}^* \cdot (\boldsymbol{f}(\boldsymbol{\xi})F(\boldsymbol{\xi})) = F(\boldsymbol{\xi}) \left(\boldsymbol{\nabla}_{\boldsymbol{\xi}}^* \cdot \boldsymbol{f}(\boldsymbol{\xi})\right) + \boldsymbol{f}(\boldsymbol{\xi}) \cdot \boldsymbol{\nabla}_{\boldsymbol{\xi}}^* F(\boldsymbol{\xi}), \tag{2.8}$$

see [88, Eq. (2.145)]. The relation between the surface gradient and the Beltrami operator on the sphere is described in the next theorem.

Theorem 2.16 ([81, Eq. (1.2.47)]). *The spherical differentiation operators satisfy*

$$\boldsymbol{\nabla}^* \cdot \boldsymbol{\nabla}^* = \boldsymbol{L}^* \cdot \boldsymbol{L}^* = \Delta^*.$$

For certain calculations, we need relations among the introduced spherical operators with respect to the curl operator. They are stated in the following lemmas.

Lemma 2.17. *Let $F \in \mathrm{C}^2(\mathbb{S})$, then it holds true that*

$$\boldsymbol{\nabla}_{\boldsymbol{\xi}}^* \wedge \boldsymbol{\nabla}_{\boldsymbol{\xi}}^* F(\boldsymbol{\xi}) = \boldsymbol{L}_{\boldsymbol{\xi}}^* F(\boldsymbol{\xi}) \qquad \textit{for all } \boldsymbol{\xi} \in \mathbb{S}.$$

Proof. Let $F \in \mathrm{C}^2(\mathbb{S})$ be given. We define a function $G \in \mathrm{C}^2(\mathbb{R}^3 \setminus \{\mathbf{0}\})$ by $G(\boldsymbol{x}) \coloneqq F(\boldsymbol{\xi})$ for all $\boldsymbol{x} = r\boldsymbol{\xi} \in \mathbb{R}^3 \setminus \{\mathbf{0}\}$. According to [79, Eq. (1.88)], the identity

$$\mathbf{0} = \boldsymbol{\nabla}_{\boldsymbol{x}} \wedge (\boldsymbol{\nabla}_{\boldsymbol{x}} G(\boldsymbol{x}))$$

holds true for all $\boldsymbol{x} \in \mathbb{R}^3$. Since G has no radial dependency, we get with Theorem 2.14 the relation

$$\begin{aligned} \mathbf{0} = \boldsymbol{\nabla}_{\boldsymbol{x}} \wedge (\boldsymbol{\nabla}_{\boldsymbol{x}} F(\boldsymbol{\xi})) &= \left(\boldsymbol{\varepsilon}^r \frac{\partial}{\partial r} + \frac{1}{r}\boldsymbol{\nabla}_{\boldsymbol{\xi}}^*\right) \wedge \left(\frac{1}{r}\boldsymbol{\nabla}_{\boldsymbol{\xi}}^*\right) F(\boldsymbol{\xi}) \\ &= -\frac{1}{r^2}\boldsymbol{L}_{\boldsymbol{\xi}}^* F(\boldsymbol{\xi}) + \frac{1}{r^2}\boldsymbol{\nabla}_{\boldsymbol{\xi}}^* \wedge \boldsymbol{\nabla}_{\boldsymbol{\xi}}^* F(\boldsymbol{\xi}). \end{aligned}$$

Multiplication by r^2 yields the desired result. □

Lemma 2.18. *Let $F \in \mathrm{C}^1(\mathbb{S})$, then the next identity holds true:*

$$\boldsymbol{\nabla}_{\boldsymbol{\xi}}^* \wedge (\boldsymbol{\xi} F(\boldsymbol{\xi})) = -\boldsymbol{\xi} \wedge \boldsymbol{\nabla}_{\boldsymbol{\xi}}^* F(\boldsymbol{\xi}) + F(\boldsymbol{\xi})\boldsymbol{\nabla}_{\boldsymbol{\xi}}^* \wedge \boldsymbol{\xi} = -\boldsymbol{L}_{\boldsymbol{\xi}}^* F(\boldsymbol{\xi}), \qquad \boldsymbol{\xi} \in \mathbb{S}.$$

Proof. From [79, Eq. (2.41)], the product rule

$$\boldsymbol{\nabla}^* \wedge (F\boldsymbol{f}) = (\boldsymbol{\nabla}^* F) \wedge \boldsymbol{f} + F(\boldsymbol{\nabla}^* \wedge \boldsymbol{f})$$

is known for all $F \in \mathrm{C}^1(\mathbb{S})$ and $\boldsymbol{f} \in \mathbf{C}^1(\mathbb{S})$. We use this in the first step of the stated equation and Eq. (2.7) in the second step. □

Lemma 2.19. *Let $F \in \mathrm{C}^2(\mathbb{R}^3)$, then with $\boldsymbol{x} = r\boldsymbol{\xi}$, where $\boldsymbol{\xi} \in \mathbb{S}$, we have*

$$\boldsymbol{\nabla}_{\boldsymbol{x}} \wedge \boldsymbol{L}_{\boldsymbol{x}} F(\boldsymbol{x}) = \frac{1}{r}\boldsymbol{\xi}\Delta_{\boldsymbol{\xi}}^* F(\boldsymbol{x}) - \boldsymbol{\nabla}_{\boldsymbol{\xi}}^* \left(\frac{1}{r} + \frac{\partial}{\partial r}\right) F(\boldsymbol{x}).$$

Proof. From [79, Eqs. (2.193),(2.195)], we have for all sufficiently often differentiable functions F and all $\boldsymbol{\xi} \in \mathbb{S}$ the relations

$$\begin{aligned}\boldsymbol{\xi} \wedge (\boldsymbol{\nabla}^*_{\boldsymbol{\xi}} \wedge \boldsymbol{\xi} F(\boldsymbol{\xi})) &= \boldsymbol{\nabla}^*_{\boldsymbol{\xi}} F(\boldsymbol{\xi}),\\ \boldsymbol{\nabla}^*_{\boldsymbol{\xi}} \wedge (\boldsymbol{\nabla}^*_{\boldsymbol{\xi}} \wedge \boldsymbol{\xi} F(\boldsymbol{\xi})) &= -\boldsymbol{\xi} \Delta^*_{\boldsymbol{\xi}} F(\boldsymbol{\xi}) + \boldsymbol{\nabla}^*_{\boldsymbol{\xi}} F(\boldsymbol{\xi}).\end{aligned}$$

With the representation of the surface gradient in spherical coordinates, see Theorem 2.14, Eq. (2.5), Lemma 2.18, and the previous two relations, we get

$$\begin{aligned}\boldsymbol{\nabla}_{\boldsymbol{x}} \wedge \boldsymbol{L}_{\boldsymbol{x}} F(\boldsymbol{x}) &= -\left(\boldsymbol{\xi} \frac{\partial}{\partial r} + \frac{1}{r} \boldsymbol{\nabla}^*_{\boldsymbol{\xi}}\right) \wedge \left(\boldsymbol{\nabla}^*_{\boldsymbol{\xi}} \wedge (\boldsymbol{\xi} F(\boldsymbol{x}))\right)\\ &= \frac{1}{r} \boldsymbol{\xi} \Delta^*_{\boldsymbol{\xi}} F(\boldsymbol{x}) - \boldsymbol{\nabla}^*_{\boldsymbol{\xi}} \left(\frac{1}{r} + \frac{\partial}{\partial r}\right) F(\boldsymbol{x}).\end{aligned}$$

□

Green's identities are a well-known and powerful tool. In our setting, of course, the surface versions, more precisely the versions on the sphere, are more useful than the classical versions.

Theorem 2.20 (Green's Surface Identities). *Let $\mathbb{D} \subseteq \mathbb{S}$ be a subset of the unit sphere with sufficiently smooth boundary $\partial\mathbb{D}$ and corresponding outer unit normal field $\boldsymbol{n}$. Furthermore, let F, $G \in \mathrm{C}^2(\overline{\mathbb{D}})$ be twice continuously differentiable functions. Then the following identities are valid:*

i) Green's first surface identity, see [88, Eq. (2.156)],

$$\int_{\mathbb{D}} \boldsymbol{\nabla}^*_{\boldsymbol{\xi}} F(\boldsymbol{\xi}) \cdot \boldsymbol{\nabla}^*_{\boldsymbol{\xi}} G(\boldsymbol{\xi}) \,\mathrm{d}\omega(\boldsymbol{\xi}) + \int_{\mathbb{D}} F(\boldsymbol{\xi}) \Delta^*_{\boldsymbol{\xi}} G(\boldsymbol{\xi}) \,\mathrm{d}\omega(\boldsymbol{\xi}) = \int_{\partial\mathbb{D}} F(\boldsymbol{\xi}) \frac{\partial}{\partial \boldsymbol{n}} G(\boldsymbol{\xi}) \,\mathrm{d}\sigma(\boldsymbol{\xi})$$

and

ii) Green's second surface identity, see [88, Eq. (2.158)],

$$\begin{aligned}&\int_{\mathbb{D}} \left(F(\boldsymbol{\xi}) \Delta^*_{\boldsymbol{\xi}} G(\boldsymbol{\xi}) - G(\boldsymbol{\xi}) \Delta^*_{\boldsymbol{\xi}} F(\boldsymbol{\xi})\right) \,\mathrm{d}\omega(\boldsymbol{\xi})\\ =&\int_{\partial\mathbb{D}} \left(F(\boldsymbol{\xi}) \frac{\partial}{\partial \boldsymbol{n}} G(\boldsymbol{\xi}) - G(\boldsymbol{\xi}) \frac{\partial}{\partial \boldsymbol{n}} F(\boldsymbol{\xi})\right) \,\mathrm{d}\sigma(\boldsymbol{\xi}),\end{aligned}$$

where $\mathrm{d}\omega$ *and* $\mathrm{d}\sigma$ *are the surface and the line measure, respectively.*

In particular, for the full sphere $\mathbb{S}$, which has no boundary, we obtain certain other integral identities, see [88, Eq. (2.159)-(2.164)]. Let $\boldsymbol{f} \in \mathbf{C}^1(\mathbb{S})$, $F \in \mathrm{C}^1(\mathbb{S})$, and $G \in \mathrm{C}^2(\mathbb{S})$ be given, then

$$\int_{\mathbb{S}} \boldsymbol{f}(\boldsymbol{\xi}) \cdot \boldsymbol{\nabla}^*_{\boldsymbol{\xi}} F(\boldsymbol{\xi}) \,\mathrm{d}\omega(\boldsymbol{\xi}) = -\int_{\mathbb{S}} F(\boldsymbol{\xi}) \boldsymbol{\nabla}^*_{\boldsymbol{\xi}} \cdot \boldsymbol{f}(\boldsymbol{\xi}) \,\mathrm{d}\omega(\boldsymbol{\xi}), \tag{2.9a}$$

$$\int_{\mathbb{S}} \boldsymbol{f}(\boldsymbol{\xi}) \cdot \boldsymbol{L}^*_{\boldsymbol{\xi}} F(\boldsymbol{\xi}) \,\mathrm{d}\omega(\boldsymbol{\xi}) = -\int_{\mathbb{S}} F(\boldsymbol{\xi}) \boldsymbol{L}^*_{\boldsymbol{\xi}} \cdot \boldsymbol{f}(\boldsymbol{\xi}) \,\mathrm{d}\omega(\boldsymbol{\xi}), \tag{2.9b}$$

$$\begin{aligned}\int_{\mathbb{S}} \boldsymbol{\nabla}^*_{\boldsymbol{\xi}} G(\boldsymbol{\xi}) \cdot \boldsymbol{\nabla}^*_{\boldsymbol{\xi}} F(\boldsymbol{\xi}) \,\mathrm{d}\omega(\boldsymbol{\xi}) &= -\int_{\mathbb{S}} F(\boldsymbol{\xi}) \Delta^*_{\boldsymbol{\xi}} G(\boldsymbol{\xi}) \,\mathrm{d}\omega(\boldsymbol{\xi}) &\text{(2.9c)}\\ &= \int_{\mathbb{S}} \boldsymbol{L}^*_{\boldsymbol{\xi}} G(\boldsymbol{\xi}) \cdot \boldsymbol{L}^*_{\boldsymbol{\xi}} F(\boldsymbol{\xi}) \,\mathrm{d}\omega(\boldsymbol{\xi}). &\text{(2.9d)}\end{aligned}$$

A particular case of the previous integral equations is given by

$$\int_{\mathbb{S}} \boldsymbol{\nabla}_{\boldsymbol{\xi}}^{*} \cdot \boldsymbol{f}(\boldsymbol{\xi}) \, \mathrm{d}\omega(\boldsymbol{\xi}) = \int_{\mathbb{S}} \boldsymbol{L}_{\boldsymbol{\xi}}^{*} \cdot \boldsymbol{f}(\boldsymbol{\xi}) \, \mathrm{d}\omega(\boldsymbol{\xi}) = 0. \tag{2.10}$$

Besides the stated $\mathbb{R}^3$-orthogonality relations, the spherical differentiation operators also provide us with further orthogonality results with respect to the $\mathbf{L}_2(\mathbb{S})$-inner product.

Corollary 2.21. *Let $F \in \mathrm{C}^1(\mathbb{S})$ and $G \in \mathrm{C}^2(\mathbb{S})$, then*

$$\int_{\mathbb{S}} \left(\boldsymbol{\nabla}_{\boldsymbol{\xi}}^{*} F(\boldsymbol{\xi}) \right) \cdot \left(\boldsymbol{L}_{\boldsymbol{\xi}}^{*} G(\boldsymbol{\xi}) \right) \, \mathrm{d}\omega(\boldsymbol{\xi}) = 0, \qquad \int_{\mathbb{S}} \left(\boldsymbol{L}_{\boldsymbol{\xi}}^{*} F(\boldsymbol{\xi}) \right) \cdot \left(\boldsymbol{\nabla}_{\boldsymbol{\xi}}^{*} G(\boldsymbol{\xi}) \right) \, \mathrm{d}\omega(\boldsymbol{\xi}) = 0.$$

Proof. Inserting $\boldsymbol{f} = \boldsymbol{L}^{*} G$ or $\boldsymbol{f} = \boldsymbol{\nabla}^{*} G$, respectively, into Eq. (2.9) and using Eq. (2.6a), we obtain the desired result. □

2.4. Scalar Spherical Harmonics

Scalar spherical harmonics form the foundation for the analysis of the magneto-electroencephalography problem in the context of a ball-shaped conductor. They are used in many applications, such as in the geosciences or for other medical imaging problems. In addition, we also need the related inner and outer harmonics, which are introduced briefly. For more information on these special functions see, for example, [81, 84, 88, 158, 173, 184].

2.4.1. Definition of Spherical Harmonics

In this section, we define the scalar spherical harmonics and state their basic properties. Some of these properties are going back to the Addition Theorem for spherical harmonics, which is also stated in this section.

Definition 2.22 (Spherical Harmonics [88, Def. 3.22]). *The set of all homogeneous (i.e. $H_n(\alpha \boldsymbol{x}) = \alpha^n H_n(\boldsymbol{x})$) harmonic polynomials H_n of degree $n \in \mathbb{N}_0$ is denoted by* $\mathrm{Harm}_n(\mathbb{R}^3)$. *For the set $\mathbb{G} \subset \mathbb{R}^3$, we define*

$$\mathrm{Harm}_n(\mathbb{G}) \coloneqq \left\{ H_n|_{\mathbb{G}} \;\middle|\; H_n \in \mathrm{Harm}_n(\mathbb{R}^3) \right\}, \qquad n \in \mathbb{N}_0.$$

The restriction $Y_n = H_n|_{\mathbb{S}}$ onto the unit sphere is called a (scalar) spherical harmonic *of degree n and is contained in* $\mathrm{Harm}_n(\mathbb{S})$.

Lemma 2.23 ([81, Lem. 3.1.2]). *All spherical harmonics $Y_n \in \mathrm{Harm}_n(\mathbb{S})$, where $n \in \mathbb{N}_0$, are infinitely often differentiable eigenfunctions of the Beltrami operator Δ^{*} to the eigenvalues $-n(n+1) =: (\Delta^{*})^{\wedge}(n)$, that is*

$$\Delta_{\boldsymbol{\xi}}^{*} Y_n(\boldsymbol{\xi}) = (\Delta^{*})^{\wedge}(n) Y_n(\boldsymbol{\xi}), \qquad \boldsymbol{\xi} \in \mathbb{S}.$$

The sequence $\{(\Delta^{*})^{\wedge}(n)\}_{n \in \mathbb{N}_0}$ is called the spherical symbol of the Beltrami operator.

Note that $\mathrm{Harm}_n(\mathbb{S}) \perp \mathrm{Harm}_m(\mathbb{S})$ whenever $n \neq m$, see [88, Thm. 3.15]. Since for all $n \in \mathbb{N}_0$ the dimension of this space is given by $\dim \mathrm{Harm}_n(\mathbb{S}) = 2n + 1$, see [88, Thm. 3.5], the following definition makes sense.

Definition 2.24 ([88, Rem. 3.25]). *For every fixed $n \in \mathbb{N}_0$ the set $\{Y_{n,j}\}_{j=1,\dots,2n+1}$ always denotes an $\mathrm{L}_2(\mathbb{S})$-orthonormal set in $\mathrm{Harm}_n(\mathbb{S})$, where n is called the* degree *and j is the* order *of $Y_{n,j}$.*

As we have already mentioned, the (scalar) spherical harmonics are closely related to the Legendre polynomials. The important and famous Addition Theorem for spherical harmonics provides a link to these polynomials.

Theorem 2.25 (Addition Theorem, [81, p. 3.1.3]). *If $\{Y_{n,j}\}_{j=1,\dots,2n+1}$ is an $\mathrm{L}_2(\mathbb{S})$-orthonormal set in $\mathrm{Harm}_n(\mathbb{S})$, where $n \in \mathbb{N}_0$, then*

$$\sum_{j=1}^{2n+1} Y_{n,j}(\boldsymbol{\xi}) Y_{n,j}(\boldsymbol{\eta}) = \frac{2n+1}{4\pi} P_n(\boldsymbol{\xi} \cdot \boldsymbol{\eta})$$

holds true for all $\boldsymbol{\xi}, \boldsymbol{\eta} \in \mathbb{S}$, where P_n is the Legendre polynomial of degree n, see Definition 2.5.

Via the Addition Theorem, we can derive several useful properties of the spherical harmonics. For example, an immediate consequence of the Addition Theorem is a closed representation for the spherical harmonics of degree zero, that is

$$\left(Y_{0,1}(\boldsymbol{\xi})\right)^2 = \sum_{j=1}^{1} Y_{0,1}(\boldsymbol{\xi}) Y_{0,1}(\boldsymbol{\xi}) = \frac{1}{4\pi} P_0(1) = \frac{1}{4\pi}. \tag{2.11}$$

This result can, for instance, also be achieved via the normalization property of the spherical harmonics. In addition, the function on the right-hand side of the Addition Theorem has the reproducing property, see [88, Lem. 3.29]. For all n, $k \in \mathbb{N}_0$ and $j = 1, \dots, 2k+1$, the reproducing property is given by

$$\frac{2n+1}{4\pi} \int_{\mathbb{S}} P_n(\boldsymbol{\eta} \cdot \boldsymbol{\xi}) Y_{k,j}(\boldsymbol{\eta}) \, \mathrm{d}\omega(\boldsymbol{\eta}) = \delta_{n,k} Y_{n,j}(\boldsymbol{\xi}), \qquad \boldsymbol{\xi} \in \mathbb{S}. \tag{2.12}$$

This property can be easily proved by using Theorem 2.25 and the orthogonality of the spherical harmonics. By means of this theorem, we also get for all $Y_n \in \mathrm{Harm}_n(\mathbb{S})$ with $n \in \mathbb{N}_0$ the following useful estimate

$$\|Y_n\|_{\mathrm{C}(\mathbb{S})} \leq \sqrt{\frac{2n+1}{4\pi}} \, \|Y_n\|_{\mathrm{L}_2(\mathbb{S})}, \tag{2.13}$$

see [88, Lem. 3.31]. Combining the Addition Theorem with Lemma 2.23, we obtain an identity of the Legendre polynomials, that is

$$\Delta^*_{\boldsymbol{\xi}} P_n(\boldsymbol{\xi} \cdot \boldsymbol{\eta}) = -n(n+1) P_n(\boldsymbol{\xi} \cdot \boldsymbol{\eta}) \tag{2.14}$$

for all $n \in \mathbb{N}_0$ and $\boldsymbol{\xi}$, $\boldsymbol{\eta} \in \mathbb{S}$, see [88, Lem. 3.29].

Via the Abel-Poisson integral formula, see [88, 158], the next corollary can be proved. This central corollary is frequently used within this thesis and is essential for the analysis of the ill-posedness of the inverse magneto-electroencephalography problem.

Corollary 2.26 ([81, Cor. 3.4.3]). *The system $\{Y_{n,j}\}_{n\in\mathbb{N}_0, j=1,\dots,2n+1}$ from Definition 2.24 is closed and represents a complete orthonormal system in $\mathrm{L}_2(\mathbb{S})$, that is*

$$\mathrm{L}_2(\mathbb{S}) = \overline{\mathrm{span}\left\{Y_{n,j} \mid n \in \mathbb{N}_0, \; j = 1, \dots, 2n+1\right\}}^{\|\cdot\|_{\mathrm{L}_2(\mathbb{S})}}.$$

From functional analysis, it is well-known that the statement in Corollary 2.26 is equivalent to

$$\lim_{N\to\infty} \left\| F - \sum_{n=0}^{N} \sum_{j=1}^{2n+1} \langle F, Y_{n,j} \rangle_{\mathrm{L}_2(\mathbb{S})} Y_{n,j} \right\|_{\mathrm{L}_2(\mathbb{S})} = 0$$

for all $F \in \mathrm{L}_2(\mathbb{S})$. This convergence, which does not necessarily hold pointwise, is also meant by the notation

$$F(\boldsymbol{\xi}) \overset{\mathrm{L}_2(\mathbb{S})}{=} \sum_{n=0}^{\infty} \sum_{j=1}^{2n+1} \langle F, Y_{n,j} \rangle_{\mathrm{L}_2(\mathbb{S})} Y_{n,j}(\boldsymbol{\xi}),$$

or more shortly,

$$F = \sum_{n=0}^{\infty} \sum_{j=1}^{2n+1} \langle F, Y_{n,j} \rangle_{\mathrm{L}_2(\mathbb{S})} Y_{n,j}.$$

The series on the right-hand side is often called a *Fourier series*. Due to the completeness, Parseval's identities, see [142, Ch. 6], [198, Thm. 12.6], or [88, Thm. 3.54], hold true. In the particular case of functions in the space $\mathrm{L}_2(\mathbb{S})$, Parseval's identities are for all F, $G \in \mathrm{L}_2(\mathbb{S})$ given by

$$\|F\|_{\mathrm{L}_2(\mathbb{S})}^2 = \sum_{n=0}^{\infty} \sum_{j=1}^{2n+1} \langle F, Y_{n,j} \rangle_{\mathrm{L}_2(\mathbb{S})}^2, \tag{2.15a}$$

$$\langle F, G \rangle_{\mathrm{L}_2(\mathbb{S})} = \sum_{n=0}^{\infty} \sum_{j=1}^{2n+1} \langle F, Y_{n,j} \rangle_{\mathrm{L}_2(\mathbb{S})} \langle G, Y_{n,j} \rangle_{\mathrm{L}_2(\mathbb{S})}. \tag{2.15b}$$

Remark 2.27. *Due to the fact that* $\{Y_{n,j}\}_{n\in\mathbb{N}_0,\, j=1,\ldots,2n+1}$ *is an* $\mathrm{L}_2(\mathbb{S})$*-orthonormal basis, it is easy to verify that, consequently,* $\{R^{-1} Y_{n,j}(R^{-1}\cdot)\}_{n\in\mathbb{N}_0,\, j=1,\ldots,2n+1}$ *is an orthonormal basis for* $\mathrm{L}_2(\mathbb{S}_R)$.

2.4.2. Inner and Outer Harmonics

In Lemma 2.23, we saw that spherical harmonics are connected with the Beltrami operator. By means of spherical harmonics, two more systems of functions that are connected to the Laplacian can be defined, see also [91, 184]. For this purpose, let a function $F\colon \mathbb{B}_R \to \mathbb{R}$ be defined by the $\mathrm{L}_2(\mathbb{B}_R)$-convergent series

$$F(\boldsymbol{x}) \overset{\mathrm{L}_2(\mathbb{B}_R)}{=} \sum_{n=0}^{\infty} \sum_{j=1}^{2n+1} F_{n,j}(r) Y_{n,j}(\boldsymbol{\xi}). \tag{2.16}$$

For almost all $r \coloneqq |\boldsymbol{x}| \in [0, R]$, the radially-dependent spherical harmonics coefficients are given by

$$F_{n,j}(r) = \int_{\mathbb{S}} F(r\boldsymbol{\xi}) Y_{n,j}(\boldsymbol{\xi}) \,\mathrm{d}\omega(\xi), \qquad n \in \mathbb{N}_0,\ j = 1, \ldots, 2n+1.$$

Now, we assume that F is a harmonic function, that is F satisfies $\Delta F = 0$. Together with Lemma 2.23 (i.e. $\Delta^* Y_{n,j} = -n(n+1)Y_{n,j}$ for all $n \in \mathbb{N}_0$, $j = 1, \dots, 2n+1$), we obtain the ordinary differential equation for the radial part

$$\left(\frac{\partial^2}{\partial r^2} + \frac{2}{r}\frac{\partial}{\partial r} - \frac{1}{r^2} n(n+1) \right) F_{n,j}(r) = 0 \tag{2.17}$$

for all $n \in \mathbb{N}_0$, $j = 1, \dots, 2n+1$. The fundamental system yields for all $n \in \mathbb{N}_0$ the identity

$$F_{n,j}(r) = C_n r^{-(n+1)} + D_n r^n. \tag{2.18}$$

In the case of the inner problem, that is searching for a harmonic solution inside a medium $\mathbb{B}_R$, we require, at least, the continuity at the origin. Hence, in this particular case, we set $C_n = 0$ for all $n \in \mathbb{N}_0$. In contrast, in the case of the outer problem, one is interested in a harmonic solution outside of a medium (i.e. $\mathbb{B}_R^{\text{ext}}$) that is regular at infinity. Hence, we set $D_n = 0$ for all $n \in \mathbb{N}_0$ in this particular case.

Before we define the inner and outer harmonics, we introduce the term *regularity at infinity* in more detail. A function $F \colon \mathbb{R}^3 \to \mathbb{R}$ is called regular at infinity if $|F(\boldsymbol{x})| \in \mathcal{O}(x^{-1})$ and if $|\boldsymbol{\nabla}_{\boldsymbol{x}} F(\boldsymbol{x})| \in \mathcal{O}(x^{-2})$ as $x \to \infty$. See, for instance, [88, p. 442] for the definition of regularity at infinity.

Based on the preliminary consideration, we make the following definition.

Definition 2.28 (Inner and Outer Harmonics). *Let $\mathbb{B}_R$ be a closed ball with radius R and let $\boldsymbol{x} \in \mathbb{B}_R$. Then the* inner harmonics *with respect to the sphere $\mathbb{S}_R$ of degree $n \in \mathbb{N}_0$ and order $j = 1, \dots, 2n+1$, see [88, Eq. (10.32)], are defined by*

$$H_{n,j}^{\text{int}}(R; \boldsymbol{x}) \coloneqq \frac{1}{R} \left(\frac{x}{R} \right)^n Y_{n,j}(\hat{\boldsymbol{x}}).$$

The outer harmonics*, see [88, Eq. (10.36)], of degree n and order j are defined by*

$$H_{n,j}^{\text{ext}}(R; \boldsymbol{y}) \coloneqq \frac{1}{R} \left(\frac{R}{y} \right)^{n+1} Y_{n,j}(\hat{\boldsymbol{y}})$$

for all $\boldsymbol{y} \in \mathbb{R}^3 \setminus \{\boldsymbol{0}\}$.

Both sets of functions provides us with several properties.

Corollary 2.29 (Properties of Inner Harmonics, [88, p. 437]). *The following properties hold true:*

i) $H_{n,j}^{\text{int}}(R; \cdot)$ *is of class* $\mathrm{C}^\infty(\mathbb{R}^3)$,

ii) $H_{n,j}^{\text{int}}(R; \cdot)$ *is harmonic in* $\mathbb{R}^3$,

iii) $H_{n,j}^{\text{int}}(R; \cdot)|_{\mathbb{S}_R} = \frac{1}{R} Y_{n,j}$, *and*

iv) $\langle H_{n,j}^{\text{int}}(R; \cdot)|_{\mathbb{S}_R}, H_{m,k}^{\text{int}}(R; \cdot)|_{\mathbb{S}_R} \rangle_{\mathrm{L}_2(\mathbb{S}_R)} = \delta_{n,m} \delta_{j,k}$.

Corollary 2.30 (Properties of Outer Harmonics, [88, p. 438]). *The following properties hold true:*

i) $H_{n,j}^{\mathrm{ext}}(R;\cdot)$ *is of class* $\mathrm{C}^\infty(\mathbb{R}^3 \setminus \{\mathbf{0}\})$,

ii) $H_{n,j}^{\mathrm{ext}}(R;\cdot)$ *is harmonic in* $\mathbb{R}^3 \setminus \{\mathbf{0}\}$,

iii) $H_{n,j}^{\mathrm{ext}}(R;\cdot)$ *is regular at infinity,*

iv) $H_{n,j}^{\mathrm{ext}}(R;\cdot)|_{\mathbb{S}_R} = \frac{1}{R} Y_{n,j}$, *and*

v) $\langle H_{n,j}^{\mathrm{ext}}(R;\cdot)|_{\mathbb{S}_R}, H_{m,k}^{\mathrm{ext}}(R;\cdot)|_{\mathbb{S}_R} \rangle_{\mathrm{L}_2(\mathbb{S}_R)} = \delta_{n,m}\delta_{j,k}$.

The inner and outer harmonics are closely related to the interior and exterior Dirichlet Problem, respectively. For more information on the Dirichlet Problem, see [79, 88], for example.

Definition 2.31 (Exterior Dirichlet Problem (EDP), [88, p. 441ff.]). *Let* $\mathbb{G} \subset \mathbb{R}^d$ *be a region with sufficiently smooth boundary* $\partial\mathbb{G}$. *Suppose that* $F \in \mathrm{C}(\partial\mathbb{G})$ *is given. We are searching for a function* $U \colon \overline{\mathbb{R}^d \setminus \mathbb{G}} \to \mathbb{R}$ *satisfying the following conditions:*

i) U *is of class* $\mathrm{C}^2(\mathbb{R}^d \setminus \mathbb{G}) \cap \mathrm{C}(\overline{\mathbb{R}^d \setminus \mathbb{G}})$,

ii) U *satisfies Laplace's equation* $\Delta U = 0$ *in* $\mathbb{R}^d \setminus \mathbb{G}$,

iii) U *is regular at infinity, and*

iv) $U|_{\partial\mathbb{G}} = F$.

It is well known that the solution of the (EDP) is uniquely determined. The proof is based on the Maximum/Minimum Principle for harmonic functions and needs the regularity at infinity. Furthermore, the solution U can be represented by an outer harmonics expansion if $d = 3$ and $\mathbb{G} = \mathbb{B}_R$, see [88].

Lemma 2.32 ([88, Eq. (10.54)]). *Let* U *be the unique solution of the (EDP) for the region* $\mathbb{G} = \mathbb{B}_R$ *with* $U|_{\mathbb{S}_R} = F \in \mathrm{C}(\mathbb{S}_R)$. *Then it has the expansion*

$$U = \sum_{n=0}^{\infty} \sum_{j=1}^{2n+1} \left\langle F, H_{n,j}^{\mathrm{ext}}(R;\cdot)|_{\mathbb{S}_R} \right\rangle_{\mathrm{L}_2(\mathbb{S}_R)} H_{n,j}^{\mathrm{ext}}(R;\cdot).$$

In addition, the series converges absolutely and uniformly on each subset $\mathbb{E} \subset \mathbb{B}_R^{\mathrm{ext}}$ *with* $\operatorname{dist}(\mathbb{E}, \mathbb{S}_R) > 0$.

2.5. Theory of Distributions

In this section, we summarize central results from the theory of distributions. For a full overview of the topic and the proofs of the results see, for instance, [123, 131]. The aim of this survey is to present an approach to solve the distributional Poisson's equation by means of convolution with the fundamental solution of Laplace's equation. This equation occurs, for instance, in the derivation of an integral equation for the electroencephalography problem.

Since distributions are continuous linear mappings from a function space into the underlying field (i.e. the set of real numbers $\mathbb{R}$), like functionals, we denote them with capital calligraphic letters in order to stick to our notation.

We start with some basic definitions and notations in Definition 2.33.

Definition 2.33 (Distribution). *Let $\mathbb{G} \subset \mathbb{R}^d$, where $d \in \mathbb{N}$, be an arbitrary set.*

i) If $\mathbb{G}$ is open, the set of test functions $\mathcal{D}(\mathbb{G})$ *is defined by*

$$\mathcal{D}(\mathbb{G}) \coloneqq \{f \colon \mathbb{G} \to \mathbb{R} \mid f \in \mathrm{C}^\infty(\mathbb{G}),\ \operatorname{supp} f \subset \mathbb{G} \text{ is compact}\},$$

see [123, Def. 1.2.1]. In addition, a sequence $\{\psi_n\}_{n\in\mathbb{N}_0} \subset \mathcal{D}(\mathbb{G})$ converges to $\psi \in \mathcal{D}(\mathbb{G})$ if for all compact sets $\mathbb{M} \subset \mathbb{G}$ and all $k \in \mathbb{N}$ it holds true that

$$\lim_{n\to\infty} \sup_{\boldsymbol{x}\in\mathbb{M}} |\partial^{\boldsymbol{\alpha}}(\psi_n(\boldsymbol{x}) - \psi(\boldsymbol{x}))| = 0,$$

where $\boldsymbol{\alpha}$ is a multi-index of order k. For arbitrary subsets $\mathbb{G} \subset \mathbb{R}^d$, we define $\mathcal{D}(\mathbb{G})$ as the set of elements in $\mathcal{D}(\mathbb{R}^d)$ with support contained in $\mathbb{G}$, see [123, p. 14].

ii) A distribution $\mathcal{V} \colon \mathcal{D}(\mathbb{G}) \to \mathbb{R}$ *is a continuous linear mapping on $\mathcal{D}(\mathbb{G})$, that is $\mathcal{V}\psi_n \to \mathcal{V}\psi$ if $\psi_n \to \psi$ as $n \to \infty$. The set of all distributions is denoted by $\mathcal{D}'(\mathbb{G})$, see [123, Def. 2.2.1].*

iii) The space of all locally integrable functions *is called $\mathbf{L}_{1,\mathrm{loc}}(\mathbb{G}, \mathbb{R}^s)$, where $s \in \mathbb{N}$, and is defined by*

$$\mathbf{L}_{1,\mathrm{loc}}(\mathbb{G}, \mathbb{R}^s) \coloneqq \{f \colon \mathbb{G} \to \mathbb{R}^s \text{ measurable} \mid f|_{\mathbb{M}} \in \mathrm{L}_1(\mathbb{M}, \mathbb{R}^s)\ \ \forall \mathbb{M} \subset \mathbb{G} \text{ compact}\}.$$

iv) Let $g \in \mathrm{L}_{1,\mathrm{loc}}(\mathbb{G})$, then the distribution

$$\mathcal{V}_g\psi \coloneqq \int_{\mathbb{R}^d} g(\boldsymbol{x})\psi(\boldsymbol{x})\,\mathrm{d}\boldsymbol{x}$$

is called a regular distribution*, see [131, Def. 15.1].*

v) Let $\mathbb{G}_1$, $\mathbb{G}_2 \subset \mathbb{R}^d$ be open sets with $\mathbb{G}_2 \subset \mathbb{G}_1$. Let $\mathcal{V} \colon \mathcal{D}(\mathbb{G}_1) \to \mathbb{R}$ be a distribution, then the restriction $\mathcal{V}|_{\mathbb{G}_2} \colon \mathcal{D}(\mathbb{G}_2) \to \mathbb{R}$ of $\mathcal{V}$ is given by $\mathcal{V}|_{\mathbb{G}_2}\psi = \mathcal{V}\mathcal{E}\psi$ for all $\psi \in \mathcal{D}(\mathbb{G}_2)$, where $\mathcal{E} \colon \mathcal{D}(\mathbb{G}_2) \to \mathcal{D}(\mathbb{G}_1)$ extends a given smooth function compactly supported in $\mathbb{G}_2$ by zero to a smooth function compactly supported in $\mathbb{G}_1$, see [123, p. 41].

vi) The support *of a distribution $\mathcal{V}$, that is $\operatorname{supp}\mathcal{V}$, is the set of points in $\mathbb{G}$ having no open neighbourhood to which the restriction of $\mathcal{V}$ is zero, see [123, Def. 2.2.1].*

vii) The partial differentiation ∂_k of a distribution $\mathcal{V} \in \mathcal{D}'(\mathbb{G})$ is understood as

$$(\partial_k\mathcal{V})\,\psi = -\mathcal{V}\,(\partial_k\psi), \qquad k = 1, \ldots, d,$$

see [123, Def. 3.1.1]. According to [123, p. 55], the derivative of the distribution exists and is unique.

For the solution of Poisson's equation, we need some particular distributions that are stated in Example 2.34.

Example 2.34. *Let $\mathbb{G} \subset \mathbb{R}^d$, where $d \in \mathbb{N}$, be given.*

i) The Delta distribution, or Dirac distribution, is defined by

$$\delta_{\boldsymbol{a}} \colon \mathcal{D}(\mathbb{G}) \to \mathbb{R}, \qquad \psi \mapsto \psi(\boldsymbol{a}), \qquad \boldsymbol{a} \in \mathbb{G},$$

see [123, Exam. 3.1.2]. It has compact support.

ii) For a multi-index $\boldsymbol{k}$ of order $k \coloneqq |\boldsymbol{k}|$, let the linear partial differential operator be given by $\partial^{\boldsymbol{k}}$. According to [123, Eq. (3.1.1)'], we define the distribution $\partial^{\boldsymbol{k}}\mathcal{V}$ for an arbitrary distribution $\mathcal{V}$ by

$$\left(\partial^{\boldsymbol{k}}\mathcal{V}\right)\psi \coloneqq (-1)^k\, \mathcal{V}\left(\partial^{\boldsymbol{k}}\psi\right) \qquad \text{for all } \psi \in \mathcal{D}\left(\mathbb{G}\right).$$

iii) Let $\partial^{\boldsymbol{k}}$ be given as in the previous item and δ be the Delta distribution, see [123, Exam. 3.1.2], then

$$\left(\partial^{\boldsymbol{k}}\delta_{\boldsymbol{a}}\right)\psi = (-1)^k \left(\partial^{\boldsymbol{k}}\psi\right)(\boldsymbol{a}) \qquad \text{for all } \psi \in \mathcal{D}\left(\mathbb{G}\right).$$

For solving partial differential equations by means of distribution theory, we have to define the fundamental solution.

Definition 2.35 (Fundamental Solution, [123, Def. 3.3.1]). *A distribution $\mathcal{V}$ is called a* fundamental solution *of the differential operator $\mathcal{P} = \sum_{\boldsymbol{k}} \alpha_{\boldsymbol{k}} \partial^{\boldsymbol{k}}$ with constant coefficients $\alpha_{\boldsymbol{k}}$ and multi-index $\boldsymbol{k}$ if $\mathcal{P}\mathcal{V} = \delta_{\boldsymbol{0}}$.*

For the application considered in this thesis, the fundamental solution of the well-known three-dimensional Laplace's equation is required.

Lemma 2.36 ([123, Thm. 3.3.2]). *Consider Laplace's equation in three dimensions (i.e. $d = 3$). The fundamental solution of the differential equation is given by the regular distribution generated by*

$$g(\boldsymbol{x}) = \frac{1}{4\pi|\boldsymbol{x}|}, \qquad \boldsymbol{x} \in \mathbb{R}^3 \setminus \{\boldsymbol{0}\}.$$

In order to obtain a solution of Poisson's equation from knowledge of the fundamental solution of Laplace's equation, we need the tool of convolution. Therefore, we make the following definitions.

Definition 2.37 ([123, Def. 4.1.1]). *Let $\mathbb{G} \subset \mathbb{R}^d$, where $d \in \mathbb{N}$, be given. If $\mathcal{V} \in \mathcal{D}'(\mathbb{G})$ and $\psi \in \mathcal{D}(\mathbb{G})$, then the* convolution $\mathcal{V} * \psi \in \mathrm{C}^\infty(\mathbb{G})$ *is defined by*

$$(\mathcal{V} * \psi)(\boldsymbol{x}) = \mathcal{V}(\psi(\boldsymbol{x} - \cdot)).$$

Definition 2.38 ([123, Def. 4.2.2]). *Let $\mathbb{G} \subset \mathbb{R}^d$, where $d \in \mathbb{N}$, be given. Let $\mathcal{V}_1$, $\mathcal{V}_2 \in \mathcal{D}'(\mathbb{G})$ be two distributions, where at least one of them has compact support. The* convolution $\mathcal{V}_1 * \mathcal{V}_2$ *of two distributions is defined to be the unique distribution $\mathcal{V}$ such that*

$$\mathcal{V}_1 * (\mathcal{V}_2 * \psi) = \mathcal{V} * \psi \qquad \text{for all } \psi \in \mathcal{D}(\mathbb{G}).$$

Under certain conditions that are stated in the next lemma, the convolution is commutative.

Lemma 2.39 ([123, Thm. 4.2.4]). *Let $\mathbb{G} \subset \mathbb{R}^d$, where $d \in \mathbb{N}$, be given. Let $\mathcal{V}_1$, $\mathcal{V}_2 \in \mathcal{D}'(\mathbb{G})$ be two distributions, where at least one of them has compact support. Then the convolution is commutative, that is*

$$\mathcal{V}_1 * \mathcal{V}_2 = \mathcal{V}_2 * \mathcal{V}_1.$$

In addition, the differential operator $\mathcal{P}$ with constant coefficients can be applied to the convolution of distributions.

Lemma 2.40 ([131, Thm. 41.3]). *Let $\mathbb{G} \subset \mathbb{R}^d$, where $d \in \mathbb{N}$, be given, let $\mathcal{V}_1$, $\mathcal{V}_2 \in \mathcal{D}'(\mathbb{G})$ be two distributions, and let $\mathcal{P}$ be a differential operator with constant coefficients. Then*

$$\mathcal{P}\left(\mathcal{V}_1 * \mathcal{V}_2\right) = \left(\mathcal{P}\mathcal{V}_1\right) * \mathcal{V}_2 = \mathcal{V}_1 * \left(\mathcal{P}\mathcal{V}_2\right).$$

Besides convolution, the translation operator is often used in the context of distributions.

Definition 2.41. *Let $\mathbb{G} \subset \mathbb{R}^d$, where $d \in \mathbb{N}$, be given and let $\boldsymbol{h} \in \mathbb{R}^d$, $\psi \in \mathcal{D}(\mathbb{G})$, and $\mathcal{V} \in \mathcal{D}'(\mathbb{G})$.*

i) The translation operator *$\tau_{\boldsymbol{h}}$ for test functions is defined by $(\tau_{\boldsymbol{h}}\psi)(\boldsymbol{x}) \coloneqq \psi(\boldsymbol{x} - \boldsymbol{h})$, see [131, Ch. X.39].*

ii) The translation operator *$\tau_{\boldsymbol{h}}$ for distributions is defined by $(\tau_{\boldsymbol{h}}\mathcal{V})\psi \coloneqq \mathcal{V}(\tau_{-\boldsymbol{h}}\psi)$ for all $\psi \in \mathcal{D}(\mathbb{G})$, see [131, Ch. X.39].*

A connection between the convolution, the Delta distribution, and the translation operator is stated in the next lemma.

Lemma 2.42 ([131, Thm. 40.2]). *Let $\mathbb{G} \subset \mathbb{R}^d$, where $d \in \mathbb{N}$, be given and let $\boldsymbol{h} \in \mathbb{R}^d$. Then for $\mathcal{V} \in \mathcal{D}'(\mathbb{G})$, it holds true that*

$$\mathcal{V} * \delta = \mathcal{V}, \qquad \mathcal{V} * \delta_{\boldsymbol{h}} = \tau_{\boldsymbol{h}}\mathcal{V}.$$

Eventually, we are able to solve the distributional Poisson's equation.

Lemma 2.43 ([131, Thm. 53.1]). *For arbitrary distributions $\mathcal{V}_1$ with compact support, the particular solution of the distributional Poisson's equation $\Delta\mathcal{V}_2 = -\mathcal{V}_1$ is given by the convolution of the distribution $\mathcal{V}_1$ and the regular distribution $\mathcal{V}_g$ defined by the fundamental solution g of Laplace's equation, that is $\mathcal{V}_2 = \mathcal{V}_1 * \mathcal{V}_g$.*

Chapter 3.

Modelling the Magnetoencephalography Problem

Magneto- and electroencephalographs are used in medical diagnostics and in recent and former medical research, see [108, 113] and the references therein. However, their use and resolution is limited by the capabilities of the devices and the ill-posedness of the corresponding inverse problems. A mathematical investigation of these inverse problems provides a precise characterization of the maximal theoretically possible capabilities of these methods.

The aim of the (vectorial) inverse magnetoencephalography (MEG) problem is the reconstruction of the primary current $\boldsymbol{J}^{\mathrm{P}}$, that is the neuronal current inside the cerebrum, from measured data of the magnetic field $\boldsymbol{B}$ outside the head. The measurements at the sensors, often called SQUIDs (i.e. superconducting quantum interference device), of the magnetoencephalograph yield data related to the magnetic field $\boldsymbol{B}$. A short technical description of a typical magnetoencephalograph and further references can be found in [33, 172] and an extensive survey in [108]. SQUIDs are required for the measurement of the human brain's magnetic field, which is more than a hundred million times smaller than the Earth's magnetic field. Recent magnetoencephalographs can have about 300 sensors, which are grouped into gradiometers and magnetometers. The about 100 magnetometers measure the normal component of the magnetic field, that is $B_{\boldsymbol{\nu}} \coloneqq \boldsymbol{\nu} \cdot \boldsymbol{B}$. Sometimes, this physical quantity is called the magnetic flux density. The vector field $\boldsymbol{\nu}$ is orthogonal to the surfaces of the sensors but not to the direction of the magnetic field. A schematic diagram of the installation is given in Fig. 3.1. In contrast to the magnetometers, the gradiometers measure certain derivatives of the magnetic field. Most magnetoencephalographs provide us with two planar gradiometer measurements per sensor surface. They yield normal component measurements of certain derivatives of $\boldsymbol{B}$ in two directions tangential to the sensor surface. Formulae describing these quantities are derived in Section 9.2 based on the results from this section. In both cases, the magnetic field $\boldsymbol{B}$ is utilized. Thus, we start with an investigation of this physical quantity.

In order to reconstruct the primary current and solve this inverse problem, we need a mathematical relation between the magnetic field and the neuronal current. This relation is based on the quasi-static approximation of Maxwell's equations. The quasi-static approach is commonly used in medical electromagnetism and verified in the work of Plonsey, see [190]. In this context, the changes of the current and the electric and magnetic fields are assumed to be so slow such that they appear to be static. In [190, 191] the authors show that the errors made by the quasi-static approach, that is the omission of propagation, capacitative and inductive effects, and the boundary considerations, are clearly negligible.

A second argument for the quasi-static approach can be found in [108].

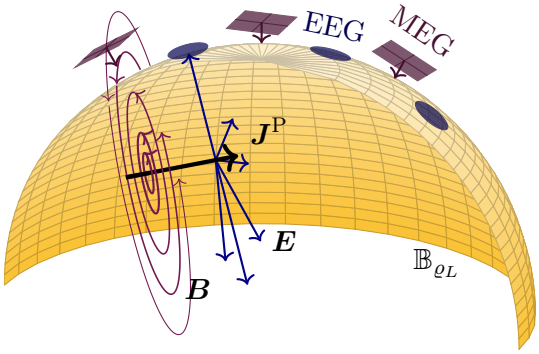

FIGURE 3.1: *The installation of the magneto-electroencephalograph. The scalp (modelled by the yellow surface) separates the space into the interior $\mathbb{B}_{\varrho_L}$ that models the head and the outer space. The neuronal current $\boldsymbol{J}^{\mathrm{P}}$ and its induced magnetic ($\boldsymbol{B}$, purple) and electric fields ($\boldsymbol{E}$, blue) are indicated. The electroencephalograph sensors (blue circles) are attached on the scalp. The magnetoencephalograph sensors (purple squares) are located in the exterior and their normal vectors $\boldsymbol{\nu}$ are suggested. Figure kindly provided by Samuel Leweke [145].*

Definition 3.1 (Quasi-static Maxwell's Equations). *In order to compute the magnetic field $\boldsymbol{B}$ caused by bio-electric sources, such as the primary current inside the brain, we use the* quasi-static approximation of Maxwell's equations*, see [190]:*

$$\boldsymbol{E} = -\boldsymbol{\nabla} u, \qquad \boldsymbol{\nabla} \cdot \boldsymbol{B} = 0, \qquad \boldsymbol{\nabla} \wedge \boldsymbol{B} = \mu_0 \boldsymbol{J}^{\mathrm{T}}.$$

Here, $\boldsymbol{E}$ is the electric field, u is the electric potential, $\boldsymbol{J}^{\mathrm{T}} = \boldsymbol{J}^{\mathrm{P}} + \sigma \boldsymbol{E}$ is the total current with the primary current $\boldsymbol{J}^{\mathrm{P}}$ and the Ohmic current $\sigma \boldsymbol{E}$, σ is the conductivity, and μ_0 is the constant permeability in vacuum. Moreover, the electric and magnetic potentials are regular at infinity.

Note that within this section, $\boldsymbol{J}^{\mathrm{T}}$ denotes the vector-valued total current and not the transposed of a vector $\boldsymbol{J}$.

The domain of all quantities occurring in the quasi-static Maxwell's equations is the space $\mathbb{R}^3$. However, the total current has its support inside the cerebrum. Thus, the magnetic field is irrotational in the exterior of the head, that is $\boldsymbol{\nabla} \wedge \boldsymbol{B} = \boldsymbol{0}$. Since the exterior of the head is a simply connected subset of $\mathbb{R}^3$, the magnetic field $\boldsymbol{B}$ is a conservative vector field. Hence, there exists a magnetic potential U such that

$$\boldsymbol{B} = \mu_0 \boldsymbol{\nabla} U \qquad \text{in } \mathbb{B}^{\mathrm{ext}}, \tag{3.1}$$

where $\mathbb{B}$ models the cerebrum. For the magneto-electroencephalography problem we distinguish between the homogeneous and the inhomogeneous case. In the homogeneous case, the observed medium, that is the head, has a positive constant conductivity $\sigma \in \mathbb{R}^+$. In contrast, the inhomogeneous case allows a spatial dependency of the conductivity of the medium.

In many other publications on this topic, see, for instance, [76, 110, 208], the Biot-Savart operator is used to describe the relation between the total current $\boldsymbol{J}^{\mathrm{T}}$ and the magnetic field as

$$\boldsymbol{B}(\boldsymbol{y}) = \frac{\mu_0}{4\pi} \int_{\mathbb{B}} \boldsymbol{J}^{\mathrm{T}}(\boldsymbol{x}) \wedge \frac{\boldsymbol{y} - \boldsymbol{x}}{|\boldsymbol{y} - \boldsymbol{x}|} \, \mathrm{d}\boldsymbol{x}, \qquad \boldsymbol{y} \in \mathbb{B}^{\mathrm{ext}}. \tag{3.2}$$

In the inverse MEG problem, we are interested in reconstructing only the primary current $\boldsymbol{J}^{\mathrm{P}}$ because it is affected by the sources in the brain tissue, see [108, 200]. Due to Maxwell's equations, the total current is the sum of the primary current and the secondary, or Ohmic,

current $\boldsymbol{J}^{\mathrm{T}} = \boldsymbol{J}^{\mathrm{P}} - \sigma\boldsymbol{\nabla}u$. It is proved in [200] that the total current in Eq. (3.2) reduces to the primary current in the case of an unbounded homogeneous medium, hence,

$$\boldsymbol{B}(\boldsymbol{y}) = \frac{\mu_0}{4\pi}\int_{\mathbb{B}} \boldsymbol{J}^{\mathrm{P}}(\boldsymbol{x}) \wedge \frac{\boldsymbol{y}-\boldsymbol{x}}{|\boldsymbol{y}-\boldsymbol{x}|}\,\mathrm{d}\boldsymbol{x}, \qquad \boldsymbol{y} \in \mathbb{B}^{\mathrm{ext}}.$$

Accordingly, in the case of an inhomogeneous medium, the inversion of the Bio-Savart operator yields a reconstruction of the total current. However, only a reconstruction of the primary current is desired. If the Biot-Savart operator is used in the inhomogeneous case misleadingly, one reconstructs parts of the primary and the secondary current, see [76].

Since different parts of the head, for example the cerebrum, the skull, and the scalp, have different conductivities and since the head is a bounded conductor, we want to use a different model. For our model, we need the following assumptions.

Assumption 3.2 (Multiple-shell Model). *We assume that*

- *the cerebrum $\mathbb{B}_{\varrho_0}$ is a closed ball with radius $\varrho_0 > 0$ and that around this ball there are L spherical shells $\mathbb{S}_{(\varrho_l,\varrho_{l+1}]}$ with $l = 0,\dots,L-1$ modelling the various head tissues, see Fig. 3.2. The radii are increasing, that is $\varrho_l < \varrho_{l+1}$ for $l = 0,\dots,L-1$, and the sphere with the largest radius ϱ_L models the head boundary;*

- *the conductivity σ is given as a piecewise constant function, that is*

$$\sigma(\boldsymbol{x}) \coloneqq \begin{cases} \sigma_0 & \text{if } \boldsymbol{x} \in \mathbb{B}_{\varrho_0}, \\ \sigma_l & \text{if } \boldsymbol{x} \in \mathbb{S}_{(\varrho_{l-1},\varrho_l]},\ l = 1,\dots,L, \\ \sigma_{L+1} = 0 & \text{if } \boldsymbol{x} \in \mathbb{B}^{\mathrm{ext}}_{\varrho_L}. \end{cases}$$

  This implies that the radial and tangential conductivity coincide in each shell. In addition, the conductivity inside the head is positive, that is $\sigma(\boldsymbol{x}) > 0$ for all $\boldsymbol{x} \in \mathbb{B}_{\varrho_L}$;

- *the neuronal current can be described as a continuous dipole distribution;*

- *the permeability is constant everywhere and equal to μ_0, which is the permeability of the vacuum, see [108];*

- *the neuronal current is only non-vanishing inside the cerebrum and $\boldsymbol{J}^{\mathrm{P}}$ is a function in $\mathbf{L}_2(\mathbb{B}_{\varrho_0})$.*

The conductivity of air is about $3\,\mathrm{fS\,m^{-1}}$ to $5\,\mathrm{fS\,m^{-1}}$ whereas the conductivity of the different tissues is about $0.01\,\mathrm{S\,m^{-1}}$ to $1\,\mathrm{S\,m^{-1}}$. Thus, the modelling error of assuming that the conductivity vanishes outside the head is acceptable.

The three-shell model is a common approach to approximate the brain structure, see [108, 125, 126, 171, 174] and the references therein. Note that also in current research the three-shell model is still considered to be sufficient, see [45, 71, 73, 74]. It can be obtained from the multiple-shell model by setting $L = 3$. The shells in the three-shell model are the fluid (cerebrospinal fluid (CSF)) $\mathbb{S}_{(\varrho_0,\varrho_1]}$, the bone (skull) $\mathbb{S}_{(\varrho_1,\varrho_2]}$, and the scalp $\mathbb{S}_{(\varrho_2,\varrho_3]}$. If $L = 0$, the head is modelled as one solid spherical conductor with constant conductivity.

In addition, there exist also multiple-shell models in the literature. For example, the scalp can be divided into a fat layer, the dermis, and the epidermis, or the skull can be split into three layers. Then the upper and lower layer are made out of bone, which is a bad

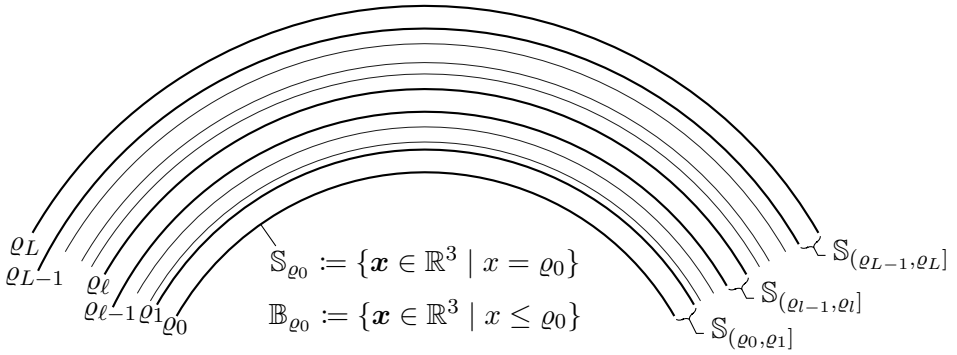

FIGURE 3.2: *The multiple-shell model of the head*

conductor, with a highly conductive middle layer in between, see [117]. However, in the case of spherical shells, their number and their conductivity does not affect the magnetic potential $\boldsymbol{B}$ in the exterior of the head at all. Note that also single-shell models exist, see [180]. Alternatively, elliptic-shell models can be used at least for the electroencephalography problem, see [46, 54, 56, 71, 95] and the references therein. In the case of a more anatomically correct conductor model, the magnetic field $\boldsymbol{B}$ can only be calculated numerically, see [108, 174, 182, 217].

We now concentrate our analysis on the multiple-shell model. With the assumptions of Assumption 3.2, the secondary current in the Biot-Savart law, see Eq. (3.2), does not vanish and we obtain Geselowitz' formula, see [94], given by

$$\begin{aligned}\boldsymbol{B}(\boldsymbol{y}) = \frac{\mu_0}{4\pi} \int_{\mathbb{B}_{\varrho_0}} \boldsymbol{J}^{\mathrm{P}}(\boldsymbol{x}) \wedge \frac{\boldsymbol{y}-\boldsymbol{x}}{|\boldsymbol{y}-\boldsymbol{x}|^3} \,\mathrm{d}\boldsymbol{x} \\ - \frac{\mu_0}{4\pi} \sum_{l=0}^{L} (\sigma_l - \sigma_{l+1}) \int_{\mathbb{S}_{\varrho_l}} u(\boldsymbol{x}) \boldsymbol{n}_{\varrho_l}(\boldsymbol{x}) \wedge \frac{\boldsymbol{y}-\boldsymbol{x}}{|\boldsymbol{y}-\boldsymbol{x}|^3} \,\mathrm{d}\omega(\hat{\boldsymbol{x}}), \qquad \boldsymbol{y} \in \overline{\mathbb{B}^{\mathrm{ext}}_{\varrho_L}},\end{aligned}$$

where $\boldsymbol{n}_{\varrho_l}$ is the unit normal vector of the surface $\mathbb{S}_{\varrho_l}$.

In order to analyze the ill-posedness of the MEG problem in detail, we are interested in a Fredholm integral equation of the first kind as a formulation of the inverse problem. For this purpose, we modify the derivation found in [73].

In [200], an approach for a ball-shaped conductor with piecewise constant conductivities on each shell is presented. This approach is used in [73] to eliminate the secondary current and a simple derivation of the magnetic and electric potentials and their relations to the neuronal current are given. In this ansatz, the operator that maps the neuronal current onto the magnetic field data is optimized for a certain decomposition (i.e. the Hodge decomposition, see Section 15.1) of the neuronal current and for a reconstruction of only a scalar-valued part of the current. In contrast, we now want to reconstruct the whole vector-valued current as a vector-valued quantity. This is why we present a slightly different derivation. The advantage of a vector-valued reconstruction is the possibility to apply certain physical principles to it, such as Hamilton's principle, Maupertuis' principle, or, more generally, the principle of stationary action; see [70] for details. In contrast, to the knowledge of the author, there is no indication that the principle of stationary action could be applied to scalar-valued parts of the current in order to obtain a unique reconstruction.

According to [42, 73, 200], the relation between the magnetic potential U^{d} generated by a single dipole with dipole moment $\boldsymbol{Q}(\boldsymbol{x})$ at the (fixed) point $\boldsymbol{x} \in \mathbb{B}_{\varrho_0}$ is given as

$$4\pi y \frac{\partial U^{\mathrm{d}}}{\partial y}(\boldsymbol{x}, \boldsymbol{y}) = -\left(\boldsymbol{Q}(\boldsymbol{x}) \wedge \boldsymbol{x}\right) \cdot \boldsymbol{\nabla}_{\boldsymbol{x}} \frac{1}{|\boldsymbol{y} - \boldsymbol{x}|}$$

with $\boldsymbol{y} \in \overline{\mathbb{B}_{\varrho_L}^{\mathrm{ext}}}$. Note that $\boldsymbol{y}$ denotes the measurement position of the magnetic potential or magnetic field, respectively. Using the Legendre expansion for $|\boldsymbol{x} - \boldsymbol{y}|^{-1}$ with $x < y$, see Eq. (2.2), and interchanging the series and the gradient, which is allowed due to [73], we get

$$4\pi y \frac{\partial U^{\mathrm{d}}}{\partial y}(\boldsymbol{x}, \boldsymbol{y}) = -\left(\boldsymbol{Q}(\boldsymbol{x}) \wedge \boldsymbol{x}\right) \cdot \sum_{k=0}^{\infty} \frac{1}{y^{k+1}} \boldsymbol{\nabla}_{\boldsymbol{x}} \left(x^k P_k(\hat{\boldsymbol{x}} \cdot \hat{\boldsymbol{y}})\right).$$

The zeroth summand equals zero because of the derivative. After dividing the equation by y, we can interchange the integration with respect to y and the series in the occurring right-hand side as shown in [73]. Finding the antiderivative with respect to y by taking into account that the magnetic potential vanishes as $y \to \infty$, we obtain

$$4\pi U^{\mathrm{d}}(\boldsymbol{x}, \boldsymbol{y}) = \left(\boldsymbol{Q}(\boldsymbol{x}) \wedge \boldsymbol{x}\right) \cdot \boldsymbol{\nabla}_{\boldsymbol{x}} \sum_{k=1}^{\infty} \frac{x^k}{y^{k+1}(k+1)} P_k(\hat{\boldsymbol{x}} \cdot \hat{\boldsymbol{y}}).$$

Note that the gradient and the series can be interchanged again, due to the same argumentation as before. Now, $\boldsymbol{J}^{\mathrm{P}}$ denotes the primary current, which is the continuous counterpart of the dipole moment $\boldsymbol{Q}$. The corresponding magnetic potential U can be obtained via the magnetic potential U^{d} of the single dipole, that is

$$U(\boldsymbol{y}) \coloneqq \int_{\mathbb{B}_{\varrho_0}} U^{\mathrm{d}}(\boldsymbol{x}, \boldsymbol{y}) \, \mathrm{d}\boldsymbol{x}, \qquad \boldsymbol{y} \in \overline{\mathbb{B}_{\varrho_L}^{\mathrm{ext}}}.$$

The integration of U^{d} with respect to the first argument over the cerebrum $\mathbb{B}_{\varrho_0}$ yields for all $\boldsymbol{y} \in \overline{\mathbb{B}_{\varrho_L}^{\mathrm{ext}}}$ the identity

$$U(\boldsymbol{y}) = \frac{1}{4\pi} \int_{\mathbb{B}_{\varrho_0}} \left(\boldsymbol{J}^{\mathrm{P}}(\boldsymbol{x}) \wedge \boldsymbol{x}\right) \cdot \boldsymbol{\nabla}_{\boldsymbol{x}} \sum_{k=1}^{\infty} \frac{x^k}{y^{k+1}(k+1)} P_k(\hat{\boldsymbol{x}} \cdot \hat{\boldsymbol{y}}) \, \mathrm{d}\boldsymbol{x}.$$

Up to this point, the derivation coincides with the one in [73]. Instead of using Gauß's Theorem, see [219], as it is done in [73], we use the circular shift of the triple product, that is $(\boldsymbol{x} \wedge \boldsymbol{y}) \cdot \boldsymbol{z} = \boldsymbol{x} \cdot (\boldsymbol{y} \wedge \boldsymbol{z})$ for all $\boldsymbol{x}$, $\boldsymbol{y}$, $\boldsymbol{z} \in \mathbb{R}^3$, see [141, Sec. 14]. Due to this novel approach, we do not need the additional assumption $\boldsymbol{J}^{\mathrm{P}}|_{\mathbb{S}_{\varrho_0}} \equiv 0$, which is used in [73]. Thus, we obtain the $\mathbf{L}_2(\mathbb{B}_{\varrho_0})$-inner product between the primary current $\boldsymbol{J}^{\mathrm{P}}$ and our desired integral kernel for all $\boldsymbol{y} \in \overline{\mathbb{B}_{\varrho_L}^{\mathrm{ext}}}$, that is

$$\begin{aligned} U(\boldsymbol{y}) &= \frac{1}{4\pi} \int_{\mathbb{B}_{\varrho_0}} \boldsymbol{J}^{\mathrm{P}}(\boldsymbol{x}) \cdot \left(\boldsymbol{x} \wedge \boldsymbol{\nabla}_{\boldsymbol{x}} \sum_{k=1}^{\infty} \frac{x^k}{y^{k+1}(k+1)} P_k(\hat{\boldsymbol{x}} \cdot \hat{\boldsymbol{y}})\right) \mathrm{d}\boldsymbol{x} \\ &= \frac{1}{4\pi} \int_{\mathbb{B}_{\varrho_0}} \boldsymbol{J}^{\mathrm{P}}(\boldsymbol{x}) \cdot \left(\boldsymbol{L}_{\boldsymbol{x}} \sum_{k=1}^{\infty} \frac{x^k}{y^{k+1}(k+1)} P_k(\hat{\boldsymbol{x}} \cdot \hat{\boldsymbol{y}})\right) \mathrm{d}\boldsymbol{x} \\ &= \frac{1}{4\pi} \int_{\mathbb{B}_{\varrho_0}} \boldsymbol{J}^{\mathrm{P}}(\boldsymbol{x}) \cdot \left(\boldsymbol{L}_{\hat{\boldsymbol{x}}}^* \sum_{k=1}^{\infty} \frac{x^k}{y^{k+1}(k+1)} P_k(\hat{\boldsymbol{x}} \cdot \hat{\boldsymbol{y}})\right) \mathrm{d}\boldsymbol{x}. \end{aligned} \tag{3.3}$$

Here, we used properties of the surface curl gradient $\boldsymbol{L}^*$ stated in Eq. (2.5) in the last step. For the sake of readability, we introduce for all $(\boldsymbol{x}, \boldsymbol{y}) \in \mathbb{B}_{\varrho_0} \times \overline{\mathbb{B}_{\varrho_L}^{\mathrm{ext}}}$ an abbreviation for the integral kernel, that is

$$\boldsymbol{k}_{\mathrm{M}}(\boldsymbol{x}, \boldsymbol{y}) \coloneqq \frac{1}{4\pi} \boldsymbol{L}_{\hat{\boldsymbol{x}}}^* \sum_{k=1}^{\infty} \frac{x^k}{y^{k+1}(k+1)} P_k(\hat{\boldsymbol{x}} \cdot \hat{\boldsymbol{y}}). \tag{3.4}$$

Eventually, the magnetic potential has the representation

$$U(\boldsymbol{y}) = \int_{\mathbb{B}_{\varrho_0}} \boldsymbol{J}^{\mathrm{P}}(\boldsymbol{x}) \cdot \boldsymbol{k}_{\mathrm{M}}(\boldsymbol{x}, \boldsymbol{y}) \, \mathrm{d}\boldsymbol{x}, \qquad \boldsymbol{y} \in \overline{\mathbb{B}_{\varrho_L}^{\mathrm{ext}}}.$$

Via Eq. (3.1), a relation between the neuronal current and the magnetic field can be found. An immediate consequence is the formal relation between the primary current and the magnetic flux density $B_{\boldsymbol{\nu}} \coloneqq \boldsymbol{\nu} \cdot \boldsymbol{B}$ in the direction of the normal vector field $\boldsymbol{\nu}$ given by

$$B_{\boldsymbol{\nu}}(\boldsymbol{y}) = \mu_0 \boldsymbol{\nu}(\boldsymbol{y}) \cdot \boldsymbol{\nabla}_{\boldsymbol{y}} \left(\int_{\mathbb{B}_{\varrho_0}} \boldsymbol{J}^{\mathrm{P}}(\boldsymbol{x}) \cdot \boldsymbol{k}_{\mathrm{M}}(\boldsymbol{x}, \boldsymbol{y}) \, \mathrm{d}\boldsymbol{x} \right), \qquad \boldsymbol{y} \in \overline{\mathbb{B}_{\varrho_L}^{\mathrm{ext}}}.$$

At this point, several questions arise: does the series representation of $\boldsymbol{k}_{\mathrm{M}}$ converge in an appropriate sense? If the series is convergent, does the equation in Eq. (3.3) make sense? Or more precisely, is the occurring integrand an $\mathrm{L}_1(\mathbb{B}_{\varrho_0})$-function? If the formula for the magnetic potential is well-defined, can we evaluate U at the measurement positions and can we apply the gradient onto U? Eventually, can the magnetic flux density be evaluated at the sensor positions?

Before we give answers to these questions, we derive an integral equation for the electroencephalography problem.

Chapter 4.

Modelling the Electroencephalography Problem

Similar to the inverse MEG problem, it is the aim of the inverse electroencephalography (EEG) problem to reconstruct the neuronal current inside the cerebrum. Besides the magnetic field, the neuronal current $\boldsymbol{J}^{\mathrm{P}}$ induces an electric potential u and its field $\boldsymbol{E}$, respectively. A schematic diagram of the installation is given in Fig. 3.1. The electric potential difference, or voltage difference, is measured via the sensors of the electroencephalograph, which is non-invasively attached on the head. For this purpose, a reference level for the potential by means of a reference electrode needs to be chosen in advance. For multi-channel recordings, it is common to substract the average as reference instead of a single reference, see [172] and the references therein. The sensor cap can generally contain about 70 sensors.

In the multiple-shell model, see Fig. 3.2, the sensors are non-invasively attached on the outer shell. In the three-shell model, this outer shell represents the scalp and could be split into more detailed (sub-)shells. It can, for example, be separated into a fat layer, the dermis, and the (outer) epidermis, see [117]. However, we name the outer shell $\mathbb{S}_{[\varrho_{L-1},\varrho_L]}$ the scalp, even if the scalp tissue is divided into detailed layers.

As proved in the next section, the number of shells, their radii, and conductivities play an important role in the derivation of the integral equation corresponding to the electric problem. This stands in contrast to the inverse MEG problem, where these quantities do not effect the magnetic potential at all under our model assumption stated in Assumption 3.2.

In analogy to the MEG problem, we start the derivation with the quasi-static version of Maxwell's equations. Recall the formulae from Definition 3.1:

$$\boldsymbol{E} = -\boldsymbol{\nabla} u, \qquad \boldsymbol{\nabla} \cdot \boldsymbol{B} = 0, \qquad \boldsymbol{\nabla} \wedge \boldsymbol{B} = \mu_0 \boldsymbol{J}^{\mathrm{T}},$$

where $\boldsymbol{E}$ is the electric field, $\boldsymbol{B}$ the magnetic field, u the electric potential, $\boldsymbol{J}^{\mathrm{T}} = \boldsymbol{J}^{\mathrm{P}} + \sigma \boldsymbol{E}$ the total current, $\boldsymbol{J}^{\mathrm{P}}$ the primary current, $\sigma \boldsymbol{E}$ the Ohmic current with the conductivity σ, and μ_0 is the constant permeability in vacuum. In the inverse EEG problem, we are interested in the reconstruction of the primary current $\boldsymbol{J}^{\mathrm{P}}$ from given measurements of the electric potential u on the scalp. Note that the total current vanishes outside the head. For the reconstruction, we transform the quasi-static version of Maxwell's equations to a vector-valued (Fredholm) integral equation of the first kind. In our setting, Assumption 3.2 is still required to hold true, except that we first assume a single dipole as the neuronal current for the derivation.

Since the divergence of the curl equals zero, see [141, Sec. 22], we obtain that the total current is divergence free in $\mathbb{R}^3$, that is

$$0 = \boldsymbol{\nabla} \cdot (\boldsymbol{\nabla} \wedge \boldsymbol{B}) = \boldsymbol{\nabla} \cdot \left(\mu_0 \boldsymbol{J}^{\mathrm{T}} \right).$$

Assuming that the conductivity is piecewise constant, see Assumption 3.2, and combining the formulae involving the electric field and potential, we obtain

$$0 = \boldsymbol{\nabla} \cdot \boldsymbol{J}^{\mathrm{T}} = \boldsymbol{\nabla} \cdot \boldsymbol{J}^{\mathrm{P}} + \sigma \boldsymbol{\nabla} \cdot \boldsymbol{E} = \boldsymbol{\nabla} \cdot \boldsymbol{J}^{\mathrm{P}} - \sigma \Delta u. \tag{4.1}$$

Under the assumption that $\operatorname{supp} \boldsymbol{J}^{\mathrm{P}} \subseteq \mathbb{B}_{\varrho_0}$, see Assumption 3.2, and in the case of a single dipole at the (fixed) position $\boldsymbol{x}$ with dipole moment $\boldsymbol{Q}$, the current can be modelled as a distribution. For the derivation of the EEG integral operator we, hence, need some basics of distribution theory, which are summarized in Section 2.5. Thus, we can model the current by

$$\boldsymbol{J}^{\mathrm{P}}(\psi) = \boldsymbol{Q}\delta_{\boldsymbol{x}}(\psi) \qquad \text{for all } \psi \in \mathcal{D}(\mathbb{B}_{\varrho_0}), \tag{4.2}$$

where δ is the Dirac distribution, see Example 2.34. The set of all test-functions $\mathcal{D}(\mathbb{B}_{\varrho_0})$ is defined in Definition 2.33. In addition, Eq. (4.2) is meant component-wise, since the dipole moment is a vector-valued quantity, that is $\boldsymbol{Q}\delta_{\boldsymbol{x}}(\psi) = \boldsymbol{Q}\psi(\boldsymbol{x})$ for all test-functions $\psi \in \mathcal{D}(\mathbb{B}_{\varrho_0})$. In this setting, we can define the divergence of the distribution by means of the scalar-valued differential operator $\mathcal{D} \coloneqq \boldsymbol{Q} \cdot \boldsymbol{\nabla} = \sum_{k=1}^{3} Q_k \partial_k$ with constant coefficients Q_k (i.e. kth component of the dipole moment $\boldsymbol{Q}$) and partial derivatives ∂_k in the kth direction for $k = 1, 2, 3$, that is

$$\boldsymbol{\nabla} \cdot (\boldsymbol{Q}\delta_{\boldsymbol{x}}(\psi)) \coloneqq \boldsymbol{Q} \cdot \boldsymbol{\nabla}\delta_{\boldsymbol{x}}(\psi) = \sum_{k=1}^{3} Q_k \partial_k \delta_{\boldsymbol{x}}(\psi) = \mathcal{D}\delta_{\boldsymbol{x}}(\psi).$$

We follow the approach in [95], where the electric potential u is split into the parts corresponding to the different regions in the three-shell model, and transfer it to the multiple-shell model, that is for fixed $\boldsymbol{x} \in \mathbb{B}_{\varrho_0}$ we set

$$u^{\mathrm{d}}(\boldsymbol{x}, \boldsymbol{y}) = \begin{cases} u_0^{\mathrm{d}}(\boldsymbol{x}, \boldsymbol{y}) & \text{if } \boldsymbol{y} \in \mathbb{B}_{\varrho_0}, \\ u_l^{\mathrm{d}}(\boldsymbol{x}, \boldsymbol{y}) & \text{if } \boldsymbol{y} \in \mathbb{S}_{(\varrho_{l-1}, \varrho_l]},\ l = 1, \dots, L, \\ u_{L+1}^{\mathrm{d}}(\boldsymbol{x}, \boldsymbol{y}) & \text{if } \boldsymbol{y} \in \mathbb{B}_{\varrho_L}^{\mathrm{ext}}. \end{cases} \tag{4.3}$$

The superscript d indicates the association of the electric potential to the single dipole distribution. Recall that L is the number of shells in the multiple-shell model, see Assumption 3.2. Therein, the conductivity σ of the tissues is assumed to be piecewise constant and equal to σ_j on the shell $\mathbb{S}_{(\varrho_{l-1}, \varrho_l]}$ for all $l = 1, \dots, L$ and σ_0 inside $\mathbb{B}_{\varrho_0}$. Thus, we obtain the following system due to the restrictions of the distributions over the particular spaces, see Definition 2.33. We denote the distributions belonging to the electric potential with $\mathcal{U}$ and further indices. This notation already suggests that the occurring distributions are regular distributions. They are given by

$$\mathcal{U}_{u_0^{\mathrm{d}}} \colon \mathcal{D}\left(\mathbb{B}_{\varrho_0}\right) \to \mathbb{R}, \qquad \sigma_0 \Delta \mathcal{U}_{u_0^{\mathrm{d}}} = \mathcal{D}\delta_{\boldsymbol{x}}, \tag{4.4a}$$

$$\mathcal{U}_{u_l^{\mathrm{d}}} \colon \mathcal{D}\left(\mathbb{S}_{(\varrho_{l-1}, \varrho_l]}\right) \to \mathbb{R}, \qquad \Delta \mathcal{U}_{u_l^{\mathrm{d}}} = 0, \tag{4.4b}$$

$$\mathcal{U}_{u_{L+1}^{\mathrm{d}}} \colon \mathcal{D}\left(\mathbb{B}_{\varrho_L}^{\mathrm{ext}}\right) \to \mathbb{R}, \qquad \Delta \mathcal{U}_{u_{L+1}^{\mathrm{d}}} = 0 \tag{4.4c}$$

with $l = 1, \dots, L$. Thus, we obtain L distributional Laplace equations from Eq. (4.4b), that is one for each shell.

In order to solve Poisson's equation stated in Eq. (4.4a), we use a classical result from the theory of distributions. We can apply Lemma 2.43 to Poisson's equation, that is $\Delta \mathcal{U}_{u_0^{\mathrm{d}}} = \sigma_0^{-1} \mathcal{D}\delta_{\boldsymbol{x}} =: \mathcal{V}$, since the distributions $\mathcal{U}_{u_0^{\mathrm{d}}}$ and $\mathcal{V}$ have compact supports. Hence, the particular solution of the distributional Poisson's equation is given by $\mathcal{U}_{u_0^{\mathrm{d}}} = -\mathcal{V} * \mathcal{V}_g$. Here, $\mathcal{V}_g$ is the regular distribution fulfilling $\Delta \mathcal{V}_g = \delta_{\mathbf{0}}$. In our setting, the representation

$g = (4\pi|\cdot|)^{-1}$ for the fundamental solution g of Laplace's equation is well-known, see also Lemma 2.36. A closer representation of the distribution $\mathcal{U}_{u_0^{\mathrm{d}}}$ is obtained by further calculating the convolution of the distributions $\mathcal{V}$ and $\mathcal{V}_g$, see Definition 2.38.

The Delta distribution and its derivative are distributions with compact support. Hence, we obtain for the particular solution with Lemma 2.40 and for the convolution with the Delta distribution, see Lemma 2.42, the representation

$$\mathcal{U}_{u_0^{\mathrm{d}}} = -\left(\frac{1}{\sigma_0}\mathcal{D}\delta_{\boldsymbol{x}}\right) * \mathcal{V}_g = -\frac{1}{\sigma_0}\mathcal{D}\left(\delta_{\boldsymbol{x}} * \mathcal{V}_g\right) = -\frac{1}{\sigma_0}\mathcal{D}\left(\tau_{\boldsymbol{x}}\mathcal{V}_g\right), \tag{4.5}$$

where τ denotes the usual translation operator $(\tau_{\boldsymbol{x}}\mathcal{V})\psi \coloneqq \mathcal{V}(\tau_{-\boldsymbol{x}}\psi)$, see Definition 2.41. For the distribution on the right-hand side, the following holds true for all $\psi \in \mathcal{D}(\mathbb{B}_{\varrho_0})$ since $\mathcal{D}$ is a differential operator of order 1, see Example 2.34:

$$-\mathcal{D}(\tau_{\boldsymbol{x}}\mathcal{V}_g)\psi = \mathcal{V}_g(\tau_{-\boldsymbol{x}}\mathcal{D}\psi) = \int_{\mathbb{R}^3} g(\boldsymbol{z})(\tau_{-\boldsymbol{x}}\mathcal{D}\psi(\boldsymbol{z}))\,\mathrm{d}\boldsymbol{z}.$$

In the next equation, we proceed by manipulating the integral on the right-hand side. We observe that the distribution on the left-hand side of this equation is regular, thus the distribution on the left-hand side of Eq. (4.5) is also regular. More precisely, we have

$$\begin{aligned}
\int_{\mathbb{R}^3} g(\boldsymbol{z})\mathcal{D}\psi(\boldsymbol{z}+\boldsymbol{x})\,\mathrm{d}\boldsymbol{z} &= -\int_{\mathbb{R}^3} (\mathcal{D}g)(\boldsymbol{z})\psi(\boldsymbol{z}+\boldsymbol{x})\,\mathrm{d}\boldsymbol{z} \\
&= -\int_{\mathbb{R}^3} (\mathcal{D}g)(\boldsymbol{y}-\boldsymbol{x})\psi(\boldsymbol{y})\,\mathrm{d}\boldsymbol{y} \\
&= -\int_{\mathbb{R}^3} \left(\boldsymbol{Q}\cdot\boldsymbol{\nabla}_{\boldsymbol{y}}\frac{1}{4\pi|\boldsymbol{y}-\boldsymbol{x}|}\right)\psi(\boldsymbol{y})\,\mathrm{d}\boldsymbol{y} \\
&= \int_{\mathbb{R}^3} \left(\boldsymbol{Q}\cdot\boldsymbol{\nabla}_{\boldsymbol{x}}\frac{1}{4\pi|\boldsymbol{y}-\boldsymbol{x}|}\right)\psi(\boldsymbol{y})\,\mathrm{d}\boldsymbol{y}.
\end{aligned}$$

Hence, for an arbitrary $\boldsymbol{x} \in \mathbb{B}_{\varrho_0}$, the distribution from Eq. (4.5) is generated by a locally integrable function that equals the mapping $\boldsymbol{y} \mapsto (4\pi\sigma_0)^{-1}\boldsymbol{Q}\cdot\boldsymbol{\nabla}_{\boldsymbol{x}}|\boldsymbol{y}-\boldsymbol{x}|^{-1}$ almost everywhere. From the equivalence class of all $\mathrm{L}_1(\mathbb{B}_{\varrho_0})$-functions generating $\mathcal{U}_{u_0^{\mathrm{d}}}$, we choose the generator u_0^{p} defined by

$$\sigma_0 u_0^{\mathrm{p}}(\boldsymbol{x},\boldsymbol{y}) = \boldsymbol{Q}\cdot\boldsymbol{\nabla}_{\boldsymbol{x}}\frac{1}{4\pi|\boldsymbol{y}-\boldsymbol{x}|}, \qquad \boldsymbol{x},\ \boldsymbol{y} \in \mathbb{B}_{\varrho_0},\ \boldsymbol{x} \neq \boldsymbol{y}. \tag{4.6}$$

In the following calculations, u_0^{p} denotes this continuous (except for the singularity) representative.

For each fixed $\boldsymbol{x} \in \mathbb{B}_{\varrho_0}$, the general solution of Poisson's equation with respect to $\boldsymbol{y} \in \mathbb{B}_{\varrho_0}$ in Eq. (4.4a) is given by the sum of the particular solution u_0^{p} depending on the right-hand side of Eq. (4.4a), see [95], and a harmonic function denoted by u_0^{h}:

$$u_0^{\mathrm{d}}(\boldsymbol{x},\boldsymbol{y}) = u_0^{\mathrm{p}}(\boldsymbol{x},\boldsymbol{y}) + u_0^{\mathrm{h}}(\boldsymbol{x},\boldsymbol{y}), \qquad \boldsymbol{x},\ \boldsymbol{y} \in \mathbb{B}_{\varrho_0}. \tag{4.7}$$

For the sake of comprehensibility, we denote explicitly the dependency of the points $\boldsymbol{x}$ and $\boldsymbol{y}$. The harmonic function can be represented by means of a fundamental system of the Laplacian. The corresponding coefficients can be determined by the boundary conditions, for which we need a solution of Laplace's equations on the other shells.

For Laplace's equation Eq. (4.4b) we can make the following considerations. The zero function is a continuous function and Eq. (4.4b) holds true in the sense of the distribution theory, hence, u_l^{d} is at least twice continuously differentiable for $l = 1, \dots, L$ and the Laplacian of u_l^{d} exists at every point $\boldsymbol{y} \in \mathbb{B}_{\varrho_0}^{\mathrm{ext}}$ and is equal to zero, see [90, p. 66]. Hence, the distributional and the classical solution of the differential equation coincide. Furthermore, on each particular shell, u_l^{d} is a twice continuously differentiable function for all $l = 1, \dots, L$. In addition, we use the widely known transmission conditions stated in [46, 95]. These Dirichlet and Neumann boundary conditions, considering that in the spherical case the normal derivative and the radial derivative coincide, are given for all $l = 0, \dots, L$ by

$$u_l^{\mathrm{d}}(\boldsymbol{x}, \boldsymbol{y}) = u_{l+1}^{\mathrm{d}}(\boldsymbol{x}, \boldsymbol{y}), \qquad \sigma_l \frac{\partial u_l^{\mathrm{d}}(\boldsymbol{x}, \boldsymbol{y})}{\partial y} = \sigma_{l+1} \frac{\partial u_{l+1}^{\mathrm{d}}(\boldsymbol{x}, \boldsymbol{y})}{\partial y}, \qquad \boldsymbol{y} \in \mathbb{S}_{\varrho_l}. \tag{4.8}$$

This system of partial differential equations and the corresponding Dirichlet and Neumann boundary conditions are, for instance, given in [45, 71] for the spherical three-shell model. Due to the Dirichlet condition, the electric potential is continuous in the second argument on the boundary spheres. Thus, Eq. (4.3) also holds true for the corresponding closed shells.

In order to solve the problem, we expand the classical solutions into series of inner and outer harmonics since they form a fundamental system for the Laplacian. For the harmonic part of the solution in the cerebrum, see Eq. (4.7), we obtain

$$u_0^{\mathrm{h}}(\boldsymbol{x}, \boldsymbol{y}) = \sum_{k=0}^{\infty} \sum_{i=1}^{2k+1} \bar{\alpha}_{k,i}^{(0)}(\boldsymbol{x}) y^k Y_{k,i}(\hat{\boldsymbol{y}}), \qquad \boldsymbol{x},\ \boldsymbol{y} \in \mathbb{B}_{\varrho_0}$$

due to its continuity at the origin. We can also give an expansion of the particular solution in Eq. (4.7) by using the same identity as in Eq. (2.2) and assuming $x < y$. Thus,

$$\begin{aligned}
\sigma_0 u_0^{\mathrm{p}}(\boldsymbol{x}, \boldsymbol{y}) &= \frac{1}{4\pi} \boldsymbol{Q} \cdot \boldsymbol{\nabla}_{\boldsymbol{x}} \sum_{k=0}^{\infty} \frac{x^k}{y^{k+1}} P_k(\hat{\boldsymbol{x}} \cdot \hat{\boldsymbol{y}}) \\
&= \boldsymbol{Q} \cdot \boldsymbol{\nabla}_{\boldsymbol{x}} \sum_{k=0}^{\infty} \sum_{i=1}^{2k+1} \frac{1}{2k+1} \frac{x^k}{y^{k+1}} Y_{k,i}(\hat{\boldsymbol{x}}) Y_{k,i}(\hat{\boldsymbol{y}}) \\
&= \sum_{k=0}^{\infty} \sum_{i=1}^{2k+1} \frac{\boldsymbol{Q} \cdot \boldsymbol{\nabla}_{\boldsymbol{x}} \left(x^k Y_{k,i}(\hat{\boldsymbol{x}}) \right)}{2k+1} \frac{1}{y^{k+1}} Y_{k,i}(\hat{\boldsymbol{y}}).
\end{aligned}$$

The interchanging of the series and the derivative is valid, see [73]. Summing up, the function u_0^{d} has for $x < y$ the representation

$$u_0^{\mathrm{d}}(\boldsymbol{x}, \boldsymbol{y}) = \sum_{k=0}^{\infty} \sum_{i=1}^{2k+1} \left(\bar{\alpha}_{k,i}^{(0)}(\boldsymbol{x}) y^k + \frac{1}{\sigma_0} \frac{\boldsymbol{Q} \cdot \boldsymbol{\nabla}_{\boldsymbol{x}} \left(x^k Y_{k,i}(\hat{\boldsymbol{x}}) \right)}{2k+1} \frac{1}{y^{k+1}} \right) Y_{k,i}(\hat{\boldsymbol{y}}). \tag{4.9}$$

For the sake of readability, we define $\bar{\beta}_{k,i}^{(0)}(\boldsymbol{x}) \coloneqq 1/(\sigma_0(2k+1)) \boldsymbol{Q} \cdot \boldsymbol{\nabla}_{\boldsymbol{x}}(x^k Y_{k,i}(\hat{\boldsymbol{x}}))$. If $L = 0$, that is the case of a single ball-shaped conductor with constant conductivity containing the dipole, only $\bar{\alpha}_{k,i}^{(0)}$ needs to be determined. This can be calculated straightforward using the Neumann condition in Eq. (4.8). Here, the conductivity σ_{L+1} vanishes, which implies that the right-hand side of the Neumann condition equals zero. Hence, we assume that $L > 0$ for the next steps of the derivation.

Since the electric potential is harmonic inside the diverse shells of our model, we can expand it into the sum of inner and outer spherical harmonics on each region. This is a particular case of the expansion into interior and exterior ellipsoidal harmonics used in [43, 95]. For all $l = 1, \dots, L+1$, we obtain

$$u_l^{\mathrm{d}}(\boldsymbol{x}, \boldsymbol{y}) = \sum_{k=0}^{\infty} \sum_{i=1}^{2k+1} \left(\bar{\alpha}_{k,i}^{(l)}(\boldsymbol{x}) y^k + \bar{\beta}_{k,i}^{(l)}(\boldsymbol{x}) \frac{1}{y^{k+1}} \right) Y_{k,i}(\hat{\boldsymbol{y}}), \qquad \boldsymbol{y} \in \mathbb{S}_{[\varrho_{l-1}, \varrho_l]}. \tag{4.10}$$

For the spherical three-shell model this formula can also be found in [32]. Inserting the expansions from Eqs. (4.9) to (4.10) into the boundary conditions from Eq. (4.8), we obtain, for $l = 0, \dots, L$, the following linear system for the coefficients:

$$0 = \varrho_l^{2k+1} \left(\bar{\alpha}_{k,i}^{(l)}(\boldsymbol{x}) - \bar{\alpha}_{k,i}^{(l+1)}(\boldsymbol{x}) \right) + \bar{\beta}_{k,i}^{(l)}(\boldsymbol{x}) - \bar{\beta}_{k,i}^{(l+1)}(\boldsymbol{x}), \tag{4.11a}$$

$$0 = \varrho_l^{2k+1} k \left(\sigma_l \bar{\alpha}_{k,i}^{(l)}(\boldsymbol{x}) - \sigma_{l+1} \bar{\alpha}_{k,i}^{(l+1)}(\boldsymbol{x}) \right) + (k+1) \left(\sigma_{l+1} \bar{\beta}_{k,i}^{(l+1)}(\boldsymbol{x}) - \sigma_l \bar{\beta}_{k,i}^{(l)}(\boldsymbol{x}) \right). \tag{4.11b}$$

For all $l = 0, \dots, L$, we gain the identities $\bar{\beta}_{0,1}^{(l)}(\boldsymbol{x}) = 0$ and $\bar{\alpha}_{0,1}^{(l)}(\boldsymbol{x}) = \bar{\alpha}_{0,1}^{(L+1)}(\boldsymbol{x})$, since $\boldsymbol{Q} \cdot \boldsymbol{\nabla}_{\boldsymbol{x}}(x^k Y_{k,i}(\hat{\boldsymbol{x}}))$ vanishes for $k = 0$. Without additional information, we cannot obtain a unique solution for the coefficients for $k = 0$. From Maxwell's equations, we have the additional information that the electric potential is regular at infinity, see Definition 3.1. Thus, $\lim_{y \to \infty} u_{L+1}^{\mathrm{d}}(\boldsymbol{x}, \boldsymbol{y}) = 0$ and we obtain $\bar{\alpha}_{k,i}^{(L+1)} \equiv 0$ for all $k \in \mathbb{N}_0$ and $i = 1, \dots, 2k+1$. Eventually, the zeroth summand in the expansion series of each particular electric potential vanishes.

Long but straightforward calculations, which are not shown here, lead to the linear dependency of $\bar{\alpha}_{k,i}^{(l)}(\boldsymbol{x})$ and $\bar{\beta}_{k,i}^{(l)}(\boldsymbol{x})$ on $\boldsymbol{Q} \cdot \boldsymbol{\nabla}_{\boldsymbol{x}}(x^k Y_{k,i}(\hat{\boldsymbol{x}}))$ for all $k \in \mathbb{N}$, $i = 1, \dots, 2n+1$, and $l = 0, \dots, L$, see [45, 95]. Based on this linear dependency, we introduce the abbreviations

$$\bar{\alpha}_{k,i}^{(l)}(\boldsymbol{x}) =: \alpha_k^{(l)} \left(\boldsymbol{Q} \cdot \boldsymbol{\nabla}_{\boldsymbol{x}}(x^k Y_{k,i}(\hat{\boldsymbol{x}})) \right),$$
$$\bar{\beta}_{k,i}^{(l)}(\boldsymbol{x}) =: \beta_k^{(l)} \left(\boldsymbol{Q} \cdot \boldsymbol{\nabla}_{\boldsymbol{x}}(x^k Y_{k,i}(\hat{\boldsymbol{x}})) \right)$$

for all $k \in \mathbb{N}$, $i = 1, \dots, 2n+1$, and all $l = 0, \dots, L$. In the particular case of $l = 0$ this leads for all $k \in \mathbb{N}$ to

$$\beta_k^{(0)} := \frac{1}{\sigma_0 (2k+1)}. \tag{4.12}$$

The remaining coefficients $\alpha_k^{(l)}$ and $\beta_k^{(l)}$ do not depend on $\boldsymbol{x}$ and i anymore for all $k \in \mathbb{N}$ and $l = 0, \dots, L$.

Using the introduced abbreviation, we obtain for $\boldsymbol{y}$ in the particular domains and $\boldsymbol{x} \in \mathbb{B}_{\varrho_0}$ the following set of equations:

$$u_l^{\mathrm{d}}(\boldsymbol{x}, \boldsymbol{y}) = \boldsymbol{Q} \cdot \left(\sum_{k=1}^{\infty} \sum_{i=1}^{2k+1} \left(\alpha_k^{(l)} y^k + \beta_k^{(l)} \frac{1}{y^{k+1}} \right) \boldsymbol{\nabla}_{\boldsymbol{x}} \left(x^k Y_{k,i}(\hat{\boldsymbol{x}}) \right) Y_{k,i}(\hat{\boldsymbol{y}}) \right), \tag{4.13}$$

for $l = 0, \dots, L+1$. These equations are also stated in [45] in the case of the three-shell model.

Since the coefficients are now independent of the order of the spherical harmonics, we are able to interchange the summation over i with the gradient. Afterwards, we apply the

Addition Theorem, see Theorem 2.25, to the expression. Independent of $l = 0, \dots, L$, this leads for all $k \in \mathbb{N}$ to the identity

$$\boldsymbol{\nabla}_{\boldsymbol{x}} \left(x^k \sum_{i=1}^{2k+1} Y_{k,i}(\hat{\boldsymbol{x}}) Y_{k,i}(\hat{\boldsymbol{y}}) \right) = \frac{2k+1}{4\pi} \boldsymbol{\nabla}_{\boldsymbol{x}} \left(x^k P_k(\hat{\boldsymbol{x}} \cdot \hat{\boldsymbol{y}}) \right).$$

Via Theorem 2.25 and Definition 2.22, we immediately obtain that for fixed $\boldsymbol{y} \in \mathbb{B}_{\varrho_0}$ the mapping $\boldsymbol{x} \mapsto x^k P_k(\hat{\boldsymbol{x}} \cdot \hat{\boldsymbol{y}})$ is a non-constant, homogeneous polynomial of degree $k \geq 1$. For different degrees, these polynomials are linearly independent. Thus, for all $k \in \mathbb{N}$ the gradients on the right-hand side of the previous equation are linearly independent.

Using the Addition Theorem, we obtain for all $l = 0, \dots, L$ the expansion

$$u_l^{\mathrm{d}}(\boldsymbol{x}, \boldsymbol{y}) = \frac{1}{4\pi} \boldsymbol{Q} \cdot \left(\sum_{k=1}^{\infty} (2k+1) \left(\alpha_k^{(l)} y^k + \beta_k^{(l)} \frac{1}{y^{k+1}} \right) \boldsymbol{\nabla}_{\boldsymbol{x}} \left(x^k P_k(\hat{\boldsymbol{x}} \cdot \hat{\boldsymbol{y}}) \right) \right). \tag{4.14}$$

Due to the linear independence with respect to $k \in \mathbb{N}$ of the functions on the right-hand side, the transmission conditions in Eq. (4.8) applied to Eq. (4.13) yield for all $k \in \mathbb{N}$ and $l = 1, \dots, L$ a system of linear equations for the expansion coefficients. This system can be obtained in total analogy to the one from Eq. (4.11) and it is given by

$$\varrho_0^{2k+1} \left(\alpha_k^{(0)} - \alpha_k^{(1)} \right) - \beta_k^{(1)} = \frac{-1}{(2k+1)\sigma_0}, \tag{4.15a}$$

$$\varrho_0^{2k+1} k \left(\sigma_0 \alpha_k^{(0)} - \sigma_1 \alpha_k^{(1)} \right) + (k+1)\sigma_1 \beta_k^{(1)} = \frac{k+1}{2k+1}, \tag{4.15b}$$

$$\varrho_l^{2k+1} \left(\alpha_k^{(l)} - \alpha_k^{(l+1)} \right) + \beta_k^{(l)} - \beta_k^{(l+1)} = 0, \tag{4.15c}$$

$$\varrho_l^{2k+1} k \left(\sigma_l \alpha_k^{(l)} - \sigma_{l+1} \alpha_k^{(l+1)} \right) + (k+1) \left(\sigma_{l+1} \beta_k^{(l+1)} - \sigma_l \beta_k^{(l)} \right) = 0. \tag{4.15d}$$

This system is also stated in [45] for the three-shell model. Note that $\beta_k^{(0)}$ and $\alpha_k^{(L+1)}$ are already known. Thus, we obtain $2L+2$ unknown variables and $2L+2$ equations to determine them for each $k \in \mathbb{N}$. Since the electric potential is measured on the scalp, we are mainly interested in the coefficients $\alpha_k^{(L)}$ and $\beta_k^{(L)}$ for the representation of u_L^{d} in Eq. (4.14). Thus, we do not need Eq. (4.15c) in the case of $l = L$. In addition, the conductivity outside the brain vanishes. Consequently, Eq. (4.15d) reduces to

$$\alpha_k^{(L)} = \frac{k+1}{k} \varrho_L^{-(2k+1)} \beta_k^{(L)}, \tag{4.16}$$

where the coefficients corresponding to the electric potential u_{L+1}^{d} do not appear. Note that Eq. (4.16) also holds true in the case of $L = 0$. Thus, the system reduces to a system with $2L+1$ equations and $2L+1$ unknown variables.

Up to this point, there exist several strategies to solve the system of linear equations, which in practice has to be done a large number of times with varying $k \in \mathbb{N}$. The straightforward method is to transfer the system into a matrix-vector representation and apply Gaussian elimination. In the case of the three-shell model, that is $L = 3$, it is stated in [73] that this matrix is ill-conditioned. The size of the corresponding matrix is $(2L+1) \times (2L+1)$. The classical Gaussian algorithm for solving this linear system requires $\mathcal{O}((2L+1)^3)$ operations, see [35].

For the sake of computing effort and stabilization effects, we further analyze this system of linear equations and present a second approach to solve the system. The aim is to achieve a tridiagonal matrix. The advantage of a tridiagonal matrix over an arbitrary matrix is the computational cost for the inversion. The solution of a system of linear equations with a tridiagonal matrix of size $(2L+1)\times(2L+1)$ can be obtained in $\mathcal{O}(2L+1)$ operations by means of the Thomas algorithm, see [35].

By means of rearranging and insertion of Eq. (4.15c) into Eq. (4.15d), we obtain for Eq. (4.15d) the identity

$$\varrho_l^{2k+1} k\,(\sigma_l-\sigma_{l+1})\,\alpha_k^{(l+1)} + ((k+1)\sigma_{l+1}+k\sigma_l)\,\beta_k^{(l+1)} - (2k+1)\sigma_l\beta_k^{(l)} = 0. \tag{4.15d$'$}$$

The coefficient $\beta_k^{(l+1)}$ in Eq. (4.15c) can be eliminated by Eq. (4.15d$'$). Thus,

$$\varrho_l^{2k+1}\left(((k+1)\sigma_{l+1}+k\sigma_l)\,\alpha_k^{(l)} - (2k+1)\sigma_{l+1}\alpha_k^{(l+1)}\right) + (k+1)\,(\sigma_{l+1}-\sigma_l)\,\beta_k^{(l)} = 0. \tag{4.15c$'$}$$

Similarly, $\beta_k^{(1)}$ can be eliminated in Eq. (4.15a) by means of Eq. (4.15b), that is

$$\varrho_0^{2k+1}\,((k+1)\sigma_1+k\sigma_0)\,\alpha_k^{(0)} - \varrho_0^{2k+1}(2k+1)\sigma_1\alpha_k^{(1)} = \frac{(k+1)(\sigma_0-\sigma_1)}{(2k+1)\sigma_0}. \tag{4.15a$'$}$$

Due to Eqs. (4.15b), (4.16), and (4.15a$'$) to (4.15d$'$), we can find a tridiagonal matrix $\mathfrak{A}_k$ and a right-hand side $\boldsymbol{b}_k$ such that $\mathfrak{A}_k\boldsymbol{z}_k = \boldsymbol{b}_k$ for all $k\in\mathbb{N}$. We summarize our results in the next lemma for the particular case of the three-shell model.

Lemma 4.1. *Let $L=3$, then the coefficients of the fundamental system expansions of the electric potential on each particular shell are for all $k\in\mathbb{N}$ uniquely determined by the solution of the system of linear equations $\mathfrak{A}_k\boldsymbol{z}_k = \boldsymbol{b}_k$. The quantities are defined by*

$$\mathfrak{A}_k \coloneqq \begin{pmatrix}
(k+1)\sigma_1+k\sigma_0 & -(2k+1)\sigma_1 & 0 & 0 & 0 & 0 & 0\\
k\sigma_0 & -k\sigma_1 & \frac{(k+1)\sigma_1}{\varrho_0^{2k+1}} & 0 & 0 & 0 & 0\\
0 & (k+1)\sigma_2+k\sigma_1 & \frac{(k+1)(\sigma_2-\sigma_1)}{\varrho_1^{2k+1}} & -(2k+1)\sigma_2 & 0 & 0 & 0\\
0 & 0 & \frac{-\sigma_1(2k+1)}{\varrho_1^{2k+1}} & k(\sigma_1-\sigma_2) & \frac{(k+1)\sigma_2+k\sigma_1}{\varrho_1^{2k+1}} & 0 & 0\\
0 & 0 & 0 & (k+1)\sigma_3+k\sigma_2 & \frac{(k+1)(\sigma_3-\sigma_2)}{\varrho_2^{2k+1}} & -(2k+1)\sigma_3 & 0\\
0 & 0 & 0 & 0 & \frac{-\sigma_2(2k+1)}{\varrho_2^{2k+1}} & k(\sigma_2-\sigma_3) & \frac{(k+1)\sigma_3+k\sigma_2}{\varrho_2^{2k+1}}\\
0 & 0 & 0 & 0 & 0 & \varrho_3^{2k+1}k & -(k+1)
\end{pmatrix}$$

$$\boldsymbol{z}_k \coloneqq \begin{pmatrix}\alpha_k^{(0)} & \alpha_k^{(1)} & \beta_k^{(1)} & \alpha_k^{(2)} & \beta_k^{(2)} & \alpha_k^{(3)} & \beta_k^{(3)}\end{pmatrix}^{\mathrm{T}},$$

$$\boldsymbol{b}_k \coloneqq \begin{pmatrix}\frac{(k+1)(\sigma_0-\sigma_1)}{\varrho_0^{2k+1}(2k+1)\sigma_0} & \frac{k+1}{\varrho_0^{2k+1}(2k+1)} & 0 & 0 & 0 & 0 & 0\end{pmatrix}^{\mathrm{T}}.$$

Lengthy but easy calculations, which were done with Mathematica [223], show that the matrix $\mathfrak{A}_k$ is a full-rank matrix for all $k\in\mathbb{N}$. Thus, the system is solvable for each $k\in\mathbb{N}$ and we are able to obtain a unique solution for the particular coefficients. However, the matrix is ill-conditioned, which is also stated in [73]. Due to the previous considerations, we set $\alpha_0^{(l)} = \beta_0^{(l)} = 0$ for all $l = 0,\dots,3$.

However, we are neither able to get a handy representation of the coefficients $\alpha_k^{(L)}$ and $\beta_k^{(L)}$ by means of the inversion of the matrix $\mathfrak{A}_k$ nor its non-tridiagonal predecessor. Nevertheless, for the convergence of the series in u_L^{d}, see Eq. (4.14), we need the asymptotic behaviour of $\alpha_k^{(L)}$ and $\beta_k^{(L)}$ as $k \to \infty$.

Inspired by an idea of P. Hashemzadeh and A.S. Fokas, and co-authors [49, 114], we can use a third approach in order to obtain the coefficients. This approach is based on the ansatz of [171, 174, 175, 226, 227] and the references therein. They use the Wronskian in order to solve Poisson's equation in Eq. (4.4a). They separate the sought function into an angular and a radial part and reduce the differential equation to a second-order linear ordinary differential equation. Then, they construct two linearly independent solutions of the homogeneous equation fulfilling the Dirichlet and Neumann boundary conditions stated in Eq. (4.8). For this construction, they use a 2×2 matrix to calculate the coefficients in Eq. (4.14). These two solutions of the homogeneous equation are combined by means of the Wronskian to construct the unique solution of the inhomogeneous equation fulfilling Eq. (4.8).

Since we have already solved the inhomogeneous differential equation, we do not need the part concerning the Wronskian of this ansatz. However, we can use the 2×2 matrix approach to solve Eq. (4.15). For $l = 0, \dots, L-1$, the Eqs. (4.15c) and (4.15d) can also be represented for fixed $k \in \mathbb{N}$ by

$$\begin{pmatrix} \varrho_l^{2k+1} & 1 \\ \varrho_l^{2k+1} k\sigma_l & -(k+1)\sigma_l \end{pmatrix} \begin{pmatrix} \alpha_k^{(l)} \\ \beta_k^{(l)} \end{pmatrix} = \begin{pmatrix} \varrho_l^{2k+1} & 1 \\ \varrho_l^{2k+1} k\sigma_{l+1} & -(k+1)\sigma_{l+1} \end{pmatrix} \begin{pmatrix} \alpha_k^{(l+1)} \\ \beta_k^{(l+1)} \end{pmatrix}.$$

The latter formula is also stated in [32] for the three-shell model. However, in the setting of [32], the conductivities of the different shells are sought and not the neuronal current. For this purpose, it is assumed that the neuronal current is made out of a fixed number of pointwise dipolar sources. For fixed conductivities we are interested in the reconstruction of the neuronal current, thus, we do not follow [32] in the following calculations.

The inversion of the right-hand side matrix is admissible if $\varrho_l^{2k+1}(2k+1)\sigma_{l+1} \neq 0$. This is the case if the tissue in the $(l+1)$th shell has a positive conductivity, which is fulfilled for all $l = 0, \dots, L-1$ due to Assumption 3.2. Thus, this is equivalent to

$$\begin{pmatrix} \alpha_k^{(l+1)} \\ \beta_k^{(l+1)} \end{pmatrix} = \frac{1}{2k+1} \begin{pmatrix} k+1+\frac{\sigma_l}{\sigma_{l+1}} k & (k+1)\left(1-\frac{\sigma_l}{\sigma_{l+1}}\right) \varrho_l^{-(2k+1)} \\ k\left(1-\frac{\sigma_l}{\sigma_{l+1}}\right) \varrho_l^{2k+1} & k+(k+1)\frac{\sigma_l}{\sigma_{l+1}} \end{pmatrix} \begin{pmatrix} \alpha_k^{(l)} \\ \beta_k^{(l)} \end{pmatrix}.$$

Recall that $\beta_k^{(0)}$ is already known from the particular solution of Poisson's equation, see Eq. (4.12), and that the representation of u_L^{d} is sought. Thus, we arrive at

$$\begin{aligned} \begin{pmatrix} \alpha_k^{(L)} \\ \beta_k^{(L)} \end{pmatrix} &= \frac{1}{(2k+1)^L} \left(\coprod_{l=0}^{L-1} \begin{pmatrix} k+1+\frac{\sigma_l}{\sigma_{l+1}} k & (k+1)\left(1-\frac{\sigma_l}{\sigma_{l+1}}\right) \varrho_l^{-(2k+1)} \\ k\left(1-\frac{\sigma_l}{\sigma_{l+1}}\right) \varrho_l^{2k+1} & k+(k+1)\frac{\sigma_l}{\sigma_{l+1}} \end{pmatrix} \right) \begin{pmatrix} \alpha_k^{(0)} \\ \beta_k^{(0)} \end{pmatrix} \\ &=: \mathfrak{M}^{(L)} \begin{pmatrix} \alpha_k^{(0)} \\ \beta_k^{(0)} \end{pmatrix}. \end{aligned} \tag{4.17}$$

The matrix product $\coprod_{l=0}^{L-1}$ is meant as follows: first, the matrix with the lowest index is stated and then, from the left-hand side, the matrix with the next higher index is multiplied,

that is, for example, $(\coprod_{l=0}^{L-1} \mathfrak{A}_l)\boldsymbol{b} \coloneqq \mathfrak{A}_{L-1} \cdots \mathfrak{A}_1 \mathfrak{A}_0 \boldsymbol{b}$. The order of multiplication is relevant, since matrix multiplication is non-commutative. The coefficients $\alpha_k^{(L)}$ and $\beta_k^{(L)}$ are linearly dependent, see Eq. (4.16). Hence, we obtain two equations for two unknowns. Let $m_{i,j}^{(L)}$ denote the entry in the ith row and the jth column of the matrix $\mathfrak{M}^{(L)}$. Note that the matrix $\mathfrak{M}^{(L)}$ and its entries also depend on the order k, which is omitted in the notation for the sake of readability. Then

$$\alpha_k^{(L)} = m_{1,1}^{(L)} \alpha_k^{(0)} + m_{1,2}^{(L)} \beta_k^{(0)}, \qquad \beta_k^{(L)} = m_{2,1}^{(L)} \alpha_k^{(0)} + m_{2,2}^{(L)} \beta_k^{(0)}.$$

Using Eq. (4.16), a straightforward calculation yields

$$\beta_k^{(L)} \left(\frac{k+1}{k} \varrho_L^{-(2k+1)} - \frac{m_{1,1}^{(L)}}{m_{2,1}^{(L)}} \right) = - \frac{m_{1,1}^{(L)} m_{2,2}^{(L)} - m_{1,2}^{(L)} m_{2,1}^{(L)}}{m_{2,1}^{(L)}} \beta_k^{(0)}.$$

With $\beta_k^{(0)} = (\sigma_0(2k+1))^{-1}$ and the formal identity $\det(\mathfrak{M}^{(L)}) = m_{1,1}^{(L)} m_{2,2}^{(L)} - m_{1,2}^{(L)} m_{2,1}^{(L)}$, we can solve this equation for $\beta_k^{(L)}$ and get

$$\beta_k^{(L)} = \frac{k}{\sigma_0(2k+1) \left(k m_{1,1}^{(L)} - (k+1) m_{2,1}^{(L)} \varrho_L^{-(2k+1)} \right)} \det\left(\mathfrak{M}^{(L)}\right).$$

The determinant of $\mathfrak{M}^{(L)}$ is calculated as

$$\begin{aligned} \det\left(\mathfrak{M}^{(L)}\right) &= \frac{1}{(2k+1)^{2L}} \prod_{l=0}^{L-1} \left(\left(k+1+\frac{\sigma_l}{\sigma_{l+1}} k \right) \left(k + (k+1)\frac{\sigma_l}{\sigma_{l+1}} \right) \right. \\ &\qquad \left. - k(k+1) \left(1 - \frac{\sigma_l}{\sigma_{l+1}} \right)^2 \right) \\ &= \frac{1}{(2k+1)^{2L}} \prod_{l=0}^{L-1} (2k+1)^2 \frac{\sigma_l}{\sigma_{l+1}} \\ &= \frac{\sigma_0}{\sigma_L}. \end{aligned}$$

Thus, we eventually obtain for all $k \in \mathbb{N}$ the representation

$$\beta_k^{(L)} = \frac{k}{\sigma_L(2k+1) \left(k m_{1,1}^{(L)} - (k+1) m_{2,1}^{(L)} \varrho_L^{-(2k+1)} \right)}. \tag{4.18}$$

Independent of the way of calculating the coefficients, we define for the sake of brevity the abbreviation

$$H_k(y) \coloneqq \alpha_k^{(L)} y^k + \beta_k^{(L)} \frac{1}{y^{k+1}}, \qquad y \in [\varrho_{L-1}, \varrho_L], \tag{4.19}$$

for all $k \in \mathbb{N}$. Recall for all $k \in \mathbb{N}$ the relation between $\alpha_k^{(L)}$ and $\beta_k^{(L)}$ in Eq. (4.16). Hence, the function H_k becomes

$$H_k(y) = \left(\frac{k+1}{k} \left(\frac{y}{\varrho_L} \right)^{2k+1} + 1 \right) \beta_k^{(L)} \frac{1}{y^{k+1}}, \qquad y \in [\varrho_{L-1}, \varrho_L]. \tag{4.20}$$

Note that H_k depends on the radius ϱ_L of the scalp for all $k \in \mathbb{N}$ and of the number of shells $L \in \mathbb{N}$. For the sake of readability, we omit this dependency in our notation. Inserting Eq. (4.20) into the expansion of u_L^{d} from Eq. (4.14), we obtain the representation

$$\begin{aligned} u_L^{\mathrm{d}}(\boldsymbol{x}, \boldsymbol{y}) &= \frac{1}{4\pi} \boldsymbol{Q} \cdot \left(\sum_{k=1}^{\infty} (2k+1) \left(\frac{k+1}{k} \left(\frac{y}{\varrho_L} \right)^{2k+1} + 1 \right) \beta_k^{(L)} \frac{1}{y^{k+1}} \boldsymbol{\nabla}_{\boldsymbol{x}} \left(x^k P_k(\hat{\boldsymbol{x}} \cdot \hat{\boldsymbol{y}}) \right) \right) \\ &= \frac{1}{4\pi} \boldsymbol{Q} \cdot \left(\sum_{k=1}^{\infty} (2k+1) H_k(y) \boldsymbol{\nabla}_{\boldsymbol{x}} \left(x^k P_k(\hat{\boldsymbol{x}} \cdot \hat{\boldsymbol{y}}) \right) \right). \end{aligned}$$

for the electric potential on the scalp corresponding to a single dipole. Often, in the literature, for fixed $\boldsymbol{x} \in \mathbb{B}_{\varrho_0}$ the restriction of $u_L^{\mathrm{d}}(\boldsymbol{x}, \cdot)$ onto the sphere $\mathbb{S}_{\varrho_L}$ is considered. Using the abbreviation

$$H_k \coloneqq H_k(\varrho_L) = \beta_k^{(L)} \frac{1}{\varrho_L^{k+1}} \frac{2k+1}{k}, \tag{4.21}$$

we can represent this restriction by

$$u_L^{\mathrm{d}}(\boldsymbol{x}, \varrho_L \hat{\boldsymbol{y}}) = \frac{1}{4\pi} \boldsymbol{Q} \cdot \left(\sum_{k=1}^{\infty} \frac{(2k+1)^2}{k} \beta_k^{(L)} \frac{1}{\varrho_L^{k+1}} \boldsymbol{\nabla}_{\boldsymbol{x}} \left(x^k P_k(\hat{\boldsymbol{x}} \cdot \hat{\boldsymbol{y}}) \right) \right).$$

For the comparison of our results with previous approaches, we also use the restriction onto the outer sphere in Chapter 15.

So far, we have derived an expansion for the electric potential corresponding to a single dipole in inner and outer harmonics based on solutions of distributional Poisson's and Laplace's equations. As we have already pointed out, this expansion coincides with previous expansions in the literature. In addition, we presented two novel approaches in order to compute the occurring coefficients. The first approach leads to a tridiagonal matrix, which reduces the computational cost for the inversion. The second approach is based on existing ideas for a recursive computation and yields a novel closed formula for the coefficients $\{\beta_k^{(L)}\}_{k \in \mathbb{N}}$. This formula is required to answer the following question: does the series derived for the electric potential converge?

Obviously, the asymptotic behaviour of $H_k(y)$ as $k \to \infty$ for all $y \in [\varrho_{L-1}, \varrho_L]$ plays an important role in order to guarantee the convergence. To this end, we analyze the asymptotic behaviour of $\beta_k^{(L)}$ as $k \to \infty$ in the next lemma.

Lemma 4.2. *Let Assumption 3.2 be fulfilled, let the number of shells $L \in \mathbb{N}_0$ be fixed, and let $\beta_k^{(L)}$ be defined as in Eq. (4.18) for $k \in \mathbb{N}$. Then*

$$\left(k \mapsto \left| \beta_k^{(L)} \right| \right) \in \mathcal{O}(k^{-1}) \text{ as } k \to \infty.$$

In the case of $L = 0$, we get the representation

$$\beta_k^{(0)} = \frac{1}{\sigma_0 (2k+1)}.$$

Proof. First, we assume $L = 0$. In this case, u_0^{d} can be measured non-invasively and from Eq. (4.12) we immediately obtain

$$\beta_k^{(0)} = \frac{1}{\sigma_0 (2k+1)} \in \mathcal{O}(k^{-1}).$$

Now, let $L > 0$. We analyze the matrix entries of $\mathfrak{M}^{(L)}$ occurring in the denominator of $\beta_k^{(L)}$. Since $\mathfrak{M}^{(L)}$ is constructed iteratively, we use a mathematical induction over L to prove the statement. For $L = 1$, we obtain

$$\mathfrak{M}^{(1)} = \frac{1}{2k+1} \begin{pmatrix} k+1+\frac{\sigma_0}{\sigma_1}k & (k+1)\left(1-\frac{\sigma_0}{\sigma_1}\right)\varrho_0^{-(2k+1)} \\ k\left(1-\frac{\sigma_0}{\sigma_1}\right)\varrho_0^{2k+1} & k+(k+1)\frac{\sigma_0}{\sigma_1} \end{pmatrix}.$$

Obviously, for a finite real constant $C^{(1)} > 0$, the following limits hold true, since $\varrho_0 < \varrho_1$ and the conductivities on each shell are positive, see Assumption 3.2:

$$\begin{aligned} \lim_{k\to\infty} \left| m_{1,1}^{(1)} \right| &= \frac{1}{2}\left(1 + \frac{\sigma_0}{\sigma_1}\right) =: C^{(1)}, \\ \lim_{k\to\infty} \left| m_{2,1}^{(1)} \varrho_1^{-(2k+1)} \right| &= 0. \end{aligned}$$

Now, we assume for an arbitrary $L \in \mathbb{N}$ that the entries in the first column of $\mathfrak{M}^{(L-1)}$ fulfil

$$\begin{aligned} \lim_{k\to\infty} \left| m_{1,1}^{(L-1)} \right| &= C^{(L-1)}, \\ \lim_{k\to\infty} \left| m_{2,1}^{(L-1)} \varrho_{L-1}^{-(2k+1)} \right| &= 0 \end{aligned}$$

for a finite real constant $C^{(L-1)} > 0$. For $\mathfrak{M}^{(L)}$, we obtain the representation

$$\mathfrak{M}^{(L)} = \frac{1}{2k+1} \begin{pmatrix} k+1+\frac{\sigma_{L-1}}{\sigma_L}k & (k+1)\left(1-\frac{\sigma_{L-1}}{\sigma_L}\right)\varrho_{L-1}^{-(2k+1)} \\ k\left(1-\frac{\sigma_{L-1}}{\sigma_L}\right)\varrho_{L-1}^{2k+1} & k+(k+1)\frac{\sigma_{L-1}}{\sigma_L} \end{pmatrix} \mathfrak{M}^{(L-1)}.$$

By performing the matrix multiplication, we get

$$\begin{aligned} m_{1,1}^{(L)} &= \frac{1}{2k+1}\left(\left(k+1+\frac{\sigma_{L-1}}{\sigma_L}k\right) m_{1,1}^{(L-1)} + (k+1)\left(1-\frac{\sigma_{L-1}}{\sigma_L}\right)\varrho_{L-1}^{-(2k+1)} m_{2,1}^{(L-1)}\right), \\ m_{2,1}^{(L)} &= \frac{1}{2k+1}\left(k\left(1-\frac{\sigma_{L-1}}{\sigma_L}\right)\varrho_{L-1}^{2k+1} m_{1,1}^{(L-1)} + \left(k+(k+1)\frac{\sigma_{L-1}}{\sigma_L}\right) m_{2,1}^{(L-1)}\right). \end{aligned}$$

For the limit, we obtain, due to the existence of the limits concerning the matrix entries of $\mathfrak{M}^{(L-1)}$, the result

$$\begin{aligned} \lim_{k\to\infty} \left| m_{1,1}^{(L)} \right| &= \lim_{k\to\infty} \left| \left(\frac{k+1}{2k+1} + \frac{\sigma_{L-1}}{\sigma_L}\frac{k}{2k+1}\right) m_{1,1}^{(L-1)} \right. \\ &\qquad \left. + \frac{k+1}{2k+1}\left(1-\frac{\sigma_{L-1}}{\sigma_L}\right)\varrho_{L-1}^{-(2k+1)} m_{2,1}^{(L-1)} \right| \\ &= \left| C^{(L-1)} \left(\lim_{k\to\infty} \frac{k+1}{2k+1} + \frac{\sigma_{L-1}}{\sigma_L} \lim_{k\to\infty} \frac{k}{2k+1} \right) \right| \\ &= \frac{1}{2}\left(1+\frac{\sigma_{L-1}}{\sigma_L}\right) C^{(L-1)} =: C^{(L)}. \end{aligned}$$

The limit exists because the limits of all summands exist. It is a finite and positive constant. In analogy, we get with $\varrho_{L-1} < \varrho_L$ the identity

$$\begin{aligned} \lim_{k\to\infty} \left| m_{2,1}^{(L)} \varrho_L^{-(2k+1)} \right| &= \lim_{k\to\infty} \left| \left(\frac{k}{2k+1}\left(1-\frac{\sigma_{L-1}}{\sigma_L}\right)\left(\frac{\varrho_{L-1}}{\varrho_L}\right)^{2k+1} m_{1,1}^{(L-1)} \right. \right. \\ &\qquad \left. \left. + \left(\frac{k}{2k+1} + \frac{k+1}{2k+1}\frac{\sigma_{L-1}}{\sigma_L}\right) m_{2,1}^{(L-1)} \varrho_{L-1}^{-(2k+1)} \left(\frac{\varrho_{L-1}}{\varrho_L}\right)^{2k+1} \right) \right| \\ &= 0. \end{aligned}$$

This concludes the induction. Finally, we obtain the desired asymptotic behaviour of the sought coefficients $\beta_k^{(L)}$ for all $L \in \mathbb{N}$, that is

$$\begin{aligned}\limsup_{k\to\infty}\left|\frac{\beta_k^{(L)}}{k^{-1}}\right| &= \lim_{k\to\infty}\left|\frac{k}{\sigma_L\left(km_{1,1}^{(L)} - (k+1)m_{2,1}^{(L)}\varrho_L^{-(2k+1)}\right)}\frac{k}{2k+1}\right| \\ &= \frac{1}{2\sigma_L}\lim_{k\to\infty}\left|\frac{1}{m_{1,1}^{(L)} - \frac{k+1}{k}m_{2,1}^{(L)}\varrho_L^{-(2k+1)}}\right| \\ &= \frac{1}{2\sigma_L}\frac{1}{C^{(L)}} < \infty. \end{aligned}$$

□

From the definition of $C^{(1)}$ and $C^{(L)}$ in the last proof, we immediately obtain the next result.

Corollary 4.3. *Let Assumption 3.2 be fulfilled, let the number of shells $L \geq 2$ be fixed, let $\beta_k^{(L)}$ be defined as in Eq. (4.18) for $k \in \mathbb{N}$, and let the sequence $\{k\beta_k^{(L)}\}_{k\in\mathbb{N}}$ be monotonically increasing. Then*

$$\sup_{k\in\mathbb{N}}\left|k\beta_k^{(L)}\right| \leq \frac{1}{2\sigma_L}\frac{1}{C^{(L)}},$$

where the constant is given recursively for $L = 2, \ldots, L$ by

$$C^{(L)} = \frac{1}{2^L}\prod_{l=1}^{L}\left(1 + \frac{\sigma_{l-1}}{\sigma_l}\right).$$

For further calculations, we need more properties of the coefficients $\beta_k^{(L)}$ for all $k \in \mathbb{N}$.

Lemma 4.4. *Let Assumption 3.2 be fulfilled and let $L \in \mathbb{N}_0$ be fixed. Then $\beta_k^{(L)} \neq 0$ for all $k \in \mathbb{N}$.*

Proof. For $L = 0$, the statement is clear due to the representation of $\beta_k^{(L)}$ from Lemma 4.2. The statement for $L > 1$ remains to be proved. Let us assume that $\beta_k^{(L)} = 0$ for an arbitrary $k \in \mathbb{N}$. Then, by means of Eq. (4.16), we get $\alpha_k^{(L)} = 0$. Inserting this into Eqs. (4.15c) and (4.15d) for $l = L - 1$, we obtain two equations for the unknown coefficients $\beta_k^{(L-1)}$ and $\alpha_k^{(L-1)}$, that is

$$\begin{aligned}\varrho_{L-1}^{2k+1}\left(\alpha_k^{(L-1)}\right) + \beta_k^{(L-1)} &= 0, \\ \varrho_{L-1}^{2k+1}k\sigma_{L-1}\alpha_k^{(L-1)} - (k+1)\sigma_{L-1}\beta_k^{(L-1)} &= 0.\end{aligned}$$

Inserting the first equation into the second, we directly obtain $\alpha_k^{(L-1)} = 0$ and, thus, $\beta_k^{(L-1)} = 0$. Consequently, this can be done inductively for $l = L-2, \ldots, 1$ and we obtain $\alpha_k^{(l)} = \beta_k^{(l)} = 0$ for all $l = 1, \ldots, L$. Finally, Eqs. (4.15a) and (4.15b) yield

$$\begin{aligned}\varrho_0^{2k+1}\alpha_k^{(0)} &= \frac{-1}{(2k+1)\sigma_0}, \\ \varrho_0^{2k+1}k\sigma_0\alpha_k^{(0)} &= \frac{k+1}{2k+1}.\end{aligned}$$

Both equations cannot be true simultaneously. Hence, we arrived at a contradiction and we conclude $\beta_k^{(L)} \neq 0$ for all $k \in \mathbb{N}$. □

After these calculations, we can concentrate our analysis on the derivation of an integral equation of the first kind for the inverse EEG problem in the case of a continuous dipole distribution. In Eq. (4.14), we found the electric potential $u_L^{\mathrm{d}}(\boldsymbol{x}, \cdot)$ in the case of a single dipole located at $\boldsymbol{x}$. In order to obtain the electric potential in the case of a continuous dipole distribution, we use the superposition principle and integrate our solution u_L^{d} over the cerebrum $\mathbb{B}_{\varrho_0}$ with respect to the first argument. We concentrate our analysis on the function u_L^{d} since this is the only part of the electric potential that can be measured non-invasively by the electroencephalograph. Note that the discrete dipole moment becomes the neuronal current $\boldsymbol{J}^{\mathrm{P}}$ in the transition to the continuous dipole distribution. This nomenclature is often used in the literature, see, for instance, [73] and the references therein.

Corollary 4.5. *Let Assumption 3.2 with $L \geq 2$ hold true. The electric potential u_L on the outer shell $\mathbb{S}_{[\varrho_{L-1}, \varrho_L]}$ is given by*

$$u_L(\boldsymbol{y}) \coloneqq \int_{\mathbb{B}_{\varrho_0}} u_L^{\mathrm{d}}(\boldsymbol{x}, \boldsymbol{y}) \, \mathrm{d}\boldsymbol{x} = \int_{\mathbb{B}_{\varrho_0}} \boldsymbol{J}^{\mathrm{P}}(\boldsymbol{x}) \cdot \boldsymbol{k}_{\mathrm{E}}(\boldsymbol{x}, \boldsymbol{y}) \, \mathrm{d}\boldsymbol{x}. \tag{4.22}$$

The occurring integral kernel has for all $(\boldsymbol{x}, \boldsymbol{y}) \in \mathbb{B}_{\varrho_0} \times \mathbb{S}_{[\varrho_{L-1}, \varrho_L]}$ the formal representation

$$\boldsymbol{k}_{\mathrm{E}}(\boldsymbol{x}, \boldsymbol{y}) \coloneqq \frac{1}{4\pi} \sum_{k=1}^{\infty} (2k+1) H_k(y) \boldsymbol{\nabla}_{\boldsymbol{x}} \left(x^k P_k(\hat{\boldsymbol{x}} \cdot \hat{\boldsymbol{y}}) \right). \tag{4.23}$$

Here, as in the inverse magnetic case, $\boldsymbol{J}^{\mathrm{P}}$ denotes the primary current that is derived from the integration of terms involving the dipole moment $\boldsymbol{Q}$.

This integral equation for the EEG problem is also stated in [45, 73] for the restriction of the electric potential onto the sphere $\mathbb{S}\varrho_L$.

In this chapter, we derived a representation of the electric potential in the outer (scalp) shell induced by a single dipole in the cerebrum. Based on the superposition principle, this result could be transferred to the continuous dipole distribution. Thus, we achieved an integral equation relating the neuronal current inside the cerebrum with the electric potential in the outside of the head.

In analogy to the modelling of the MEG problem, some additional questions arise: does the series in the representation of $\boldsymbol{k}_{\mathrm{E}}$ converge? Is the integrand in Eq. (4.22) integrable? And can we evaluate the electric potential at the sensor positions?

In order to simultaneously answer the open questions for the MEG and EEG problem, we introduce a particular class of integral equations with corresponding kernels in the next part.

Part II.

Solving the Direct Problem

Chapter 5.

Preliminaries

In this part, we solve the direct problem related to the MEG and EEG integral equation, that is determining the magnetic flux density and the electric potential from a given neuronal current. For both problems, we have already derived two integral equations relating these physical quantities with each other in the previous part. In this context, some of the open questions can be answered: are the two occurring integral kernels, which are stated in Eq. (3.4) and Eq. (4.23), respectively, and their corresponding integral equations well-defined? Can we state a formula for the solution of the related direct problem? Is the achieved potential smooth enough for our application?

In this preliminary chapter, we give an overview over the mathematical foundations that are required in order to solve the direct MEG and EEG problem. For the answers to these questions, some special functions are required. We need an orthonormal basis in the vector-valued space $\mathbf{L}_2(\mathbb{B}_{\varrho_0})$ for analyzing the direct problem. Based on a separation ansatz, this basis consists of two types of functions. The first type is given by a scalar-valued orthonormal system on the interval, which is presented in Section 5.1. The second type of functions, which is presented in Section 5.2, is a vector-valued version of the already introduced spherical harmonics on the sphere. The vector-valued spherical orthonormal system is also used for the analysis of the integral kernels. For this purpose, a related vector-valued analogue of the Legendre polynomials is introduced in Section 5.3 and corresponding inner and outer vector spherical harmonics are described in Section 5.4. Completing the list of used vector-valued orthonormal functions, we introduce a (vector-valued) orthonormal basis for $\mathbf{L}_2(\mathbb{B}_{\varrho_0})$ in Section 5.5.

5.1. Orthonormal Systems on the Interval

We have already introduced some special functions on the interval, namely the Jacobi polynomials, in Section 2.2. Therein, we stated that within this work mainly two particular cases of Jacobi polynomials are used. The first particular case is given by the Legendre polynomials, which are defined in Definition 2.5 and are important functions in the context of spherical harmonics. The second particular case of Jacobi polynomials considered in this work is used as the radial part of an orthonormal system on the ball.

The Jacobi polynomials are defined over the interval $[-1, 1]$. For the construction of orthonormal basis functions on the ball, a transformation of these polynomials to the interval $[0, R]$ is required. This particular orthonormal basis is first used by the author in [147, 162] and includes Jacobi polynomials with $\alpha = 0$ and $\beta > -1$. This basis is also used in Definition 5.33. There, the historical origin of these functions is stated. Now, we consider only its radial part and define an abbreviation for these functions.

Definition 5.1. *For $R > 0$, the functions $Q_m^{(\beta)}(R;\cdot)$ of degree $m \in \mathbb{N}_0$ and $\beta > -1$ are defined by means of the Jacobi polynomials via*

$$Q_m^{(\beta)}(R;r) \coloneqq \sqrt{\frac{4m+2\beta+2}{R^3}} \left(\frac{r}{R}\right)^{\beta-1/2} P_m^{(0,\beta)}\left(2\frac{r^2}{R^2}-1\right), \qquad r \in (0,R].$$

With this definition, we can easily establish completeness and orthonormality of this system.

Corollary 5.2. *For every $\beta > -1$ the system $\{Q_m^{(\beta)}(R;\cdot)\}_{m\in\mathbb{N}_0}$ from Definition 5.1 forms an orthonormal basis for $\mathrm{L}_2^w([0,R])$, where $w(r) \coloneqq r^2$.*

Proof. We start with Theorem 2.8 for the Jacobi polynomials $P_m^{(0,\beta)}$ and their orthogonality. Then, we use the substitution $x = 2r^2/R^2 - 1$. Thus,

$$\begin{aligned}
\frac{2^{\beta+1}}{2m+\beta+1}\delta_{m,n} &= \int_{-1}^{1} (1+x)^\beta P_m^{(0,\beta)}(x) P_n^{(0,\beta)}(x)\,\mathrm{d}x \\
&= \int_0^R \left(2\frac{r^2}{R^2}\right)^\beta P_m^{(0,\beta)}\left(2\frac{r^2}{R^2}-1\right) P_n^{(0,\beta)}\left(2\frac{r^2}{R^2}-1\right)\frac{4r}{R^2}\,\mathrm{d}r \\
&= \frac{2^{\beta+2}}{R^{2\beta+2}} \int_0^R r^{2\beta+1} P_m^{(0,\beta)}\left(2\frac{r^2}{R^2}-1\right) P_n^{(0,\beta)}\left(2\frac{r^2}{R^2}-1\right)\mathrm{d}r \\
&= \frac{2^{\beta+2}}{\sqrt{4m+2\beta+2}\sqrt{4n+2\beta+2}} \int_0^R Q_m^{(\beta)}(R;r) Q_n^{(\beta)}(R;r) r^2\,\mathrm{d}r.
\end{aligned}$$

Concluding, the functions $Q_m^{(\beta)}(R;\cdot)$ with $m \in \mathbb{N}_0$ are $\mathrm{L}_2^w([0,R])$-orthonormal. Due to Theorem 2.9, the set of all these functions is a basis for $\mathrm{L}_2^w([0,R])$. □

Lemma 5.3. *For all $\beta \geq 1/2$ and all $m \in \mathbb{N}_0$, we get*

$$\max_{r\in[0,R]} \left|Q_m^{(\beta)}(R;r)\right| = \sqrt{\frac{4m+2\beta+2}{R^3}} \binom{m+\beta}{m} \leq \sqrt{6} R^{-3/2} \frac{(m+\beta)^{m+1/2}}{m!}.$$

Proof. From [158, Eq. (10.10)], we have the inequality

$$\binom{m+\beta}{m} \leq \frac{(m+\beta)^m}{m!}$$

for all $m \in \mathbb{N}_0$. By using this estimate and Theorem 2.7, we get

$$\begin{aligned}
\max_{r\in[0,R]} \left|Q_m^{(\beta)}(R;r)\right| &= \max_{r\in[0,R]} \left(\sqrt{\frac{4m+2\beta+2}{R^3}} \left(\frac{r}{R}\right)^{\beta-1/2} \left|P_m^{(0,\beta)}\left(2\frac{r^2}{R^2}-1\right)\right|\right) \\
&= \sqrt{\frac{4m+2\beta+2}{R^3}} \binom{m+\beta}{m} \\
&\leq \sqrt{\frac{4m+2\beta+2}{R^3}} \frac{(m+\beta)^m}{m!} \\
&\leq \sqrt{6} R^{-3/2} \frac{(m+\beta)^{m+1/2}}{m!}.
\end{aligned}$$

In the last step, we used $2 \leq 2m + 4\beta$ for all $m \in \mathbb{N}_0$. □

5.2. Vector Spherical Harmonics

In this section, we give a short overview over two systems of vector-valued spherical harmonics and their properties. The first system goes back to P.M. Morse and H. Feshbach and is often used in geomathematics because it separates vector-valued functions into their normal and tangential parts. In addition, the system going back to A.R. Edmonds is used for problems in (electro-) magnetism in order to separate vector fields into parts belonging to inner and outer sources. For more information, see [79, 81, 84, 88], for instance, and the references therein.

5.2.1. Definition of Vector Spherical Harmonics

First, we define an abbreviation for three (differential) operators on the sphere that we use for the construction of $\mathbf{L}_2(\mathbb{S})$-orthonormal vector-valued spherical harmonics systems. The occurring differential operators are defined in Theorem 2.14.

Definition 5.4 ([88, Eq. (5.17)-(5.19)]). *We define the operators* $\boldsymbol{o}^{(i)} \colon \mathrm{C}^1(\mathbb{S}) \to \mathbf{C}^0(\mathbb{S})$ *by*

$$\boldsymbol{o}_{\boldsymbol{\xi}}^{(1)} F(\boldsymbol{\xi}) \coloneqq \boldsymbol{\xi} F(\boldsymbol{\xi}), \quad \boldsymbol{o}_{\boldsymbol{\xi}}^{(2)} F(\boldsymbol{\xi}) \coloneqq \boldsymbol{\nabla}_{\boldsymbol{\xi}}^* F(\boldsymbol{\xi}), \quad \boldsymbol{o}_{\boldsymbol{\xi}}^{(3)} F(\boldsymbol{\xi}) \coloneqq \boldsymbol{L}_{\boldsymbol{\xi}}^* F(\boldsymbol{\xi})$$

for all $F \in \mathrm{C}^1(\mathbb{S})$ *and* $\boldsymbol{\xi} \in \mathbb{S}$.

The following orthonormal properties of these operators can be shown based on Eq. (2.6a) and Corollary 2.21.

Lemma 5.5 ([81, Lem. 12.1.1]). *Let* F, $G \in \mathrm{C}^1(\mathbb{S})$. *Then the following statements are valid:*

i) For all $\boldsymbol{\xi} \in \mathbb{S}$, *we get* $\boldsymbol{o}_{\boldsymbol{\xi}}^{(i)} F(\boldsymbol{\xi}) \cdot \boldsymbol{o}_{\boldsymbol{\xi}}^{(j)} F(\boldsymbol{\xi}) = 0$ *for all* $i \neq j$ *with* i, $j = 1, 2, 3$.

ii) If $\langle F, G \rangle_{\mathrm{L}_2(\mathbb{S})} = 0$, *then* $\langle \boldsymbol{o}^{(i)} F, \boldsymbol{o}^{(j)} G \rangle_{\mathbf{L}_2(\mathbb{S})} = 0$ *for all* i, $j = 1, 2, 3$.

For certain statements, the adjoints of the $\boldsymbol{o}^{(i)}$-operators are needed. For example, for the calculation of the classical vector-valued reproducing kernels, see [81].

Corollary 5.6 ([88, Eq. (5.25)-(5.27)]). *The adjoint operators* $O^{(i)} \colon \mathbf{C}^1(\mathbb{S}) \to \mathrm{C}(\mathbb{S})$ *of* $\boldsymbol{o}^{(i)}$ *(with respect to the* $\mathbf{L}_2(\mathbb{S})$- *and* $\mathrm{L}_2(\mathbb{S})$*-inner products, respectively) are represented by*

$$O_{\boldsymbol{\xi}}^{(1)} \boldsymbol{f}(\boldsymbol{\xi}) = \boldsymbol{\xi} \cdot \mathcal{P}_{\mathrm{nor}} \boldsymbol{f}(\boldsymbol{\xi}), \quad O_{\boldsymbol{\xi}}^{(2)} \boldsymbol{f}(\boldsymbol{\xi}) = -\boldsymbol{o}_{\boldsymbol{\xi}}^{(2)} \cdot \mathcal{P}_{\tan} \boldsymbol{f}(\boldsymbol{\xi}), \quad O_{\boldsymbol{\xi}}^{(3)} \boldsymbol{f}(\boldsymbol{\xi}) = -\boldsymbol{o}_{\boldsymbol{\xi}}^{(3)} \cdot \mathcal{P}_{\tan} \boldsymbol{f}(\boldsymbol{\xi})$$

if $\boldsymbol{\xi} \in \mathbb{S}$ *and* $\boldsymbol{f} \in \mathbf{C}^1(\mathbb{S})$. *The operators* $\mathcal{P}_{\mathrm{nor}}$, $\mathcal{P}_{\tan}$ *are the projections onto the normal and tangential part of* $\boldsymbol{f}$, *respectively, as defined in Eq.* (2.3).

Lemma 5.7 ([88, Lem. 5.1]). *Let* $F \in \mathrm{C}^2(\mathbb{S})$. *Then the following statements hold true:*

i) If i, $j = 1, 2, 3$ *with* $i \neq j$, *then* $O_{\boldsymbol{\xi}}^{(i)} \boldsymbol{o}_{\boldsymbol{\xi}}^{(j)} F(\boldsymbol{\xi}) = 0$ *for all* $\boldsymbol{\xi} \in \mathbb{S}$.

ii) If $i = 1, 2, 3$ *and* $\boldsymbol{\xi} \in \mathbb{S}$, *then*

$$O_{\boldsymbol{\xi}}^{(i)} \boldsymbol{o}_{\boldsymbol{\xi}}^{(i)} F(\boldsymbol{\xi}) = \begin{cases} F(\boldsymbol{\xi}) & \text{if } i = 1, \\ -\Delta_{\boldsymbol{\xi}}^* F(\boldsymbol{\xi}) & \text{if } i = 2, 3. \end{cases}$$

With these preliminaries, we define the Morse-Feshbach vector spherical harmonics, see [169, 170], in analogy to the scalar-valued case.

Definition 5.8 (Morse-Feshbach Vector Spherical Harmonics, [81, Ch. 12.2]). *Let* $Y_n \in \mathrm{Harm}_n(\mathbb{S})$*, then the vector field*

$$\boldsymbol{y}_n^{(i)} \coloneqq \boldsymbol{o}^{(i)} Y_n, \qquad i = 1,\, 2,\, 3,\, n \in \mathbb{N}_{0_i}$$

is called a Morse-Feshbach vector spherical harmonics *of type* i *and order* n*, where*

$$0_i \coloneqq \begin{cases} 0 & \text{if } i = 1, \\ 1 & \text{if } i = 2, 3 \end{cases} \qquad \text{and} \qquad \mathbb{N}_{0_i} \coloneqq \begin{cases} \mathbb{N}_0 & \text{if } i = 1, \\ \mathbb{N} & \text{if } i = 2, 3. \end{cases}$$

Due to the definition of the $\boldsymbol{o}^{(i)}$-operators, the vector field $\boldsymbol{y}_n^{(1)}$ is a normal field and the fields $\boldsymbol{y}_n^{(2)}$ and $\boldsymbol{y}_n^{(3)}$ are tangential vector fields for all $n \in \mathbb{N}_{0_i}$.

Let the set of scalar-valued spherical harmonics $\{Y_{n,j}\}_{n\in\mathbb{N}_0,\, j=1,\ldots,2n+1}$ be defined as in Definition 2.22, then we define the corresponding Morse-Feshbach vector spherical harmonics by

$$\boldsymbol{y}_{n,j}^{(i)} \coloneqq \left(\mu_n^{(i)}\right)^{-1/2} \boldsymbol{o}^{(i)} Y_{n,j} \tag{5.1}$$

for $i = 1,\, 2,\, 3$, $n \in \mathbb{N}_{0_i}$, and $j = 1, \ldots, 2n+1$, with the normalization factor

$$\mu_n^{(i)} \coloneqq \begin{cases} 1 & \text{if } i = 1, \\ -(\Delta^*)^\wedge(n) = n(n+1) & \text{if } i = 2, 3. \end{cases} \tag{5.2}$$

If $\{Y_{n,j}\}_{n\in\mathbb{N}_0,\, j=1,\ldots,2n+1}$ is an $\mathrm{L}_2(\mathbb{S})$-orthonormal set of (scalar) spherical harmonics, then $\{\boldsymbol{y}_{n,j}^{(i)}\}_{i=1,2,3,\, n\in\mathbb{N}_{0_i},\, j=1,\ldots,2n+1}$ is an $\mathbf{L}_2(\mathbb{S})$-orthonormal system of vector spherical harmonics, see Lemma 5.5. Using a linear combination of the Morse-Feshbach vector spherical harmonics, a second system can be defined, see [61]. First, a related set of operators $\tilde{\boldsymbol{o}}^{(i)} \colon \mathrm{C}^1(\mathbb{S}) \to \mathbf{C}^0(\mathbb{S})$ for $i = 1,\, 2,\, 3$ is defined, see [88, Ch. 5.13]:

$$\begin{aligned} \tilde{\boldsymbol{o}}_{\boldsymbol{\xi}}^{(1)} F(\boldsymbol{\xi}) &\coloneqq \boldsymbol{o}_{\boldsymbol{\xi}}^{(1)} \left(\mathcal{D} + \frac{1}{2}\right) F(\boldsymbol{\xi}) - \boldsymbol{o}_{\boldsymbol{\xi}}^{(2)} F(\boldsymbol{\xi}), \\ \tilde{\boldsymbol{o}}_{\boldsymbol{\xi}}^{(2)} F(\boldsymbol{\xi}) &\coloneqq \boldsymbol{o}_{\boldsymbol{\xi}}^{(1)} \left(\mathcal{D} - \frac{1}{2}\right) F(\boldsymbol{\xi}) + \boldsymbol{o}_{\boldsymbol{\xi}}^{(2)} F(\boldsymbol{\xi}), \\ \tilde{\boldsymbol{o}}_{\boldsymbol{\xi}}^{(3)} F(\boldsymbol{\xi}) &\coloneqq \boldsymbol{o}_{\boldsymbol{\xi}}^{(3)} F(\boldsymbol{\xi}) \end{aligned}$$

for all $F \in \mathrm{C}^1(\mathbb{S})$, where the pseudodifferential operator $\mathcal{D} \coloneqq (-\Delta^* + 1/4)^{1/2}$ of order 1 is characterized by its infinitely often differentiable eigenfunctions $Y_{n,j}$ to the eigenvalues $n + 1/2$, that is

$$\mathcal{D} Y_{n,j} = \left(n + \frac{1}{2}\right) Y_{n,j}, \qquad n \in \mathbb{N}_0, j = 1, \ldots, 2n+1.$$

For more details on the operator and its inverse, the single layer operator, see [91]. Using the singular values of the operator $\mathcal{D}$, an alternative operator $\tilde{\boldsymbol{o}}_n^{(i)} \colon \mathrm{C}^1(\mathbb{S}) \to \mathbf{C}^0(\mathbb{S})$ for $i = 1$,

2, 3 can be defined for all $n \in \mathbb{N}_{0_i}$, see [81] or [88, Eq. (5.282)-(5.284)], for instance. Let $Y_n \in \mathrm{Harm}_n(\mathbb{S})$, then we define for all $n \in \mathbb{N}_{0_i}$ the operators

$$\tilde{\boldsymbol{o}}_n^{(1)} Y_n(\boldsymbol{\xi}) \coloneqq (n+1)\boldsymbol{o}_{\boldsymbol{\xi}}^{(1)} Y_n(\boldsymbol{\xi}) - \boldsymbol{o}_{\boldsymbol{\xi}}^{(2)} Y_n(\boldsymbol{\xi}), \tag{5.3a}$$

$$\tilde{\boldsymbol{o}}_n^{(2)} Y_n(\boldsymbol{\xi}) \coloneqq n\boldsymbol{o}_{\boldsymbol{\xi}}^{(1)} Y_n(\boldsymbol{\xi}) + \boldsymbol{o}_{\boldsymbol{\xi}}^{(2)} Y_n(\boldsymbol{\xi}), \tag{5.3b}$$

$$\tilde{\boldsymbol{o}}_n^{(3)} Y_n(\boldsymbol{\xi}) \coloneqq \tilde{\boldsymbol{o}}^{(3)} Y_n(\boldsymbol{\xi}) = \boldsymbol{o}_{\boldsymbol{\xi}}^{(3)} Y_n(\boldsymbol{\xi}). \tag{5.3c}$$

In contrast to the $\tilde{\boldsymbol{o}}^{(i)}$-operators, the operator $\tilde{\boldsymbol{o}}_n^{(i)}$ depends on $n \in \mathbb{N}_{0_i}$ if $i = 1$ or $i = 2$. However, we have $\tilde{\boldsymbol{o}}^{(i)} Y_n = \tilde{\boldsymbol{o}}_n^{(i)} Y_n$ for all $i = 1, 2, 3$ and $n \in \mathbb{N}_{0_i}$.

Definition 5.9 (Edmonds Vector Spherical Harmonics, [88, Def. 5.54]). *Let $Y_n \in \mathrm{Harm}_n(\mathbb{S})$, then the vector field*

$$\tilde{\boldsymbol{y}}_n^{(i)} \coloneqq \tilde{\boldsymbol{o}}_n^{(i)} Y_n, \qquad i = 1, 2, 3,\ n \in \mathbb{N}_{0_i}$$

is called an Edmonds vector spherical harmonic *of type i and degree n.*

Hence, we call a function an Edmonds vector spherical harmonic of type i, degree n, and order j if it has the representation

$$\tilde{\boldsymbol{y}}_{n,j}^{(1)} \coloneqq \sqrt{\frac{n+1}{2n+1}}\boldsymbol{y}_{n,j}^{(1)} - \sqrt{\frac{n}{2n+1}}\boldsymbol{y}_{n,j}^{(2)}, \tag{5.4a}$$

$$\tilde{\boldsymbol{y}}_{n,j}^{(2)} \coloneqq \sqrt{\frac{n}{2n+1}}\boldsymbol{y}_{n,j}^{(1)} + \sqrt{\frac{n+1}{2n+1}}\boldsymbol{y}_{n,j}^{(2)}, \tag{5.4b}$$

$$\tilde{\boldsymbol{y}}_{n,j}^{(3)} \coloneqq \boldsymbol{y}_{n,j}^{(3)} \tag{5.4c}$$

for all $n \in \mathbb{N}$, see [88, Eq. (5.309)-(5.311)], and we set $\tilde{\boldsymbol{y}}_{0,1}^{(1)} \coloneqq \boldsymbol{y}_{0,1}^{(1)}$ for $n = 0$.

Lemma 5.10 ([88, Thm. 5.56]). *The Edmonds vector spherical harmonics of type i, degree n, and order j are orthogonal in $\mathbf{L}_2(\mathbb{S})$.*

Inverting the system of linear equations given in Eq. (5.4), we get a representation of the Morse-Feshbach vector spherical harmonics in terms of the Edmonds vector spherical harmonics for all $n \in \mathbb{N}_{0_i}$, $j = 1, \ldots, 2n+1$, see [88, Eq. (5.312)-(5.314)]:

$$\boldsymbol{y}_{n,j}^{(1)} = \sqrt{\frac{n+1}{2n+1}}\tilde{\boldsymbol{y}}_{n,j}^{(1)} + \sqrt{\frac{n}{2n+1}}\tilde{\boldsymbol{y}}_{n,j}^{(2)}, \tag{5.5a}$$

$$\boldsymbol{y}_{n,j}^{(2)} = -\sqrt{\frac{n}{2n+1}}\tilde{\boldsymbol{y}}_{n,j}^{(1)} + \sqrt{\frac{n+1}{2n+1}}\tilde{\boldsymbol{y}}_{n,j}^{(2)}, \tag{5.5b}$$

$$\boldsymbol{y}_{n,j}^{(3)} = \tilde{\boldsymbol{y}}_{n,j}^{(3)}. \tag{5.5c}$$

Although the two systems are just linear combinations of each other, they possess different properties. In the next paragraphs, we give a short overview of these properties.

5.2.2. Orthogonality and Completeness of Vector Spherical Harmonics

In analogy to the scalar-valued case, we consider homogeneous harmonic polynomials.

Definition 5.11 ([81, Def. 12.3.1]). *A vector field* $\boldsymbol{h}_n\colon \mathbb{R}^3 \to \mathbb{R}^3$, $n \in \mathbb{N}_0$, *is called a* homogeneous harmonic vector polynomial *of degree* n *if* $\boldsymbol{h}_n \cdot \boldsymbol{\varepsilon}^i$ *is a homogeneous harmonic polynomial of degree* n *for every* $i = 1, 2, 3$.

Using the abbreviation

$$\mathrm{Harm}_n(\mathbb{R}^3)\boldsymbol{\varepsilon}^i \coloneqq \left\{ H_n\boldsymbol{\varepsilon}^i \;\middle|\; H_n \in \mathrm{Harm}_n(\mathbb{R}^3) \right\},$$

we characterize the space of all homogeneous harmonic vector polynomials of degree n by

$$\bigoplus_{i=1}^{3} \mathrm{Harm}_n(\mathbb{R}^3)\boldsymbol{\varepsilon}^i.$$

The restriction of homogeneous harmonic scalar polynomials of degree n to the unit sphere $\mathbb{S}$ is a scalar spherical harmonic by definition. In the vectorial case, however, such a restriction of homogeneous harmonic vector polynomials of degree n does not yield a Morse-Feshbach vector spherical harmonic of degree n.

Definition 5.12 ([81, Def. 12.3.2]). *For* $n \in \mathbb{N}_0$, $H_n \in \mathrm{Hom}_n(\mathbb{R}^3)$, *and* $i = 1, 2, 3$, *the extensions of the operators* $\tilde{\boldsymbol{o}}_n^{(i)}\colon \mathbb{R}^3 \to \mathbb{R}^3$ *are defined for* $\boldsymbol{x} \in \mathbb{R}^3$ *by*

$$\begin{aligned}
\tilde{\boldsymbol{o}}_n^{(1)} H_n(\boldsymbol{x}) &\coloneqq ((2n+1)\boldsymbol{x} - x^2\boldsymbol{\nabla}_{\boldsymbol{x}})H_n(\boldsymbol{x}),\\
\tilde{\boldsymbol{o}}_n^{(2)} H_n(\boldsymbol{x}) &\coloneqq \boldsymbol{\nabla}_{\boldsymbol{x}} H_n(\boldsymbol{x}),\\
\tilde{\boldsymbol{o}}_n^{(3)} H_n(\boldsymbol{x}) &\coloneqq \boldsymbol{x} \wedge \boldsymbol{\nabla}_{\boldsymbol{x}} H_n(\boldsymbol{x}).
\end{aligned}$$

In the case of $H_n(r\boldsymbol{\xi}) = r^n Y_n(\boldsymbol{\xi})$, we can see that $(\tilde{\boldsymbol{o}}_n^{(i)} H_n(\boldsymbol{x}))|_{x=1}$ coincides with the previous definition of the $\tilde{\boldsymbol{o}}_n^{(i)}$-operators in Eq. (5.3) for $i = 1, 2, 3$ by using the representation of the gradient in polar coordinates: let $\boldsymbol{x} = r\boldsymbol{\xi}$, $\boldsymbol{\xi} \in \mathbb{S}$, then

$$\begin{aligned}
\boldsymbol{\nabla}_{\boldsymbol{x}}\left(r^n Y_n(\boldsymbol{\xi})\right) &= \left(\boldsymbol{\xi}\frac{\partial}{\partial r} + \frac{1}{r}\boldsymbol{\nabla}_{\boldsymbol{\xi}}^*\right)\left(r^n Y_n(\boldsymbol{\xi})\right)\\
&= r^{n-1}\left(n\boldsymbol{\xi} + \boldsymbol{\nabla}_{\boldsymbol{\xi}}^*\right) Y_n(\boldsymbol{\xi})\\
&= r^{n-1}\left(n\boldsymbol{o}_{\boldsymbol{\xi}}^{(1)} Y_n(\boldsymbol{\xi}) + \boldsymbol{o}_{\boldsymbol{\xi}}^{(2)} Y_n(\boldsymbol{\xi})\right)\\
&= r^{n-1}\tilde{\boldsymbol{o}}_n^{(2)} Y_n(\boldsymbol{\xi}). \qquad (5.6)
\end{aligned}$$

The relation corresponding to $i = 3$ can be easily seen by using Eq. (2.5). Hence, regarding the construction of the Edmonds vector spherical harmonics, we observe that these functions are restrictions of harmonic polynomials to the unit sphere.

Lemma 5.13 ([81, Lem. 12.3.3]). *Let* $H_n \in \mathrm{Harm}_n(\mathbb{R}^3)$, *where* $n \in \mathbb{N}_0$. *Then* $\tilde{\boldsymbol{o}}_n^{(i)} H_n$ *is a homogeneous harmonic vector polynomial of degree* $\deg^{(i)}(n)$ *(i.e.* $\tilde{\boldsymbol{o}}_n^{(i)} H_n$ *is an element of* $\oplus_{j=1}^{3} \mathrm{Harm}_{\deg^{(i)}(n)}(\mathbb{R}^3)\boldsymbol{\varepsilon}^j$*) for* $i = 1, 2, 3$, *where we use the abbreviation*

$$\deg^{(i)}(n) \coloneqq \begin{cases} n+1 & \text{if } i = 1,\\ n-1 & \text{if } i = 2,\\ n & \text{if } i = 3. \end{cases}$$

If $\deg^{(i)}(n) < 0$, *then* $\tilde{\boldsymbol{o}}_n^{(i)} H_n = 0$.

In contrast to this result, the Morse-Feshbach vector spherical harmonics of type $i = 1$, 2 are restrictions of vector polynomials of mixed degree, which is easy to see by using Lemma 5.13 and Eq. (5.5). Due to this property, we define the vector-valued space $\mathbf{harm}_n(\mathbb{S})$ by means of the Edmonds vector spherical harmonics. In contrast to this approach, spaces by means of the Morse-Feshbach vector spherical harmonics are constructed in [81].

Definition 5.14 (Vector-valued $\mathbf{harm}_n^{(i)}(\mathbb{S})$-Spaces, [88, Ch. 5.14]). *Let $n \in \mathbb{N}_0$, the set $\mathbf{harm}_n^{(i)}(\mathbb{S})$ denotes the set of all Edmonds vector spherical harmonics of type i and order n. More precisely,*

$$\begin{aligned}
\mathbf{harm}_0(\mathbb{S}) &\coloneqq \mathbf{harm}_0^{(1)}(\mathbb{S}), \\
\mathbf{harm}_n(\mathbb{S}) &\coloneqq \bigoplus_{i=1}^{3} \mathbf{harm}_n^{(i)}(\mathbb{S}), \qquad n \geq 1, \\
\mathbf{harm}_{p,\dots,q}^{(i)}(\mathbb{S}) &\coloneqq \bigoplus_{n=p}^{q} \mathbf{harm}_n^{(i)}(\mathbb{S}), \qquad p, q \in \mathbb{N},\ p \leq q.
\end{aligned}$$

Note that if $\tilde{\boldsymbol{o}}_n^{(i)} Y_n \in \mathbf{harm}_n^{(i)}(\mathbb{S})$, the n in $\mathbf{harm}_n^{(i)}(\mathbb{S})$ represents the degree of the scalar spherical harmonics Y_n and does not represent the degree $\deg^{(i)}(n)$ of $\tilde{\boldsymbol{o}}_n^{(i)} Y_n$ before the restriction onto the unit sphere.

Using the orthogonality of the (scalar) spherical harmonics, Lemma 5.5, and the properties of the $\tilde{\boldsymbol{o}}_n^{(i)}$-operators, it is easy to see that $\mathbf{harm}_n^{(i)}(\mathbb{S})$ is $\mathbf{L}_2(\mathbb{S})$-orthogonal to $\mathbf{harm}_m^{(i)}(\mathbb{S})$ if $n \neq m$. In order to expand functions by means of these vector spherical harmonics, we need the following result.

Theorem 5.15. *Let the two sets of vector spherical harmonics $\{\boldsymbol{y}_{n,j}^{(i)}\}_{i=1,2,3,\, n\in\mathbb{N}_{0_i},\, j=1,\dots,2n+1}$ and $\{\tilde{\boldsymbol{y}}_{n,j}^{(i)}\}_{i=1,2,3,\, n\in\mathbb{N}_{0_i},\, j=1,\dots,2n+1}$ be defined as in Eqs. (5.1) and (5.4), respectively. Then the following statements are valid:*

i) The two systems of vector spherical harmonics are closed in $\mathbf{C}(\mathbb{S})$ with respect to the $\|\cdot\|_{\mathbf{C}(\mathbb{S})}$-norm, see [81, Thm. 12.3.5].

ii) The two systems are complete in $\mathbf{L}_2(\mathbb{S})$ with respect to the $\langle\cdot,\cdot\rangle_{\mathbf{L}_2(\mathbb{S})}$-inner product, see [88, Thm. 5.56].

A more recent proof of the $\mathbf{L}_2(\mathbb{S})$-completeness of the Morse-Feshbach system involving Bernstein's kernels is given in [83]. Hence, all $\boldsymbol{f} \in \mathbf{L}_2(\mathbb{S})$ have the unique expansions

$$\boldsymbol{f} = \sum_{i=1}^{3} \sum_{n=0_i}^{\infty} \sum_{j=1}^{2n+1} \left\langle \boldsymbol{f}, \boldsymbol{y}_{n,j}^{(i)} \right\rangle_{\mathbf{L}_2(\mathbb{S})} \boldsymbol{y}_{n,j}^{(i)} = \sum_{i=1}^{3} \sum_{n=0_i}^{\infty} \sum_{j=1}^{2n+1} \left\langle \boldsymbol{f}, \tilde{\boldsymbol{y}}_{n,j}^{(i)} \right\rangle_{\mathbf{L}_2(\mathbb{S})} \tilde{\boldsymbol{y}}_{n,j}^{(i)}.$$

5.2.3. Harmonicity of Vector Spherical Harmonics

Since the Beltrami operator plays an important role in the theory of the scalar-valued spherical harmonics, we now discuss its role in the vector-valued setting. As usual, the vector-valued Laplacian is defined as the component-wise application of the (scalar) Laplacian. Analogously, we define the vectorial Beltrami operator $\boldsymbol{\Delta}^*$. If $\boldsymbol{f} \in \mathbf{C}^2(\mathbb{S})$ is of the form

$$\boldsymbol{f}(\boldsymbol{\xi}) = \sum_{j=1}^{3} \boldsymbol{\varepsilon}^j F_j(\boldsymbol{\xi}), \qquad \boldsymbol{\xi} \in \mathbb{S},$$

then, in accordance with [81, Eq. (12.5.1.)], we define

$$\boldsymbol{\Delta}^* \boldsymbol{f}(\boldsymbol{\xi}) \coloneqq \sum_{j=1}^{3} \boldsymbol{\varepsilon}^j \Delta^* F_j(\boldsymbol{\xi}), \qquad \boldsymbol{\xi} \in \mathbb{S}. \tag{5.7}$$

We can now apply the vectorial Beltrami operator to Morse-Feshbach vector spherical harmonics.

Corollary 5.16 ([81, Eq. (12.5.2.)]). *If $Y_n \in \operatorname{Harm}_n(\mathbb{S})$, then*

$$\begin{aligned}
\boldsymbol{\Delta}^* \boldsymbol{o}^{(1)} Y_n &= (-n(n+1) - 2)\boldsymbol{o}^{(1)} Y_n + 2\boldsymbol{o}^{(2)} Y_n, \\
\boldsymbol{\Delta}^* \boldsymbol{o}^{(2)} Y_n &= 2n(n+1)\boldsymbol{o}^{(1)} Y_n - n(n+1)\boldsymbol{o}^{(2)} Y_n, \\
\boldsymbol{\Delta}^* \boldsymbol{o}^{(3)} Y_n &= -n(n+1)\boldsymbol{o}^{(3)} Y_n.
\end{aligned}$$

This shows that the Morse-Feshbach vector spherical harmonics are not eigenfunctions of the (vectorial) Beltrami operator given in Eq. (5.7). However, in [81] another vectorial differential operator is constructed that has the Morse-Feshbach vector spherical harmonics as eigenfunctions. Now, we are able to define a new differential operator ${}^*\boldsymbol{\Delta}_{\boldsymbol{\xi}}$ by means of the vectorial Beltrami operator that has the Morse-Feshbach vector spherical harmonics as eigenfunctions.

Lemma 5.17 ([81, p. 333]). *Let ${}^*\boldsymbol{\Delta}_{\boldsymbol{\xi}}$ be given by*

$${}^*\boldsymbol{\Delta}_{\boldsymbol{\xi}} \boldsymbol{f}(\boldsymbol{\xi}) \coloneqq \boldsymbol{\Delta}^*_{\boldsymbol{\xi}} \boldsymbol{f}(\boldsymbol{\xi}) - 2\boldsymbol{L}^*_{\boldsymbol{\xi}} \wedge \boldsymbol{f}(\boldsymbol{\xi}) - 2\boldsymbol{f}(\boldsymbol{\xi})$$

for all $\boldsymbol{f} \in \mathbf{C}^2(\mathbb{S})$. Then ${}^*\boldsymbol{\Delta}_{\boldsymbol{\xi}} \boldsymbol{y}^{(i)}_{n,j}(\boldsymbol{\xi}) = -n(n+1)\boldsymbol{y}^{(i)}_{n,j}(\boldsymbol{\xi})$ for all $i = 1, 2, 3$, $n \in \mathbb{N}_{0_i}$, and $j = 1, \ldots, 2n+1$.

Lemma 5.18 ([81, Lem. 12.5.3]). *If $F \colon \mathbb{S} \to \mathbb{R}$ and $\boldsymbol{f} \colon \mathbb{S} \to \mathbb{R}^3$ are sufficiently smooth, then*

$$\begin{aligned}
{}^*\boldsymbol{\Delta} \boldsymbol{o}^{(i)} F &= \boldsymbol{o}^{(i)} \Delta^* F, \\
O^{(i)} \, {}^*\boldsymbol{\Delta} \boldsymbol{f} &= \Delta^* O^{(i)} \boldsymbol{f}
\end{aligned}$$

holds for $i = 1, 2, 3$.

In contrast, the Edmonds vector spherical harmonics are eigenfunctions of the vectorial Beltrami operator defined in Eq. (5.7), see [88, Thm. 5.56], that is

$$\boldsymbol{\Delta}^* \tilde{\boldsymbol{o}}^{(1)}_n Y_n = -(n+1)(n+2)\tilde{\boldsymbol{o}}^{(1)}_n Y_n, \tag{5.8a}$$
$$\boldsymbol{\Delta}^* \tilde{\boldsymbol{o}}^{(2)}_n Y_n = -n(n-1)\tilde{\boldsymbol{o}}^{(2)}_n Y_n, \tag{5.8b}$$
$$\boldsymbol{\Delta}^* \tilde{\boldsymbol{o}}^{(3)}_n Y_n = -n(n+1)\tilde{\boldsymbol{o}}^{(2)}_n Y_n. \tag{5.8c}$$

Hence, the vector fields $\boldsymbol{x} \mapsto \tilde{\boldsymbol{o}}^{(i)}_n H_n(\boldsymbol{x})$ with $\boldsymbol{x} \in \mathbb{R}^3$ and $i = 1, 2, 3$ satisfy

$$\boldsymbol{\Delta} \tilde{\boldsymbol{o}}^{(i)}_n H_n = \mathbf{0}, \qquad i = 1, 2, 3, \tag{5.9}$$

where $H_n(\boldsymbol{x}) \coloneqq r^n Y_n(\boldsymbol{\xi})$ with $\boldsymbol{x} = r\boldsymbol{\xi}$, see [88, Rem. 5.66].

5.2.4. Decomposition of $\mathbf{L}_2(\mathbb{S})$ via Vector Spherical Harmonics

Due to the orthogonality properties, we are able to decompose the space $\mathbf{L}_2(\mathbb{S})$ by means of the Morse-Feshbach vector spherical harmonics. Any vector field can be written out as $\boldsymbol{f}(\boldsymbol{\xi}) = \sum_{i=1}^{3} \boldsymbol{o}_{\boldsymbol{\xi}}^{(i)} F_i(\boldsymbol{\xi})$ for $\boldsymbol{\xi} \in \mathbb{S}$ with uniquely determined functions $F_i \colon \mathbb{S} \to \mathbb{R}$, see [81]. Sometimes this decomposition is named after Helmholtz. In [79], it is called the *spherical Helmholtz decomposition*.

Theorem 5.19 (Spherical Helmholtz Decomposition, [88, Thm. 12.4.1]). *Let the function $\boldsymbol{f} \colon \mathbb{S} \to \mathbb{R}^3$ be a continuously differentiable vector field. Then there exist uniquely determined functions $F_1 \in \mathrm{C}^1(\mathbb{S})$, $F_2, F_3 \in \mathrm{C}^2(\mathbb{S})$ satisfying*

$$\int_{\mathbb{S}} F_i(\boldsymbol{\xi}) \, \mathrm{d}\omega(\boldsymbol{\xi}) = 0, \qquad i = 2,\ 3$$

such that $\boldsymbol{f} = \sum_{i=1}^{3} \boldsymbol{o}^{(i)} F_i$.

Note that without the constraint $\int_{\mathbb{S}} F_i(\boldsymbol{\xi}) \, \mathrm{d}\omega(\boldsymbol{\xi}) = 0$ for $i = 2, 3$ we only get uniqueness up to an additional constant for those F_i.

Thus, the Morse-Feshbach vector spherical harmonics yield an orthogonal decomposition into the normal and the tangential part of a function, see [81, Ch. 12.4], that is

$$\begin{aligned} \mathbf{L}_2^{(i)}(\mathbb{S}) &= \overline{\{\boldsymbol{o}^{(i)} F \mid F \in \mathrm{C}^\infty(\mathbb{S})\}}^{\|\cdot\|_{\mathbf{L}_2(\mathbb{S})}}, \\ \mathbf{L}_2(\mathbb{S}) &= \mathbf{L}_2^{(1)}(\mathbb{S}) \oplus \mathbf{L}_2^{(2)}(\mathbb{S}) \oplus \mathbf{L}_2^{(3)}(\mathbb{S}). \end{aligned} \tag{5.10}$$

Finally, we can decompose every vector field $\boldsymbol{f} \in \mathbf{L}_2(\mathbb{S})$ into $\boldsymbol{f} = \sum_{i=1}^{3} \boldsymbol{f}^{(i)}$ with $\boldsymbol{f}^{(i)} \in \mathbf{L}_2^{(i)}(\mathbb{S})$ and

$$\boldsymbol{f}^{(i)} = \sum_{n=0_i}^{\infty} \sum_{j=1}^{2n+1} \left\langle \boldsymbol{f}, \boldsymbol{y}_{n,j}^{(i)} \right\rangle_{\mathbf{L}_2(\mathbb{S})} \boldsymbol{y}_{n,j}^{(i)} \tag{5.11}$$

for $i = 1, 2, 3$. Here, we used the notation introduced after Corollary 2.26.

The Edmonds vector spherical harmonics, of course, do not provide us with a decomposition into normal and tangential parts. In contrast, the Edmonds vector spherical harmonics decompose a harmonic gradient field into parts that are related to the inner harmonics and parts that are related to the outer harmonics. This can be seen in the following lemma.

Lemma 5.20 ([79, Thm. 2.54]). *Let r, $R > 0$ and $\boldsymbol{x} = r\boldsymbol{\xi}$, $\boldsymbol{\xi} \in \mathbb{S}$, then we get*

$$\begin{aligned} \boldsymbol{\nabla}_{\boldsymbol{x}} H_{n,j}^{\mathrm{int}}(R; \boldsymbol{x}) &= \frac{1}{R^2} \left(\frac{r}{R} \right)^{n-1} \sqrt{n(2n+1)} \tilde{\boldsymbol{y}}_{n,j}^{(2)}(\boldsymbol{\xi}), \\ -\boldsymbol{\nabla}_{\boldsymbol{x}} H_{n,j}^{\mathrm{ext}}(R; \boldsymbol{x}) &= \frac{1}{R^2} \left(\frac{R}{r} \right)^{n+2} \sqrt{(n+1)(2n+1)} \tilde{\boldsymbol{y}}_{n,j}^{(1)}(\boldsymbol{\xi}) \end{aligned}$$

for $n \in \mathbb{N}_{0_i}$, $i = 1, 2$, respectively, and $j = 1, \ldots, 2n+1$.

Every vector field $\boldsymbol{f} \in \mathbf{L}_2(\mathbb{S})$ can also be represented by

$$\boldsymbol{f} = \sum_{i=1}^{3} \tilde{\boldsymbol{f}}^{(i)}, \qquad \tilde{\boldsymbol{f}}^{(i)} = \sum_{n=0_i}^{\infty} \sum_{j=1}^{2n+1} \left\langle \boldsymbol{f}, \tilde{\boldsymbol{y}}_{n,j}^{(i)} \right\rangle_{\mathbf{L}_2(\mathbb{S})} \tilde{\boldsymbol{y}}_{n,j}^{(i)}, \quad i = 1, 2, 3,$$

in the $\mathbf{L}_2(\mathbb{S})$-sense due to Eq. (5.4), Theorem 5.15, and Lemma 5.10.

5.3. Vector Legendre Polynomials

In Eq. (3.4) and Eq. (4.23), we show that the integral kernels of the magnetoencephalography as well as the electroencephalography integral equation are given as the surface curl operator or the gradient, respectively, applied to (a series of) Legendre polynomials. In addition, in the previous section, we state that these particular differential operators are closely related to the Morse-Feshbach and Edmonds vector spherical harmonics. In analogy to the two systems of vector spherical harmonics, we now define two sets of vector-valued Legendre polynomials.

Definition 5.21 (Vector Legendre Polynomials [88, Lem. 5.63]). *Let $\boldsymbol{\xi}$, $\boldsymbol{\eta} \in \mathbb{S}$ and P_n be defined as in Definition 2.5, then for $i = 1, 2, 3$ and $n \in \mathbb{N}_{0_i}$*

$$\begin{aligned}\boldsymbol{p}_n^{(i)}(\boldsymbol{\xi},\boldsymbol{\eta}) &\coloneqq \left(\mu_n^{(i)}\right)^{-1/2} \boldsymbol{o}_{\boldsymbol{\xi}}^{(i)} P_n(\boldsymbol{\xi}\cdot\boldsymbol{\eta}),\\ \tilde{\boldsymbol{p}}_n^{(i)}(\boldsymbol{\xi},\boldsymbol{\eta}) &\coloneqq \left(\tilde{\mu}_n^{(i)}\right)^{-1/2} \tilde{\boldsymbol{o}}_{\boldsymbol{\xi}}^{(i)} P_n(\boldsymbol{\xi}\cdot\boldsymbol{\eta})\end{aligned}$$

are called the Morse-Feshbach and Edmonds vector Legendre polynomials, respectively, of type i and degree n, where

$$\tilde{\mu}_n^{(i)} \coloneqq \begin{cases} (n+1)(2n+1) & \text{if } i = 1,\\ n(2n+1) & \text{if } i = 2,\\ n(n+1) & \text{if } i = 3.\end{cases}$$

Recall that $\boldsymbol{o}_{\boldsymbol{\xi}}^{(i)}$ is defined as in Definition 5.4 and 0_i as in Definition 5.8 for $i = 1, 2, 3$. In analogy to Eq. (5.4), vector Legendre polynomials of one type can be represented as linear combinations of the other type:

$$\tilde{\boldsymbol{p}}_n^{(1)}(\boldsymbol{\xi},\boldsymbol{\eta}) = \sqrt{\frac{n+1}{2n+1}}\boldsymbol{p}_n^{(1)}(\boldsymbol{\xi},\boldsymbol{\eta}) - \sqrt{\frac{n}{2n+1}}\boldsymbol{p}_n^{(2)}(\boldsymbol{\xi},\boldsymbol{\eta}) \tag{5.12a}$$

$$\tilde{\boldsymbol{p}}_n^{(2)}(\boldsymbol{\xi},\boldsymbol{\eta}) = \sqrt{\frac{n}{2n+1}}\boldsymbol{p}_n^{(1)}(\boldsymbol{\xi},\boldsymbol{\eta}) + \sqrt{\frac{n+1}{2n+1}}\boldsymbol{p}_n^{(2)}(\boldsymbol{\xi},\boldsymbol{\eta}), \tag{5.12b}$$

$$\tilde{\boldsymbol{p}}_n^{(3)}(\boldsymbol{\xi},\boldsymbol{\eta}) = \boldsymbol{p}_n^{(3)}(\boldsymbol{\xi},\boldsymbol{\eta}). \tag{5.12c}$$

For the analysis of the MEG and EEG integral kernels, certain estimates of the vector Legendre polynomials are required, which are stated below.

Lemma 5.22. *Let $\boldsymbol{\xi}$, $\boldsymbol{\eta} \in \mathbb{S}$, then the vector Legendre polynomials fulfil for all $i = 1, 2, 3$ and $n \in \mathbb{N}_{0_i}$ the estimates*

$$|\boldsymbol{p}_n^{(i)}(\boldsymbol{\xi},\boldsymbol{\eta})| \leq \sqrt{\mu_n^{(i)}} \quad \text{and} \quad |\tilde{\boldsymbol{p}}_n^{(i)}(\boldsymbol{\xi},\boldsymbol{\eta})| \leq \sqrt{\tilde{\mu}_n^{(i)}}.$$

Proof. The first statement is proved in [88, Lem. 5.23]. Thus, we only prove the inequality concerning $\tilde{\boldsymbol{p}}_n^{(1)}$ because the proof of $\tilde{\boldsymbol{p}}_n^{(2)}$ can be obtained equally and the third is clear due

to $\tilde{\boldsymbol{p}}_n^{(3)} = \boldsymbol{p}_n^{(3)}$. By means of the orthogonality, see Lemma 5.5, we obtain

$$\begin{aligned}
\left|\tilde{\boldsymbol{p}}_n^{(1)}(\boldsymbol{\xi},\boldsymbol{\eta})\right|^2 &= \left|\sqrt{\frac{n+1}{2n+1}}\boldsymbol{p}_n^{(1)}(\boldsymbol{\xi},\boldsymbol{\eta}) - \sqrt{\frac{n}{2n+1}}\boldsymbol{p}_n^{(2)}(\boldsymbol{\xi},\boldsymbol{\eta})\right|^2 \\
&= \frac{n+1}{2n+1}\left|\boldsymbol{p}_n^{(1)}(\boldsymbol{\xi},\boldsymbol{\eta})\right|^2 + \frac{n}{2n+1}\left|\boldsymbol{p}_n^{(2)}(\boldsymbol{\xi},\boldsymbol{\eta})\right|^2 \\
&\leq \frac{n+1}{2n+1} + \frac{n}{2n+1}n(n+1) \leq \frac{2n^2(n+1)}{2n+1} \\
&\leq \frac{(2n+1)^2(n+1)}{2n+1} = (2n+1)(n+1). \qquad \square
\end{aligned}$$

Corollary 5.23. *For all $n \in \mathbb{N}_{0_i}$ and all $\boldsymbol{\xi} \in \mathbb{S}$, we get with Lemma 5.22 the estimates*

$$\begin{aligned}
\left|\boldsymbol{\Delta}_{\boldsymbol{\xi}}^* \boldsymbol{p}_n^{(1)}(\boldsymbol{\xi},\boldsymbol{\eta})\right| &\leq 4n(n+1), \\
\left|\boldsymbol{\Delta}_{\boldsymbol{\xi}}^* \boldsymbol{p}_n^{(2)}(\boldsymbol{\xi},\boldsymbol{\eta})\right| &\leq 3n^{3/2}(n+1)^{3/2}, \\
\left|\boldsymbol{\Delta}_{\boldsymbol{\xi}}^* \boldsymbol{p}_n^{(3)}(\boldsymbol{\xi},\boldsymbol{\eta})\right| &\leq n^{3/2}(n+1)^{3/2}.
\end{aligned}$$

Proof. For $n = 0$, the estimates are clear. For $n \in \mathbb{N}$, we use Corollary 5.16 combined with Theorem 2.25 that provides us with formulae to interchange the Beltrami operator with the $\boldsymbol{o}^{(i)}$ operator in the definition of the vectorial Legendre polynomials, see Definition 5.21. Thus, in the case $i = 1$, we have

$$\left|\boldsymbol{\Delta}_{\boldsymbol{\xi}}^* \boldsymbol{p}_n^{(1)}(\boldsymbol{\xi},\boldsymbol{\eta})\right| \leq \left|(-n(n+1)-2)\boldsymbol{p}_n^{(1)}(\boldsymbol{\xi},\boldsymbol{\eta}) + 2\boldsymbol{p}_n^{(2)}(\boldsymbol{\xi},\boldsymbol{\eta})\right|.$$

Next, we apply the triangle inequality to the right-hand side and Lemma 5.22 to each summand and obtain the desired estimate, that is

$$\begin{aligned}
\left|\boldsymbol{\Delta}_{\boldsymbol{\xi}}^* \boldsymbol{p}_n^{(1)}(\boldsymbol{\xi},\boldsymbol{\eta})\right| &\leq (n(n+1)+2) + 2\sqrt{n(n+1)} \\
&\leq n(n+1) + n + 1 + 2\sqrt{(n+1)(n+1)} \\
&\leq n(n+1) + n(n+1) + 2n(n+1).
\end{aligned}$$

The other two cases can be estimated analogously. $\square$

With this preliminary work, we can formulate the Addition Theorem in the vectorial case, see [88]. This Addition Theorem will be frequently used within this thesis.

Theorem 5.24 (Addition Theorem [88, Thm. 5.46]). *Let $\boldsymbol{\xi}$, $\boldsymbol{\eta} \in \mathbb{S}$ and $\boldsymbol{y}_{n,j}^{(i)}$ be defined as in Eq. (5.1) for $i = 1, 2, 3$, $n \in \mathbb{N}_{0_i}$, and $j = 1, \ldots, 2n+1$. Then the following holds true:*

$$\sum_{j=1}^{2n+1} \boldsymbol{y}_{n,j}^{(i)}(\boldsymbol{\xi}) Y_{n,j}(\boldsymbol{\eta}) = \frac{2n+1}{4\pi} \boldsymbol{p}_n^{(i)}(\boldsymbol{\xi},\boldsymbol{\eta}). \tag{5.13}$$

In accordance with [88, Thm. 5.64], an immediate consequence of this formula is for all $n \in \mathbb{N}_{0_i}$ the identity

$$\sum_{j=1}^{2n+1} \tilde{\boldsymbol{y}}_{n,j}^{(i)}(\boldsymbol{\xi}) Y_{n,j}(\boldsymbol{\eta}) = \frac{2n+1}{4\pi} \tilde{\boldsymbol{p}}_n^{(i)}(\boldsymbol{\xi},\boldsymbol{\eta}), \qquad \boldsymbol{\xi},\ \boldsymbol{\eta} \in \mathbb{S}. \tag{5.14}$$

Thus, we obtain a useful norm estimate for the vector spherical harmonics, which is taken from [88, Lem. 5.37] in the case of Edmonds vector spherical harmonics and from [88, Lem. 5.38] for Morse-Feshbach vector spherical harmonics.

Corollary 5.25. *Let* $\boldsymbol{y}_{n,j}^{(i)}$ *be defined as in Eq.* (5.1) *and* $\tilde{\boldsymbol{y}}_{n,j}^{(i)}$ *as in Eq.* (5.4) *for* $i = 1, 2, 3$, $n \in \mathbb{N}_{0_i}$, *and* $j = 1, \dots, 2n+1$. *Then we have*

$$\sum_{j=1}^{2n+1} \left|\boldsymbol{y}_{n,j}^{(i)}(\boldsymbol{\xi})\right|^2 = \sum_{j=1}^{2n+1} \left|\tilde{\boldsymbol{y}}_{n,j}^{(i)}(\boldsymbol{\xi})\right|^2 = \frac{2n+1}{4\pi}$$

and, thus,

$$\left\|\boldsymbol{y}_{n,j}^{(i)}\right\|_{\mathbf{C}(\mathbb{S})} \leq \sqrt{\frac{2n+1}{4\pi}}, \qquad \left\|\tilde{\boldsymbol{y}}_{n,j}^{(i)}\right\|_{\mathbf{C}(\mathbb{S})} \leq \sqrt{\frac{2n+1}{4\pi}}.$$

Note that the proof in the case of the Edmonds vector spherical harmonics is an immediate consequence of the Morse-Feshbach proof if the orthogonality of the Morse-Feshbach vector spherical harmonics is used wisely.

The vectorial Addition Theorem provides us with a kind of reproducing property of the vector Legendre polynomials.

Corollary 5.26 ([88, Thm. 5.64]). *Consider the Morse-Feshbach vector Legendre polynomials, then*

$$\int_{\mathbb{S}} \boldsymbol{y}_{n,j}^{(i)}(\boldsymbol{\xi}) \cdot \boldsymbol{p}_k^{(\iota)}(\boldsymbol{\xi}, \boldsymbol{\eta}) \,\mathrm{d}\omega(\boldsymbol{\xi}) = \frac{4\pi}{2n+1} Y_{n,j}(\boldsymbol{\eta}) \delta_{n,k} \delta_{i,\iota}, \qquad \boldsymbol{\eta} \in \mathbb{S},$$

for all $i, \iota \in \{1, 2, 3\}$, $k \in \mathbb{N}_{0_\iota}$, $n \in \mathbb{N}_{0_i}$, *and* $j = 1, \dots, 2n+1$.

Proof. We simply calculate the inner product by means of the vectorial Addition Theorem 5.24 and get for all $i, \iota \in \{1, 2, 3\}$, $k \in \mathbb{N}_{0_\iota}$, $n \in \mathbb{N}_{0_i}$, and $j = 1, \dots, 2n+1$ the identity

$$\begin{aligned}\int_{\mathbb{S}} \boldsymbol{y}_{n,j}^{(i)}(\boldsymbol{\xi}) \cdot \boldsymbol{p}_k^{(\iota)}(\boldsymbol{\xi}, \boldsymbol{\eta}) \,\mathrm{d}\omega(\boldsymbol{\xi}) &= \sum_{l=1}^{2k+1} \frac{4\pi}{2k+1} \int_{\mathbb{S}} \boldsymbol{y}_{n,j}^{(i)}(\boldsymbol{\xi}) \cdot \boldsymbol{y}_{k,l}^{(\iota)}(\boldsymbol{\xi}) \,\mathrm{d}\omega(\boldsymbol{\xi}) Y_{k,l}(\boldsymbol{\eta}) \\ &= \frac{4\pi}{2n+1} Y_{n,j}(\boldsymbol{\eta}) \delta_{n,k} \delta_{i,\iota}.\end{aligned}$$

□

5.4. Vector Outer Harmonics

Gradient fields, such as the magnetic field, of harmonic functions are closely related to gradients of inner and outer harmonics, which are introduced in Section 2.4.2. Thus, we can define the vector-valued analogues of outer harmonics by applying the gradient to them. Due to the usage of the gradient, these vector outer harmonics are related to the Edmonds vector spherical harmonics. In this section, some properties of vector outer harmonics are summarized. For the proofs and more details, see [79, 184], for example.

Definition 5.27 (Vector Outer Harmonics [79, Def. 2.55]). *The* vector outer harmonics $\boldsymbol{h}_{n,j}^{(i)}(R; \cdot)$ *of degree* n, *order* j, *and type* i *belonging to the sphere* $\mathbb{S}_R$ *are defined*

by

$$\begin{aligned}\boldsymbol{h}_{n,j}^{(1)}(R;\boldsymbol{x}) &\coloneqq \frac{1}{R}\left(\frac{R}{x}\right)^{n+2}\tilde{\boldsymbol{y}}_{n,j}^{(1)}(\hat{\boldsymbol{x}}),\\ \boldsymbol{h}_{n,j}^{(2)}(R;\boldsymbol{x}) &\coloneqq \frac{1}{R}\left(\frac{R}{x}\right)^{n}\tilde{\boldsymbol{y}}_{n,j}^{(2)}(\hat{\boldsymbol{x}}),\\ \boldsymbol{h}_{n,j}^{(3)}(R;\boldsymbol{x}) &\coloneqq \frac{1}{R}\left(\frac{R}{x}\right)^{n+1}\tilde{\boldsymbol{y}}_{n,j}^{(3)}(\hat{\boldsymbol{x}})\end{aligned}$$

for $n \in \mathbb{N}_{0_i}$, $j = 1,\dots,2n+1$, *and* $\boldsymbol{x} \in \mathbb{R}^3 \setminus \{\mathbf{0}\}$.

Like their scalar-valued analogues, they satisfy the following properties.

Remark 5.28 ([79, Rem. 2.56]). *The vector outer harmonics* $\boldsymbol{h}_{n,j}^{(i)}(R;\cdot)$ *satisfy the listed properties:*

- $\boldsymbol{h}_{n,j}^{(i)}(R;\cdot)$ *is of class* $\mathbf{C}^\infty(\mathbb{R}^3 \setminus \{\mathbf{0}\})$,
- $\boldsymbol{\Delta}_{\boldsymbol{x}}\boldsymbol{h}_{n,j}^{(i)}(R;\boldsymbol{x}) = \mathbf{0}$ *for* $\boldsymbol{x} \in \mathbb{R}^3 \setminus \{\mathbf{0}\}$, *that is every component function satisfies the Laplace equation,*
- $\boldsymbol{h}_{n,j}^{(i)}(R;\cdot)|_{\mathbb{S}_R} = \frac{1}{R}\tilde{\boldsymbol{y}}_{n,j}^{(i)}$,
- $\langle \boldsymbol{h}_{n,j}^{(i)}(R;\cdot)|_{\mathbb{S}_R}, \boldsymbol{h}_{m,l}^{(k)}(R;\cdot)|_{\mathbb{S}_R}\rangle_{\mathbf{L}_2(\mathbb{S}_R)} = \delta_{i,k}\delta_{n,m}\delta_{j,l}$, *and*
- $|\boldsymbol{h}_{n,j}^{(i)}(R;\boldsymbol{x})| \in \mathcal{O}(x^{-2})$ *as* $x \to \infty$.

With these functions, for all $\boldsymbol{x} \in \mathbb{R}^3 \setminus \{\mathbf{0}\}$ the relation

$$\boldsymbol{\nabla}_{\boldsymbol{x}}\left(\frac{1}{x^{n+1}}Y_{n,j}(\hat{\boldsymbol{x}})\right) = -\frac{\sqrt{(2n+1)(n+1)}}{x^{n+2}}\tilde{\boldsymbol{y}}_{n,j}^{(1)}(\hat{\boldsymbol{x}}) \tag{5.15a}$$

$$= -\frac{\sqrt{(2n+1)(n+1)}}{R^{n+1}}\boldsymbol{h}_{n,j}^{(1)}(R;\boldsymbol{x}) \tag{5.15b}$$

holds true, see [79, Eq. (2.233)]. Later, we also need an estimate of the vector outer harmonics of type 1 for $x \geq r > R$, which is derived via Corollary 5.25:

$$\left|\boldsymbol{h}_{n,j}^{(1)}(R;\boldsymbol{x})\right| = \left|\frac{R^{n+1}}{x^{n+2}}\tilde{\boldsymbol{y}}_{n,j}^{(1)}(\hat{\boldsymbol{x}})\right| \leq \frac{R^{n+1}}{r^{n+2}}\sqrt{\frac{2n+1}{4\pi}}. \tag{5.16}$$

In analogy to Definition 5.14, we introduce the $\mathbf{harm}_n^{(i)}(\overline{\mathbb{B}_R^{\mathrm{ext}}})$-spaces.

Definition 5.29 ([184, Ch. 7.2.1]). *Let* $\boldsymbol{h}_{n,j}^{(i)}(R;\cdot)$ *be defined as in Definition 5.27 for* $i = 1, 2, 3$, $n \in \mathbb{N}_{0_i}$, *and* $j = 1,\dots,2n+1$. *Then we define*

$$\mathbf{harm}_n^{(i)}\left(\overline{\mathbb{B}_R^{\mathrm{ext}}}\right) \coloneqq \operatorname{span}\left\{\boldsymbol{h}_{n,j}^{(i)}(R;\cdot)\;\middle|\; j = 1,\dots,2n+1\right\},$$

for $i = 1, 2, 3$ *and* $n \in \mathbb{N}_{0_i}$, *and for* $n \in \mathbb{N}$ *we define*

$$\begin{aligned}\mathbf{harm}_0\left(\overline{\mathbb{B}_R^{\mathrm{ext}}}\right) &\coloneqq \mathbf{harm}_0^{(1)}\left(\overline{\mathbb{B}_R^{\mathrm{ext}}}\right),\\ \mathbf{harm}_n\left(\overline{\mathbb{B}_R^{\mathrm{ext}}}\right) &\coloneqq \bigoplus_{i=1}^{3}\mathbf{harm}_n^{(i)}\left(\overline{\mathbb{B}_R^{\mathrm{ext}}}\right).\end{aligned}$$

In addition, we define for $i = 1,\ 2,\ 3$ *the spaces*

$$\mathbf{harm}\left(\overline{\mathbb{B}_R^{\mathrm{ext}}}\right) \coloneqq \overline{\mathrm{span}\left\{\boldsymbol{h}_{n,j}^{(i)}(R;\cdot)\;\middle|\; i=1,2,3,\ n\in\mathbb{N}_{0_i},\ j=1,\dots,2n+1\right\}}^{\|\cdot\|_{\mathbf{C}(\overline{\mathbb{B}_R^{\mathrm{ext}}})}},$$
$$\mathbf{harm}^{(i)}\left(\overline{\mathbb{B}_R^{\mathrm{ext}}}\right) \coloneqq \overline{\mathrm{span}\left\{\boldsymbol{h}_{n,j}^{(i)}(R;\cdot)\;\middle|\; n\in\mathbb{N}_{0_i},\ j=1,\dots,2n+1\right\}}^{\|\cdot\|_{\mathbf{C}(\overline{\mathbb{B}_R^{\mathrm{ext}}})}}.$$

These spaces can also be defined on the exterior of a regular surface, see, for example, [29] for its definition. Note that a sphere is a particular regular surface.

Definition 5.30 (Regular Surface and Runge Sphere). *The set* $\Sigma \subset \mathbb{R}^3$ *is called a* regular surface *if it satisfies the following conditions:*

i) Σ *splits the* $\mathbb{R}^3$ *into the (open) bounded region* Σ^{int} *(inner space) and the (open) unbounded region* Σ^{ext} *(outer space) defined by* $\Sigma^{\mathrm{ext}} = \mathbb{R}^3 \setminus \overline{\Sigma^{\mathrm{int}}}$.

ii) Σ *is a closed and compact surface with no double points.*

iii) The origin 0 *is contained in* Σ^{int}.

iv) Σ *is a* C^2*-surface, that is* Σ *is locally* C^2*-smooth.*

A sphere $\mathbb{S}_R$ *is called a* Runge sphere *if* $0 < R < \sigma \coloneqq \inf_{\boldsymbol{x}\in\Sigma} x$.

Runge spheres are often considered in the context of gravity modelling, see, for instance, [27]. There, the Runge sphere that is the inner spherical best approximation of the Earth's surface is called a Bjerhammar sphere.

Lemma 5.31 ([184, Lem. 7.2.3]). *Let* Σ *be a regular surface and let the vector outer harmonics* $\boldsymbol{h}_{n,j}^{(i)}(R;\cdot)$ *for* $i = 1,2,3$, $n \in \mathbb{N}_{0_i}$, *and* $j = 1,\dots,2n+1$ *be defined as in Definition 5.27. Then the system* $\{\boldsymbol{h}_{n,j}^{(i)}(R;\cdot)|_\Sigma\}_{i=1,2,3,\ n\in\mathbb{N}_{0_i},\ j=1,\dots,2n+1}$ *is linearly independent.*

Now, a completeness result is of note.

Corollary 5.32 ([184, Thm. 7.2.5]). *Let* Σ *be a regular surface and let* $\mathbb{S}_R$ *be a Runge sphere of this surface. In addition, let* $\{\boldsymbol{h}_{n,j}^{(i)}(R;\cdot)\}_{i=1,2,3,\ n\in\mathbb{N}_0,\ j=1,\dots,2n+1}$ *be a system of vector outer harmonics as defined in Definition 5.27 . Then the following statements hold true:*

i) $$\mathbf{L}_2(\Sigma) = \overline{\mathrm{span}\left\{\boldsymbol{h}_{n,j}^{(i)}(R;\cdot)|_\Sigma\;\middle|\; i=1,2,3,\ n\in\mathbb{N}_{0_i},\ j=1,\dots,2n+1\right\}}^{\|\cdot\|_{\mathbf{L}_2(\Sigma)}},$$

ii) $$\mathbf{C}(\Sigma) = \overline{\mathrm{span}\left\{\boldsymbol{h}_{n,j}^{(i)}(R;\cdot)|_\Sigma\;\middle|\; i=1,2,3,\ n\in\mathbb{N}_{0_i},\ j=1,\dots,2n+1\right\}}^{\|\cdot\|_{\mathbf{C}(\Sigma)}}.$$

Hence, we obtain that every function $\boldsymbol{f} \in \mathbf{L}_2(\Sigma)$ *with* $\Sigma \subset \overline{\mathbb{B}_r^{\mathrm{ext}}}$ *has the* $\mathbf{L}_2(\Sigma)$*-expansion*

$$\boldsymbol{f} = \sum_{i=1}^{3}\sum_{n=0_i}^{\infty}\sum_{j=1}^{2n+1}\left\langle \boldsymbol{f}, \boldsymbol{h}_{n,j}^{(i)}(R;\cdot)\right\rangle_{\mathbf{L}_2(\Sigma)} \boldsymbol{h}_{n,j}^{(i)}(R;\cdot)|_\Sigma.$$

5.5. Orthonormal Systems on the Ball

In this section, we define scalar- and vector-valued orthonormal systems on the ball. These systems are required for decomposing the neuronal current in the analysis of the magneto-electroencephalography problem using the multiple-shell model. We have already stated some orthonormal systems on the real line and on the sphere. Now, we combine these results in order to obtain an orthonormal system on the ball $\mathbb{B}_R$ with radius $R > 0$. Thus, we use the separation ansatz

$$G(\boldsymbol{x}) = G_{\mathrm{rad}}(x)Y(\hat{\boldsymbol{x}}) \qquad \text{for all } \boldsymbol{x} \in \mathbb{B}_R \setminus \{\mathbf{0}\}\,.$$

This ansatz has an advantage for the construction of the $\mathrm{L}_2(\mathbb{B}_R)$-orthogonality. The occurring integral can be split into a radial and an angular integral by means of Fubini's Theorem for Lebesgue-integrals, see, for example, [19]. On the other hand, this separation might not be defined at the origin, since the function $\boldsymbol{x} \mapsto \hat{\boldsymbol{x}}$ is not defined at the origin. However, this is not a problem in the sense of $\mathrm{L}_2(\mathbb{B}_R)$.

This separation ansatz is widely used for the construction of orthonormal functions on the ball, see, for instance, [1, 13, 59, 144, 158, 215]. As in the literature, we choose the spherical harmonics for the construction of the angular part of the orthonormal system on the ball. This particular construction yields scalar-valued functions. If vector-valued functions are required, one can easily substitute the scalar spherical harmonics with a set of vector-valued spherical harmonics, such as the Edmonds vector spherical harmonics.

Definition 5.33. *The following two systems can be defined for m, $n \in \mathbb{N}_0$, $j = 1, \ldots, 2n+1$, where R is the radius of the ball $\mathbb{B}_R$:*

$$G^{\mathrm{I}}_{m,n,j}(R;\boldsymbol{x}) \coloneqq \sqrt{\frac{4m+2n+3}{R^3}} P_m^{(0,n+1/2)}\left(2\frac{x^2}{R^2}-1\right)\left(\frac{x}{R}\right)^n Y_{n,j}(\hat{\boldsymbol{x}}),$$

$$G^{\mathrm{II}}_{m,n,j}(R;\boldsymbol{x}) \coloneqq \sqrt{\frac{4m+3}{R^3}} P_m^{(0,2)}\left(2\frac{x}{R}-1\right) Y_{n,j}(\hat{\boldsymbol{x}})$$

for $x \in (0, R]$, $\hat{\boldsymbol{x}} \in \mathbb{S}$.

The system $\{G^{\mathrm{I}}_{m,n,j}(R;\cdot)\}_{m,n\in\mathbb{N}_0,\, j=1,\ldots,2n+1}$ goes back to L. Ballani, J. Engels, E.W. Grafarend, and H.M. Dufour, see [13, 59]. Here, the nomenclature introduced in [157, 158] is used. The other system goes back to C.C. Tscherning, see [215]. Note that the functions $G^{\mathrm{II}}_{m,n,j}(R;\cdot)$ have a discontinuity at the origin for all $m \in \mathbb{N}_0$, $n \in \mathbb{N}$, and $j = 1, \ldots, 2n+1$.

Corollary 5.34. *The two sets of orthonormal functions $\{G^{\mathrm{I}}_{m,n,j}(R;\cdot)\}_{m,n\in\mathbb{N}_0,\, j=1,\ldots,2n+1}$ and $\{G^{\mathrm{II}}_{m,n,j}(R;\cdot)\}_{m,n\in\mathbb{N}_0,\, j=1,\ldots,2n+1}$ are both complete orthonormal systems in $\mathrm{L}_2(\mathbb{B}_R)$.*

For our application, we need another orthonormal basis. To this end, we construct a generalization of the system I.

Definition 5.35. *Let $R > 0$ be the radius of the ball, then the functions $G_{m,n,j}(R;\cdot)$ for m, $n \in \mathbb{N}_0$, $j = 1, \ldots, 2n+1$ are defined for all $\boldsymbol{x} \in \mathbb{B}_R \setminus \{\mathbf{0}\}$ by*

$$\begin{aligned} G_{m,n,j}(R;\boldsymbol{x}) &\coloneqq Q_m^{(t_n+1/2)}(R;x)Y_{n,j}(\hat{\boldsymbol{x}}) \\ &= \sqrt{\frac{4m+2t_n+3}{R^3}} P_m^{(0,t_n+1/2)}\left(2\frac{x^2}{R^2}-1\right)\left(\frac{x}{R}\right)^{t_n} Y_{n,j}(\hat{\boldsymbol{x}}), \end{aligned} \tag{5.17}$$

where the polynomials $Q_m^{(t_n+1/2)}(R;\cdot)$ *are given in Definition 5.1 with the sequence* $\{t_n\}_{n\in\mathbb{N}_0}$ *satisfying the property* $\inf_{n\in\mathbb{N}_0} t_n > -3/2$.

In the particular case $t_n = n$ for all $n \in \mathbb{N}_0$, we immediately obtain $G_{m,n,j}(R;\cdot) = G^{\mathrm{I}}_{m,n,j}(R;\cdot)$ for all $m,\, n \in \mathbb{N}_0$, $j = 1,\ldots,2n+1$. The case $t_n = n-1$ for all $n \in \mathbb{N}_0$ is plotted on the unit sphere in Fig. 5.1 and on a plane in Fig. 5.2. Independent of the choice for the sequence $\{t_n\}_{n\in\mathbb{N}_0}$, this definition forms an orthonormal and complete system in $\mathrm{L}_2(\mathbb{B}_R)$. This property is proved in the next lemma.

Lemma 5.36. *The system* $\{G_{m,n,j}(R;\cdot)\}_{m,n\in\mathbb{N}_0,\, j=1,\ldots,2n+1}$ *is a complete orthonormal system in* $\mathrm{L}_2(\mathbb{B}_R)$.

Proof. With the $\mathrm{L}_2(\mathbb{S})$-orthogonality of the spherical harmonics and, according to Corollary 5.2, the $\mathrm{L}_2^w([0,R])$-orthogonality of the radial orthonormal basis with respect to $w(x) = x^2$ for $x \in [0,R]$ we obtain

$$\begin{aligned}
&\langle G_{m,n,j}(R;\cdot), G_{\mu,\nu,\iota}(R;\cdot)\rangle_{\mathrm{L}_2(\mathbb{B}_R)} \\
&= \int_0^R Q_m^{(t_n+1/2)}(R;x) Q_\mu^{(t_n+1/2)}(R;x) x^2 \,\mathrm{d}x \int_{\mathbb{S}} Y_{n,j}(\hat{\boldsymbol{x}}) Y_{\nu,\iota}(\hat{\boldsymbol{x}}) \,\mathrm{d}\omega(\hat{\boldsymbol{x}}) \\
&= \delta_{\mu,m}\delta_{\nu,n}\delta_{\iota,j}.
\end{aligned}$$

The existence of the integral is guaranteed by the requirement that $\inf_{n\in\mathbb{N}_0} t_n \geq -3/2$, which is required for the conditions in Corollary 5.2. Thus, the presented system is an orthonormal system on the ball. The completeness of the Jacobi polynomials with respect to the weight function, see Corollary 5.2, and the completeness of the spherical harmonics, see Corollary 2.26, provides us with the completeness of $\{G_{m,n,j}(R;\cdot)\}_{m,n\in\mathbb{N}_0,\, j=1,\ldots,2n+1}$. Hence, $\{G_{m,n,j}(R;\cdot)\}_{m,n\in\mathbb{N}_0,\, j=1,\ldots,2n+1}$ is an orthonormal basis for $\mathrm{L}_2(\mathbb{B}_R)$. □

For a vector-valued analogue of this orthonormal basis on the ball, we use the Edmonds vector spherical harmonics, see Definition 5.9, for the angular part of the separation ansatz. Thus, we obtain the next definition.

Definition 5.37. *Let* $R > 0$ *be the radius of the ball* $\mathbb{B}_R$*, then the functions* $\boldsymbol{g}^{(i)}_{m,n,j}(R;\cdot)$ *and* $\tilde{\boldsymbol{g}}^{(i)}_{m,n,j}(R;\cdot)$ *for* $m,\, n \in \mathbb{N}_{0_i}$*,* $j = 1,\ldots,2n+1$*, and* $i = 1,\, 2,\, 3$ *are defined by*

$$\begin{aligned}
\boldsymbol{g}^{(i)}_{m,n,j}(R;\boldsymbol{x}) &\coloneqq Q_m^{(t_n^{(i)}+1/2)}(R;x)\boldsymbol{y}^{(i)}_{n,j}(\hat{\boldsymbol{x}}) \qquad (5.18a)\\
&= \sqrt{\frac{4m+2t_n^{(i)}+3}{R^3}} P_m^{(0,t_n^{(i)}+1/2)}\left(2\frac{x^2}{R^2}-1\right)\left(\frac{x}{R}\right)^{t_n^{(i)}} \boldsymbol{y}^{(i)}_{n,j}(\hat{\boldsymbol{x}}),\\
\tilde{\boldsymbol{g}}^{(i)}_{m,n,j}(R;\boldsymbol{x}) &\coloneqq Q_m^{(t_n^{(i)}+1/2)}(R;x)\tilde{\boldsymbol{y}}^{(i)}_{n,j}(\hat{\boldsymbol{x}}). \qquad (5.18b)
\end{aligned}$$

The polynomials $Q_m^{(t_n^{(i)}+1/2)}(R;\cdot)$ *are given in Definition 5.1, where the sequence* $\{t_n^{(i)}\}_{n\in\mathbb{N}_{0_i}}$ *has to fulfil the property* $\inf_{n\in\mathbb{N}_{0_i}} t_n^{(i)} > -3/2$.

Plots of some vector-valued orthonormal basis functions can be found in Chapter 19, in particular in Figs. 19.3 and 19.5. In the next lemma, we expand arbitrary functions of $\mathbf{L}_2(\mathbb{B}_R)$ into the new basis systems from Definition 5.37, which is an application of [198, Thm. 4.18] for general Hilbert spaces.

Lemma 5.38. *Both systems of functions* $\{\boldsymbol{g}^{(i)}_{m,n,j}(R;\cdot)\}_{i=1,2,3,\, m\in\mathbb{N}_0,\, n\in\mathbb{N}_{0_i},\, j=1,\dots,2n+1}$ *and* $\{\tilde{\boldsymbol{g}}^{(i)}_{m,n,j}(R;\cdot)\}_{i=1,2,3,\, m\in\mathbb{N}_0,\, n\in\mathbb{N}_{0_i},\, j=1,\dots,2n+1}$ *are complete orthonormal systems in the space* $\mathbf{L}_2(\mathbb{B}_R)$*. Thus, all* $\boldsymbol{f}\in\mathbf{L}_2(\mathbb{B}_R)$ *can be expanded by the Fourier expansions*

$$\boldsymbol{f} = \sum_{i=1}^{3}\sum_{m=0}^{\infty}\sum_{n=0_i}^{\infty}\sum_{j=1}^{2n+1} f^{\wedge}(i,m,n,j)\boldsymbol{g}^{(i)}_{m,n,j}(R;\cdot), \tag{5.19a}$$

$$= \sum_{i=1}^{3}\sum_{m=0}^{\infty}\sum_{n=0_i}^{\infty}\sum_{j=1}^{2n+1} f^{\wedge}[i,m,n,j]\tilde{\boldsymbol{g}}^{(i)}_{m,n,j}(R;\cdot). \tag{5.19b}$$

The Fourier coefficients are given by

$$f^{\wedge}(i,m,n,j) = \int_{\mathbb{B}_R} \boldsymbol{f}(\boldsymbol{x})\cdot\boldsymbol{g}^{(i)}_{m,n,j}(R;\boldsymbol{x})\,\mathrm{d}\boldsymbol{x},$$

$$f^{\wedge}[i,m,n,j] = \int_{\mathbb{B}_R} \boldsymbol{f}(\boldsymbol{x})\cdot\tilde{\boldsymbol{g}}^{(i)}_{m,n,j}(R;\boldsymbol{x})\,\mathrm{d}\boldsymbol{x}.$$

Proof. The proof is similar to the one of Lemma 5.36, where the required completeness of the Edmonds vector spherical harmonics is given by Theorem 5.15 and the orthogonality by Lemma 5.10. Note that a different sequence $t^{(i)}_n$ can be chosen for each type i, due to the orthogonality of Edmonds vector spherical harmonics of different types. □

As a particular case of the result stated in [118, Ch. 3], we obtain the next lemma.

Lemma 5.39. *Convergence in Eq.* (5.19) *is unconditional, that is it converges regardless of the order of summation.*

For certain applications, it is interesting which orthonormal basis functions are harmonic. Due to the construction of the Morse-Feshbach vector spherical harmonics, we cannot expect harmonicity of most functions $\boldsymbol{g}^{(i)}_{m,n,j}$. Thus, we restrict ourselves to the orthonormal basis based on the Edmonds vector spherical harmonics.

Lemma 5.40. *Let the exponents* $t^{(i)}_n$ *for* $i=1,\ 2,\ 3$ *and all* $n\in\mathbb{N}_{0_i}$ *be given by*

$$t^{(i)}_n \coloneqq \begin{cases} n+1 & \text{if } i=1,\\ n-1 & \text{if } i=2,\\ n & \text{if } i=3. \end{cases}$$

Then the basis functions $\tilde{\boldsymbol{g}}^{(i)}_{m,n,j}(R;\cdot)$ *are harmonic in* $\mathbb{B}_R$ *in the following cases:*

$$\boldsymbol{\Delta}\tilde{\boldsymbol{g}}^{(i)}_{m,n,j}(R;\cdot)=\boldsymbol{0} \quad\Leftrightarrow\quad m=0,\ n\in\mathbb{N}_{0_i},\ \text{and } j=1,\dots,2n+1.$$

Proof. The calculation is straightforward with the representation of the Laplacian in spherical coordinates, see Theorem 2.14, and the eigenfunctions of the vectorial Beltrami operator, see Eq. (5.8).

$$\boldsymbol{\Delta}_{\boldsymbol{x}}\tilde{\boldsymbol{g}}^{(i)}_{m,n,j}(R;\boldsymbol{x}) = \left(\frac{\partial^2}{\partial x^2}+\frac{2}{x}\frac{\partial}{\partial x}+\boldsymbol{\Delta}^{*}_{\boldsymbol{x}}\right) Q^{(t^{(i)}_n+1/2)}_m(R;x)\tilde{\boldsymbol{y}}^{(i)}_{n,j}(\hat{\boldsymbol{x}})$$

$$= \begin{cases} \left(\frac{\mathrm{d}^2}{\mathrm{d}x^2}+\frac{2}{x}\frac{\mathrm{d}}{\mathrm{d}x}-(n+1)(n+2)\right) Q^{(t^{(1)}_n+1/2)}_m(R;x) & \text{if } i=1,\\ \left(\frac{\mathrm{d}^2}{\mathrm{d}x^2}+\frac{2}{x}\frac{\mathrm{d}}{\mathrm{d}x}-n(n-1)\right) Q^{(t^{(2)}_n+1/2)}_m(R;x) & \text{if } i=2,\\ \left(\frac{\mathrm{d}^2}{\mathrm{d}x^2}+\frac{2}{x}\frac{\mathrm{d}}{\mathrm{d}x}-n(n+1)\right) Q^{(t^{(3)}_n+1/2)}_m(R;x) & \text{if } i=3. \end{cases}$$

Thus, we obtain three different second-order linear ordinary differential equations for the radial part. For each fixed $n \in \mathbb{N}_{0_i}$, their fundamental systems are given by $\{x^{n+1}, x^{-(n+2)}\}$ for $i = 1$, $\{x^{n-1}, x^{-n}\}$ for $i = 2$, and $\{x^n, x^{-(n+1)}\}$ for $i = 3$. Comparing this with the definition of $Q_m^{(t_n^{(i)}+1/2)}(R; x)$, we obtain the stated parameters. □

Lemma 5.41. *Let the exponents be defined by $t_n^{(2)} \coloneqq n - 1$ for all $n \in \mathbb{N}$. Then the basis functions $\tilde{\boldsymbol{g}}_{m,n,j}^{(i)}(R; \cdot)$ are solenoidal or divergence-free, that is $\boldsymbol{\nabla} \cdot \tilde{\boldsymbol{g}}_{m,n,j}^{(i)}(R; \cdot) = 0$ in $\mathbb{B}_R$, in the following cases:*

$$\boldsymbol{\nabla} \cdot \tilde{\boldsymbol{g}}_{m,n,j}^{(i)}(R; \cdot) = 0 \quad \Leftrightarrow \quad \begin{cases} i = 2,\ m = 0,\ n \in \mathbb{N},\ j = 1, \dots, 2n+1, \\ i = 3,\ m \in \mathbb{N}_0,\ n \in \mathbb{N},\ j = 1, \dots, 2n+1. \end{cases}$$

For arbitrary regions $\mathbb{G} \subset \mathbb{R}^3$, a vector field $\boldsymbol{f} \in \mathbf{C}^1(\mathbb{G})$ is said to be solenoidal if $\int_\Gamma \boldsymbol{f}(\boldsymbol{x}) \cdot \boldsymbol{\nu}(\boldsymbol{x}) \, \mathrm{d}\omega(\boldsymbol{x}) = 0$ for every closed and sufficiently smooth surface $\Gamma \subset \mathbb{G}$, see [79, Def. 5.8]. In the considered case, however, this coincides with the definition of $\boldsymbol{f}$ being divergence-free due to Gauß's Theorem.

Proof. The calculation is straightforward with the representation of the divergence in spherical coordinates, see Theorem 2.14:

$$\boldsymbol{\nabla}_{\boldsymbol{x}} \cdot \tilde{\boldsymbol{g}}_{m,n,j}^{(i)}(R; \boldsymbol{x}) = \left(\hat{\boldsymbol{x}} \frac{\partial}{\partial x} + \frac{1}{x} \boldsymbol{\nabla}_{\hat{\boldsymbol{x}}}^* \right) \cdot \left(Q_m^{(t_n^{(i)}+1/2)}(R; x) \tilde{\boldsymbol{y}}_{n,j}^{(i)}(\hat{\boldsymbol{x}}) \right).$$

Due to Eq. (2.6), it is easy to see that this equation is equal to zero if $i = 3$. In the case $i = 1$, we obtain with the relation $\tilde{\boldsymbol{y}}_{n,j}^{(i)} = (\tilde{\mu}_n^{(i)})^{-1/2} \tilde{\boldsymbol{o}}_n^{(i)} Y_{n,j}$, Definition 5.9, Eqs. (2.4) and (5.3), Lemma 2.23, and Theorem 2.16 for all $m \in \mathbb{N}_0$, $n \in \mathbb{N}_0$, and $j = 1, \dots, 2n+1$ the differential equation

$$\begin{aligned} &\boldsymbol{\nabla}_{\boldsymbol{x}} \cdot \tilde{\boldsymbol{g}}_{m,n,j}^{(1)}(R; \boldsymbol{x}) \\ &= (\tilde{\mu}_n^{(1)})^{-1/2} \left((n+1) \frac{\partial}{\partial x} + \frac{1}{x} \boldsymbol{\nabla}_{\hat{\boldsymbol{x}}}^* \cdot ((n+1)\hat{\boldsymbol{x}} - \boldsymbol{\nabla}_{\hat{\boldsymbol{x}}}^*) \right) Q_m^{(t_n^{(1)}+1/2)}(R; x) Y_{n,j}(\hat{\boldsymbol{x}}) \\ &= (\tilde{\mu}_n^{(1)})^{-1/2} \left((n+1) \frac{\partial}{\partial x} + \frac{1}{x} \left(2(n+1) - \Delta_{\hat{\boldsymbol{x}}}^* \right) \right) Q_m^{(t_n^{(1)}+1/2)}(R; x) Y_{n,j}(\hat{\boldsymbol{x}}) \\ &= (\tilde{\mu}_n^{(1)})^{-1/2} \left(\left((n+1) \frac{\mathrm{d}}{\mathrm{d}x} + \frac{1}{x}(n+2)(n+1) \right) Q_m^{(t_n^{(1)}+1/2)}(R; x) \right) Y_{n,j}(\hat{\boldsymbol{x}}). \end{aligned}$$

Thus, the problem reduces for all $n \in \mathbb{N}_0$ to a first-order linear ordinary differential equation, that is

$$\left((n+1) \frac{\mathrm{d}}{\mathrm{d}x} + \frac{1}{x}(n+2)(n+1) \right) Q_m^{(t_n^{(1)}+1/2)}(R; x) \stackrel{!}{=} 0. \tag{5.20}$$

The fundamental system is given by $\{x^{-n-2}\}_{n \in \mathbb{N}_0}$, which cannot be expressed in terms of $Q_m^{(t_n^{(1)}+1/2)}(R; x)$ because these functions consist of Jacobi polynomials of degree $m \in \mathbb{N}_0$ and the function $x \mapsto x^{t_n^{(1)}}$ with $\inf_{n \in \mathbb{N}_0} t_n^{(1)} > -3/2$. Thus, Eq. (5.20) cannot be fulfilled and, hence, all orthonormal basis functions corresponding to $i = 1$ are not solenoidal.

In the case of $i = 2$, we obtain with a similar calculation for all $n \in \mathbb{N}$ the first-order linear ordinary differential equation

$$\left(n \frac{\mathrm{d}}{\mathrm{d}x} - \frac{1}{x} n(n-1) \right) Q_m^{(t_n^{(2)}+1/2)}(R; x) = 0.$$

For each $n \in \mathbb{N}$, the fundamental system is given by $\{x^{n-1}\}$. Combined with $t_n^{(2)} = n - 1$ for all $n \in \mathbb{N}$, this implies $m = 0$. □

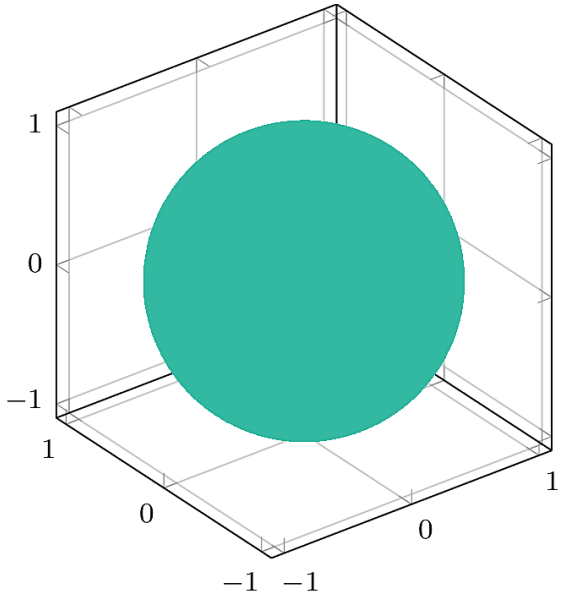

(a) $G_{m,n,j}(R;\cdot)$ *for* $m = 0$, $n = 0$, $j = 1$

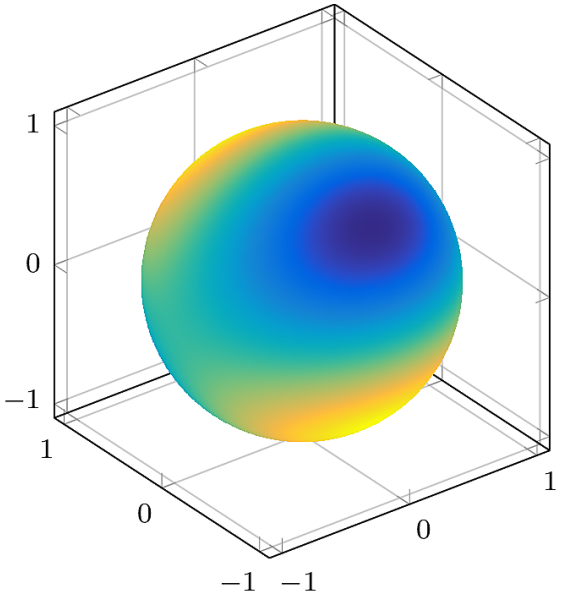

(b) $G_{m,n,j}(R;\cdot)$ *for* $m = 0$, $n = 2$, $j = 4$

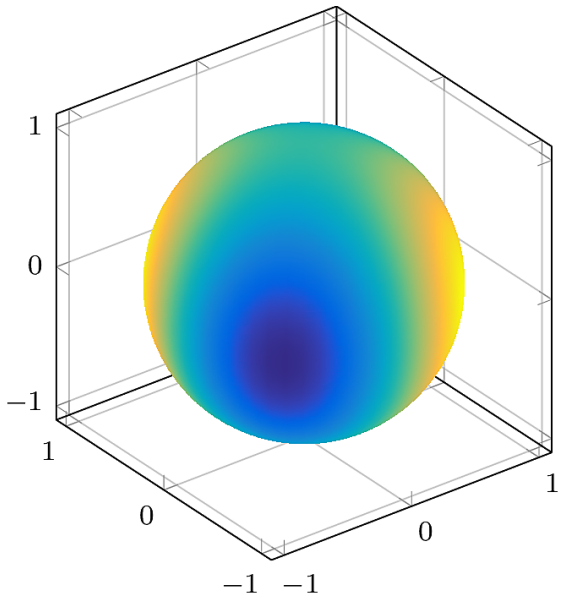

(c) $G_{m,n,j}(R;\cdot)$ *for* $m = 1$, $n = 2$, $j = 4$

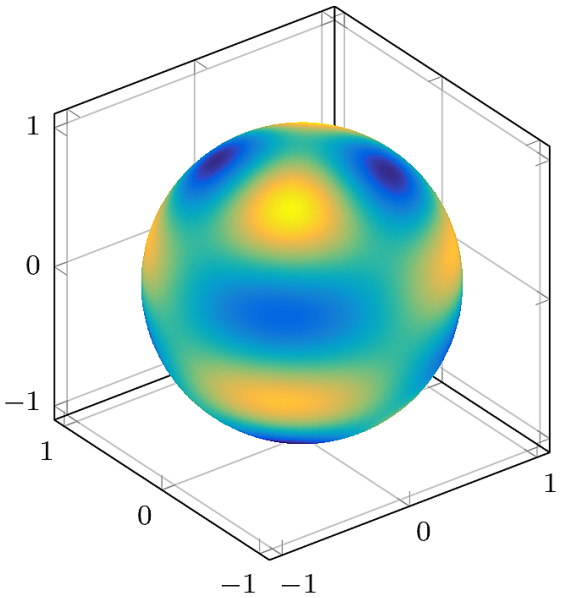

(d) $G_{m,n,j}(R;\cdot)$ *for* $m = 5$, $n = 5$, $j = 3$

FIGURE 5.1: *The functions* $G_{m,n,j}(R;\cdot)$ *in the case* $t_n := n-1$, $R = 1$ *for different parameters* m, n, j *are plotted on the unit sphere. For the particular parameters see the respective caption. The maximum is always yellow and the minimum is blue.*

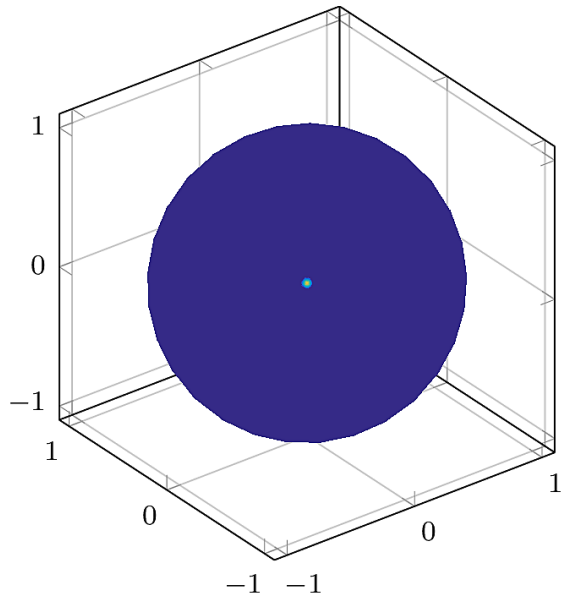

(a) $G_{m,n,j}(R;\cdot)$ *for* $m = 0$, $n = 0$, $j = 1$

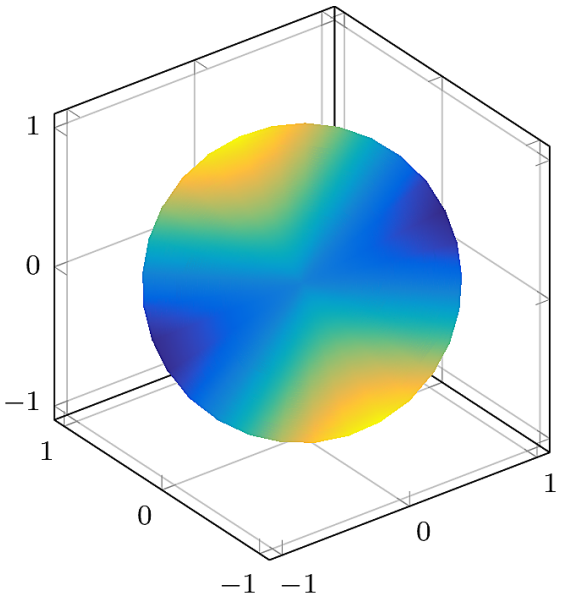

(b) $G_{m,n,j}(R;\cdot)$ *for* $m = 0$, $n = 2$, $j = 4$

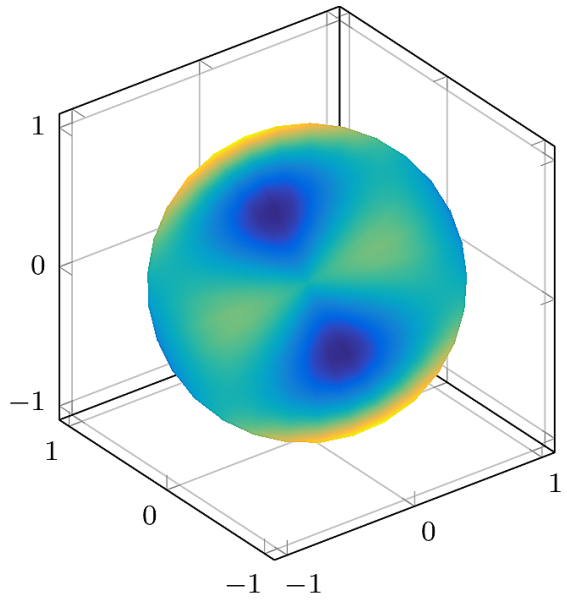

(c) $G_{m,n,j}(R;\cdot)$ *for* $m = 1$, $n = 2$, $j = 4$

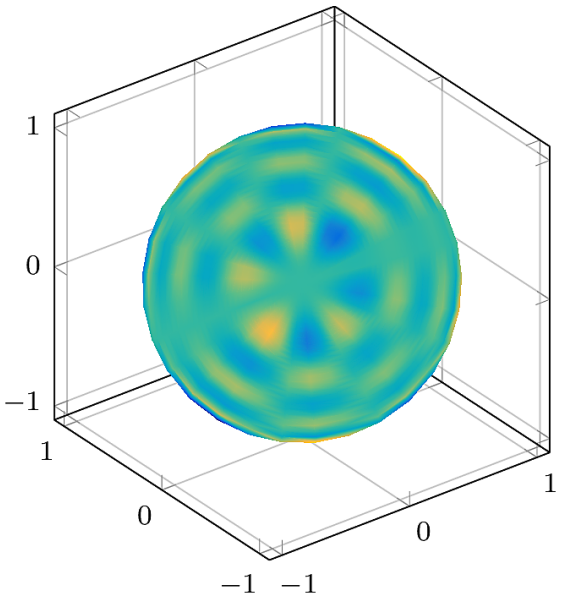

(d) $G_{m,n,j}(R;\cdot)$ *for* $m = 5$, $n = 5$, $j = 3$

FIGURE 5.2: *The functions* $G_{m,n,j}(R;\cdot)$ *in the case* $t_n := n-1$, $R = 1$ *for different parameters* m, n, j *are plotted at the plane through the origin with normal vector* $(1, 1, -1)^{\mathrm{T}}$. *For the particular parameters see the respective caption. The maximum is always yellow and the minimum is blue.*

Chapter 6.

Vector Legendre-type Integral Kernels

In this chapter, we define and consider two particular classes of Fredholm integral kernels: the continuous and the star-shaped vector Legendre-type integral kernels. The classical Fredholm integral kernels and their equations are discussed, for example, in [77]. Important integral equations in the context of potential theory are discussed in [135], for instance.

As mentioned before, two vector-valued integral kernels, which lie at the heart of the magneto-encephalography problem, are defined in Eq. (3.4) and Eq. (4.23). For each kernel, there is an integral equation relating the neuronal current to the measured quantity, that is either the magnetic flux density or the electric potential. The aim of the class of integral kernels introduced in this chapter is to simultaneously cover both magneto-electroencephalography integral kernels. Thus, the definition of this kernels should be generalizing on the one side, such that both problems are covered, but also be restrictive enough to handle the corresponding integral operator.

These kernels are formally defined in Section 6.1 via a series representation. Thus, in Section 6.1, the convergence of this series in an appropriate sense is analyzed, which yields the well-definedness of these kernels. The relation between the kernels occurring in the inverse MEG and EEG problem and this particular class of kernels is analyzed in Section 6.2. Eventually, we consider in Section 6.3 further properties of this particular class of kernels that are required for the well-definedness of the corresponding integral equations.

6.1. Definition and Well-definedness

The definition of the continuous vector Legendre-type integral kernel is inspired by the familiar series of Legendre polynomials previously stated in Eq. (2.2), that is

$$\frac{1}{4\pi|\boldsymbol{x}-\boldsymbol{y}|} = \frac{1}{4\pi}\sum_{k=0}^{\infty}\frac{x^k}{y^{k+1}}P_k(\hat{\boldsymbol{x}}\cdot\hat{\boldsymbol{y}}), \qquad \boldsymbol{x},\ \boldsymbol{y}\in\mathbb{R}^3,\ x<y.$$

This integral kernel occurs, for example, in the inverse gravimetric problem, that is the reconstruction of the mass density distribution ϱ inside the Earth $\mathbb{E}$ by the gravitational potential V in the outer space. Both quantities are linked by means of Newton's Law of Gravitation, whose formula is given by

$$V(\boldsymbol{y}) = \frac{1}{4\pi}\int_{\mathbb{E}}\frac{\varrho(\boldsymbol{x})}{|\boldsymbol{x}-\boldsymbol{y}|}\,\mathrm{d}\boldsymbol{x}, \qquad \boldsymbol{y}\in\mathbb{R}^3\setminus\mathbb{E}.$$

This famous integral equation is not the only one of this kind. All solutions V of Poisson's equation $\Delta V = \varrho$ can be represented by such an integral equation. In this context, the stated integral kernel is called the three-dimensional Newtonian kernel. In Part IV, we come back to this integral equation. Besides this, Poisson's equation occurs in diverse surface

reconstruction problems, in the context of diffusion processes, in electrostatics, and in the magneto-electroencephalography problem, see, for instance, [64, 79, 117, 204].

As we have already seen, the sought density is a vector-valued quantity in the case of the magneto-encephalography problem. For this purpose, we need a vector-valued integral kernel that fits to the vector calculus in spherical geometries. We accomplish this by replacing the scalar Legendre polynomials with a vectorial counterpart, see Definition 5.21. In addition, we allow a more general setting for the part that depends on the radius.

We call kernels that fulfil the conditions of the next definition *continuous vector Legendre-type integral kernels* (continuous VLI kernels) because the Morse-Feshbach vector Legendre polynomials build a foundation for these integral kernels. At the end of this chapter, we see that we can also use the Edmonds vector Legendre polynomials instead of the Morse-Feshbach vector Legendre polynomials in order to achieve kernels with similar properties. In addition, in the literature, see [88, 89], the (Morse-Feshbach) vector Legendre polynomials are sometimes also called *vector Legendre kernels*. After some analysis of this kernel, we prove in Corollary 6.12 that the adjective *continuous* is justified.

Definition 6.1 (Continuous Vector Legendre-type Integral Kernel). *Let the inner set $\mathbb{G}_{\text{in}} \subset \mathbb{R}^3$ be a compact, region containing the origin with $\sup_{\boldsymbol{x}\in\mathbb{G}_{\text{in}}} x = R > 0$. Moreover, let the outer set $\mathbb{G}_{\text{out}} \subset \mathbb{R}^3 \setminus \mathbb{G}_{\text{in}}$ be an unbounded region with $\inf_{\boldsymbol{y}\in\mathbb{G}_{\text{out}}} y > R$, see Fig. 6.1. For an arbitrary $\iota \in \{1, 2, 3\}$, we define the kernel $\boldsymbol{k}^{(\iota)}$ by*

$$\boldsymbol{k}^{(\iota)}(\boldsymbol{x}, \boldsymbol{y}) \coloneqq \sum_{k=0_\iota}^{\infty} \gamma_k(y) x^{t_k} \boldsymbol{p}_k^{(\iota)}(\hat{\boldsymbol{x}}, \hat{\boldsymbol{y}}), \qquad (\boldsymbol{x}, \boldsymbol{y}) \in \mathbb{G}_{\text{in}} \times \mathbb{G}_{\text{out}}.$$

Let the occurring quantities fulfil the following assumptions:

i) The real sequence of exponents $\{t_k\}_{k\in\mathbb{N}_{0_\iota}}$ is bounded from below by zero, that is $\inf_{k\in\mathbb{N}_{0_\iota}, \gamma_k\neq 0} t_k \geq 0$.

ii) The asymptotic behaviour of $\{t_k\}_{k\in\mathbb{N}_{0_\iota}}$ can be characterized by $\sup_{k\in\mathbb{N}_{0_\iota}} R^{t_k-k} < \infty$.

iii) Each function γ_k is continuous and satisfies for all $\boldsymbol{y} \in \mathbb{G}_{\text{out}}$ the inequality

$$|\gamma_k(y)| \leq \frac{\Gamma_k}{y^{k+1+\delta_{0_\iota,0}\delta_{k,0}}}$$

for all $k \in \mathbb{N}_{0_\iota}$ with $\{\Gamma_k\}_{k\in\mathbb{N}_{0_\iota}} \subset \mathbb{R}_0^+$. In addition, let $M \in \mathbb{N}_0$ be fixed such that the mapping $(k \mapsto \Gamma_k)$ is an element of $\mathcal{O}(k^M)$.

The corresponding integral equation is called the continuous VLI equation.

Note that we often use non-bold letters as the abbreviation for the absolute value of bold letter quantities. In this particular case, however, $\boldsymbol{k}^{(\iota)}$ names the vectorial kernel and k the summation index of this kernel. Examples of continuous VLI kernels in the context of the magneto-electroencephalography problem can be found in Section 6.2.

Let us briefly discuss the stated assumptions and their respective aim. The convergence of the series in the Newtonian kernel is achieved by a dominating convergent power series. Thus, by means of the asymptotic behaviour of the sequence $\{t_k\}_{k\in\mathbb{N}_{0_\iota}}$ and the upper bound of $\{\gamma_k\}_{k\in\mathbb{N}_{0_\iota}}$ this convergence is ensured for the continuous VLI kernel. The boundedness

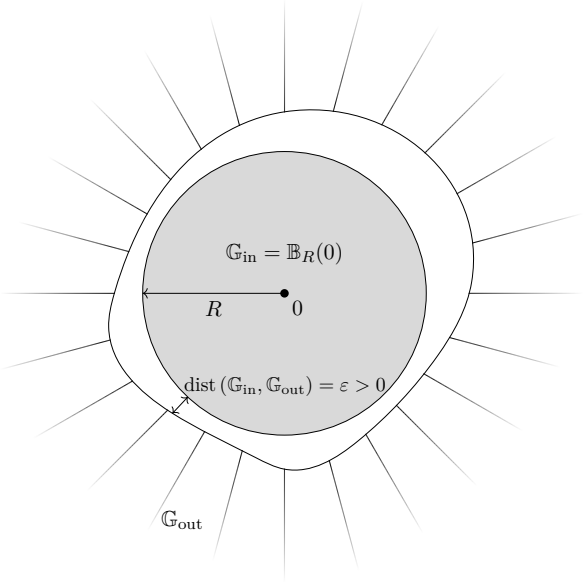

FIGURE 6.1: *The compact inner region* $\mathbb{G}_{\text{in}}$ *in the particular case of* $\mathbb{G}_{\text{in}} \coloneqq \mathbb{B}_R$ *and the unbounded outer region* $\mathbb{G}_{\text{out}}$ *with* $\text{dist}(\mathbb{G}_{\text{in}}, \mathbb{G}_{\text{out}}) = \varepsilon > 0$ *and* $\inf_{\boldsymbol{y} \in \mathbb{G}_{\text{out}}} y = R + \varepsilon$.

from below of $\{t_k\}_{k \in \mathbb{N}_{0_\iota}}$ is required for certain smoothness results, such as continuity or integrability. Both statements are proved later.

In certain cases, a moderate degree of smoothness is sufficient. For this purpose, we define the *star-shaped VLI kernel*.

Definition 6.2 (Star-shaped VLI Kernel). *Let* $\mathbb{G}_{\text{star}} \subset \mathbb{R}^3$ *be a compact star domain with vantage point zero and* $\sup_{\boldsymbol{x} \in \mathbb{G}_{\text{star}}} x = R$. *Let* $\mathbb{G}_{\text{out}} \subset \mathbb{R}^3 \setminus \mathbb{G}_{\text{star}}$ *be an unbounded outer region with* $\inf_{\boldsymbol{y} \in \mathbb{G}_{\text{out}}} y > R$. *For an arbitrary* $\iota \in \{1, 2, 3\}$, *we define the kernel* $\boldsymbol{k}^{(\iota)}$ *by*

$$\boldsymbol{k}^{(\iota)}(\boldsymbol{x}, \boldsymbol{y}) \coloneqq \sum_{k=0_\iota}^{\infty} \gamma_k(y) x^{t_k} \boldsymbol{p}_k^{(\iota)}(\hat{\boldsymbol{x}}, \hat{\boldsymbol{y}}), \qquad (\boldsymbol{x}, \boldsymbol{y}) \in (\mathbb{G}_{\text{star}} \setminus \{\boldsymbol{0}\}) \times \mathbb{G}_{\text{out}}.$$

The sequences $\{t_k\}_{k \in \mathbb{N}_{0_\iota}}$ *and* $\{\gamma_k\}_{k \in \mathbb{N}_{0_\iota}}$ *fulfil the assumptions of the continuous VLI kernel. In addition, we enhance the range of the exponent sequence such that*

$$\inf_{k \in \mathbb{N}_{0_\iota}, \gamma_k \not\equiv 0} t_k \geq -1.$$

Note that the attribute *star-shaped* belongs to a property of the region $\mathbb{G}_{\text{star}}$ and is not a property of the kernel itself.

The domain of the star-shaped VLI kernel is given by $\operatorname{dom} \boldsymbol{k}^{(\iota)} = (\mathbb{G}_{\text{star}} \setminus \{\boldsymbol{0}\}) \times \mathbb{G}_{\text{out}}$, since the origin can be a singularity of $\boldsymbol{k}^{(\iota)}(\cdot, \boldsymbol{y})$ for all $\boldsymbol{y} \in \mathbb{G}_{\text{out}}$. However, in the sense of $\mathbf{L}_2(\mathbb{G}_{\text{star}} \times \mathbb{G}_{\text{out}})$ this is not a problem.

Comparing the definitions of the continuous VLI and the star-shaped VLI kernel, we immediately obtain the next corollary.

Corollary 6.3. *Let* $\boldsymbol{k}^{(\iota)}$ *be a star-shaped VLI kernel. Then* $(\boldsymbol{x}, \boldsymbol{y}) \mapsto x\boldsymbol{k}^{(\iota)}(\boldsymbol{x}, \boldsymbol{y})$ *is a continuous VLI kernel for all* $(\boldsymbol{x}, \boldsymbol{y}) \in \mathbb{G}_{\text{star}} \times \mathbb{G}_{\text{out}}$.

The star domain can be characterized in spherical coordinates similar to the ball. Each point depends on the angle and the radius, which for the star domain differs from angle to angle. More precisely, with a measurable function $\zeta\colon \mathbb{S} \to [0, R]$ we have

$$\mathbb{G}_{\text{star}} = \left\{ \boldsymbol{x} \in \mathbb{R}^3 \;\middle|\; \boldsymbol{x} = \zeta(\hat{\boldsymbol{x}})\hat{\boldsymbol{x}},\ \hat{\boldsymbol{x}} \in \mathbb{S} \right\}.$$

Of course, by a change of variables we obtain for all $\boldsymbol{f} \in \mathbf{L}_2(\mathbb{G}_{\text{star}})$ the identity

$$\int_{\mathbb{G}_{\text{star}}} \boldsymbol{f}(\boldsymbol{x}) \,\mathrm{d}\boldsymbol{x} = \int_{\mathbb{S}} \int_0^{\zeta(\hat{\boldsymbol{x}})} \boldsymbol{f}(\boldsymbol{x}) x^2 \,\mathrm{d}x \,\mathrm{d}\omega(\hat{\boldsymbol{x}}). \tag{6.1}$$

Why do we consider two different kinds of integral kernels? The continuous VLI kernel is regular in $\mathbb{G}_{\text{in}}$, which leads us to its uniform boundedness. This property helps us to handle the integral kernel by interchanging limits. However, we are ultimately interested in the corresponding integral equation. In contrast to the continuous VLI kernel, the star-shaped VLI kernel cannot be handled as easily due to the singularity at the origin. Fortunately, the Jacobian determinant occurring in the integration over $\mathbb{G}_{\text{star}}$ in Eq. (6.1) flattens the singularity of the star-shaped VLI kernel. Hence, we are able to weaken the conditions for the exponent $\{t_k\}_{k\in\mathbb{N}_{0_\iota}}$ for star-shaped domains. Then, by means of Corollary 6.3, we are able to transfer properties of the continuous VLI kernel to the star-shaped one.

First, we prove that both kernels $\boldsymbol{k}^{(\iota)}$ from Definition 6.1 and Definition 6.2 are well-defined, that is the series of the kernels converge in an appropriate sense. To this end and for the forthcoming convergence result, we need an essential property of the geometric series, which is summarized in the next theorem.

Theorem 6.4 (Convergence of the Power Series). *Let $|q| < 1$ and $M \in \mathbb{R}$ be fixed, then the series*

$$\sum_{k=0}^{\infty} k^M q^k < \infty$$

converges absolutely. This also implies $\lim_{k\to\infty} k^M q^k = 0$.

Proof. Consider the series as a power series in q with coefficients k^M. Its radius of convergence is given by

$$\frac{1}{\limsup_{k\to\infty} \sqrt[k]{k^M}} = \frac{1}{\left(\lim_{k\to\infty} \sqrt[k]{k}\right)^M} = 1.$$

Thus, the series converges absolutely for all $|q| < 1$. □

The next lemma is a powerful tool for the convergence analysis of the integral kernel and the well-definedness of its induced integral equation. Its proof is based on the convergence of the power series stated in the foregoing theorem.

Lemma 6.5. *The continuous VLI kernel $\boldsymbol{k}^{(\iota)}$ is bounded, that is*

$$\left|\boldsymbol{k}^{(\iota)}(\boldsymbol{x}, \boldsymbol{y})\right| \leq B \qquad \text{for all } (\boldsymbol{x}, \boldsymbol{y}) \in \mathbb{G}_{\text{in}} \times \mathbb{G}_{\text{out}},$$

where the bound B is defined by

$$B \coloneqq \left(\sup_{k\in\mathbb{N}_{0_\iota}} R^{t_k - k} \right) \sum_{k=0_\iota}^{\infty} \Gamma_k \sqrt{\mu_k^{(\iota)}} \frac{R^k}{(R+\varepsilon)^{k+1+\delta_{0_\iota,0}\delta_{k,0}}} < \infty.$$

Proof. Due to the construction of $\mathbb{G}_{\text{in}}$ and $\mathbb{G}_{\text{out}}$, there exists an $\varepsilon > 0$ such that $0 \leq x \leq \sup_{\boldsymbol{x} \in \mathbb{G}_{\text{in}}} x = R < R + \varepsilon \leq \inf_{\boldsymbol{y} \in \mathbb{G}_{\text{out}}} y \leq y$ for all $(\boldsymbol{x}, \boldsymbol{y}) \in \mathbb{G}_{\text{in}} \times \mathbb{G}_{\text{out}}$. In addition, Lemma 5.22 provides us with the estimate

$$\left| \boldsymbol{p}_k^{(\iota)}(\hat{\boldsymbol{x}}, \hat{\boldsymbol{y}}) \right| \leq \sqrt{\mu_k^{(\iota)}}$$

for all $k \in \mathbb{N}_{0_\iota}$ and all $(\boldsymbol{x}, \boldsymbol{y}) \in \mathbb{G}_{\text{in}} \times \mathbb{G}_{\text{out}}$. Thus, under the assumptions in Definition 6.1 we immediately obtain the estimate

$$\begin{aligned} \left| \boldsymbol{k}^{(\iota)}(\boldsymbol{x}, \boldsymbol{y}) \right| &= \left| \sum_{k=0_\iota}^{\infty} \gamma_k(y) x^{t_k} \boldsymbol{p}_k^{(\iota)}(\hat{\boldsymbol{x}}, \hat{\boldsymbol{y}}) \right| \\ &\leq \left(\sup_{k \in \mathbb{N}_{0_\iota}} R^{t_k - k} \right) \sum_{k=0_\iota}^{\infty} \Gamma_k \sqrt{\mu_k^{(\iota)}} \frac{R^k}{y^{k+1+\delta_{0_\iota,0}\delta_{k,0}}} \\ &\leq \left(\sup_{k \in \mathbb{N}_{0_\iota}} R^{t_k - k} \right) \sum_{k=0_\iota}^{\infty} \Gamma_k \sqrt{\mu_k^{(\iota)}} \frac{R^k}{(R+\varepsilon)^{k+1+\delta_{0_\iota,0}\delta_{k,0}}} \\ &= B. \end{aligned}$$

The convergence properties of the geometric power series, see Theorem 6.4, the fact that

$$\left(k \mapsto \sqrt{\mu_k^{(\iota)}} \Gamma_k \right) \in \mathcal{O}\left(k^{M+1} \right),$$

and $\sup_{k \in \mathbb{N}_{0_\iota}} R^{t_k - k} < \infty$ ensure the convergence of the series. This implies $B < \infty$. □

Using this result, we can establish absolute and uniform convergence of the series in the continuous VLI kernel.

Theorem 6.6. *Let $\boldsymbol{k}^{(\iota)}$ be a continuous VLI kernel. The series in its definition, that is*

$$\sum_{k=0_\iota}^{\infty} \gamma_k(y) x^{t_k} \boldsymbol{p}_k^{(\iota)}(\hat{\boldsymbol{x}}, \hat{\boldsymbol{y}}),$$

converges absolutely and uniformly in $\mathbb{G}_{\text{in}} \times \mathbb{G}_{\text{out}}$.

Proof. For the convergence of the series we analyze the following bounding series

$$\left| \sum_{k=K+1}^{\infty} \gamma_k(y) x^{t_k} \boldsymbol{p}_k^{(\iota)}(\hat{\boldsymbol{x}}, \hat{\boldsymbol{y}}) \right| \leq \left(\sup_{k \in \mathbb{N}_{0_\iota}} R^{t_k - k} \right) \sum_{k=K+1}^{\infty} \Gamma_k \sqrt{\mu_k^{(\iota)}} \frac{R^k}{(R+\varepsilon)^{k+1+\delta_{0_\iota,0}\delta_{k,0}}}.$$

The employed estimate is similar to the one from the foregoing result, see Lemma 6.5. The power series on the right-hand side converges to 0 as $K \to \infty$, due to the convergence properties of the geometric series, see Theorem 6.4. The right-hand side is also independent of $(\boldsymbol{x}, \boldsymbol{y}) \in \mathbb{G}_{\text{in}} \times \mathbb{G}_{\text{out}}$. Thus, uniform convergence follows. □

For the star-shaped VLI kernel, we are able to obtain a comparable result.

Lemma 6.7. *The series in the definition of the star-shaped VLI kernel converges absolutely and pointwise for all $(\boldsymbol{x}, \boldsymbol{y}) \in (\mathbb{G}_{\text{star}} \setminus \{\mathbf{0}\}) \times \mathbb{G}_{\text{out}}$.*

Note that we do not obtain the uniform convergence in $\mathbb{G}_{\text{star}}$ in this case, due to the singularity at the origin.

Proof. Let $\boldsymbol{k}^{(\iota)}$ be the star-shaped VLI kernel given by

$$\boldsymbol{k}^{(\iota)}(\boldsymbol{x},\boldsymbol{y}) = \sum_{k=0_\iota}^{\infty} \gamma_k(y) x^{t_k} \boldsymbol{p}_k^{(\iota)}(\hat{\boldsymbol{x}},\hat{\boldsymbol{y}}), \qquad (\boldsymbol{x},\boldsymbol{y}) \in \mathbb{G}_{\text{star}} \times \mathbb{G}_{\text{out}}.$$

Then $(\boldsymbol{x},\boldsymbol{y}) \mapsto x\boldsymbol{k}^{(\iota)}(\boldsymbol{x},\boldsymbol{y})$ is a continuous VLI kernel for all $(\boldsymbol{x},\boldsymbol{y}) \in \mathbb{G}_{\text{star}} \times \mathbb{G}_{\text{out}}$, see Corollary 6.3. Thus, the series

$$\sum_{k=0_\iota}^{\infty} \gamma_k(y) x^{t_k+1} \boldsymbol{p}_k^{(\iota)}(\hat{\boldsymbol{x}},\hat{\boldsymbol{y}})$$

converges absolutely and pointwise for all $(\boldsymbol{x},\boldsymbol{y}) \in \mathbb{G}_{\text{star}} \times \mathbb{G}_{\text{out}}$ by means of Theorem 6.6. For the series of the star-shaped VLI kernel, we obtain for all $(\boldsymbol{x},\boldsymbol{y}) \in (\mathbb{G}_{\text{star}} \setminus \{\boldsymbol{0}\}) \times \mathbb{G}_{\text{out}}$ the estimate

$$\begin{aligned}\left| \sum_{k=K+1}^{\infty} \gamma_k(y) x^{t_k} \boldsymbol{p}_k^{(\iota)}(\hat{\boldsymbol{x}},\hat{\boldsymbol{y}}) \right| &= \left| \frac{1}{x} \sum_{k=K+1}^{\infty} \gamma_k(y) x^{t_k+1} \boldsymbol{p}_k^{(\iota)}(\hat{\boldsymbol{x}},\hat{\boldsymbol{y}}) \right| \\ &\leq \frac{1}{x} \left(\sup_{k \in \mathbb{N}_{0_\iota}} R^{t_k-k} \right) \sum_{k=K+1}^{\infty} \Gamma_k \sqrt{\mu_k^{(\iota)}} \frac{R^{k+1}}{(R+\varepsilon)^{k+1+\delta_{0_\iota,0}\delta_{k,0}}}.\end{aligned}$$

Here, the right-hand side converges to zero as $K \to \infty$. □

In the next lemma, we show that the $\boldsymbol{o}_{\hat{\boldsymbol{x}}}^{(\iota)}$-operators can be interchanged with the series of the integral kernel. We use this result when the interchanging of differential operators with components of the vectorial kernel is analyzed. In addition, we know from Eq. (3.4) that the integral kernel of the MEG problem is given by the surface curl of a Legendre polynomial series. In contrast, the EEG integral kernel is given by a series of gradients of Legendre polynomials, see Eq. (4.23). In order to find a collective representation of both integral kernels, the interchanging of the differential operators and the series is necessary.

Lemma 6.8. *For the continuous VLI kernel $\boldsymbol{k}^{(\iota)}$, the following holds true:*

- *We can interchange the $\boldsymbol{o}_{\hat{\boldsymbol{x}}}^{(\iota)}$-operator included in the vectorial Legendre polynomials with the series, that is*

$$\boldsymbol{k}^{(\iota)}(\boldsymbol{x},\boldsymbol{y}) = \boldsymbol{o}_{\hat{\boldsymbol{x}}}^{(\iota)} \sum_{k=0_\iota}^{\infty} \left(\mu_k^{(\iota)}\right)^{-1/2} \gamma_k(y) x^{t_k} P_k(\hat{\boldsymbol{x}} \cdot \hat{\boldsymbol{y}}), \qquad (\boldsymbol{x},\boldsymbol{y}) \in \mathbb{G}_{\text{in}} \times \mathbb{G}_{\text{out}}. \tag{6.2}$$

- *The series in Eq.* (6.2) *converges absolutely and uniformly.*

The interchanging also holds true for the star-shaped VLI kernel for all $(\boldsymbol{x},\boldsymbol{y}) \in (\mathbb{G}_{\text{star}} \setminus \{\boldsymbol{0}\}) \times \mathbb{G}_{\text{out}}$.

Proof. In the case of $\iota = 1$, there is nothing to prove for the interchanging and the convergence, since $\boldsymbol{o}^{(1)}$ is only a multiplication operator independent of the summation index $k \in \mathbb{N}_0$ and the corresponding normalization factor equals one for all degrees.

In the two other cases, we need to check if the occurring differential operator and the series can be interchanged. Theorem 6.6 provides us with the uniform convergence of the term-by-term differentiated series. According to properties of uniformly convergent series, see [197], the pointwise convergence of the non-differentiated series remains to be shown. For the non-differentiated series, we get for all $(\boldsymbol{x}, \boldsymbol{y}) \in \mathbb{G}_{\text{in}} \times \mathbb{G}_{\text{out}}$ the estimate

$$\begin{aligned}&\left| \sum_{k=K+1}^{\infty} \left(\mu_k^{(\iota)}\right)^{-1/2} \gamma_k(y) x^{t_k} P_k(\hat{\boldsymbol{x}} \cdot \hat{\boldsymbol{y}}) \right| \\ &\leq \left(\sup_{k \in \mathbb{N}_{0_\iota}} R^{t_k - k} \right) \sum_{k=K+1}^{\infty} \Gamma_k \left(\mu_k^{(\iota)}\right)^{-1/2} \frac{R^k}{(R+\varepsilon)^{k+1+\delta_{0_\iota,0}\delta_{k,0}}}.\end{aligned}$$

The right-hand side converges to zero as $K \to \infty$ due to the assumptions in Definition 6.1 and Theorem 6.4. Since both series converge uniformly, an interchanging of $\boldsymbol{o}_{\hat{\boldsymbol{x}}}^{(\iota)}$ and the series is valid.

Let us now consider the case of the star-shaped VLI kernel. Then, by means of Corollary 6.3, we get for all $(\boldsymbol{x}, \boldsymbol{y}) \in (\mathbb{G}_{\text{star}} \setminus \{\boldsymbol{0}\}) \times \mathbb{G}_{\text{out}}$ the identity

$$\begin{aligned}x\boldsymbol{k}^{(\iota)}(\boldsymbol{x}, \boldsymbol{y}) &= \boldsymbol{o}_{\hat{\boldsymbol{x}}}^{(\iota)} \sum_{k=0_\iota}^{\infty} \left(\mu_k^{(\iota)}\right)^{-1/2} \gamma_k(y) x^{t_k+1} P_k(\hat{\boldsymbol{x}} \cdot \hat{\boldsymbol{y}}) \\ &= x\boldsymbol{o}_{\hat{\boldsymbol{x}}}^{(\iota)} \sum_{k=0_\iota}^{\infty} \left(\mu_k^{(\iota)}\right)^{-1/2} \gamma_k(y) x^{t_k} P_k(\hat{\boldsymbol{x}} \cdot \hat{\boldsymbol{y}}).\end{aligned}$$

□

Some of the next statements hold true for the continuous VLI kernel as well as the star-shaped VLI kernel. Thus, we use the notation *continuous/star-shaped VLI kernel* if a statement holds true for both kinds of kernels.

Concluding, in this section, we defined the continuous/star-shaped VLI kernels via a series representation of Morse-Feshbach vector Legendre polynomials. We proved that the series is well-defined since it converges at least absolutely and pointwise. In addition, we found a dominating convergent power series for the continuous VLI kernel that is independent of $(\boldsymbol{x}, \boldsymbol{y}) \in \mathbb{G}_{\text{in}} \times \mathbb{G}_{\text{out}}$. Due to this estimate, the series of the continuous VLI kernel converges uniformly. Furthermore, the differential operators occurring in the definition of the Morse-Feshbach vector Legendre polynomials can be interchanged with the series.

6.2. Examples: Magneto-electroencephalography Kernels

So far, we have defined a particular class of integral kernels. In the introduction of this chapter, we claimed that the integral kernels occurring in the MEG and EEG problem are kernels of this particular class. Before we further investigate properties of continuous/ star-shaped VLI kernels in Section 6.3, we prove this statement.

We start with the integral kernel corresponding to the MEG problem. In Eq. (3.4), the representation

$$\boldsymbol{k}_{\text{M}}(\boldsymbol{x}, \boldsymbol{y}) = \frac{1}{4\pi} \boldsymbol{L}_{\hat{\boldsymbol{x}}}^* \sum_{k=1}^{\infty} \frac{x^k}{y^{k+1}(k+1)} P_k(\hat{\boldsymbol{x}} \cdot \hat{\boldsymbol{y}}), \qquad (\boldsymbol{x}, \boldsymbol{y}) \in \mathbb{B}_{\varrho_0} \times \overline{\mathbb{B}_{\varrho_L}^{\text{ext}}}$$

is derived for this kernel. Recall that we consider the multiple-shell model in the MEG problem, see Assumption 3.2. According to this model, the inner region of the continuous/star-shaped VLI is given by the cerebrum that is modelled as a closed ball with radius ϱ_0. Then the MEG integral kernel has for all $(\boldsymbol{x}, \boldsymbol{y}) \in \mathbb{B}_{\varrho_0} \times \overline{\mathbb{B}_{\varrho_L}^{\text{ext}}}$ the following alternative representations:

$$\boldsymbol{k}_{\text{M}}(\boldsymbol{x}, \boldsymbol{y}) = \frac{1}{4\pi} \boldsymbol{L}_{\hat{\boldsymbol{x}}}^* \sum_{k=1}^{\infty} \frac{x^k}{y^{k+1}(k+1)} P_k(\hat{\boldsymbol{x}} \cdot \hat{\boldsymbol{y}}) \tag{6.3a}$$

$$= \frac{1}{4\pi} \sum_{k=1}^{\infty} \frac{x^k}{y^{k+1}(k+1)} \boldsymbol{L}_{\hat{\boldsymbol{x}}}^* P_k(\hat{\boldsymbol{x}} \cdot \hat{\boldsymbol{y}}) \tag{6.3b}$$

$$= \frac{1}{4\pi} \sum_{k=1}^{\infty} \frac{x^k \sqrt{k(k+1)}}{y^{k+1}(k+1)} \boldsymbol{p}_k^{(3)}(\hat{\boldsymbol{x}}, \hat{\boldsymbol{y}}) \tag{6.3c}$$

$$= \frac{1}{4\pi} \sum_{k=1}^{\infty} \sqrt{\frac{k}{k+1}} \frac{x^k}{y^{k+1}} \boldsymbol{p}_k^{(3)}(\hat{\boldsymbol{x}}, \hat{\boldsymbol{y}}). \tag{6.3d}$$

Note that the interchanging of the differential operator and the series is valid due to Lemma 6.8. The vector Legendre polynomials are given in Definition 5.21. Thus, we eventually obtain that the kernel of the inverse MEG problem is a particular case of the continuous/star-shaped VLI kernel.

Lemma 6.9. *Let Assumption 3.2 with $L \geq 1$ be fulfilled. The integral kernel $\boldsymbol{k}_{\text{M}}$ given by*

$$\boldsymbol{k}_{\text{M}}(\boldsymbol{x}, \boldsymbol{y}) = \frac{1}{4\pi} \sum_{k=1}^{\infty} \sqrt{\frac{k}{k+1}} \frac{x^k}{y^{k+1}} \boldsymbol{p}_k^{(3)}(\hat{\boldsymbol{x}}, \hat{\boldsymbol{y}}), \qquad (\boldsymbol{x}, \boldsymbol{y}) \in \mathbb{B}_{\varrho_0} \times \overline{\mathbb{B}_{\varrho_L}^{\text{ext}}}, \tag{6.4}$$

is a continuous/star-shaped VLI kernel, see Definitions 6.1 and 6.2. In addition, we have type $\iota = 3$ and the exponents $t_k \coloneqq k$ for all $k \in \mathbb{N}$. The corresponding functions $\{\gamma_k\}_{k \in \mathbb{N}}$ given by

$$\gamma_k(y) \coloneqq \Gamma_k \frac{1}{y^{k+1}} \coloneqq \frac{1}{4\pi} \sqrt{\frac{k}{k+1}} \frac{1}{y^{k+1}} \qquad \text{for all } \boldsymbol{y} \in \overline{\mathbb{B}_{\varrho_L}^{\text{ext}}}$$

satisfy for an $\varepsilon > 0$ the estimates

$$|\gamma_k(y)| \leq \frac{1}{4\pi} \sqrt{\frac{k}{k+1}} \frac{1}{y^{k+1}},$$

$$\sup_{\boldsymbol{y} \in \overline{\mathbb{B}_{\varrho_L}^{\text{ext}}}} |\gamma_k'(y)| \leq \frac{1}{4\pi} \sqrt{k(k+1)} (\varrho_0 + \varepsilon)^{-(k+2)},$$

$$\sup_{\boldsymbol{y} \in \overline{\mathbb{B}_{\varrho_L}^{\text{ext}}}} |\gamma_k''(y)| \leq \frac{1}{4\pi} \sqrt{k(k+1)} (k+2) (\varrho_0 + \varepsilon)^{-(k+3)}.$$

Finally, we set $\gamma_0 \coloneqq \Gamma_0 \coloneqq 0$.

Proof. By means of the multiple-shell model, we immediately obtain $\inf_{\boldsymbol{y} \in \overline{\mathbb{B}_{\varrho_L}^{\text{ext}}}} y \geq \varrho_L > \varrho_0$, which satisfies the requirements on the domains. Moreover, we set $\iota = 3$ and determine for

all $k \in \mathbb{N}$ the exponent by $t_k = k \geq 1$. It is easy to verify that $\sup_{k\in\mathbb{N}} \varrho_0^{k-k} = 1 < \infty$ and that

$$|\gamma_k(y)| \leq \frac{\Gamma_k}{y^{k+1}} = \frac{\Gamma_k}{y^{k+1+\delta_{0_\iota,0}\delta_{k,0}}} \qquad \text{for all } \boldsymbol{y} \in \overline{\mathbb{B}_{\varrho_L}^{\text{ext}}}$$

with $(k \mapsto \Gamma_k \coloneqq \sqrt{k/(k+1)}/(4\pi)) \in \mathcal{O}(1)$ as $k \to \infty$. Since the origin is not contained in the outer region, the function γ_k is an arbitrarily often continuously differentiable function for all $k \in \mathbb{N}$. In addition, there exists an $\varepsilon \coloneqq (2(\varrho_L - \varrho_0))^{-1} > 0$ such that

$$\begin{aligned}
\sup_{\boldsymbol{y}\in\overline{\mathbb{B}_{\varrho_L}^{\text{ext}}}} |\gamma_k'(y)| &= \sup_{\boldsymbol{y}\in\overline{\mathbb{B}_{\varrho_L}^{\text{ext}}}} \left|\frac{-\Gamma_k(k+1)}{y^{k+2}}\right| \leq \frac{1}{4\pi}\sqrt{k(k+1)}(\varrho_0+\varepsilon)^{-(k+2)}, \\
\sup_{\boldsymbol{y}\in\overline{\mathbb{B}_{\varrho_L}^{\text{ext}}}} |\gamma_k''(y)| &= \sup_{\boldsymbol{y}\in\overline{\mathbb{B}_{\varrho_L}^{\text{ext}}}} \left|\frac{\Gamma_k(k+1)(k+2)}{y^{k+3}}\right| \leq \frac{1}{4\pi}\sqrt{k(k+1)}(k+2)(\varrho_0+\varepsilon)^{-(k+3)}. \qquad \square
\end{aligned}$$

Now, we consider the integral kernel corresponding to the EEG problem. In Eq. (4.23), a representation of this kernel is stated, that is

$$\boldsymbol{k}_{\text{E}}(\boldsymbol{x},\boldsymbol{y}) \coloneqq \frac{1}{4\pi}\sum_{k=1}^{\infty}(2k+1)H_k(y)\boldsymbol{\nabla}_{\boldsymbol{x}}\left(x^k P_k(\hat{\boldsymbol{x}}\cdot\hat{\boldsymbol{y}})\right), \qquad (\boldsymbol{x},\boldsymbol{y}) \in \mathbb{B}_{\varrho_0} \times \mathbb{S}_{[\varrho_{L-1},\varrho_L]}.$$

In order to fit into the setting of the continuous/star-shaped VLI kernels, further manipulation of the right-hand side is required. For the gradient term of the right-hand side, we use Eq. (5.6) since the Legendre polynomials of degree $k \in \mathbb{N}_0$ are elements of $\text{Harm}_k(\mathbb{S})$, see Theorem 2.25. Thus, via Definition 5.21, we get for all $k \in \mathbb{N}$ the identity

$$\begin{aligned}
\boldsymbol{\nabla}_{\boldsymbol{x}}\left(x^k P_k(\hat{\boldsymbol{x}}\cdot\hat{\boldsymbol{y}})\right) &= x^{k-1}\tilde{\boldsymbol{o}}_{n,\boldsymbol{\xi}}^{(2)} P_k(\hat{\boldsymbol{x}}\cdot\hat{\boldsymbol{y}}) \\
&= \sqrt{k(2k+1)}x^{k-1}\tilde{\boldsymbol{p}}_n^{(2)}(\hat{\boldsymbol{x}},\hat{\boldsymbol{y}}).
\end{aligned}$$

For $k = 0$, the gradient of the constant function vanishes. Hence, the integral kernel has for all $(\boldsymbol{x},\boldsymbol{y}) \in \mathbb{B}_{\varrho_0} \times \mathbb{S}_{[\varrho_{L-1},\varrho_L]}$ several alternative representations:

$$\begin{aligned}
\boldsymbol{k}_{\text{E}}(\boldsymbol{x},\boldsymbol{y}) &= \frac{1}{4\pi}\sum_{k=1}^{\infty}\sqrt{k(2k+1)^3}H_k(y)x^{k-1}\tilde{\boldsymbol{p}}_k^{(2)}(\hat{\boldsymbol{x}},\hat{\boldsymbol{y}}) && \text{(6.5a)} \\
&= \frac{1}{4\pi}\sum_{k=1}^{\infty}(2k+1)H_k(y)\boldsymbol{\nabla}_{\boldsymbol{x}}\left(x^k P_k(\hat{\boldsymbol{x}}\cdot\hat{\boldsymbol{y}})\right) && \text{(6.5b)} \\
&= \frac{1}{4\pi}\boldsymbol{\nabla}_{\boldsymbol{x}}\sum_{k=1}^{\infty}(2k+1)H_k(y)x^k P_k(\hat{\boldsymbol{x}}\cdot\hat{\boldsymbol{y}}), && \text{(6.5c)}
\end{aligned}$$

where the interchanging of the differential operator and the series in the last step is valid due to Lemma 6.8.

Lemma 6.10. *Let Assumption 3.2 be fulfilled, where the multiple-shell model has at least two shells, that is $L \geq 2$. Under this condition, the kernel given by*

$$\boldsymbol{k}_{\text{E}}(\boldsymbol{x},\boldsymbol{y}) = \frac{1}{4\pi}\sum_{k=1}^{\infty}\sqrt{k(2k+1)^3}H_k(y)x^{k-1}\tilde{\boldsymbol{p}}_k^{(2)}(\hat{\boldsymbol{x}},\hat{\boldsymbol{y}}) \qquad (6.6)$$

for all $(\boldsymbol{x},\boldsymbol{y}) \in \mathbb{B}_{\varrho_0} \times \mathbb{S}_{[\varrho_{L-1},\varrho_L]}$ *with* H_k *given as in Eq.* (4.20) *combined with Eq.* (4.18)*, is a linear combination of two continuous/star-shaped VLI kernels in the sense of Definition 6.1 or Definition 6.2, respectively. Thus, the series converges uniformly in* $\mathbb{B}_{\varrho_0} \times \mathbb{S}_{[\varrho_{L-1},\varrho_L]}$*. In addition, the series and the differential operator appearing in the vector Legendre polynomial can be interchanged.*

Proof. First, we define for all $(\boldsymbol{x},\boldsymbol{y}) \in \mathbb{B}_{\varrho_0} \times \mathbb{S}_{[\varrho_{L-1},\varrho_L]}$ the two functions

$$\begin{aligned}\boldsymbol{f}^{(1)}(\boldsymbol{x},\boldsymbol{y}) &\coloneqq \frac{1}{4\pi}\sum_{k=1}^{\infty}(2k+1)kH_k(y)x^{k-1}\boldsymbol{p}_k^{(1)}(\hat{\boldsymbol{x}},\hat{\boldsymbol{y}}),\\ \boldsymbol{f}^{(2)}(\boldsymbol{x},\boldsymbol{y}) &\coloneqq \frac{1}{4\pi}\sum_{k=1}^{\infty}\sqrt{\mu_k^{(2)}}(2k+1)H_k(y)x^{k-1}\boldsymbol{p}_k^{(2)}(\hat{\boldsymbol{x}},\hat{\boldsymbol{y}}).\end{aligned}$$

Second, we prove that these two functions are star-shaped VLI kernels. In both cases, we obtain that the inner region $\mathbb{B}_{\varrho_0}$ is a star-shaped bounded region with $\sup_{\boldsymbol{x}\in\mathbb{B}_{\varrho_0}} x = \varrho_0$ and that $\inf_{\boldsymbol{y}\in\mathbb{S}_{[\varrho_{L-1},\varrho_L]}} y > \varrho_{L-1} > \varrho_0$ since $L \geq 2$. In addition, we define the exponent by $t_k \coloneqq k-1$ for all $k \in \mathbb{N}_0$, which implies $\inf_{k\in\mathbb{N}_0,\gamma_k\not\equiv 0} t_k \geq -1$. Also, we have $\sup_{k\in\mathbb{N}_0} \varrho_0^{t_k-k} = \varrho_0^{-1} < \infty$.

In the case of $\boldsymbol{f}^{(1)}$, we choose the following parameters for $k \in \mathbb{N}_0$ in order to satisfy Definition 6.2 for $\iota = 1$. For the sequence of functions $\{\gamma_k\}_{k\in\mathbb{N}_0}$, we choose

$$\gamma_k(y) \coloneqq \frac{k(2k+1)}{4\pi}H_k(y), \qquad \boldsymbol{y} \in \mathbb{S}_{[\varrho_{L-1},\varrho_L]}.$$

Note that $\gamma_0 \equiv 0$. Hence, we can also start the summation by $k = 1$ and do not get a singularity at the origin. By means of Lemma 4.2, we obtain that $(k \mapsto |\beta_k^{(L)}|) \in \mathcal{O}(k^{-1})$ if $L \geq 0$. Thus, for its asymptotic behaviour, we obtain for all $\boldsymbol{y} \in \mathbb{S}_{[\varrho_{L-1},\varrho_L]}$ the estimate

$$\begin{aligned}|\gamma_k(y)| &= \frac{k(2k+1)}{4\pi}\,|H_k(y)|\\ &= \frac{k(2k+1)}{4\pi}\left|\left(\frac{k+1}{k}\left(\frac{y}{\varrho_L}\right)^{2k+1}+1\right)\right|\left|\beta_k^{(L)}\right||y|^{-(k+1)}\\ &\leq \frac{(2k+1)^2}{4\pi}\left|\beta_k^{(L)}\right||y|^{-(k+1)}\\ &=: \frac{\Gamma_k}{y^{k+1+\delta_{0_1,0}\delta_{k,0}}}\end{aligned}$$

with $\Gamma_k \coloneqq (2k+1)^2(4\pi)^{-1}|\beta_k^{(L)}| \in \mathbb{R}_0^+$. The constant Γ_k grows polynomially in k with order 1, due to Lemma 4.2. Thus, $\boldsymbol{f}^{(1)}$ is a star-shaped VLI kernel in the sense of Definition 6.2. Similarly, in the case of $\boldsymbol{f}^{(2)}$, we obtain a star-shaped VLI kernel by choosing the same parameters and setting $\gamma_k(y) \coloneqq (4\pi)^{-1}(2k+1)\sqrt{k(k+1)}H_k(y)$ for $k \in \mathbb{N}$ and $\gamma_0 \equiv 0$. Both functions are also continuous VLI kernels as in Definition 6.1 because the zeroth summand vanishes and $\inf_{k\in\mathbb{N}_0,\gamma_k\not\equiv 0} t_k = 0$.

Recall that the Edmonds and Morse-Feshbach vector Legendre polynomials are related by Eq. (5.12b), that is

$$\begin{aligned}\sqrt{\tilde{\mu}_k^{(2)}}\tilde{\boldsymbol{p}}_k^{(2)} &= \sqrt{\tilde{\mu}_k^{(2)}}\left(\sqrt{\frac{k}{2k+1}}\boldsymbol{p}_k^{(1)}+\sqrt{\frac{k+1}{2k+1}}\boldsymbol{p}_k^{(2)}\right)\\ &= k\boldsymbol{p}_k^{(1)}+\sqrt{k(k+1)}\boldsymbol{p}_k^{(2)},\end{aligned}$$

where the normalization factor $\tilde{\mu}_k^{(2)} = k(2k+1)$ is given for all $k \in \mathbb{N}$ in Definition 5.21 and $\mu_k^{(2)} = k(k+1)$ in Eq. (5.2). Since both series occurring in $\boldsymbol{f}^{(1)}$ and $\boldsymbol{f}^{(2)}$ converge (uniformly), see Theorem 6.6, the series in $\boldsymbol{k}_{\mathrm{E}} = \boldsymbol{f}^{(1)} + \boldsymbol{f}^{(2)}$ converges (uniformly). □

Summing up, the representation of $\boldsymbol{k}_{\mathrm{E}}$ consists of a linear combination of two continuous/star-shaped VLI kernels. We analyzed the convergence of the occurring series by taking into account the asymptotic behaviour of the coefficients $\beta_k^{(L)}$ stated in Lemma 4.2. The coefficients depend on the radii of the different shells and their conductivities.

In the frequently used special case of the homogeneous setting, that is the same constant conductivity on each shell, a closed representation of $\{H_k\}_{k\in\mathbb{N}}$ is known and the convergence is given, see Example 6.11.

Example 6.11. *In the homogeneous case, that is all conductivities are equal ($\sigma_l = \sigma_0$ for all $l = 0, \dots, L$), we do not need to distinguish between the different shells. Hence, we can assume that the number of shells is greater than one and the matrix $\mathfrak{M}^{(L)}$ equals the identity matrix, see Eq.* (4.17)*. Thus, via Eq.* (4.18) *we get that $\beta_k^{(l)} = \beta_k^{(0)} = (\sigma_0(2k+1))^{-1}$ for all $k \in \mathbb{N}$ and all $l = 0, \dots, L$ and, as in the inhomogeneous case, $\alpha_0^{(0)} = \beta_0^{(0)} = 0$. The integral kernel is for all $(\boldsymbol{x}, \boldsymbol{y}) \in \mathbb{B}_{\varrho_0} \times \mathbb{S}_{[\varrho_{L-1}, \varrho_L]}$ (i.e. $x \le \varrho_0 < \varrho_{L-1} \le y$) given by*

$$\boldsymbol{k}_{\mathrm{E}}(\boldsymbol{x}, \boldsymbol{y}) = \frac{1}{4\pi} \sum_{k=1}^{\infty} \sqrt{k(2k+1)^3} \left(\frac{k+1}{k} \left(\frac{y}{\varrho_L} \right)^{2k+1} + 1 \right) \beta_k^{(0)} \frac{x^{k-1}}{y^{k+1}} \tilde{\boldsymbol{p}}_k^{(2)}(\hat{\boldsymbol{x}}, \hat{\boldsymbol{y}}).$$

Thus, for the homogeneous inverse EEG problem, we also obtain the asymptotic behaviour of the sequence $\{\beta_k^{(0)}\}_{k\in\mathbb{N}}$ required for the convergence of the series, see Lemma 4.2. For the restriction to the sphere $\mathbb{S}_{\varrho_L}$, we obtain $H_k = (\sigma_0 k)^{-1} \varrho_L^{-(k+1)}$, see Eq. (4.21)*, and*

$$\boldsymbol{k}_{\mathrm{E}}(\boldsymbol{x}, \varrho_L \hat{\boldsymbol{y}}) = \frac{1}{4\pi\sigma_0} \sum_{k=1}^{\infty} \sqrt{\frac{(2k+1)^3}{k}} \frac{x^{k-1}}{\varrho_L^{k+1}} \tilde{\boldsymbol{p}}_k^{(2)}(\hat{\boldsymbol{x}}, \hat{\boldsymbol{y}}). \tag{6.7}$$

6.3. Further Properties

For the analysis of the integral operator induced by the continuous/star-shaped VLI kernel, we need more properties than the well-definedness of the integral kernel. We start by establishing the continuity of the continuous VLI kernel using the uniform convergence and boundedness of the occurring series.

Corollary 6.12. *The following statements hold true:*

i) The continuous VLI kernel $\boldsymbol{k}^{(\iota)}$ is continuous in both arguments.

ii) The star-shaped VLI kernel $\boldsymbol{k}^{(\iota)}(\boldsymbol{x}, \boldsymbol{y})$ is continuous for all $(\boldsymbol{x}, \boldsymbol{y}) \in (\mathbb{G}_{\mathrm{star}} \setminus \{\boldsymbol{0}\}) \times \mathbb{G}_{\mathrm{out}}$.

Proof. i) For each $k \in \mathbb{N}_{0_\iota}$, the function $\boldsymbol{h}_k \colon \mathbb{G}_{\mathrm{in}} \times \mathbb{G}_{\mathrm{out}} \to \mathbb{R}^3$ defined by

$$\boldsymbol{h}_k(\boldsymbol{x}, \boldsymbol{y}) \coloneqq \gamma_k(y) x^{t_k} \boldsymbol{p}_k^{(\iota)}(\hat{\boldsymbol{x}}, \hat{\boldsymbol{y}})$$

is continuous because of the continuity of γ_k, the fact that $\inf_{k\in\mathbb{N}_{0_\iota}, \gamma_k \not\equiv 0} t_k \ge 0$, and the properties of the vectorial Legendre polynomials. The uniform convergence of the series $\sum_{k=0_\iota}^{\infty} \boldsymbol{h}_k$ is proved in Theorem 6.6. This yields the desired continuity of the limit $\boldsymbol{k}^{(\iota)}$.

ii) Due to Corollary 6.3, $x\boldsymbol{k}^{(\iota)}(\boldsymbol{x},\boldsymbol{y})$ is a continuous VLI kernel for all $(\boldsymbol{x},\boldsymbol{y}) \in \mathbb{G}_{\text{star}} \times \mathbb{G}_{\text{out}}$ and, hence, continuous in both arguments by means of the previous item. Thus, $\boldsymbol{k}^{(\iota)}(\boldsymbol{x},\boldsymbol{y})$ is continuous for all $(\boldsymbol{x},\boldsymbol{y}) \in (\mathbb{G}_{\text{star}} \setminus \{\boldsymbol{0}\}) \times \mathbb{G}_{\text{out}}$. □

Now, we are interested in integrability results of the continuous/star-shaped VLI kernel $\boldsymbol{k}^{(\iota)}$. An immediate consequence of the continuity of the continuous VLI kernel and the boundedness of sets $\mathbb{G}_{\text{in}}$ and $\mathbb{G}_{\text{star}}$, respectively, is the next corollary.

Corollary 6.13. *The following statements hold true, where B is the upper bound given in Lemma 6.5:*

i) The continuous VLI kernel $\boldsymbol{k}^{(\iota)}(\cdot,\boldsymbol{y})$ is an $\mathbf{L}_2(\mathbb{G}_{\text{in}})$-function for all fixed $\boldsymbol{y} \in \mathbb{G}_{\text{out}}$ fulfilling

$$\left\|\boldsymbol{k}^{(\iota)}(\cdot,\boldsymbol{y})\right\|^2_{\mathbf{L}_2(\mathbb{G}_{\text{in}})} \leq B^2 \text{vol}(\mathbb{G}_{\text{in}}) < \infty.$$

ii) The star-shaped VLI kernel $\boldsymbol{k}^{(\iota)}(\cdot,\boldsymbol{y})$ is an $\mathbf{L}_2(\mathbb{G}_{\text{star}})$-function for all fixed $\boldsymbol{y} \in \mathbb{G}_{\text{out}}$ with

$$\left\|\boldsymbol{k}^{(\iota)}(\cdot,\boldsymbol{y})\right\|^2_{\mathbf{L}_2(\mathbb{G}_{\text{star}})} \leq B^2 4\pi R^3 < \infty.$$

The series of the integral kernels $\boldsymbol{k}^{(\iota)}(\cdot,\boldsymbol{y})$ converge in the $\mathbf{L}_2(\mathbb{G}_{\text{in}})$- and $\mathbf{L}_2(\mathbb{G}_{\text{star}})$-sense, respectively.

Proof. The convergence of the series and the finiteness of the norms can be obtained by the same estimates. Thus, we restrict ourselves to the calculation of the norms.

i) The region $\mathbb{G}_{\text{in}}$ is bounded by Definition 6.1. Due to Corollary 6.12, we have $\boldsymbol{k}^{(\iota)}(\cdot,\boldsymbol{y}) \in \mathbf{C}(\mathbb{G}_{\text{in}}) \subset \mathbf{L}_2(\mathbb{G}_{\text{in}})$ for all fixed $\boldsymbol{y} \in \mathbb{G}_{\text{out}}$. With the result from Lemma 6.5, we estimate the norm for all $\boldsymbol{y} \in \mathbb{G}_{\text{out}}$ by

$$\left\|\boldsymbol{k}^{(\iota)}(\cdot,\boldsymbol{y})\right\|^2_{\mathbf{L}_2(\mathbb{G}_{\text{in}})} = \int_{\mathbb{G}_{\text{in}}} \left(\boldsymbol{k}^{(\iota)}(\boldsymbol{x},\boldsymbol{y})\right)^2 \,\mathrm{d}\boldsymbol{x} \leq B^2 \,\text{vol}(\mathbb{G}_{\text{in}}) < \infty.$$

ii) For the second statement, we need to estimate the $\mathbf{L}_2(\mathbb{G}_{\text{star}})$-norm of the star-shaped VLI kernel $\boldsymbol{k}^{(\iota)}(\cdot,\boldsymbol{y})$. For this purpose, we use properties of the vectorial Legendre polynomials from Definition 5.21 and Lemma 5.22. Thus, for all $\boldsymbol{y} \in \mathbb{G}_{\text{out}}$ we get the estimate

$$\begin{aligned}
\left\|\boldsymbol{k}^{(\iota)}(\cdot,\boldsymbol{y})\right\|^2_{\mathbf{L}_2(\mathbb{G}_{\text{star}})} &= \int_{\mathbb{G}_{\text{star}}} \left(\sum_{k=0_\iota}^{\infty} \gamma_k(y) x^{t_k} \boldsymbol{p}_k^{(\iota)}(\hat{\boldsymbol{x}},\hat{\boldsymbol{y}})\right)^2 \mathrm{d}\boldsymbol{x} \\
&\leq \int_{\mathbb{G}_{\text{star}}} \left(\sum_{k=0_\iota}^{\infty} |\gamma_k(y)|\, x^{t_k} \sqrt{\mu_k^{(\iota)}}\right)^2 \mathrm{d}\boldsymbol{x} \\
&= \int_{\mathbb{S}} \int_0^{\zeta(\hat{\boldsymbol{x}})} \left(\sum_{k=0_\iota}^{\infty} |\gamma_k(y)|\, x^{t_k+1} \sqrt{\mu_k^{(\iota)}}\right)^2 \mathrm{d}x \,\mathrm{d}\omega(\hat{\boldsymbol{x}}) \\
&\leq \left(\sum_{k=0_\iota}^{\infty} |\gamma_k(y)|\, R^{t_k+1} \sqrt{\mu_k^{(\iota)}}\right)^2 \int_{\mathbb{S}} \int_0^{\zeta(\hat{\boldsymbol{x}})} \mathrm{d}x \,\mathrm{d}\omega(\hat{\boldsymbol{x}})
\end{aligned}$$

$$\leq 4\pi R \left(\sup_{k \in \mathbb{N}_{0_\iota}} R^{t_k - k} \right)^2 \left(\sum_{k=0_\iota}^{\infty} \Gamma_k \sqrt{\mu_k^{(\iota)}} \frac{R^{k+1}}{(R+\varepsilon)^{k+1+\delta_{0_\iota,0}\delta_{k,0}}} \right)^2$$
$$= B^2 4\pi R^3 < \infty.$$

The latter estimate is valid due to Lemma 6.5 and Definition 6.2, and properties of the power series, see Theorem 6.4. □

In the continuous/star-shaped VLI equation, the kernel is integrated together with a function $\boldsymbol{f} \in \mathbf{L}_2(\mathbb{G})$. For later use, we want to interchange the series in the kernel with the integration. This is permitted by the strong convergence of the series proved in Corollary 6.13, see, for instance, [225, Ch. V].

Corollary 6.14. *Let $\mathbb{G} \subseteq \mathbb{G}_{\text{in}}$ or $\mathbb{G} \subseteq \mathbb{G}_{\text{star}}$, respectively, be a region inside the inner region and let $\boldsymbol{f} \in \mathbf{L}_2(\mathbb{G})$. Then the following holds true for the continuous/star-shaped VLI kernel:*

$$\int_{\mathbb{G}} \boldsymbol{f}(\boldsymbol{x}) \cdot \boldsymbol{k}^{(\iota)}(\boldsymbol{x}, \boldsymbol{y}) \, \mathrm{d}\boldsymbol{x} = \sum_{k=0_\iota}^{\infty} \int_{\mathbb{G}} \boldsymbol{f}(\boldsymbol{x}) \cdot \left(\gamma_k(y) x^{t_k} \boldsymbol{p}_k^{(\iota)}(\hat{\boldsymbol{x}}, \hat{\boldsymbol{y}}) \right) \mathrm{d}\boldsymbol{x}.$$

The integrability of the continuous/star-shaped VLI kernel with respect to the first argument is a consequence of this corollary. For its proof, the Cartesian unit vectors in $\mathbb{R}^3$ are used as the function $\boldsymbol{f}$.

Corollary 6.15. *Let $\mathbb{G} \subseteq \mathbb{G}_{\text{in}}$ or $\mathbb{G} \subseteq \mathbb{G}_{\text{star}}$, respectively, be a region inside the inner region. Then we are able to interchange the integration over $\mathbb{G}$ with the series in the definition of the continuous/star-shaped VLI kernel. More precisely, for all $\boldsymbol{y} \in \mathbb{G}_{\text{out}}$, we get*

$$\int_{\mathbb{G}} \boldsymbol{k}^{(\iota)}(\boldsymbol{x}, \boldsymbol{y}) \, \mathrm{d}\boldsymbol{x} = \sum_{k=0_\iota}^{\infty} \int_{\mathbb{G}} \gamma_k(y) x^{t_k} \boldsymbol{p}_k^{(\iota)}(\hat{\boldsymbol{x}}, \hat{\boldsymbol{y}}) \, \mathrm{d}\boldsymbol{x}.$$

The weak convergence of the series in Corollary 6.14 enables us to expand Corollary 6.13 to the second slot of the kernel, that is to establish $\mathbf{L}_2(\mathbb{G}_{\text{in}} \times \mathbb{G}_{\text{out}})$ regularity of $\boldsymbol{k}^{(\iota)}$.

Lemma 6.16. *The following statements hold true:*

i) The continuous VLI kernel $\boldsymbol{k}^{(\iota)}$ is an $\mathbf{L}_2(\mathbb{G}_{\text{in}} \times \mathbb{G}_{\text{out}})$-function.

ii) The star-shaped VLI kernel $\boldsymbol{k}^{(\iota)}$ is an $\mathbf{L}_2(\mathbb{G}_{\text{star}} \times \mathbb{G}_{\text{out}})$-function.

Proof. Inserting the series representation of the continuous/star-shaped VLI kernel into the norm and using the weak convergence of the series, see Corollary 6.14, we obtain

$$\int_{\mathbb{G}_{\text{out}}} \int_{\mathbb{G}_{\text{in}}} \left(\boldsymbol{k}^{(\iota)}(\boldsymbol{x}, \boldsymbol{y}) \right)^2 \mathrm{d}\boldsymbol{x} \, \mathrm{d}\boldsymbol{y}$$
$$= \int_{\mathbb{G}_{\text{out}}} \int_{\mathbb{G}_{\text{in}}} \left(\sum_{k=0_\iota}^{\infty} \gamma_k(y) x^{t_k} \boldsymbol{p}_k^{(\iota)}(\hat{\boldsymbol{x}}, \hat{\boldsymbol{y}}) \right)^2 \mathrm{d}\boldsymbol{x} \, \mathrm{d}\boldsymbol{y}$$
$$= \int_{\mathbb{G}_{\text{out}}} \sum_{k=0_\iota}^{\infty} \sum_{l=0_\iota}^{\infty} \gamma_k(y) \gamma_l(y) \int_{\mathbb{G}_{\text{in}}} x^{t_k + t_l} \boldsymbol{p}_k^{(\iota)}(\hat{\boldsymbol{x}}, \hat{\boldsymbol{y}}) \cdot \boldsymbol{p}_l^{(\iota)}(\hat{\boldsymbol{x}}, \hat{\boldsymbol{y}}) \, \mathrm{d}\boldsymbol{x} \, \mathrm{d}\boldsymbol{y}. \tag{6.8}$$

If the right-hand side exists, then it equals the $\mathbf{L}_2(\mathbb{G}_{\text{in}} \times \mathbb{G}_{\text{out}})$-norm of $\boldsymbol{k}^{(\iota)}$ to the power of two. This is obtained by means of Tonelli's Theorem, see [19, Thm. 23.6]. The latter identity also holds true in the case of $\mathbb{G}_{\text{star}}$ instead of $\mathbb{G}_{\text{in}}$.

i) Using the estimate of the vectorial Legendre polynomials, see Lemma 5.22 and the fact that $x \leq R$ since $\boldsymbol{x} \in \mathbb{G}_{\text{in}}$, and the assumptions on $\{\gamma_k\}_{k\in\mathbb{N}_{0_\iota}}$ from Definition 6.1, we obtain the estimate

$$\begin{aligned}
&\int_{\mathbb{G}_{\text{out}}} \int_{\mathbb{G}_{\text{in}}} \left(\boldsymbol{k}^{(\iota)}(\boldsymbol{x},\boldsymbol{y})\right)^2 \,\mathrm{d}\boldsymbol{x}\,\mathrm{d}\boldsymbol{y} \\
&\leq \int_{\mathbb{G}_{\text{out}}} \left(\sum_{k=0_\iota}^{\infty} |\gamma_k(y)|\, R^{t_k} \sqrt{\mu_k^{(\iota)}} \right)^2 \operatorname{vol}(\mathbb{G}_{\text{in}})\,\mathrm{d}\boldsymbol{y} \\
&\leq \int_{\mathbb{G}_{\text{out}}} \left(\sum_{k=0_\iota}^{\infty} \frac{\Gamma_k}{y^{k+1+\delta_{0_\iota,0}\delta_{k,0}}} R^{t_k} \sqrt{\mu_k^{(\iota)}} \right)^2 \operatorname{vol}(\mathbb{G}_{\text{in}})\,\mathrm{d}\boldsymbol{y} \\
&\leq \operatorname{vol}(\mathbb{G}_{\text{in}}) \int_{\mathbb{B}_{R+\varepsilon}^{\text{ext}}} \left(\sum_{k=0_\iota}^{\infty} \frac{\Gamma_k}{y^{k+1+\delta_{0_\iota,0}\delta_{k,0}}} R^{t_k} \sqrt{\mu_k^{(\iota)}} \right)^2 \mathrm{d}\boldsymbol{y} \\
&= \operatorname{vol}(\mathbb{G}_{\text{in}}) \int_{\mathbb{S}} \int_{R+\varepsilon}^{\infty} \left(\sum_{k=0_\iota}^{\infty} \frac{\Gamma_k}{y^{k+1+\delta_{0_\iota,0}\delta_{k,0}}} R^{t_k} \sqrt{\mu_k^{(\iota)}} \right)^2 y^2 \,\mathrm{d}y\; \mathrm{d}\omega(\hat{\boldsymbol{y}}) \\
&= 4\pi \operatorname{vol}(\mathbb{G}_{\text{in}}) \int_{R+\varepsilon}^{\infty} \left(\sum_{k=0_\iota}^{\infty} \frac{\Gamma_k}{y^{k+\delta_{0_\iota,0}\delta_{k,0}}} R^{t_k} \sqrt{\mu_k^{(\iota)}} \right)^2 \mathrm{d}y \\
&= 4\pi \operatorname{vol}(\mathbb{G}_{\text{in}}) \int_{R+\varepsilon}^{\infty} \sum_{k=0_\iota}^{\infty} \sum_{l=0_\iota}^{\infty} \frac{\Gamma_k\Gamma_l}{y^{k+l+\delta_{0_\iota,0}(\delta_{k,0}+\delta_{l,0})}} R^{t_k+t_l} \sqrt{\mu_k^{(\iota)}\mu_l^{(\iota)}}\,\mathrm{d}y.
\end{aligned}$$

In the third estimate, we extend the integration region to a region that has a known parametrization. Eventually, the integral reduces to a one-dimensional integral with respect to y. In the next step, we want to interchange the series and the integration. We define the auxiliary functions $f_{k,l}\colon [R+\varepsilon,\infty) \to \mathbb{R}$ by

$$f_{k,l}(y) \coloneqq \Gamma_k\Gamma_l y^{-(k+l+\delta_{0_\iota,0}(\delta_{k,0}+\delta_{l,0}))} R^{t_k+t_l} \sqrt{\mu_k^{(\iota)}\mu_l^{(\iota)}}$$

for all k, $l \in \mathbb{N}_{0_\iota}$. Due to the assumptions on $\{\Gamma_k\}_{k\in\mathbb{N}_{0_\iota}}$, each function $f_{k,l}$ is non-negative and $f_{k,l} \in \mathrm{L}_2([R+\varepsilon,\infty))$. For this property of $f_{k,l}$, the term $\delta_{0_\iota,0}(\delta_{k,0}+\delta_{l,0})$ is required to achieve the integrability for k, $l = 0$. This condition has its origin in the inequality for γ_k from Definition 6.1. An immediate consequence of Beppo Levi's Theorem for series, see [19, Ch. 15], provides us with the possibility to interchange. Hence,

$$\begin{aligned}
&\int_{\mathbb{G}_{\text{out}}} \int_{\mathbb{G}_{\text{in}}} \left(\boldsymbol{k}^{(\iota)}(\boldsymbol{x},\boldsymbol{y})\right)^2 \,\mathrm{d}\boldsymbol{x}\,\mathrm{d}\boldsymbol{y} \\
&\leq 4\pi \operatorname{vol}(\mathbb{G}_{\text{in}}) \sum_{k=0_\iota}^{\infty} \sum_{l=0_\iota}^{\infty} \int_{R+\varepsilon}^{\infty} \frac{\Gamma_k\Gamma_l}{y^{k+l+\delta_{0_\iota,0}(\delta_{k,0}+\delta_{l,0})}} R^{t_k+t_l} \sqrt{\mu_k^{(\iota)}\mu_l^{(\iota)}}\,\mathrm{d}y \\
&= 4\pi \operatorname{vol}(\mathbb{G}_{\text{in}}) \sum_{k=0_\iota}^{\infty} \sum_{l=0_\iota}^{\infty} \Gamma_k\Gamma_l R^{t_k+t_l} \sqrt{\mu_k^{(\iota)}\mu_l^{(\iota)}} \int_{R+\varepsilon}^{\infty} \frac{1}{y^{k+l+\delta_{0_\iota,0}(\delta_{k,0}+\delta_{l,0})}}\,\mathrm{d}y \\
&= 4\pi \operatorname{vol}(\mathbb{G}_{\text{in}}) \sum_{k=0_\iota}^{\infty} \sum_{l=0_\iota}^{\infty} \Gamma_k\Gamma_l R^{t_k+t_l} \sqrt{\mu_k^{(\iota)}\mu_l^{(\iota)}} \frac{(R+\varepsilon)^{-(k+l+\delta_{0_\iota,0}(\delta_{k,0}+\delta_{l,0})-1)}}{(k+l+\delta_{0_\iota,0}(\delta_{k,0}+\delta_{l,0})-1)}
\end{aligned}$$

$$
\begin{aligned}
&= 4\pi \operatorname{vol}(\mathbb{G}_{\text{in}}) \sum_{k=0_\iota}^{\infty} \sum_{l=0_\iota}^{\infty} \Gamma_k \Gamma_l R^{t_k+t_l} \sqrt{\mu_k^{(\iota)} \mu_l^{(\iota)}} (R+\varepsilon)^{-(k+l+\delta_{0_\iota,0}(\delta_{k,0}+\delta_{l,0})-1)} \\
&\leq 4\pi \operatorname{vol}(\mathbb{G}_{\text{in}}) \left(\sum_{k=0_\iota}^{\infty} \Gamma_k \sqrt{\mu_k^{(\iota)}} \frac{R^{t_k}}{(R+\varepsilon)^{k+\delta_{0_\iota,0}\delta_{k,0}-1/2}} \right)^2 \\
&\leq 4\pi \operatorname{vol}(\mathbb{G}_{\text{in}}) \left(\sup_{k\in\mathbb{N}_{0_\iota}} R^{t_k-k} \right)^2 \left(\sum_{k=0_\iota}^{\infty} \Gamma_k \sqrt{\mu_k^{(\iota)}} \frac{R^{k}}{(R+\varepsilon)^{k+\delta_{0_\iota,0}\delta_{k,0}-1/2}} \right)^2 \\
&\leq 4\pi \operatorname{vol}(\mathbb{G}_{\text{in}}) B^2 (R+\varepsilon)^3 < \infty.
\end{aligned}
$$

ii) The estimate for the star-shaped VLI kernel is similar to the previous one. For the inner integral, we obtain

$$
\begin{aligned}
&\int_{\mathbb{G}_{\text{out}}} \int_{\mathbb{G}_{\text{star}}} \left(\boldsymbol{k}^{(\iota)}(\boldsymbol{x},\boldsymbol{y})\right)^2 \,\mathrm{d}\boldsymbol{x}\,\mathrm{d}\boldsymbol{y} \\
&= \int_{\mathbb{G}_{\text{out}}} \sum_{k=0_\iota}^{\infty} \sum_{l=0_\iota}^{\infty} \gamma_k(y)\gamma_l(y) \int_{\mathbb{G}_{\text{star}}} x^{t_k+t_l} \boldsymbol{p}_k^{(\iota)}(\hat{\boldsymbol{x}},\hat{\boldsymbol{y}}) \cdot \boldsymbol{p}_l^{(\iota)}(\hat{\boldsymbol{x}},\hat{\boldsymbol{y}}) \,\mathrm{d}\boldsymbol{x}\,\mathrm{d}\boldsymbol{y} \\
&= \int_{\mathbb{G}_{\text{out}}} \sum_{k=0_\iota}^{\infty} \sum_{l=0_\iota}^{\infty} \gamma_k(y)\gamma_l(y) \int_{\mathbb{S}} \left(\int_0^{\zeta(\hat{\boldsymbol{x}})} x^{t_k+t_l+2} \,\mathrm{d}x \right) \boldsymbol{p}_k^{(\iota)}(\hat{\boldsymbol{x}},\hat{\boldsymbol{y}}) \cdot \boldsymbol{p}_l^{(\iota)}(\hat{\boldsymbol{x}},\hat{\boldsymbol{y}}) \,\mathrm{d}\omega(\hat{\boldsymbol{x}})\,\mathrm{d}\boldsymbol{y} \\
&= \int_{\mathbb{G}_{\text{out}}} \sum_{k=0_\iota}^{\infty} \sum_{l=0_\iota}^{\infty} \gamma_k(y)\gamma_l(y) \int_{\mathbb{S}} \frac{1}{t_k+t_l+3} \left(\zeta(\hat{\boldsymbol{x}})\right)^{t_k+t_l+3} \boldsymbol{p}_k^{(\iota)}(\hat{\boldsymbol{x}},\hat{\boldsymbol{y}}) \cdot \boldsymbol{p}_l^{(\iota)}(\hat{\boldsymbol{x}},\hat{\boldsymbol{y}}) \,\mathrm{d}\omega(\hat{\boldsymbol{x}})\,\mathrm{d}\boldsymbol{y} \\
&\leq \int_{\mathbb{G}_{\text{out}}} \sum_{k=0_\iota}^{\infty} \sum_{l=0_\iota}^{\infty} |\gamma_k(y)|\,|\gamma_l(y)| \int_{\mathbb{S}} \frac{1}{t_k+t_l+3} R^{t_k+t_l+3} \sqrt{\mu_k^{(\iota)}\mu_l^{(\iota)}} \,\mathrm{d}\omega(\hat{\boldsymbol{x}})\,\mathrm{d}\boldsymbol{y} \\
&\leq 4\pi \int_{\mathbb{G}_{\text{out}}} \sum_{k=0_\iota}^{\infty} \sum_{l=0_\iota}^{\infty} |\gamma_k(y)|\,|\gamma_l(y)|\, R^{t_k+t_l+3} \sqrt{\mu_k^{(\iota)}\mu_l^{(\iota)}} \,\mathrm{d}\boldsymbol{y}.
\end{aligned}
$$

Now, we can apply the previous estimates to this equation and eventually obtain

$$
\left\|\boldsymbol{k}^{(\iota)}\right\|^2_{\mathbf{L}_2(\mathbb{G}_{\text{star}}\times\mathbb{G}_{\text{out}})} < \infty. \qquad \square
$$

Besides interchanging the series with integration, we are also interested in interchanging with certain differential operators. If the sequence $\{t_k\}_{k\in\mathbb{N}_{0_\iota}}$ is chosen in such a way that $\boldsymbol{k}^{(\iota)}(\cdot,\boldsymbol{y})$ is componentwise harmonic for all $\boldsymbol{y}\in\mathbb{G}_{\text{out}}$, then based on Harnack's First Theorem, see [135, Ch. X.1], the interchanging of the derivatives in the next theorem with respect to $\boldsymbol{x}$ and the series is valid.

Theorem 6.17. *We can interchange the following differential operators with respect to $\boldsymbol{x}$ with the series in the representation of the continuous VLI kernel $\boldsymbol{k}^{(\iota)}$:*

i) The surface divergence $\boldsymbol{\nabla}^*_{\hat{\boldsymbol{x}}}\cdot$, the surface curl gradient $\boldsymbol{L}^*_{\hat{\boldsymbol{x}}}$, and the surface gradient $\boldsymbol{\nabla}^*_{\hat{\boldsymbol{x}}}$ applied to each component $(\boldsymbol{k}^{(\iota)})_j$ for $j=1,\,2,\,3$ of the kernel

ii) The differential operators $\frac{\partial}{\partial x}$, the divergence if $\inf_{k\in\mathbb{N}_{0_\iota},\gamma_k\neq 0} t_k \geq 1$ and $(k\mapsto t_k)\in\mathcal{O}(k^M)$ for a fixed $M\in\mathbb{N}_0$, and the gradient applied to each component $(\boldsymbol{k}^{(\iota)})_j$ of the kernel for $j=1,\,2,\,3$

iii) The Beltrami operator $\boldsymbol{\Delta}^*_{\hat{\boldsymbol{x}}}$

iv) The differential operators $\frac{\partial^2}{\partial x^2}$ *and the Laplacian* $\boldsymbol{\Delta}_{\boldsymbol{x}}$ *if* $\inf_{k\in\mathbb{N}_{0_\iota},\gamma_k\neq 0} t_k \geq 2$ *and* $(k \mapsto t_k) \in \mathcal{O}(k^M)$ *for a fixed* $M \in \mathbb{N}_0$

In addition, all term-by-term differentiated series converge uniformly.

If the supremum of $\boldsymbol{x}$ over $\mathbb{G}_{\text{in}}$ is given by $R > 1$, we are able to reduce the additional requirements stated in the foregoing theorem. In this case, the assumption on $\{t_k\}_{k\in\mathbb{N}_{0_\iota}}$ from Definition 6.1, that is $\sup_{k\in\mathbb{N}_{0_\iota}} R^{t_k-k} < \infty$, already imply the assumed asymptotic behaviour of the mapping $k \mapsto t_k$ for all $k \in \mathbb{N}_{0_\iota}$.

Proof. From Theorem 6.6, it is known that the series

$$\sum_{k=0_\iota}^{\infty} \gamma_k(y) x^{t_k} \boldsymbol{p}_k^{(\iota)}(\hat{\boldsymbol{x}}, \hat{\boldsymbol{y}})$$

converges uniformly for all $(\boldsymbol{x}, \boldsymbol{y}) \in \mathbb{G}_{\text{in}} \times \mathbb{G}_{\text{out}}$. Thus, we need to prove for all cases that the term-by-term differentiated series converge uniformly. For this purpose, we need certain derivatives. With $\hat{\boldsymbol{x}} = \hat{\boldsymbol{x}}(\varphi, t)$, fixed $\boldsymbol{y} \in \mathbb{G}_{\text{out}}$, and the derivatives from Theorem 2.15, we get

$$\boldsymbol{o}^{(2)}_{\hat{\boldsymbol{x}}}(\hat{\boldsymbol{x}} \cdot \hat{\boldsymbol{y}}) = (\hat{\boldsymbol{y}} - (\hat{\boldsymbol{x}} \cdot \hat{\boldsymbol{y}})\hat{\boldsymbol{x}}), \tag{6.9a}$$

$$\frac{1}{\sqrt{1-t^2}} \frac{\partial}{\partial \varphi} \boldsymbol{o}^{(2)}_{\hat{\boldsymbol{x}}}(\hat{\boldsymbol{x}} \cdot \hat{\boldsymbol{y}}) = -((\hat{\boldsymbol{x}} \cdot \hat{\boldsymbol{y}})\boldsymbol{\varepsilon}^{\varphi} + (\boldsymbol{\varepsilon}^{\varphi} \cdot \hat{\boldsymbol{y}})\hat{\boldsymbol{x}}), \tag{6.9b}$$

$$\sqrt{1-t^2} \frac{\partial}{\partial t} \boldsymbol{o}^{(2)}_{\hat{\boldsymbol{x}}}(\hat{\boldsymbol{x}} \cdot \hat{\boldsymbol{y}}) = -\left((\hat{\boldsymbol{x}} \cdot \hat{\boldsymbol{y}})\boldsymbol{\varepsilon}^{t} + \left(\boldsymbol{\varepsilon}^{t} \cdot \hat{\boldsymbol{y}}\right)\hat{\boldsymbol{x}}\right), \tag{6.9c}$$

and

$$\boldsymbol{o}^{(3)}_{\hat{\boldsymbol{x}}}(\hat{\boldsymbol{x}} \cdot \hat{\boldsymbol{y}}) = \hat{\boldsymbol{x}} \wedge \hat{\boldsymbol{y}}, \tag{6.9d}$$

$$\frac{1}{\sqrt{1-t^2}} \frac{\partial}{\partial \varphi} \boldsymbol{o}^{(3)}_{\hat{\boldsymbol{x}}}(\hat{\boldsymbol{x}} \cdot \hat{\boldsymbol{y}}) = \boldsymbol{\varepsilon}^{\varphi} \wedge \hat{\boldsymbol{y}}, \tag{6.9e}$$

$$\sqrt{1-t^2} \frac{\partial}{\partial t} \boldsymbol{o}^{(3)}_{\hat{\boldsymbol{x}}}(\hat{\boldsymbol{x}} \cdot \hat{\boldsymbol{y}}) = \boldsymbol{\varepsilon}^{t} \wedge \hat{\boldsymbol{y}}. \tag{6.9f}$$

i) For the angular derivative, we investigate the case $\iota = 1$ separately. By means of Lemma 6.8, the abbreviation

$$\boldsymbol{k}^{(\iota)}(\boldsymbol{x}, \boldsymbol{y}) =: \boldsymbol{o}^{(1)}_{\hat{\boldsymbol{x}}} H(\boldsymbol{x}, \boldsymbol{y}), \qquad (\boldsymbol{x}, \boldsymbol{y}) \in \mathbb{G}_{\text{in}} \times \mathbb{G}_{\text{out}},$$

and the product rule, see [141, Sec. 22], we obtain for $i = 1, 2, 3$ the relation

$$\begin{aligned} \boldsymbol{o}^{(i)}_{\hat{\boldsymbol{x}}} \cdot \boldsymbol{k}^{(\iota)}(\boldsymbol{x}, \boldsymbol{y}) &= \boldsymbol{o}^{(i)}_{\hat{\boldsymbol{x}}} \cdot \left(\boldsymbol{o}^{(1)}_{\hat{\boldsymbol{x}}} H(\boldsymbol{x}, \boldsymbol{y})\right) \\ &= H(\boldsymbol{x}, \boldsymbol{y}) \left(\boldsymbol{o}^{(i)}_{\hat{\boldsymbol{x}}} \cdot \hat{\boldsymbol{x}}\right) + \hat{\boldsymbol{x}} \cdot \boldsymbol{o}^{(i)}_{\hat{\boldsymbol{x}}} H(\boldsymbol{x}, \boldsymbol{y}). \end{aligned}$$

Both series converge uniformly, due to Theorem 6.6 and Lemma 6.8. This implies the uniform convergence of the term-by-term differentiated series with respect to the angular derivatives.

In the remaining two cases, that is $\iota = 2, 3$, we have to investigate the uniform convergence of the term-by-term differentiated series manually. Due to the structure of the surface divergence and surface curl gradients, see Theorem 2.14, we estimate the following two series. This estimate is also sufficient for the interchanging of the gradient with each component of the kernel. With the derivatives from Theorem 2.15 and Eq. (6.9), we obtain for all $(\boldsymbol{x}, \boldsymbol{y}) \in \mathbb{G}_{\text{in}} \times \mathbb{G}_{\text{out}}$ the estimate

$$
\begin{aligned}
&\left| \sum_{k=K+1}^{\infty} \frac{1}{\sqrt{1-t^2}} \frac{\partial}{\partial \varphi} \left(\gamma_k(y) x^{t_k} \boldsymbol{p}_k^{(\iota)}(\hat{\boldsymbol{x}}, \hat{\boldsymbol{y}}) \right) \right| \\
&= \left| \sum_{k=K+1}^{\infty} \left(\mu_k^{(\iota)} \right)^{-1/2} \gamma_k(y) x^{t_k} \frac{1}{\sqrt{1-t^2}} \frac{\partial}{\partial \varphi} \left(P_k'(\hat{\boldsymbol{x}} \cdot \hat{\boldsymbol{y}}) \boldsymbol{o}_{\hat{\boldsymbol{x}}}^{(\iota)}(\hat{\boldsymbol{x}} \cdot \hat{\boldsymbol{y}}) \right) \right| \\
&= \left| \sum_{k=K+1}^{\infty} \left(\mu_k^{(\iota)} \right)^{-1/2} \gamma_k(y) x^{t_k} \left(P_k''(\hat{\boldsymbol{x}} \cdot \hat{\boldsymbol{y}}) (\boldsymbol{\varepsilon}^{\varphi} \cdot \hat{\boldsymbol{y}}) \boldsymbol{o}_{\hat{\boldsymbol{x}}}^{(\iota)}(\hat{\boldsymbol{x}} \cdot \hat{\boldsymbol{y}}) \right. \right. \\
&\qquad \left. \left. + P_k'(\hat{\boldsymbol{x}} \cdot \hat{\boldsymbol{y}}) \frac{1}{\sqrt{1-t^2}} \frac{\partial}{\partial \varphi} \boldsymbol{o}_{\hat{\boldsymbol{x}}}^{(\iota)}(\hat{\boldsymbol{x}} \cdot \hat{\boldsymbol{y}}) \right) \right| \\
&\leq 2 \sum_{k=K+1}^{\infty} \left(\mu_k^{(\iota)} \right)^{-1/2} \left| \gamma_k(y) x^{t_k} \right| \left(\left| P_k''(\hat{\boldsymbol{x}} \cdot \hat{\boldsymbol{y}}) \right| + \left| P_k'(\hat{\boldsymbol{x}} \cdot \hat{\boldsymbol{y}}) \right| \right) \\
&\leq \left(\sup_{k \in \mathbb{N}_{0_\iota}} R^{t_k - k} \right) \sum_{k=K+1}^{\infty} \left(\Gamma_k \left(\mu_k^{(\iota)} \right)^{-1/2} \left(\frac{(k+2)(k+1)k(k-1)}{4} + k(k+1) \right) \right. \\
&\qquad \left. \times \frac{R^k}{(R+\varepsilon)^{k+1+\delta_{0_\iota,0}\delta_{k,0}}} \right).
\end{aligned}
$$

The latter estimate is valid due to Eq. (2.1) and our assumptions. The right-hand side of this inequality converges to zero as $K \to \infty$, see Theorem 6.4. Similarly, we obtain for all $(\boldsymbol{x}, \boldsymbol{y}) \in \mathbb{G}_{\text{in}} \times \mathbb{G}_{\text{out}}$ the estimate

$$
\begin{aligned}
&\left| \sum_{k=K+1}^{\infty} \sqrt{1-t^2} \frac{\partial}{\partial t} \left(\gamma_k(y) x^{t_k} \boldsymbol{p}_k^{(\iota)}(\hat{\boldsymbol{x}}, \hat{\boldsymbol{y}}) \right) \right| \\
&\leq \left(\sup_{k \in \mathbb{N}_{0_\iota}} R^{t_k - k} \right) \sum_{k=K+1}^{\infty} \left(\Gamma_k \left(\mu_k^{(\iota)} \right)^{-1/2} \left(\frac{(k+2)(k+1)k(k-1)}{4} + k(k+1) \right) \right. \\
&\qquad \left. \times \frac{R^k}{(R+\varepsilon)^{k+1+\delta_{0_\iota,0}\delta_{k,0}}} \right),
\end{aligned}
$$

where the right-hand side tends to zero as $K \to \infty$, see Theorem 6.4. Summing these results up, we obtain the uniform convergence of these term-by-term differentiated series. The desired result follows immediately via the definition of the surface curl and the surface divergence operators.

ii) In order to interchange the divergence with respect to $\boldsymbol{x}$ and the series, we need analogous estimates to the ones in the previous item. In contrast, they need to include the additional factor x^{-1} caused by the representation of the gradient in spherical coordinates for the angular part. Thus, we solely investigate for the absolute value of

$\boldsymbol{x} \in \mathbb{G}_{\text{in}}$ the estimate

$$\left|\frac{1}{x}x^{t_k}\right| = x^{t_k-1} \leq \left(\sup_{k\in\mathbb{N}_{0_\iota}} R^{t_k-k}\right) R^{k-1},$$

which holds true due to the assumption $\inf_{k\in\mathbb{N}_{0_\iota},\gamma_k\neq 0} t_k \geq 1$.

We continue with the radial derivative with respect to x. We obtain for $\iota = 1, 2, 3$ and all $(\boldsymbol{x}, \boldsymbol{y}) \in \mathbb{G}_{\text{in}} \times \mathbb{G}_{\text{out}}$ the estimate

$$\begin{aligned}
&\left|\sum_{k=K+1}^{\infty} \frac{\partial}{\partial x}\left(\gamma_k(y)x^{t_k}\boldsymbol{p}_k^{(\iota)}(\hat{\boldsymbol{x}},\hat{\boldsymbol{y}})\right)\right| \\
=&\left|\sum_{k=K+1}^{\infty} \gamma_k(y)t_k x^{t_k-1}\boldsymbol{p}_k^{(\iota)}(\hat{\boldsymbol{x}},\hat{\boldsymbol{y}})\right| \\
\leq&\left(\sup_{k\in\mathbb{N}_{0_\iota}} R^{t_k-k}\right)\sum_{k=K+1}^{\infty}\Gamma_k\sqrt{\mu_k^{(\iota)}}t_k\frac{R^{k-1}}{(R+\varepsilon)^{k+1+\delta_{0_\iota,0}\delta_{k,0}}} \to 0 \quad (\text{as } K\to\infty).
\end{aligned}$$

In the last step, we used the estimate of the vectorial Legendre polynomials from Lemma 5.22. The convergence to zero is obtained by the assumptions on the sequences $\{\Gamma_k\}_{k\in\mathbb{N}_{0_\iota}}$ and $\{t_k\}_{k\in\mathbb{N}_{0_\iota}}$, and Theorem 6.4. Thus, the uniform convergence of this series follows, which permits the interchanging of the radial derivative and the series.

Combining this with the results of the previous item and Theorem 2.14, we obtain the interchanging of the divergence with respect to $\boldsymbol{x}$ and the series.

iii) For the interchanging with the Beltrami operator, we use estimates of $|\boldsymbol{\Delta}^*_{\hat{\boldsymbol{x}}}\boldsymbol{p}_k^{(\iota)}(\hat{\boldsymbol{x}},\hat{\boldsymbol{y}})|$ from Corollary 5.23. Hence, we get for the series with the term-by-term angular derivative the estimate

$$\begin{aligned}
&\left|\sum_{k=K+1}^{\infty}\boldsymbol{\Delta}^*_{\hat{\boldsymbol{x}}}\left(\gamma_k(y)x^{t_k}\boldsymbol{p}_k^{(\iota)}(\hat{\boldsymbol{x}},\hat{\boldsymbol{y}})\right)\right| \\
\leq 4&\left(\sup_{k\in\mathbb{N}_{0_\iota}} R^{t_k-k}\right)\sum_{k=K+1}^{\infty}\Gamma_k\left(k^{3/2}(k+1)^{3/2}\right)\frac{R^k}{(R+\varepsilon)^{k+1+\delta_{0_\iota,0}\delta_{k,0}}}.
\end{aligned}$$

The right-hand side converges to zero as $K\to\infty$. Thus, we obtain the sought convergence, see Theorem 6.4, and we are able to interchange the Beltrami operator with the series in $\boldsymbol{k}^{(\iota)}$.

iv) The representation of the Laplacian in spherical coordinates is given in Theorem 2.14. For the second-order radial derivative, we immediately obtain the uniform convergence of the term-by-term differentiated series in $\mathbb{G}_{\text{in}} \times \mathbb{G}_{\text{out}}$ by

$$\begin{aligned}
&\left|\sum_{k=K+1}^{\infty} \frac{\partial^2}{\partial x^2}\left(\gamma_k(y)x^{t_k}\boldsymbol{p}_k^{(\iota)}(\hat{\boldsymbol{x}},\hat{\boldsymbol{y}})\right)\right| \\
=&\left|\sum_{k=K+1}^{\infty} \gamma_k(y)t_k(t_k-1)x^{t_k-2}\boldsymbol{p}_k^{(\iota)}(\hat{\boldsymbol{x}},\hat{\boldsymbol{y}})\right| \\
\leq&\left(\sup_{k\in\mathbb{N}_{0_\iota}} R^{t_k-k}\right)\sum_{k=K+1}^{\infty}\Gamma_k t_k(t_k-1)\sqrt{\mu_k^{(\iota)}}\frac{R^{k-2}}{(R+\varepsilon)^{k+1+\delta_{0_\iota,0}\delta_{k,0}}} \to 0 \quad (\text{as } K\to\infty),
\end{aligned}$$

due to the assumptions on $\{\Gamma_k\}_{k\in\mathbb{N}_{0_\iota}}$ and $\{t_k\}_{k\in\mathbb{N}_{0_\iota}}$, see Theorem 6.4. Recall that $\inf_{k\in\mathbb{N}_{0_\iota},\gamma_k\not\equiv 0} t_k \geq 2$. Similarly, we obtain an estimate for the first-order radial derivative. The estimates made in the previous item can be used for the angular derivatives, that is

$$\begin{aligned}&\left|\sum_{k=K+1}^{\infty}\frac{1}{x^2}\boldsymbol{\Delta}^*_{\hat{\boldsymbol{x}}}\left(\gamma_k(y)x^{t_k}\boldsymbol{p}_k^{(\iota)}(\hat{\boldsymbol{x}},\hat{\boldsymbol{y}})\right)\right|\\ &\leq 4\left(\sup_{k\in\mathbb{N}_{0_\iota}}R^{t_k-k}\right)\sum_{k=K+1}^{\infty}\Gamma_k k^{3/2}(k+1)^{3/2}\frac{R^{k-2}}{(R+\varepsilon)^{k+1+\delta_{0_\iota,0}\delta_{k,0}}}\to 0\quad(\text{as } K\to\infty).\end{aligned}$$

The latter estimate is valid, due to Corollary 5.23. Combining these arguments, we obtain the uniform convergence of the term-by-term differentiated series. Thus, we are able to interchange the Laplacian with the series in $\boldsymbol{k}^{(\iota)}$. □

Besides applying differential operators with respect to the first argument of the continuous VLI kernel, we also want to apply differential operators with respect to the second argument to the kernel. Here, the results also hold true for the star-shaped VLI kernel.

Theorem 6.18. *We can interchange the following differential operators with respect to $\boldsymbol{y}$ with the series in the representation of the continuous/star-shaped VLI kernel $\boldsymbol{k}^{(\iota)}$:*

i) The surface divergence $\boldsymbol{\nabla}^*_{\hat{\boldsymbol{y}}}\cdot$, the surface curl gradient $\boldsymbol{L}^*_{\hat{\boldsymbol{y}}}$, and the surface gradient $\boldsymbol{\nabla}^*_{\hat{\boldsymbol{y}}}$ applied to each component $(\boldsymbol{k}^{(\iota)})_j$ for $j=1,\,2,\,3$ of the kernel

ii) The differential operators $\frac{\partial}{\partial y}$, the divergence if $\{\gamma_k\}_{k\in\mathbb{N}_{0_\iota}}$ is a sequence of continuously differentiable functions fulfilling

$$\sup_{\boldsymbol{y}\in\mathbb{G}_{\text{out}}}|\gamma_k'(y)|\leq\Gamma_k(R+\varepsilon)^{-(k+N_1)}$$

with $N_1\in\mathbb{N}_0$ for all $k\in\mathbb{N}_{0_\iota}$ with $(k\mapsto\Gamma_k)\in\mathcal{O}(k^M)$ for a fixed $M\in\mathbb{N}_0$, and the gradient applied to each component $(\boldsymbol{k}^{(\iota)})_j$ for $j=1,\,2,\,3$ of the kernel

iii) The Beltrami operator $\boldsymbol{\Delta}^*_{\hat{\boldsymbol{y}}}$

iv) The differential operators $\frac{\partial^2}{\partial y^2}$ and the Laplacian $\boldsymbol{\Delta}_{\boldsymbol{y}}$ if $\{\gamma_k\}_{k\in\mathbb{N}_{0_\iota}}$ is a sequence of twice continuously differentiable functions fulfilling

$$\begin{aligned}\sup_{\boldsymbol{y}\in\mathbb{G}_{\text{out}}}|\gamma_k'(y)|&\leq\Gamma_k(R+\varepsilon)^{-(k+N_1)},\\ \sup_{\boldsymbol{y}\in\mathbb{G}_{\text{out}}}|\gamma_k''(y)|&\leq\Gamma_k(R+\varepsilon)^{-(k+N_2)}\end{aligned}$$

with $N_1,\,N_2\in\mathbb{N}_0$ for all $k\in\mathbb{N}_{0_\iota}$ with $(k\mapsto\Gamma_k)\in\mathcal{O}(k^M)$ for a fixed $M\in\mathbb{N}_0$

Furthermore, under the appropriate conditions, all term-by-term differentiated series converge uniformly in the case of the continuous VLI kernel and in the $\mathbf{L}_2(\mathbb{G}_{\text{star}}\times\mathbb{G}_{\text{out}})$-sense in the case of the star-shaped VLI kernel.

Proof. We start with the proof for the continuous VLI kernel.

i) In the case of the surface divergence, we obtain with $\hat{\boldsymbol{y}} = \hat{\boldsymbol{y}}(\varphi, t)$ and $\hat{\boldsymbol{x}}$ independent of these φ, t the identities

$$\frac{1}{\sqrt{1-t^2}} \frac{\partial}{\partial \varphi} \boldsymbol{o}_{\hat{\boldsymbol{x}}}^{(2)}(\hat{\boldsymbol{x}} \cdot \hat{\boldsymbol{y}}) = \boldsymbol{\varepsilon}^{\varphi} - (\hat{\boldsymbol{x}} \cdot \boldsymbol{\varepsilon}^{\varphi})\hat{\boldsymbol{x}},$$
$$\sqrt{1-t^2} \frac{\partial}{\partial t} \boldsymbol{o}_{\hat{\boldsymbol{x}}}^{(2)}(\hat{\boldsymbol{x}} \cdot \hat{\boldsymbol{y}}) = \boldsymbol{\varepsilon}^{t} - (\hat{\boldsymbol{x}} \cdot \boldsymbol{\varepsilon}^{t})\hat{\boldsymbol{x}}.$$

Thus, the same estimates as in Item i) of Theorem 6.17 concerning the surface divergence operators with respect to $\hat{\boldsymbol{x}}$ also hold true in this case.

In the case of the surface curl gradient, the argumentation concerning the angular part is the same as in Item i) of Theorem 6.17, since $\boldsymbol{L}_{\hat{\boldsymbol{y}}}^{*} P_k(\hat{\boldsymbol{x}} \cdot \hat{\boldsymbol{y}}) = -\boldsymbol{L}_{\hat{\boldsymbol{x}}}^{*} P_k(\hat{\boldsymbol{x}} \cdot \hat{\boldsymbol{y}})$, which implies

$$\boldsymbol{p}_k^{(3)}(\hat{\boldsymbol{x}}, \hat{\boldsymbol{y}}) = -\boldsymbol{p}_k^{(3)}(\hat{\boldsymbol{y}}, \hat{\boldsymbol{x}}), \qquad \hat{\boldsymbol{x}},\ \hat{\boldsymbol{y}} \in \mathbb{S}.$$

Eventually, all term-by-term differentiated series with respect to $\hat{\boldsymbol{y}}$ converge uniformly and we are able to interchange the surface curl and divergence operator with respect to $\hat{\boldsymbol{y}}$ with the series in $\boldsymbol{k}^{(\iota)}$.

ii) We split the divergence with respect to $\boldsymbol{y}$ into the radial and angular derivatives, see Theorem 2.14. For the radial derivative, we investigate the estimate by using Lemma 5.22 and for all $(\boldsymbol{x}, \boldsymbol{y}) \in \mathbb{G}_{\text{in}} \times \mathbb{G}_{\text{out}}$ obtain

$$\begin{aligned}
&\left| \sum_{k=K+1}^{\infty} \frac{\partial}{\partial y} \left(\gamma_k(y) x^{t_k} \boldsymbol{p}_k^{(\iota)}(\hat{\boldsymbol{x}}, \hat{\boldsymbol{y}}) \right) \right| \\
&= \left| \sum_{k=K+1}^{\infty} \gamma_k'(y) x^{t_k} \boldsymbol{p}_k^{(\iota)}(\hat{\boldsymbol{x}}, \hat{\boldsymbol{y}}) \right| \\
&\leq \left(\sup_{k \in \mathbb{N}_{0_\iota}} R^{t_k - k} \right) \sum_{k=K+1}^{\infty} \Gamma_k \sqrt{\mu_k^{(\iota)}} \frac{R^k}{(R+\varepsilon)^{k+N_1}} \to 0 \qquad (\text{as } K \to \infty),
\end{aligned}$$

see Theorem 6.4. Hence, the term-by-term differentiated series converges uniformly. For the angular part, we use the result of the previous item combined with the estimate

$$\left| \frac{\gamma_k(y) x^{t_k}}{y} \right| \leq \Gamma_k \frac{R^{t_k}}{(R+\varepsilon)^{k+N_1}} \leq \left(\sup_{k \in \mathbb{N}_{0_\iota}} R^{t_k - k} \right) \Gamma_k \frac{R^k}{(R+\varepsilon)^{k+N_1}},$$

which is valid for all $(\boldsymbol{x}, \boldsymbol{y}) \in \mathbb{G}_{\text{in}} \times \mathbb{G}_{\text{out}}$. Finally, the uniform convergence allows the desired interchanging.

iii) For the Beltrami operator with respect to $\hat{\boldsymbol{y}}$, we observe that the relation

$$\begin{aligned}
\boldsymbol{\Delta}_{\hat{\boldsymbol{y}}}^{*} \boldsymbol{p}_k^{(\iota)}(\hat{\boldsymbol{x}}, \hat{\boldsymbol{y}}) &= \left(\mu_k^{(\iota)} \right)^{-1/2} \frac{4\pi}{2k+1} \sum_{l=1}^{2k+1} \boldsymbol{o}_{\hat{\boldsymbol{x}}}^{(\iota)} Y_{k,l}(\hat{\boldsymbol{x}}) \Delta_{\hat{\boldsymbol{y}}}^{*} Y_{k,l}(\hat{\boldsymbol{y}}) \\
&= -\frac{4\pi}{2k+1} \frac{k(k+1)}{\sqrt{\mu_k^{(\iota)}}} \sum_{l=1}^{2k+1} \boldsymbol{o}_{\hat{\boldsymbol{x}}}^{(\iota)} Y_{k,l}(\hat{\boldsymbol{x}}) Y_{k,l}(\hat{\boldsymbol{y}}) \\
&= -k(k+1) \boldsymbol{p}_k^{(\iota)}(\hat{\boldsymbol{x}}, \hat{\boldsymbol{y}})
\end{aligned}$$

holds true for all $\hat{\boldsymbol{x}}$, $\hat{\boldsymbol{y}} \in \mathbb{S}$ and $k \in \mathbb{N}_{0_\iota}$. This implies the uniform convergence of the term-by-term differentiated series in analogy to the previous estimates. Together with Item i) of Theorem 6.17, we obtain the desired interchanging.

iv) We split the Laplacian into its radial derivatives and the Beltrami operator. For the second-order radial derivative, we get with Theorem 6.4 for all $(\boldsymbol{x}, \boldsymbol{y}) \in \mathbb{G}_{\text{in}} \times \mathbb{G}_{\text{out}}$ the estimate

$$\begin{aligned}
&\left| \sum_{k=K+1}^{\infty} \frac{\partial^2}{\partial y^2} \left(\gamma_k(y) x^{t_k} \boldsymbol{p}_k^{(\iota)}(\hat{\boldsymbol{x}}, \hat{\boldsymbol{y}}) \right) \right| \\
&= \left| \sum_{k=K+1}^{\infty} \gamma_k''(y) x^{t_k} \boldsymbol{p}_k^{(\iota)}(\hat{\boldsymbol{x}}, \hat{\boldsymbol{y}}) \right| \\
&\leq \left(\sup_{k \in \mathbb{N}_{0_\iota}} R^{t_k - k} \right) \sum_{k=K+1}^{\infty} \Gamma_k \sqrt{\mu_k^{(\iota)}} \frac{R^k}{(R+\varepsilon)^{k+N_2}} \to 0 \qquad (\text{as } K \to \infty).
\end{aligned}$$

The result that concerns the remaining derivative can be proved similarly. For the angular derivative, we combine the estimate in the previous item with $x \leq R$ and obtain the uniform convergence of the term-by-term differentiated series. Finally, we can interchange the Laplacian with respect to $\boldsymbol{y}$ and the series in $\boldsymbol{k}^{(\iota)}$.

Due to Corollary 6.3, the function $(\boldsymbol{x}, \boldsymbol{y}) \mapsto x\boldsymbol{k}^{(\iota)}(\boldsymbol{x}, \boldsymbol{y})$ is a continuous VLI kernel for all $(\boldsymbol{x}, \boldsymbol{y}) \in \mathbb{G}_{\text{star}} \times \mathbb{G}_{\text{out}}$ if $\boldsymbol{k}^{(\iota)}$ is a star-shaped VLI kernel. Let $\mathcal{D}$ denote one of the differential operators stated above. For all $(\boldsymbol{x}, \boldsymbol{y}) \in (\mathbb{G}_{\text{star}} \setminus \{\boldsymbol{0}\}) \times \mathbb{G}_{\text{out}}$, we get the identity

$$\begin{aligned}
\mathcal{D}_{\boldsymbol{y}} \boldsymbol{k}^{(\iota)}(\boldsymbol{x}, \boldsymbol{y}) &= \frac{1}{x} \mathcal{D}_{\boldsymbol{y}} \sum_{k=0_\iota}^{\infty} \gamma_k(y) x^{t_k+1} \boldsymbol{p}_k^{(\iota)}(\hat{\boldsymbol{x}}, \hat{\boldsymbol{y}}) \\
&= \sum_{k=0_\iota}^{\infty} x^{t_k} \mathcal{D}_{\boldsymbol{y}} \left(\gamma_k(y) \boldsymbol{p}_k^{(\iota)}(\hat{\boldsymbol{x}}, \hat{\boldsymbol{y}}) \right).
\end{aligned}$$

Under the stated conditions, the series occurring in the function $(\boldsymbol{x}, \boldsymbol{y}) \mapsto \boldsymbol{k}^{(\iota)}(\boldsymbol{x}, \boldsymbol{y})$ can be interchanged with all the differential operators. Moreover, the non-differentiated and the term-by-term differentiated series converge uniformly. The convergence is obtained similarly to the proof of Corollary 6.13 combined with the previous considerations. □

Not only these few derivatives are of note in the following investigations. We also need continuity of the Jacobian matrix of the kernel $\boldsymbol{k}^{(\iota)}$ and a bound for its elements.

Lemma 6.19. *Let $\boldsymbol{k}^{(\iota)}$ be a continuous/star-shaped VLI kernel. In addition, let the sequence of* continuously *differentiable functions $\{\gamma_k\}_{k \in \mathbb{N}_{0_\iota}}$ satisfy*

$$\sup_{\boldsymbol{y} \in \mathbb{G}_{\text{out}}} |\gamma_k'(y)| \leq \Gamma_k (R+\varepsilon)^{-(k+N_1)}$$

with $N_1 \in \mathbb{N}_0$ for all $k \in \mathbb{N}_{0_\iota}$ with $(k \mapsto \Gamma_k) \in \mathcal{O}(k^M)$ for a fixed $M \in \mathbb{N}_0$. Then, for all $\boldsymbol{x} \in \mathbb{G}_{\text{in}}$ and all $\boldsymbol{x} \in \mathbb{G}_{\text{star}} \setminus \{\boldsymbol{0}\}$, respectively, the mapping

$$\boldsymbol{y} \mapsto \left(\text{jac}_{\boldsymbol{y}} \left(\boldsymbol{k}^{(\iota)}(\boldsymbol{x}, \boldsymbol{y}) \right) \right)^{\mathrm{T}}, \qquad \boldsymbol{y} \in \mathbb{G}_{\text{out}},$$

is continuous. The functions in each entry of the occurring matrix are bounded for all l, $j \in \{1,2,3\}$ *by*

$$\left|\left(\mathrm{jac}_{\boldsymbol{y}}\left(\boldsymbol{k}^{(\iota)}(\boldsymbol{x},\boldsymbol{y})\right)\right)_{j,l}\right| \leq \sum_{k=0_\iota}^{\infty} \bar{\Gamma}_k \frac{x^{t_k}}{(R+\varepsilon)^{k+N_1}},$$

where $\{\bar{\Gamma}_k\}_{k\in\mathbb{N}_{0_\iota}}$ *is an appropriate sequence with* $(k \mapsto \bar{\Gamma}_k) \in \mathcal{O}(k^{\tilde{M}})$ *for a fixed* $\tilde{M} \in \mathbb{N}_0$.

Proof. First, we assume that $\boldsymbol{k}^{(\iota)}$ is a continuous VLI kernel. By $(\boldsymbol{k}^{(\iota)})_j$ for $j = 1,\ 2, 3$ we denote the jth component of the vector-valued kernel $\boldsymbol{k}^{(\iota)}$, that is

$$\left(\boldsymbol{k}^{(\iota)}(\boldsymbol{x},\boldsymbol{y})\right)_j = \sum_{k=0_\iota}^{\infty} \gamma_k(y) x^{t_k} \left(\boldsymbol{p}_k^{(\iota)}(\hat{\boldsymbol{x}},\hat{\boldsymbol{y}})\right)_j, \qquad (\boldsymbol{x},\boldsymbol{y}) \in \mathbb{G}_{\mathrm{in}} \times \mathbb{G}_{\mathrm{out}}. \tag{6.10}$$

Due to the structure of the Jacobian matrix, we get the identity

$$\left(\mathrm{jac}_{\boldsymbol{y}}\left(\boldsymbol{k}^{(\iota)}(\boldsymbol{x},\boldsymbol{y})\right)\right)^{\mathrm{T}} = \left(\boldsymbol{\nabla}_{\boldsymbol{y}}\left(\boldsymbol{k}^{(\iota)}(\boldsymbol{x},\boldsymbol{y})\right)_1, \boldsymbol{\nabla}_{\boldsymbol{y}}\left(\boldsymbol{k}^{(\iota)}(\boldsymbol{x},\boldsymbol{y})\right)_2, \boldsymbol{\nabla}_{\boldsymbol{y}}\left(\boldsymbol{k}^{(\iota)}(\boldsymbol{x},\boldsymbol{y})\right)_3\right).$$

Thus, we analyze the matrix column by column. According to Theorem 6.18, the gradient $\boldsymbol{\nabla}_{\boldsymbol{y}}(\boldsymbol{k}^{(\iota)}(\boldsymbol{x},\boldsymbol{y}))_j$ exists for all $j = 1,\ 2,\ 3$. The gradient and the series in the kernel can be interchanged, where the term-by-term differentiated series also converges uniformly.

In addition, for each for $j = 1,\ 2,\ 3$ the function given by

$$(\boldsymbol{x},\boldsymbol{y}) \mapsto \gamma_k(y) x^{t_k} \left(\boldsymbol{p}_k^{(\iota)}(\hat{\boldsymbol{x}},\hat{\boldsymbol{y}})\right)_j$$

is, as a composition of continuously differentiable functions in $\boldsymbol{y}$, continuously differentiable. Together with the uniform convergence, we obtain the continuous differentiability of $(\boldsymbol{k}^{(\iota)}(\boldsymbol{x},\boldsymbol{y}))_j$ for all $j = 1,\ 2,\ 3$. Thus, the mapping

$$\boldsymbol{y} \mapsto \left(\mathrm{jac}_{\boldsymbol{y}}\left(\boldsymbol{k}^{(\iota)}(\boldsymbol{x},\boldsymbol{y})\right)\right)^{\mathrm{T}}$$

is continuous. For $l,\ j \in \{1,2,3\}$, we obtain via the calculations in the proof of Theorem 6.18 the estimate

$$\left|\left(\boldsymbol{\nabla}_{\boldsymbol{y}}\left(\boldsymbol{k}^{(\iota)}(\boldsymbol{x},\boldsymbol{y})\right)_j\right)_l\right| \leq \sum_{k=0_\iota}^{\infty} \bar{\Gamma}_k \frac{x^{t_k}}{(R+\varepsilon)^{k+N_1}}, \qquad (\boldsymbol{x},\boldsymbol{y}) \in \mathbb{G}_{\mathrm{in}} \times \mathbb{G}_{\mathrm{in}},$$

where $\bar{\Gamma}_k$ is an appropriate polynomial in $k \in \mathbb{N}_{0_\iota}$. Thus, the functions in each entry of the Jacobian matrix are bounded by the same bound.

Second, let $\boldsymbol{k}^{(\iota)}$ be a star-shaped VLI kernel. Then $(\boldsymbol{x},\boldsymbol{y}) \mapsto x\boldsymbol{k}^{(\iota)}(\boldsymbol{x},\boldsymbol{y})$ is a continuous VLI kernel, see Corollary 6.3. Thus,

$$\boldsymbol{y} \mapsto \left(\mathrm{jac}_{\boldsymbol{y}}\left(\boldsymbol{k}^{(\iota)}(\boldsymbol{x},\boldsymbol{y})\right)\right)^{\mathrm{T}} = \frac{1}{x}\left(\mathrm{jac}_{\boldsymbol{y}}\left(x\boldsymbol{k}^{(\iota)}(\boldsymbol{x},\boldsymbol{y})\right)\right)^{\mathrm{T}}$$

is continuous for all $\boldsymbol{x} \in \mathbb{G}_{\mathrm{star}} \setminus \{\boldsymbol{0}\}$. The estimates for the matrix entries are obtained similarly. □

The results obtained above for the continuous/star-shaped VLI kernel using the Morse-Feshbach vector Legendre polynomials can be transferred to a kernel using the Edmonds vector Legendre polynomials instead. This transfer is of interest since the integral kernel of the EEG problem consists of Edmonds vector Legendre polynomials, see Eq. (6.4).

Lemma 6.20. *Let $\iota \in \{1,2,3\}$ be fixed, let the quantities $\{\gamma_k\}_{k\in\mathbb{N}_{0_\iota}}$ and $\{t_k\}_{k\in\mathbb{N}_{0_\iota}}$ fulfil the assumption of Definition 6.1, and let a kernel be defined by*

$$\tilde{\boldsymbol{k}}^{(\iota)}(\boldsymbol{x},\boldsymbol{y}) \coloneqq \sum_{k=0_\iota}^{\infty} \gamma_k(y) x^{t_k} \tilde{\boldsymbol{p}}_k^{(\iota)}(\hat{\boldsymbol{x}},\hat{\boldsymbol{y}}), \qquad (\boldsymbol{x},\boldsymbol{y}) \in \mathbb{G}_{\text{in}} \times \mathbb{G}_{\text{out}}, \tag{6.11}$$

where $\tilde{\boldsymbol{p}}_k^{(\iota)}$ is defined in Definition 5.21. Then

i) the series is bounded and converges absolutely and uniformly;

ii) it can be represented as a finite linear combination of continuous VLI kernels;

iii) the kernel $\tilde{\boldsymbol{k}}^{(\iota)}$ is a $\mathbf{C}(\mathbb{G}_{\text{in}} \times \mathbb{G}_{\text{out}})$-function and an $\mathbf{L}_2(\mathbb{G}_{\text{in}} \times \mathbb{G}_{\text{out}})$-function;

iv) due to the linearity of integration and differentiation, the results in Corollary 6.14 and Theorems 6.17 and 6.18 also hold true for $\tilde{\boldsymbol{k}}^{(\iota)}$.

Proof. i) Using the estimate of Lemma 5.22 for the polynomials $\tilde{\boldsymbol{p}}_k^{(\iota)}$ for all $k \in \mathbb{N}_{0_\iota}$ in the proof of Theorem 6.6, we immediately obtain the convergence results. With Lemma 6.5, we achieve the boundedness.

ii) In the case of $\iota = 3$, there is nothing to prove. The other two cases are similar to each other, which is why we restrict ourselves to the case of $\iota = 1$. Due to the absolute convergence of the series, we obtain with Eq. (5.12a) for all $(\boldsymbol{x},\boldsymbol{y}) \in \mathbb{G}_{\text{in}} \times \mathbb{G}_{\text{out}}$ the identity

$$\begin{aligned}
\tilde{\boldsymbol{k}}^{(1)}(\boldsymbol{x},\boldsymbol{y}) &= \sum_{k=0}^{\infty} \gamma_k(y) x^{t_k} \tilde{\boldsymbol{p}}_k^{(1)}(\hat{\boldsymbol{x}},\hat{\boldsymbol{y}}) \\
&= \sum_{k=0}^{\infty} \gamma_k(y) x^{t_k} \left(\sqrt{\frac{k+1}{2k+1}} \boldsymbol{p}_k^{(1)}(\hat{\boldsymbol{x}},\hat{\boldsymbol{y}}) - \sqrt{\frac{k}{2k+1}} \boldsymbol{p}_k^{(2)}(\hat{\boldsymbol{x}},\hat{\boldsymbol{y}}) \right) \\
&= \sum_{k=0}^{\infty} \gamma_k(y) x^{t_k} \sqrt{\frac{k+1}{2k+1}} \boldsymbol{p}_k^{(1)}(\hat{\boldsymbol{x}},\hat{\boldsymbol{y}}) - \sum_{k=1}^{\infty} \gamma_k(y) x^{t_k} \sqrt{\frac{k}{2k+1}} \boldsymbol{p}_k^{(2)}(\hat{\boldsymbol{x}},\hat{\boldsymbol{y}}).
\end{aligned}$$

Comparing both series with the definition of the continuous VLI kernel in Definition 6.1, we get the desired result.

Due to the representation of $\tilde{\boldsymbol{k}}^{(\iota)}$ by means of a finite linear combination of continuous VLI kernels and the linearity of differentiation and integration, the remaining two statements are clear. □

Corollary 6.21. *Let $\iota \in \{1,2,3\}$ be fixed, let the quantities $\{\gamma_k\}_{k\in\mathbb{N}_{0_\iota}}$ and $\{t_k\}_{k\in\mathbb{N}_{0_\iota}}$ fulfil the assumption of Definition 6.2, and let a kernel be defined by*

$$\tilde{\boldsymbol{k}}^{(\iota)}(\boldsymbol{x},\boldsymbol{y}) \coloneqq \sum_{k=0_\iota}^{\infty} \gamma_k(y) x^{t_k} \tilde{\boldsymbol{p}}_k^{(\iota)}(\hat{\boldsymbol{x}},\hat{\boldsymbol{y}}), \qquad (\boldsymbol{x},\boldsymbol{y}) \in \mathbb{G}_{\text{star}} \times \mathbb{G}_{\text{out}}, \tag{6.12}$$

where $\tilde{\boldsymbol{p}}_k^{(\iota)}$ is defined in Definition 5.21. Then

i) the series converges absolutely and pointwise for all $(\boldsymbol{x}, \boldsymbol{y}) \in (\mathbb{G}_{\text{star}} \setminus \{\mathbf{0}\}) \times \mathbb{G}_{\text{out}}$*;*

ii) the kernel can be represented as a finite linear combination of continuous/star-shaped VLI kernels;

iii) the kernel $\tilde{\boldsymbol{k}}^{(\iota)}$ *is a* $\mathbf{C}((\mathbb{G}_{\text{star}} \setminus \{\mathbf{0}\}) \times \mathbb{G}_{\text{out}})$*- and an* $\mathbf{L}_2(\mathbb{G}_{\text{star}} \times \mathbb{G}_{\text{out}})$*-function;*

iv) due to the linearity of integration, Corollary 6.14 also holds true for $\tilde{\boldsymbol{k}}^{(\iota)}$*.*

Proof. The first statement can be proved similarly to Lemma 6.7 via the estimate of the Edmonds vector Legendre polynomials in Lemma 5.22. The remaining statements can be proved in analogy to Lemma 6.20. □

Since the MEG and EEG kernels are continuous/star-shaped VLI kernels (or at least a linear combination of these kernels), all proven properties hold also true for $\boldsymbol{k}_{\text{M}}$ and $\boldsymbol{k}_{\text{E}}$. In particular, we are able to interchange all differential operators from Theorem 6.17 and Theorem 6.18 with their series. For these two particular integral kernels, some of these derivatives vanish. This is summarized in the next theorems.

Theorem 6.22. *For the MEG integral kernel* $\boldsymbol{k}_{\text{M}}$*, the following statements are true, where all occurring differential operators can be interchanged with the series:*

i) $\boldsymbol{\nabla}^*_{\hat{\boldsymbol{x}}} \cdot \boldsymbol{k}_{\text{M}}(\boldsymbol{x}, \boldsymbol{y}) = \boldsymbol{\nabla}_{\boldsymbol{x}} \cdot \boldsymbol{k}_{\text{M}}(\boldsymbol{x}, \boldsymbol{y}) = 0$ *for all* $\boldsymbol{y} \in \overline{\mathbb{B}^{\text{ext}}_{\varrho_L}}$*,*

ii) $\boldsymbol{\nabla}_{\boldsymbol{y}} \cdot \boldsymbol{k}_{\text{M}}(\boldsymbol{x}, \boldsymbol{y}) = 0$ *for all* $\boldsymbol{x} \in \mathbb{B}_{\varrho_0}$*,*

iii) $\boldsymbol{\Delta}_{\boldsymbol{y}} \boldsymbol{k}_{\text{M}}(\boldsymbol{x}, \boldsymbol{y}) = \mathbf{0}$ *for all* $\boldsymbol{x} \in \mathbb{B}_{\varrho_0}$*, and*

iv) $\boldsymbol{\Delta}_{\boldsymbol{x}} \boldsymbol{k}_{\text{M}}(\boldsymbol{x}, \boldsymbol{y}) = \mathbf{0}$ *for all* $\boldsymbol{y} \in \overline{\mathbb{B}^{\text{ext}}_{\varrho_L}}$*.*

In addition, $\boldsymbol{k}_{\text{M}}(\boldsymbol{x}, \cdot) \in \mathbf{C}^\infty(\operatorname{int} \mathbb{B}^{\text{ext}}_{\varrho_L})$ *for all* $\boldsymbol{x} \in \mathbb{B}_{\varrho_0}$ *and* $\boldsymbol{k}_{\text{M}}(\cdot, \boldsymbol{y}) \in \mathbf{C}^\infty(\operatorname{int} \mathbb{B}_{\varrho_0})$ *for all* $\boldsymbol{y} \in \overline{\mathbb{B}^{\text{ext}}_{\varrho_L}}$*.*

Recall that the vectorial Laplacian in the last two items is meant component-wise, see Eq. (5.9).

Proof. According to Theorems 6.17 and 6.18, the series of the kernel can be interchanged with the four differential operators. The assumptions on $\{\gamma_k\}_{k \in \mathbb{N}}$ required for this purpose are fulfilled, see Lemma 6.9. In the case of Item iv), we are able to start the series by $k = 2$ since $\Delta_{\boldsymbol{x}}(x \boldsymbol{p}_1^{(3)}(\hat{\boldsymbol{x}}, \hat{\boldsymbol{y}})) = \mathbf{0}$. Note that another representation of $\boldsymbol{k}_{\text{M}}$ from Eq. (6.3) is used for the proof depending on the applied differential operator.

i) We get the result since for each summand in Eq. (6.3b) the divergence and the surface divergence are equal to zero, that is

$$\boldsymbol{\nabla}_{\boldsymbol{x}} \cdot \left(x^k \boldsymbol{L}^*_{\hat{\boldsymbol{x}}} P_k(\hat{\boldsymbol{x}} \cdot \hat{\boldsymbol{y}}) \right) = \left(k x^{k-1} \hat{\boldsymbol{x}} \cdot \boldsymbol{L}^*_{\hat{\boldsymbol{x}}} P_k(\hat{\boldsymbol{x}} \cdot \hat{\boldsymbol{y}}) + x^{k-1} \boldsymbol{\nabla}^*_{\hat{\boldsymbol{x}}} \cdot \boldsymbol{L}^*_{\hat{\boldsymbol{x}}} P_k(\hat{\boldsymbol{x}} \cdot \hat{\boldsymbol{y}}) \right) = 0$$

for all $k \in \mathbb{N}$ and $(\boldsymbol{x}, \boldsymbol{y}) \in \mathbb{B}_{\varrho_0} \times \overline{\mathbb{B}^{\text{ext}}_{\varrho_L}}$. Here, we used certain orthogonality statements from Eq. (2.6).

ii) Similar to the proof of the foregoing item, we obtain with Eq. (6.3b) the relation

$$\boldsymbol{\nabla}_{\boldsymbol{y}} \cdot \boldsymbol{k}_{\mathrm{M}}(\boldsymbol{x},\boldsymbol{y}) = \frac{1}{4\pi} \sum_{k=1}^{\infty} \boldsymbol{\nabla}_{\boldsymbol{y}} \cdot \left(\frac{x^k}{y^{k+1}(k+1)} \boldsymbol{L}^*_{\hat{\boldsymbol{x}}} P_k(\hat{\boldsymbol{x}} \cdot \hat{\boldsymbol{y}}) \right) = 0,$$

since $\boldsymbol{L}^*_{\hat{\boldsymbol{x}}} P_k(\hat{\boldsymbol{x}} \cdot \hat{\boldsymbol{y}}) = -\boldsymbol{L}^*_{\hat{\boldsymbol{y}}} P_k(\hat{\boldsymbol{x}} \cdot \hat{\boldsymbol{y}})$ for all $(\boldsymbol{x},\boldsymbol{y}) \in \mathbb{B}_{\varrho_0} \times \overline{\mathbb{B}^{\mathrm{ext}}_{\varrho_L}}$.

iii) For all $(\boldsymbol{x},\boldsymbol{y}) \in \mathbb{B}_{\varrho_0} \times \overline{\mathbb{B}^{\mathrm{ext}}_{\varrho_L}}$, we get the relation

$$\begin{aligned}
\boldsymbol{\Delta}_{\boldsymbol{y}} \boldsymbol{k}_{\mathrm{M}}(\boldsymbol{x},\boldsymbol{y}) &= \frac{1}{4\pi} \boldsymbol{\Delta}_{\boldsymbol{y}} \left(\sum_{k=1}^{\infty} \frac{x^k}{y^{k+1}(k+1)} \boldsymbol{p}^{(3)}_k(\hat{\boldsymbol{x}},\hat{\boldsymbol{y}}) \right) \\
&= \frac{1}{4\pi} \sum_{k=1}^{\infty} \frac{x^k}{k+1} \boldsymbol{\Delta}_{\boldsymbol{y}} \left(y^{-(k+1)} \boldsymbol{p}^{(3)}_k(\hat{\boldsymbol{x}},\hat{\boldsymbol{y}}) \right) \\
&= \frac{1}{4\pi} \sum_{k=1}^{\infty} \sum_{j=1}^{2k+1} \frac{4\pi}{2k+1} \frac{x^k}{k+1} \boldsymbol{y}^{(3)}_{n,j}(\hat{\boldsymbol{x}}) \Delta_{\boldsymbol{y}} \left(y^{-(k+1)} Y_{n,j}(\hat{\boldsymbol{y}}) \right) \\
&= \boldsymbol{0},
\end{aligned}$$

where we used the Addition Theorem for vectorial Legendre polynomials, see Theorem 5.24. The mapping $\boldsymbol{y} \mapsto y^{-(k+1)} Y_{n,j}(\hat{\boldsymbol{y}})$ is a harmonic function for $\boldsymbol{y} \neq \boldsymbol{0}$, see Corollary 2.30. Thus, each summand of the series vanishes.

iv) In analogy to the previous calculation, we obtain for all $(\boldsymbol{x},\boldsymbol{y}) \in \mathbb{B}_{\varrho_0} \times \overline{\mathbb{B}^{\mathrm{ext}}_{\varrho_L}}$ the relation

$$\begin{aligned}
\boldsymbol{\Delta}_{\boldsymbol{y}} \boldsymbol{k}_{\mathrm{M}}(\boldsymbol{x},\boldsymbol{y}) &= \boldsymbol{\Delta}_{\boldsymbol{y}} \sum_{k=1}^{\infty} \Gamma_k \frac{x^k}{y^{k+1}} \boldsymbol{p}^{(3)}_k(\hat{\boldsymbol{x}},\hat{\boldsymbol{y}}) \\
&= -\sum_{k=1}^{\infty} \Gamma_k x^k \boldsymbol{\Delta}_{\boldsymbol{y}} \left(\frac{1}{y^{k+1}} \boldsymbol{p}^{(3)}_k(\hat{\boldsymbol{y}},\hat{\boldsymbol{x}}) \right).
\end{aligned}$$

In the last step, we used Theorem 2.15, which permutes the arguments of the vector Legendre polynomial and changes the sign. The vector Legendre polynomials of type 3 and order k are eigenfunctions of the vectorial Beltrami operator to the eigenvalue $-k(k+1)$, see Corollary 5.16 combined with Theorem 2.25 and Eq. (2.14). Eventually, we obtain that the function $\boldsymbol{y} \mapsto y^{-(k+1)} \boldsymbol{p}^{(3)}_k(\hat{\boldsymbol{x}},\hat{\boldsymbol{y}})$ is harmonic for all $\hat{\boldsymbol{x}} \in \mathbb{S}$.

Summing up, we obtain the harmonicity in the interior, that is $\boldsymbol{\Delta}_{\boldsymbol{y}} \boldsymbol{k}_{\mathrm{M}}(\boldsymbol{x},\boldsymbol{y}) = \boldsymbol{0}$ for all $\boldsymbol{x} \in \mathbb{B}_{\varrho_0}$.

The stated smoothness of the kernel is a consequence of the harmonicity of the kernel on this particular region, see [64]. □

For further analysis of the direct or inverse EEG problem, respectively, we need more properties of the integral kernel. Due to the particular vector Legendre polynomial occurring in the integral kernel, we are able to prove certain properties of the kernel $\boldsymbol{k}_{\mathrm{E}}$.

Theorem 6.23. *Let the kernel $\boldsymbol{k}_{\mathrm{E}}$ be defined as in Lemma 6.10, where $L \geq 2$. Then for all $(\boldsymbol{x},\boldsymbol{y}) \in \mathbb{B}_{\varrho_0} \times \mathbb{S}_{[\varrho_{L-1},\varrho_L]}$ the following statements are true:*

i) $\boldsymbol{L}^*_{\hat{\boldsymbol{x}}} \cdot \boldsymbol{k}_{\mathrm{E}}(\boldsymbol{x},\boldsymbol{y}) = 0$ for all $\boldsymbol{y} \in \mathbb{S}_{[\varrho_{L-1},\varrho_L]}$,

ii) $\boldsymbol{\nabla}_{\boldsymbol{x}} \cdot \boldsymbol{k}_{\mathrm{E}}(\boldsymbol{x}, \boldsymbol{y}) = 0$ *for all* $\boldsymbol{y} \in \mathbb{S}_{[\varrho_{L-1}, \varrho_L]}$,

iii) $\boldsymbol{\Delta}_{\boldsymbol{x}} \boldsymbol{k}_{\mathrm{E}}(\boldsymbol{x}, \boldsymbol{y}) = \mathbf{0}$ *for all* $\boldsymbol{y} \in \mathbb{S}_{[\varrho_{L-1}, \varrho_L]}$,

iv) $\boldsymbol{L}^*_{\hat{\boldsymbol{y}}} \cdot \boldsymbol{k}_{\mathrm{E}}(\boldsymbol{x}, \boldsymbol{y}) = 0$ *for all* $\boldsymbol{x} \in \mathbb{B}_{\varrho_0}$, *and*

v) $\boldsymbol{\Delta}_{\boldsymbol{y}} \boldsymbol{k}_{\mathrm{E}}(\boldsymbol{x}, \boldsymbol{y}) = \mathbf{0}$ *for all* $\boldsymbol{x} \in \mathbb{B}_{\varrho_0}$.

Proof. We use the different representations of the kernel collected in Eq. (6.5) for the proof. All occurring (linear) differential operators can be interchanged with the series in the representation of $\boldsymbol{k}_{\mathrm{E}}$ due to Theorems 6.17 and 6.18 and Lemma 6.20.

i) We immediately obtain

$$\boldsymbol{L}^*_{\hat{\boldsymbol{x}}} \cdot \boldsymbol{k}_{\mathrm{E}}(\boldsymbol{x}, \boldsymbol{y}) = \frac{1}{4\pi} \sum_{k=1}^{\infty} \sqrt{k(2k+1)^3} H_k(y) x^{k-1} \boldsymbol{L}^*_{\hat{\boldsymbol{x}}} \cdot \tilde{\boldsymbol{p}}_k^{(2)}(\hat{\boldsymbol{x}}, \hat{\boldsymbol{y}}) = 0,$$

since for all $F \in \mathrm{C}^2(\mathbb{B}_{\varrho_0})$ the equation $\boldsymbol{L}^*_{\hat{\boldsymbol{x}}} \cdot \boldsymbol{o}^{(i)}_{\hat{\boldsymbol{x}}} F(\boldsymbol{x}) = 0$ holds true for $i = 1, 2$, see Eqs. (2.4) and (2.6).

ii) We interchange the series and the derivative and obtain with $\boldsymbol{\nabla} \cdot \boldsymbol{\nabla} = \Delta$ and the Addition Theorem, see Theorem 2.25, the identity

$$\boldsymbol{\nabla}_{\boldsymbol{x}} \cdot \boldsymbol{k}_{\mathrm{E}}(\boldsymbol{x}, \boldsymbol{y}) = \sum_{k=1}^{\infty} \sum_{i=1}^{2k+1} H_k(y) \Delta_{\boldsymbol{x}} \left(x^k Y_{k,i}(\hat{\boldsymbol{x}}) \right) Y_{k,i}(\hat{\boldsymbol{y}}) = 0.$$

iii) With Eq. (5.9) and $\boldsymbol{\nabla}_{\boldsymbol{x}} x^k (P_k(\hat{\boldsymbol{x}} \cdot \hat{\boldsymbol{y}})) = x^{k-1} \sqrt{\tilde{\mu}_k^{(2)}} \tilde{\boldsymbol{p}}_k^{(2)}$, we obtain

$$\boldsymbol{\Delta}_{\boldsymbol{x}} \boldsymbol{k}_{\mathrm{E}}(\boldsymbol{x}, \boldsymbol{y}) = \frac{1}{4\pi} \sum_{k=1}^{\infty} (2k+1) H_k(y) \boldsymbol{\Delta}_{\boldsymbol{x}} \left(\boldsymbol{\nabla}_{\boldsymbol{x}} x^k P_k(\hat{\boldsymbol{x}} \cdot \hat{\boldsymbol{y}}) \right) = \mathbf{0}.$$

iv) First, we prove that $\|H_k'\|_{\mathrm{C}([\varrho_{L-1}, \varrho_L])} \leq \Gamma_k \varrho_{L-1}^{-(k+2)}$ with some sequence $(k \mapsto \Gamma_k) \in \mathcal{O}(1)$ in order to fulfil the assumptions of Theorem 6.18. That is

$$\begin{aligned} \|H_k'\|_{\mathrm{C}([\varrho_{L-1}, \varrho_L])} &= \sup_{y \in [\varrho_{L-1}, \varrho_L]} \left| (k+1) \left(\left(\frac{y}{\varrho_L} \right)^{2k+1} - 1 \right) \right| \left| \beta_k^{(L)} \right| \left| \frac{1}{y^{k+2}} \right| \\ &\leq 2(k+1) \left| \beta_k^{(L)} \right| \frac{1}{\varrho_{L-1}^{k+2}}. \end{aligned}$$

Thus, the mapping $k \mapsto \Gamma_k \coloneqq (k+1)|\beta_k^{(L)}|$ is in $\mathcal{O}(1)$. Using Schwarz's Theorem, see [197], Theorem 2.15, and Item i), we obtain

$$\begin{aligned} \boldsymbol{L}^*_{\hat{\boldsymbol{y}}} \cdot \boldsymbol{k}_{\mathrm{E}}(\boldsymbol{x}, \boldsymbol{y}) &= \frac{1}{4\pi} \boldsymbol{L}^*_{\hat{\boldsymbol{y}}} \cdot \boldsymbol{\nabla}_{\boldsymbol{x}} \sum_{k=1}^{\infty} (2k+1) H_k(y) x^k P_k(\hat{\boldsymbol{x}} \cdot \hat{\boldsymbol{y}}) \\ &= \frac{1}{4\pi} \boldsymbol{\nabla}_{\boldsymbol{x}} \cdot \boldsymbol{L}^*_{\hat{\boldsymbol{y}}} \sum_{k=1}^{\infty} (2k+1) H_k(y) x^k P_k(\hat{\boldsymbol{x}} \cdot \hat{\boldsymbol{y}}) \\ &= -\boldsymbol{L}^*_{\hat{\boldsymbol{x}}} \cdot \boldsymbol{k}_{\mathrm{E}}(\boldsymbol{x}, \boldsymbol{y}) = 0. \end{aligned}$$

v) In analogy to the previous item, we can prove that the asymptotic behaviour of H_k'' required in Theorem 6.18 is fulfilled. We immediately obtain from Eq. (4.19) together with Corollaries 2.29 and 2.30 that $\Delta_{\boldsymbol{y}} \left(H_k(y) Y_{k,i}(\hat{\boldsymbol{y}}) \right) = 0$ for all $k \in \mathbb{N}$, $i = 1, \ldots, 2k+1$. Thus,

$$\boldsymbol{\Delta}_{\boldsymbol{y}} \boldsymbol{k}_{\mathrm{E}}(\hat{\boldsymbol{x}}, \boldsymbol{x}) = \sum_{k=1}^{\infty} \sum_{i=1}^{2k+1} \Delta_{\boldsymbol{y}} \left(H_k(y) Y_{k,i}(\hat{\boldsymbol{y}}) \right) \boldsymbol{\nabla}_{\boldsymbol{x}} \left(x^k Y_{k,i}(\hat{\boldsymbol{x}}) \right) = \boldsymbol{0}. \qquad \square$$

Chapter 7.

Vector Legendre-type Integral Operators

In this chapter, we define the integral equation and operator corresponding to the continuous/ star-shaped VLI kernel. In Section 7.1, we state the definition of the integral operator and some examples. Motivated by these examples, we call the function obtained by the integration of a vector-valued density and the continuous/star-shaped VLI kernel a potential. In Section 7.2, we prove that this name is reasonable from a mathematical point of view, since the resulting function is under certain additional assumptions continuously differentiable. Eventually, in Section 7.3, we solve the corresponding direct problem via a Fourier series expansion of the density. For this purpose, we restrict ourselves to the case of ball-shaped domains.

7.1. Definition of the Integral Operators

We consider the continuous VLI operator of the first kind corresponding to the continuous VLI kernel from Chapter 6. Recall that the value of ι will be determined by the particular problem. Integral equations of the first kind are widely discussed in the literature, see, for instance, [63, 102, 127]. However, in most settings both regions $\mathbb{G}_{\text{int}}$ and $\mathbb{G}_{\text{out}}$ coincide or the outer region $\mathbb{G}_{\text{out}}$ needs to be compact. Since in our case the compactness of $\mathbb{G}_{\text{out}}$ is not assumed, we cannot come back to these results.

Definition 7.1 (Continuous VLI Operator). *The* continuous VLI operator $\mathcal{T}$ *is for all* $\boldsymbol{f} \in \mathbf{L}_2(\mathbb{G}_{\text{in}})$ *and* $\boldsymbol{y} \in \mathbb{G}_{\text{out}}$ *defined by*

$$\begin{aligned}(\mathcal{T}\boldsymbol{f})(\boldsymbol{y}) &\coloneqq \int_{\mathbb{G}_{\text{in}}} \boldsymbol{f}(\boldsymbol{x}) \cdot \boldsymbol{k}^{(\iota)}(\boldsymbol{x}, \boldsymbol{y}) \, \mathrm{d}\boldsymbol{x} \\ &= \int_{\mathbb{G}_{\text{in}}} \boldsymbol{f}(\boldsymbol{x}) \cdot \left(\sum_{k=0_\iota}^{\infty} \gamma_k(y) x^{t_k} \boldsymbol{p}_k^{(\iota)}(\hat{\boldsymbol{x}}, \hat{\boldsymbol{y}}) \right) \mathrm{d}\boldsymbol{x},\end{aligned}$$

where the continuous VLI kernel $\boldsymbol{k}^{(\iota)}$ *for fixed* $\iota = 1,\ 2,\ 3$ *is defined in Definition 6.1.*

In this thesis, we call the function V generated by the continuous VLI operator, that is $V = \mathcal{T}\boldsymbol{f}$, the *(scalar) potential*. In Section 7.2, we verify that this notation is meaningful, since V is a continuously differentiable function and in many applications, such as the inverse gravimetric problem or the inverse electroencephalography problem, this nomenclature is established. In addition, we call the function $\boldsymbol{f}$ the *density* of the scalar potential.

According to Definition 7.1, we can define a star-shaped VLI operator via Definition 6.2.

Definition 7.2 (Star-shaped VLI Operator). *The* star-shaped VLI operator $\mathcal{T}$ *is for all* $\boldsymbol{f} \in \mathbf{L}_2(\mathbb{G}_{\mathrm{star}})$ *and* $\boldsymbol{y} \in \mathbb{G}_{\mathrm{out}}$ *defined by*

$$\begin{aligned}(\mathcal{T}\boldsymbol{f})(\boldsymbol{y}) &\coloneqq \int_{\mathbb{G}_{\mathrm{star}}} \boldsymbol{f}(\boldsymbol{x}) \cdot \boldsymbol{k}^{(\iota)}(\boldsymbol{x}, \boldsymbol{y}) \,\mathrm{d}\boldsymbol{x} \\ &= \int_{\mathbb{G}_{\mathrm{star}}} \boldsymbol{f}(\boldsymbol{x}) \cdot \left(\sum_{k=0_\iota}^{\infty} \gamma_k(y) x^{t_k} \boldsymbol{p}_k^{(\iota)}(\hat{\boldsymbol{x}}, \hat{\boldsymbol{y}}) \right) \mathrm{d}\boldsymbol{x},\end{aligned}$$

where $\boldsymbol{k}^{(\iota)}$ *for fixed* $\iota = 1, 2, 3$ *is defined in Definition 6.2.*

For the continuous/star-shaped VLI operator, it is not immediately clear by the definition of $\mathcal{T}$ that the function $\mathcal{T}\boldsymbol{f}$ can be evaluated at every position $\boldsymbol{y} \in \mathbb{G}_{\mathrm{out}}$. However, within the next results, we see that this notation makes sense and that the potential can be evaluated at any of these positions.

It is well known from other integral equations, such as the convolution, that properties of the kernel can be transferred to the potential. We are mainly interested in results concerning the smoothness and integrability of $\mathcal{T}\boldsymbol{f}$. For example, the differentiability of the potential is required in order to calculate a gradient field of it and the $\mathrm{L}_2(\mathbb{G}_{\mathrm{out}})$-integrability is required for embedding the potential into particular Hilbert spaces.

Using the Cauchy-Schwarz inequality, we immediately obtain that $\mathcal{T}$ continuously maps from $\mathbf{L}_2(\mathbb{G}_{\mathrm{in}})$ or $\mathbf{L}_2(\mathbb{G}_{\mathrm{star}})$, respectively, to $\mathrm{L}_2(\mathbb{G}_{\mathrm{out}})$ if the kernel is an $\mathbf{L}_2$-function over its domain. More precisely, for $\mathbb{G} \in \{\mathbb{G}_{\mathrm{in}}, \mathbb{G}_{\mathrm{star}}\}$ and $\boldsymbol{f} \in \mathbf{L}_2(\mathbb{G})$ we have

$$\begin{aligned}\|\mathcal{T}\boldsymbol{f}\|_{\mathrm{L}_2(\mathbb{G}_{\mathrm{out}})}^2 &= \int_{\mathbb{G}_{\mathrm{out}}} \left(\int_{\mathbb{G}} \boldsymbol{f}(\boldsymbol{x}) \cdot \boldsymbol{k}^{(\iota)}(\boldsymbol{x}, \boldsymbol{y}) \,\mathrm{d}\boldsymbol{x} \right)^2 \mathrm{d}\boldsymbol{y} \\ &\leq \int_{\mathbb{G}_{\mathrm{out}}} \int_{\mathbb{G}} (\boldsymbol{f}(\boldsymbol{x}))^2 \,\mathrm{d}\boldsymbol{x} \int_{\mathbb{G}} (\boldsymbol{k}^{(\iota)}(\boldsymbol{x}, \boldsymbol{y}))^2 \,\mathrm{d}\boldsymbol{x} \,\mathrm{d}\boldsymbol{y} \\ &= \|\boldsymbol{f}\|_{\mathbf{L}_2(\mathbb{G})}^2 \left\|\boldsymbol{k}^{(\iota)}\right\|_{\mathbf{L}_2(\mathbb{G} \times \mathbb{G}_{\mathrm{out}})}^2 < \infty.\end{aligned}$$

This estimate proves the next corollary.

Corollary 7.3. *The function* $\mathcal{T}\boldsymbol{f}$ *is an* $\mathrm{L}_2(\mathbb{G}_{\mathrm{out}})$*-function if*

i) $\boldsymbol{f} \in \mathbf{L}_2(\mathbb{G}_{\mathrm{in}})$ *and the operator* $\mathcal{T} \colon \mathbf{L}_2(\mathbb{G}_{\mathrm{in}}) \to \mathrm{L}_2(\mathbb{G}_{\mathrm{out}})$ *is a continuous VLI operator, or*

ii) $\boldsymbol{f} \in \mathbf{L}_2(\mathbb{G}_{\mathrm{star}})$ *and the operator* $\mathcal{T} \colon \mathbf{L}_2(\mathbb{G}_{\mathrm{star}}) \to \mathrm{L}_2(\mathbb{G}_{\mathrm{out}})$ *is a star-shaped VLI operator.*

In addition, in these particular cases $\mathcal{T}$ *is a linear and bounded operator.*

Now, we list some applications related to the continuous/star-shaped VLI equation.

Example 7.4 (Magnetoencephalography Problem). *Let the MEG integral kernel* $\boldsymbol{k}_{\mathrm{M}}$ *be defined as in Eq.* (3.4)*. Then we define the corresponding linear and bounded continuous/ star-shaped VLI operator* $\mathcal{T}_U \colon \mathbf{L}_2(\mathbb{B}_{\varrho_0}) \to \mathrm{L}_2(\overline{\mathbb{B}_{\varrho_L}^{\mathrm{ext}}})$ *by*

$$\mathcal{T}_U \boldsymbol{J}^{\mathrm{P}} \coloneqq \int_{\mathbb{B}_{\varrho_0}} \boldsymbol{J}^{\mathrm{P}}(\boldsymbol{x}) \cdot \boldsymbol{k}_{\mathrm{M}}(\boldsymbol{x}, \cdot) \,\mathrm{d}\boldsymbol{x},$$

where $\boldsymbol{J}^{\mathrm{P}}$ *denotes the neuronal current and* $\mathbb{B}_{\varrho_0}$ *models the cerebrum. More details on the underlying multiple-shell model can be found in Assumption 3.2. In this particular case, the operator is denoted by* $\mathcal{T}_U$ *since it maps the neuronal current onto the magnetic potential* U*.*

Example 7.5 (Electroencephalography Problem). *Let the EEG integral kernel $\boldsymbol{k}_{\mathrm{E}}$ be defined as in Eq. (4.23). Then we define the corresponding linear and bounded integral operator $\mathcal{T}_{\mathrm{E}}\colon \mathbf{L}_2(\mathbb{B}_{\varrho_0}) \to \mathrm{L}_2(\mathbb{S}_{[\varrho_{L-1},\varrho_L]})$ by*

$$\mathcal{T}_{\mathrm{E}}\boldsymbol{J}^{\mathrm{P}} \coloneqq \int_{\mathbb{B}_{\varrho_0}} \boldsymbol{J}^{\mathrm{P}}(\boldsymbol{x}) \cdot \boldsymbol{k}_{\mathrm{E}}(\boldsymbol{x},\cdot)\,\mathrm{d}\boldsymbol{x},$$

where $\boldsymbol{J}^{\mathrm{P}}$ denotes the neuronal current, $\mathbb{B}_{\varrho_0}$ models the cerebrum, and $\mathbb{S}_{[\varrho_{L-1},\varrho_L]}$ is the outer shell of the multiple-shell head model. The operator $\mathcal{T}_{\mathrm{E}}$ can be expressed as a linear combination of two continuous/star-shaped VLI operators, see Lemma 6.10.

Example 7.6 (Earth's Magnetization). *From [15, 28, 93], it is known that the Earth's magnetic potential Φ of the crust can be expressed as*

$$\Phi(\boldsymbol{y}) = -\frac{1}{4\pi}\int_{\mathbb{B}_R} \boldsymbol{m}(\boldsymbol{y}) \cdot \frac{\boldsymbol{x}-\boldsymbol{y}}{|\boldsymbol{x}-\boldsymbol{y}|^3}\,\mathrm{d}\boldsymbol{x}, \qquad \boldsymbol{y} \in \mathbb{R}^3, \tag{7.1}$$

where $\boldsymbol{m} \in \mathbf{L}_2(\mathbb{B}_R)$ denotes the Earth's crust magnetization and $R > 0$ the Earth's radius. In addition, the Earth's crust magnetization has its support inside the Earth's crust, which is modelled as a thin spherical shell inside the Earth. If the magnetic potential is measured in the exterior of the Earth, we can embed this integral equation into the context of the continuous VLI equation. For all $(\boldsymbol{x},\boldsymbol{y}) \in \mathbb{B}_R \times \overline{\mathbb{B}^{\mathrm{ext}}_{R+\varepsilon}}$ with a fixed $\varepsilon > 0$, the corresponding vector-valued integral kernel is given by

$$\begin{aligned}
\frac{\boldsymbol{x}-\boldsymbol{y}}{|\boldsymbol{x}-\boldsymbol{y}|^3} &= -\boldsymbol{\nabla}_{\boldsymbol{x}} \frac{1}{|\boldsymbol{x}-\boldsymbol{y}|} \\
&= -\boldsymbol{\nabla}_{\boldsymbol{x}} \sum_{k=0}^{\infty} \frac{x^k}{y^{k+1}} P_k(\hat{\boldsymbol{x}}\cdot\hat{\boldsymbol{y}}) \\
&= -\frac{1}{4\pi}\sum_{k=0}^{\infty}\sum_{i=1}^{2k+1} (2n+1)\frac{1}{y^{k+1}}\boldsymbol{\nabla}_{\boldsymbol{x}}\left(x^k Y_{k,i}(\hat{\boldsymbol{y}})\right) Y_{k,i}(\hat{\boldsymbol{y}}) \\
&= -\frac{1}{4\pi}\sum_{k=1}^{\infty}\sum_{i=1}^{2k+1} (2n+1)\left(\tilde{\mu}_k^{(2)}\right)^{1/2}\frac{1}{y^{k+1}} x^{k-1} Y_{k,i}(\hat{\boldsymbol{y}})\tilde{\boldsymbol{y}}_{k,i}^{(2)}(\hat{\boldsymbol{x}}) \\
&= -\sum_{k=1}^{\infty}\left(\tilde{\mu}_k^{(2)}\right)^{1/2}\frac{x^{k-1}}{y^{k+1}}\tilde{\boldsymbol{p}}_k^{(2)}(\hat{\boldsymbol{x}},\hat{\boldsymbol{y}}).
\end{aligned}$$

We used Corollary 2.10, Lemma 6.20, Theorem 2.25, and Eq. (5.6) in this calculation. Setting $t_k \coloneqq k-1$, $\gamma_0 \equiv 0$, and $\gamma_k(y) = (\tilde{\mu}_k^{(2)})^{1/2} y^{-(k+1)}/(4\pi)$ for all $k \in \mathbb{N}$, we immediately obtain that the kernel in Eq. (7.1) is a continuous VLI kernel. Thus, the operator mapping the Earth's crust magnetization onto the potential is a linear and bounded operator mapping from $\mathbf{L}_2(\mathbb{B}_R)$ to $\mathrm{L}_2(\overline{\mathbb{B}^{\mathrm{ext}}_{R+\varepsilon}})$.

7.2. Continuity and Differentiability of the Potential

In the case of a star-shaped VLI equation, a singularity or discontinuity of the integral kernel can occur at the origin if at least one exponent t_k is negative. For non-singular integral kernels, a higher smoothness order of the potential $V = \mathcal{T}\boldsymbol{f}$ can be achieved a-priori in a more general context.

Lemma 7.7. *Let $\boldsymbol{k} \in \mathbf{L}_2(\mathbb{G}_1 \times \mathbb{G}_2)$ be an integral kernel with a compact (inner) region $\mathbb{G}_1 \subset \mathbb{R}^d$ and a non-empty (outer) region $\mathbb{G}_2 \subset \mathbb{R}^d$, where $d \in \mathbb{N}$. In addition, let $\boldsymbol{k}(\boldsymbol{x}, \cdot) \in \mathbf{C}(\mathbb{G}_2)$ for almost all $\boldsymbol{x} \in \mathbb{G}_1$. If there exists a constant $C \geq 0$ with $|\boldsymbol{k}(\boldsymbol{x}, \boldsymbol{y})| \leq C < \infty$ for all $(\boldsymbol{x}, \boldsymbol{y}) \in \mathbb{G}_1 \times \mathbb{G}_2$, then the operator $\mathcal{T} \colon \mathbf{L}_2(\mathbb{G}_1) \to \mathrm{C}(\mathbb{G}_2)$ with $\mathcal{T}\boldsymbol{f} = \int_{\mathbb{G}_1} \boldsymbol{f}(\boldsymbol{x}) \cdot \boldsymbol{k}(\boldsymbol{x}, \cdot)\, \mathrm{d}\boldsymbol{x}$ is bounded.*

Proof. Let $\boldsymbol{f} \in \mathbf{L}_2(\mathbb{G}_1)$ be arbitrary. Let $\{\boldsymbol{y}_n\}_{n \in \mathbb{N}_0} \subset \mathbb{G}_2$ be a sequence with $\lim_{n\to\infty} \boldsymbol{y}_n = \boldsymbol{y} \in \mathbb{G}_2$. We define for all $n \in \mathbb{N}_0$ and almost all $\boldsymbol{x} \in \mathbb{G}_1$ a sequence of functions g_n by

$$g_n(\boldsymbol{x}) \coloneqq \boldsymbol{f}(\boldsymbol{x}) \cdot \boldsymbol{k}(\boldsymbol{x}, \boldsymbol{y}_n).$$

The functions fulfil $g_n \in \mathrm{L}_2(\mathbb{G}_1)$ for all $n \in \mathbb{N}_0$, due to the Cauchy-Schwarz inequality, the uniform boundedness of the integral kernel $\boldsymbol{k}$, and the compactness of $\mathbb{G}_1$, that is

$$\int_{\mathbb{G}_1} |g_n(\boldsymbol{x})|\, \mathrm{d}\boldsymbol{x} \leq \|\boldsymbol{f}\|_{\mathbf{L}_2(\mathbb{G}_1)} \left(\int_{\mathbb{G}_1} C^2\, \mathrm{d}\boldsymbol{x} \right)^{1/2} = C\sqrt{\mathrm{vol}\,(\mathbb{G}_1)}\, \|\boldsymbol{f}\|_{\mathbf{L}_2(\mathbb{G}_1)} < \infty.$$

The continuity of $\boldsymbol{k}$ in the second argument yields the limit

$$\lim_{n\to\infty} g_n(\boldsymbol{x}) = \boldsymbol{f}(\boldsymbol{x}) \cdot \lim_{n\to\infty} \boldsymbol{k}(\boldsymbol{x}, \boldsymbol{y}_n) = \boldsymbol{f}(\boldsymbol{x}) \cdot \boldsymbol{k}(\boldsymbol{x}, \boldsymbol{y})$$

(almost) everywhere. In addition, the estimate

$$|g_n(\boldsymbol{x})| = |\boldsymbol{f}(\boldsymbol{x}) \cdot \boldsymbol{k}(\boldsymbol{x}, \boldsymbol{y}_n)| \leq |\boldsymbol{f}(\boldsymbol{x})|\, |\boldsymbol{k}(\boldsymbol{x}, \boldsymbol{y}_n)| \leq C\, |\boldsymbol{f}(\boldsymbol{x})| \eqqcolon g(\boldsymbol{x})$$

holds true (almost) everywhere. The dominating function g is an $\mathrm{L}_2(\mathbb{G}_1) \subset \mathrm{L}_1(\mathbb{G}_1)$-function, due to the compactness of $\mathbb{G}_1$. Hence, the Dominated Convergence Theorem yields

$$\lim_{n\to\infty} \int_{\mathbb{G}_1} \boldsymbol{f}(\boldsymbol{x}) \cdot \boldsymbol{k}(\boldsymbol{x}, \boldsymbol{y}_n)\, \mathrm{d}\boldsymbol{x} = \int_{\mathbb{G}_1} \lim_{n\to\infty} \boldsymbol{f}(\boldsymbol{x}) \cdot \boldsymbol{k}(\boldsymbol{x}, \boldsymbol{y}_n)\, \mathrm{d}\boldsymbol{x} = \int_{\mathbb{G}_1} \boldsymbol{f}(\boldsymbol{x}) \cdot \boldsymbol{k}(\boldsymbol{x}, \boldsymbol{y})\, \mathrm{d}\boldsymbol{y}.$$

Thus, the continuity of $(\mathcal{T}\boldsymbol{f})$ is given by

$$\lim_{n\to\infty} (\mathcal{T}\boldsymbol{f})(\boldsymbol{y}_n) = \lim_{n\to\infty} \int_{\mathbb{G}_1} \boldsymbol{f}(\boldsymbol{x}) \cdot \boldsymbol{k}(\boldsymbol{x}, \boldsymbol{y}_n)\, \mathrm{d}\boldsymbol{x} = (\mathcal{T}\boldsymbol{f})(\boldsymbol{y}).$$

For the operator norm, we obtain

$$\|T\|_{\mathcal{L}} = \sup_{\substack{\boldsymbol{f} \in \mathbf{L}_2(\mathbb{G}_1) \\ \|\boldsymbol{f}\|_{\mathbf{L}_2(\mathbb{G}_1)} = 1}} \sup_{\boldsymbol{y} \in \mathbb{G}_2} |(\mathcal{T}\boldsymbol{f})(\boldsymbol{y})| \leq C\sqrt{\mathrm{vol}\,(\mathbb{G}_1)},$$

which provides us with the continuity of the linear operator. □

This lemma can be applied to our particular case in the next theorem.

Theorem 7.8. *Let $\mathcal{T}$ be the continuous VLI operator from Definition 7.1 and let $\boldsymbol{f} \in \mathbf{L}_2(\mathbb{G}_{\mathrm{in}})$. Then $\mathcal{T}\boldsymbol{f}$ is a continuous function, that is $\mathcal{T}\boldsymbol{f} \in \mathrm{C}(\mathbb{G}_{\mathrm{out}})$. Hence, the identity*

$$(\mathcal{T}\boldsymbol{f})(\boldsymbol{y}) = \int_{\mathbb{G}_{\mathrm{in}}} \boldsymbol{f}(\boldsymbol{x}) \cdot \boldsymbol{k}^{(\iota)}(\boldsymbol{x}, \boldsymbol{y})\, \mathrm{d}\boldsymbol{x}$$

holds pointwise for all $\boldsymbol{y} \in \mathbb{G}_{\mathrm{out}}$. In addition, the operator $\mathcal{T} \colon \mathbf{L}_2(\mathbb{G}_{\mathrm{in}}) \to \mathrm{C}(\mathbb{G}_{\mathrm{out}})$ is bounded.

Proof. From Lemma 6.5, we immediately obtain the uniform boundedness of the continuous VLI kernel $\boldsymbol{k}^{(\iota)}$ for all $(\boldsymbol{x}, \boldsymbol{y}) \in \mathbb{G}_{\text{in}} \times \mathbb{G}_{\text{out}}$. Together with Corollary 6.12 and Lemma 6.16 all assumptions of Lemma 7.7 are fulfilled. Due to this lemma, the continuous VLI operator $\mathcal{T}$ maps from $\mathbf{L}_2(\mathbb{G}_{\text{in}})$ to $\mathrm{C}(\mathbb{G}_{\text{out}})$. This implies the continuity of the function $\mathcal{T}\boldsymbol{f}$. □

We now continue with some differentiability considerations of the given continuous VLI kernel. For this purpose, we state the next general result.

Lemma 7.9 (Differentiability of Fredholm Integral Equations). *Let $\boldsymbol{k}\colon \mathbb{G}_1 \times \mathbb{G}_2 \to \mathbb{R}^d$, with $d \in \mathbb{N}$, be a kernel function with a compact (inner) region $\mathbb{G}_1 \subset \mathbb{R}^d$ and a non-empty (outer) region $\mathbb{G}_2 \subset \mathbb{R}^d$. We define the integrand function h by*

$$h(\boldsymbol{x}, \boldsymbol{y}) \coloneqq \boldsymbol{f}(\boldsymbol{x}) \cdot \boldsymbol{k}(\boldsymbol{x}, \boldsymbol{y}), \qquad (\boldsymbol{x}, \boldsymbol{y}) \in \mathbb{G}_1 \times \mathbb{G}_2.$$

Let $\mathcal{D}_{\boldsymbol{y}}$ be a first-order differential operator with respect to $\boldsymbol{y}$. If the four conditions

- $\boldsymbol{f} \in \mathbf{L}_2(\mathbb{G}_1)$,
- $\boldsymbol{k}(\cdot, \boldsymbol{y}) \in \mathbf{L}_2(\mathbb{G}_1)$ *for all* $\boldsymbol{y} \in \mathbb{G}_2$,
- $\boldsymbol{k}(\boldsymbol{x}, \cdot) \in \mathbf{C}^1(\mathbb{G}_2)$ *for almost all* $\boldsymbol{x} \in \mathbb{G}_1$, *and*
- *there exists a function* $g \in \mathrm{L}_1(\mathbb{G}_1)$ *with* $|\mathcal{D}_{\boldsymbol{y}} h(\boldsymbol{x}, \boldsymbol{y})| \leq g(\boldsymbol{x})$ *for almost all* $\boldsymbol{x} \in \mathbb{G}_1$

are fulfilled, we can interchange the differential operator and the integration, that is

$$\mathcal{D}_{\boldsymbol{y}} \int_{\mathbb{G}_1} \boldsymbol{f}(\boldsymbol{x}) \cdot \boldsymbol{k}(\boldsymbol{x}, \boldsymbol{y}) \,\mathrm{d}\boldsymbol{x} = \int_{\mathbb{G}_1} \mathcal{D}_{\boldsymbol{y}} \left(\boldsymbol{f}(\boldsymbol{x}) \cdot \boldsymbol{k}(\boldsymbol{x}, \boldsymbol{y}) \right) \,\mathrm{d}\boldsymbol{x} \qquad \text{for all } \boldsymbol{y} \in \mathbb{G}_2.$$

Proof. Applying the theorem of differentiation under the integral sign onto the function h, see [19, Cor. 16.3], we obtain the desired result. □

In addition, we observe that the identity

$$\boldsymbol{\nabla}_{\boldsymbol{y}} \left(\boldsymbol{f}(\boldsymbol{x}) \cdot \boldsymbol{k}^{(\iota)}(\boldsymbol{x}, \boldsymbol{y}) \right) = \left(\mathrm{jac}_{\boldsymbol{y}} \left(\boldsymbol{k}^{(\iota)}(\boldsymbol{x}, \boldsymbol{y}) \right) \right)^{\mathrm{T}} \boldsymbol{f}(\boldsymbol{x}) \tag{7.2}$$

holds true for all $(\boldsymbol{x}, \boldsymbol{y}) \in \mathbb{G}_{\text{in}} \times \mathbb{G}_{\text{out}}$ and all $\boldsymbol{f} \in \mathbf{L}_2(\mathbb{G}_{\text{in}})$ if the conditions of Lemma 6.19 are fulfilled. In this case, the kernel $\boldsymbol{k}^{(\iota)}$ is continuously differentiable with respect to the second argument, see Lemma 6.19. The multiplication on the right-hand side is a classical matrix-vector multiplication. This provides us with the existence of the right-hand side of this equation.

Lemma 7.10. *Let $\mathbb{G} \in \{\mathbb{G}_{\text{in}}, \mathbb{G}_{\text{star}}\}$ and let $\boldsymbol{k}^{(\iota)}$ be a continuous/star-shaped VLI kernel fulfilling the differentiability conditions from Lemma 6.19. Then there exists a function $g \in \mathrm{L}_1(\mathbb{G})$ such that for almost all $\boldsymbol{x} \in \mathbb{G}$ and all $\boldsymbol{y} \in \mathbb{G}_{\text{out}}$ we have*

$$\left| \left(\mathrm{jac}_{\boldsymbol{y}} \left(\boldsymbol{k}^{(\iota)}(\boldsymbol{x}, \boldsymbol{y}) \right) \right)^{\mathrm{T}} \boldsymbol{f}(\boldsymbol{x}) \right| \leq g(\boldsymbol{x}).$$

Proof. Since all assumptions of Lemma 6.19 are fulfilled, we immediately obtain the continuity of the Jacobian matrix. For the remaining statement, we consider for almost all $\boldsymbol{x} \in \mathbb{G}_{\text{in}}$ the estimate

$$\begin{aligned}
\left|\boldsymbol{\nabla}_{\boldsymbol{y}}\left(\boldsymbol{f}(\boldsymbol{x}) \cdot \boldsymbol{k}^{(\iota)}(\boldsymbol{x},\boldsymbol{y})\right)\right| &= \left|\sum_{l=1}^{3} (\boldsymbol{f}(\boldsymbol{x}))_l \boldsymbol{\nabla}_{\boldsymbol{y}}\left(\boldsymbol{k}^{(\iota)}(\boldsymbol{x},\boldsymbol{y})\right)_l\right| \\
&\leq \sum_{l=1}^{3} \left|(\boldsymbol{f}(\boldsymbol{x}))_l\right| \left|\boldsymbol{\nabla}_{\boldsymbol{y}}\left(\boldsymbol{k}^{(\iota)}(\boldsymbol{x},\boldsymbol{y})\right)_l\right| \\
&= \sum_{l=1}^{3} \left|(\boldsymbol{f}(\boldsymbol{x}))_l\right| \left(\sum_{j=1}^{3} \left(\left(\boldsymbol{\nabla}_{\boldsymbol{y}}\left(\boldsymbol{k}^{(\iota)}(\boldsymbol{x},\boldsymbol{y})\right)_l\right)_j\right)^2\right)^{1/2} \\
&\leq \left(\sum_{l=1}^{3} \left|(\boldsymbol{f}(\boldsymbol{x}))_l\right|^2\right)^{1/2} \left(\sum_{l=1}^{3}\sum_{j=1}^{3} \left(\operatorname{jac}_{\boldsymbol{y}}\left(\boldsymbol{k}^{(\iota)}(\boldsymbol{x},\boldsymbol{y})\right)\right)_{l,j}^2\right)^{1/2} \\
&\leq \left|\boldsymbol{f}(\boldsymbol{x})\right| \left(\sum_{l=1}^{3}\sum_{j=1}^{3} \left(\sum_{k=0_\iota}^{\infty} \bar{\Gamma}_k \frac{x^{t_k}}{(R+\varepsilon)^{k+N_1}}\right)^2\right)^{1/2} \\
&= 3\left|\boldsymbol{f}(\boldsymbol{x})\right| \sum_{k=0_\iota}^{\infty} \bar{\Gamma}_k \frac{x^{t_k}}{(R+\varepsilon)^{k+N_1}} \\
&=: g(\boldsymbol{x}).
\end{aligned}$$

Now, we verify that $g \in \mathrm{L}_1(\mathbb{G}_{\text{in}})$. Thus, by means of Theorem 6.4, we obtain the estimate

$$\begin{aligned}
\int_{\mathbb{G}_{\text{in}}} |g(\boldsymbol{x})| \,\mathrm{d}\boldsymbol{x} &\leq 3\left(\int_{\mathbb{G}_{\text{in}}} \boldsymbol{f}(\boldsymbol{x})^2 \,\mathrm{d}\boldsymbol{x}\right)^{1/2} \left(\int_{\mathbb{G}_{\text{in}}} \left(\sum_{k=0_\iota}^{\infty} \bar{\Gamma}_k \frac{x^{t_k}}{(R+\varepsilon)^{k+N_1}}\right)^2 \mathrm{d}\boldsymbol{x}\right)^{1/2} \\
&\leq 3\left\|\boldsymbol{f}\right\|_{\mathbf{L}_2(\mathbb{G}_{\text{in}})} \sqrt{\operatorname{vol}\left(\mathbb{G}_{\text{in}}\right)} \sup_{k\in\mathbb{N}_{0_\iota}} \left(R^{t_k-k}\right) \left(\sum_{k=0_\iota}^{\infty} \bar{\Gamma}_k \frac{R^k}{(R+\varepsilon)^{k+N_1}}\right) < \infty.
\end{aligned}$$

It only remains to prove that $g \in \mathrm{L}_1(\mathbb{G}_{\text{star}})$ in the star-shaped VLI case. Using Theorem 6.4, we get the estimate

$$\begin{aligned}
\int_{\mathbb{G}_{\text{star}}} |g(\boldsymbol{x})| \,\mathrm{d}\boldsymbol{x} &\leq 3\left\|\boldsymbol{f}\right\|_{\mathbf{L}_2(\mathbb{G}_{\text{star}})} \left(\int_{\mathbb{S}} \int_0^{\zeta(\eta)} \left(\sum_{k=0_\iota}^{\infty} \bar{\Gamma}_k \frac{x^{t_k+1}}{(R+\varepsilon)^{k+N_1}}\right)^2 \mathrm{d}x \,\mathrm{d}\omega(\hat{\boldsymbol{x}})\right)^{1/2} \\
&\leq 3\left\|\boldsymbol{f}\right\|_{\mathbf{L}_2(\mathbb{G}_{\text{star}})} \left(\sum_{k=0_\iota}^{\infty} \bar{\Gamma}_k \frac{R^{t_k+1}}{(R+\varepsilon)^{k+N_1}}\right) \left(\int_{\mathbb{S}} \int_0^{\zeta(\eta)} \mathrm{d}x \,\mathrm{d}\omega(\hat{\boldsymbol{x}})\right)^{1/2} \\
&\leq 6\sqrt{\pi R}\left\|\boldsymbol{f}\right\|_{\mathbf{L}_2(\mathbb{G}_{\text{star}})} \sup_{k\in\mathbb{N}_{0_\iota}} \left(R^{t_k-k}\right) \sum_{k=0_\iota}^{\infty} \bar{\Gamma}_k \frac{R^{k+1}}{(R+\varepsilon)^{k+N_1}} < \infty. \qquad \square
\end{aligned}$$

With these preliminary studies, we are able to prove the existence of the gradient of $\mathcal{T}\boldsymbol{f}$, where $\mathcal{T}$ is the continuous/star-shaped VLI operator.

Theorem 7.11. *Let $\mathbb{G} \in \{\mathbb{G}_{\text{in}}, \mathbb{G}_{\text{star}}\}$, $\boldsymbol{f} \in \mathbf{L}_2(\mathbb{G})$, and let $\boldsymbol{k}^{(\iota)}$ be the continuous/star-shaped VLI kernel fulfilling the assumptions of Lemma 7.10. Then the gradient of the potential corresponding to the continuous/star-shaped VLI operator $\mathcal{T}\boldsymbol{f}$ exists and can be interchanged with the integration for all $\boldsymbol{y} \in \mathbb{G}_{\text{out}}$, such that*

$$(\boldsymbol{\nabla}(\mathcal{T}\boldsymbol{f}))(\boldsymbol{y}) = \int_{\mathbb{G}} \left(\operatorname{jac}_{\boldsymbol{y}} \left(\boldsymbol{k}^{(\iota)}(\boldsymbol{x}, \boldsymbol{y})\right)\right)^{\mathrm{T}} \boldsymbol{f}(\boldsymbol{x}) \,\mathrm{d}\boldsymbol{x}. \tag{7.3}$$

Proof. Due to Lemma 7.10, the integral on right-hand side of Eq. (7.3) exists. With Eq. (7.2), we obtain the existence of the integral given by

$$\int_{\mathbb{G}} \boldsymbol{\nabla}_{\boldsymbol{y}} \left(\boldsymbol{f}(\boldsymbol{x}) \cdot \boldsymbol{k}^{(\iota)}(\boldsymbol{x}, \boldsymbol{y})\right) \,\mathrm{d}\boldsymbol{x}.$$

The assumptions of this theorem and the results in Lemmas 6.16 and 7.10 guarantee that all conditions of Lemma 7.9 are fulfilled. Hence, we can interchange the integration with the gradient and obtain

$$\boldsymbol{\nabla}_{\boldsymbol{y}} \int_{\mathbb{G}} \boldsymbol{f}(\boldsymbol{x}) \cdot \boldsymbol{k}^{(\iota)}(\boldsymbol{x}, \boldsymbol{y}) \,\mathrm{d}\boldsymbol{x} = \int_{\mathbb{G}} \boldsymbol{\nabla}_{\boldsymbol{y}} \left(\boldsymbol{f}(\boldsymbol{x}) \cdot \boldsymbol{k}^{(\iota)}(\boldsymbol{x}, \boldsymbol{y})\right) \,\mathrm{d}\boldsymbol{x}.$$

Eventually, Eq. (7.2) yields the desired result. □

Corollary 7.12. *If the assumptions of Theorem 7.11 are fulfilled, then $\boldsymbol{\nabla}(\mathcal{T}\boldsymbol{f})$ is continuous.*

Proof. Let $\{\boldsymbol{y}_n\}_{n\in\mathbb{N}_0} \subset \mathbb{G}_{\text{out}}$ be a convergent sequence with $\lim_{n\to\infty} \boldsymbol{y}_n = \boldsymbol{y} \in \mathbb{G}_{\text{out}}$. Then Theorem 7.11 yields

$$\lim_{n\to\infty} (\boldsymbol{\nabla}(\mathcal{T}\boldsymbol{f}))(\boldsymbol{y}_n) = \lim_{n\to\infty} \int_{\mathbb{B}_{\varrho_0}} \left(\operatorname{jac}_{\boldsymbol{y}} \left(\boldsymbol{k}^{(\iota)}(\boldsymbol{x}, \boldsymbol{y}_n)\right)\right)^{\mathrm{T}} \cdot \boldsymbol{f}(\boldsymbol{x}) \,\mathrm{d}\boldsymbol{x}.$$

Due to Lemma 7.10 and the Dominated Convergence Theorem, we are able to interchange the integration and the limit. Thus,

$$\begin{aligned}
\lim_{n\to\infty} (\boldsymbol{\nabla}(\mathcal{T}\boldsymbol{f}))(\boldsymbol{y}_n) &= \int_{\mathbb{B}_{\varrho_0}} \left(\lim_{n\to\infty} \operatorname{jac}_{\boldsymbol{y}} \left(\boldsymbol{k}^{(\iota)}(\boldsymbol{x}, \boldsymbol{y}_n)\right)\right)^{\mathrm{T}} \cdot \boldsymbol{f}(\boldsymbol{x}) \,\mathrm{d}\boldsymbol{x} \\
&= \int_{\mathbb{B}_{\varrho_0}} \left(\operatorname{jac}_{\boldsymbol{y}} \left(\boldsymbol{k}^{(\iota)}(\boldsymbol{x}, \boldsymbol{y})\right)\right)^{\mathrm{T}} \cdot \boldsymbol{f}(\boldsymbol{x}) \,\mathrm{d}\boldsymbol{x} \\
&= (\boldsymbol{\nabla}(\mathcal{T}\boldsymbol{f}))(\boldsymbol{y}),
\end{aligned}$$

which implies the continuity of the stated function. □

For second order derivatives, a similar result can be obtained. We concentrate our calculations on the Laplacian of $\mathcal{T}\boldsymbol{f}$.

Theorem 7.13. *Let $\mathbb{G} \in \{\mathbb{G}_{\text{in}}, \mathbb{G}_{\text{star}}\}$, $\boldsymbol{f} \in \mathbf{L}_2(\mathbb{G})$, and let $\boldsymbol{k}^{(\iota)}$ be a continuous/star-shaped VLI kernel, where $\{\gamma_k\}_{k\in\mathbb{N}_{0_\iota}}$ is a sequence of twice continuously differentiable functions fulfilling*

$$\begin{aligned}
\sup_{\boldsymbol{y}\in\mathbb{G}_{\text{out}}} |\gamma_k'(y)| &\leq \Gamma_k (R+\varepsilon)^{-(k+N_1)}, \\
\sup_{\boldsymbol{y}\in\mathbb{G}_{\text{out}}} |\gamma_k''(y)| &\leq \Gamma_k (R+\varepsilon)^{-(k+N_2)}
\end{aligned}$$

for all $k \in \mathbb{N}_{0_\iota}$ with $(k \mapsto \Gamma_k) \in \mathcal{O}(k^M)$ for a fixed $M \in \mathbb{N}_0$ and N_1, $\mathbb{N}_2 \in \mathbb{N}_0$. Then the Laplacian of the corresponding potential, that is $\mathcal{T}\boldsymbol{f}$, exists and can be interchanged with the integration, such that for all $\boldsymbol{y} \in \mathbb{G}_{\text{out}}$ we have

$$(\Delta(\mathcal{T}\boldsymbol{f}))(\boldsymbol{y}) = \int_{\mathbb{G}} \boldsymbol{f}(\boldsymbol{x}) \cdot (\boldsymbol{\Delta}_{\boldsymbol{y}} \boldsymbol{k}^{(\iota)}(\boldsymbol{x}, \boldsymbol{y})) \, \mathrm{d}\boldsymbol{x}. \tag{7.4}$$

Proof. For the interchanging of the integral and the differential, we observe

$$\begin{aligned}
(\Delta(\mathcal{T}\boldsymbol{f}))(\boldsymbol{y}) &= \Delta_{\boldsymbol{y}} \int_{\mathbb{G}} \boldsymbol{f}(\boldsymbol{x}) \cdot \boldsymbol{k}^{(\iota)}(\boldsymbol{x}, \boldsymbol{y}) \, \mathrm{d}\boldsymbol{x} \\
&= \boldsymbol{\nabla}_{\boldsymbol{y}} \cdot \boldsymbol{\nabla}_{\boldsymbol{y}} \int_{\mathbb{G}} \boldsymbol{f}(\boldsymbol{x}) \cdot \boldsymbol{k}^{(\iota)}(\boldsymbol{x}, \boldsymbol{y}) \, \mathrm{d}\boldsymbol{x} \\
&= \boldsymbol{\nabla}_{\boldsymbol{y}} \cdot \int_{\mathbb{G}} \boldsymbol{\nabla}_{\boldsymbol{y}} \left(\boldsymbol{f}(\boldsymbol{x}) \cdot \boldsymbol{k}^{(\iota)}(\boldsymbol{x}, \boldsymbol{y}) \right) \mathrm{d}\boldsymbol{x},
\end{aligned}$$

where the interchanging is valid due to Theorem 7.11. Now, we need to check if we can also interchange the second differential operator with the integration. Thus, we verify that all assumptions of the theorem of differentiation under the integral sign, see [19, Cor. 16.3], are fulfilled. We define for almost all $(\boldsymbol{x}, \boldsymbol{y}) \in \mathbb{G} \times \mathbb{G}_{\text{out}}$ the auxiliary function

$$\boldsymbol{h}(\boldsymbol{x}, \boldsymbol{y}) \coloneqq \boldsymbol{\nabla}_{\boldsymbol{y}} \left(\boldsymbol{f}(\boldsymbol{x}) \cdot \boldsymbol{k}^{(\iota)}(\boldsymbol{x}, \boldsymbol{y}) \right).$$

We immediately obtain $\boldsymbol{h}(\cdot, \boldsymbol{y}) \in \mathbf{L}_1(\mathbb{G})$ via Lemma 7.10. For its derivative, we obtain with an appropriate polynomial $k \mapsto \bar{\Gamma}_k$ and the proof of Theorem 6.18 the estimate

$$\begin{aligned}
|\boldsymbol{\nabla}_{\boldsymbol{y}} \cdot \boldsymbol{h}(\boldsymbol{x}, \boldsymbol{y})| &= \left| \boldsymbol{\nabla}_{\boldsymbol{y}} \cdot \left(\boldsymbol{\nabla}_{\boldsymbol{y}} \left(\boldsymbol{f}(\boldsymbol{x}) \cdot \boldsymbol{k}^{(\iota)}(\boldsymbol{x}, \boldsymbol{y}) \right) \right) \right| \\
&= \left| \Delta_{\boldsymbol{y}} \left(\boldsymbol{f}(\boldsymbol{x}) \cdot \boldsymbol{k}^{(\iota)}(\boldsymbol{x}, \boldsymbol{y}) \right) \right| \\
&= \left| \left(\boldsymbol{f}(\boldsymbol{x}) \cdot (\boldsymbol{\Delta}_{\boldsymbol{y}} \boldsymbol{k}^{(\iota)}(\boldsymbol{x}, \boldsymbol{y})) \right) \right| \\
&\leq |\boldsymbol{f}(\boldsymbol{x})| \, |\boldsymbol{\Delta}_{\boldsymbol{y}} \boldsymbol{k}^{(\iota)}(\boldsymbol{x}, \boldsymbol{y})| \\
&\leq |\boldsymbol{f}(\boldsymbol{x})| \sum_{k=0_\iota}^{\infty} \bar{\Gamma}_k \frac{x^{t_k}}{(R+\varepsilon)^{k+N_2}} \\
&\eqqcolon g(\boldsymbol{x}).
\end{aligned}$$

Here, g is an $\mathrm{L}_2(\mathbb{G})$-function. For the case $\mathbb{G} = \mathbb{G}_{\text{in}}$, we have

$$\int_{\mathbb{G}_{\text{in}}} g(\boldsymbol{x})^2 \, \mathrm{d}\boldsymbol{x} \leq \int_{\mathbb{G}_{\text{in}}} |\boldsymbol{f}(\boldsymbol{x})|^2 \, \mathrm{d}\boldsymbol{x} \left(\sum_{k=0_\iota}^{\infty} \bar{\Gamma}_k \frac{R^{t_k}}{(R+\varepsilon)^{k+N_2}} \right)^2 < \infty,$$

see also the proof of Lemma 7.10 for the detailed estimates. In analogy, we obtain for the case $\mathbb{G} = \mathbb{G}_{\text{star}}$ the estimates

$$\int_{\mathbb{G}_{\text{star}}} g(\boldsymbol{x})^2 \, \mathrm{d}\boldsymbol{x} = \int_{\mathbb{S}} \int_0^{\zeta(\hat{\boldsymbol{x}})} \left| \boldsymbol{f}(\boldsymbol{x}) \sum_{k=0_\iota}^{\infty} \bar{\Gamma}_k \frac{x^{t_k+1}}{(R+\varepsilon)^{k+N_2}} \right|^2 \mathrm{d}x \, \mathrm{d}\omega(\hat{\boldsymbol{x}}) < \infty.$$

The smoothness of $\boldsymbol{h}$ remains to be verified.

First, we investigate the case of the continuous VLI operator. We analyze $H(\boldsymbol{x}, \boldsymbol{y}) \coloneqq \boldsymbol{\nabla}_{\boldsymbol{y}} \cdot \boldsymbol{h}(\boldsymbol{x}, \boldsymbol{y}) = \boldsymbol{f}(\boldsymbol{x}) \cdot \boldsymbol{\Delta}_{\boldsymbol{y}} \boldsymbol{k}^{(\iota)}(\boldsymbol{x}, \boldsymbol{y})$ for almost all $(\boldsymbol{x}, \boldsymbol{y}) \in \mathbb{G}_{\text{in}} \times \mathbb{G}_{\text{out}}$. According to Theorem 6.18,

the Laplacian with respect to $\boldsymbol{y}$ and the series in $\boldsymbol{k}^{(\iota)}$ can be interchanged. In addition, this second-order term-by-term differentiated series converges uniformly. We obtain the relation

$$\boldsymbol{\Delta}_{\boldsymbol{y}}\boldsymbol{k}^{(\iota)}(\boldsymbol{x},\boldsymbol{y}) = \sum_{k=0_\iota}^{\infty} \boldsymbol{\Delta}_{\boldsymbol{y}}\left(\gamma_k(y)x^{t_k}\boldsymbol{p}_k^{(\iota)}(\hat{\boldsymbol{x}},\hat{\boldsymbol{y}})\right).$$

Each summand of this series is continuous as a composition of continuous functions. Due to the uniform convergence and the fact that $\boldsymbol{f}$ is independent of $\boldsymbol{y}$, we get $H(\boldsymbol{x},\cdot) \in \mathbf{C}(\mathbb{G}_{\text{out}})$ for almost all $\boldsymbol{x} \in \mathbb{G}_{\text{in}}$. With the often used trick, that is multiplying and dividing H by $x \in (0,R]$, and Corollary 6.3, we immediately obtain that $H(\boldsymbol{x},\cdot) \in \mathbf{C}(\mathbb{G}_{\text{out}})$ if the kernel $\boldsymbol{k}^{(\iota)}$ is the star-shaped VLI kernel. Summing up, $\boldsymbol{h}(\boldsymbol{x},\cdot)$ is continuously differentiable for almost all $\boldsymbol{x}$ on the corresponding domain. Combining these two results with the theorem of differentiation under the integral sign, we are able to interchange the remaining differential operator with the integration. Finally, for all $\boldsymbol{y} \in \mathbb{G}_{\text{out}}$ we obtain the identity

$$\begin{aligned}(\Delta(\mathcal{T}\boldsymbol{f}))(\boldsymbol{y}) &= \Delta_{\boldsymbol{y}} \int_{\mathbb{G}} \boldsymbol{f}(\boldsymbol{x}) \cdot \boldsymbol{k}^{(\iota)}(\boldsymbol{x},\boldsymbol{y}) \,\mathrm{d}\boldsymbol{x} \\ &= \int_{\mathbb{G}} \Delta_{\boldsymbol{y}} \left(\boldsymbol{f}(\boldsymbol{x}) \cdot \boldsymbol{k}^{(\iota)}(\boldsymbol{x},\boldsymbol{y})\right) \,\mathrm{d}\boldsymbol{x} \\ &= \int_{\mathbb{G}} \boldsymbol{f}(\boldsymbol{x}) \cdot \left(\boldsymbol{\Delta}_{\boldsymbol{y}}\boldsymbol{k}^{(\iota)}(\boldsymbol{x},\boldsymbol{y})\right) \,\mathrm{d}\boldsymbol{x},\end{aligned}$$

since $\boldsymbol{f}$ is independent of $\boldsymbol{y}$. □

7.3. Solution of the Direct Problem

Having defined the continuous/star-shaped VLI equation and analyzed the well-posedness of the related direct problem, we proceed by solving the corresponding direct problem. In order to do so, we restrict ourselves to a particular setting that fits to our desired application, that is $\mathbb{G}_{\text{in}} \coloneqq \mathbb{B}_R$. For this purpose, we expand the density $\boldsymbol{f}$ via an appropriate vector-valued orthonormal basis for $\mathbf{L}_2(\mathbb{B}_R)$. We call this expansion the Morse-Feshbach expansion of $\boldsymbol{f}$ since the orthonormal basis system on the ball using the Morse-Feshbach vector spherical harmonics is employed, see Definition 5.37. This expansion is used to find a series representation of the potential. In addition, since in the case of the MEG problem a relation between the neuronal current and the magnetic field is desired, we also calculate the series representation for the corresponding gradient field.

Assumption 7.14. *Let the inner set $\mathbb{G}_{\text{in}} \coloneqq \mathbb{G}_{\text{star}} \coloneqq \mathbb{B}_R$ be a ball with radius $R > 0$ and let the function $\boldsymbol{f}$ be expandable into the $\mathbf{L}_2(\mathbb{B}_R)$-convergent series*

$$\boldsymbol{f}(\boldsymbol{x}) \overset{\mathrm{L}_2(\mathbb{B}_R)}{=} \sum_{i=1}^{3} \sum_{n=0_i}^{\infty} \sum_{j=1}^{2n+1} f_{n,j}^{(i)}(x)\boldsymbol{y}_{n,j}^{(i)}(\hat{\boldsymbol{x}}),$$

where $\boldsymbol{y}_{n,j}^{(i)}$ are the Morse-Feshbach vector spherical harmonics from Definition 5.8. Here, the functions $f_{n,j}^{(i)}$ with $i = 1, 2, 3$, $n \in \mathbb{N}_{0_i}$, and $j = 1, \ldots, 2n+1$ are defined as the Morse-Feshbach expansion coefficients at a certain radius, that is

$$f_{n,j}^{(i)}(x) \coloneqq \int_{\mathbb{S}} \boldsymbol{f}(x\hat{\boldsymbol{x}}) \cdot \boldsymbol{y}_{n,j}^{(i)}(\hat{\boldsymbol{x}}) \,\mathrm{d}\omega(\hat{\boldsymbol{x}}) \qquad \text{for almost all } x \in [0,R].$$

By means of this representation, we are able to calculate the $\mathbf{L}_2(\mathbb{B}_R)$-norm of the function $\boldsymbol{f}$, which is useful for forthcoming estimates.

Theorem 7.15. *If $\boldsymbol{f} \in \mathbf{L}_2(\mathbb{B}_R)$, then it holds true that*

$$\|\boldsymbol{f}\|_{\mathbf{L}_2(\mathbb{B}_R)} = \left(\sum_{i=1}^{3} \sum_{n=0_i}^{\infty} \sum_{j=1}^{2n+1} \int_0^R \left(x f_{n,j}^{(i)}(x) \right)^2 \mathrm{d}x \right)^{1/2}. \tag{7.5}$$

Proof. From the strong convergence of the series, we obtain the weak convergence, see, for instance, [225, Ch. V]. More precisely, we have

$$\sum_{i=1}^{3} \sum_{n=0_i}^{\infty} \sum_{j=1}^{2n+1} \left\langle f_{n,j}^{(i)}(|\cdot|) \boldsymbol{y}_{n,j}^{(i)}(\hat{\cdot}), \boldsymbol{g} \right\rangle_{\mathbf{L}_2(\mathbb{B}_R)} = \left\langle \sum_{i=1}^{3} \sum_{n=0_i}^{\infty} \sum_{j=1}^{2n+1} f_{n,j}^{(i)}(|\cdot|) \boldsymbol{y}_{n,j}^{(i)}(\hat{\cdot}), \boldsymbol{g} \right\rangle_{\mathbf{L}_2(\mathbb{B}_R)}$$

for all $\boldsymbol{g} \in \mathbf{L}_2(\mathbb{B}_R)$. We obtain the desired interchanging for the series with respect to i, n, j and the integral over $\mathbb{B}_R$. Thus, we eventually obtain the relation

$$\begin{aligned}
&\|\boldsymbol{f}\|_{\mathbf{L}_2(\mathbb{B}_R)}^2 \\
&= \int_{\mathbb{B}_R} (\boldsymbol{f}(\boldsymbol{x}))^2 \,\mathrm{d}\boldsymbol{x} = \int_{\mathbb{B}_R} \left(\sum_{i=1}^{3} \sum_{n=0_i}^{\infty} \sum_{j=1}^{2n+1} f_{n,j}^{(i)}(x) \boldsymbol{y}_{n,j}^{(i)}(\hat{\boldsymbol{x}}) \right)^2 \mathrm{d}\boldsymbol{x} \\
&= \sum_{i=1}^{3} \sum_{n=0_i}^{\infty} \sum_{j=1}^{2n+1} \sum_{\kappa=1}^{3} \sum_{m=0_\kappa}^{\infty} \sum_{l=1}^{2m+1} \int_{\mathbb{B}_R} f_{n,j}^{(i)}(x) \boldsymbol{y}_{n,j}^{(i)}(\hat{\boldsymbol{x}}) \cdot \left(f_{m,l}^{(\kappa)}(x) \boldsymbol{y}_{m,l}^{(\kappa)}(\hat{\boldsymbol{x}}) \right) \mathrm{d}\boldsymbol{x} \\
&= \sum_{i=1}^{3} \sum_{n=0_i}^{\infty} \sum_{j=1}^{2n+1} \sum_{\kappa=1}^{3} \sum_{m=0_\kappa}^{\infty} \sum_{l=1}^{2m+1} \int_0^R f_{n,j}^{(i)}(x) f_{m,l}^{(\kappa)}(y) x^2 \,\mathrm{d}x \int_{\mathbb{S}} \boldsymbol{y}_{n,j}^{(i)}(\hat{\boldsymbol{x}}) \cdot \boldsymbol{y}_{m,l}^{(\kappa)}(\hat{\boldsymbol{x}}) \,\mathrm{d}\omega(\hat{\boldsymbol{x}}) \\
&= \sum_{i=1}^{3} \sum_{n=0_i}^{\infty} \sum_{j=1}^{2n+1} \int_0^R \left(x f_{n,j}^{(i)}(x) \right)^2 \mathrm{d}x.
\end{aligned}$$

□

Now, we insert the Morse-Feshbach expansion of $\boldsymbol{f}$ from Assumption 7.14 into the continuous/star-shaped VLI equation. Further calculations require to interchange the integration and the series. First, we prove that this interchanging is valid.

Theorem 7.16. *If $\boldsymbol{f}$ fulfils Assumption 7.14, then the continuous/star-shaped VLI operator for all $\boldsymbol{y} \in \mathbb{G}_{\mathrm{out}}$ has the representation*

$$\begin{aligned}
(\mathcal{T}\boldsymbol{f})(\boldsymbol{y}) &= \int_{\mathbb{B}_R} \boldsymbol{f}(\boldsymbol{x}) \cdot \boldsymbol{k}^{(\iota)}(\boldsymbol{x}, \boldsymbol{y}) \,\mathrm{d}\boldsymbol{x} \\
&= \sum_{i=1}^{3} \sum_{n=0_i}^{\infty} \sum_{j=1}^{2n+1} \sum_{k=0_\iota}^{\infty} \int_{\mathbb{B}_R} f_{n,j}^{(i)}(x) \boldsymbol{y}_{n,j}^{(i)}(\hat{\boldsymbol{x}}) \cdot \left(\gamma_k(y) x^{t_k} \boldsymbol{p}_k^{(\iota)}(\hat{\boldsymbol{x}}, \hat{\boldsymbol{y}}) \right) \mathrm{d}\boldsymbol{x}.
\end{aligned}$$

Proof. The density $\boldsymbol{f}$ fulfils Assumption 7.14, which is equivalent to the strong convergence of the series. Due to this property, we again obtain the weak convergence. Finally, Corollary 6.14 provides us with the possibility to interchange the integration and the series with respect to k. □

Using this preliminary study, we are able to further simplify the direct operator corresponding to the continuous/star-shaped VLI equation, which reduces the integral to a one-dimensional one.

Corollary 7.17. *Let Assumption 7.14 be fulfilled. Then the continuous/star-shaped VLI operator yields*

$$(\mathcal{T}\boldsymbol{f})(\boldsymbol{y}) = 4\pi \sum_{n=0_\iota}^{\infty} \sum_{j=1}^{2n+1} \frac{1}{2n+1} \left(\int_0^R f_{n,j}^{(\iota)}(x) x^{t_n+2} \,\mathrm{d}x \right) \gamma_n(y) Y_{n,j}(\hat{\boldsymbol{y}}) \tag{7.6}$$

for all $\boldsymbol{y} \in \mathbb{G}_{\mathrm{out}}$.

Proof. Theorem 7.16 provides us with the possibility to interchange the series and the integration. In the second step, we use a kind of reproducing property of the vectorial Legendre polynomials, see Corollary 5.26. Eventually, we get the stated relation, that is

$$\begin{aligned}(\mathcal{T}\boldsymbol{f})(\boldsymbol{y}) &= \sum_{i=1}^{3} \sum_{n=0_i}^{\infty} \sum_{j=1}^{2n+1} \sum_{k=0_\iota}^{\infty} \left(\gamma_k(y) \int_0^R f_{n,j}^{(i)}(x) x^{t_k+2} \,\mathrm{d}x \int_{\mathbb{S}} \boldsymbol{y}_{n,j}^{(i)}(\hat{\boldsymbol{x}}) \cdot \boldsymbol{p}_k^{(\iota)}(\hat{\boldsymbol{x}}, \hat{\boldsymbol{y}}) \,\mathrm{d}\omega(\hat{\boldsymbol{x}}) \right) \\ &= 4\pi \sum_{n=0_\iota}^{\infty} \sum_{j=1}^{2n+1} \frac{1}{2n+1} \left(\int_0^R f_{n,j}^{(\iota)}(x) x^{t_n+2} \,\mathrm{d}x \right) \gamma_n(y) Y_{n,j}(\hat{\boldsymbol{y}}). \end{aligned}$$

□

On the right-hand side of Eq. (7.6), a series is stated. We need to examine the type of convergence of this series. So far, we obtained uniform convergence in the continuous VLI case and $\mathbf{L}_2(\mathbb{G}_{\mathrm{out}})$-convergence in the star-shaped VLI case.

Theorem 7.18. *If Assumption 7.14 is fulfilled, then the series on the right-hand side of Eq.* (7.6) *converges uniformly in* $\mathbb{G}_{\mathrm{out}}$. *In addition, the series converges in the* $\mathrm{L}_2(\mathbb{G}_{\mathrm{out}})$*-sense.*

Proof. In order to estimate the series, we use the triangle inequality for the absolute value. Then, we apply the Cauchy-Schwarz inequality twice, first for the integral and second for the series. In combination with the estimate for the functions γ_n for $n \in \mathbb{N}_{0_\iota}$, the Addition Theorem, see Theorem 2.25, and Theorem 7.15 we get for all $N \in \mathbb{N}$ and $(\boldsymbol{x}, \boldsymbol{y}) \in \mathbb{B}_R \times \mathbb{G}_{\mathrm{out}}$ the estimate

$$\begin{aligned}&\left| \sum_{n=N}^{\infty} \sum_{j=1}^{2n+1} \frac{1}{2n+1} \left(\int_0^R f_{n,j}^{(\iota)}(x) x^{t_n+2} \,\mathrm{d}x \right) \gamma_n(y) Y_{n,j}(\hat{\boldsymbol{y}}) \right| \\ &\leq \sum_{n=N}^{\infty} \sum_{j=1}^{2n+1} \frac{1}{2n+1} \left| \int_0^R f_{n,j}^{(\iota)}(x) x^{t_n+2} \,\mathrm{d}x \right| \sup_{\boldsymbol{y} \in \mathbb{G}_{\mathrm{out}}} |\gamma_n(y)| \, |Y_{n,j}(\hat{\boldsymbol{y}})| \\ &\leq \sum_{n=N}^{\infty} \sum_{j=1}^{2n+1} \frac{1}{2n+1} \left(\int_0^R \left(f_{n,j}^{(\iota)}(x) x \right)^2 \mathrm{d}x \int_0^R x^{2t_n+2} \,\mathrm{d}x \right)^{1/2} \frac{\Gamma_n}{(R+\varepsilon)^{n+1}} \, |Y_{n,j}(\hat{\boldsymbol{y}})| \\ &\leq \left(\sum_{n=N}^{\infty} \sum_{j=1}^{2n+1} \frac{\Gamma_n^2}{(2n+1)^2(2t_n+3)} \frac{R^{2t_n+3}}{(R+\varepsilon)^{2n+2}} \left(Y_{n,j}(\hat{\boldsymbol{y}}) \right)^2 \right)^{1/2} \\ &\qquad \times \left(\sum_{n=N}^{\infty} \sum_{j=1}^{2n+1} \int_0^R \left(f_{n,j}^{(\iota)}(x) x \right)^2 \mathrm{d}x \right)^{1/2} \\ &\leq \left(\sup_{n \in \mathbb{N}_{0_\iota}} R^{t_n - n} \right) \left(\frac{R}{4\pi} \sum_{n=N}^{\infty} \frac{\Gamma_n^2}{(2n+1)(2t_n+3)} \left(\frac{R}{R+\varepsilon} \right)^{2n+2} \right)^{1/2} \|\boldsymbol{f}\|_{\mathbf{L}_2(\mathbb{B}_R)} . \end{aligned}$$

Due to the requirements in Definition 6.1 and properties of the power series, see Theorem 6.4, we obtain the convergence of the right-hand side to zero as $N \to \infty$ and, hence, the uniform convergence of the series. For the convergence in $\mathrm{L}_2(\mathbb{G}_{\mathrm{out}})$-sense, we need to verify that

$$\lim_{N\to\infty} \int_{\mathbb{G}_{\mathrm{out}}} \left| \sum_{n=N}^{\infty} \sum_{j=1}^{2n+1} \frac{1}{2n+1} \left(\int_0^R f_{n,j}^{(\iota)}(x) x^{t_n+2} \,\mathrm{d}x \right) \gamma_n(y) Y_{n,j}(\hat{\boldsymbol{y}}) \right|^2 \mathrm{d}\boldsymbol{y} = 0.$$

By combining the previous estimates with the ones from the proof of Lemma 6.16, we get the desired result, that is

$$\begin{aligned}
&\int_{\mathbb{G}_{\mathrm{out}}} \left| \sum_{n=N}^{\infty} \sum_{j=1}^{2n+1} \frac{1}{2n+1} \left(\int_0^R f_{n,j}^{(\iota)}(x) x^{t_n+2} \,\mathrm{d}x \right) \gamma_n(y) Y_{n,j}(\hat{\boldsymbol{y}}) \right|^2 \mathrm{d}\boldsymbol{y} \\
&\leq \int_{\mathbb{G}_{\mathrm{out}}} \left(\sum_{n=N}^{\infty} \sum_{j=1}^{2n+1} \frac{1}{2n+1} \left(\int_0^R \left(f_{n,j}^{(\iota)}(x) x \right)^2 \mathrm{d}x \right)^{1/2} \left(\int_0^R x^{2t_n+2} \,\mathrm{d}x \right)^{1/2} \frac{\Gamma_n}{y^{n+1}} \left| Y_{n,j}(\hat{\boldsymbol{y}}) \right| \right)^2 \mathrm{d}\boldsymbol{y} \\
&\leq \frac{1}{4\pi} \int_{\mathbb{G}_{\mathrm{out}}} \left(\sum_{n=N}^{\infty} \frac{\Gamma_n^2}{(2n+1)(2t_n+3)} \frac{R^{2t_n+3}}{y^{2n+2}} \right) \left(\sum_{n=N}^{\infty} \sum_{j=1}^{2n+1} \int_0^R \left(f_{n,j}^{(\iota)}(x) x \right)^2 \mathrm{d}x \right) \mathrm{d}\boldsymbol{y} \\
&\leq \|\boldsymbol{f}\|_{\mathbf{L}_2(\mathbb{B}_R)}^2 \int_{R+\varepsilon}^{\infty} \left(\sum_{n=N}^{\infty} \frac{\Gamma_n^2}{2n+1} \frac{R^{2t_n+3}}{y^{2n}} \right) \mathrm{d}y \\
&= \|\boldsymbol{f}\|_{\mathbf{L}_2(\mathbb{B}_R)}^2 \left(\sup_{n\in\mathbb{N}} R^{t_n-n} \right)^2 \sum_{n=N}^{\infty} \frac{\Gamma_n^2}{(2n-1)(2n+1)} \frac{R^{2n+3}}{(R+\varepsilon)^{2n-1}} \to 0 \quad (\text{as } N \to \infty). \qquad \square
\end{aligned}$$

Theorem 7.8 provides us with the continuity of $\mathcal{T}\boldsymbol{f}$ in the case of the continuous VLI operator. In the case of the star-shaped VLI kernel, which includes $\inf_{n\in\mathbb{N}_{0_\iota},\gamma_n\not\equiv 0} t_n \geq -1$, we cannot achieve a uniform bound of the integral kernel due to a possible singularity. By means of the previous theorem, however, we are able to prove the continuity of $\mathcal{T}\boldsymbol{f}$ in the ball case even if the corresponding integral kernel is not bounded.

Corollary 7.19. *Let Assumption 7.14 be fulfilled. Then $\mathcal{T}\boldsymbol{f}$ obtained from the continuous/ star-shaped VLI kernel is a continuous function in $\mathbb{G}_{\mathrm{out}}$.*

Proof. Due to Theorem 7.18, we get the uniform convergence of

$$(\mathcal{T}\boldsymbol{f})(\boldsymbol{y}) = 4\pi \sum_{n=0_\iota}^{\infty} \sum_{j=1}^{2n+1} \frac{1}{2n+1} \left(\int_0^R f_{n,j}^{(\iota)}(x) x^{t_n+2} \,\mathrm{d}x \right) \gamma_n(y) Y_{n,j}(\hat{\boldsymbol{y}})$$

in $\mathbb{G}_{\mathrm{out}}$. Each summand of the series on the right-hand side is continuous in $\boldsymbol{y}$, due to the conditions on $\{\gamma_n\}_{n\in\mathbb{N}_{0_\iota}}$ in Definition 6.1 or Definition 6.2, respectively, and the continuity of the spherical harmonics. Combining these two statements, we get $\mathcal{T}\boldsymbol{f} \in \mathrm{C}(\mathbb{G}_{\mathrm{out}})$. $\square$

In certain applications, the function $\mathcal{T}\boldsymbol{f}$ on the domain $\mathbb{S}_R$ is of interest. In this case, we cannot expect uniform or even pointwise convergence of the series, due to the missing power series. However, another type of convergence can be proved under certain circumstances.

Theorem 7.20. *Let Assumption 7.14 be fulfilled, which implies*

$$\boldsymbol{f}(\boldsymbol{x}) \overset{\mathbf{L}_2(\mathbb{B}_R)}{=} \sum_{i=1}^{3} \sum_{n=0_i}^{\infty} \sum_{j=1}^{2n+1} f_{n,j}^{(i)}(x) \boldsymbol{y}_{n,j}^{(i)}(\hat{\boldsymbol{x}}).$$

In addition, let the sequence of functions $\{\gamma_n\}_{n\in\mathbb{N}_{0_i}}$ *be evaluable for* $y = R$ *and let them fulfil the additional condition*

$$|\gamma_n(R)| \leq \Gamma_n R^{-(n+1+\delta_{0_\iota,0}\delta_{n,0})}$$

for all $n \in \mathbb{N}_{0_i}$*, where for all* $n \in \mathbb{N}_{0_i}$ *it holds true that*

$$\Gamma_n \leq c\sqrt{(2n+1)^2(2t_n+3)}$$

with $c \in \mathbb{R}_0^+$*. Then we can expand and restrict* $\mathcal{T}\boldsymbol{f}$ *obtained from the continuous/star-shaped VLI operator onto the sphere with radius* R*. This function is denoted by* $(\mathcal{T}\boldsymbol{f})|_{\mathbb{S}_R}$*. In addition, the series in* $(\mathcal{T}\boldsymbol{f})|_{\mathbb{S}_R}$ *converges in the sense of* $\mathrm{L}_2(\mathbb{S}_R)$*. It is represented by the expression*

$$(\mathcal{T}\boldsymbol{f})(\boldsymbol{y}) \overset{\mathrm{L}_2(\mathbb{S}_R)}{=} 4\pi \sum_{n=0_\iota}^{\infty} \sum_{j=1}^{2n+1} \frac{1}{2n+1} \left(\int_0^R f_{n,j}^{(\iota)}(x) x^{t_n+2} \,\mathrm{d}x \right) \gamma_n(R) Y_{n,j}(\hat{\boldsymbol{y}}).$$

Proof. Due to our assumption, the domain of $\mathcal{T}\boldsymbol{f}$ can be extended to $\mathbb{S}_R$. An immediate consequence of Corollary 7.17 and the requirements on $\{\gamma_n\}_{n\in\mathbb{N}_{0_\iota}}$ yield the desired representation. The convergence in the $\mathbf{L}_2(\mathbb{S}_R)$-sense remains to be proved. Since the set $\{R^{-1}Y_{n,j}\}_{n\in\mathbb{N}_0,j=1,\dots,2n+1}$ is an orthonormal basis for $\mathbf{L}_2(\mathbb{S}_R)$, we can use a property of Parseval's identity, see [198, Thm. 12.6], combined with the Cauchy-Schwarz inequality to obtain the relation

$$\begin{aligned}
&\|(\mathcal{T}\boldsymbol{f})|_{\mathbb{S}_R}\|_{\mathrm{L}_2(\mathbb{S}_R)}^2 = \sum_{n=0}^{\infty} \sum_{j=1}^{2n+1} \left\langle (\mathcal{T}\boldsymbol{f})|_{\mathbb{S}_R}, \frac{1}{R} Y_{n,j} \right\rangle_{\mathrm{L}_2(\mathbb{S}_R)}^2 \\
&= (4\pi R)^2 \sum_{n=0_\iota}^{\infty} \sum_{j=1}^{2n+1} \frac{1}{(2n+1)^2} \left(\int_0^R f_{n,j}^{(\iota)}(x) x^{t_n+2} \,\mathrm{d}x \right)^2 (\gamma_n(R))^2 \\
&\leq (4\pi R)^2 \sum_{n=0_\iota}^{\infty} \sum_{j=1}^{2n+1} \frac{\Gamma_n^2}{(2n+1)^2} \frac{1}{R^{2n+2+2\delta_{0_\iota,0}\delta_{n,0}}} \int_0^R \left(f_{n,j}^{(\iota)}(x) x \right)^2 \mathrm{d}x \int_0^R x^{2t_n+2} \,\mathrm{d}x \\
&\leq (4\pi R)^2 \sum_{n=0_\iota}^{\infty} \sum_{j=1}^{2n+1} \frac{\Gamma_n^2}{(2n+1)^2(2t_n+3)} \frac{R^{2t_n+3}}{R^{2n+2+2\delta_{0_\iota,0}\delta_{n,0}}} \int_0^R \left(f_{n,j}^{(\iota)}(x) x \right)^2 \mathrm{d}x \\
&\leq (4\pi)^2 \max\left\{R^3, R\right\} \left(\sup_{n\in\mathbb{N}_{0_\iota}} R^{t_n-n} \right)^2 \sum_{n=0_\iota}^{\infty} \sum_{j=1}^{2n+1} \frac{\Gamma_n^2}{(2n+1)^2(2t_n+3)} \int_0^R \left(f_{n,j}^{(\iota)}(x) x \right)^2 \mathrm{d}x \\
&\leq (4\pi)^2 \max\left\{R^3, R\right\} c^2 \left(\sup_{n\in\mathbb{N}_{0_\iota}} R^{t_n-n} \right)^2 \sum_{n=0_\iota}^{\infty} \sum_{j=1}^{2n+1} \int_0^R \left(f_{n,j}^{(\iota)}(x) x \right)^2 \mathrm{d}x \\
&= (4\pi)^2 \max\left\{R^3, R\right\} c^2 \left(\sup_{n\in\mathbb{N}_{0_\iota}} R^{t_n-n} \right)^2 \|\boldsymbol{f}\|_{\mathbf{L}_2(\mathbb{G}_{\mathrm{in}})}^2 < \infty,
\end{aligned}$$

which implies the desired result. □

We have already seen that the gradient with respect to $\boldsymbol{y}$ and the integration over $\mathbb{B}_R$ in the definition of $\mathcal{T}\boldsymbol{f}$ can be interchanged. Now, we are able to find an explicit representation of the gradient of $\mathcal{T}\boldsymbol{f}$ by means of the Morse-Feshbach expansion of $\boldsymbol{f}$.

Lemma 7.21. *Let Assumption 7.14 be fulfilled and let*

$$\sup_{\boldsymbol{y}\in\mathbb{G}_{\text{out}}} |\gamma_n'(y)| \leq \Gamma_n (R+\varepsilon)^{-(n+N_1)},$$

where $N_1 \in \mathbb{N}_0$, for all $n \in \mathbb{N}_{0_\iota}$ with $(n \mapsto \Gamma_n) \in \mathcal{O}(n^M)$ for a fixed $M \in \mathbb{N}_0$ hold true. Then the gradient of the potential achieved via the continuous/star-shaped VLI operator from Definition 7.1 is given by

$$(\boldsymbol{\nabla}(\mathcal{T}\boldsymbol{f}))(\boldsymbol{y}) = 4\pi \sum_{n=0_\iota}^{\infty} \sum_{j=1}^{2n+1} \frac{1}{2n+1} \left(\int_0^R f_{n,j}^{(\iota)}(x) x^{t_n+2} \,\mathrm{d}x \right) \boldsymbol{\nabla}_{\boldsymbol{y}} \left(\gamma_n(y) Y_{n,j}(\hat{\boldsymbol{y}}) \right)$$

for all $\boldsymbol{y} \in \mathbb{G}_{\text{out}}$. In addition, the series on the right-hand side converges uniformly.

Proof. Corollary 7.17 provides us with the identity

$$(\mathcal{T}\boldsymbol{f})(\boldsymbol{y}) = 4\pi \sum_{n=0_\iota}^{\infty} \sum_{j=1}^{2n+1} \frac{1}{2n+1} \left(\int_0^R f_{n,j}^{(\iota)}(x) x^{t_n+2} \,\mathrm{d}x \right) \gamma_n(y) Y_{n,j}(\hat{\boldsymbol{y}})$$

for all $\boldsymbol{y} \in \mathbb{G}_{\text{out}}$. Theorem 7.18 yields the uniform convergence of the series. Now, we want to interchange the gradient and the series. For this purpose, the uniform convergence of the term-by-term differentiated series remains to be proved. First, we separately analyze the part that depends on $\boldsymbol{y}$. To this end, we will utilize the Euclidean orthogonality of the Morse-Feshbach vector spherical harmonics. For all $n \in \mathbb{N}$ and $\boldsymbol{y} \in \mathbb{G}_{\text{out}}$, we get

$$\begin{aligned}
\left| \boldsymbol{\nabla}_{\boldsymbol{y}} \left(\gamma_n(y) Y_{n,j}(\hat{\boldsymbol{y}}) \right) \right|^2 &= \left| \left(\hat{\boldsymbol{y}} \frac{\partial}{\partial y} + \frac{1}{y} \boldsymbol{\nabla}_{\hat{\boldsymbol{y}}}^* \right) \left(\gamma_n(y) Y_{n,j}(\hat{\boldsymbol{y}}) \right) \right|^2 \\
&= \left| \gamma_n'(y) \hat{\boldsymbol{y}} Y_{n,j}(\hat{\boldsymbol{y}}) + \frac{\gamma_n(y)}{y} \boldsymbol{\nabla}_{\hat{\boldsymbol{y}}}^* Y_{n,j}(\hat{\boldsymbol{y}}) \right|^2 \\
&= \left(\gamma_n'(y) \right)^2 \left| \boldsymbol{y}_{n,j}^{(1)}(\hat{\boldsymbol{y}}) \right|^2 + n(n+1) \frac{\gamma_n^2(y)}{y^2} \left| \boldsymbol{y}_{n,j}^{(2)}(\hat{\boldsymbol{y}}) \right|^2 \\
&\leq \frac{\Gamma_n^2}{(R+\varepsilon)^{2n+2N_1}} \left(Y_{n,j}(\hat{\boldsymbol{y}}) \right)^2 + \frac{n(n+1)\Gamma_n^2}{(R+\varepsilon)^{2n+4}} \left| \boldsymbol{y}_{n,j}^{(2)}(\hat{\boldsymbol{y}}) \right|^2 \\
&\leq n(n+1)\Gamma_n^2 \left(\frac{1}{(R+\varepsilon)^{2n+2N_1}} \left(Y_{n,j}(\hat{\boldsymbol{y}}) \right)^2 + \frac{1}{(R+\varepsilon)^{2n+4}} \left| \boldsymbol{y}_{n,j}^{(2)}(\hat{\boldsymbol{y}}) \right|^2 \right).
\end{aligned} \tag{7.7}$$

For $n = 0$ and $\iota = 1$, we obtain for all $\boldsymbol{y} \in \mathbb{G}_{\text{out}}$ the identity

$$\left| \boldsymbol{\nabla}_{\boldsymbol{y}} \left(\gamma_0(y) Y_{0,1}(\hat{\boldsymbol{y}}) \right) \right|^2 = \left| \gamma_0'(y) \hat{\boldsymbol{y}} Y_{0,1}(\hat{\boldsymbol{y}}) \right|^2 = 4\pi \left| \gamma_0'(y) \right|^2.$$

Similar estimates as made in the previous uniform convergence statements, the assumption on $\{\Gamma_n\}_{n\in\mathbb{N}_{0_\iota}}$, Eqs. (7.5) and (7.7), Theorem 2.25, and Corollary 5.25 are used in the next

inequality. Thus, with $N \in \mathbb{N}$, we get

$$
\begin{aligned}
&\left| \sum_{n=N}^{\infty} \sum_{j=1}^{2n+1} \frac{1}{2n+1} \left(\int_0^R f_{n,j}^{(\iota)}(x) x^{t_n+2} \,\mathrm{d}x \right) \boldsymbol{\nabla}_{\boldsymbol{y}} \left(\gamma_n(y) Y_{n,j}(\hat{\boldsymbol{y}}) \right) \right| \\
&\leq \left| \sum_{n=N}^{\infty} \sum_{j=1}^{2n+1} \frac{1}{2n+1} \left(\int_0^R \left(f_{n,j}^{(\iota)}(x) x \right)^2 \mathrm{d}x \int_0^R x^{2t_n+2} \,\mathrm{d}x \right)^{1/2} \boldsymbol{\nabla}_{\boldsymbol{y}} \left(\gamma_n(y) Y_{n,j}(\hat{\boldsymbol{y}}) \right) \right| \\
&\leq \left(\sum_{n=N}^{\infty} \sum_{j=1}^{2n+1} \frac{1}{(2n+1)^2 (2t_n+3)} R^{2t_n+3} \left| \boldsymbol{\nabla}_{\boldsymbol{y}} \left(\left(\gamma_n(y) Y_{n,j}(\hat{\boldsymbol{y}}) \right) \right) \right|^2 \right)^{1/2} \|\boldsymbol{f}\|_{\mathbf{L}_2(\mathbb{B}_R)} \\
&\leq \left(\sum_{n=N}^{\infty} \sum_{j=1}^{2n+1} \frac{n(n+1)\Gamma_n^2}{(2n+1)^2 (2t_n+3)} R^{2t_n+3} \left(\frac{\left(Y_{n,j}(\hat{\boldsymbol{y}}) \right)^2}{(R+\varepsilon)^{2n+2N_1}} + \frac{|\boldsymbol{y}_{n,j}^{(2)}(\hat{\boldsymbol{y}})|^2}{(R+\varepsilon)^{2n+4}} \right) \right)^{1/2} \|\boldsymbol{f}\|_{\mathbf{L}_2(\mathbb{B}_R)} \\
&\leq \frac{1}{\sqrt{4\pi}} \left(\sum_{n=N}^{\infty} \frac{n(n+1)\Gamma_n^2}{(2n+1)(2t_n+3)} \left(\frac{R^{2t_n+3}}{(R+\varepsilon)^{2n+2N_1}} + \frac{R^{2t_n+3}}{(R+\varepsilon)^{2n+4}} \right) \right)^{1/2} \|\boldsymbol{f}\|_{\mathbf{L}_2(\mathbb{B}_R)} \\
&\leq \frac{1}{\sqrt{4\pi}} \left(\sup_{n \in \mathbb{N}_{0_\iota}} R^{t_n - n} \right) \left(\sum_{n=N}^{\infty} \frac{n(n+1)\Gamma_n^2}{(2n+1)(2t_n+3)} \left(\frac{R^{2n+3}}{(R+\varepsilon)^{2n+2N_1}} + \frac{R^{2n+3}}{(R+\varepsilon)^{2n+4}} \right) \right)^{1/2} \|\boldsymbol{f}\|_{\mathbf{L}_2(\mathbb{B}_R)}
\end{aligned}
$$

which converges to zero as $N \to \infty$. Eventually, the term-by-term differentiated series converges uniformly and, hence, we are able to interchange the gradient and the series. □

For our application, we later need the representation in terms of the radial integral of the potential $\mathcal{T}\boldsymbol{f}$. However, a closed representation of the potential of the continuous/star-shaped VLI direct problem can be obtained by expanding the functions $f_{n,j}^{(\iota)}$ that occur in the radial integral in Eq. (7.6). This allows to fully evaluate the integral

$$
\int_0^R f_{n,j}^{(\iota)}(x) x^{t_n+2} \,\mathrm{d}x. \tag{7.8}
$$

To this end, we employ a generalized Fourier expansion for $f_{n,j}^{(\iota)}$. Theorem 2.9 provides us with a variety of complete orthonormal systems for weighted spaces $\mathrm{L}_2^w([0,R])$. Equation (7.8) is derived by the integration over a ball and a separation into radial and angular components, see Assumption 7.14. Due to the Jacobian determinant x^2 therein, we choose the weight function $w(x) \coloneqq x^2$ for $x \in [0,R]$. This is consistent with our approach for the construction of an orthonormal basis on the ball from Definition 5.37. Thus, we choose for all $m \in \mathbb{N}_0$ and all $n \in \mathbb{N}_{0_\iota}$ the functions

$$
Q_m^{(t_n+1/2)}(R;x) = \sqrt{\frac{4m+2t_n+3}{R^3}} \left(\frac{x}{R} \right)^{t_n} P_m^{(0,t_n+1/2)} \left(2\frac{x^2}{R^2} - 1 \right), \qquad x \in [0,R],
$$

as the basis functions for the space $\mathrm{L}_2^w([0,R])$, see Corollary 5.2. In addition, for all $n \in \mathbb{N}_{0_\iota}$ with $\gamma_n \equiv 0$, we set $t_n \coloneqq 0$. Then the condition $\inf_{n \in \mathbb{N}_{0_\iota}} t_n > -3/2$ is fulfilled for all $n \in \mathbb{N}_{0_\iota}$.

We can now interpret the radial integral in Eq. (7.8) as an inner product in the Hilbert space $\mathrm{L}_2^w([0,R])$ for all $n \in \mathbb{N}_{0_\iota}$, $j = 1, \ldots, 2n+1$.

Lemma 7.22. *Let Assumption 7.14 be fulfilled and let the setting of Definition 7.1 be given. In addition, we set $t_n \coloneqq 0$ for all $n \in \mathbb{N}_{0_\iota}$ for which $\gamma_n \equiv 0$. Then, we define $h_n(x) \coloneqq x^{t_n}$*

for all $x \in [0,R]$ and all $n \in \mathbb{N}_{0_\iota}$. Let the weight function be given by $w(x) \coloneqq x^2$. Then $f_{n,j}^{(\iota)}$ and h_n are $\mathrm{L}_2^w([0,R])$-functions for all $n \in \mathbb{N}_{0_\iota}$ and $j = 1,\dots,2n+1$. In addition, the functions h_n have for all $n \in \mathbb{N}_{0_\iota}$ the alternative representation

$$h_n = \sqrt{\frac{R^{2t_n+3}}{2t_n+3}} Q_0^{(t_n+1/2)}(R;\cdot) \tag{7.9}$$

and the following relation holds true

$$\left\langle f_{n,j}^{(\iota)}, h_n \right\rangle_{\mathrm{L}_2^w([0,R])} = \int_0^R f_{n,j}^{(\iota)}(x) x^{t_n+2}\,\mathrm{d}x. \tag{7.10}$$

Proof. If $f_{n,j}^{(\iota)}$ and h_n are $\mathrm{L}_2^w([0,R])$-functions for all $n \in \mathbb{N}_{0_\iota}$ and $j = 1,\dots,2n+1$, then the formula Eq. (7.10) is clear by the definition of the $\mathrm{L}_2^w([0,R])$-inner product, see Definition 2.2. In this case, Eq. (7.8) reduces to

$$\begin{aligned}\int_0^R f_{n,j}^{(\iota)}(x) x^{t_n+2}\,\mathrm{d}x &= \int_0^R f_{n,j}^{(\iota)}(x) h_n(x) x^2\,\mathrm{d}x \\ &= \left\langle f_{n,j}^{(\iota)}, h_n \right\rangle_{\mathrm{L}_2^w([0,R])}.\end{aligned}$$

However, it remains to verify that $f_{n,j}^{(\iota)}$ and h_n are $\mathrm{L}_2^w([0,R])$-functions for all $n \in \mathbb{N}_{0_\iota}$ and $j = 1,\dots,2n+1$. For the functions $f_{n,j}^{(\iota)}$, we obtain the estimate

$$\sum_{i=1}^{3} \sum_{n=0_i}^{\infty} \sum_{j=1}^{2n+1} \int_0^R \left(x f_{n,j}^{(i)}(x) \right)^2 \mathrm{d}x < \infty,$$

due to Eq. (7.5) and $\boldsymbol{f} \in \mathbf{L}_2(\mathbb{B}_R)$. Since the integrands are non-negative, each summand of the series must be finite. In particular, for all $n \in \mathbb{N}_{0_i}$, $j = 1,\dots,2n+1$, and for $i = \iota$, we have

$$\left\| f_{n,j}^{(\iota)} \right\|_{\mathrm{L}_2^w([0,R])}^2 = \int_0^R \left(f_{n,j}^{(\iota)}(x) \right)^2 x^2\,\mathrm{d}x < \infty.$$

Thus, $f_{n,j}^{(\iota)} \in \mathrm{L}_2^w([0,R])$. The remaining function h_n with $n \in \mathbb{N}_{0_\iota}$, coincides with a multiple of the single basis function $Q_0^{(t_n+1/2)}(R;\cdot) \in \mathrm{L}_2^w([0,R])$, that is

$$\begin{aligned}Q_0^{(t_n+1/2)}(R;x) &= \sqrt{\frac{2t_n+3}{R^3}} \left(\frac{x}{R}\right)^{t_n} P_0^{(0,t_n+1/2)}\left(2\frac{x^2}{R^2} - 1\right) \\ &= \sqrt{\frac{2t_n+3}{R^{2t_n+3}}} x^{t_n} = \sqrt{\frac{2t_n+3}{R^{2t_n+3}}} h_n(x).\end{aligned}$$

The latter identity holds true, since the Jacobi polynomial of degree $m = 0$ is a constant function equal to one, that is $P_0^{(0,t_n+1/2)}(r) \equiv 1$ for all $r \in [-1,1]$ independent of t_n. □

By means of the latter result, we are able to expand the functions $f_{n,j}^{(\iota)}$ for $n \in \mathbb{N}_{0_\iota}$ for which $\gamma_n \not\equiv 0$ and $j = 1,\dots,2n+1$.

Lemma 7.23. *Let the condition of Lemma 7.22 be fulfilled. For each fixed $n \in \mathbb{N}_{0_\iota}$ and all $j = 1, \dots, 2n+1$, the functions $f_{n,j}^{(\iota)}$ can be expanded into a generalized Fourier series, that is*

$$f_{n,j}^{(\iota)} = \sum_{m=0}^{\infty} f^{\wedge}\{\iota, m, n, j\} Q_m^{(t_n+1/2)}(R;\cdot), \tag{7.11}$$

where the series converges strongly in the $\mathrm{L}_2^w([0,R])$-sense. The corresponding Fourier coefficients are defined for all $m \in \mathbb{N}_0$, $n \in \mathbb{N}_{0_\iota}$, and $j = 1, \dots, 2n+1$ by

$$f^{\wedge}\{\iota, m, n, j\} \coloneqq \Big\langle f_{n,j}^{(\iota)}, Q_m^{(t_n+1/2)}(R;\cdot) \Big\rangle_{\mathrm{L}_2^w([0,R])}. \tag{7.12}$$

Via this expansion, we are able to calculate the integral in Eq. (7.8) without additional assumptions on the (generalized Fourier) coefficients $f^{\wedge}\{\iota, m, n, j\}$, where $m \in \mathbb{N}_0$, $n \in \mathbb{N}_{0_\iota}$, and $j = 1, \dots, 2n+1$.

Lemma 7.24. *If Assumption 7.14 is fulfilled and $\{t_n\}_{n\in\mathbb{N}_{0_\iota}}$ is defined as in Lemma 7.22, then*

$$\int_0^R f_{n,j}^{(\iota)}(x) x^{t_n+2} \,\mathrm{d}x = f^{\wedge}\{\iota, 0, n, j\} \sqrt{\frac{R^{2t_n+3}}{2t_n+3}}$$

for all $n \in \mathbb{N}_{0_\iota}$ and $j = 1, \dots, 2n+1$.

Proof. Inserting the expansion from Eq. (7.11) in Eq. (7.8), we eventually obtain by means of Lemma 7.22 and Parseval's identity, see [142, Ch. 6], the relation

$$\begin{aligned}
\int_0^R f_{n,j}^{(\iota)}(x) x^{t_n+2} \,\mathrm{d}x &= \Big\langle f_{n,j}^{(\iota)}, h_n \Big\rangle_{\mathrm{L}_2^w([0,R])} \\
&= \sum_{m=0}^{\infty} \Big\langle f_{n,j}^{(\iota)}, Q_m^{(t_n+1/2)}(R;\cdot) \Big\rangle_{\mathrm{L}_2^w([0,R])} \Big\langle h_n, Q_m^{(t_n+1/2)}(R;\cdot) \Big\rangle_{\mathrm{L}_2^w([0,R])} \\
&= \sum_{m=0}^{\infty} f^{\wedge}\{\iota, m, n, j\} \Big\langle h_n, Q_m^{(t_n+1/2)}(R;\cdot) \Big\rangle_{\mathrm{L}_2^w([0,R])} \\
&= f^{\wedge}\{\iota, 0, n, j\} \sqrt{\frac{R^{2t_n+3}}{2t_n+3}}
\end{aligned} \tag{7.13}$$

for all $n \in \mathbb{N}_{0_\iota}$, $j = 1, \dots, 2n+1$. The last step is valid because of Eq. (7.9) and the orthogonality of the functions $Q_m^{(t_n+1/2)}(R;\cdot)$, where $m \in \mathbb{N}_0$, that is

$$\begin{aligned}
\Big\langle h_n, Q_m^{(t_n+1/2)}(R;\cdot) \Big\rangle_{\mathrm{L}_2^w([0,R])} &= \sqrt{\frac{R^{2t_n+3}}{2t_n+3}} \Big\langle Q_0^{(t_n+1/2)}(R;\cdot), Q_m^{(t_n+1/2)}(R;\cdot) \Big\rangle_{\mathrm{L}_2^w([0,R])} \\
&= \sqrt{\frac{R^{2t_n+3}}{2t_n+3}} \delta_{m,0}.
\end{aligned}$$

□

Summing up, we first separated the density $\boldsymbol{f}$ into a radial and an angular part, see Assumption 7.14. Note that such an ansatz is common in many (scalar-valued) physical problems, for example the magneto-electroencephalography problems or the inverse gravimetric problem, which are discussed in more detail in the next chapters. Here, the angular part was

expanded by means of Morse-Feshbach vector spherical harmonics. Then, we expanded the radial part into orthogonal functions on $[0, R]$. Instead of this approach, we could directly expand the $\mathbf{L}_2(\mathbb{B}_R)$-function $\boldsymbol{f}$ by means of a Fourier series. To this end, we have already defined an appropriate vector-valued orthonormal bases for $\mathbf{L}_2(\mathbb{B}_R)$ in Definition 5.37.

Theorem 7.25. *Let $\boldsymbol{f} \in \mathbf{L}_2(\mathbb{B}_R)$ and let $\{\boldsymbol{g}^{(i)}_{m,n,j}(R;\cdot)\}_{i=1,2,3,m\in\mathbb{N}_0,n\in\mathbb{N}_{0_i},j=1,\dots,2n+1}$ be the vector-valued orthonormal basis for $\mathbf{L}_2(\mathbb{B}_R)$ defined in Definition 5.37, that is*

$$\boldsymbol{g}^{(i)}_{m,n,j}(R;\boldsymbol{x}) = Q_m^{(t_n+1/2)}(R;x)\boldsymbol{y}^{(i)}_{n,j}(\hat{\boldsymbol{x}}), \qquad \boldsymbol{x} \in \mathbb{B}_R$$

for all $i = 1, 2, 3$, $m \in \mathbb{N}_0$, $n \in \mathbb{N}_{0_i}$ for which $\gamma_n \not\equiv 0$, and $j = 1, \dots, 2n+1$. In the case $\gamma_n \equiv 0$, we define $t_n \coloneqq 0$ and get $\boldsymbol{g}^{(i)}_{m,n,j}(R;\boldsymbol{x}) = Q_m^{(1/2)}(R;x)\boldsymbol{y}^{(i)}_{n,j}(\hat{\boldsymbol{x}})$. Then the identity

$$f^\wedge(i,m,n,j) \coloneqq \left\langle \boldsymbol{f}, \boldsymbol{g}^{(i)}_{m,n,j}(R;\cdot)\right\rangle_{\mathbf{L}_2(\mathbb{B}_R)} = f^\wedge\{i,m,n,j\}$$

holds true for all $i = 1, 2, 3$, $m \in \mathbb{N}_0$, $n \in \mathbb{N}_{0_i}$, and $j = 1, \dots, 2n+1$.

Note that in the general definition of the vector-valued orthonormal basis the sequence $\{t_n\}_{n\in\mathbb{N}_{0_i}}$ also depends on the index i. For the sake of readability, this dependence is omitted in this section because only one fixed direction $i = \iota$ plays a role for the continuous/star-shaped VLI equation.

Proof. Since $\boldsymbol{f}$, $\boldsymbol{g}^{(i)}_{m,n,j}(R;\cdot) \in \mathbf{L}_2(\mathbb{B}_R)$, for all $i = 1, 2, 3$, $m \in \mathbb{N}_0$, $n \in \mathbb{N}_{0_i}$, and $j = 1, \dots, 2n+1$ we obtain with Fubini's Theorem for Lebesgue-integrals the identity

$$\begin{aligned}
\left\langle \boldsymbol{f}, \boldsymbol{g}^{(i)}_{m,n,j}(R;\cdot)\right\rangle_{\mathbf{L}_2(\mathbb{B}_R)} &= \int_{\mathbb{B}_R} \boldsymbol{f}(\boldsymbol{x}) \cdot \left(Q_m^{(t_n+1/2)}(R;x)\boldsymbol{y}^{(i)}_{n,j}(\hat{\boldsymbol{x}})\right) \mathrm{d}\boldsymbol{x} \\
&= \int_0^R \int_{\mathbb{S}} \boldsymbol{f}(\boldsymbol{x}) \cdot \left(Q_m^{(t_n+1/2)}(R;x)\boldsymbol{y}^{(i)}_{n,j}(\hat{\boldsymbol{x}})\right) \mathrm{d}\omega(\hat{\boldsymbol{x}})x^2 \,\mathrm{d}x \\
&= \int_0^R f^{(i)}_{n,j}(x) Q_m^{(t_n+1/2)}(R;x)x^2 \,\mathrm{d}x \\
&= \left\langle f^{(i)}_{n,j}, Q_m^{(t_n+1/2)}(R;\cdot)\right\rangle_{\mathrm{L}_2^w([0,R])} \\
&= f^\wedge\{i,m,n,j\},
\end{aligned}$$

see Eq. (7.12). □

By means of the Fourier expansion of $\boldsymbol{f}$, we can achieve another representation of the potential $\mathcal{T}\boldsymbol{f}$ generated by the continuous/star-shaped VLI operator.

Theorem 7.26. *Let $\boldsymbol{f} \in \mathbf{L}_2(\mathbb{B}_R)$. This implies Assumption 7.14.*

i) Then, for all $\boldsymbol{y} \in \mathbb{G}_{\mathrm{out}}$, the continuous/star-shaped VLI operator has the representation

$$(\mathcal{T}\boldsymbol{f})(\boldsymbol{y}) = 4\pi \sum_{n=0_\iota}^{\infty} \sum_{j=1}^{2n+1} \frac{R^{t_n+3/2}}{(2n+1)\sqrt{2t_n+3}} f^\wedge(\iota,0,n,j)\gamma_n(y)Y_{n,j}(\hat{\boldsymbol{y}}). \tag{7.14}$$

ii) Let the estimate

$$|\gamma_n'(y)| \le \frac{\Gamma_n}{y^{n+1+N_1}},$$

where $N_1 \in \mathbb{N}$, hold true for all $n \in \mathbb{N}_{0_\iota}$ with $(n \mapsto \Gamma_n) \in \mathcal{O}(n^M)$ for a fixed $M \in \mathbb{N}_0$. Then, for all $\boldsymbol{y} \in \mathbb{G}_{\text{out}}$, the gradient of the continuous/star-shaped VLI operator applied to the density has the representation

$$(\boldsymbol{\nabla}(\mathcal{T}\boldsymbol{f}))(\boldsymbol{y}) = 4\pi \sum_{n=0_\iota}^{\infty} \sum_{j=1}^{2n+1} \frac{R^{t_n+3/2}}{(2n+1)\sqrt{2t_n+3}} f^\wedge(\iota,0,n,j) \boldsymbol{\nabla}_{\boldsymbol{y}} \left(\gamma_n(y) Y_{n,j}(\hat{\boldsymbol{y}})\right).$$

The occurring series converge absolutely and uniformly. In addition, the series converge in the $\mathrm{L}_2(\mathbb{G}_{\text{out}})$ or $\mathbf{L}_2(\mathbb{G}_{\text{out}})$-sense, respectively.

Proof. We only need to verify that $\boldsymbol{f} \in \mathbf{L}_2(\mathbb{B}_R)$ implies the Assumption 7.14. Then all conditions of Corollary 7.17, Theorem 7.18, and Lemma 7.21 are fulfilled. Thus, we can insert the results of Lemma 7.24 and Theorem 7.25 into the derived representations of $\mathcal{T}\boldsymbol{f}$ and $\boldsymbol{\nabla}(\mathcal{T}\boldsymbol{f})$. The $\mathbf{L}_2(\mathbb{G}_{\text{out}})$-convergence of the series in $\boldsymbol{\nabla}(\mathcal{T}\boldsymbol{f})$ can be shown in total analogy to the $\mathrm{L}_2(\mathbb{G}_{\text{out}})$-convergence of the series in Eq. (7.14) from Theorem 7.18 combined with the estimates in Eq. (7.7).

Since $\boldsymbol{f} \in \mathbf{L}_2(\mathbb{B}_R)$, we can represent $\boldsymbol{f}$ by the Fourier series

$$\boldsymbol{f} = \sum_{i=1}^{3} \sum_{m=0}^{\infty} \sum_{n=0_i}^{\infty} \sum_{j=1}^{2n+1} f^\wedge(i,m,n,j) \boldsymbol{g}^{(i)}_{m,n,j}(R;\cdot),$$

which we will use for calculating $f^{(i)}_{n,j}$. Changing the order of summation, see Lemma 5.39, and inserting Eq. (5.18) into the Fourier series of $\boldsymbol{f}$, we obtain for almost all $x \in [0,R]$ the relation

$$\begin{aligned}
f^{(i)}_{n,j}(x) &= \int_{\mathbb{S}} \boldsymbol{f}(x\hat{\boldsymbol{x}}) \cdot \boldsymbol{y}^{(i)}_{n,j}(\hat{\boldsymbol{x}}) \,\mathrm{d}\omega(\hat{\boldsymbol{x}}) \\
&= \int_{\mathbb{S}} \left(\sum_{\tilde{i}=1}^{3} \sum_{\tilde{n}=0_i}^{\infty} \sum_{\tilde{j}=1}^{2\tilde{n}+1} \left(\sum_{m=0}^{\infty} f^\wedge(\tilde{i},m,\tilde{n},\tilde{j}) Q_m^{(t_{\tilde{n}}+1/2)}(R;x) \right) \boldsymbol{y}^{(\tilde{i})}_{\tilde{n},\tilde{j}}(\hat{\boldsymbol{x}}) \right) \cdot \boldsymbol{y}^{(i)}_{n,j}(\hat{\boldsymbol{x}}) \,\mathrm{d}\omega(\hat{\boldsymbol{x}}) \\
&= \sum_{\tilde{i}=1}^{3} \sum_{\tilde{n}=0_i}^{\infty} \sum_{\tilde{j}=1}^{2\tilde{n}+1} \int_{\mathbb{S}} \left(\sum_{m=0}^{\infty} f^\wedge(\tilde{i},m,\tilde{n},\tilde{j}) Q_m^{(t_{\tilde{n}}+1/2)}(R;x) \boldsymbol{y}^{(\tilde{i})}_{\tilde{n},\tilde{j}}(\hat{\boldsymbol{x}}) \right) \cdot \boldsymbol{y}^{(i)}_{n,j}(\hat{\boldsymbol{x}}) \,\mathrm{d}\omega(\hat{\boldsymbol{x}}) \\
&= \sum_{\tilde{i}=1}^{3} \sum_{\tilde{n}=0_i}^{\infty} \sum_{\tilde{j}=1}^{2\tilde{n}+1} \sum_{m=0}^{\infty} f^\wedge(\tilde{i},m,\tilde{n},\tilde{j}) Q_m^{(t_{\tilde{n}}+1/2)}(R;x) \int_{\mathbb{S}} \boldsymbol{y}^{(\tilde{i})}_{\tilde{n},\tilde{j}}(\hat{\boldsymbol{x}}) \cdot \boldsymbol{y}^{(i)}_{n,j}(\hat{\boldsymbol{x}}) \,\mathrm{d}\omega(\hat{\boldsymbol{x}}) \\
&= \sum_{m=0}^{\infty} f^\wedge(i,m,n,j) Q_m^{(t_n+1/2)}(R;x).
\end{aligned}$$

Hence, the Morse-Feshbach expansion of $\boldsymbol{f}$ from Assumption 7.14 is given by

$$\begin{aligned}
\boldsymbol{f}(\boldsymbol{x}) &\overset{\mathbf{L}_2(\mathbb{B}_R)}{=} \sum_{i=1}^{3} \sum_{n=0_i}^{\infty} \sum_{j=1}^{2n+1} \left(\sum_{m=0}^{\infty} f^\wedge(i,m,n,j) Q_m^{(t_n+1/2)}(R;x) \right) \boldsymbol{y}^{(i)}_{n,j}(\hat{\boldsymbol{x}}) \\
&= \sum_{i=1}^{3} \sum_{n=0_i}^{\infty} \sum_{j=1}^{2n+1} f^{(i)}_{n,j}(x) \boldsymbol{y}^{(i)}_{n,j}(\hat{\boldsymbol{x}}).
\end{aligned}$$

□

Summing up, we proved that the potential obtained by applying the continuous/star-shaped VLI operator to the density $\boldsymbol{f} \in \mathbf{L}_2(\mathbb{B}_R)$ is continuous. In the case of $\mathbb{G}_{\text{in}} \coloneqq \mathbb{G}_{\text{star}} \coloneqq \mathbb{B}_R$, we could furthermore solve the direct problem related to the continuous/star-shaped VLI operator of the first kind. We were able to construct an orthonormal basis in the domain of the continuous/star-shaped VLI operator that allows a precise calculation of the direct problem. In this case, the image of the star-shaped VLI operator consists of continuous and differentiable functions, which permits a representation of $\boldsymbol{\nabla}(\mathcal{T}\boldsymbol{f})$.

In Chapter 6, we consider an integral kernel containing Edmonds vector Legendre polynomials, see Corollary 6.21. Now, we will see that all results of this section can be transferred to the following related problem that is based on Corollary 6.21. Recall that the EEG operator $\mathcal{T}_{\text{E}}$ for the multiple-shell model is a particular case of the operator defined in the next theorem.

Theorem 7.27. *Let $\iota \in \{1,2,3\}$ be fixed, let the quantities $\{\gamma_k\}_{k\in\mathbb{N}_{0_\iota}}$ and $\{t_k\}_{k\in\mathbb{N}_{0_\iota}}$ fulfil the assumption of Definition 6.2, and let a kernel be defined by*

$$\tilde{\boldsymbol{k}}^{(\iota)}(\boldsymbol{x},\boldsymbol{y}) \coloneqq \sum_{k=0_\iota}^{\infty} \gamma_k(y) x^{t_k} \tilde{\boldsymbol{p}}_k^{(\iota)}(\hat{\boldsymbol{x}},\hat{\boldsymbol{y}}), \qquad (\boldsymbol{x},\boldsymbol{y}) \in \mathbb{G}_{\text{star}} \times \mathbb{G}_{\text{out}}, \tag{7.15}$$

where $\tilde{\boldsymbol{p}}_k^{(\iota)}$ is defined in Definition 5.21. Let $\boldsymbol{f} \in \mathbf{L}_2(\mathbb{B}_R)$, then it can be expanded by

$$\boldsymbol{f} = \sum_{i=1}^{3} \sum_{m=0}^{\infty} \sum_{n=0_i}^{\infty} \sum_{j=1}^{2n+1} f^{\wedge}[i,m,n,j] \tilde{\boldsymbol{g}}_{m,n,j}^{(i)},$$

$$f_{n,j}^{(i),\sim}(x) \coloneqq \int_{\mathbb{S}} \boldsymbol{f}(\boldsymbol{x}) \cdot \tilde{\boldsymbol{y}}_{n,j}^{(i)}(\hat{\boldsymbol{x}}) \, \mathrm{d}\omega(\hat{\boldsymbol{x}})$$

for almost all $x \in [0,R]$. The potential $\tilde{\mathcal{T}}\boldsymbol{f}$ has the representations

$$\begin{aligned}
\left(\tilde{\mathcal{T}}\boldsymbol{f}\right)(\boldsymbol{y}) &\coloneqq \int_{\mathbb{B}_R} \boldsymbol{f}(\boldsymbol{x}) \cdot \tilde{\boldsymbol{k}}^{(\iota)}(\boldsymbol{x},\boldsymbol{y}) \, \mathrm{d}\boldsymbol{x} \\
&= 4\pi \sum_{n=0_\iota}^{\infty} \sum_{j=1}^{2n+1} \frac{R^{t_n+3/2}}{(2n+1)\sqrt{2t_n+3}} f^{\wedge}[\iota,m,n,j] \gamma_n(y) Y_{n,j}(\hat{\boldsymbol{y}}) \\
&= 4\pi \sum_{n=0_\iota}^{\infty} \sum_{j=1}^{2n+1} \frac{1}{2n+1} \left(\int_0^R f_{n,j}^{(\iota),\sim}(x) x^{t_n+2} \, \mathrm{d}x \right) \gamma_n(y) Y_{n,j}(\hat{\boldsymbol{y}}).
\end{aligned}$$

The series converge absolutely and uniformly.

Proof. In the case of $\iota = 3$, there is nothing to prove since the kernel $\tilde{\boldsymbol{k}}^{(\iota)}$ is a star-shaped VLI kernel and the Fourier expansion of $\boldsymbol{f}$ coincides with the Morse-Feshbach expansion. The two remaining cases can be proved similarly. Hence, we restrict ourselves to the case of $\iota = 1$ and obtain the relation

$$\begin{aligned}
&\left(\tilde{\mathcal{T}}\boldsymbol{f}\right)(\boldsymbol{y}) = \int_{\mathbb{B}_R} \boldsymbol{f}(\boldsymbol{x}) \cdot \tilde{\boldsymbol{k}}^{(1)}(\boldsymbol{x},\boldsymbol{y}) \, \mathrm{d}\boldsymbol{x} \\
&= \int_{\mathbb{B}_R} \boldsymbol{f}(\boldsymbol{x}) \cdot \left(\sum_{k=0}^{\infty} \gamma_k(y) x^{t_k} \tilde{\boldsymbol{p}}_k^{(1)}(\hat{\boldsymbol{x}},\hat{\boldsymbol{y}}) \right) \mathrm{d}\boldsymbol{x} \\
&= \int_{\mathbb{B}_R} \boldsymbol{f}(\boldsymbol{x}) \cdot \left(\sum_{k=0}^{\infty} \gamma_k(y) \sqrt{\frac{k+1}{2k+1}} x^{t_k} \boldsymbol{p}_k^{(1)}(\hat{\boldsymbol{x}},\hat{\boldsymbol{y}}) - \sum_{k=1}^{\infty} \gamma_k(y) \sqrt{\frac{k}{2k+1}} x^{t_k} \boldsymbol{p}_k^{(2)}(\hat{\boldsymbol{x}},\hat{\boldsymbol{y}}) \right) \mathrm{d}\boldsymbol{x}.
\end{aligned}$$

The series can be split into two convergent series, due to Lemma 6.20 or Corollary 6.21, respectively. Each series in the integral of the right-hand side coincides with a continuous/star-shaped VLI kernel, where the functions γ_k for all $k \in \mathbb{N}_{0_\iota}$ in Definition 6.1 needs to be replaced by $\gamma_k\sqrt{(k+1)/(2k+1)}$ and $-\gamma_k\sqrt{k/(2k+1)}$, respectively. Thus, by means of Corollary 7.17 and Theorem 7.26, the linearity of the integration yields

$$\begin{aligned}
&\left(\tilde{\mathcal{T}}\boldsymbol{f}\right)(\boldsymbol{y}) \\
&= 4\pi \sum_{n=0}^{\infty} \sum_{j=1}^{2n+1} \int_0^R \left(\sqrt{\frac{n+1}{(2n+1)^3}} f_{n,j}^{(1)}(x) - \sqrt{\frac{n}{(2n+1)^3}} f_{n,j}^{(2)}(x) \right) x^{t_n+2} \,\mathrm{d}x \, \gamma_n(y) Y_{n,j}(\hat{\boldsymbol{y}}) \\
&= 4\pi \sum_{n=0}^{\infty} \sum_{j=1}^{2n+1} \frac{R^{t_n+3/2}}{(2n+1)\sqrt{2t_n+3}} \left(\sqrt{\frac{n+1}{2n+1}} f^{\wedge}(1,0,n,j) - \right. \\
&\qquad \left. \sqrt{\frac{n}{2n+1}} f^{\wedge}(2,0,n,j) \right) \gamma_n(y) Y_{n,j}(\hat{\boldsymbol{y}}).
\end{aligned}$$

Due to the construction of $\tilde{\boldsymbol{g}}_{m,n,j}^{(1)}$, we obtain

$$\begin{aligned}
f^{\wedge}[1,n,m,j] &= \left\langle \boldsymbol{f}, \tilde{\boldsymbol{g}}_{m,n,j}^{(1)} \right\rangle_{\mathbf{L}_2(\mathbb{B}_R)} \\
&= \sqrt{\frac{n+1}{2n+1}} \left\langle \boldsymbol{f}, \boldsymbol{g}_{m,n,j}^{(1)} \right\rangle_{\mathbf{L}_2(\mathbb{B}_R)} - \sqrt{\frac{n}{2n+1}} \left\langle \boldsymbol{f}, \boldsymbol{g}_{m,n,j}^{(2)} \right\rangle_{\mathbf{L}_2(\mathbb{B}_R)} \\
&= \sqrt{\frac{n+1}{2n+1}} f^{\wedge}(1,m,n,j) - \sqrt{\frac{n}{2n+1}} f^{\wedge}(2,m,n,j)
\end{aligned}$$

and, similarly,

$$f_{n,j}^{(1),\sim} = \sqrt{\frac{n+1}{2n+1}} f_{n,j}^{(1)} - \sqrt{\frac{n}{2n+1}} f_{n,j}^{(2)}. \tag{7.16}$$

The set of orthonormal functions $\tilde{\boldsymbol{g}}_{m,n,j}^{(i)}$ for $i = 1,2,3$, $m \in \mathbb{N}_0$, $n \in \mathbb{N}_{0_i}$, and $j = 1,\ldots,2n+1$ is a complete system in $\mathbf{L}_2(\mathbb{B}_R)$, just as the system $\{\boldsymbol{g}_{m,n,j}^{(i)}\}_{i=1,2,3, m\in\mathbb{N}_0, n\in\mathbb{N}_{0_i}, j=1,\ldots,2n+1}$, see Lemma 5.38. Hence, we obtain the desired result. □

After having solved the direct problem related to the continuous/star-shaped VLI equation, that is the calculation of the potential $\mathcal{T}\boldsymbol{f}$ for a given density $\boldsymbol{f}$, we can proceed by applying this knowledge to the electroencephalography problem. However, for the analysis of the magnetoencephalography problem we are interested in further calculating $\boldsymbol{\nabla}(\mathcal{T}\boldsymbol{f})$. For this purpose, we first define a particular class of continuous/star-shaped VLI operators.

Chapter 8.

A Harmonic Vector Legendre-type Integral Operator

In Theorems 6.22 and 6.23, we prove that the MEG and EEG integral kernels are harmonic functions in both arguments. In contrast, the continuous/star-shaped VLI kernel is not necessarily a harmonic function. This motivates us to define a particular subclass of star-shaped VLI kernels that are harmonic, which we call the *harmonic VLI kernels*. However, this class does not necessarily contain all harmonic star-shaped VLI kernels. This particular class is of interest, since the kernel occurring in the MEG integral equation is such a harmonic VLI kernel.

8.1. Definition

The harmonic VLI operator induced by the harmonic VLI kernel has the same structure as the star-shaped VLI operator from Chapter 6. The reduction in generality is given by a more precise formulation of the corresponding integral kernel. In addition, we can proceed by further calculating the gradient field corresponding to the potential obtained by this integral equation. In the following, we consider the harmonic VLI kernel $\boldsymbol{k}^{(\iota)}$ from the next definition.

Definition 8.1 (Harmonic VLI Kernel). *Let $\mathbb{B}_R \subset \mathbb{R}^3$ be a ball with radius $R > 0$ and let $\mathbb{G}_{\text{out}} \subset \mathbb{B}_R^{\text{ext}}$ be a region with $\inf_{\boldsymbol{y}\in\mathbb{G}_{\text{out}}} y > R$. We define the* harmonic VLI kernel $\boldsymbol{k}^{(\iota)}$ *for an arbitrary $\iota \in \{1,2,3\}$ by*

$$\boldsymbol{k}^{(\iota)}(\boldsymbol{x},\boldsymbol{y}) \coloneqq \sum_{k=1}^{\infty} \frac{\Gamma_k}{y^{k+1}} x^{t_k} \boldsymbol{p}_k^{(\iota)}(\hat{\boldsymbol{x}},\hat{\boldsymbol{y}}), \qquad (\boldsymbol{x},\boldsymbol{y}) \in \mathbb{B}_R \times \mathbb{G}_{\text{out}}.$$

The occurring quantities fulfil the following assumptions:

i) The real sequence $\{t_k\}_{k\in\mathbb{N}}$ is bounded from below by -1, that is $\inf_{k\in\mathbb{N},\Gamma_k\neq 0} t_k \geq -1$.

ii) The asymptotic behaviour of $\{t_k\}_{k\in\mathbb{N}}$ can be characterized by $\sup_{k\in\mathbb{N}} R^{t_k-k} < \infty$.

iii) The sequence $\{\Gamma_k\}_{k\in\mathbb{N}} \subset \mathbb{R}$ satisfies $(k \mapsto |\Gamma_k|) \in \mathcal{O}(k^M)$ for fixed $M \in \mathbb{N}_0$.

Note that we only consider this particular case in this chapter. Hence, an additional distinctive notation for the kernel is not necessary. Obviously, $\mathbb{B}_R$ is a bounded star domain with vantage point zero and $\sup_{\boldsymbol{x}\in\mathbb{B}_R} x \leq R$. In addition, it is easy to verify that the harmonic VLI kernel is a star-shaped VLI kernel from Definition 6.2.

Lemma 8.2. *The kernel defined in Definition 8.1 is a star-shaped VLI kernel with $\gamma_k(y) \coloneqq \Gamma_k y^{-(k+1)}$ for all $k \in \mathbb{N}$.*

Proof. Obviously, the assumptions of the star-shaped VLI kernel from Definition 6.2 concerning the domain and the asymptotic behaviour of $\{t_k\}_{k\in\mathbb{N}}$ are fulfilled. By choosing $\gamma_k(y) \coloneqq \Gamma_k y^{-(k+1)}$ for all $k \in \mathbb{N}$, the last assumption is satisfied for all $\boldsymbol{y} \in \mathbb{G}_{\text{out}}$, since here we start the summation at $k = 1$. □

Due to the more precise representation of $\{\gamma_k\}_{k\in\mathbb{N}}$, we are able to analyze the behaviour of the functions at infinity.

Lemma 8.3. *There exist an $\varepsilon > 0$ such that for all $k \in \mathbb{N}$ the functions $\{\gamma_k\}_{k\in\mathbb{N}}$, that appear in Lemma 8.2 and correspond to the harmonic VLI kernel, satisfy the estimates*

$$\begin{aligned}\sup_{\boldsymbol{y}\in\mathbb{G}_{\text{out}}} |\gamma_k'(y)| &\leq (k+1)\,|\Gamma_k|\,(R+\varepsilon)^{-(k+2)},\\ \sup_{\boldsymbol{y}\in\mathbb{G}_{\text{out}}} |\gamma_k''(y)| &\leq (k+1)(k+2)\,|\Gamma_k|\,(R+\varepsilon)^{-(k+3)}.\end{aligned}$$

In addition, we have $(k \mapsto (k+1)|\Gamma_k|) \in \mathcal{O}(k^{M+1})$ and $(k \mapsto (k+1)(k+2)|\Gamma_k|) \in \mathcal{O}(k^{M+2})$ for a fixed $M \in \mathbb{N}_0$, respectively.

Proof. We first calculate for all $\boldsymbol{y} \in \mathbb{G}_{\text{out}}$, $k \in \mathbb{N}$ the first- and second-order derivatives of γ_k, that is

$$\begin{aligned}\gamma_k'(y) &= \frac{\mathrm{d}}{\mathrm{d}y}\left(\Gamma_k y^{-(k+1)}\right) = -(k+1)\Gamma_k y^{-(k+2)},\\ \gamma_k''(y) &= \frac{\mathrm{d}^2}{\mathrm{d}y^2}\left(\Gamma_k y^{-(k+1)}\right) = (k+1)(k+2)\Gamma_k y^{-(k+3)}.\end{aligned}$$

Due to the construction of the regions in Definition 8.1, there exists an $\varepsilon > 0$ such that $\sup_{\boldsymbol{x}\in\mathbb{B}_R} = R < R + \varepsilon \leq y$ for all $y \in \mathbb{G}_{\text{out}}$. For the suprema, we obtain for all $k \in \mathbb{N}$ the bounds

$$\begin{aligned}\sup_{\boldsymbol{y}\in\mathbb{G}_{\text{out}}} |\gamma_k'(y)| &= (k+1)\,|\Gamma_k| \sup_{\boldsymbol{y}\in\mathbb{G}_{\text{out}}} \left|y^{-(k+2)}\right| \leq (k+1)\,|\Gamma_k|\,(R+\varepsilon)^{-(k+2)},\\ \sup_{\boldsymbol{y}\in\mathbb{G}_{\text{out}}} |\gamma_k''(y)| &\leq (k+1)(k+2)\,|\Gamma_k|\,(R+\varepsilon)^{-(k+3)}.\end{aligned}$$

The asymptotic behaviour of $\{\Gamma_k\}_{k\in\mathbb{N}}$ is given by the assumptions in Definition 8.1. □

Since the harmonic VLI kernel $\boldsymbol{k}^{(\iota)}$ is a star-shaped VLI kernel, we can use the results from Chapter 7 in order to obtain the potential. In addition, we can use (vector) outer harmonics to gain another representation of the potential.

Theorem 8.4. *Let $\boldsymbol{f} \in \mathbf{L}_2(\mathbb{B}_R)$ and $r > R$ be arbitrary. Then the following identities concerning the harmonic VLI operator hold true for all $\boldsymbol{y} \in \mathbb{G}_{\text{out}}$:*

$$\begin{aligned}(\mathcal{T}\boldsymbol{f})(\boldsymbol{y}) &= 4\pi \sum_{n=1}^{\infty} \sum_{j=1}^{2n+1} \frac{\Gamma_n}{(2n+1)\sqrt{2t_n+3}} f^{\wedge}(\iota,0,n,j) \frac{R^{t_n+3/2}}{r^n} H_{n,j}^{\text{ext}}(r;\boldsymbol{y})\\ &= 4\pi \sum_{n=1}^{\infty} \sum_{j=1}^{2n+1} \frac{\Gamma_n}{2n+1} \left(\int_0^R f_{n,j}^{(\iota)}(x) x^{t_n+2}\,\mathrm{d}x\right) \frac{1}{y^{n+1}} Y_{n,j}(\hat{\boldsymbol{y}}),\end{aligned}$$

$$
\begin{aligned}
(\boldsymbol{\nabla}(\mathcal{T}\boldsymbol{f}))(\boldsymbol{y}) &= -4\pi \sum_{n=1}^{\infty} \sum_{j=1}^{2n+1} \Gamma_n \sqrt{\frac{n+1}{(2n+1)(2t_n+3)}} f^{\wedge}(\iota,0,n,j) \frac{R^{t_n+3/2}}{r^{n+1}} \boldsymbol{h}_{n,j}^{(1)}(r;\boldsymbol{y}) \\
&= -4\pi \sum_{n=1}^{\infty} \sum_{j=1}^{2n+1} \Gamma_n \sqrt{\frac{n+1}{2n+1}} \left(\int_0^R f_{n,j}^{(\iota)}(x) x^{t_n+2} \, \mathrm{d}x \right) \frac{1}{r^{n+1}} \boldsymbol{h}_{n,j}^{(1)}(r;\boldsymbol{y}).
\end{aligned}
$$

Here, the series converge uniformly in $\mathbb{G}_{\text{out}}$ *and in the* $\mathrm{L}_2(\mathbb{G}_{\text{out}})$*-sense.*

Proof. We start with the representation of $\mathcal{T}\boldsymbol{f}$, which is provided by Corollary 7.17 and Theorem 7.26, that is

$$
(\mathcal{T}\boldsymbol{f})(\boldsymbol{y}) = 4\pi \sum_{n=0_\iota}^{\infty} \sum_{j=1}^{2n+1} \frac{R^{t_n+3/2}}{(2n+1)\sqrt{2t_n+3}} f^{\wedge}(\iota,0,n,j) \gamma_n(y) Y_{n,j}(\hat{\boldsymbol{y}}).
$$

Inserting the particular set of function $\{\gamma_n\}_{n\in\mathbb{N}_{0_\iota}}$ into this equation, see Lemma 8.2, we observe that the potential depends on the functions $\boldsymbol{y} \mapsto y^{-(n+1)} Y_{n,j}(\hat{\boldsymbol{y}})$ for all $n \in \mathbb{N}$, $j = 1, \ldots, 2n+1$. In addition, we are able to start the series by $n = 1$. Furthermore, for all $r > R$, $n \in \mathbb{N}$, and $j = 1, \ldots, 2n+1$ we obtain the relation

$$
\frac{1}{y^{n+1}} Y_{n,j}(\hat{\boldsymbol{y}}) = \frac{1}{r^n} H_{n,j}^{\text{ext}}(r;\boldsymbol{y}), \qquad \boldsymbol{y} \in \mathbb{G}_{\text{out}},
$$

where the scalar-valued outer harmonics $H_{n,j}^{\text{ext}}$ are defined in Definition 2.28. Combining these thoughts, we get the first relation for the potential $\mathcal{T}\boldsymbol{f}$.

For the gradient of the potential, we make the following considerations. By means of Lemma 8.3, all assumptions of Lemma 7.21 and Theorem 7.26 Item ii) hold true, which provides us for all $\boldsymbol{y} \in \mathbb{G}_{\text{out}}$ with the representation

$$
(\boldsymbol{\nabla}(\mathcal{T}\boldsymbol{f}))(\boldsymbol{y}) = 4\pi \sum_{n=0_\iota}^{\infty} \sum_{j=1}^{2n+1} \frac{R^{t_n+3/2}}{(2n+1)\sqrt{2t_n+3}} f^{\wedge}(\iota,0,n,j) \boldsymbol{\nabla}_{\boldsymbol{y}} \left(\gamma_n(y) Y_{n,j}(\hat{\boldsymbol{y}}) \right).
$$

Now, we need to calculate the gradient of the right-hand side of the previous equation. For this purpose, we use Eq. (5.15b). Thus, the gradient term is given for all $\boldsymbol{y} \in \mathbb{G}_{\text{out}}$, $n \in \mathbb{N}$, and $j = 1 \ldots, 2n+1$ by

$$
\boldsymbol{\nabla}_{\boldsymbol{y}} \left(\frac{\Gamma_n}{y^{n+1}} Y_{n,j}(\hat{\boldsymbol{y}}) \right) = -\frac{\sqrt{(2n+1)(n+1)}\Gamma_n}{r^{n+1}} \boldsymbol{h}_{n,j}^{(1)}(r;\boldsymbol{y}).
$$

Inserting this in the representation of $\boldsymbol{\nabla}(\mathcal{T}\boldsymbol{f})$, we arrive at the desired result.

In both cases, we obtain with Lemma 7.24 and Theorem 7.25 the second stated formulae. The desired convergence is obtained by Theorem 7.26, since $\gamma_n'(y) = -(n+1)\Gamma_n y^{-(n+2)}$ for all $\boldsymbol{y} \in \mathbb{G}_{\text{out}}$ (in this case $N_1 \coloneqq 1$). □

For the function $\mathcal{T}\boldsymbol{f}$, we prove the $\mathrm{L}_2(\mathbb{S}_R)$-convergence of its series for the continuous/star-shaped VLI operator $\mathcal{T}$ in Theorem 7.20. However, we could not formulate a corresponding result for $\boldsymbol{\nabla}(\mathcal{T}\boldsymbol{f})$. Eventually, we are able to prove this result in the case of the harmonic VLI operator.

Lemma 8.5. *Let Assumption 7.14 be fulfilled. In addition, let the estimate*

$$\Gamma_n \leq c\sqrt{\frac{(2n+1)(2t_n+3)}{n+1}}$$

hold true for all $n \in \mathbb{N}$ with a constant $c \in \mathbb{R}_0^+$. Then we can expand and restrict $\boldsymbol{\nabla}(\mathcal{T}\boldsymbol{f})$ generated by the harmonic VLI kernel onto the sphere with radius R. This function is denoted by $(\boldsymbol{\nabla}(\mathcal{T}\boldsymbol{f}))|_{\mathbb{S}_R}$. In addition, its series converges in the sense of $\mathbf{L}_2(\mathbb{S}_R)$. It is represented by the expression

$$(\boldsymbol{\nabla}(\mathcal{T}\boldsymbol{f}))(R\hat{\boldsymbol{y}}) \overset{\mathbf{L}_2(\mathbb{S}_R)}{=} -4\pi \sum_{n=1}^{\infty}\sum_{j=1}^{2n+1} \Gamma_n \sqrt{\frac{n+1}{2n+1}} \left(\int_0^R f_{n,j}^{(\iota)}(x) x^{t_n+2}\,\mathrm{d}x\right) \frac{1}{R^{n+1}} \tilde{\boldsymbol{y}}_{n,j}^{(1)}(\hat{\boldsymbol{y}}).$$

Proof. The representation of $\boldsymbol{\nabla}(\mathcal{T}\boldsymbol{f})$ from Theorem 8.4 can be formally extended to $\mathbb{S}_R$. In addition, for all $n \in \mathbb{N}_0$ and $j = 1, \ldots, 2n+1$ we have

$$\boldsymbol{h}_{n,j}^{(1)}(r;\boldsymbol{y}) = \left(\frac{r}{R}\right)^{n+1} \boldsymbol{h}_{n,j}^{(1)}(R;\boldsymbol{y}), \qquad \boldsymbol{y} \in \mathbb{G}_{\mathrm{out}},$$

which can be obtained from the definition of the vector outer harmonics of type 1, see Definition 5.27. Thus,

$$\boldsymbol{\nabla}(\mathcal{T}\boldsymbol{f}) = -4\pi \sum_{n=1}^{\infty}\sum_{j=1}^{2n+1} \Gamma_n \sqrt{\frac{n+1}{2n+1}} \left(\int_0^R f_{n,j}^{(\iota)}(x) x^{t_n+2}\,\mathrm{d}x\right) \left(\frac{r}{R}\right)^{n+1} \frac{1}{r^{n+1}} \boldsymbol{h}_{n,j}^{(1)}(R;\cdot).$$

We obtain with Remark 5.28, $\boldsymbol{h}_{n,j}^{(1)}(R;\cdot)|_{\mathbb{S}_R} = \frac{1}{R}\tilde{\boldsymbol{y}}_{n,j}^{(1)}$, and a property of Parseval's identity, see [198, Thm. 12.6], a representation for the norm:

$$\begin{aligned}
\|(\boldsymbol{\nabla}(\mathcal{T}\boldsymbol{f}))|_{\mathbb{S}_R}\|_{\mathbf{L}_2(\mathbb{S}_R)}^2 &= 16\pi^2 \sum_{n=1}^{\infty}\sum_{j=1}^{2n+1} \Gamma_n^2 \frac{n+1}{2n+1} \left(\int_0^R f_{n,j}^{(\iota)}(x) x^{t_n+2}\,\mathrm{d}x\right)^2 \frac{1}{R^{2n+2}} \\
&\leq 16\pi^2 \sum_{n=1}^{\infty}\sum_{j=1}^{2n+1} \Gamma_n^2 \frac{n+1}{2n+1} \int_0^R \left(f_{n,j}^{(\iota)}(x)x\right)^2 \mathrm{d}x \int_0^R x^{2t_n+2}\,\mathrm{d}x \frac{1}{R^{2n+2}} \\
&= 16\pi^2 \sum_{n=1}^{\infty}\sum_{j=1}^{2n+1} \Gamma_n^2 \frac{n+1}{(2n+1)(2t_n+3)} \int_0^R \left(f_{n,j}^{(\iota)}(x)x\right)^2 \mathrm{d}x R^{2t_n-2n+1} \\
&\leq 16\pi^2 c^2 R \left(\sup_{n\in\mathbb{N}} R^{t_n-n}\right)^2 \|\boldsymbol{f}\|_{\mathbf{L}_2(\mathbb{B}_{\varrho_0})}^2 < \infty.
\end{aligned}$$

In the second step, we used the Cauchy-Schwarz inequality for integrals, and the representation of the density norm from Eq. (7.5) in the last step. □

Having defined the harmonic VLI integral kernel and having analyzed the related direct problem, we analyze the eponymous property of the harmonic VLI kernels in the next section.

8.2. Harmonicity of the Kernel and Potential

From Theorem 6.18, we know that many differential operators interchange with the series of the continuous/star-shaped VLI kernel. In the case of the harmonic VLI kernel, we are able to explicitly calculate the result with respect to $\boldsymbol{\Delta}_{\boldsymbol{y}}$. Recall that the vectorial Laplacian is meant component-wise.

Lemma 8.6. *For the harmonic VLI kernel $\boldsymbol{k}^{(\iota)}$, we have $\boldsymbol{\Delta}_{\boldsymbol{y}}\boldsymbol{k}^{(\iota)}(\boldsymbol{x},\boldsymbol{y}) = \boldsymbol{0}$ for all $(\boldsymbol{x},\boldsymbol{y}) \in (\mathbb{B}_R \setminus \{\boldsymbol{0}\}) \times \mathbb{G}_{\text{out}}$. In addition, $\boldsymbol{k}^{(\iota)}(\boldsymbol{x},\cdot) \in \mathbf{C}^{\infty}(\operatorname{int}\mathbb{G}_{\text{out}})$ for all $\boldsymbol{x} \in \mathbb{B}_R \setminus \{\boldsymbol{0}\}$.*

Proof. According to Theorem 6.18, the series of the kernel can be interchanged with the differential operator. The assumptions on $\{\gamma_k\}_{k\in\mathbb{N}}$ required for this purpose are fulfilled, see Lemma 8.3. For all $(\boldsymbol{x},\boldsymbol{y}) \in \mathbb{B}_R \times \mathbb{G}_{\text{out}}$, we get the relation

$$\begin{aligned}
\boldsymbol{\Delta}_{\boldsymbol{y}}\boldsymbol{k}^{(\iota)}(\boldsymbol{x},\boldsymbol{y}) &= \boldsymbol{\Delta}_{\boldsymbol{y}} \sum_{k=1}^{\infty} \frac{\Gamma_k}{y^{k+1}} x^{t_k} \boldsymbol{p}_k^{(\iota)}(\hat{\boldsymbol{x}},\hat{\boldsymbol{y}}) \\
&= \sum_{k=1}^{\infty} \Gamma_k x^{t_k} \boldsymbol{\Delta}_{\boldsymbol{y}} \left(y^{-(k+1)} \boldsymbol{p}_k^{(\iota)}(\hat{\boldsymbol{x}},\hat{\boldsymbol{y}}) \right) \\
&= \sum_{k=1}^{\infty} \sum_{j=1}^{2k+1} \frac{4\pi}{2k+1} \Gamma_k x^{t_k} \boldsymbol{y}_{k,j}^{(\iota)}(\hat{\boldsymbol{x}}) \Delta_{\boldsymbol{y}} \left(y^{-(k+1)} Y_{k,j}(\hat{\boldsymbol{y}}) \right) \\
&= \boldsymbol{0},
\end{aligned}$$

where we used the Addition Theorem for vectorial Legendre polynomials, see Theorem 5.24. The mapping $\boldsymbol{y} \mapsto y^{-(k+1)} Y_{k,j}(\hat{\boldsymbol{y}})$ is a harmonic function for $\boldsymbol{y} \neq \boldsymbol{0}$, see Corollary 2.30. Thus, each summand of the series vanishes. The stated smoothness of the kernel is a consequence of the harmonicity of the kernel on this particular region, see [64]. □

By means of the foregoing lemma, we are able to prove one advantage of the harmonic VLI operator. Based on the integral representation of the forward operator $\mathcal{T}$ and the fact that, under certain assumptions, the Laplacian can be interchanged with the integration, we can achieve the harmonicity of the potential $\mathcal{T}\boldsymbol{f}$.

Theorem 8.7. *The potential $\mathcal{T}\boldsymbol{f}$ is a harmonic function in $\mathbb{G}_{\text{out}}$, that is $\Delta(\mathcal{T}\boldsymbol{f}) = 0$ for all $\boldsymbol{f} \in \mathbf{L}_2(\mathbb{B}_R)$.*

Proof. We immediately obtain

$$(\Delta(\mathcal{T}\boldsymbol{f}))(\boldsymbol{y}) = \int_{\mathbb{B}_R} \boldsymbol{f}(\boldsymbol{x}) \cdot \left(\boldsymbol{\Delta}_{\boldsymbol{y}}\boldsymbol{k}^{(\iota)}(\boldsymbol{x},\boldsymbol{y})\right) \mathrm{d}\boldsymbol{x} = 0,$$

due to Theorem 7.13. Note that the assumptions of this theorem are fulfilled by means of Lemma 8.3. Lemma 8.6 provides us with $\boldsymbol{\Delta}_{\boldsymbol{y}}\boldsymbol{k}^{(\iota)}(\boldsymbol{x},\boldsymbol{y}) = \boldsymbol{0}$ for all $(\boldsymbol{x},\boldsymbol{y}) \in (\mathbb{B}_R \setminus \{\boldsymbol{0}\}) \times \mathbb{G}_{\text{out}}$. Thus, the integral vanishes. □

Since $\mathcal{T}\boldsymbol{f}$ is a harmonic function in the outer region, we want to link the potential obtained by the harmonic VLI operator to a solution of the exterior Dirichlet problem. For this purpose, we need the regularity at infinity of $\mathcal{T}\boldsymbol{f}$.

Lemma 8.8. *The potential generated by the harmonic VLI operator, that is $V = \mathcal{T}\boldsymbol{f}$, for a given density $\boldsymbol{f} \in \mathbf{L}_2(\mathbb{B}_R)$ is regular at infinity.*

Proof. Via Theorem 8.4 and by means of outer harmonics, we obtain a representation of $\mathcal{T}\boldsymbol{f}$ for all $\boldsymbol{y} \in \mathbb{G}_{\text{out}}$ given by

$$(\mathcal{T}\boldsymbol{f})(\boldsymbol{y}) = 4\pi \sum_{n=1}^{\infty} \sum_{j=1}^{2n+1} \frac{\Gamma_n}{(2n+1)\sqrt{2t_n+3}} f^{\wedge}(\iota,0,n,j) \frac{R^{t_n+3/2}}{r^n} H_{n,j}^{\text{ext}}(r;\boldsymbol{y}).$$

In addition, the convergence of the series is absolute and uniform in $\mathbb{G}_{\text{out}}$. The outer harmonics are regular at infinity, see Corollary 2.30. For the regularity at infinity of the potential, we need to check if $\mathcal{T}\boldsymbol{f} \in \mathcal{O}(|\cdot|^{-1})$. For this purpose, we analyze the convergence of the series in $(\mathcal{T}\boldsymbol{f})(\boldsymbol{y})y$. We obtain with the Cauchy-Schwarz inequality, Theorem 7.15, the Addition Theorem 2.25, and the fact that $y \geq R + \varepsilon$ for all $\boldsymbol{y} \in \mathbb{G}_{\text{out}}$ the estimate

$$\begin{aligned}
&4\pi \left| \sum_{n=N}^{\infty} \sum_{j=1}^{2n+1} \frac{\Gamma_n}{(2n+1)\sqrt{2t_n+3}} f^{\wedge}(\iota,0,n,j) \frac{R^{t_n+3/2}}{y^n} Y_{n,j}(\hat{\boldsymbol{y}}) \right| \\
\leq &4\pi \left(\sum_{n=N}^{\infty} \sum_{j=1}^{2n+1} \frac{\Gamma_n^2}{(2n+1)^2(2t_n+3)} \frac{R^{2t_n+3}}{y^{2n}} Y_{n,j}(\hat{\boldsymbol{y}}) Y_{n,j}(\hat{\boldsymbol{y}}) \right)^{1/2} \|\boldsymbol{f}\|_{\mathbf{L}_2(\mathbb{B}_R)} \cdot \\
\leq &\sqrt{4\pi} \sup_{n\in\mathbb{N}} \left(R^{t_n-n} \right) \left(\sum_{n=N}^{\infty} \frac{\Gamma_n^2}{(2n+1)(2t_n+3)} \frac{R^{2n+3}}{(R+\varepsilon)^{2n}} \right)^{1/2} \|\boldsymbol{f}\|_{\mathbf{L}_2(\mathbb{B}_R)} \cdot
\end{aligned}$$

The right-hand side converges to zero as $N \to \infty$. Thus, $|(\mathcal{T}\boldsymbol{f})(\boldsymbol{y})y| < \infty$ uniformly for all $\boldsymbol{y} \in \mathbb{G}_{\text{out}}$ and, consequently, $\limsup_{y\to\infty} |(\mathcal{T}\boldsymbol{f})(\boldsymbol{y})y| < \infty$. With the same estimates and the representation of the gradient in Theorem 8.4, we obtain $\limsup_{y\to\infty} |y^2(\boldsymbol{\nabla}_{\boldsymbol{y}}(\mathcal{T}\boldsymbol{f})(\boldsymbol{y}))| < \infty$ and, hence, the regularity at infinity. □

The harmonicity and regularity at infinity of the potential provide us with the possibility to use knowledge about the exterior Dirichlet problem in this setting. Summing up, $\mathcal{T}\boldsymbol{f}$ satisfies all assumptions for the corresponding exterior Dirichlet problem.

Lemma 8.9. *Let $\mathbb{G}_{\text{out}} \subset \mathbb{R}^3$ be the outer region of the harmonic VLI equation. Consider the potential $V \coloneqq \mathcal{T}\boldsymbol{f}$ for $\boldsymbol{f} \in \mathbf{L}_2(\mathbb{B}_R)$. Then*

i) V satisfies Laplace's equation $\Delta V = 0$ in $\operatorname{int}(\mathbb{G}_{\text{out}})$,

ii) V is of class $\mathrm{C}^2(\operatorname{int}(\mathbb{G}_{\text{out}})) \cap \mathrm{C}(\mathbb{G}_{\text{out}})$, and

iii) V is regular at infinity.

Proof. i) From Theorem 8.7, we immediately obtain that V is harmonic.

ii) Since V is a harmonic function, it is of class $\mathrm{C}^{\infty}(\operatorname{int}(\mathbb{G}_{\text{out}}))$. Thus, we only need to verify $V \in \mathrm{C}(\mathbb{G}_{\text{out}})$, which has already been proved in Theorem 7.8.

iii) This is proved in Lemma 8.8. □

Thus, with given boundary values, the potential V generated by the harmonic VLI operator is the unique solution of the exterior Dirichlet problem. In the particular case of $\mathbb{G}_{\text{out}} = \overline{\mathbb{B}_r^{\text{ext}}}$, we also obtain the following result.

Corollary 8.10. *Let $\mathbb{G}_{\text{out}} \coloneqq \overline{\mathbb{B}_r^{\text{ext}}}$, where $r > R$, and let $\boldsymbol{f} \in \mathbf{L}_2(\mathbb{B}_R)$ be given. Then $V \coloneqq \mathcal{T}\boldsymbol{f}$ from Lemma 8.9 is the unique solution of the exterior Dirichlet problem, that is $\Delta V = 0$ in $\mathbb{B}_r^{\text{ext}}$ with boundary values $(\mathcal{T}\boldsymbol{f})|_{\mathbb{S}_r}$, see Definition 2.31. It is given by*

$$V = \sum_{n=0}^{\infty} \sum_{j=1}^{2n+1} V^{\wedge}(n,j) H_{n,j}^{\text{ext}}(r;\cdot)$$

with the abbreviation $V^{\wedge}(n,j) \coloneqq \langle (\mathcal{T}\boldsymbol{f})|_{\mathbb{S}_r}, H_{n,j}^{\text{ext}}(r;\cdot)\rangle_{\mathrm{L}_2(\mathbb{S}_r)}$. The coefficients satisfy

$$V^{\wedge}(n,j) = 4\pi \frac{\Gamma_n}{(2n+1)\sqrt{2t_n+3}} \frac{R^{t_n+3/2}}{r^n} f^{\wedge}(\iota,0,n,j), \tag{8.1}$$

for all $n \in \mathbb{N}$ and $j = 1,\dots,2n+1$, and $V^{\wedge}(0,1) = 0$.

Proof. The potential V fulfils all assumptions of a solution of the exterior Dirichlet problem, see Definition 2.31 and Lemma 8.9. Lemma 2.32 provides us with its representation. Theorem 8.4 states another expansion of the potential V, which reads

$$V(\boldsymbol{y}) = 4\pi \sum_{n=1}^{\infty} \sum_{j=1}^{2n+1} \frac{\Gamma_n}{(2n+1)\sqrt{2t_n+3}} f^{\wedge}(\iota,0,n,j) \frac{R^{t_n+3/2}}{r^n} H_{n,j}^{\text{ext}}(r;\boldsymbol{y}), \qquad \boldsymbol{y} \in \mathbb{G}_{\text{out}}.$$

Hence, we can calculate the coefficients $V^{\wedge}(n,j)$ for all $n \in \mathbb{N}$, $j = 1,\dots,2n+1$ by means of Corollary 2.30 and arrive at

$$\begin{aligned} & V^{\wedge}(n,j) \\ &= \left\langle V|_{\mathbb{S}_r}, H_{n,j}^{\text{ext}}(r;\cdot)|_{\mathbb{S}_r} \right\rangle_{\mathrm{L}_2(\mathbb{S}_r)} \\ &= 4\pi \frac{\Gamma_n}{(2n+1)\sqrt{2t_n+3}} f^{\wedge}(\iota,0,n,j) \frac{R^{t_n+3/2}}{r^n}. \end{aligned}$$

□

Now, we have all tools at hand in order to analyze the direct problem of the magneto-electroencephalography problem.

Chapter 9.

Direct Magnetoencephalography Problem

9.1. Measurements from Magnetometers

For the analysis of the direct MEG problem, recall that the multiple-shell model assumptions from Assumption 3.2 hold true. In Eq. (3.3), a connection between the magnetic potential and the neuronal current is stated. First, we want to verify that this integral equation is well-defined and the evaluation of the corresponding potential makes sense. By using the results on the continuous/star-shaped VLI equation, we immediately obtain that the series in the MEG integral kernel converges, see Theorem 6.6, and that the integrand in Eq. (3.3) is integrable over the region $\mathbb{B}_{\varrho_0}$, see Corollary 7.3. Hence, the integral equation is well-defined. For this result, we use the assumption that the neuronal current is an $\mathbf{L}_2(\mathbb{B}_{\varrho_0})$-function, see Assumption 3.2. Accordingly, Eq. (3.3) initially holds true almost everywhere. However, Chapter 7 provides us with more results concerning the potential

$$U(\boldsymbol{y}) = \int_{\mathbb{B}_{\varrho_0}} \boldsymbol{J}^{\mathrm{P}}(\boldsymbol{x}) \cdot \boldsymbol{k}_{\mathrm{M}}(\boldsymbol{x}, \boldsymbol{y}) \, \mathrm{d}\boldsymbol{x}, \qquad \boldsymbol{y} \in \overline{\mathbb{B}^{\mathrm{ext}}_{\varrho_L}}.$$

The magnetic potential is an $\mathrm{L}_2(\overline{\mathbb{B}^{\mathrm{ext}}_{\varrho_L}})$-function, see Corollary 7.3, and the linear operator $\mathcal{T}_U \colon \mathbf{L}_2(\mathbb{B}_{\varrho_0}) \to \mathrm{L}_2(\overline{\mathbb{B}^{\mathrm{ext}}_{\varrho_L}})$ with $\mathcal{T}_U \boldsymbol{J}^{\mathrm{P}} = U$ is bounded. In addition, U is a $\mathrm{C}(\overline{\mathbb{B}^{\mathrm{ext}}_{\varrho_L}})$-function, see Theorem 7.8. In other words, the magnetic potential is a continuous function $U \colon \overline{\mathbb{B}^{\mathrm{ext}}_{\varrho_L}} \to \mathbb{R}$, hence Eq. (3.3) holds pointwise for all $\boldsymbol{y} \in \overline{\mathbb{B}^{\mathrm{ext}}_{\varrho_L}}$.

Since the magnetic field $\boldsymbol{B}$ is, in the exterior of the head, given as the gradient of the magnetic potential U, see, for instance, [73, 200] or Eq. (3.1), that is

$$\boldsymbol{B}(\boldsymbol{y}) = \mu_0 \boldsymbol{\nabla}_{\boldsymbol{y}} U(\boldsymbol{y}), \qquad \boldsymbol{y} \in \overline{\mathbb{B}^{\mathrm{ext}}_{\varrho_L}},$$

we still need a higher smoothness of U. This smoothness is obtained by Theorem 7.11. All the assumptions therein are fulfilled, see Assumption 3.2 and Lemma 6.9. Due to Corollary 7.12, the magnetic field is a continuous function in $\overline{\mathbb{B}^{\mathrm{ext}}_{\varrho_L}}$.

An immediate consequence is the relation between the primary current and the magnetic flux density $B_{\boldsymbol{\nu}}$ in the direction of the normal vector field $\boldsymbol{\nu}$ given by

$$B_{\boldsymbol{\nu}}(\boldsymbol{y}) = \mu_0 \boldsymbol{\nu}(\boldsymbol{y}) \cdot \boldsymbol{\nabla}_{\boldsymbol{y}} \left(\int_{\mathbb{B}_{\varrho_0}} \boldsymbol{J}^{\mathrm{P}}(\boldsymbol{x}) \cdot \boldsymbol{k}_{\mathrm{M}}(\boldsymbol{x}, \boldsymbol{y}) \, \mathrm{d}\boldsymbol{x} \right), \qquad \boldsymbol{y} \in \overline{\mathbb{B}^{\mathrm{ext}}_{\varrho_L}}. \tag{9.1}$$

Summing up, we eventually obtain the mathematical formulation of the inverse MEG problem and its corresponding continuous/star-shaped VLI operator.

Problem 9.1 (The MEG Problem). *Let Assumption 3.2 with $L \geq 1$ be fulfilled. It is the aim to reconstruct the primary current $\boldsymbol{J}^{\mathrm{P}}$ from a finite set of $\ell_{\mathrm{M}} \in \mathbb{N}_0$ given measurements*

of $B_{\boldsymbol{\nu}}$, where the relation between those two quantities is given for $\ell = 1, \dots, \ell_{\mathrm{M}}$ by

$$\mathcal{A}_{\mathrm{M}} \boldsymbol{J}^{\mathrm{P}} = \sum_{\ell=1}^{\ell_{\mathrm{M}}} B_{\boldsymbol{\nu}}(\boldsymbol{y}_\ell) \boldsymbol{\varepsilon}^\ell = \sum_{\ell=1}^{\ell_{\mathrm{M}}} \boldsymbol{\nu}(\boldsymbol{y}_\ell) \cdot \boldsymbol{B}(\boldsymbol{y}_\ell) \boldsymbol{\varepsilon}^\ell$$

with the measurement positions $\{\boldsymbol{y}_\ell \mid \ell = 1, \dots, \ell_{\mathrm{M}}\} \subset \overline{\mathbb{B}^{\mathrm{ext}}_{\varrho_L}}$. Note that $\boldsymbol{\varepsilon}^\ell$ for $\ell = 1, \dots, \ell_{\mathrm{M}}$ denotes the standard Cartesian basis in $\mathbb{R}^{\ell_{\mathrm{M}}}$. The MEG forward operator $\mathcal{T}_{\mathrm{M}} \colon \mathbf{L}_2(\mathbb{B}_{\varrho_0}) \to \mathrm{C}(\overline{\mathbb{B}^{\mathrm{ext}}_{\varrho_L}})$ and the linear operator $\mathcal{A}_{\mathrm{M}} \colon \mathbf{L}_2(\mathbb{B}_{\varrho_0}) \to \mathbb{R}^{\ell_{\mathrm{M}}}$ are defined by

$$\left(\mathcal{T}_{\mathrm{M}} \boldsymbol{J}^{\mathrm{P}}\right)(\boldsymbol{y}) \coloneqq \mu_0 \boldsymbol{\nabla}_{\boldsymbol{y}} \int_{\mathbb{B}_{\varrho_0}} \boldsymbol{J}^{\mathrm{P}}(\boldsymbol{x}) \cdot \boldsymbol{k}_{\mathrm{M}}(\boldsymbol{x}, \boldsymbol{y}) \, \mathrm{d}\boldsymbol{x}, \qquad \boldsymbol{y} \in \overline{\mathbb{B}^{\mathrm{ext}}_{\varrho_L}}, \tag{9.2a}$$

$$\mathcal{A}_{\mathrm{M}} \boldsymbol{J}^{\mathrm{P}} \coloneqq \sum_{\ell=1}^{\ell_{\mathrm{M}}} \boldsymbol{\nu}(\boldsymbol{y}_\ell) \cdot \left(\mathcal{T}_{\mathrm{M}} \boldsymbol{J}^{\mathrm{P}}\right)(\boldsymbol{y}_\ell) \boldsymbol{\varepsilon}^\ell. \tag{9.2b}$$

The corresponding magnetic potential has the form

$$U(\boldsymbol{y}) = \int_{\mathbb{B}_{\varrho_0}} \boldsymbol{J}^{\mathrm{P}}(\boldsymbol{x}) \cdot \boldsymbol{k}_{\mathrm{M}}(\boldsymbol{x}, \boldsymbol{y}) \, \mathrm{d}\boldsymbol{x}, \qquad \boldsymbol{y} \in \overline{\mathbb{B}^{\mathrm{ext}}_{\varrho_L}}.$$

Recall that the integral kernel $\boldsymbol{k}_{\mathrm{M}}$ is given by

$$\boldsymbol{k}_{\mathrm{M}}(\boldsymbol{x}, \boldsymbol{y}) \coloneqq \frac{1}{4\pi} \sum_{k=1}^{\infty} \sqrt{\frac{k}{k+1}} \frac{x^k}{y^{k+1}} \boldsymbol{p}_k^{(3)}(\hat{\boldsymbol{x}}, \hat{\boldsymbol{y}}), \qquad (\boldsymbol{x}, \boldsymbol{y}) \in \mathbb{B}_{\varrho_0} \times \overline{\mathbb{B}^{\mathrm{ext}}_{\varrho_L}}.$$

After formulating the well-defined MEG problem, we consider the solution of the direct problem. Recall that the occurring MEG kernel $\boldsymbol{k}_{\mathrm{M}}$ is a harmonic VLI kernel. Thus, we can use the results from Chapter 8 in order to solve the direct MEG problem. Eventually, we obtain a representation of the magnetic field or potential, respectively, generated by the neuronal current.

Due to Theorem 7.11, we are able to interchange the gradient with the integration. In the resulting representation in Eq. (9.3), the vector on the left-hand side of the integrand is called the lead field of the MEG channel measuring the field at location $\boldsymbol{y}$ in direction ν, see [108, 180] and the references therein. The relation between the magnetic flux density and the lead field is given by

$$\boldsymbol{\nu}(\boldsymbol{y}) \cdot \boldsymbol{B}(\boldsymbol{y}) = \mu_0 \int_{\mathbb{B}_{\varrho_0}} \left(\boldsymbol{\nu}(\boldsymbol{y}) \cdot \left(\mathrm{jac}_{\boldsymbol{y}} \left(\boldsymbol{k}_{\mathrm{M}}(\boldsymbol{x}, \boldsymbol{y})\right)\right)^{\mathrm{T}}\right) \cdot \boldsymbol{J}^{\mathrm{P}}(\boldsymbol{x}) \, \mathrm{d}\boldsymbol{x}, \qquad \boldsymbol{y} \in \overline{\mathbb{B}^{\mathrm{ext}}_{\varrho_L}}. \tag{9.3}$$

Recall the definition of the vector-valued basis functions on the ball in Definition 5.37 and the one of the scalar-valued basis functions on the interval $[0, \varrho_0]$ in Definition 5.1. In addition, Edmonds vector spherical harmonics, see Definition 5.9, are used. Note that the sequence $\{t_n\}_{n \in \mathbb{N}_{0_\iota}}$ also occurs in the definition of the orthonormal basis functions, see Definition 5.37.

Theorem 9.2. *Let the neuronal current fulfil Assumption 3.2 with $L \geq 1$. Then we can expand $\boldsymbol{J}^{\mathrm{P}}$ as*

$$\boldsymbol{J}^{\mathrm{P}} = \sum_{i=1}^{3} \sum_{m=0}^{\infty} \sum_{n=0_i}^{\infty} \sum_{j=1}^{2n+1} J^{\wedge}[i, m, n, j] \tilde{\boldsymbol{g}}^{(i)}_{m,n,j}(\varrho_0; \cdot)$$

with $t_n \coloneqq n$ *and we define for* $i = 1, 2, 3$, $n \in \mathbb{N}_{0_i}$, *and* $j = 1, \ldots, 2n+1$ *the functions*

$$J_{n,j}^{(i),\sim} \coloneqq \sum_{m=0}^{\infty} J^{\wedge}[i,m,n,j] Q_m^{(n+1/2)}(\varrho_0;\cdot).$$

The uniformly converging series in the representation of the magnetic field and the magnetic potential, respectively, are given for all $\boldsymbol{y} \in \overline{\mathbb{B}}_{\varrho_L}^{\mathrm{ext}}$ *and for their restriction onto the sphere* $\mathbb{S}_{\varrho_0}$ *in the sense of* $\mathbf{L}_2(\mathbb{S}_{\varrho_0})$ *and* $\mathrm{L}_2(\mathbb{S}_{\varrho_0})$, *respectively, by the expressions*

$$U(\boldsymbol{y}) = \sum_{n=1}^{\infty} \sum_{j=1}^{2n+1} \frac{\sqrt{n}}{\sqrt{n+1}(2n+1)} \int_0^{\varrho_0} J_{n,j}^{(3),\sim}(x) x^{n+2} \,\mathrm{d}x \frac{1}{y^{n+1}} Y_{n,j}(\hat{\boldsymbol{y}}), \tag{9.4a}$$

$$\boldsymbol{B}(\boldsymbol{y}) = -\mu_0 \sum_{n=1}^{\infty} \sum_{j=1}^{2n+1} \sqrt{\frac{n}{2n+1}} \int_0^{\varrho_0} J_{n,j}^{(3),\sim}(x) x^{n+2} \,\mathrm{d}x \frac{1}{\varrho_0^{n+1}} \boldsymbol{h}_{n,j}^{(1)}(\varrho_0;\boldsymbol{y}). \tag{9.4b}$$

Proof. We get the representations for U and $\boldsymbol{B}$ from Theorem 8.4 in combination with Lemma 6.9 and $\Gamma_n = \sqrt{n/(n+1)}/(4\pi)$. Note that $t_n = n$ for all $n \in \mathbb{N}$ and that the Morse-Feshbach and Edmonds vector spherical harmonics of type $\iota = 3$ coincide. The convergence results concerning the magnetic potential in Eq. (9.4a) are proved in Theorems 7.18 and 7.20. The assumptions therein are fulfilled due to Lemma 6.9 combined with Theorem 7.26. In order to apply Theorem 7.20 and Lemma 8.5, we need to verify their conditions, that is

$$|\gamma_n(\varrho_0)| = \Gamma_n \varrho_0^{-(n+1)},$$

where for all $n \in \mathbb{N}$ the next estimate holds true:

$$\Gamma_n = \frac{1}{4\pi}\sqrt{\frac{n}{n+1}} \leq \sqrt{\frac{(2n+1)(2n+3)}{n+1}} \leq \sqrt{(2n+1)^2(2n+3)}.$$

The uniform convergence of the series in Eq. (9.4b) holds true because of Lemma 7.21. The $\mathbf{L}_2(\mathbb{S}_{\varrho_0})$-convergence is given by Lemma 8.5. □

By means of Lemma 7.24 and Theorem 7.25, we obtain for the remaining integration in Eq. (9.4) the result

$$\int_0^{\varrho_0} J_{n,j}^{(3),\sim}(x) x^{n+2} \,\mathrm{d}x = J^{\wedge}[3,0,n,j] \sqrt{\frac{\varrho_0^{2n+3}}{2n+3}} \tag{9.5}$$

for all $n \in \mathbb{N}$, $j = 1, \ldots, 2n+1$. Recall that the approach used in Chapter 7 is based on a separation of the neuronal current into a radial and an angular part. This kind of separation is a common approach, which has already been used for certain MEG and EEG decompositions, see [48, 71, 72], or in other fields, for instance, in the inverse gravimetric problem, see [161], or the inverse geomagnetic problem, see [12]. However, to the knowledge of the author, for the first time it is used by means of the Edmonds vector spherical harmonics. Therefore, we call this separation the Edmonds approach. In the case of the MEG problem, however, these two approaches coincide. Nevertheless, this nomenclature will make sense when the MEG problem is combined with the EEG problem. In [48, 71], a decomposition of the current into complex vector spherical harmonics is used. A comparison between the results in the literature and the ones from this section is presented in Chapter 15.

Remark 9.3. *For the MEG direct problem, it is irrelevant whether the Morse-Feshbach or the Edmonds vector spherical harmonics are used for the decomposition of the neuronal current. Only the part of the neuronal current belonging to the type $\iota = 3$ of the Morse-Feshbach vector spherical harmonics does contribute to the magnetic potential and its field. This type coincides with type $\iota = 3$ of the Edmonds vector spherical harmonics.*

Now, we find an answer to the question: 'can we represent (parts of) the neuronal current if the function describing the magnetic potential or field, respectively, is completely known?' We solve this task by stating a relation between the Fourier coefficients of the neuronal current $J^\wedge[i,m,n,j]$ for $i = 1,2,3$, $m \in \mathbb{N}_0$, $n \in \mathbb{N}_{0_i}$, and $j = 1,\dots,2n+1$ and some expansion coefficients of the magnetic potential and the magnetic field, respectively. This relation is necessary in order to describe the neuronal current by means of the given magnetic potential. Thus, we are ultimately seeking for a solution of the inverse problem. For this purpose, we first need suitable expansions for both quantities. In Chapter 8, certain SVDs for the integral operator were stated. However, we focus on an expansion in (vector-valued) outer harmonics, in order to compare our results with the literature.

Theorem 9.4. *Let the neuronal current fulfil Assumption 3.2 with $L \geq 1$,*

- *then the corresponding magnetic potential U and its outer harmonics coefficients given by $U_{\varrho_L}^\wedge(n,j) \coloneqq \langle U|_{\mathbb{S}_{\varrho_L}}, H_{n,j}^{\mathrm{ext}}(\varrho_L;\cdot)|_{\mathbb{S}_{\varrho_L}}\rangle_{\mathrm{L}_2(\mathbb{S}_{\varrho_L})}$ are uniquely determined by*

$$\begin{aligned} U(\boldsymbol{y}) &= \sum_{n=0}^{\infty}\sum_{j=1}^{2n+1} U_{\varrho_L}^\wedge(n,j) H_{n,j}^{\mathrm{ext}}(\varrho_L;\boldsymbol{y}), \qquad \boldsymbol{y} \in \overline{\mathbb{B}_{\varrho_L}^{\mathrm{ext}}}, \\ U_{\varrho_L}^\wedge(n,j) &= \frac{\sqrt{n}}{\varrho_L^n\sqrt{n+1}(2n+1)} \int_0^{\varrho_0} J_{n,j}^{(3),\sim}(x) x^{n+2}\,\mathrm{d}x \\ &= \sqrt{\frac{n\varrho_0^3}{(n+1)(2n+1)^2(2n+3)}} \left(\frac{\varrho_0}{\varrho_L}\right)^n J^\wedge[3,0,n,j] \end{aligned} \tag{9.6}$$

  for $n \in \mathbb{N}_0$, $j = 1,\dots,2n+1$;

- *then the corresponding magnetic field $\boldsymbol{B}$ and its vector outer harmonics coefficients $B_{\varrho_L}^\wedge(n,j) \coloneqq \langle \boldsymbol{B}|_{\mathbb{S}_{\varrho_L}}, \boldsymbol{h}_{n,j}^{(1)}(\varrho_L;\cdot)|_{\mathbb{S}_{\varrho_L}}\rangle_{\mathbf{L}_2(\mathbb{S}_{\varrho_L})}$ are uniquely determined by*

$$\begin{aligned} \boldsymbol{B}(\boldsymbol{y}) &= \sum_{n=0}^{\infty}\sum_{j=1}^{2n+1} B_{\varrho_L}^\wedge(n,j) \boldsymbol{h}_{n,j}^{(1)}(\varrho_L;\cdot), \qquad \boldsymbol{y} \in \overline{\mathbb{B}_{\varrho_L}^{\mathrm{ext}}}, \\ B_{\varrho_L}^\wedge(n,j) &= -\frac{\mu_0}{\varrho_L^{n+1}}\sqrt{\frac{n}{2n+1}} \int_0^{\varrho_0} J_{n,j}^{(3),\sim}(x) x^{n+2}\,\mathrm{d}x \\ &= -\mu_0\sqrt{\frac{n\varrho_0}{(2n+1)(2n+3)}} \left(\frac{\varrho_0}{\varrho_L}\right)^{n+1} J^\wedge[3,0,n,j] \end{aligned}$$

  for $n \in \mathbb{N}_0$, $j = 1,\dots,2n+1$.

For all $\boldsymbol{y} \in \overline{\mathbb{B}_{\varrho_L}^{\mathrm{ext}}}$, the occurring series converge absolutely and uniformly in both cases.

Proof. The magnetic potential is regular at infinity and harmonic in the exterior of the head, see Maxwell's equations in Definition 3.1:

$$0 = \boldsymbol{\nabla}\cdot\boldsymbol{B} = \mu_0 \boldsymbol{\nabla}\cdot\boldsymbol{\nabla} U = \mu_0 \Delta U \qquad \text{in } \overline{\mathbb{B}_{\varrho_L}^{\mathrm{ext}}}.$$

From Lemma 2.32, we obtain the unique outer harmonic representation of U. We use the relation $y^{-(n+1)}Y_{n,j}(\hat{\boldsymbol{y}}) = \varrho_L^{-n} H_{n,j}^{\mathrm{ext}}(\varrho_L; \boldsymbol{y})$ and the calculations from Theorem 9.2 and Eq. (9.5) to obtain the desired result. From Eq. (5.15), we relate the gradient of the scalar outer harmonics to the vector outer harmonics of type $i = 1$. For the magnetic field we, hence, obtain with Eq. (3.1) the relation

$$B_{\varrho_L}^{\wedge}(n,j) = -\mu_0 U_{\varrho_L}^{\wedge}(n,j) \frac{\sqrt{(n+1)(2n+1)}}{\varrho_L} \tag{9.7}$$

for all $n \in \mathbb{N}$, $j = 1, \ldots, 2n+1$. This completes the proof. □

Thus, by means of Maxwell's equations and the continuous VLI equation, we are able to formulate an integral equation modelling the relation between the neuronal current inside the brain and the measured magnetic potential in the exterior. Moreover, we used an Edmonds vector spherical harmonics decomposition of the neuronal current in order to solve the direct problem. A relation between the expansion coefficients of the measured quantities and the Fourier coefficients of the neuronal current is stated in Theorem 9.4.

9.2. Measurements from Gradiometers

Within our numerical tests with real data, the data is obtained by magnetoencephalographs that are part of the Elekta Neuromag Vectorview system, see [172]. This system provides us with additional 204 measurements, see [33, 172]. For each sensor surface, the normal vector $\boldsymbol{\nu}$ is constant and the sensor surface possesses two perpendicular tangential vectors $\boldsymbol{\upsilon}_1$ and $\boldsymbol{\upsilon}_2$. On each sensor surface, the two directional derivatives (in direction of the tangential vectors) of the normal component of the magnetic field, $B^{\boldsymbol{\upsilon}_1}$ and $B^{\boldsymbol{\upsilon}_2}$, are measured. They are defined for all $\boldsymbol{y} \in \overline{\mathbb{B}_{\varrho_L}^{\mathrm{ext}}}$ by

$$\begin{aligned} B^{\boldsymbol{\upsilon}_1}(\boldsymbol{y}) &\coloneqq \boldsymbol{\upsilon_1} \cdot (\boldsymbol{\nabla}_{\boldsymbol{y}} B_{\boldsymbol{\nu}}(\boldsymbol{y})), \\ B^{\boldsymbol{\upsilon}_2}(\boldsymbol{y}) &\coloneqq \boldsymbol{\upsilon_2} \cdot (\boldsymbol{\nabla}_{\boldsymbol{y}} B_{\boldsymbol{\nu}}(\boldsymbol{y})). \end{aligned}$$

In order to further manipulate these expressions, we use the representation of the magnetic field from Theorem 9.4 and get

$$B_{\boldsymbol{\nu}}(\boldsymbol{y}) = \sum_{n=1}^{\infty} \sum_{j=1}^{2n+1} B_{\varrho_L}^{\wedge}(n,j) \boldsymbol{\nu}(\boldsymbol{y}) \cdot \boldsymbol{h}_{n,j}^{(1)}(\varrho_L; \boldsymbol{y}), \qquad \boldsymbol{y} \in \overline{\mathbb{B}_{\varrho_L}^{\mathrm{ext}}}, \tag{9.8}$$

$$B_{\varrho_L}^{\wedge}(n,j) = -\frac{\mu_0}{{\varrho_L}^{n+1}} \sqrt{\frac{n}{2n+1}} \int_0^{\varrho_0} J_{n,j}^{(3),\sim}(x) x^{n+2} \,\mathrm{d}x, \tag{9.9}$$

where $n \in \mathbb{N}$, $j = 1, \ldots, 2n+1$. Next, we calculate the gradient of the normal component of the magnetic field.

Lemma 9.5. *The gradient of the normal component of the magnetic field $B_{\boldsymbol{\nu}}$ is given for all $\boldsymbol{y} \in \overline{\mathbb{B}}_{\varrho_L}^{\text{ext}}$ by*

$$\begin{aligned}\boldsymbol{\nabla}_{\boldsymbol{y}} B_{\boldsymbol{\nu}}(\boldsymbol{y}) = \sum_{n=1}^{\infty} \sum_{j=1}^{2n+1} B_{\varrho_L}^{\wedge}(n,j) \Bigg(&+ \sqrt{\frac{n+1}{2n+1}} \boldsymbol{\nu}(\boldsymbol{y}) Y_{n,j}(\hat{\boldsymbol{y}}) \\ &+ (\boldsymbol{\nu}(\boldsymbol{y}) \cdot \hat{\boldsymbol{y}}) \left(-(n+3) \sqrt{\frac{n+1}{2n+1}} \boldsymbol{y}_{n,j}^{(1)}(\hat{\boldsymbol{y}}) + (n+2) \sqrt{\frac{n}{2n+1}} \boldsymbol{y}_{n,j}^{(2)}(\hat{\boldsymbol{y}}) \right) \\ &+ \sqrt{\frac{n(n+1)^2}{2n+1}} \hat{\boldsymbol{y}} \left(\boldsymbol{\nu}(\boldsymbol{y}) \cdot \boldsymbol{y}_{n,j}^{(2)}(\hat{\boldsymbol{y}}) \right) - \sqrt{\frac{n}{2n+1}} (\boldsymbol{\nu}(\boldsymbol{y}) \cdot \boldsymbol{\nabla}_{\hat{\boldsymbol{y}}}^{*}) \boldsymbol{y}_{n,j}^{(2)}(\hat{\boldsymbol{y}}) \Bigg) \Bigg).\end{aligned}$$

Proof. The detailed proof can be found in the appendix, see Appendix A. □

Due to the complicated structure of the function $\boldsymbol{\nabla} B_{\boldsymbol{\nu}}$, we are not able to obtain an SVD of the operator mapping the neuronal current onto B^{υ_1} or B^{υ_2}, respectively.

In addition, even with an SVD of these operators more theoretical information on the neuronal current cannot be obtained (from it) than by means of the full magnetic field. The reason for this is that $\boldsymbol{\nabla}_{\boldsymbol{y}} B_{\boldsymbol{\nu}}$ depends on the same Fourier coefficients of $\boldsymbol{J}^{\mathrm{P}}$ as the magnetic field itself. Thus, we concentrate our theoretical investigations on the magnetic potential and its field.

On the other hand, from the numerical point of view, these additional 204 measurements can help to improve the numerical results by easing the lack of data and stabilizing the influence of the data noise. Further foundations and calculations that are required for the implementation of $\boldsymbol{\nabla}_{\boldsymbol{y}} B_{\boldsymbol{\nu}}(\boldsymbol{y})$ for the representation in Lemma 9.5 can also be found in the appendix, see Appendix A. However, the implementation itself would exceed the scope of this thesis and is left for future investigations.

Chapter 10.

Direct Electroencephalography Problem

In Eq. (4.23), an integral equation corresponding to the EEG problem for the multiple-shell model is stated. In Lemma 6.10, it is verified that this integral equation can be constructed by a linear combination of two continuous/star-shaped VLI kernels. Thus, we can use results for the continuous/star-shaped VLI operator in order to solve the direct problem related to the integral equation stated in Eq. (4.22) for the electric potential.

This integral equation for the potential restricted onto $\mathbb{S}_{\varrho_L}$ can also be found in [45, 73]. Therein, however, Gauß's Theorem, see [219], for the integration and the Helmholtz decomposition for the neuronal current is used in order to solve the problem, see also [47, 71]. Now, for the first time this problem is solved by means of the Edmonds vector spherical harmonics, which we call the Edmonds approach. A comparison of the different approaches is given in Chapter 15.

Note that the electroencephalograph measures potential differences, that is

$$u_L(\boldsymbol{y}) - u_L(\boldsymbol{z}) = \int_{\mathbb{B}_{\varrho_0}} \boldsymbol{J}^{\mathrm{P}}(\boldsymbol{x}) \cdot (\boldsymbol{k}_{\mathrm{E}}(\boldsymbol{x}, \boldsymbol{y}) - \boldsymbol{k}_{\mathrm{E}}(\boldsymbol{x}, \boldsymbol{z}))\, \mathrm{d}\boldsymbol{x}, \qquad \boldsymbol{y},\ \boldsymbol{z} \in \mathbb{S}_{[\varrho_{L-1}, \varrho_L]}.$$

The integral kernel resulting from the subtraction of $\boldsymbol{k}_{\mathrm{E}}$ evaluated at different measurement positions is often called the EEG lead field, see [181].

For the well-definedness of the EEG problem, two central questions need to be answered. The first question is whether the integral in Eq. (4.22) exists and the second one is whether the electric potential can be evaluated at the sensor positions. Due to the considerations in Lemma 6.10, we can understand the integral kernel $\boldsymbol{k}_{\mathrm{E}}$ as a linear combination of two continuous/star-shaped VLI kernels. The results from Chapter 7 combined with the linearity of the integration provide us with the answers to these questions.

Corollary 10.1. *Let Assumption 3.2 with $L \geq 2$ hold true. The electric potential u_L on the scalp given by Eq.* (4.22) *is well-defined and a $\mathrm{C}(\mathbb{S}_{[\varrho_{L-1}, \varrho_L]}) \subset \mathrm{L}_2(\mathbb{S}_{[\varrho_{L-1}, \varrho_L]})$-function.*

Proof. The integrability of the function $u_L^{\mathrm{d}}(\cdot, \boldsymbol{y})$ from Lemma 6.10 for all $\boldsymbol{y} \in \mathbb{S}_{[\varrho_{L-1}, \varrho_L]}$ is given by Lemma 6.20 combined with Lemma 6.10 and the Cauchy-Schwarz inequality. From Corollary 7.3 and Theorem 7.8, we obtain that the function

$$u(\boldsymbol{y}) \coloneqq \int_{\mathbb{B}_{\varrho_0}} \boldsymbol{J}^{\mathrm{P}}(\boldsymbol{x}) \cdot \boldsymbol{k}_{\mathrm{E}}(\boldsymbol{x}, \boldsymbol{y})\, \mathrm{d}\boldsymbol{x}, \qquad \boldsymbol{y} \in \overline{\mathbb{B}^{\mathrm{ext}}_{\varrho_0+\varepsilon}},$$

is, as the sum of two potentials obtained by continuous VLI operators, see Lemma 6.10, an $\mathrm{L}_2(\overline{\mathbb{B}^{\mathrm{ext}}_{\varrho_0+\varepsilon}})$ and a $\mathrm{C}(\overline{\mathbb{B}^{\mathrm{ext}}_{\varrho_0+\varepsilon}})$-function with an arbitrary $\varepsilon > 0$. Using $\varepsilon \coloneqq \varrho_{L-1} - \varrho_0$, its restriction onto $\mathbb{S}_{[\varrho_{L-1}, \varrho_L]}$ is also continuous and an $\mathrm{L}_2(\mathbb{S}_{[\varrho_{L-1}, \varrho_L]})$-function since $\mathbb{S}_{[\varrho_{L-1}, \varrho_L]} \subset \overline{\mathbb{B}^{\mathrm{ext}}_{\varrho_0+\varepsilon}}$. □

Now, we are able to formulate the inverse EEG problem for the multiple-shell model. We assume that the reference potential for the voltage difference is equal to zero.

Problem 10.2 (The EEG Problem). *Let Assumption 3.2 with $L \geq 2$ hold true. In the inverse EEG problem, one is interested in finding the primary current $\boldsymbol{J}^{\mathrm{P}}$ from a finite set of measurements of the electric potential u_L on the scalp at the sensor positions $\{\boldsymbol{y}_\ell \in \mathbb{S}_{[\varrho_{L-1},\varrho_L]} \mid \ell = \ell_{\mathrm{M}}+1,\dots,\ell_{\mathrm{M}}+\ell_{\mathrm{E}}\}$. The relation between the neuronal current and the electric potential is given by*

$$\mathcal{A}_{\mathrm{E}}\boldsymbol{J}^{\mathrm{P}} = \sum_{\ell=1}^{\ell_{\mathrm{E}}} u_L(\boldsymbol{y}_{\ell_{\mathrm{M}}+\ell})\boldsymbol{\varepsilon}^\ell.$$

Note that $\boldsymbol{\varepsilon}^\ell$ for $\ell = 1,\dots,\ell_{\mathrm{E}}$ denotes the standard Cartesian basis in $\mathbb{R}^{\ell_{\mathrm{E}}}$. The EEG forward operator $\mathcal{T}_{\mathrm{E}}\colon \mathbf{L}_2(\mathbb{B}_{\varrho_0}) \to \mathrm{C}(\mathbb{S}_{[\varrho_{L-1},\varrho_L]})$ and the corresponding linear operator $\mathcal{A}_{\mathrm{E}}\colon \mathbf{L}_2(\mathbb{B}_{\varrho_0}) \to \mathbb{R}^{\ell_{\mathrm{E}}}$ are defined by

$$\left(\mathcal{T}_{\mathrm{E}}\boldsymbol{J}^{\mathrm{P}}\right)(\boldsymbol{y}) \coloneqq \int_{\mathbb{B}_{\varrho_0}} \boldsymbol{J}^{\mathrm{P}}(\boldsymbol{x}) \cdot \boldsymbol{k}_{\mathrm{E}}(\boldsymbol{x},\boldsymbol{y})\,\mathrm{d}\boldsymbol{x}, \qquad \boldsymbol{y} \in \mathbb{S}_{[\varrho_{L-1},\varrho_L]}, \tag{10.1}$$

$$\mathcal{A}_{\mathrm{E}}\boldsymbol{J}^{\mathrm{P}} \coloneqq \sum_{\ell=1}^{\ell_{\mathrm{E}}} \left(\mathcal{T}_{\mathrm{E}}\boldsymbol{J}^{\mathrm{P}}\right)(\boldsymbol{y}_{\ell_{\mathrm{M}}+\ell})\boldsymbol{\varepsilon}^\ell. \tag{10.2}$$

The occurring kernel is given in Lemma 6.10, that is

$$\boldsymbol{k}_{\mathrm{E}}(\boldsymbol{x},\boldsymbol{y}) = \frac{1}{4\pi}\sum_{k=1}^{\infty} \sqrt{k(2k+1)^3} H_k(y) x^{k-1} \tilde{\boldsymbol{p}}_k^{(2)}(\hat{\boldsymbol{x}},\hat{\boldsymbol{y}}), \qquad (\boldsymbol{x},\boldsymbol{y}) \in \mathbb{B}_{\varrho_0} \times \mathbb{S}_{[\varrho_{L-1},\varrho_L]}.$$

Note that the counter for the sensor positions starts at $\ell_{\mathrm{M}}+1$, where ℓ_M is the number of MEG measurements, in order to simplify a combination of the inverse MEG and EEG problem later.

For the next result, recall the definition of the orthonormal vector-valued basis functions on the ball in Definition 5.37, in which the sequence $\{t_n\}_{n\in\mathbb{N}}$ occurs. The used scalar-valued basis functions on the interval $[0,\varrho_0]$ are given in Definition 5.1. In addition, Edmonds vector spherical harmonics, see Definition 5.9, are used. Now, we are able to present the direct solution of the EEG problem. Thus, we use the Edmonds approach in order to solve the EEG problem.

Theorem 10.3. *Let Assumption 3.2 with $L \geq 2$ be fulfilled. Then $\boldsymbol{J}^{\mathrm{P}}$ can be expanded as*

$$\boldsymbol{J}^{\mathrm{P}} = \sum_{i=1}^{3}\sum_{m=0}^{\infty}\sum_{n=0_i}^{\infty}\sum_{j=1}^{2n+1} J^\wedge[i,m,n,j]\tilde{\boldsymbol{g}}_{m,n,j}^{(i)}(\varrho_0;\cdot)$$

with $t_n \coloneqq n-1$ and we define for $i = 1,\ 2,\ 3$, $n \in \mathbb{N}_{0_i}$, and $j = 1,\dots,2n+1$ the functions

$$J_{n,j}^{(i),\sim} \coloneqq \sum_{m=0}^{\infty} J^\wedge[i,m,n,j] Q_m^{(n-1/2)}(\varrho_0;\cdot).$$

In addition, the electric potential on the scalp has for all $\boldsymbol{y} \in \mathbb{S}_{[\varrho_{L-1},\varrho_L]}$ the representation

$$u_L(\boldsymbol{y}) = \int_{\mathbb{B}_{\varrho_0}} \boldsymbol{J}^{\mathrm{P}}(\boldsymbol{x}) \cdot \boldsymbol{k}_{\mathrm{E}}(\boldsymbol{x},\boldsymbol{y})\,\mathrm{d}\boldsymbol{x} \tag{10.3a}$$

$$= \sum_{n=1}^{\infty}\sum_{j=1}^{2n+1} \varrho_0^{n+1/2} J^\wedge[2,0,n,j]\sqrt{n} H_n(y) Y_{n,j}(\hat{\boldsymbol{y}}) \tag{10.3b}$$

$$= \sum_{n=1}^{\infty}\sum_{j=1}^{2n+1} \sqrt{n(2n+1)} H_n(y) \int_0^{\varrho_0} J_{n,j}^{(2),\sim}(x) x^{n+1}\,\mathrm{d}x Y_{n,j}(\hat{\boldsymbol{y}}). \tag{10.3c}$$

The occurring series converges absolutely and uniformly.

Proof. By means of Theorem 7.27, we define with $\iota = 2$ and for all $n \in \mathbb{N}$ the quantities $\gamma_n(y) \coloneqq (4\pi)^{-1}\sqrt{n(2n+1)^3}H_n(y)$ and $t_n \coloneqq n-1$, where the domain of the former is $\boldsymbol{y} \in \mathbb{B}^{\text{ext}}_{\varrho_0+\varepsilon}$ with $\varepsilon \coloneqq \varrho_{L-1} - \varrho_0$. Therefore, the equations hold true for all $\boldsymbol{y} \in \mathbb{S}_{[\varrho_{L-1},\varrho_L]}$ in particular. □

In contrast to the MEG operator from Chapter 9, the EEG operator $\mathcal{T}_{\text{E}}$ maps into a range of functions over the spherical shell $\mathbb{S}_{[\varrho_{L-1},\varrho_L]}$. The EEG sensors need to be attached non-invasively onto the head, since the electric potential cannot be measured in the circumambient air, which is a really bad conductor. The conductivity of the air is modelled as zero, see also the note after Assumption 3.2. Note that the outer shell $\mathbb{S}_{[\varrho_{L-1},\varrho_L]}$ does not necessarily need to be the scalp or a part of it. The outer shell can also model a layer of paste used for the attachment. However, the paste is not attached equally around the entire head which will then lead to a model error.

In the literature, the electric potential u_L is often restricted onto the sphere $\mathbb{S}_{\varrho_L}$. In this case, we get

$$u_L(\varrho_L\hat{\boldsymbol{y}}) = \sum_{n=0}^{\infty}\sum_{j=1}^{2n+1} u_L^{\wedge}(n,j)\frac{1}{\varrho_L}Y_{n,j}(\hat{\boldsymbol{y}}), \qquad \hat{\boldsymbol{y}} \in \mathbb{S}.$$

Here, the Fourier coefficients are given for all $n \in \mathbb{N}$, $j = 1,\dots,2n+1$ by

$$\begin{aligned} u_L^{\wedge}(n,j) &\coloneqq \left\langle u_L|_{\mathbb{S}_{\varrho_L}}, \frac{1}{\varrho_L}Y_{n,j}\right\rangle_{\mathrm{L}_2(\mathbb{S}_{\varrho_L})} \\ &= \varrho_L\sqrt{n(2n+1)}H_n(\varrho_L)\int_0^{\varrho_0} J_{n,j}^{(2),\sim}(x)x^{n+1}\,\mathrm{d}x \qquad (10.4a) \\ &= \frac{\varrho_0^{n+1/2}}{\varrho_L^n}\frac{2n+1}{\sqrt{n}}\beta_n^{(L)}J^{\wedge}[2,0,n,j] \qquad (10.4b) \end{aligned}$$

and $u_L^{\wedge}(0,1) = 0$.

By solving Eq. (10.4b) for $\beta_n^{(L)}$ for all $n \in \mathbb{N}$, we are able to state the next relation for all $n \in \mathbb{N}$, $j = 1,\dots,2n+1$ by means of H_n from Eq. (4.20), that is

$$\begin{aligned} J^{\wedge}[2,0,n,j]H_n(y) &= J^{\wedge}[2,0,n,j]\left(\frac{n+1}{n}\left(\frac{y}{\varrho_L}\right)^{2n+1}+1\right)\beta_n^{(L)}\frac{1}{y^{n+1}} \\ &= \frac{1}{2n+1}\left(\frac{n+1}{n}\left(\frac{y}{\varrho_L}\right)^{2n+1}+1\right)\frac{1}{y^{n+1}}\left(\frac{\varrho_L}{\varrho_0}\right)^n\sqrt{\frac{n}{\varrho_0}}u_L^{\wedge}(n,j). \end{aligned}$$

Due to this formula, we observe that the electric potential in the shell $\mathbb{S}_{[\varrho_{L-1},\varrho_L]}$ is completely known if it is known on the sphere $\mathbb{S}_{\varrho_L}$. A similar result is also known for the Earth's magnetic field, see [12]. Thus, a consequence of the previous result is the next theorem.

Theorem 10.4. *Let the assumptions of Theorem 10.3 be fulfilled. Then the electric potential has for all $\boldsymbol{y} \in \mathbb{S}_{[\varrho_{L-1},\varrho_L]}$ the representation*

$$u_L(\boldsymbol{y}) = \sum_{n=0}^{\infty}\sum_{j=1}^{2n+1}\left(\frac{n+1}{2n+1}\left(\frac{y}{\varrho_L}\right)^{2n+1}+\frac{n}{2n+1}\right)\left(\frac{\varrho_L}{y}\right)^n u_L^{\wedge}(n,j)\frac{1}{y}Y_{n,j}(\hat{\boldsymbol{y}}) \qquad (10.5)$$

with $u_L^{\wedge}(0,1) = 0$. *For all* $n \in \mathbb{N}$ *and* $j = 1, \ldots, 2n+1$, *we have*

$$u_L^{\wedge}(n,j) = \frac{1}{\varrho_L^n} \sqrt{\frac{(2n+1)^3}{n}} \beta_n^{(L)} \int_0^{\varrho_0} J_{n,j}^{(2),\sim}(x) x^{n+1} \, \mathrm{d}x.$$

In this part, we defined three particular classes of integral kernels, which are related to each other, namely the continuous VLI, the star-shaped VLI, and the harmonic VLI kernels. We analyzed these kernels in detail and defined corresponding integral operators, which are well-defined. We stated certain examples of these kernels, such as the MEG and EEG integral kernel, which we are mainly interested in. Eventually, we solved the direct problems related to these integral equations in the general setting as well as for the particular problems.

Since we have now solved the direct problem, we are interested in a solution of the inverse problem, that is a solution of the integral equation itself.

Part III.

Solving the Inverse Problem

Chapter 11.

Introduction to Inverse Problems

A large class of mathematical and physical problems are the inverse problems. A broad overview is given in [63, 148, 194], for instance. Whereas direct problems calculate an effect from a given cause, inverse problems infer the cause from observed effects. Important examples are the calculation of the evolution backwards in time and the calculation of physical quantities in some medium by means of knowledge from outside of the medium. The last problem class includes the inverse gravimetric problem and the inverse electroencephalography problem, both of which are discussed in this thesis. In all cases, the solution f is mapped onto the data g by means of the corresponding forward operator $\mathcal{T}$, that is $\mathcal{T}f = g$. The domain of the operator $\operatorname{dom}\mathcal{T}$ is a subset of $\mathcal{X}$ and the range of the operator $\operatorname{ran}\mathcal{T}$ is a subset of $\mathcal{Y}$, where $\mathcal{X}$ and $\mathcal{Y}$ are certain spaces. We denote the null space of the operator $\mathcal{T}$ by $\ker\mathcal{T} \subset \mathcal{X}$.

Inverse problems are discussed in detail in [34, 63, 100, 102, 127, 136, 148, 193, 194], for instance. Further foundations of functional analysis can be found in [124, 142, 198]. Here, we summarize the essential results required for the analysis of the inverse magneto-electroencephalography problem.

Most inverse problems have in common that they are ill-posed or improperly posed problems because of the discontinuity of the mapping from the data to the solution. Other reasons for the ill-posedness are the non-uniqueness of the solution or the lack of a solution of the problem. A well-known characterization of ill-posed problems goes back to Hadamard, see [106, 107].

Definition 11.1 (Ill-Posedness (Hadamard), [148, Def. 1.1.1]). *Let $\mathcal{X}$, $\mathcal{Y}$ be normed spaces and let $\mathcal{T}\colon \mathcal{X} \to \mathcal{Y}$ be a mapping between them. The problem $(\mathcal{T}, \mathcal{X}, \mathcal{Y})$ is* well-posed *if the following properties hold true:*

i) The equation $\mathcal{T}f = g$ has a solution f for every $g \in \mathcal{Y}$;

ii) the solution f is uniquely determined;

iii) the solution f depends continuously on the data.

If one of these properties is violated, the problem is ill-posed.

In order to solve ill-posed inverse problems, one is interested in a best fitting solution. If $\operatorname{ran}\mathcal{T} \neq \mathcal{Y}$, then the equation $\mathcal{T}f = g$ does not necessarily have a solution for all $g \in \mathcal{Y}$.

Definition 11.2 ([63, Def. 2.1]). *Let $\mathcal{X}$, $\mathcal{Y}$ be normed spaces and let $\mathcal{T}\colon \mathcal{X} \to \mathcal{Y}$ be a bounded linear operator.*

i) The element $f^* \in \mathcal{X}$ is called the least-squares solution *of $\mathcal{T}f^* = g$ if*

$$\|\mathcal{T}f^* - g\|_{\mathcal{X}} = \inf_{f\in\mathcal{X}} \|\mathcal{T}f - g\|_{\mathcal{X}}\,.$$

ii) The function f^+ is called best-approximate solution *of $\mathcal{T}f^+ = g$ if it is a least-squares solution with*

$$f^+ \coloneqq \inf \{\|f\|_{\mathcal{X}} \mid f \text{ is a least-squares solution of } \mathcal{T}f = g\} .$$

The solution f^+ is a least-squares solution if and only if it is a solution of the *normal equation*, that is $\mathcal{T}^*\mathcal{T}f^+ = \mathcal{T}^*g$, see [63, Thm. 2.6]. We will later see, that the best-approximate solution is unique if $g \in \operatorname{ran}\mathcal{T} \oplus (\operatorname{ran}\mathcal{T})^\perp$. This can be further characterized by means of the well-known Moore-Penrose inverse operator.

Definition 11.3 (Moore-Penrose Inverse, [63, Def. 2.2]). *Let $\mathcal{X}$, $\mathcal{Y}$ be Hilbert spaces and let $\mathcal{T}\colon \mathcal{X} \to \mathcal{Y}$ be a bounded linear operator. Then the generalized inverse or* Moore-Penrose inverse *$\mathcal{T}^+$ of $\mathcal{T}$ is defined as the unique linear extension of $\bar{\mathcal{T}}^{-1}$ to*

$$\operatorname{dom}\mathcal{T}^+ \coloneqq \operatorname{ran}\mathcal{T} \oplus (\operatorname{ran}\mathcal{T})^\perp$$

with

$$\ker\mathcal{T}^+ = (\operatorname{ran}\mathcal{T})^\perp ,$$

where

$$\bar{\mathcal{T}} \coloneqq \mathcal{T}|_{(\ker\mathcal{T})^\perp}\colon (\ker\mathcal{T})^\perp \to \operatorname{ran}\mathcal{T}.$$

The Moore-Penrose inverse is closely related to the best-approximate solution and a least-squares solution.

Theorem 11.4 ([63, Thm. 2.5]). *Let $g \in \operatorname{dom}\mathcal{T}^+$. Then $\mathcal{T}f = g$ has a unique best-approximate solution, which is given by $f^+ = \mathcal{T}^+g$. The set of all least-squares solution is given by $f^+ + \ker\mathcal{T}$.*

Theorem 11.5 (Properties of the Moore-Penrose Inverse). *Let $\mathcal{X}$, $\mathcal{Y}$ be Hilbert spaces and $\mathcal{T}\colon \mathcal{X} \to \mathcal{Y}$ be a bounded linear operator. The Moore-Penrose inverse $\mathcal{T}^+$ satisfies the following properties:*

i) Let $g \in \operatorname{dom}\mathcal{T}^+$. Then $f \in \mathcal{X}$ is a least-squares solution of $\mathcal{T}f = g$ if and only if the normal equation *$\mathcal{T}^*\mathcal{T}f = \mathcal{T}^*$ holds true, see [63, Thm. 2.6].*

ii) The space $\mathcal{Y}$ can be decomposed into $\mathcal{Y} = \operatorname{ran}(\mathcal{T}) \oplus (\operatorname{ran}\mathcal{T})^\perp$ if and only if the range of $\mathcal{T}$ is closed, see [194, Thm. 2.1.8].

iii) The range of the Moore-Penrose inverse can also be represented by $\operatorname{ran}\mathcal{T}^+ = (\ker\mathcal{T})^\perp$, see [63, Prop. 2.3].

iv) The Moore-Penrose inverse $\mathcal{T}^+$ is continuous and, hence, bounded if and only if the range of $\mathcal{T}$ is closed, see [63, Prop. 2.4].

Based on these properties of the Moore-Penrose inverse, another characterization of ill-posed problems is given. In [194, Ch. 2.1], it is stated that only the cases remain interesting where $\mathcal{T}^+$ is unbounded.

Definition 11.6 (Ill-Posedness (Nashed), [177]). *Let $\mathcal{X}$, $\mathcal{Y}$ be normed spaces and let $\mathcal{T}\colon \mathcal{X} \to \mathcal{Y}$ be a mapping between them. The problem $(\mathcal{T}, \mathcal{X}, \mathcal{Y})$ is* ill-posed according to Nashed *if* $\operatorname{ran}\mathcal{T} \neq \overline{\operatorname{ran}\mathcal{T}}$.

A large class of inverse problems is generated by compact operators.

Definition 11.7 (Compact Operator [224, Ch. X]). *Let $\mathcal{X}$, $\mathcal{Y}$ be normed spaces and let $\mathcal{T}\colon \mathcal{X} \to \mathcal{Y}$ be a linear operator. The operator $\mathcal{T}$ is called compact if $\mathcal{T}\mathbb{B}_{\mathcal{X}}$ is relatively compact in $\mathcal{Y}$, where $\mathbb{B}_{\mathcal{X}}$ denotes the unit ball in $\mathcal{X}$.*

A linear operator $\mathcal{T}$ is called compact if the image of every closed ball in $\mathcal{X}$ is relatively compact in $\mathcal{Y}$. By means of basic functional analysis properties, it is easy to verify that compact operators cannot have a bounded inverse if the range is infinite-dimensional. Thus, at least one property from Hadamard's characterization is violated.

Lemma 11.8 ([198, Thm. 4.18]). *Let $\mathcal{T}\colon \mathcal{X} \to \mathcal{Y}$ be a compact operator between two normed spaces. In addition, let $\mathcal{X}$ be infinite-dimensional. Then $\mathcal{T}$ cannot have a bounded inverse.*

Corollary 11.9 ([63, Prop. 2.7]). *Let $\mathcal{T}\colon \mathcal{X} \to \mathcal{Y}$ be a compact operator between two normed spaces. In addition, let $\mathcal{X}$ be infinite-dimensional. Then $\mathcal{T}^+$ is a densely defined unbounded linear operator with closed graph.*

On the other hand, compact operators between Hilbert spaces provide us with a useful tool for solving the inverse problem, that is the singular value expansion of an operator given by the Spectral Theorem. The singular value expansion can be understood as the infinite-dimensional analogue of the well-known singular value decomposition for matrices. Therefore, we use SVD as its abbreviation.

Theorem 11.10 (Spectral Theorem, [63, Ch. 2.2]). *Let $\mathcal{X}$, $\mathcal{Y}$ be Hilbert spaces and let $\mathcal{T}\colon \mathcal{X} \to \mathcal{Y}$ be a compact operator. Then there exist an orthonormal system $\{f_k\}_{k\in\mathbb{N}}$ of $\mathcal{X}$, an orthonormal system $\{g_k\}_{k\in\mathbb{N}}$ of $\mathcal{Y}$, and a decreasing sequence of numbers with $\lambda_1 \geq \lambda_2 \geq \ldots > 0$ and $\lim_{k\to\infty} \lambda_k = 0$ such that*

$$\mathcal{T}f = \sum_{k=1}^{\infty} \lambda_k \langle f, f_k\rangle_{\mathcal{X}} g_k \qquad \text{for all } f \in \mathcal{X}. \tag{11.1}$$

More precisely, λ_k^2 are the eigenvalues of the self-adjoint operator $\mathcal{T}^*\mathcal{T}$ and λ_k are called singular values *of $\mathcal{T}$. The set $\{f_k, g_k; \lambda_k\}_{k\in\mathbb{N}}$ is called the* singular system.

The expansion in Eq. (11.1) is called a *singular value decomposition* or sometimes a *singular value expansion*. Note that the singular values are often assumed to be positive as in Theorem 11.10. However, for a given expansion as in Eq. (11.1) that also has negative values of λ_k for some (or all) $k \in \mathbb{N}$, we can always make the singular values positive by flipping the sign of the corresponding orthonormal basis functions. In addition, $\{f_k\}_{k\in\mathbb{N}}$ is an orthonormal basis in $(\ker\mathcal{T})^\perp$ and $\{g_k\}_{k\in\mathbb{N}}$ is an orthonormal basis in $\overline{\operatorname{ran}\mathcal{T}}$.

Corollary 11.11 ([63, p. 37]). *Let $\mathcal{X}$, $\mathcal{Y}$ be Hilbert spaces and let $\mathcal{T}\colon \mathcal{X} \to \mathcal{Y}$ be a compact operator with the SVD from Eq.* (11.1)*. Then its adjoint operator $\mathcal{T}^*\colon \mathcal{Y} \to \mathcal{X}$ defined by*

$$\langle \mathcal{T}f, g\rangle_{\mathcal{Y}} = \langle f, \mathcal{T}^* g\rangle_{\mathcal{X}} \qquad \text{for all } (f, g) \in \mathcal{X} \times \mathcal{Y}$$

has the SVD

$$\mathcal{T}^* g = \sum_{k=1}^{\infty} \lambda_k \langle g, g_k \rangle_{\mathcal{Y}} f_k \qquad \text{for all } g \in \mathcal{Y}.$$

Recall that, according to [198, Thm. 4.12], the range of a bounded, linear operator between two Hilbert spaces and the null space of its adjoint are related by

$$\ker \mathcal{T}^* = (\operatorname{ran} \mathcal{T})^{\perp}, \qquad (\ker \mathcal{T})^{\perp} = \overline{\operatorname{ran} \mathcal{T}^*}. \tag{11.2}$$

Using the SVD, the Moore-Penrose inverse can be derived by inverting the singular values.

Theorem 11.12 ([63, Thm. 2.8]). *Let $\mathcal{X}$, $\mathcal{Y}$ be Hilbert spaces and let $\mathcal{T}\colon \mathcal{X} \to \mathcal{Y}$ be a compact linear operator. Let $\{f_k, g_k; \lambda_k\}_{k\in\mathbb{N}}$ be the corresponding singular system and $g \in \operatorname{dom} \mathcal{T}^+$. Then the singular value expansion of $\mathcal{T}^+$ is given by*

$$\mathcal{T}^+ g = \sum_{k=1}^{\infty} \lambda_k^{-1} \langle g, g_k \rangle_{\mathcal{Y}} f_k.$$

Often, the condition $g \in \operatorname{ran} \mathcal{T}$ is hard to verify. However, $g \in \operatorname{ran} \mathcal{T}$ if and only if $g \in \overline{\operatorname{ran} \mathcal{T}}$ and a summability condition called *Picard's criterion* is fulfilled.

Theorem 11.13 (Picard's Criterion, [63, Thm. 2.8]). *Let $\mathcal{X}$, $\mathcal{Y}$ be Hilbert spaces and let $\mathcal{T}\colon \mathcal{X} \to \mathcal{Y}$ be a compact linear operator with singular system $\{f_k, g_k; \lambda_k\}_{k\in\mathbb{N}}$. Then $\mathcal{T} f = g$ has a solution if and only if $g \in \overline{\operatorname{ran} \mathcal{T}} = (\ker \mathcal{T}^*)^{\perp}$ and Picard's criterion, that is*

$$\sum_{k=1}^{\infty} \lambda_k^{-2} \left| \langle g, g_k \rangle_{\mathcal{Y}} \right|^2 < \infty,$$

is fulfilled.

If the singular values decay faster, Picard's criterion forces a stricter condition on the decay of the Fourier coefficients of g, see, for instance, [63, p. 40]. This allows to characterize the degree of ill-posedness of the problem $\mathcal{T} f = g$. A problem is called mildly (modestly) ill-posed if $\lambda_n \in \mathcal{O}(n^{-\alpha})$ for some $\alpha \in \mathbb{R}^+$, and severely ill-posed otherwise, that is if $\lambda \in \mathcal{O}(e^{-n})$, see also [148, 214].

Chapter 12.

Ill-Posedness of the VLI Problem

12.1. Continuous and Star-shaped Problem

Now, we are interested in the solution of the inverse magneto-electroencephalography problem. Again, in order to solve the inverse MEG problem as well as the inverse EEG problem at once, we first consider the ill-posedness of the continuous/star-shaped VLI problem. The inverse problem induced by the continuous/star-shaped VLI operator is the reconstruction or calculation of the density $\boldsymbol{f}$ from a given potential V. Definition 11.1 presents a criterion according to Hadamard to decide whether an inverse problem is ill-posed or not.

By means of the representation of $\mathcal{T}\boldsymbol{f}$ in Theorem 7.26, we can prove that the operator $\mathcal{T}$ is compact, even if the region $\mathbb{G}_{\text{out}}$ is not compact. In [97], the compactness of a Fredholm integral operator is shown using certain assumptions that are violated by the continuous/ star-shaped VLI operator. Via the alternative proof of the next theorem, this result can be conserved due to the special structure of the integral kernel. Consequently, the inverse problem $\mathcal{T}\boldsymbol{f} = V$ is ill-posed.

Theorem 12.1. *The continuous/star-shaped VLI operator* $\mathcal{T}\colon \mathbf{L}_2(\mathbb{B}_R) \to \mathrm{L}_2(\mathbb{G}_{\text{out}})$ *is compact and nuclear.*

Proof. Due to [225, Ch. X.2], each nuclear operator is compact. Thus, it remains to prove that $\mathcal{T}$ is a nuclear operator, that is $\mathcal{T}\boldsymbol{f}$ has for all $\boldsymbol{f} \in \mathbf{L}_2(\mathbb{B}_R)$ in $\mathrm{L}_2(\mathbb{G}_{\text{out}})$ the strongly convergent representation

$$\mathcal{T}\boldsymbol{f} \overset{\mathbf{L}_2(\mathbb{B}_R)}{=} \sum_{l=0}^{\infty} c_l \langle \boldsymbol{f}, \boldsymbol{f}_l \rangle_{\mathbf{L}_2(\mathbb{B}_R)} g_l,$$

where $\{\boldsymbol{f}_l\}_{l\in\mathbb{N}_0} \subset \mathbf{L}_2(\mathbb{B}_R)$, $\{g_l\}_{l\in\mathbb{N}_0} \subset \mathrm{L}_2(\mathbb{G}_{\text{out}})$, and $\{c_l\}_{l\in\mathbb{N}_0} \subset \mathbb{R}$ are sequences fulfilling

$$\sup_{l\in\mathbb{N}_0} \|g_l\|_{\mathrm{L}_2(\mathbb{G}_{\text{out}})} < \infty, \quad \sup_{l\in\mathbb{N}_0} \|\boldsymbol{f}_l\|_{\mathbf{L}_2(\mathbb{B}_R)} < \infty, \quad \sum_{l=0}^{\infty} |c_l| < \infty.$$

Since $\mathbf{L}_2(\mathbb{B}_R)$ is a Hilbert space, the operator $\mathcal{T}$ has the required series representation, see Eq. (7.14). In our particular setting, the above stated conditions can be represented by

- $\sup_{n,j} \|\boldsymbol{g}_{0,n,j}^{(\iota)}\|_{\mathbf{L}_2(\mathbb{B}_R)} < \infty$,
- $\sup_{n,j} \|(n+1)^2 R^n \gamma_n(|\cdot|) Y_{n,j}(\hat{\cdot})\|_{\mathrm{L}_2(\mathbb{G}_{\text{out}})} < \infty$, and
- $\sum_{n=0_\iota}^{\infty} |\frac{R^{t_n - n + 3/2}}{(n+1)^2\sqrt{2t_n+3}}| < \infty$.

The first condition is immediately satisfied due to the normalization property of the orthonormal basis functions. The second condition is implied by the asymptotic behaviour of the functions γ_n, where $n \in \mathbb{N}_{0_\iota}$. The last condition is fulfilled due to the assumptions on the sequence $\{t_n\}_{n\in\mathbb{N}_{0_\iota}}$. Finally, the series from Eq. (7.14) has to converge strongly in the $\mathrm{L}_2(\mathbb{G}_{\mathrm{out}})$-topology, which is established by Theorem 7.26. □

In order to find a 'solution', we need to analyze this ill-posedness of the continuous/star-shaped VLI problem in detail. Such a sought solution could be the best-approximate solution of the inverse problem, for example. We start with the non-injectivity and characterize the null space by means of the previous results. Recall the representation of the potential $\mathcal{T}\boldsymbol{f}$ from Eq. (7.14), that is

$$(\mathcal{T}\boldsymbol{f})(\boldsymbol{y}) = 4\pi \sum_{n=0_\iota}^{\infty} \sum_{j=1}^{2n+1} \frac{R^{t_n+3/2}}{(2n+1)\sqrt{2t_n+3}} f^\wedge(\iota,0,n,j)\gamma_n(y)Y_{n,j}(\hat{\boldsymbol{y}}).$$

Note that the parameter ι is determined by the actual problem at hand. The density $\boldsymbol{f}$ has the $\mathbf{L}_2(\mathbb{B}_R)$-convergent Fourier expansion

$$\boldsymbol{f} = \sum_{i=1}^{3} \sum_{m=0}^{\infty} \sum_{n=0_i}^{\infty} \sum_{j=1}^{2n+1} f^\wedge(i,m,n,j)\boldsymbol{g}_{m,n,j}^{(i)}(R;\cdot).$$

Obviously, only the summands for $i = \iota$ and $m = 0$ occur in the representation of $\mathcal{T}\boldsymbol{f}$. The other summands have no influence on the potential. Thus, the continuous/star-shaped VLI operator $\mathcal{T}\colon \mathbf{L}_2(\mathbb{B}_R) \to \mathrm{L}_2(\mathbb{G}_{\mathrm{out}})$ is not injective and, hence, $\ker\mathcal{T} \neq \{0\}$. We can characterize the orthogonal complement of the operator null space as follows.

Lemma 12.2. *Let $\mathcal{T}\colon \mathbf{L}_2(\mathbb{B}_R) \to \mathrm{L}_2(\mathbb{G}_{\mathrm{out}})$ be the continuous/star-shaped VLI operator with $\mathbb{G}_{\mathrm{in}} \coloneqq \mathbb{B}_R$, then*

$$(\ker\mathcal{T})^\perp = \overline{\operatorname{span}\left\{\boldsymbol{g}_{0,n,j}^{(\iota)}(R;\cdot) \;\middle|\; n \in \{n' \in \mathbb{N}_{0_\iota}, \gamma_{n'} \not\equiv 0\},\ j = 1,\dots,2n+1\right\}}. \tag{12.1}$$

Consequently, $(\ker\mathcal{T})^\perp$ is a proper subset of $\mathbf{L}_2(\mathbb{B}_R)$ and $\mathcal{T}$ is not injective.

In order to find a representation of the best-approximate solution, one is interested in the SVD of the operator $\mathcal{T}$, see Theorem 11.12. The SVD of the continuous/star-shaped VLI operator exists because $\mathcal{T}$ is compact, see Theorem 11.10. However, we are not able to formulate the SVD in this general setting, but we can consider the restriction of $\mathcal{T}$ to a sphere $\mathbb{S}_r$. This particular case is of interest, since in many applications the data is collected from (approximately) spherical sensor arrangements, such as satellite orbits, magnetoencephalography devices, or electroencephalography sensor caps, see [87, 108] and the references therein.

Definition 12.3. *Let $r \geq \inf_{\boldsymbol{y}\in\mathbb{G}_{\mathrm{out}}} y > R$ be an arbitrary radius. Let for all $k \in \mathbb{N}_{0_\iota}$ the functions γ_k from Definition 6.1 be continuously extendable for $y = r$. Then the restricted operator $\mathcal{T}|_{\mathbb{S}_r}\colon \mathbf{L}_2(\mathbb{B}_R) \to \mathrm{L}_2(\mathbb{S}_r)$ is defined by*

$$\mathcal{T}|_{\mathbb{S}_r}\boldsymbol{f} \coloneqq \left(\int_{\mathbb{B}_R} \boldsymbol{f}(\boldsymbol{x}) \cdot \boldsymbol{k}^{(\iota)}(\boldsymbol{x},\cdot)\,\mathrm{d}\boldsymbol{x}\right)\Big|_{\mathbb{S}_r}, \tag{12.2}$$

$$(\mathcal{T}|_{\mathbb{S}_r}\boldsymbol{f})(\boldsymbol{y}) = 4\pi \sum_{n=0_\iota}^{\infty} \sum_{j=1}^{2n+1} \frac{R^{t_n+3/2}}{(2n+1)\sqrt{2t_n+3}} f^\wedge(\iota,0,n,j)\gamma_n(r)Y_{n,j}(\hat{\boldsymbol{y}}),$$

where $\boldsymbol{k}^{(\iota)}$ is the continuous/star-shaped VLI kernel from Definition 6.1.

It is possible that $\mathbb{S}_r$ is not a proper subset of $\mathbb{G}_{\text{out}}$. However, for the the calculation of the direct solution and the convergence statements this is not a problem, since $r \geq \inf_{\boldsymbol{y}\in\mathbb{G}_{\text{out}}} y > R$. Thus, Theorem 7.26 is still valid in this case. This also implies the uniform convergence of the occurring series, which allows its pointwise evaluation in Definition 12.3. In addition, the potential $(\mathcal{T}|_{\mathbb{S}_r}\boldsymbol{f})(\boldsymbol{y})$ only depends on the angular part of $\boldsymbol{y}$ since $\boldsymbol{y} = r\hat{\boldsymbol{y}}$ for all $\boldsymbol{y} \in \mathbb{S}_r$. Hence, $\{\gamma_n(r)\}_{n\in\mathbb{N}_{0_\iota}}$ is only a sequence of constants depending on n.

By means of this definition, we are able to formulate the SVD of $\mathcal{T}|_{\mathbb{S}_r}$.

Theorem 12.4. *Let $\mathcal{T}|_{\mathbb{S}_r}\colon \mathbf{L}_2(\mathbb{B}_R) \to \mathrm{L}_2(\mathbb{S}_r)$ be the restricted operator defined in Definition 12.3. Then*

i) the orthogonal complement of the null space $(\ker \mathcal{T}|_{\mathbb{S}_r})^\perp \subset \mathbf{L}_2(\mathbb{B}_R)$ is given by

$$(\ker \mathcal{T}|_{\mathbb{S}_r})^\perp = \overline{\operatorname{span}\left\{\boldsymbol{g}_{0,n,j}^{(\iota)}(R;\cdot) \;\middle|\; n \in \{n' \in \mathbb{N}_{0_\iota}, \gamma_{n'}(r) \neq 0\},\ j = 1,\dots,2n+1\right\}}.$$

ii) $\{\boldsymbol{g}_{0,n,j}^{(\iota)}(R;\cdot)\}_{n\in\{n'\in\mathbb{N}_{0_\iota}|\gamma_{n'}(r)\neq 0\},j=1,\dots,2n+1}$ is an orthonormal basis for the orthogonal complement of the null space $(\ker \mathcal{T}|_{\mathbb{S}_r})^\perp \subset \mathbf{L}_2(\mathbb{B}_R)$,

iii) an orthonormal basis for $\mathrm{L}_2(\mathbb{S}_r)$ is given by $\{r^{-1}Y_{n,j}\}_{n\in\mathbb{N}_0,j=1,\dots,2n+1}$, and

iv) the singular values of $\mathcal{T}|_{\mathbb{S}_r}$ are given for all $n \in \{n' \in \mathbb{N}_{0_\iota} \mid \gamma_{n'}(r) \neq 0\}$ independent of j by

$$\lambda_n \coloneqq 4\pi r\sqrt{\frac{R^3}{2t_n+3}}\frac{R^{t_n}}{2n+1}\gamma_n(r).$$

Eventually, we obtain an SVD of $\mathcal{T}|_{\mathbb{S}_r}$, that is

$$\mathcal{T}|_{\mathbb{S}_r}\boldsymbol{f} = \sum_{n=0_\iota}^{\infty}\sum_{j=1}^{2n+1}\lambda_n\Big\langle \boldsymbol{f}, \boldsymbol{g}_{0,n,j}^{(\iota)}(R;\cdot)\Big\rangle_{\mathbf{L}_2(\mathbb{B}_R)}\frac{1}{r}Y_{n,j}.$$

Proof. The first statement is clear by combining the orthonormal basis from Lemma 5.38 with the characterization of the null space of $\mathcal{T}$, see Lemma 12.2. Due to Remark 2.27, an orthonormal basis for $\mathrm{L}_2(\mathbb{S}_r)$ is given by $\{r^{-1}Y_{n,j}\}_{n\in\mathbb{N}_0,j=1,\dots,2n+1}$. The forward operator has the Fourier series

$$\begin{aligned}(\mathcal{T}|_{\mathbb{S}_r}\boldsymbol{f})(\boldsymbol{y}) &= 4\pi \sum_{\substack{n=0_\iota\\ \gamma_n(r)\neq 0}}^{\infty}\sum_{j=1}^{2n+1}\frac{R^{t_n+3/2}}{(2n+1)\sqrt{2t_n+3}}f^\wedge(\iota,0,n,j)\gamma_n(r)Y_{n,j}(\hat{\boldsymbol{y}})\\ &= \sum_{\substack{n=0_\iota\\ \gamma_n(r)\neq 0}}^{\infty}\sum_{j=1}^{2n+1}4\pi r\gamma_n(r)\frac{R^{t_n+3/2}}{(2n+1)\sqrt{2t_n+3}}f^\wedge(\iota,0,n,j)\frac{1}{r}Y_{n,j}(\hat{\boldsymbol{y}}).\end{aligned}$$

□

By means of the Spectral Theorem for $\mathcal{T}|_{\mathbb{S}_r}$ and the Moore-Penrose inverse, we are able to further simplify the inverse problem of finding the density $\boldsymbol{f} \in \mathbf{L}_2(\mathbb{B}_R)$ for a given potential $V \in \mathrm{L}_2(\mathbb{S}_r)$ with $V = \mathcal{T}|_{\mathbb{S}_r}\boldsymbol{f}$. For this purpose, we investigate the behaviour of the singular values.

Corollary 12.5. *The singular values* $\{\lambda_n\}_{n\in\{n'\in\mathbb{N}_{0_\iota}\,|\,\gamma_{n'}(r)\neq 0\}}$ *of* $\mathcal{T}|_{\mathbb{S}_r}$ *stated in Theorem 12.4 form a sequence of non-zero real numbers converging to zero.*

Proof. Obviously, $\gamma_n(r) \neq 0$ for all $n \in \{n' \in \mathbb{N}_{0_\iota} \mid \gamma_{n'}(r) \neq 0\}$ and $R > 0$. Thus, each singular value λ_n is non-zero for all $n \in \{n' \in \mathbb{N}_{0_\iota} \mid \gamma_{n'}(r) \neq 0\}$. Due to the assumptions on $\{t_n\}_{n\in\{n'\in\mathbb{N}_{0_\iota}\,|\,\gamma_{n'}(r)\neq 0\}}$ and R, the estimate

$$\begin{aligned} 0 \leq |\lambda_n| &:= \left| 4\pi \sqrt{\frac{R^3}{2t_n+3}} \frac{R^{t_n} r}{2n+1} |\gamma_n(r)| \right| \\ &\leq 4\pi \sqrt{\frac{R^3}{2t_n+3}} \frac{R^{t_n} r}{2n+1} \frac{\Gamma_n}{r^{n+1+\delta_{0_\iota,0}\delta_{n,0}}} \\ &\leq 4\pi r \sup_{n\in\mathbb{N}_{0_\iota}} R^{t_n-n}\Gamma_n \sqrt{\frac{R^3}{2t_n+3}} \frac{R^n}{r^{n+1+\delta_{0_\iota,0}\delta_{n,0}}} \end{aligned}$$

holds true for all $n \in \{n' \in \mathbb{N}_{0_\iota} \mid \gamma_{n'}(r) \neq 0\}$. The right-hand side converges to zero as $R < r$, see Theorem 6.4. Using the Squeeze Theorem, we obtain $\lim_{n\to\infty} \lambda_n = 0$. □

By means of the SVD, we immediately obtain a representation of the unique best-approximate solution of the inverse problem.

Corollary 12.6. *According to Theorem 11.12, the unique best-approximate solution* $\boldsymbol{f}^+$ *of* $\mathcal{T}|_{\mathbb{S}_r}\boldsymbol{f} = V$ *for a potential* $V \in \operatorname{dom}\mathcal{T}|^+_{\mathbb{S}_r}$ *in the domain of the Moore-Penrose inverse* $\mathcal{T}|^+_{\mathbb{S}_r}$ *is given by*

$$\begin{aligned} \boldsymbol{f}^+ &= \mathcal{T}|^+_{\mathbb{S}_r} V \\ &= \frac{1}{4\pi} \sum_{\substack{n=0_\iota \\ \gamma_n(r)\neq 0}}^{\infty} \sum_{j=1}^{2n+1} \sqrt{\frac{2t_n+3}{R^3}} \frac{2n+1}{R^{t_n} r \gamma_n(r)} \left\langle V|_{\mathbb{S}_r}, \frac{1}{r} Y_{n,j} \right\rangle_{\mathrm{L}_2(\mathbb{S}_r)} \boldsymbol{g}^{(\iota)}_{0,n,j}(R;\cdot). \end{aligned}$$

Due to the asymptotic behaviour of $\{\lambda_n\}_{n\in\{n'\in\mathbb{N}_{0_\iota}\,|\,\gamma_{n'}(r)\neq 0\}}$, *we immediately obtain the lack of continuity of the operator* $\mathcal{T}|^+_{\mathbb{S}_r}$.

Recall that the domain of $\mathcal{T}|^+_{\mathbb{S}_r}$ is given by $\operatorname{dom}(\mathcal{T}|^+_{\mathbb{S}_r}) = \operatorname{ran}(\mathcal{T}|_{\mathbb{S}_r}) \oplus (\operatorname{ran}\mathcal{T}|_{\mathbb{S}_r})^\perp$.

In order to reconstruct the density $\boldsymbol{f}$ of $\mathcal{T}|_{\mathbb{S}_r}\boldsymbol{f} = V$, it is necessary and sufficient that the potential fulfils $V \in (\ker\mathcal{T}|^*_{\mathbb{S}_r})^\perp = \overline{\operatorname{ran}\mathcal{T}|_{\mathbb{S}_r}}$ and that Picard's criterion is satisfied.

Lemma 12.7. *Picard's criterion is given by*

$$\sum_{\substack{n=0_\iota \\ \gamma_n(r)\neq 0}}^{\infty} \sum_{j=1}^{2n+1} \lambda_n^{-2} \left\langle V|_{\mathbb{S}_r}, \frac{1}{r} Y_{n,j} \right\rangle^2_{\mathrm{L}_2(\mathbb{S}_r)} < \infty. \tag{12.3}$$

The problem $\mathcal{T}|_{\mathbb{S}_r}\boldsymbol{f} = V$ *has a solution if and only if* $V \in \overline{\operatorname{ran}\mathcal{T}|_{\mathbb{S}_r}}$ *and Eq.* (12.3) *holds true.*

In this section, we analyzed the null space of the continuous/star-shaped VLI operator and the SVD of its restriction onto a sphere in the outer region. For a harmonic VLI operator, we are also able to find an SVD in a larger outer region. This is investigated in the next section.

12.2. Harmonic VLI Problem

In the previous section, we found an SVD of the continuous/star-shaped VLI operator but only for the particular case of its restriction onto a sphere in the outer region. In Theorem 12.4, the SVD is stated and the convergence of the singular values to zero is proved in Corollary 12.5. Using the Spectral Theorem, the best-approximate solution $\boldsymbol{f}^+$ is stated in Corollary 12.6. These results naturally hold true for the harmonic VLI operator by setting $\gamma_n(y) \coloneqq \Gamma_n y^{-(n+1)}$ for $n \in \mathbb{N}$ and $\gamma_0 \equiv 0$.

In certain applications, it is not sufficient to analyze the restriction of an operator to a sphere. For example, satellite orbits or the magnetometer sensor positions are not located on a perfectly shaped sphere. However, in Section 12.1, we were not able to state a result for the non-restricted operator, since we were not able to find a Hilbert space and an orthonormal basis system for $\overline{\operatorname{ran}\mathcal{T}}$ in this general context, even though such a system must exist due to the compactness of $\mathcal{T}$, see Theorem 12.1.

Therefore, we now consider the case of the harmonic VLI operator, where the set of functions $\{\gamma_n\}_{n\in\mathbb{N}}$ is determined more precisely. If we additionally restrict ourselves to the case of $\mathbb{G}_{\text{out}} \coloneqq \overline{\mathbb{B}_r^{\text{ext}}}$ with $R < r < \infty$, we are able to find appropriate orthonormal basis systems and Hilbert spaces for $\overline{\operatorname{ran}\mathcal{T}}$ as well as for the operator mapping $\boldsymbol{f}$ onto the gradient field of the potential $\mathcal{T}\boldsymbol{f}$, that is $\boldsymbol{\nabla}(\mathcal{T}\boldsymbol{f})$.

In order to find the SVD for the non-restricted operator $\mathcal{T}$, we first construct appropriate Hilbert spaces in the domain and range of the operator. A Hilbert space in the domain of the operator, that is $\mathbf{L}_2(\mathbb{B}_R)$, has already been used for the continuous/star-shaped VLI operator. For the other Hilbert space, we construct an orthonormal basis by using a definition from [88, Ch. 10.8] that is repeated in the next lemma.

Lemma 12.8. *Let the outer space be given by the exterior of a sphere with radius $r > R$, that is $\mathbb{G}_{\text{out}} \coloneqq \overline{\mathbb{B}_r^{\text{ext}}}$ with $R < r < \infty$. On the outer space $\overline{\mathbb{B}_r^{\text{ext}}}$, the set of square-integrable harmonic functions*

$$\operatorname{Harm}\left(\overline{\mathbb{B}_r^{\text{ext}}}\right) \coloneqq \left\{ F \in \mathrm{C}^2\left(\overline{\mathbb{B}_r^{\text{ext}}}\right) \;\middle|\; \int_{\overline{\mathbb{B}_r^{\text{ext}}}} (F(\boldsymbol{y}))^2 \,\mathrm{d}\boldsymbol{y} < \infty,\ \Delta F = 0 \text{ in } \mathbb{B}_r^{\text{ext}} \right\}$$

is a closed subset of $\mathrm{L}_2(\overline{\mathbb{B}_r^{\text{ext}}})$. Moreover, the system that is comprised of the functions

$$S_{n,j}(r;\boldsymbol{x}) \coloneqq \sqrt{\frac{2n-1}{r}} H_{n,j}^{\text{ext}}(r;\boldsymbol{x}), \qquad \boldsymbol{x} \in \overline{\mathbb{B}_r^{\text{ext}}}$$

for $n \in \mathbb{N}$, $j = 1, \ldots, 2n+1$ constitutes a complete orthonormal system in the Hilbert space $(\operatorname{Harm}(\overline{\mathbb{B}_r^{\text{ext}}}), \langle\cdot,\cdot\rangle_{\mathrm{L}_2(\overline{\mathbb{B}_r^{\text{ext}}})})$.

Proof. The definition of the space $\operatorname{Harm}(\overline{\mathbb{B}_r^{\text{ext}}})$ can also be found in [88, Ch. 10.8]. Therein, it is stated that the system of outer harmonics $\{H_{n,j}^{\text{ext}}(r;\cdot)\}_{n\in\mathbb{N},j=1,\ldots,2n+1}$ constitutes a complete orthogonal system in $\operatorname{Harm}(\overline{\mathbb{B}_r^{\text{ext}}})$. Note that the function $H_{0,1}^{\text{ext}}(r;\cdot)$ is not an element of the space $\operatorname{Harm}(\overline{\mathbb{B}_r^{\text{ext}}})$, since it is not square-integrable with a finite norm. Thus, the system only needs to be normalized. For $n, m \in \mathbb{N}$, $j = 1, \ldots, 2n+1$, and $l = 1, \ldots, 2m+1$ we obtain the identity

$$\begin{aligned}\left\langle H_{n,j}^{\text{ext}}(r;\cdot), H_{m,l}^{\text{ext}}(r;\cdot)\right\rangle_{\mathrm{L}_2(\overline{\mathbb{B}_r^{\text{ext}}})} &= \int_{\mathbb{S}} Y_{n,j}(\hat{\boldsymbol{x}}) Y_{m,l}(\hat{\boldsymbol{x}}) \,\mathrm{d}\omega(\hat{\boldsymbol{x}}) \int_r^\infty \frac{r^{n+m}}{x^{n+m+2}} x^2 \,\mathrm{d}x \\ &= \delta_{m,n}\delta_{j,l} \frac{r}{2n-1}.\end{aligned}$$

□

Now, we have all components of the SVD at hand.

Theorem 12.9. *Let* $(\mathrm{Harm}(\overline{\mathbb{B}_r^{\mathrm{ext}}}), \langle\cdot,\cdot\rangle_{\mathrm{L}_2(\overline{\mathbb{B}_r^{\mathrm{ext}}})})$ *be defined as in Lemma 12.8. Let the operator* $\mathcal{T}$ *be given by*

$$\mathcal{T}\colon \boldsymbol{f} \mapsto \int_{\mathbb{B}_R} \boldsymbol{f}(\boldsymbol{x}) \cdot \boldsymbol{k}^{(\iota)}(\boldsymbol{x},\cdot)\,\mathrm{d}\boldsymbol{x}$$

with the harmonic VLI kernel $\boldsymbol{k}^{(\iota)}$ *from Definition 8.1. Then*

i) $\mathcal{T}\colon \mathbf{L}_2(\mathbb{B}_R) \to (\mathrm{Harm}(\overline{\mathbb{B}_r^{\mathrm{ext}}}), \langle\cdot,\cdot\rangle_{\mathrm{L}_2(\overline{\mathbb{B}_r^{\mathrm{ext}}})})$,

ii) an orthonormal basis for the orthogonal complement of the null space $(\ker\mathcal{T})^{\perp} \subset \mathbf{L}_2(\mathbb{B}_R)$ *is given by* $\{\boldsymbol{g}_{0,n,j}^{(\iota)}(R;\cdot)\}_{n\in\{n'\in\mathbb{N}\mid\Gamma_{n'}\neq 0\}\,,j=1,\dots,2n+1}$,

iii) an orthonormal basis for $(\mathrm{Harm}(\overline{\mathbb{B}_r^{\mathrm{ext}}}), \langle\cdot,\cdot\rangle_{\mathrm{L}_2(\overline{\mathbb{B}_r^{\mathrm{ext}}})})$ *is given by means of the basis from Lemma 12.8, that is* $\{S_{n,j}(r;\cdot)\}_{n\in\mathbb{N},j=1,\dots,2n+1}$, *and*

iv) the singular values of $\mathcal{T}$ *are given for all* $n \in \{n'\in\mathbb{N}\mid\Gamma_{n'}\neq 0\}$ *by*

$$\lambda_n := 4\pi \frac{\Gamma_n}{(2n+1)\sqrt{(2t_n+3)(2n-1)}} \frac{R^{t_n+3/2}}{r^{n-1/2}}.$$

Eventually, we obtain the SVD of the harmonic VLI operator $\mathcal{T}$, *that is*

$$\mathcal{T}\boldsymbol{f} = \sum_{\substack{n=1\\ \Gamma_n\neq 0}}^{\infty} \sum_{j=1}^{2n+1} \lambda_n \Big\langle \boldsymbol{f}, \boldsymbol{g}_{0,n,j}^{(\iota)}(R;\cdot)\Big\rangle_{\mathbf{L}_2(\mathbb{B}_R)} S_{n,j}(r;\cdot).$$

Proof. i) Theorem 8.7 provides us with the required smoothness and harmonicity of $\mathcal{T}\boldsymbol{f}$. The integrability is proved in Corollary 7.3.

ii) This statement is obviously fulfilled by Lemmas 5.38 and 12.2. Note that $\gamma_n \not\equiv 0$ implies $\Gamma_n \neq 0$ for all $n \in \mathbb{N}$ since $\gamma_n(y) = \Gamma_n y^{-(n+1)}$ and $y > R$, see also Lemma 8.2. Thus, $\ker\mathcal{T} \neq \{0\}$ and, hence, $\mathcal{T}$ is not injective.

iii) This statement has already been proved in Lemma 12.8.

iv) Due to Corollary 8.10 and Lemma 12.8, we obtain an expansion of $\mathcal{T}\boldsymbol{f}$ by

$$\begin{aligned}\mathcal{T}\boldsymbol{f} &= \sum_{n=1}^{\infty}\sum_{j=1}^{2n+1} V^{\wedge}(n,j) H_{n,j}^{\mathrm{ext}}(r;\cdot)\\ &= \sum_{n=1}^{\infty}\sum_{j=1}^{2n+1} V^{\wedge}(n,j)\sqrt{\frac{r}{2n-1}}\, S_{n,j}(r;\cdot).\end{aligned}$$

Note that $V^{\wedge}(n,j) = 0$ for all $n \in \{n'\in\mathbb{N}\mid\Gamma_{n'}=0\}$ and $j = 1,\dots,2n+1$. For all $n \in \{n'\in\mathbb{N}\mid\Gamma_{n'}\neq 0\}$ and $j = 1,\dots,2n+1$, the coefficients are given by

$$\begin{aligned}&\langle \mathcal{T}\boldsymbol{f}, S_{n,j}(r;\cdot)\rangle_{\mathrm{L}_2(\overline{\mathbb{B}_r^{\mathrm{ext}}})}\\ &= V^{\wedge}(n,j)\sqrt{\frac{r}{2n-1}}\\ &= 4\pi \frac{\Gamma_n}{(2n+1)\sqrt{(2t_n+3)(2n-1)}} \frac{R^{t_n+3/2}}{r^{n-1/2}} \Big\langle \boldsymbol{f}, \boldsymbol{g}_{0,n,j}^{(\iota)}(R;\cdot)\Big\rangle_{\mathbf{L}_2(\mathbb{B}_R)}.\end{aligned}$$

The singular values for all $n \in \{n' \in \mathbb{N} \mid \Gamma_{n'} = 0\}$ are, via Eq. (8.1), given by

$$\lambda_n = 4\pi \frac{\Gamma_n}{(2n+1)\sqrt{(2t_n+3)(2n-1)}} \frac{R^{t_n+3/2}}{r^{n-1/2}},$$

which are obviously finite non-zero numbers as $\inf_{n\in\mathbb{N},\Gamma_n\neq 0} t_n \geq -1$. □

Now, let $V = \mathcal{T}\boldsymbol{f}$ be the potential of $\boldsymbol{f}$. Due to Lemma 8.9, V is the unique solution of the corresponding exterior Dirichlet problem. By means of Lemma 2.32, it can be represented by an expansion in outer harmonics. Thus, we get

$$V(\boldsymbol{y}) = \sum_{n=1}^{\infty} \sum_{j=1}^{2n+1} V^{\wedge}(n,j) H_{n,j}^{\mathrm{ext}}(r;\boldsymbol{y}), \qquad \boldsymbol{y} \in \mathbb{G}_{\mathrm{out}},$$

with $V^{\wedge}(n,j) \coloneqq \langle V|_{\mathbb{S}_r}, r^{-1}Y_{n,j}\rangle_{\mathrm{L}_2(\mathbb{S}_r)}$ for all $n \in \mathbb{N}$, $j = 1,\ldots,2n+1$. Via Theorem 8.4 and orthogonality properties of the outer harmonics, the coefficients $V^{\wedge}(n,j)$ are given by

$$\begin{aligned} V^{\wedge}(n,j) &= \left\langle (\mathcal{T}\boldsymbol{f})|_{\mathbb{S}_r}, H_{n,j}^{\mathrm{ext}}(r;\cdot)|_{\mathbb{S}_r} \right\rangle_{\mathrm{L}_2(\mathbb{S}_r)} \\ &= 4\pi \frac{\Gamma_n}{(2n+1)\sqrt{2t_n+3}} \frac{R^{t_n+3/2}}{r^n} f^{\wedge}(\iota,0,n,j) \\ &= \sqrt{\frac{2n-1}{r}} \lambda_n f^{\wedge}(\iota,0,n,j) \end{aligned} \tag{12.4}$$

for all $n \in \mathbb{N}$ and $j = 1,\ldots,2n+1$. In addition, we have an relation between the Fourier coefficients and the outer harmonics coefficients, that is

$$\langle V, S_{n,j}(r;\cdot)\rangle_{\mathrm{L}_2(\overline{\mathbb{B}_r^{\mathrm{ext}}})} = \sqrt{\frac{r}{2n-1}} V^{\wedge}(n,j). \tag{12.5}$$

Furthermore, the SVD of $\mathcal{T}$ stated in Theorem 12.9 leads to the next theorem.

Theorem 12.10. *Let $\mathcal{T}\colon \mathbf{L}_2(\mathbb{B}_R) \to (\mathrm{Harm}(\overline{\mathbb{B}_r^{\mathrm{ext}}}), \langle\cdot,\cdot\rangle_{\mathrm{L}_2(\overline{\mathbb{B}_r^{\mathrm{ext}}})})$ be the harmonic VLI operator with the integral kernel defined in Definition 8.1. Then the inverse problem $\mathcal{T}\boldsymbol{f} = V$ of finding the density $\boldsymbol{f} \in \mathbf{L}_2(\mathbb{B}_R)$ to a given potential $V \in \operatorname{ran}\mathcal{T}$ is (severely) ill-posed, since the singular values of $\mathcal{T}$ decay exponentially fast to zero.*

Proof. The proof is mainly based on the SVD of $\mathcal{T}$. By means of the singular values λ_n for $n \in \{n' \in \mathbb{N} \mid \Gamma_{n'} \neq 0\}$ and the estimate $\inf_{n\in\mathbb{N},\Gamma_n\neq 0} t_n \geq -1$, we obtain

$$\begin{aligned} 0 \leq |\lambda_n| &= 4\pi \frac{|\Gamma_n|}{(2n+1)\sqrt{(2t_n+3)(2n-1)}} \frac{R^{t_n+3/2}}{r^{n-1/2}} \\ &\leq 4\pi \left(\sup_{n\in\mathbb{N}} R^{t_n-n} \right) \frac{|\Gamma_n|}{2n+1} \sqrt{\frac{R^3}{r(2t_n+3)(2n-1)}} \frac{R^n}{r^n}. \end{aligned}$$

Due to the assumption in Definition 8.1, the mapping $n \mapsto \Gamma_n$ is of polynomial growth in n at most. Hence, via the Squeeze Theorem, we get $\lim_{n\to\infty} \Gamma_n (R/r)^n = 0$. The singular values are exponentially decreasing, which implies a severely ill-posed problem. □

The singular values of the Moore-Penrose inverse operator are given by $\{\lambda_n^{-1}\}_{n\in\mathbb{N}}$, see Theorem 11.12, which immediately implies its unboundedness.

By means of the SVD and the adjoint operator $\mathcal{T}^*$, we are able to further characterize the closure of the operator range $\overline{\operatorname{ran}\mathcal{T}} = (\ker\mathcal{T}^*)^\perp$. The adjoint operator of a (Fredholm) integral operator between two Lebesgue spaces can be easily calculated by using Fubini's Theorem. Thus, we obtain the identity

$$\mathcal{T}^*V = \int_{\mathbb{B}_r^{\mathrm{ext}}} V(\boldsymbol{y})\boldsymbol{k}^{(\iota)}(\cdot,\boldsymbol{y})\,\mathrm{d}\boldsymbol{y}.$$

Alternatively, the representation of the adjoint operator $\mathcal{T}^*$ given by

$$\mathcal{T}^*V = \sum_{\substack{n=1\\ \Gamma_n\neq 0}}^{\infty}\sum_{j=1}^{2n+1} \lambda_n \langle V, S_{n,j}(r;\cdot)\rangle_{\mathrm{L}_2(\overline{\mathbb{B}_r^{\mathrm{ext}}})}\boldsymbol{g}_{0,n,j}^{(\iota)}(R,\cdot)$$

is an immediate consequence of the Spectral Theorem for the SVD of the adjoint operator, see Corollary 11.11. By means of the last formula, we get

$$(\ker\mathcal{T}^*)^\perp = \overline{\operatorname{span}\left\{S_{n,j}(r;\cdot) \mid n\in\{n'\in\mathbb{N}\mid \Gamma_{n'}\neq 0\},\ j=1,\dots,2n+1\right\}}. \tag{12.6}$$

Another consequence of the Spectral Theorem for the operator $\mathcal{T}$ is Picard's criterion, see Theorem 11.13, which complements the investigation of the SVD.

Corollary 12.11. *Let $\mathcal{T}\colon \mathbf{L}_2(\mathbb{B}_R) \to (\mathrm{Harm}(\overline{\mathbb{B}_r^{\mathrm{ext}}}), \langle\cdot,\cdot\rangle_{\mathrm{L}_2(\overline{\mathbb{B}_r^{\mathrm{ext}}})})$ be the harmonic VLI operator with the integral kernel defined in Definition 8.1. In addition, let the potential $V\in(\ker\mathcal{T}^*)^\perp$ be given. Then the inverse problem $\mathcal{T}\boldsymbol{f}=V$ of finding the density $\boldsymbol{f}$ has a unique best-approximate solution if and only if Picard's criterion holds, that is*

$$\begin{aligned}&\sum_{\substack{n=1\\ \Gamma_n\neq 0}}^{\infty}\sum_{j=1}^{2n+1} \lambda_n^{-2}\left|\langle V, S_{n,j}(r;\cdot)\rangle_{\mathrm{L}_2(\overline{\mathbb{B}_r^{\mathrm{ext}}})}\right|^2\\ &= \frac{1}{16\pi^2}\sum_{\substack{n=1\\ \Gamma_n\neq 0}}^{\infty}\sum_{j=1}^{2n+1} \frac{(2t_n+3)(2n-1)(2n+1)^2}{\Gamma_n^2}\frac{r^{2n-1}}{R^{2t_n+3}}\left|\langle V, S_{n,j}(r;\cdot)\rangle_{\mathrm{L}_2(\overline{\mathbb{B}_r^{\mathrm{ext}}})}\right|^2 < \infty.\end{aligned}$$

Then the solution $\boldsymbol{f}^+$ is given by the Fourier series

$$\boldsymbol{f}^+ = \frac{1}{4\pi}\sum_{\substack{n=1\\ \Gamma_n\neq 0}}^{\infty}\sum_{j=1}^{2n+1}\frac{2n+1}{\Gamma_n}\sqrt{\frac{(2t_n+3)(2n-1)}{R^3}}\frac{r^{n-1/2}}{R^{t_n}}\langle V, S_{n,j}(r;\cdot)\rangle_{\mathrm{L}_2(\overline{\mathbb{B}_r^{\mathrm{ext}}})}\boldsymbol{g}_{0,n,j}^{(\iota)}(R;\cdot).$$

Proof. See Theorem 11.13 for a formulation of Picard's criterion. Since $V\in\operatorname{dom}\mathcal{T}^+$, we can apply Theorem 11.12 to obtain the best-approximate solution

$$\begin{aligned}\boldsymbol{f}^+ &= \sum_{\substack{n=1\\ \Gamma_n\neq 0}}^{\infty}\sum_{j=1}^{2n+1}\lambda_n^{-1}\langle V, S_{n,j}(r;\cdot)\rangle_{\mathrm{L}_2(\overline{\mathbb{B}_r^{\mathrm{ext}}})}\boldsymbol{g}_{0,n,j}^{(\iota)}(R;\cdot)\\ &= \frac{1}{4\pi}\sum_{\substack{n=1\\ \Gamma_n\neq 0}}^{\infty}\sum_{j=1}^{2n+1}\frac{2n+1}{\Gamma_n}\sqrt{\frac{(2t_n+3)(2n-1)}{R^3}}\frac{r^{n-1/2}}{R^{t_n}}\langle V, S_{n,j}(r;\cdot)\rangle_{\mathrm{L}_2(\overline{\mathbb{B}_r^{\mathrm{ext}}})}\boldsymbol{g}_{0,n,j}^{(\iota)}(R;\cdot).\end{aligned}$$

□

Inserting Eq. (12.5) into the representation of the best-approximate solution $\boldsymbol{f}^+$, we obtain the identity

$$\begin{aligned}\boldsymbol{f}^+(\boldsymbol{x}) &\overset{\mathbf{L}_2(\mathbb{B}_R)}{=} \frac{1}{4\pi}\sum_{\substack{n=1\\ \Gamma_n\neq 0}}^{\infty}\sum_{j=1}^{2n+1}\frac{2n+1}{\Gamma_n}\sqrt{\frac{(2t_n+3)(2n-1)}{R^3}}\frac{r^{n-1/2}}{R^{t_n}}V^{\wedge}(n,j)\sqrt{\frac{r}{2n-1}}\boldsymbol{g}_{0,n,j}^{(\iota)}(R;\boldsymbol{x})\\ &= \frac{1}{4\pi}\sum_{\substack{n=1\\ \Gamma_n\neq 0}}^{\infty}\sum_{j=1}^{2n+1}\frac{2n+1}{\Gamma_n}\sqrt{\frac{2t_n+3}{R^3}}\frac{r^n}{R^{t_n}}V^{\wedge}(n,j)\boldsymbol{g}_{0,n,j}^{(\iota)}(R;\boldsymbol{x}) \qquad (12.7)\\ &= \frac{1}{4\pi}\sum_{\substack{n=1\\ \Gamma_n\neq 0}}^{\infty}\sum_{j=1}^{2n+1}\frac{2n+1}{\Gamma_n}\frac{2t_n+3}{R^3}\frac{r^n}{R^{t_n}}V^{\wedge}(n,j)\left(\frac{x}{R}\right)^{t_n}\boldsymbol{y}_{n,j}^{(\iota)}(\hat{\boldsymbol{x}})\end{aligned}$$

in the sense of $\mathbf{L}_2(\mathbb{B}_R)$. Note that the factor r^n/R^{t_n} is related to the downward continuation of the data from the outer region, where, for example, sensors are located, to the inner region, where $\boldsymbol{f}^+$ is located. Similar results concerning the Spectral Theorem and the representation of the unique best-approximate solution can be derived for the operator $\mathcal{B}\boldsymbol{f} \coloneqq -\boldsymbol{\nabla}(\mathcal{T}\boldsymbol{f})$ for all $\boldsymbol{f} \in \mathbf{L}_2(\mathbb{B}_{\varrho_0})$. First, we define an appropriate function space for the operator range, see Definition 5.29.

Definition 12.12. *The space of all vector outer harmonics of type* 1 *that are contained in* $\mathbf{L}_2(\overline{\mathbb{B}_r^{\mathrm{ext}}})$ *is denoted by*

$$\mathbf{Harm}\left(\overline{\mathbb{B}_r^{\mathrm{ext}}}\right) \coloneqq \overline{\bigoplus_{n=1}^{\infty}\mathbf{harm}_n^{(1)}\left(\overline{\mathbb{B}_r^{\mathrm{ext}}}\right)}^{\|\cdot\|_{\mathbf{L}_2(\overline{\mathbb{B}_r^{\mathrm{ext}}})}}$$

and equipped with the $\langle\cdot,\cdot\rangle_{\mathbf{L}_2(\overline{\mathbb{B}_r^{\mathrm{ext}}})}$*-inner product. An orthonormal basis for* $\mathbf{Harm}\left(\overline{\mathbb{B}_r^{\mathrm{ext}}}\right)$ *is then given by*

$$\boldsymbol{s}_{n,j}(r;\cdot) \coloneqq \sqrt{\frac{2n+1}{r}}\boldsymbol{h}_{n,j}^{(1)}(r;\cdot)$$

for all $n \in \mathbb{N}$ *and* $j = 1,\ldots,2n+1$.

Due to the construction of $\mathbf{Harm}(\overline{\mathbb{B}_r^{\mathrm{ext}}})$, it is clear that $\{\boldsymbol{s}_{n,j}(r;\cdot)\}_{n\in\mathbb{N},j=1,\ldots,2n+1}$ forms an orthonormal basis for $\mathbf{Harm}(\overline{\mathbb{B}_r^{\mathrm{ext}}})$. The normalization factor can be easily calculated. For this purpose, let n, $m \in \mathbb{N}$, $j = 1,\ldots,2n+1$, and $k = 1,\ldots,2m+1$, then

$$\begin{aligned}\left\langle \boldsymbol{h}_{n,j}^{(1)}(r;\cdot), \boldsymbol{h}_{m,k}^{(1)}(r;\cdot)\right\rangle_{\mathbf{L}_2(\overline{\mathbb{B}_r^{\mathrm{ext}}})} &= \int_{\overline{\mathbb{B}_r^{\mathrm{ext}}}}\boldsymbol{h}_{n,j}^{(1)}(r;\boldsymbol{y})\boldsymbol{h}_{m,k}^{(1)}(r;\boldsymbol{y})\,\mathrm{d}\boldsymbol{y}\\ &= \int_{\overline{\mathbb{B}_r^{\mathrm{ext}}}}\frac{r^{n+m+2}}{y^{n+m+4}}\tilde{\boldsymbol{y}}_{n,j}^{(1)}(\hat{\boldsymbol{y}})\tilde{\boldsymbol{y}}_{m,k}^{(1)}(\hat{\boldsymbol{y}})\,\mathrm{d}\boldsymbol{y}\\ &= \int_r^{\infty}\frac{r^{n+m+2}}{y^{n+m+2}}\,\mathrm{d}y\int_{\mathbb{S}}\tilde{\boldsymbol{y}}_{n,j}^{(1)}(\hat{\boldsymbol{y}})\tilde{\boldsymbol{y}}_{m,k}^{(1)}(\hat{\boldsymbol{y}})\,\mathrm{d}\omega(\hat{\boldsymbol{y}})\\ &= \left[\frac{-r^{2n+2}}{(2n+1)y^{2n+1}}\right]\Bigg|_{y=r}^{\infty}\delta_{n,m}\delta_{j,k}\\ &= \frac{r}{2n+1}\delta_{n,m}\delta_{j,k}.\end{aligned}$$

Having a suitable basis at hand, we can find the SVD of the operator $\mathcal{B}$.

Theorem 12.13. *Let the operator* $\mathcal{B}\colon \mathbf{L}_2(\mathbb{B}_R) \to \mathbf{Harm}(\overline{\mathbb{B}_r^{\mathrm{ext}}})$*, where* $r > R$*, be defined by* $\mathcal{B}\boldsymbol{f} \coloneqq -\boldsymbol{\nabla}(\mathcal{T}\boldsymbol{f})$ *for all* $\boldsymbol{f} \in \mathbf{L}_2(\mathbb{B}_{\varrho_0})$ *with the harmonic VLI operator* $\mathcal{T}$ *from Theorem 12.10. Then the operator* $\mathcal{B}$ *has the following properties:*

i) $\mathcal{B}$ *is not injective as*

$$(\ker \mathcal{B})^{\perp} = \overline{\operatorname{span}\left\{ \boldsymbol{g}_{0,n,j}^{(\iota)}(R;\cdot) \;\middle|\; n \in \{n' \in \mathbb{N} \mid \Gamma_{n'} \neq 0\}\,, j = 1,\dots,2n+1 \right\}}.$$

ii) The set $\{\boldsymbol{g}_{0,n,j}^{(\iota)}(R;\cdot), \boldsymbol{s}_{n,j}(r;\cdot); \lambda_n\}_{n\in\{n'\in\mathbb{N}|\Gamma_{n'}\neq 0\}\,,j=1,\dots,2n+1}$ *is the corresponding singular system with the singular values*

$$\lambda_n \coloneqq 4\pi\Gamma_n \sqrt{\frac{n+1}{(2n+1)^2(2t_n+3)}}\frac{R^{t_n+3/2}}{r^{n+1/2}}.$$

iii) The corresponding Moore-Penrose inverse operator $\mathcal{B}^{+}$ *is unbounded.*

iv) The closure of the operator range $\operatorname{ran}\mathcal{B}$ *is given by*

$$\overline{\operatorname{ran}\mathcal{B}} = \overline{\operatorname{span}\left\{\boldsymbol{s}_{n,j}(r;\cdot) \mid n \in \{n' \in \mathbb{N} \mid \Gamma_{n'} \neq 0\}\,, j = 1,\dots,2n+1\right\}}.$$

v) For given $\boldsymbol{V} \in \overline{\operatorname{ran}\mathcal{B}}$*, Picard's criterion is given by*

$$\sum_{\substack{n=1\\ \Gamma_n\neq 0}}^{\infty}\sum_{j=1}^{2n+1} \lambda_n^{-2}\left|\left\langle \boldsymbol{V}, \boldsymbol{s}_{n,j}^{(1)}(r;\cdot)\right\rangle_{\mathbf{Harm}\left(\overline{\mathbb{B}_r^{\mathrm{ext}}}\right)}\right|^2 < \infty.$$

vi) The unique best-approximate solution $\boldsymbol{f}^{+}$ *of the inverse problem is for all* $\boldsymbol{V} \in \overline{\operatorname{ran}\mathcal{B}}$ *given by*

$$\boldsymbol{f}^{+} = \frac{1}{4\pi}\sum_{\substack{n=1\\ \Gamma_n\neq 0}}^{\infty}\sum_{j=1}^{2n+1} \lambda_n^{-1}\left\langle \boldsymbol{V}, \boldsymbol{s}_{n,j}^{(1)}(r;\cdot)\right\rangle_{\mathbf{Harm}\left(\overline{\mathbb{B}_r^{\mathrm{ext}}}\right)} \boldsymbol{g}_{0,n,j,}^{(\iota)}(R;\cdot).$$

Proof. From Theorem 8.4, we get the expansion

$$\mathcal{B}\boldsymbol{f} = 4\pi\sum_{n=1}^{\infty}\sum_{j=1}^{2n+1}\Gamma_n\sqrt{\frac{n+1}{(2n+1)(2t_n+3)}} f^{\wedge}(\iota,0,n,j)\frac{R^{t_n+3/2}}{r^{n+1}}\boldsymbol{h}_{n,j}^{(1)}(r;\cdot). \tag{12.8}$$

i) Due to the construction of $\mathcal{B}$, we immediately obtain $\{0\} \neq \ker\mathcal{T} \subset \ker\mathcal{B}$. Eq. (12.8) provide us with the representation of the operator null space.

ii) The SVD and the singular values are a direct consequence of the representation in Eq. (12.8) and the choice of the orthonormal basis. The singular values are obviously non-zero numbers with $\lim_{n\to\infty}\lambda_n = 0$.

iii) The unboundedness of the Moore-Penrose inverse operator follows immediately from the SVD and the asymptotic behaviour of the singular values, which converge to zero as $n \to \infty$.

iv) This is an immediate consequence of the SVD and the fact that $\overline{\operatorname{ran}\mathcal{B}} = (\ker\mathcal{B}^*)^\perp$.

v) Inserting the SVD in Theorem 11.13, we get the desired result.

vi) The representation of the unique best-approximate solution can be achieved by using Theorem 11.12 in combination with the SVD. □

In Theorem 8.4, the absolute and uniform convergence of the series in Eq. (12.8) is proved. However, we are able to extend the operator onto $\mathbb{S}_R$, where the series converges in the $\mathbf{L}_2(\mathbb{S}_R)$-sense after all.

Theorem 12.14. *Let $\boldsymbol{f} \in \mathbf{L}_2(\mathbb{B}_R)$ and let the coefficients Γ_n fulfil*

$$|\Gamma_n| \leq c\sqrt{\frac{(2n+1)(2t_n+3)}{n+1}}$$

for an arbitrary $c \in \mathbb{R}_0^+$ and for all $n \in \mathbb{N}$. Then $(\mathcal{B}\boldsymbol{f})|_{\mathbb{S}_R} \in \mathbf{L}_2(\mathbb{S}_R)$.

Proof. Via the definition of the vector outer harmonics, see Definition 5.27, we get

$$\frac{1}{r^{n+1}}\boldsymbol{h}_{n,j}^{(1)}(r;\boldsymbol{y}) = \frac{1}{R^{n+1}}\boldsymbol{h}_{n,j}^{(1)}(R;\boldsymbol{y})$$

and $\boldsymbol{h}_{n,j}^{(1)}(R;\cdot)|_{\mathbb{S}_R} = \frac{1}{R}\tilde{\boldsymbol{y}}_{n,j}^{(1)}$ for all $n \in \mathbb{N}$ and $j = 1,\ldots,2n+1$. Thus,

$$\begin{aligned}(\mathcal{B}\boldsymbol{f})|_{\mathbb{S}_R} &= \left(4\pi\sum_{n=1}^{\infty}\sum_{j=1}^{2n+1}\Gamma_n\sqrt{\frac{n+1}{(2n+1)(2t_n+3)}}f^\wedge(\iota,0,n,j)\frac{R^{t_n+3/2}}{r^{n+1}}\boldsymbol{h}_{n,j}^{(1)}(r;\cdot)\right)\Bigg|_{\mathbb{S}_R}\\ &\overset{\mathbf{L}_2(\mathbb{S}_R)}{=} 4\pi\sum_{n=1}^{\infty}\sum_{j=1}^{2n+1}\Gamma_n\sqrt{\frac{n+1}{(2n+1)(2t_n+3)}}f^\wedge(\iota,0,n,j)R^{t_n-n+1/2}\frac{1}{R}\tilde{\boldsymbol{y}}_{n,j}^{(1)}(\hat{\boldsymbol{y}}).\end{aligned}$$

For the $\mathbf{L}_2(\mathbb{S}_R)$-norm, using a property of Parseval's identity, see [198, Thm. 12.6], and the fact that $\{R^{-1}\tilde{\boldsymbol{y}}_{n,j}^{(i)}\}_{i=1,2,3,n\in\mathbb{N}_{0_i},j=1,\ldots,2n+1}$ is an orthonormal basis in $\mathbf{L}_2(\mathbb{S}_R)$, we get the identity

$$\begin{aligned}\|(\mathcal{B}\boldsymbol{f})|_{\mathbb{S}_R}\|_{\mathbf{L}_2(\mathbb{S}_R)}^2 &= 16\pi^2\sum_{n=1}^{\infty}\sum_{j=1}^{2n+1}\Gamma_n^2\frac{n+1}{(2n+1)(2t_n+3)}\left(f^\wedge(\iota,0,n,j)\right)^2R^{2t_n-2n+1}\\ &\leq 16\pi^2R\left(\sup_{n\in\mathbb{N}}R^{t_n-n}\right)^2\sum_{n=1}^{\infty}\sum_{j=1}^{2n+1}\Gamma_n^2\frac{n+1}{(2n+1)(2t_n+3)}\left(f^\wedge(\iota,0,n,j)\right)^2\\ &\leq 16\pi^2c^2R\left(\sup_{n\in\mathbb{N}}R^{t_n-n}\right)^2\sum_{n=1}^{\infty}\sum_{j=1}^{2n+1}\left(f^\wedge(\iota,0,n,j)\right)^2\\ &\leq 16\pi^2c^2R\left(\sup_{n\in\mathbb{N}}R^{t_n-n}\right)^2\|\boldsymbol{f}\|_{\mathbf{L}_2(\mathbb{B}_R)}^2 < \infty.\end{aligned}$$

□

12.3. Uniqueness Constraints for the Continuous VLI Problem

In Section 12.1, we prove that the continuous/star-shaped VLI operator has an infinite-dimensional null space and formulate its expansion via an orthonormal basis. Indeed, the null space also remains infinite-dimensional in the case of the harmonic VLI problem or the scalar-valued analogues considered in Part IV. SVDs of the mentioned integral operators are stated, which lead to the unique best-approximate solution by means of the Moore-Penrose inverse operator. However, the best-approximate solution may not be the realistic density of the problem. In certain applications, structures of the density are known a-priori that may not be covered by the best-approximate solution. For instance, in Example 7.6, the sought density has its support only inside a spherical shell.

In this section, we want to achieve a unique solution of the inverse problem by means of additional constraints. Therefore, a solution of the inverse problem $V = \mathcal{T}\boldsymbol{f}$ needs to exist. Thus, we formulate the next proposition valid for this entire section.

Assumption 12.15. *Let $\mathcal{T}$ be the vector continuous/star-shaped VLI operator and let the outer space be given by $\mathbb{G}_{\text{out}} \coloneqq \overline{\mathbb{B}_r^{\text{ext}}}$ with $r > R \coloneqq \sup_{\boldsymbol{x}\in\mathbb{G}_{\text{in}}} x$. We assume that the potential $V = \mathcal{T}\boldsymbol{f}$ with density $\boldsymbol{f} \in \mathbf{L}_2(\mathbb{G}_{\text{in}})$*

i) restricted to $\mathbb{S}_r$ is an $\mathrm{L}_2(\mathbb{S}_r)$-function,

ii) is harmonic in the outer space, that is $\Delta V = 0$ in $\mathbb{G}_{\text{out}}$,

iii) is regular at infinity, and

iv) satisfies Picard's criterion.

From Theorem 7.26 and Corollary 7.19, two expansions of the potential are known if the inner region is given by a ball with radius R; they are

$$\begin{aligned}(\mathcal{T}\boldsymbol{f})(\boldsymbol{y}) &= 4\pi \sum_{n=0_\iota}^{\infty} \sum_{j=1}^{2n+1} \frac{R^{t_n+3/2}}{(2n+1)\sqrt{2t_n+3}} f^{\wedge}(\iota,0,n,j)\gamma_n(y)Y_{n,j}(\hat{\boldsymbol{y}}) \\ &= 4\pi \sum_{n=0_\iota}^{\infty} \sum_{j=1}^{2n+1} \frac{1}{2n+1} \left(\int_0^R f_{n,j}^{(\iota)}(x) x^{t_n+2} \,\mathrm{d}x \right) \gamma_n(y)Y_{n,j}(\hat{\boldsymbol{y}}).\end{aligned}$$

The spherical harmonics $\{Y_{n,j}\}_{n\in\mathbb{N}_{0_\iota}, j=1,\dots,2n+1}$ are a set of linearly independent functions. Hence, the harmonicity constraint on V from Assumption 12.15 can only be fulfilled if for each $n \in \mathbb{N}_{0_\iota}$, $j = 1,\dots,2n+1$ the function $\boldsymbol{y} \mapsto \gamma_n(y)Y_{n,j}(\hat{\boldsymbol{y}})$ with $\boldsymbol{y} \in \mathbb{G}_{\text{out}}$ is a harmonic function. However, only the inner and outer harmonics can satisfy this requirement. In addition, V needs to be regular at infinity. We arrive for all $n \in \mathbb{N}_{0_\iota}$ at

$$\gamma_n(y) \coloneqq \frac{\Gamma_n}{y^{n+1}} \qquad \text{for all } \boldsymbol{y} \in \mathbb{G}_{\text{out}}$$

with some sequence $\{\Gamma_n\}_{n\in\mathbb{N}_{0_\iota}} \subset \mathbb{R}$. Due to convergence requirements, we need a polynomial growth condition $(n \mapsto |\Gamma_n|) \in \mathcal{O}(n^M)$ for fixed $M \in \mathbb{N}_0$. This condition is similar to the one

for the harmonic VLI kernel. On the other hand, V solves the exterior Dirichlet problem, see Corollary 8.10. It has, hence, the expansion

$$V = \sum_{n=0}^{\infty} \sum_{j=1}^{2n+1} V^{\wedge}(n,j) H_{n,j}^{\mathrm{ext}}(r;\cdot)$$

in $\mathbb{G}_{\mathrm{out}}$ with the abbreviation $V^{\wedge}(n,j) \coloneqq \langle V|_{\mathbb{S}_r}, r^{-1}Y_{n,j}\rangle_{\mathrm{L}_2(\mathbb{S}_r)}$. The coefficients satisfy

$$V^{\wedge}(n,j) = 4\pi \frac{\Gamma_n}{(2n+1)\sqrt{2t_n+3}} \frac{R^{t_n+3/2}}{r^n} f^{\wedge}(\iota,0,n,j), \tag{12.9a}$$

$$V^{\wedge}(n,j) = 4\pi \frac{\Gamma_n}{2n+1} \frac{1}{r^n} \int_0^R f_{n,j}^{(\iota)}(x) x^{t_n+2} \,\mathrm{d}x \tag{12.9b}$$

for all $n \in \mathbb{N}_{0_\iota}$, $j = 1, \ldots, 2n+1$ and $V^{\wedge}(0,1) = 0$ in the case of $\iota = 2, 3$. Vice versa, the density can be represented by means of the Fourier expansion, that is

$$\boldsymbol{f}(\boldsymbol{x}) \overset{\mathbf{L}_2(\mathbb{B}_R)}{=} \sum_{i=1}^{3} \sum_{n=0_i}^{\infty} \sum_{j=1}^{2n+1} f_{n,j}^{(i)}(x) \boldsymbol{y}_{n,j}^{(i)}(\hat{\boldsymbol{x}}) \tag{12.10a}$$

$$\overset{\mathbf{L}_2(\mathbb{B}_R)}{=} \sum_{i=1}^{3} \sum_{m=0}^{\infty} \sum_{n=0_i}^{\infty} \sum_{j=1}^{2n+1} f^{\wedge}(i,m,n,j) \boldsymbol{g}_{m,n,j}^{(i)}(R;\boldsymbol{x}). \tag{12.10b}$$

Via Eq. (12.9), only information for $i = \iota$ can be obtained. Additional knowledge is required for the remaining two directions of the density $\boldsymbol{f}$. To this end, assumptions on the directional part of the function $\boldsymbol{f}$ are necessary. This will be discussed in Section 12.3.2. On the other hand, only information for $m = 0$ is obtained by Eq. (12.9). Therefore, additional uniqueness constraints for the radial part of $\boldsymbol{f}$ are required.

12.3.1. Radial Uniqueness Constraints

In order to apply radial uniqueness constraints to the problem, we decompose the density into a radial and an angular part. The angular part is represented by (vector) spherical harmonics, see Eq. (12.10) or Eq. (14.7). Depending on $\iota \in \{1,2,3\}$ given by the underlying problem, the function $f_{n,j}^{(\iota)}$ is only given for $n \geq 0_\iota$. In order to cover both cases for 0_ι with one notation, we introduce the function $D_{n,j} \in \mathrm{L}_2^w([0,R])$, where $w(x) \coloneqq x^2$, which is defined for all $n \in \mathbb{N}_0$, $j = 1, \ldots, 2n+1$ by

$$D_{n,j} \coloneqq \begin{cases} f_{n,j}^{(\iota)} & \text{in the vector-valued case for all } n \in \mathbb{N}_{0_\iota},\ j = 1, \ldots, 2n+1, \\ 0 & \text{in the vector-valued case for all } i = 2,\ 3 \text{ and } (n,j) = (0,1). \end{cases} \tag{12.11}$$

The introduction of this abbreviation has also an other background. In a forthcoming part of this thesis, we will analyze an integral equation related to the continuous/star-shaped VLI equation consisting of a scalar-valued density and scalar-valued integral kernel. Then, by choosing the function $D_{n,j}$ for all $n \in \mathbb{N}_0$, $j = 1, \ldots, 2n+1$ appropriately, the additional uniqueness constraints from this section can be immediately applied to the scalar-valued case.

With the introduced notation, the outer harmonics coefficients of the potential V are eventually given by

$$V^{\wedge}(n,j) = 4\pi \frac{\Gamma_n}{2n+1} \frac{1}{r^n} \int_0^R D_{n,j}(x) x^{t_n+2} \,\mathrm{d}x, \tag{12.12}$$

where the angular part does not occur. The remaining integral provides us with the part of $D_{n,j}$ that is parallel to $Q_0^{(t_n+1/2)}(R,\cdot)$ since

$$\int_0^R D_{n,j}(x) x^{t_n+2} \,\mathrm{d}x = \sqrt{\frac{2t_n+3}{R^{2t_n+3}}} \Big\langle D_{n,j}, Q_0^{(t_n+1/2)}(R,\cdot) \Big\rangle_{\mathrm{L}_2^w([0,R])}.$$

See the proof of Lemma 7.24 for more details. However, by means of additional radial uniqueness constraints, we are able to transfer information from the part of $D_{n,j}$ that is parallel to $Q_0^{(t_n+1/2)}(R,\cdot)$ to the orthogonal part. The application of this approach to the scalar-valued case has already been published by the author in [147, 162].

The occurring radial uniqueness constraints are often motivated by structure-related constraints. For example, it could be known a-priori that a density or a density deviation only occurs in a particular layer (spherical shell) of the underlying body $\mathbb{B}_R$. Then, it would be appropriate to assume that this density (deviation) has its support inside this layer. This directly leads to the layer density constraint, which is a radial uniqueness constraint and is presented in Example 12.17. However, we first state the general setting.

Lemma 12.16. *Let each function $D_{n,j} \in \mathrm{L}_2^w([0,R])$ with the weight function $w(x) \coloneqq x^2$ be a multiple of an $\mathrm{L}_2^w([0,R])$-function $B_{n,j}$, that is*

$$D_{n,j} \coloneqq d_{n,j} B_{n,j},$$

with real coefficients $d_{n,j} \in \mathbb{R}$ for all $n \in \mathbb{N}_0$, $j = 1,\dots,2n+1$. Then

$$V^{\wedge}(n,j) = 4\pi \frac{\Gamma_n d_{n,j}}{2n+1} \frac{1}{r^n} \int_0^R B_{n,j}(x) x^{t_n+2} \,\mathrm{d}x.$$

The function $D_{n,j}$ can be represented for almost all $x \in [0,R]$ by

$$D_{n,j}(x) = \frac{1}{4\pi} \frac{2n+1}{\Gamma_n} r^n V^{\wedge}(n,j) \left(\int_0^R B_{n,j}(x) x^{t_n+2} \,\mathrm{d}x \right)^{-1} B_{n,j}(x)$$

if $B_{n,j}$ is not $\mathrm{L}_2^w([0,R])$-orthogonal to $Q_0^{(t_n+1/2)}(R,\cdot)$.

We obtain a unique representation for $f_{n,j}^{(\iota)}$ and a unique representation for $\boldsymbol{f}$ if the density with the minimum norm fulfilling Lemma 12.16 is sought. This implies $f_{n,j}^{(i)} = 0$ for $i \neq \iota$ and for all $n \in \mathbb{N}_{0_i}$, $j = 1,\dots,2n+1$.

Proof. Inserting the identity $D_{n,j} = d_{n,j} B_{n,j}$ into Eq. (12.12), we get

$$V^{\wedge}(n,j) = 4\pi \frac{\Gamma_n}{2n+1} \frac{1}{r^n} \int_0^R B_{n,j}(x) x^{t_n+2} \,\mathrm{d}x d_{n,j}.$$

Solving this equation for $d_{n,j}$, we obtain the desired representation for $D_{n,j}$. □

A more detailed proof of this lemma for particular functions $B_{n,j}$ can be found in [162]. In the scalar-valued case, see [147, 161, 162], this approach is used to obtain the harmonic solution, the quasi-harmonic solution, that is $\Delta_{\boldsymbol{x}}(F(\boldsymbol{x})x^{-p}) \equiv 0$ for $p \in \mathbb{R}_0^+$, a generalization of the harmonic solution, and a layer-density. These are summarized in the next example.

Example 12.17. *A few examples of additional radial uniqueness constraints are listed in Table 12.1, which is also valid for the scalar-valued case if* $\mathbb{N}_{0_\iota}$ *is understood as* $\mathbb{N}_0$.

Constraint	$B_{n,j}(x)$	Conditions	Integral
Generalized Harmonicity	$\coloneqq \frac{x^{\kappa_n}}{R^{\kappa_n+1}}$	$\inf_{n\in\mathbb{N}_{0_\iota}} \kappa_n > -\frac{3}{2}$	$\int_0^R B_{n,j}(x)x^{t_n+2}\,\mathrm{d}x = \frac{R^{t_n+2}}{\kappa_n+t_n+3}$
Minimum Norm	$\coloneqq \frac{x^{t_n}}{R^{t_n+1}}$	$\inf_{n\in\mathbb{N}_{0_\iota}} t_n > -1$	$\int_0^R B_{n,j}(x)x^{t_n+2}\,\mathrm{d}x = \frac{R^{t_n+2}}{2t_n+3}$
Layer Density	$\coloneqq \chi_{[\tau,\tau+\delta]}(x)$	$\tau, \tau+\delta \in [0,R]$, $\delta > 0$	$\int_0^R B_{n,j}(x)x^{t_n+2}\,\mathrm{d}x = \frac{(\tau+\delta)^{t_n+3}-\tau^{t_n+3}}{t_n+3}$

TABLE 12.1: *Several radial uniqueness constraints, which only need to hold in the* $\mathrm{L}_2^w([0,R])$*-sense, and their resulting integrals. Note that* χ *denotes the indicator function, that is* $\chi_A(x) = 0$ *if* $x \notin A$ *and* $\chi_A(x) = 1$ *if* $x \in A$.

In the case of the generalized harmonicity constraint, the functions $B_{n,j}$ *and, hence,* $D_{n,j}$ *have a singularity at the origin for negative values of* κ_n *and at least a discontinuity in the case of* $\kappa_n = 0$. *However, in the sense of* $\mathrm{L}_2^w([0,R])$ *this is not a problem if* $\inf_{n\in\mathbb{N}_0} \kappa_n > -3/2$.

The name of the generalized harmonicity constraint is attributed to the scalar-valued case. Here, for $\kappa_n \coloneqq n$ *for all* $n \in \mathbb{N}_0$, *we obtain*

$$F(\boldsymbol{x}) \overset{\mathrm{L}_2(\mathbb{B}_R)}{=} \sum_{n=0}^{\infty}\sum_{j=1}^{2n+1} d_{n,j}\frac{x^n}{R^{n+1}}Y_{n,j}(\hat{\boldsymbol{x}}),$$

which is harmonic due to properties of the inner harmonics. In the vector-valued case, the harmonicity is only obtained for $\iota = 3$, *since only these Morse-Feshbach vector spherical harmonics are eigenfunctions of the Beltrami operator, see Corollary 5.16. The quasi-harmonic solution in the scalar case is obtained for* $\kappa_n = n + p$ *with fixed* $p \in \mathbb{R}_0^+$, *which is the background for its name. Here,* $\Delta_{\boldsymbol{x}}(F(\boldsymbol{x})x^{-p}) \equiv 0$ *and for* $p = 0$ *the density* F *is assumed to be harmonic. However, this condition is not sufficient for the harmonicity of a vector-valued density. This particular case is discussed in more detail in the next section.*

The minimum norm condition is closely related to the best-approximate solution. In this context, we assume that the sought density has the smallest norm among all densities fulfilling Eq. (12.12). *In [161], a descriptively proof for the connection between the minimum norm condition and the particular radial uniqueness constraint in Table 12.1 is stated.*

In addition, a surface density condition is presented in [147], which has its origin in the scalar inverse gravimetric problem. Therein, time-variable fields with relatively short time-scales have their main variation on the Earth's surface or relatively small layers close

to the Earth's surface. So far, the volumetric density F of the inverse problem has been considered. The shift from a volumetric density to a surface density is not as straightforward as the previous radial uniqueness constraints. For this purpose, the integral equation of interest has to be understood in a distributional sense. The regular distribution induced by the density is replaced by a singular distribution similar to the well-known Delta distribution, that is

$$(F\delta_{\mathbb{S}_R})\psi \coloneqq \langle F, \psi \rangle_{\mathrm{L}_2(\mathbb{S}_R)}$$

for all test functions ψ. Then, again a formula for the coefficients $V^\wedge(n,j)$ can be found. However, this approach does not fit perfectly to the context of the VLI equation and has no relevance for the magneto-electroencephalography problem as our main application. Therefore, it is not presented here in detail. For more information, see the author's publication [147].

12.3.2. Directional Uniqueness Constraints

In this section, we concentrate on directional uniqueness constraints. Using knowledge of the harmonic VLI operator, we obtain

$$V^\wedge(n,j) = 4\pi \frac{\Gamma_n}{2n+1} \frac{1}{r^n} \int_0^R f_{n,j}^{(\iota)}(x) x^{t_n+2} \,\mathrm{d}x$$

for all $n \in \mathbb{N}_{0_\iota}$, $j = 1, \ldots, 2n+1$ via the Fourier expansion of $\boldsymbol{f}$ in Eq. (12.10). Due to the structure of the continuous/star-shaped VLI kernel, we are only able to obtain information for $f_{n,j}^{(i)}$ in the case of $i = \iota$. The other two directions are in the null space of the operator. Via the minimum norm condition, which yields the best-approximate solution, we can always achieve a unique solution $\boldsymbol{f}^+$. Then $\boldsymbol{f}^+$ is only non-zero in the direction of $i = \iota$.

By means of additional directional uniqueness constraints, we are, in certain cases, able to transfer the information obtained for $i = \iota$ to other directions. By additional directional uniqueness constraints we understand assumptions like $\boldsymbol{f}$ is a solenoidal ($\boldsymbol{\nabla} \cdot \boldsymbol{f} = 0$) or irrotational ($\boldsymbol{\nabla} \wedge \boldsymbol{f} = \boldsymbol{0}$) vector field if $\boldsymbol{f}$ is sufficiently often differentiable inside $\mathbb{B}_R$.

However, these additional directional uniqueness constraints alone do not yield a unique solution. Since not all parts of $f_{n,j}^{(\iota)}(x)$ for $n \in \mathbb{N}_{0_\iota}$, $j = 1, \ldots, 2n+1$ can be obtained by the stated Fourier coefficients relation in Eq. (12.12), we always need additional radial uniqueness constraints. For the sake of simplicity, we choose the minimum norm condition as the additional radial uniqueness constraint for all directional constraints. However, it is possible to replace this constraint with every constraint in Table 12.1 and others.

Theorem 12.18 (Solenoidal). *Let the density $\boldsymbol{f} \in \mathbf{L}_2(\mathbb{B}_R)$ be sufficiently smooth and let the gradient be interchangeable with the series in Eq.* (12.10)*. Then we can compute a unique minimum norm solenoidal density fulfilling $\mathcal{T}\boldsymbol{f} = V$.*

Proof. First, we observe for each $n \in \mathbb{N}$, $j = 1, \ldots, 2n+1$ that

$$\begin{aligned} 0 &= \boldsymbol{\nabla}_{\boldsymbol{x}} \cdot \left(\sum_{i=1}^{3} f_{n,j}^{(i)}(x) \boldsymbol{y}_{n,j}^{(i)}(\hat{\boldsymbol{x}}) \right) \\ &= \sum_{i=1}^{3} \left(\frac{\mathrm{d} f_{n,j}^{(i)}(x)}{\mathrm{d}x} \hat{\boldsymbol{x}} \cdot \boldsymbol{y}_{n,j}^{(i)}(\hat{\boldsymbol{x}}) + \frac{f_{n,j}^{(i)}(x)}{x} \boldsymbol{\nabla}_{\hat{\boldsymbol{x}}}^* \cdot \boldsymbol{y}_{n,j}^{(i)}(\hat{\boldsymbol{x}}) \right) \end{aligned}$$

$$= \frac{\mathrm{d}f_{n,j}^{(1)}(x)}{\mathrm{d}x}\hat{\boldsymbol{x}} \cdot \boldsymbol{y}_{n,j}^{(1)}(\hat{\boldsymbol{x}}) + \sum_{i=1}^{2}\left(\frac{f_{n,j}^{(i)}(x)}{x}\boldsymbol{\nabla}_{\hat{\boldsymbol{x}}}^{*} \cdot \boldsymbol{y}_{n,j}^{(i)}(\hat{\boldsymbol{x}})\right)$$
$$= \left(\frac{\mathrm{d}f_{n,j}^{(1)}(x)}{\mathrm{d}x} + \frac{2f_{n,j}^{(1)}(x)}{x} - \frac{\sqrt{n(n+1)}f_{n,j}^{(2)}(x)}{x}\right) Y_{n,j}(\hat{\boldsymbol{x}}). \tag{12.13}$$

Here, we used the representation of the gradient in spherical coordinates, see Theorem 2.14, the orthogonality relation from Eq. (2.6), and the definition of the Morse-Feshbach vector spherical harmonics in Eq. (5.1). Due to the density being divergence-free, we obtain a relation between the direction corresponding to the type $i = 1$ and the direction corresponding to $i = 2$, see Eq. (12.13). From the divergence-free condition, we obtain for $n = 0$ the additional equation

$$\frac{\mathrm{d}f_{0,1}^{(1)}(x)}{\mathrm{d}x} + \frac{2f_{0,1}^{(1)}(x)}{x} = 0, \qquad x \in (0, R].$$

This first-order homogeneous differential equation has, with a coefficient $c_{0,1}^{(1)} \in \mathbb{R}$, the solution

$$f_{0,1}^{(1)}(x) = \frac{c_{0,1}^{(1)}}{x^2}, \qquad x \in [0, R].$$

From the condition $\boldsymbol{f} \in \mathbf{L}_2(\mathbb{B}_R)$, Fubini's Theorem, and the Jacobian determinant, we get $f_{0,1}^{(1)} \in \mathrm{L}_2^w([0, R])$ with $w(x) \coloneqq x^2$. Thus, $c_{0,1}^{(1)} = 0$.

Now, let $\iota = 1$ be given. Then, $f_{n,j}^{(1)}$ is completely known by $\mathcal{T}\boldsymbol{f} = V$ and the minimum norm condition. Thus, we solve Eq. (12.13) for the unconstrained direction $f_{n,j}^{(2)}$. This leads for all $n \in \mathbb{N}$, $j = 1, \ldots, 2n + 1$ to the relation

$$f_{n,j}^{(2)}(x) = \frac{1}{\sqrt{n(n+1)}}\left(x\frac{\mathrm{d}f_{n,j}^{(1)}(x)}{\mathrm{d}x} + 2f_{n,j}^{(1)}(x)\right). \tag{12.14}$$

Eventually, if the normal vector field part of $\boldsymbol{f}$ is known, we are able to calculate the functions $f_{n,j}^{(2)}$, which represent one tangential direction of $\boldsymbol{f}$, from the knowledge of $f_{n,j}^{(1)}$ via Eq. (12.14).

Vice versa, for given $\iota = 2$, we obtain from Eq. (12.13) a first-order linear ordinary differential equation for the normal direction of the density. Solving this equation for $f_{n,j}^{(1)}$, we obtain, with some coefficients $c_{n,j}^{(2)} \in \mathbb{R}$, for all $n \in \mathbb{N}$, $j = 1, \ldots, 2n + 1$ the solution

$$f_{n,j}^{(1)}(x) = \frac{c_{n,j}^{(2)}}{x^2} + \frac{\sqrt{n(n+1)}}{x^2}\int_0^x t f_{n,j}^{(2)}(t)\,\mathrm{d}t. \tag{12.15}$$

Due to the minimum norm assumption and $\mathcal{T}\boldsymbol{f} = V$, we already know that

$$f_{n,j}^{(2)}(x) = c_{n,j}^{(3)}\frac{x^{t_n}}{R^{t_n+1}}, \qquad x \in [0, R],$$

with $\inf_{n \in \mathbb{N}_{0\iota}, \Gamma_n \neq 0} t_n > -1$ and some constants $c_{n,j}^{(3)} \in \mathbb{R}$ for all $n \in \mathbb{N}$, $j = 1, \ldots, 2n + 1$, see Table 12.1. With this representation and a lengthy calculation, we can prove that the function $f_{n,j}^{(1)}$ from Eq. (12.15) satisfies $f_{n,j}^{(1)} \in \mathrm{L}_2^w([0, R])$ if and only if $c_{n,j}^{(2)} = 0$ for all $n \in \mathbb{N}$, $j = 1, \ldots, 2n + 1$. Hence, under the assumption that $\boldsymbol{f}$ is the solution of $\mathcal{T}\boldsymbol{f} = V$, that

is solenoidal with the smallest $\mathbf{L}_2(\mathbb{B}_R)$-norm, the functions $f_{n,j}^{(1)}$ and $f_{n,j}^{(2)}$ are for all $n \in \mathbb{N}$, $j = 1, \ldots, 2n+1$ related by

$$f_{n,j}^{(1)}(x) = \frac{\sqrt{n(n+1)}}{x^2} \int_0^x t f_{n,j}^{(2)}(t)\,\mathrm{d}t. \tag{12.16}$$

In the case of $\iota = 3$, we directly obtain the minimum norm solution since the solenoidal condition does not affect this direction of the density, see Eq. (12.13). □

As an immediate consequence, we obtain a comparable result under the assumption that the vector field $\boldsymbol{f}$ is surface divergence-free, that is $\boldsymbol{\nabla}^* \cdot \boldsymbol{f} = 0$.

Corollary 12.19 (Surface Divergence-free). *Let the density $\boldsymbol{f} \in \mathbf{L}_2(\mathbb{B}_R)$ be sufficiently smooth and let the surface gradient be interchangeable with the series in Eq.* (12.10)*. Then we can compute a unique minimum norm surface divergence-free density.*

Proof. The proof is similar to the previous one. Therefore, we only concentrate on the differences. Again, under the assumption that the differential operator can be interchanged with the series, we get

$$\begin{aligned} 0 &= \boldsymbol{\nabla}_{\hat{\boldsymbol{x}}}^* \cdot \left(\sum_{i=1}^{3} f_{n,j}^{(i)}(x) \boldsymbol{y}_{n,j}^{(i)}(\hat{\boldsymbol{x}}) \right) \\ &= \left(2 f_{n,j}^{(1)}(x) - \sqrt{n(n+1)} f_{n,j}^{(2)}(x) \right) Y_{n,j}(\hat{\boldsymbol{x}}). \end{aligned}$$

Hence, we obtain a one-to-one relation between $f_{n,j}^{(1)}$ and $f_{n,j}^{(2)}$ given by

$$f_{n,j}^{(1)} = \frac{\sqrt{n(n+1)}}{2} f_{n,j}^{(2)} \tag{12.17}$$

for all $n \in \mathbb{N}$, $j = 1, \ldots, 2n+1$ and $f_{0,1}^{(1)} = 0$. □

Another tangential differential operator that occurs in the context of vector spherical harmonics is the $\boldsymbol{L}^*$ operator. Thus, the additional directional constraint discussed next is $\boldsymbol{L}^* \cdot \boldsymbol{f} = 0$.

Lemma 12.20 (Surface Curl-free). *Let the density $\boldsymbol{f} \in \mathbf{L}_2(\mathbb{B}_R)$ be sufficiently smooth and let the surface curl be interchangeable with the series in Eq.* (12.10)*. Suppose that $\boldsymbol{L}^* \cdot \boldsymbol{f} = 0$. Then the functions $f_{n,j}^{(3)}$ vanish for all $n \in \mathbb{N}$, $j = 1, \ldots, 2n+1$ in the cases $\iota \in \{1, 2\}$ and in the case of $\iota = 3$ the problem $\mathcal{T}\boldsymbol{f} = V$ does not have a solution.*

Proof. Again, under the assumption that the surface curl gradient interchanges with the series, we obtain with Eqs. (2.4) and (2.6) and Theorem 2.16 that

$$\begin{aligned} 0 &= \boldsymbol{L}_{\hat{\boldsymbol{x}}}^* \cdot \left(\sum_{i=1}^{3} f_{n,j}^{(i)}(x) \boldsymbol{y}_{n,j}^{(i)}(\hat{\boldsymbol{x}}) \right) \\ &= \sum_{i=1}^{3} \left(f_{n,j}^{(i)}(x) \boldsymbol{L}_{\hat{\boldsymbol{x}}}^* \cdot \boldsymbol{y}_{n,j}^{(i)}(\hat{\boldsymbol{x}}) \right) \\ &= f_{n,j}^{(3)}(x) \boldsymbol{L}_{\hat{\boldsymbol{x}}}^* \cdot \boldsymbol{y}_{n,j}^{(3)}(\hat{\boldsymbol{x}}) \\ &= -\sqrt{n(n+1)} f_{n,j}^{(3)}(x) Y_{n,j}(\hat{\boldsymbol{x}}) \end{aligned} \tag{12.18}$$

for all $n \in \mathbb{N}$, $j = 1, \dots, 2n+1$. Consequently, $f_{n,j}^{(3)}$ vanishes independent of the former results. In addition, we neither gain further conditions on $f_{n,j}^{(1)}$ nor on $f_{n,j}^{(2)}$. □

In contrast, by means of the classical curl operator, we can obtain more information on the density. This is shown in the next theorem for an irrotational, or curl-free, vector field $\boldsymbol{f}$.

Theorem 12.21 (Irrotational). *Let the density $\boldsymbol{f} \in \mathbf{L}_2(\mathbb{B}_R)$ be sufficiently smooth and let the curl operator be interchangeable with the series in Eq.* (12.10)*. Then we can obtain further information of the irrotational density if $\iota \in \{1, 2\}$.*

Proof. Due to the allowed interchanging, we obtain by means of Eq. (2.6) and Lemmas 2.17 to 2.19 that

$$\begin{aligned}
\mathbf{0} &= \boldsymbol{\nabla}_{\boldsymbol{x}} \wedge \left(\sum_{i=1}^{3} f_{n,j}^{(i)}(x) \boldsymbol{y}_{n,j}^{(i)}(\hat{\boldsymbol{x}}) \right) \\
&= \sum_{i=1}^{3} \left(\boldsymbol{\nabla}_{\boldsymbol{x}} \wedge \left(f_{n,j}^{(i)}(x) \boldsymbol{y}_{n,j}^{(i)}(\hat{\boldsymbol{x}}) \right) \right) \\
&= \sum_{i=1}^{2} \left(\frac{\mathrm{d} f_{n,j}^{(i)}(x)}{\mathrm{d}x} \hat{\boldsymbol{x}} \wedge \boldsymbol{y}_{n,j}^{(i)}(\hat{\boldsymbol{x}}) + \frac{f_{n,j}^{(i)}(x)}{x} \boldsymbol{\nabla}_{\hat{\boldsymbol{x}}}^{*} \wedge \boldsymbol{y}_{n,j}^{(i)}(\hat{\boldsymbol{x}}) \right) \\
&\quad + \frac{1}{\sqrt{n(n+1)}} \boldsymbol{\nabla}_{\boldsymbol{x}} \wedge \boldsymbol{L}_{\hat{\boldsymbol{x}}}^{*} \left(f_{n,j}^{(3)}(x) Y_{n,j}(\hat{\boldsymbol{x}}) \right) \\
&= \left(\frac{\mathrm{d} f_{n,j}^{(2)}(x)}{\mathrm{d}x} - \sqrt{n(n+1)} \frac{f_{n,j}^{(1)}(x)}{x} + \frac{f_{n,j}^{(2)}(x)}{x} \right) \boldsymbol{y}_{n,j}^{(3)}(\hat{\boldsymbol{x}}) \\
&\quad - \frac{\sqrt{n(n+1)}}{x} f_{n,j}^{(3)}(x) \boldsymbol{y}_{n,j}^{(1)}(\hat{\boldsymbol{x}}) - \left(\frac{f_{n,j}^{(3)}(x)}{x} + \frac{\mathrm{d} f_{n,j}^{(3)}(x)}{\mathrm{d}x} \right) \boldsymbol{y}_{n,j}^{(2)}(\hat{\boldsymbol{x}}).
\end{aligned}$$

Hence, we get for all $n \in \mathbb{N}$, $j = 1, \dots, 2n+1$, and $x \in (0, R]$ the equations

$$f_{n,j}^{(3)}(x) \equiv 0, \tag{12.19a}$$

$$f_{n,j}^{(1)}(x) = \frac{1}{\sqrt{n(n+1)}} \left(x \frac{\mathrm{d} f_{n,j}^{(2)}(x)}{\mathrm{d}x} + f_{n,j}^{(2)}(x) \right) \tag{12.19b}$$

$$\Leftrightarrow \qquad f_{n,j}^{(2)}(x) = \frac{c_{n,j}^{(3)}}{x} + \frac{\sqrt{n(n+1)}}{x} \int_0^x f_{n,j}^{(1)}(t) \, \mathrm{d}t, \tag{12.19c}$$

where the constant $c_{n,j}^{(3)} \in \mathbb{R}$ needs to be determined by further conditions for all $n \in \mathbb{N}$, $j = 1, \dots, 2n+1$. For example, from the continuity of $f_{n,j}^{(1)}$ at the origin, we immediately obtain $c_{n,j}^{(3)} = 0$ for all $n \in \mathbb{N}$, $j = 1, \dots, 2n+1$. □

The last presented additional uniqueness constraint for the vector-valued case is neither a pure radial nor a pure directional uniqueness constraint. In the case of a scalar-valued density F and the problem $\mathcal{S}F = V$, we have already seen that the harmonicity constraint for the density reduces to a solely radial constraint, see Example 12.17. This fact is based on the chosen basis system for the analysis of the forward operator and Eq. (12.12). However, an additional radial uniqueness constraint alone cannot be enough for the vector-valued density to be harmonic since the Morse-Feshbach vector spherical harmonics of type $i = 1$, 2

are not eigenfunctions of the vectorial Beltrami operator, see Corollary 5.16. In contrast, in Lemma 5.40 a characterization of the harmonic functions in $\mathbf{L}_2(\mathbb{B}_R)$ is given. Now, we discuss in detail the harmonicity constraint, that is $\boldsymbol{\Delta} \boldsymbol{f} = \mathbf{0}$, for sufficiently smooth $\boldsymbol{f} \in \mathbf{L}_2(\mathbb{B}_R)$. The Morse-Feshbach vector spherical harmonics of type $i = 3$ coincide with the Edmonds vector spherical harmonics, which are indeed eigenfunctions of the vectorial Beltrami operator. From the proof of Lemma 5.40, we immediately obtain by means of the fundamental system that

$$f_{n,j}^{(3)}(x) = c_{n,j}^{(5)} x^{-(n+1)} + d_{n,j}^{(5)} x^n,$$

where $c_{n,j}^{(5)}$, $d_{n,j}^{(5)} \in \mathbb{R}$ for all $n \in \mathbb{N}$, $j = 1, \ldots, 2n+1$. Since $f_{n,j}^{(3)} \in \mathrm{L}_2^w([0,R])$, we get $c_{n,j}^{(5)} = 0$ for all $n \in \mathbb{N}$, $j = 1, \ldots, 2n+1$. The other coefficients remain to be determined.

Now, let $\iota = 3$ be given and let the density $\boldsymbol{f}$ be harmonic. Then the coefficients $\{d_{n,j}^{(5)}\}_{n\in\mathbb{N}, j=1,\ldots,2n+1}$ of $f_{n,j}^{(3)}$, which is given by

$$f_{n,j}^{(3)}(x) = d_{n,j}^{(5)} x^n, \tag{12.20}$$

are uniquely determined by Eq. (12.12). However, with this approach we are not able to gain more information about the remaining two directions of the current. Therefore, the minimum norm condition is additionally required to obtain a unique harmonic solution of the problem $\mathcal{T}\boldsymbol{f} = V$.

For $\iota = 1, 2$, we can uniquely determine the respective other direction from the information on $f_{n,j}^{(\iota)}$ obtained from Eq. (12.12). Since the Morse-Feshbach vector spherical harmonics of type $i \neq 3$ are not eigenfunctions of the Beltrami operator, we convert the corresponding density expansion into an expansion based on the Edmonds vector spherical harmonics. From the proof of Lemma 5.40, a fundamental system for the vector-valued Laplacian is known, that is $\{x^{n+1}, x^{-(n+2)}\}$ for $i = 1$ and $\{x^{n-1}, x^{-n}\}$ for $i = 2$. Since the final functions have to be elements of $\mathrm{L}_2^w([0,R])$, we can reduce the possible ansatz functions to certain linear combinations of the fundamental system. For all $n \in \mathbb{N}_0$, only x^{n+1} remains for $i = 1$, whereas for $i = 2$ we have x^{n-1} for $n > 1$ and $\{1, x^{-1}\}$ for $n = 1$. In addition, the function $\boldsymbol{x} \mapsto \tilde{\boldsymbol{y}}_{n,j}^{(2)}(\hat{\boldsymbol{x}})$ is only continuous if the angular part is constant, which is not the case for all $n \in \mathbb{N}$, see Eq. (5.4b). The functions $\boldsymbol{x} \mapsto x^{-1}\tilde{\boldsymbol{y}}_{n,j}^{(2)}(\hat{\boldsymbol{x}})$ are never continuous at the origin. Thus, the candidates further reduce to x^{n-1} for $i = 2$ with $n > 1$.

It is now the aim to combine the two directions $f_{n,j}^{(1)}(x)$ and $f_{n,j}^{(2)}(x)$ in such a way that the corresponding part of the density $\boldsymbol{f}$ is parallel to an Edmonds vector spherical harmonic for almost all $x \in [0,R]$. Based on Eq. (5.4), we have two opportunities to combine these two functions. We first choose for all $n \in \mathbb{N}$, $j = 1, \ldots, 2n+1$ the relation

$$f_{n,j}^{(2)} = -\sqrt{\frac{n}{n+1}} f_{n,j}^{(1)}. \tag{12.21}$$

Then we get for all $n \in \mathbb{N}$, $j = 1, \ldots, 2n+1$ the identity

$$\begin{aligned}
&f_{n,j}^{(2)}(x)\boldsymbol{y}_{n,j}^{(2)}(\hat{\boldsymbol{x}}) + f_{n,j}^{(1)}(x)\boldsymbol{y}_{n,j}^{(1)}(\hat{\boldsymbol{x}}) \\
&= -\sqrt{\frac{n}{n+1}} f_{n,j}^{(1)}(x)\boldsymbol{y}_{n,j}^{(2)}(\hat{\boldsymbol{x}}) + f_{n,j}^{(1)}(x)\boldsymbol{y}_{n,j}^{(1)}(\hat{\boldsymbol{x}}) \\
&= \sqrt{\frac{2n+1}{n+1}} f_{n,j}^{(1)}(x) \left(-\sqrt{\frac{n}{2n+1}}\boldsymbol{y}_{n,j}^{(2)}(\hat{\boldsymbol{x}}) + \sqrt{\frac{n+1}{2n+1}}\boldsymbol{y}_{n,j}^{(1)}(\hat{\boldsymbol{x}}) \right)
\end{aligned}$$

$$= \sqrt{\frac{2n+1}{n+1}} f_{n,j}^{(1)}(x) \tilde{\boldsymbol{y}}_{n,j}^{(1)}(\hat{\boldsymbol{x}}),$$

where we used Eq. (5.4) in the last step. Based on the preliminary considerations, we obtain a unique condition for the harmonicity of the right-hand side of the latter equation. This condition is given for all $n \in \mathbb{N}_0$ and $x \in [0, R]$ by $f_{n,j}^{(1)}(x) = c_{n,j}^{(5)} x^{n+1}$. The remaining coefficients $\{c_{n,j}^{(5)}\}_{n \in \mathbb{N}_0, j=1,\dots,2n+1}$ are uniquely determined by Eq. (12.12).

On the other hand, there exist a second approach to combine Morse-Feshbach vector spherical harmonics of type $i = 1, 2$ to Edmonds vector spherical harmonics. Thus, we choose for all $n \in \mathbb{N}$, $j = 1, \dots, 2n+1$ the relation

$$f_{n,j}^{(2)} = \sqrt{\frac{n+1}{n}} f_{n,j}^{(1)}. \tag{12.22}$$

Then we get for all $n \in \mathbb{N}$, $j = 1, \dots, 2n+1$ the identity

$$\begin{aligned}
& f_{n,j}^{(2)}(x) \boldsymbol{y}_{n,j}^{(2)}(\hat{\boldsymbol{x}}) + f_{n,j}^{(1)}(x) \boldsymbol{y}_{n,j}^{(1)}(\hat{\boldsymbol{x}}) \\
&= \sqrt{\frac{n+1}{n}} f_{n,j}^{(1)}(x) \boldsymbol{y}_{n,j}^{(2)}(\hat{\boldsymbol{x}}) + f_{n,j}^{(1)}(x) \boldsymbol{y}_{n,j}^{(1)}(\hat{\boldsymbol{x}}) \\
&= \sqrt{\frac{2n+1}{n}} f_{n,j}^{(1)}(x) \left(\sqrt{\frac{n+1}{2n+1}} \boldsymbol{y}_{n,j}^{(2)}(\hat{\boldsymbol{x}}) + \sqrt{\frac{n}{2n+1}} \boldsymbol{y}_{n,j}^{(1)}(\hat{\boldsymbol{x}}) \right) \\
&= \sqrt{\frac{2n+1}{n}} f_{n,j}^{(1)}(x) \tilde{\boldsymbol{y}}_{n,j}^{(2)}(\hat{\boldsymbol{x}}),
\end{aligned}$$

where again we used Eq. (5.4) in the last step. According to the fundamental system, we need to choose the function $f_{n,j}^{(1)}(x) = d_{n,j}^{(5)} x^{n-1}$ for all $n \in \mathbb{N}$ with $n > 1$ and $x \in [0, R]$ to obtain harmonicity. Here, the coefficients $d_{n,j}^{(5)}$ are for all $n \in \mathbb{N}$, $j = 1, \dots, 2n+1$ uniquely determined by Eq. (12.12). This preliminary considerations are summarized in the next theorem.

Theorem 12.22. *Let the continuous/star-shaped VLI operator for ι be given. Let for all $n \in \mathbb{N}_{0_\iota}$, $j = 1, \dots, 2n+1$ the radial assumptions*

$$f_{n,j}^{(\iota)}(x) = d_{n,j} \begin{cases} x^{n-1} & \text{if } \iota = 1, \text{or} \\ x^{n+1} & \text{if } \iota = 1, \\ x^{n-1} & \text{if } \iota = 2, \text{or} \\ x^{n+1} & \text{if } \iota = 2, \\ x^{n} & \text{if } \iota = 3 \end{cases}$$

be satisfied, where we set $d_{n,j} = 0$ in the case of x^{n-1} for $n = 1$ and $\iota \in \{1, 2\}$. If $\boldsymbol{f}$ is assumed to be harmonic with minimum norm, then $\boldsymbol{f} \in \mathbf{L}_2(\mathbb{B}_R)$ is uniquely determined by the potential.

Proof. We start with the case $\iota = 3$. Then, by means of the radial assumption, each function $\boldsymbol{x} \mapsto f_{n,j}^{(3)}(x) \boldsymbol{y}_{n,j}^{(3)}(\hat{\boldsymbol{x}})$ is harmonic, see Lemma 5.40. The coefficients $\{d_{n,j}\}_{n \in \mathbb{N}_{0_\iota}, j=1,\dots,2n+1}$ are uniquely determined by Eq. (12.12). Due to the minimum norm assumption and the $\mathbf{L}_2(\mathbb{B}_R)$-orthogonality of the vector spherical harmonics, we obtain $f_{n,j}^{(1)} = f_{n,j}^{(2)} = 0$ for all $n \in \mathbb{N}_{0_i}$, $j = 1, \dots, 2n+1$ and, hence, a unique solution of the inverse problem $\mathcal{T}\boldsymbol{f} = V$.

Consider the case $\iota = 1$. Then for both stated radial uniqueness constraints, we obtain a unique representation for the direction corresponding to the Morse-Feshbach vector spherical harmonics of type ι, that is $f^{(1)}_{n,j}$, by means of Lemma 12.16 or Eq. (12.12). If the radial constraint $f^{(\iota)}_{n,j}(x) = d_{n,j}x^{n-1}$ is given, we immediately obtain a unique representation of $f^{(2)}_{n,j}$ using Eq. (12.22) such that $\boldsymbol{f}$ is harmonic. On the other hand, if the radial constraint $f^{(\iota)}_{n,j}(x) = d_{n,j}x^{n+1}$ is used, we can calculate $f^{(2)}_{n,j}$ by Eq. (12.21) in order to achieve a harmonic density. The additional minimum norm condition yields $f^{(3)}_{n,j} = 0$ for all $n \in \mathbb{N}$, $j = 1, \dots, 2n+1$.

Finally, the proof for $\iota = 2$ is the same as the one for $\iota = 1$ with permuted roles of $i = 1$ and $i = 2$. □

The results achieved within this section are summarized in Table 12.2. Therein, based on the chosen additional directional uniqueness constraint and the parameter ι corresponding to the operator $\mathcal{T}$, the directions of the density that are affected by the uniqueness constraints are listed. For example, if $\iota = 1$ is given by the underlying problem and the current is assumed to be solenoidal then $f^{(2)}_{n,j}$ can be calculated from knowledge of $f^{(1)}_{n,j}$ and their relation is stated in Eq. (12.16).

Condition	$\iota = 1$	$\iota = 2$	$\iota = 3$
$\boldsymbol{\nabla} \cdot \boldsymbol{f} = 0$	$f^{(2)}_{n,j}$, Eq. (12.14)	$f^{(1)}_{n,j}$, Eq. (12.16)	–
$\boldsymbol{\nabla}^* \cdot \boldsymbol{f} = 0$	$f^{(2)}_{n,j}$, Eq. (12.17)	$f^{(1)}_{n,j}$, Eq. (12.17)	–
$\boldsymbol{L}^* \cdot \boldsymbol{f} = 0$	$f^{(3)}_{n,j} = 0$, Eq. (12.18)	$f^{(3)}_{n,j} = 0$, Eq. (12.18)	$f^{(3)}_{n,j} = 0$, Eq. (12.18)
$\boldsymbol{\nabla} \wedge \boldsymbol{f} = \boldsymbol{0}$	$f^{(2)}_{n,j}$, Eq. (12.19c)	$f^{(1)}_{n,j}$, Eq. (12.19b)	$f^{(3)}_{n,j} = 0$ Eq. (12.19a)
	$f^{(3)}_{n,j} = 0$ Eq. (12.19a)	$f^{(3)}_{n,j} = 0$ Eq. (12.19a)	
$\boldsymbol{\Delta f} = \boldsymbol{0}$	$f^{(2)}_{n,j}$, Eq. (12.21)	$f^{(1)}_{n,j}$, Eq. (12.22)	
	$f^{(3)}_{n,j} = 0$	$f^{(3)}_{n,j} = 0$	$f^{(3)}_{n,j}$, Eq. (12.20)

TABLE 12.2: *Computable radial functions for given $f^{(\iota)}_{n,j}$ under the respective directional condition*

Chapter 13.

Inverse Magneto-electroencephalography Problem

In the case of the multiple-shell model, where L is the number of shells, we derive a harmonic VLI operator for the MEG problem in Chapter 9 as well as a linear combination of continuous VLI operators for the EEG problem in Chapter 10. Recall that components of the magnetic field $\boldsymbol{B}$, such as the magnetic flux density, can be measured by the magnetoencephalograph outside the head $\mathbb{B}_{\varrho_L}$. In addition, electroencephalography electrodes can measure electric potential differences u_L on the scalp. Now, we combine these two problems in order to gain more information about the neuronal current $\boldsymbol{J}^{\mathrm{P}}$ inside the brain $\mathbb{B}_{\varrho_0}$. The corresponding integral equations are given by

$$
\begin{aligned}
u_L(\boldsymbol{y}) &= \int_{\mathbb{B}_{\varrho_0}} \boldsymbol{J}^{\mathrm{P}}(\boldsymbol{x}) \cdot \boldsymbol{k}_{\mathrm{E}}(\boldsymbol{x},\boldsymbol{y}) \,\mathrm{d}\boldsymbol{x}, && \boldsymbol{y} \in \mathbb{S}_{[\varrho_{L-1},\varrho_L]},\\
U(\boldsymbol{y}) &= \int_{\mathbb{B}_{\varrho_0}} \boldsymbol{J}^{\mathrm{P}}(\boldsymbol{x}) \cdot \boldsymbol{k}_{\mathrm{M}}(\boldsymbol{x},\boldsymbol{y}) \,\mathrm{d}\boldsymbol{x}, && \boldsymbol{y} \in \overline{\mathbb{B}^{\mathrm{ext}}_{\varrho_L}},\\
\boldsymbol{B}(\boldsymbol{y}) &= \mu_0 \boldsymbol{\nabla}_{\boldsymbol{y}} \left(\int_{\mathbb{B}_{\varrho_0}} \boldsymbol{J}^{\mathrm{P}}(\boldsymbol{x}) \cdot \boldsymbol{k}_{\mathrm{M}}(\boldsymbol{x},\boldsymbol{y}) \,\mathrm{d}\boldsymbol{x} \right), && \boldsymbol{y} \in \overline{\mathbb{B}^{\mathrm{ext}}_{\varrho_L}}.
\end{aligned}
$$

The precise problems are formulated in Problems 9.1 and 10.2.

We have already analyzed the well-definedness of the two direct problems related to these integral equations by means of the continuous/star-shaped VLI operator. This includes the integrability of the integrand and the evaluation of the resulting functions at the sensor positions. Since a reconstruction of the neuronal current $\boldsymbol{J}^{\mathrm{P}}$ is desired, the corresponding inverse problems are considered. Due to the compactness of the occurring integral operators, see Theorem 12.1, we already know that these inverse problems are ill-posed. For the first time this has been realized for general bioelectromagnetic inverse problems in living conductors in [119]. Therefore, it is sometimes called the Helmholtz principle, see [115]. Since then it has been extensively discussed in the literature, see [38, 40–42, 44–48, 50, 51, 53, 55, 71–73, 75, 181]. Therein, by means of an inversion of the electric potential or the magnetic field, certain parts of the neuronal current are reconstructed. The neuronal current itself is assumed to be a collection of dipoles or a continuous dipole distribution. In [47], a survey over the non-uniqueness is given. In general, the neuronal current is decomposed into a variety of ways in order to achieve these results. An overview of these decompositions in comparison to the Edmonds approach pursued in this thesis is given in Chapter 15.

An often pursued approach is a separation of the neuronal current into an angular and a radial part. However, we use the Edmonds expansion of the angular part of the neuronal current, which is new for this problem. This enables a more precise characterization of the null space of the EEG integral operator and the possibility to combine the results of the MEG and EEG null space characterizations. Besides a decomposition for the angular part, we also use a generalized Fourier expansion of the radial part by means of Jacobi polynomials.

This allows an even more precise characterization of the null spaces of both operators. For the harmonic VLI operator, a representation of the null space is given in Theorems 12.9 and 12.13. Thereout, two problems concerning the non-uniqueness of the inverse MEG and EEG problem arise:

(A) Not all directions of the neuronal current can be reconstructed, even if the measured quantities are completely known;

(B) not all parts of the reconstructable directions can be calculated from the measured quantities.

In summary, the dimension of the null space is infinite. Besides the non-uniqueness of the inverse MEG and EEG problem, more challenges for the inversion emerge:

(C) The inversion of the MEG and EEG problem includes a downward continuation, which makes them severely unstable.

(D) In the real data situation, the continuous fields and potentials cannot be measured as a whole. Due to the construction of the magneto- and electroencephalograph, only about 170 discrete data points are obtained per measurement time point. This is known as the lack of data.

(E) The obtained data is noisy. The white noise of the magnetometers and gradiometers is at most $5\,\mathrm{fT\,Hz^{-1/2}}$ or $5\,\mathrm{fT\,cm^{-1}\,Hz^{-1/2}}$, respectively, in the case of frequencies in the magnitude of 60 to 70 Hz for 96 % of the sensors and at most $10\,\mathrm{fT\,Hz^{-1/2}}$ or $10\,\mathrm{fT\,cm^{-1}\,Hz^{-1/2}}$ for all sensors, see [62]. Typical neuromagnetic signals are in the range 50 to 500 fT, see [108]. A typical adult human EEG signal is about 10 to 50 µV in amplitude when measured from the scalp, see [10], whereas the root mean square noise across all EEG sensors is smaller than 0.4 µV, see [62].

(F) Besides technical noise, the measured quantities can be influenced by certain effects, such as head, eye, jaw, or neck movements, the magnetic fields generated by the heart, particles attached or implanted to the body, and non-human outer fields and currents, see [104].

Now, we analyze the ill-posedness in the sense of Hadamard, see Definition 11.1, of the inverse magneto-electroencephalography problem in detail.

13.1. Non-uniqueness

First, we concentrate on the non-uniqueness of the inverse problem. To this end, we assume that a solution exists and that the neuronal current fulfils Assumption 3.2 with the multiple-shell model containing at least two shells. Then we are able to formulate its unique Fourier series by

$$\boldsymbol{J}^{\mathrm{P}} = \sum_{i=1}^{3} \sum_{m=0}^{\infty} \sum_{n=0_i}^{\infty} \sum_{j=1}^{2n+1} J^{\wedge}[i,m,n,j] \tilde{\boldsymbol{g}}^{(i)}_{m,n,j}(\varrho_0;\cdot), \tag{13.1}$$

where the occurring vector-valued basis functions are defined in Definition 5.37. They consist of Edmonds vector spherical harmonics and an orthonormal set of radial basis functions,

see Definition 5.1. Note that the index i denotes the direction of the current that belongs to the Edmonds vector spherical harmonics of this type, whereas n is the degree and j the order of the spherical harmonics. The summation index m belongs to the generalized Fourier expansion of the radial part. More precisely, with $i = 1, 2, 3$, $m \in \mathbb{N}_0$, $n \in \mathbb{N}_{0_i}$, and $j = 1, \dots, 2n+1$, we have

$$\tilde{\boldsymbol{g}}^{(i)}_{m,n,j}(\varrho_0; \boldsymbol{x}) \coloneqq Q_m^{(t_n^{(i)}+1/2)}(\varrho_0; x)\tilde{\boldsymbol{y}}^{(i)}_{n,j}(\hat{\boldsymbol{x}}) \tag{13.2}$$

with

$$t_n^{(i)} \coloneqq \begin{cases} n+1 & \text{if } i = 1, \\ n-1 & \text{if } i = 2, \\ n & \text{if } i = 3. \end{cases} \tag{13.3}$$

Note that the direction corresponding to $i = 1$ is in the null space of $\mathcal{T}_{\mathrm{M}}$ as well as in the null space of $\mathcal{T}_{\mathrm{E}}$. However, in order to state a complete orthonormal basis of $\mathbf{L}_2(\mathbb{B}_{\varrho_0})$ and to expand the neuronal current in Eq. (13.1) we need to determine $\{t_n^{(1)}\}_{n\in\mathbb{N}_0}$. We chose the sequence of exponents in such a way that a characterization of the harmonic and anharmonic orthonormal basis functions based on Lemma 5.40 is possible.

For solving the inverse problems, let us assume that the measured magnetic field $\boldsymbol{B}$ and the electric potential u_L are completely known. Then we get the representations

$$\begin{aligned} \boldsymbol{B}(\boldsymbol{y}) &= \sum_{n=0}^{\infty}\sum_{j=1}^{2n+1} B_{\varrho_L}^{\wedge}(n,j)\boldsymbol{h}^{(1)}_{n,j}(\varrho_L; \boldsymbol{y}), \\ u_L(\boldsymbol{y}) &= \sum_{n=0}^{\infty}\sum_{j=1}^{2n+1} \left(\frac{n+1}{2n+1}\left(\frac{y}{\varrho_L}\right)^{2n+1} + \frac{n}{2n+1}\right)\left(\frac{\varrho_L}{y}\right)^n u_L^{\wedge}(n,j)\frac{1}{y}Y_{n,j}(\hat{\boldsymbol{y}}), \end{aligned}$$

where $\boldsymbol{y} \in \mathbb{B}^{\mathrm{ext}}_{\varrho_L}$ in the case of the magnetic field and $\boldsymbol{y} \in \mathbb{S}_{[\varrho_{L-1},\varrho_L]}$ in the case of the electric potential. The expansion coefficients are defined for all $n \in \mathbb{N}_0$, $j = 1, \dots, 2n+1$ by

$$\begin{aligned} B_{\varrho_L}^{\wedge}(n,j) &\coloneqq \int_{\mathbb{S}_{\varrho_L}} \boldsymbol{B}(\varrho_L\hat{\boldsymbol{y}}) \cdot \boldsymbol{h}^{(1)}_{n,j}(\varrho_L; \varrho_L\hat{\boldsymbol{y}}) \,\mathrm{d}\omega(\hat{\boldsymbol{y}}), \\ u_L^{\wedge}(n,j) &\coloneqq \frac{1}{\varrho_L}\int_{\mathbb{S}_{\varrho_L}} u_L(\varrho_L\hat{\boldsymbol{y}})Y_{n,j}(\hat{\boldsymbol{y}}) \,\mathrm{d}\omega(\hat{\boldsymbol{y}}). \end{aligned}$$

For the neuronal current, we eventually obtain by Theorems 9.4 and 10.3 $B_{\varrho_L}^{\wedge}(0,1) = u_L^{\wedge}(0,1) = 0$ and for all $n \in \mathbb{N}$, $j = 1, \dots, 2n+1$ the relations

$$J^{\wedge}[3,0,n,j] = -\frac{1}{\mu_0}\sqrt{\frac{(2n+1)(2n+3)}{n\varrho_0}}\left(\frac{\varrho_L}{\varrho_0}\right)^{n+1} B_{\varrho_L}^{\wedge}(n,j), \tag{13.4a}$$

$$J^{\wedge}[2,0,n,j] = \sqrt{\frac{n}{(2n+1)^2\varrho_0}}\frac{1}{\beta_n^{(L)}}\left(\frac{\varrho_L}{\varrho_0}\right)^n u_L^{\wedge}(n,j), \tag{13.4b}$$

where the coefficients $\beta_n^{(L)}$ are given in Eq. (4.18) for all $n \in \mathbb{N}$. Thus, we observe that not all parts of the neuronal current can be reconstructed, even if the measured quantities are completely known. Only the part of the neuronal current that belongs to the Edmonds vector spherical harmonics of type 2 and the toroidal part belonging to the Edmonds vector

spherical harmonics of type 3 are related to the measured quantities. The portion of the neuronal current that belongs to the Edmonds vector spherical harmonics of type 1 can neither be reconstructed from MEG nor EEG data. A comparable result is stated in [47], wherein a decomposition by means of Morse-Feshbach vector spherical harmonics is used. The advantage of Edmonds vector spherical harmonics over the Morse-Feshbach vector spherical harmonics is a more precise characterization of the reconstructable parts, which will become clear in Chapter 15.

As we have already mentioned, we further improve previous modellings by characterizing the reconstructable parts by expanding the radial part of the neuronal current via orthonormal polynomials. We can see in Eq. (13.4) that almost all summands of the series with respect to m vanish. Only the summand corresponding to $m = 0$ contributes to the electric potential and the magnetic field. In this case, the basis function of degree $m = 0$ for the radial part reduces to

$$\begin{aligned} Q_0^{(t_n^{(i)}+1/2)}(\varrho_0; x) &= \sqrt{\frac{2t_n^{(i)}+3}{\varrho_0^3}} \left(\frac{x}{\varrho_0}\right)^{t_n^{(i)}} P_0^{(0,t_n^{(i)}+1/2)}\left(2\frac{x^2}{\varrho_0^2}-1\right) \\ &= \sqrt{\frac{2t_n^{(i)}+3}{\varrho_0^3}} \left(\frac{x}{\varrho_0}\right)^{t_n^{(i)}}, \end{aligned}$$

since the Jacobi polynomials of degree zero are equal to one. The corresponding orthonormal basis functions on the ball are for all $n \in \mathbb{N}$, $j = 1, \ldots, 2n+1$ given by

$$\tilde{\boldsymbol{g}}_{0,n,j}^{(2)}(\varrho_0; \boldsymbol{x}) = \sqrt{\frac{2n+1}{\varrho_0^3}} \left(\frac{x}{\varrho_0}\right)^{n-1} \tilde{\boldsymbol{y}}_{n,j}^{(2)}(\hat{\boldsymbol{x}}), \tag{13.5a}$$

$$\tilde{\boldsymbol{g}}_{0,n,j}^{(3)}(\varrho_0; \boldsymbol{x}) = \sqrt{\frac{2n+3}{\varrho_0^3}} \left(\frac{x}{\varrho_0}\right)^{n} \tilde{\boldsymbol{y}}_{n,j}^{(3)}(\hat{\boldsymbol{x}}). \tag{13.5b}$$

Due to Lemma 5.40, these functions are harmonic, that is $\boldsymbol{\Delta}\tilde{\boldsymbol{g}}_{0,n,j}^{(2)}(\varrho_0; \cdot) = \boldsymbol{0}$ as well as $\boldsymbol{\Delta}\tilde{\boldsymbol{g}}_{0,n,j}^{(3)}(\varrho_0; \cdot) = \boldsymbol{0}$. Here, the Laplace operator is applied componentwise. Combining this with the characterization of the solenoidality of the orthonormal basis function from Lemma 5.40, we obtain the next result. Only the part of the neuronal current that is solenoidal and harmonic can be reconstructed from MEG and EEG data.

However, based on quasi-static Maxwell's equations, there is no indication that the neuronal current is harmonic. We summarize our considerations concerning the non-harmonicity of the inverse MEG and EEG problem in the case of a multiple-shell model in the next theorem.

Theorem 13.1. *Let Assumption 3.2 with $L \geq 2$ be fulfilled. Let the neuronal current be expanded in the orthonormal basis based on the Edmonds vector spherical harmonics in Eq.* (13.2)*. Then only the part of the neuronal current that is solenoidal and harmonic can be reconstructed. Hence, the reconstructable part is given by*

$$\boldsymbol{J}^{\mathrm{P}} = \sum_{i=2}^{3} \sum_{n=1}^{\infty} \sum_{j=1}^{2n+1} J^{\wedge}[i,0,n,j] \tilde{\boldsymbol{g}}_{0,n,j}^{(i)}(\varrho_0; \cdot).$$

The Fourier coefficients are uniquely determined by Eq. (13.4)*. This can be formulated, see*

Lemma 12.2, equivalently by

$$(\ker \mathcal{T}_{\mathrm{M}})^{\perp} = \overline{\operatorname{span}\left\{ \tilde{\boldsymbol{g}}^{(3)}_{0,n,j}(\varrho_0;\cdot) \;\middle|\; n \in \mathbb{N}, j = 1,\dots,2n+1 \right\}},$$
$$(\ker \mathcal{T}_{\mathrm{E}})^{\perp} = \overline{\operatorname{span}\left\{ \tilde{\boldsymbol{g}}^{(2)}_{0,n,j}(\varrho_0;\cdot) \;\middle|\; n \in \mathbb{N}, j = 1,\dots,2n+1 \right\}}.$$

The occurring operators are defined in Problems 9.1 and 10.2.

Besides the non-uniqueness of the reconstruction, we need to tackle more problems to solve the inverse MEG and EEG problem. We have to handle the lack of data. In the case of the inverse MEG problem, we do not measure the whole magnetic field $\boldsymbol{B}$ but only the magnetic flux density $B_{\boldsymbol{\nu}}$ at a small number of sensor positions. Here, $\boldsymbol{\nu}$ is the normal vector of the sensor surface. Thus, a substantial amount of information on the magnetic field is lost. In addition, typical MEG devices have about 100 magnetometers, which yield about 100 measurements of $B_{\boldsymbol{\nu}}$. The same problem occurs in the case of EEG measurements, where the sensor cap provides us with about 70 measurements of the electric potential difference.

13.2. Instability

According to Hadamard's definition of ill-posedness, an inverse problem is stable if the solution continuously depends on the data. Since compact operators cannot have a bounded inverse, this is not fulfilled for the solution of the magneto-electroencephalography problem. By means of the singular values of a compact operator, we are able to further characterize the instability.

We have already found a Hilbert space and an orthonormal basis for the orthogonal complement of the operator null spaces, see Theorem 13.1. For the image of the three operators $\mathcal{T}_U$, $\mathcal{T}_{\mathrm{M}}$, and $\mathcal{T}_{\mathrm{E}}$, we make the following considerations. The operator $\mathcal{T}_U \colon \mathbf{L}_2(\mathbb{B}_{\varrho_0}) \to \operatorname{Harm}(\overline{\mathbb{B}^{\mathrm{ext}}_{\varrho_L}})$ mapping $\boldsymbol{J}^{\mathrm{P}}$ to the magnetic potential U is a harmonic VLI operator since the integral kernel $\boldsymbol{k}_{\mathrm{M}}$ is a harmonic VLI kernel, see Lemma 6.9. Thus, we can use the results from Theorem 12.9 with $t_n \coloneqq n$ and $\Gamma_n \coloneqq (4\pi)^{-1}\sqrt{n/(n+1)}$ in order to state an SVD for $\mathcal{T}_U$ with the singular values $\{\lambda^U_n\}_{n\in\mathbb{N}}$. Since the magnetic field is given by the gradient of the magnetic potential, that is $\mathcal{T}_{\mathrm{M}}\boldsymbol{J}^{\mathrm{P}} = \mu_0 \boldsymbol{\nabla}(\mathcal{T}_U \boldsymbol{J}^{\mathrm{P}})$, we can use the results of Theorem 12.13 for its SVD. The corresponding singular values are denoted by $\{\lambda^{\mathrm{M}}_n\}_{n\in\mathbb{N}}$. Here, $t_n \coloneqq n$ and $\Gamma_n \coloneqq \mu_0(4\pi)^{-1}\sqrt{n/(n+1)}$. For the operator $\mathcal{T}_{\mathrm{E}} \colon \mathbf{L}_2(\mathbb{B}_{\varrho_0}) \to \mathcal{Z}$, an SVD remains to be found. In Theorem 10.4 a first expansion of the electric potential on the outer shell is stated. This provides us with the idea for the definition of a new Hilbert space with an adequate orthonormal basis.

Lemma 13.2. *For all $n \in \mathbb{N}$ and $j = 1,\dots,2n+1$, let a system of continuously differentiable functions be given by*

$$Z_{n,j}(\boldsymbol{y}) \coloneqq \left(\frac{n+1}{2n+1} \left(\frac{y}{\varrho_L} \right)^{2n+1} + \frac{n}{2n+1} \right) \left(\frac{\varrho_L}{y} \right)^{n} \frac{1}{y} Y_{n,j}(\hat{\boldsymbol{y}}), \qquad \boldsymbol{y} \in \mathbb{S}_{[\varrho_{L-1},\varrho_L]}.$$

The space $\operatorname{span}\{Z_{n,j}\}_{n\in\mathbb{N},j=1,\dots,2n+1}$ *can be equipped with the inner product*

$$\langle f, g \rangle_{\mathcal{Z}} \coloneqq \left\langle f|_{\mathbb{S}_{\varrho_L}}, g|_{\mathbb{S}_{\varrho_L}} \right\rangle_{\mathrm{L}_2(\mathbb{S}_{\varrho_L})}.$$

The completion of $\operatorname{span}\{Z_{n,j} \mid n \in \mathbb{N}, j = 1, \dots, 2n+1\}$ *with respect to the norm induced by this inner product is the Hilbert space*

$$\mathcal{Z}(\mathbb{S}_{[\varrho_{L-1},\varrho_L]}) := \mathcal{Z} := \overline{\operatorname{span}\{Z_{n,j} \mid n \in \mathbb{N}, j = 1, \dots, 2n+1\}}^{\|\cdot\|_{\mathcal{Z}}},$$

where $\{Z_{n,j}\}_{n\in\mathbb{N},j=1,\dots,2n+1}$ *is an orthonormal basis.*

Note that the space $\mathcal{Z}$ is isometrically isomorphic to the space $\mathrm{L}_2(\mathbb{S}_{\varrho_L})$.

Proof. It can easily be verified that $\langle\cdot,\cdot\rangle_{\mathcal{Z}}$ is an inner product on $\operatorname{span}\{Z_{n,j}\}_{n\in\mathbb{N},j=1,\dots,2n+1}$, since $\langle\cdot,\cdot\rangle_{\mathcal{Z}}$ is a symmetric bilinear form over $\operatorname{span}\{Z_{n,j}\}_{n\in\mathbb{N},j=1,\dots,2n+1}$ and $\langle F,F\rangle_{\mathcal{Z}} \geq 0$ for all $F \in \operatorname{span}\{Z_{n,j}\}_{n\in\mathbb{N},j=1,\dots,2n+1}$. We get for all $F \in \operatorname{span}\{Z_{n,j}\}_{n\in\mathbb{N},j=1,\dots,2n+1}$ the representation $F = \sum_{n=1}^{N}\sum_{j=1}^{2n+1} c_{n,j}Z_{n,j}$. From $0 = \langle F,F\rangle_{\mathcal{Z}}$, we immediately obtain $0 \equiv F|_{\mathbb{S}_{\varrho_L}} = \sum_{n=1}^{N}\sum_{j=1}^{2n+1} c_{n,j}\varrho_L^{-1}Y_{n,j}$. Since the spherical harmonics are linearly independent, we get $c_{n,j} = 0$ for all $n \leq N$ and $j = 1, \dots, 2n+1$ and, consequently, $F \equiv 0$. The system $\{Z_{n,j}\}_{n\in\mathbb{N},j=1,\dots,2n+1}$ is, due to the construction of $\mathcal{Z}$, obviously a basis. For the orthonormality, we obtain

$$\langle Z_{n,j}, Z_{m,k}\rangle_{\mathcal{Z}} = \int_{\mathbb{S}_{\varrho_L}} \frac{1}{\varrho_L^2} Y_{n,j}(\hat{\boldsymbol{y}})Y_{m,k}(\hat{\boldsymbol{y}})\,\mathrm{d}\omega(\hat{\boldsymbol{y}}) = \delta_{n,m}\delta_{j,k}. \qquad \square$$

Note that this is no contradiction to the well-known statements according to which harmonic functions are uniquely determined by their boundary values. In the case of harmonic functions over the shell $\mathbb{S}_{[\varrho_{L-1},\varrho_L]}$, the fundamental system is given by the set of all inner and all outer harmonics. The boundary of the shell is given by the two spheres $\mathbb{S}_{\varrho_{L-1}}$ and $\mathbb{S}_{\varrho_L}$. However, in the subspace $\mathcal{Z}$ the inner and outer harmonics are not independent. Therefore, the information obtained on one boundary is sufficient to determine a function in $\mathcal{Z}$.

By means of this Hilbert space, we are able to find an SVD of the EEG forward operator $\mathcal{T}_{\mathrm{E}}$.

Theorem 13.3. *The EEG forward operator* $\mathcal{T}_{\mathrm{E}}$ *maps from* $\mathbf{L}_2(\mathbb{B}_{\varrho_0})$ *to* $\mathcal{Z}$. *In addition, the singular system of* $\mathcal{T}_{\mathrm{E}}$ *is given by* $\{\tilde{\boldsymbol{g}}^{(2)}_{0,n,j}(\varrho_0;\cdot), Z_{n,j}; \lambda^{\mathrm{E}}_n\}_{n\in\mathbb{N},j=1,\dots,2n+1}$ *with the singular values*

$$\lambda^{\mathrm{E}}_n := \lambda^{\mathrm{E}}_{n,j} := \frac{\varrho_0^{n+1/2}}{\varrho_L^n}\frac{2n+1}{\sqrt{n}}\beta^{(L)}_n, \qquad n \in \mathbb{N},\ j = 1, \dots, 2n+1.$$

Note that $\beta^{(L)}_n \neq 0$ *due to Lemma 4.4. In addition,* $\lim_{n\to\infty}\lambda^{\mathrm{E}}_n = 0$.

Proof. From Theorem 10.3, it is known that only the system $\{\tilde{\boldsymbol{g}}^{(2)}_{0,n,j}(\varrho_0;\cdot)\}_{n\in\mathbb{N},j=1,\dots,2n+1}$ contributes to the electric potential. In addition, $H_n \not\equiv 0$ for all $n \in \mathbb{N}$. Thus, the set $\{\tilde{\boldsymbol{g}}^{(2)}_{0,n,j}\}_{n\in\mathbb{N},j=1,\dots,2n+1}$ is an orthonormal basis for $(\ker\mathcal{T}_{\mathrm{E}})^{\perp}$. Eq. (10.5) provides us with a Fourier expansion of $\mathcal{T}_{\mathrm{E}}\boldsymbol{J}^{\mathrm{P}}$, that is

$$u_L(\boldsymbol{y}) = \sum_{n=0}^{\infty}\sum_{j=1}^{2n+1} u_L^{\wedge}(n,j)Z_{n,j}(\boldsymbol{y}),$$

where the coefficients are given by means of Eq. (10.4). This eventually yields the desired representation of the singular values. Since $\varrho_0 < \varrho_L$ and $\beta^{(L)}_n \in \mathcal{O}(n^{-1})$, we get $\lim_{n\to\infty}\lambda^{\mathrm{E}}_n = 0$ exponentially fast. $\square$

$\mathcal{T}$	ONB for $(\ker \mathcal{T})^{\perp}$	ONS for $\overline{\operatorname{ran} \mathcal{T}}$	SV λ_n
$\mathcal{T}_U$	$\{\tilde{\boldsymbol{g}}^{(3)}_{0,n,j}(\varrho_0;\cdot)\}$, $t_n \coloneqq n$	$\{S_{n,j}(\varrho_L;\cdot)\}$	$\sqrt{\frac{n\varrho_0^3\varrho_L}{(n+1)(2n+1)^2(2n+3)(2n-1)}}\left(\frac{\varrho_0}{\varrho_L}\right)^n$
$\mathcal{T}_{\mathrm{M}}$	$\{\tilde{\boldsymbol{g}}^{(3)}_{0,n,j}(\varrho_0;\cdot)\}$, $t_n \coloneqq n$	$\{-\boldsymbol{s}_{n,j}(\varrho_L;\cdot)\}$	$\mu_0\sqrt{\frac{n\varrho_0\varrho_L}{(2n+1)^2(2n+3)}}\left(\frac{\varrho_0}{\varrho_L}\right)^{n+1}$
$\mathcal{T}_{\mathrm{E}}$	$\{\tilde{\boldsymbol{g}}^{(2)}_{0,n,j}(\varrho_0;\cdot)\}$, $t_n \coloneqq n-1$	$\{Z_{n,j}\}$	$(2n+1)\sqrt{\frac{\varrho_0}{n}}\beta_n^{(L)}\left(\frac{\varrho_0}{\varrho_L}\right)^n$

TABLE 13.1: *The SVD of the operators occurring in the inverse MEG and EEG problem. Here, the range of the parameters is $n \in \mathbb{N}$ and $j = 1, \dots, 2n+1$ in each set.*

By means of this SVD, we obtain for the adjoint operator $\mathcal{T}_{\mathrm{E}}^*\colon \mathcal{Z} \to \mathbf{L}_2(\mathbb{B}_{\varrho_0})$ the representation

$$\begin{aligned}\mathcal{T}_{\mathrm{E}}^* u_L &= \int_{\mathbb{S}_{\varrho_L}} u_L(\boldsymbol{y}) \boldsymbol{k}_{\mathrm{E}}(\cdot, \boldsymbol{y}) \,\mathrm{d}\boldsymbol{y} \\ &= \sum_{n=1}^{\infty} \sum_{j=1}^{2n+1} \lambda_n^{\mathrm{E}} u_L^{\wedge}(n,j) \tilde{\boldsymbol{g}}^{(2)}_{0,n,j}(\varrho_0;\cdot).\end{aligned}$$

This implies by means of $\lambda_n^{\mathrm{E}} \neq 0$ for all $n \in \mathbb{N}$ that

$$\overline{\operatorname{ran} \mathcal{T}_{\mathrm{E}}} = (\ker \mathcal{T}_{\mathrm{E}}^*)^{\perp} = \mathcal{Z}. \tag{13.6}$$

For the familiar special case of a homogeneous spherical brain model, we get the next result.

Example 13.4. *In the homogeneous case, see Example 6.11, with the constant conductivity σ_0, we obtain for all $n \in \mathbb{N}$, $j = 1, \dots, 2n+1$ the Fourier coefficients*

$$u_L^{\wedge}(n,j) = \left(\frac{\varrho_0}{\varrho_L}\right)^n \sqrt{\frac{\varrho_0}{n}} \frac{1}{\sigma_0} J^{\wedge}[2,0,n,j]$$

and $u_L^{\wedge}(0,1) = 0$.

Eventually, for the forward operator restricted to the sphere $\mathbb{S}_{\varrho_L}$ as well as for the operator mapping onto the electric potential on the shell $\mathbb{S}_{[\varrho_{L-1},\varrho_L]}$, we are able to state an SVD. Note that in all three cases, that is $\{\lambda_n^U\}_{n\in\mathbb{N}}$, $\{\lambda_n^{\mathrm{M}}\}_{n\in\mathbb{N}}$, and $\{\lambda_n^{\mathrm{E}}\}_{n\in\mathbb{N}}$ the singular values are independent of the order j. We summarize the SVDs in Table 13.1.

Now, we analyze the asymptotic behaviour of the singular values. Recall that $\beta_n^{(L)} \in \mathcal{O}(n^{-1})$ as $n \to \infty$, see Lemma 4.2. For the inverse MEG and EEG problem, we immediately obtain with $\varrho_0 < \varrho_L$ the limits

$$\lim_{n\to\infty} \lambda_n^U = \lim_{n\to\infty} \lambda_n^{\mathrm{M}} = \lim_{n\to\infty} \lambda_n^{\mathrm{E}} = 0.$$

Concluding, in all three cases the corresponding Moore-Penrose inverse operator is not bounded. This is not surprising due to the compactness of the forward operators. However, the singular values of the three problems all have the factor $(\varrho_0/\varrho_L)^n$ in common. Due to this factor, the singular values decay to zero exponentially fast. Thus, the corresponding inverse problems are severely ill-posed. This factor is generated by the upward continuation from the

$\mathcal{T}$	RHS	$\overline{\operatorname{ran}\mathcal{T}}$	Summability Condition
$\mathcal{T}_U$	U	$\operatorname{Harm}(\overline{\mathbb{B}^{\operatorname{ext}}_{\varrho_L}})$	$\sum_{n=1}^{\infty}\sum_{j=1}^{2n+1}\left(\lambda_n^U\right)^{-2}\langle U, S_{n,j}(\varrho_L;\cdot)\rangle^2_{\mathrm{L}_2(\overline{\mathbb{B}^{\operatorname{ext}}_{\varrho_L}})}<\infty$
$\mathcal{T}_{\mathrm{M}}$	$\boldsymbol{B}$	$\mathbf{Harm}\left(\overline{\mathbb{B}^{\operatorname{ext}}_{\varrho_L}}\right)$	$\sum_{n=1}^{\infty}\sum_{j=1}^{2n+1}\left(\lambda_n^{\mathrm{M}}\right)^{-2}\langle \boldsymbol{B}, \boldsymbol{s}_{n,j}(\varrho_L;\cdot)\rangle^2_{\mathbf{Harm}(\overline{\mathbb{B}^{\operatorname{ext}}_{\varrho_L}})}<\infty$
$\mathcal{T}_{\mathrm{E}}$	u_L	$\mathcal{Z}$	$\sum_{n=1}^{\infty}\sum_{j=1}^{2n+1}\left(\lambda_n^{\mathrm{E}}\right)^{-2}\langle u_L, Z_{n,j}\rangle^2_{\mathcal{Z}}<\infty$

TABLE 13.2: *Picard's criterion for the continuous magneto-electroencephalography problem.*

activity inside the cerebrum with radius ϱ_0 to the measurement positions on and outside the head. Note that in the case of the downward continuation of spaceborne gravity data, the ratio of the mean radius of Earth's surface ϱ_{Earth} to the satellite altitude is approximately $\varrho_{\mathrm{Earth}}/(\varrho_{\mathrm{Earth}} + 450\,\mathrm{km}) \approx 0.9340$, see, for example, [91]. In contrast, in our synthetic test case, see Eq. (19.2), the ratio of the approximated scalp radius to the radius of the cerebrum is $\varrho_0/\varrho_L \approx 0.8353$. In addition, the ratio of the approximated human head radius to the radius of the magnetoencephalograph sensor Runge sphere $\mathbb{S}_{R_{\mathrm{sen}}}$ is even worse, that is $\varrho_0/R_{\mathrm{sen}} \approx 0.6676$.

Due to the instability of the MEG and EEG operators, the level of noise, see Item (E), and the defective data, see Item (F) on page 174, have a major impact on the solution. Therefore, a regularization method is needed to solve the inverse problems properly.

13.3. Existence of a Solution

By means of the Spectral Theorem for linear compact operators, we can use Picard's criterion as a necessary and sufficient criterion for the existence of a solution. This criterion consists of two requirements. First, the measured quantity has to be in the orthogonal complement of the adjoint operator null space. For the operators of the inverse magneto-electroencephalography problem, we collect the results from Eqs. (12.6) and (13.6) and Theorem 12.13. Therein, the closure of the ranges is characterized by the closure of the span of certain orthogonal basis functions. In addition, the singular values of the operators $\mathcal{T}_U$ and $\mathcal{T}_{\mathrm{M}}$ are non-zero for all $n \in \mathbb{N}$. Thus, the span contains all orthogonal basis functions of the particular Hilbert spaces. Eventually, the closures of the ranges coincide with the whole Hilbert spaces. This is summarized in Table 13.2. The second requirement of Picard's criterion is a summability condition and also listed in Table 13.2. It regulates the asymptotic behaviour of the measured quantity's Fourier coefficients. For this purpose, the singular values of the operators are needed and stated in Table 13.1.

However, this result obtained by Picard's criterion is merely a theoretical result. We can only apply Picard's criterion to our problem if the measured quantities or their Fourier coefficients, respectively, are completely known. In the actual inverse magneto-electroencephalography problem, only a few noisy measurements of the electric potential and the magnetic field are known, see Problems 9.1 and 10.2.

Concluding, in Sections 13.1 to 13.3 we established that the reconstruction of the neuronal current by means of MEG and EEG data is severely ill-posed, since the solution is not unique and the singular values decay exponentially fast to zero. In order to get rid of the non-uniqueness, certain additional uniqueness constraints are presented in the next section.

For the purpose of handling the instability, we use regularization methods to solve the inverse problem. An introduction to the theory of regularization methods is given in Section 16.2. The regularization methods also help to handle the lack of data and to manage the noise in the data.

13.4. Additional Uniqueness Constraints

By means of our previous considerations, we see that the reconstruction of the neuronal current from MEG and EEG data is not unique, see, for example, Theorem 13.1. However, we obtain a unique best-approximate solution of the inverse magneto-electroencephalography problem by means of the Moore-Penrose pseudoinverse operator if we restrict the domains of the operators to the orthogonal complements of their null spaces, if the electric potential and magnetic field is completely known, and if we assume that Picard's criterion, see Table 13.2, is fulfilled. Thus, further solutions of the inverse problem can be generated by adding elements from the null space to the best-approximate solution. In this setting, two types of non-uniqueness can be distinguished. First, not all directions of the current can be reconstructed and second, the reconstructable direction contains silent parts. Thus, we need additional uniqueness constraints in order to achieve a unique representation. In Section 12.3, we present additional radial and directional uniqueness constraints for the continuous VLI equation, which are adjusted to the inverse MEG and EEG problem here.

In the MEG as well as the EEG direct problem, after a separation into an angular and a radial part of the neuronal current we get for all $n \in \mathbb{N}$, $j = 1, \ldots, 2n+1$ the integral

$$\int_0^{\varrho_0} J_{n,j}^{(i),\sim}(x) x^{t_n^{(i)}+2} \,\mathrm{d}x$$

with $t_n^{(i)}$ given in Eq. (13.3), see Theorems 9.2 and 10.3. In both cases, infinitely many choices of the function $J_{n,j}^{(i),\sim}$ lead to the same value of the integral, see also [161, 162]. Thus, for each $i = 2, 3$ we can choose additional radial uniqueness constraints from Table 12.1, such as the generalized harmonicity constraint or the layer density constraint. In order to obtain a unique reconstruction, we furthermore need to assume $J_{n,j}^{(1),\sim} = 0$ for all $n \in \mathbb{N}_0$, $j = 1, \ldots, 2n+1$.

Theorem 13.5. *Let Assumption 3.2 with $L \geq 2$ be fulfilled. Let the magnetic field and the electric potential fulfil Picard's criterion summarized in Table 13.2. Let the neuronal current be of the form*

$$\boldsymbol{J}^{\mathrm{P}}(\boldsymbol{x}) \overset{\mathrm{L}_2(\mathbb{B}_{\varrho_0})}{=} \sum_{i=2}^{3} \sum_{n=1}^{\infty} \sum_{j=1}^{2n+1} \kappa_{n,j}^{(i)} D_{n,j}^{(i)}(x) \tilde{\boldsymbol{y}}_{n,j}^{(i)}(\hat{\boldsymbol{x}})$$

with given functions $D_{n,j}^{(i)}$ that are not $\mathrm{L}_2^w([0,\varrho_0])$-orthogonal to $Q_0^{(t_n^{(i)}+1/2)}(\varrho_0;\cdot)$, see also Eq. (13.2). Then the neuronal current can be uniquely reconstructed from the magnetic field and the electric potential by

$$\begin{aligned}\boldsymbol{J}^{\mathrm{P}}(\boldsymbol{x}) \overset{\mathrm{L}_2(\mathbb{B}_{\varrho_0})}{=} &\sum_{n=1}^{\infty} \sum_{j=1}^{2n+1} \sqrt{\frac{n}{(2n+1)^3}} \frac{1}{\beta_n^{(L)}} \varrho_L^n u_L^{\wedge}(n,j) \left(\int_0^{\varrho_0} D_{n,j}^{(2)}(x) x^{n+1} \,\mathrm{d}x \right)^{-1} D_{n,j}^{(2)}(x) \tilde{\boldsymbol{y}}_{n,j}^{(2)}(\hat{\boldsymbol{x}}) \\ &- \sum_{n=1}^{\infty} \sum_{j=1}^{2n+1} \frac{1}{\mu_0} \sqrt{\frac{2n+1}{n}} \varrho_L^{n+1} B_{\varrho_L}^{\wedge}(n,j) \left(\int_0^{\varrho_0} D_{n,j}^{(3)}(x) x^{n+2} \,\mathrm{d}x \right)^{-1} D_{n,j}^{(3)}(x) \tilde{\boldsymbol{y}}_{n,j}^{(3)}(\hat{\boldsymbol{x}}).\end{aligned}$$

Proof. From Eq. (13.4), we have for all $n \in \mathbb{N}$, $j = 1, \ldots, 2n+1$ the relations

$$J^{\wedge}[2,0,n,j] = \sqrt{\frac{n}{(2n+1)^2 \varrho_0}} \frac{1}{\beta_n^{(L)}} \left(\frac{\varrho_L}{\varrho_0}\right)^n u_L^{\wedge}(n,j), \tag{13.7a}$$

$$J^{\wedge}[3,0,n,j] = -\frac{1}{\mu_0} \sqrt{\frac{(2n+1)(2n+3)}{n \varrho_0}} \left(\frac{\varrho_L}{\varrho_0}\right)^{n+1} B_{\varrho_L}^{\wedge}(n,j). \tag{13.7b}$$

For $i = 2, 3$, the left-hand sides of these two equations can be reformulated by means of Eq. (7.13) to

$$J^{\wedge}[i,0,n,j] \sqrt{\frac{\varrho_0^{2t_n^{(i)}+3}}{2t_n^{(i)}+3}} = \int_0^{\varrho_0} J_{n,j}^{(i),\sim}(x) x^{t_n^{(i)}+2} \, \mathrm{d}x.$$

Due to the assumption $J_{n,j}^{(i),\sim} = \kappa_{n,j}^{(i)} D_{n,j}^{(i)}$, we obtain for the coefficients

$$\kappa_{n,j}^{(i)} = \sqrt{\frac{\varrho_0^{2t_n^{(i)}+3}}{2t_n^{(i)}+3}} \left(\int_0^{\varrho_0} D_{n,j}^{(i)}(x) x^{t_n^{(i)}+2} \, \mathrm{d}x \right)^{-1} J^{\wedge}[i,0,n,j].$$

Inserting these results into the expansion of the neuronal current, we obtain the stated result. □

The layer density constraint has been used before in the case of the scalar inverse MEG and EEG problems in [73], that is

$$D_{n,j}^{(i)}(x) \coloneqq \chi_{[\tau,\tau+\delta]}(x), \qquad x \in [0, \varrho_0]$$

with $[\tau, \tau+\delta] \subset [0, \varrho_0]$.

Besides this radial uniqueness constraint, we discuss further additional uniqueness constraints, such as the minimum norm approach and the harmonicity constraint.

Minimum-Norm Estimate

The minimum norm solution is a widely discussed approach for several non-unique inverse problems. It occurs in the inverse gravimetric problem, see, for instance, [161] and the references therein. Therein, a novel proof for the uniqueness under the minimum-norm assumption is presented. This approach is transferred by the author in [147, 162] to a more general setting that also covers the scalar inverse MEG and EEG problems.

A disadvantage of using the minimum norm approach for the scalar MEG and EEG problem is the lack of a physical or medical indication. Due to the principle of stationary action, certain physical quantities minimize their action, see [70]. However, this does not necessarily hold true for certain arbitrary scalar parts of the neuronal current. Therefore, the minimum-norm estimate (MNE) makes more sense for the vector-valued reconstruction of the entire neuronal current, which is not a new tool to the MEG and EEG reconstruction, see [108, 115, 216]. Classically, a discrete problem is analyzed. This can be achieved by evaluating the lead field at the sensor positions and expanding the neuronal current as a linear combination of these lead fields. Then, the problem can be reduced to the inversion of an $\ell \times \ell$-matrix, where ℓ is the number of measurement positions. Thus, the MNE

yields the neuronal current with the smallest overall amplitude, see also [109]. This can be transferred to the continuous setting by searching for the neuronal current with the smallest $\mathbf{L}_2(\mathbb{B}_{\varrho_0})$-norm fulfilling the measurements. This situation coincides with the best-approximate solution, which is obtained by the Moore-Penrose inverse. There also exists a discrete variant of the Moore-Penrose inverse and the resulting solution is known as the minimum-norm pseudoinverse (MNP), see [96]. The best-approximate solution obtained from the magnetic field and the electric potential is stated in the next theorem. Besides this, a variety of uniqueness approaches exists for the discrete case, such as the weighted MNE, the Tikhonov regularization, the maximum likelihood approach, and the Backus-Gilbert approach. Without additional knowledge of the neuronal current, they all result in the MNE solution, see [115] and the references therein.

Theorem 13.6 (Best-Approximate Solution). *Let Assumption 3.2 with $L \geq 2$ be fulfilled. Let the magnetic field and the electric potential fulfil Picard's criterion summarized in Table 13.2. Then the unique best-approximate solution $\boldsymbol{J}^+$ of the neuronal current $\boldsymbol{J}^{\mathrm{P}}$ is given by*

$$\begin{aligned}\boldsymbol{J}^+(\boldsymbol{x}) \overset{\mathrm{L}_2(\mathbb{B}_{\varrho_0})}{=} &\sum_{n=1}^{\infty}\sum_{j=1}^{2n+1}\frac{\sqrt{n}}{(2n+1)\sqrt{\varrho_0}\beta_n^{(L)}}\left(\frac{\varrho_L}{\varrho_0}\right)^n\langle u_L, Z_{n,j}\rangle_{\mathcal{Z}}\tilde{\boldsymbol{g}}^{(2)}_{0,n,j}(\varrho_0;\boldsymbol{x})\\ &+\sum_{n=1}^{\infty}\sum_{j=1}^{2n+1}\sqrt{\frac{(2n+1)^2(2n+3)}{n\varrho_0\varrho_L\mu_0^2}}\left(\frac{\varrho_L}{\varrho_0}\right)^{n+1}\langle \boldsymbol{B}, \boldsymbol{s}_{n,j}(\varrho_L;\cdot)\rangle_{\mathbf{L}_2(\mathbb{B}^{\mathrm{ext}}_{\varrho_L})}\tilde{\boldsymbol{g}}^{(3)}_{0,n,j}(\varrho_0;\boldsymbol{x}).\end{aligned}$$

Proof. In order to state the best-approximate solution $\boldsymbol{J}^+$ of the joint problem, we define for $(\boldsymbol{y},\boldsymbol{z}) \in \mathbb{B}^{\mathrm{ext}}_{\varrho_L} \times \mathbb{S}_{[\varrho_{L-1},\varrho_L]}$ the corresponding forward operator by

$$\mathcal{T}\colon \mathbf{L}_2\left(\mathbb{B}_{\varrho_0}\right) \to \mathbf{Harm}\left(\overline{\mathbb{B}^{\mathrm{ext}}_{\varrho_L}}\right) \times \mathcal{Z}, \qquad (\mathcal{T}\boldsymbol{J})\left(\boldsymbol{y},\boldsymbol{z}\right) \coloneqq \left((\mathcal{T}_{\mathrm{M}}\boldsymbol{J})(\boldsymbol{y}), (\mathcal{T}_{\mathrm{E}}\boldsymbol{J})(\boldsymbol{z})\right).$$

The space $\mathbf{Harm}(\overline{\mathbb{B}^{\mathrm{ext}}_{\varrho_L}}) \times \mathcal{Z}$ is a Hilbert space equipped with the inner product $\langle \boldsymbol{f},\boldsymbol{g}\rangle \coloneqq \langle \boldsymbol{f}_H,\boldsymbol{g}_H\rangle_{\mathbf{L}_2(\overline{\mathbb{B}^{\mathrm{ext}}_r})} + \langle f_{\mathcal{Z}}, g_{\mathcal{Z}}\rangle_{\mathcal{Z}}$ for all functions of the form $\boldsymbol{f} = (\boldsymbol{f}_H, f_{\mathcal{Z}}) \in \mathbf{Harm}(\overline{\mathbb{B}^{\mathrm{ext}}_{\varrho_L}}) \times \mathcal{Z}$. Orthonormal basis functions are given for all $i = 2,\, 3$, $n \in \mathbb{N}$, and $j = 1,\ldots,2n+1$ by

$$\boldsymbol{W}^{(i)}_{n,j}(\boldsymbol{y},\boldsymbol{z}) \coloneqq \begin{cases}(0, Z_{n,j}(\boldsymbol{z})) & \text{if } i = 2,\\ (\boldsymbol{s}_{n,j}(\varrho_L;\boldsymbol{y}), 0) & \text{if } i = 3,\end{cases} \qquad (\boldsymbol{y},\boldsymbol{z}) \in \mathbb{B}^{\mathrm{ext}}_{\varrho_L} \times \mathbb{S}_{[\varrho_{L-1},\varrho_L]}.$$

Thus, based on the results collected in Table 13.1, we obtain an SVD of $\mathcal{T}$ by

$$\mathcal{T}\boldsymbol{J} = \sum_{i=2}^{3}\sum_{n=1}^{\infty}\sum_{j=1}^{2n+1}\lambda_n^{(i)}\left\langle \boldsymbol{J}, \tilde{\boldsymbol{g}}^{(i)}_{0,n,j}(\varrho_0;\cdot)\right\rangle_{\mathbf{L}_2(\mathbb{B}_{\varrho_0})}\boldsymbol{W}^{(i)}_{n,j},$$

where $\lambda_n^{(2)} \coloneqq \lambda_n^{\mathrm{E}}$ and $\lambda_n^{(3)} \coloneqq \lambda_n^{\mathrm{M}}$. Picard's criterion for the joint problem is fulfilled if Picard's conditions for the two problems are fulfilled separately, see Table 13.2. According to Theorem 11.12, the corresponding Moore-Penrose generalized inverse operator has the representation

$$\begin{aligned}\mathcal{T}^+\left(\boldsymbol{B}, u_L\right) &= \sum_{i=2}^{3}\sum_{n=1}^{\infty}\sum_{j=1}^{2n+1}\lambda_n^{(i)}\left\langle (\boldsymbol{B}, u_L), \boldsymbol{W}^{(i)}_{n,j}\right\rangle\tilde{\boldsymbol{g}}^{(i)}_{0,n,j}(\varrho_0;\cdot)\\ &= \sum_{n=1}^{\infty}\sum_{j=1}^{2n+1}\lambda_n^{(2)}\langle u_L, Z_{n,j}\rangle_{\mathcal{Z}}\tilde{\boldsymbol{g}}^{(2)}_{0,n,j}(\varrho_0;\cdot) + \sum_{n=1}^{\infty}\sum_{j=1}^{2n+1}\lambda_n^{(3)}\langle \boldsymbol{B}, \boldsymbol{s}_{n,j}(\varrho_L;\cdot)\rangle_{\mathbf{L}_2(\mathbb{B}^{\mathrm{ext}}_{\varrho_L})}\tilde{\boldsymbol{g}}^{(3)}_{0,n,j}(\varrho_0;\cdot). \qquad \square\end{aligned}$$

Harmonicity Constraint

In the case of the inverse gravimetric problem, see [161], or the scalar-valued inverse MEG or EEG problem, see [162], the harmonicity constraint yields a unique reconstruction. In these cases, the reconstructable quantity is assumed to be harmonic in the interior of the observed body. However, in the case of the reconstruction of the vector-valued neuronal current, we are not able to achieve a unique solution by means of the harmonicity constraint alone. In this case, we assume that the neuronal current is harmonic, that is $\boldsymbol{\Delta} \boldsymbol{J}^{\mathrm{P}} = \mathbf{0}$, where the Laplacian is applied componentwise. The direction of the neuronal current belonging to the Edmonds vector spherical harmonics of type 1 is silent for the magnetoencephalograph as well as the electroencephalograph. Due to Lemma 5.40, this direction of the neuronal current has a harmonic part. Nevertheless, if the harmonicity of the current is assumed, we cannot reconstruct this part. However, if we additionally assume that the neuronal current is solenoidal or does not have a direction belonging to the Edmonds vector spherical harmonics of type 1, we can obtain a unique harmonic reconstruction.

Theorem 13.7 (Harmonicity Constraint). *Let Assumption 3.2 with $L \geq 2$ be fulfilled. Let the magnetic field and the electric potential fulfil Picard's criterion summarized in Table 13.2. In addition, let the current be solenoidal and harmonic. Then we obtain a unique reconstruction that coincides with the best-approximate solution given in Theorem 13.6.*

Proof. Via Lemma 5.41, we immediately obtain a characterization of the solenoidal basis functions. We see directly that all orthonormal basis functions corresponding to $i = 1$ are not solenoidal. By means of Lemma 5.40, we obtain a relationship between the orthonormal basis indices and the harmonic basis functions. Thus, only the orthonormal basis functions from Eq. (13.2) with $i = 2$, 3 and $m = 0$ contribute to the harmonic solution. A comparison with the representation of the neuronal current in Theorem 13.6 yields the desired result. □

Part IV.

Scalar General Integral Problem

Chapter 14.

Scalar Continuous VLI Operator

In the previous parts, we studied the vector continuous/star-shaped VLI kernel and its corresponding integral equation extensively. In contrast, many applications, such as the inverse gravimetric problem, are given by scalar-valued integral kernels. However, this setting can easily be covered by the vector-valued case.

For the analysis of the inverse magneto-electroencephalography problem, these corresponding scalar-valued integral operators are also of interest. In the literature, see, for instance, [47, 48, 50, 71–75], several approaches for solving the inverse magneto-encephalography are presented. In most of these approaches, the occurring densities and integral kernels reduce to scalar-valued functions. Since we want to compare our vector-valued approach to these scalar-valued approaches, further calculations and adaptations of the methods in the literature are required. This comparison can be found in Chapter 15.

To this end, the analysis of a scalar continuous/star-shaped VLI kernel and its induced integral equation is necessary. As a welcome side effect, we confirm existing results concerning the inverse gravimetric problem using this approach, which also validates our results. For this purpose, we first define the scalar continuous VLI kernel.

Definition 14.1 (Scalar Continuous VLI Kernel). *Let $\mathbb{G}_{\text{in}} \subset \mathbb{R}^3$ be a compact (inner) region containing the origin with $\sup_{\boldsymbol{x}\in\mathbb{G}_{\text{in}}} x = R$. Let $\mathbb{G}_{\text{out}} \subset \mathbb{R}^3 \setminus \mathbb{G}_{\text{in}}$ be the unbounded outer region with $\inf_{\boldsymbol{y}\in\mathbb{G}_{\text{out}}} y > R$. The* scalar continuous VLI kernel *is defined by*

$$K(\boldsymbol{x},\boldsymbol{y}) \coloneqq \sum_{k=0}^{\infty} \gamma_k(y) x^{t_k} P_k(\hat{\boldsymbol{x}} \cdot \hat{\boldsymbol{y}}), \qquad (\boldsymbol{x},\boldsymbol{y}) \in \mathbb{G}_{\text{in}} \times \mathbb{G}_{\text{out}}, \tag{14.1}$$

where the occurring quantities fulfil the same three assumptions formulated in Definition 6.1:

i) The real sequence of exponents $\{t_k\}_{k\in\mathbb{N}_0}$ fulfils $\inf_{k\in\mathbb{N}_0,\gamma_k\not\equiv 0} t_k \geq 0$.

ii) The asymptotic behaviour of $\{t_k\}_{k\in\mathbb{N}_0}$ can be characterized by $\sup_{k\in\mathbb{N}_0} R^{t_k-k} < \infty$.

iii) Each function γ_k with $k \in \mathbb{N}_0$ is continuous and for all $\boldsymbol{y} \in \mathbb{G}_{\text{out}}$ it holds that

$$|\gamma_k(y)| \leq \frac{\Gamma_k}{y^{k+1+\delta_{k,0}}},$$

where $\{\Gamma_k\}_{k\in\mathbb{N}_0} \subset \mathbb{R}_0^+$ is a sequence of non-negative constants. In addition, let $M \in \mathbb{N}_0$ be fixed such that $(k \mapsto \Gamma_k) \in \mathcal{O}(k^M)$.

Recall that P_k denotes the scalar Legendre polynomial of degree $k \in \mathbb{N}_0$. In analogy to the vector-valued case, we can also define a star-shaped version of this kernel.

Definition 14.2 (Scalar Star-shaped VLI Kernel). *Let $\mathbb{G}_{\text{star}} \subset \mathbb{R}^3$ be a compact star domain with vantage point zero and $\sup_{\boldsymbol{x}\in\mathbb{G}_{\text{star}}} x = R$. Let $\mathbb{G}_{\text{out}} \subset \mathbb{R}^3 \setminus \mathbb{G}_{\text{star}}$ be the unbounded outer region with $\inf_{\boldsymbol{y}\in\mathbb{G}_{\text{out}}} y > R$. We define the* scalar star-shaped VLI kernel K *by*

$$K(\boldsymbol{x},\boldsymbol{y}) \coloneqq \sum_{k=0}^{\infty} \gamma_k(y) x^{t_k} P_k(\hat{\boldsymbol{x}} \cdot \hat{\boldsymbol{y}}), \qquad (\boldsymbol{x},\boldsymbol{y}) \in (\mathbb{G}_{\text{star}} \setminus \{\boldsymbol{0}\}) \times \mathbb{G}_{\text{out}}.$$

The sequences $\{t_k\}_{k\in\mathbb{N}_0}$ and $\{\gamma_k\}_{k\in\mathbb{N}_0}$ fulfil the assumptions of the scalar continuous VLI kernel. As an extension, the sequence of exponents $\{t_k\}_{k\in\mathbb{N}_0}$ is only required to satisfy

$$\inf_{k\in\mathbb{N}_0,\gamma_k\neq 0} t_k \geq -1.$$

In previous works of the author, see [147, 162], a particular case of the scalar star-shaped VLI kernel formulated in this chapter is used and analyzed in detail. More precisely, the case $\gamma_k \coloneqq \Gamma_k y^{-(k+1)}$, where $k \in \mathbb{N}_0$, is considered therein. Here, we summarize the generalization of these previous considerations.

However, we start with some examples that demonstrate that scalar continuous/star-shaped VLI equations of this type arise in different applications. The already mentioned famous example, the inverse gravimetric problem, of such an integral kernel is presented first. This problem first appears in [204] and is discussed extensively in the literature [16, 168, 183, 189, 196, 204, 220]. An overview of potential theory, which is closely related to the inverse gravimetric problem, can be found in [135], for instance. Of course, this problem is also covered by our approach in [147, 162].

Example 14.3 (Inverse Gravimetric Problem – Part I). *Let $\gamma_k(y) \coloneqq \gamma y^{-(k+1)}$, where $\gamma > 0$ is the gravitational constant, and let $t_k \coloneqq k$ for all $k \in \mathbb{N}_0$. Using Eq. (2.2), we obtain for the integral kernel*

$$\begin{aligned} K(\boldsymbol{x},\boldsymbol{y}) &= \sum_{k=0}^{\infty} \gamma \frac{x^k}{y^{k+1}} P_k(\hat{\boldsymbol{x}} \cdot \hat{\boldsymbol{y}}) \\ &= \frac{\gamma}{|\boldsymbol{x}-\boldsymbol{y}|}. \end{aligned}$$

In addition, let $\mathbb{G}_{\text{in}}$ be the Earth. Then the gravitational potential V outside the Earth is given by Newton's Law of Gravitation, that is

$$V(\boldsymbol{y}) = \gamma \int_{\mathbb{G}_{\text{in}}} \frac{\varrho(\boldsymbol{x})}{|\boldsymbol{x}-\boldsymbol{y}|} \,\mathrm{d}\boldsymbol{x},$$

with the mass density distribution $\varrho \in \mathrm{L}_2(\mathbb{G}_{\text{in}})$ to be found. Let R be the radius of the Earth's Bjerhammar sphere. Then the mapping $y \mapsto (R/y)^{k+1}$ is sometimes called the transfer function because it transfers information from the Earth's interior to the measurement positions.

Now, additional examples of these integral kernels are presented. Two of them are listed in the next example and discussed in more detail in Chapter 15. Therein, the corresponding derivations are executed. These integral equations are improvements of results from [73].

Example 14.4. *In the context of medical imaging, the following two examples are analyzed, where parts of the neuronal current inside the brain $\mathbb{B}_{\varrho_0}$ are reconstructed from data outside the head. In both cases, the functions γ_k are given by $\gamma_k \coloneqq \Gamma_k y^{-(k+1)}$ for all $k \in \mathbb{N}_0$.*

i) The inverse MEG problem by means of the Hodge decomposition: $\Gamma_k \coloneqq k/(4\pi)$ *for all* $k \in \mathbb{N}_0$, $t_k \coloneqq k-1$ *for all* $k \in \mathbb{N}$, *and* $t_0 = 0$. *See Theorem 15.3 for more details.*

ii) The inverse EEG problem by means of the Helmholtz decomposition: in this case, the potential consists of the sum of two integral equations, where the first is given by a scalar continuous VLI equation and the second by a scalar star-shaped VLI equation. See Eq. (15.14) *and Theorem 15.6 for more details.*

iii) The homogeneous inverse EEG problem restricted onto the scalp by means of the Helmholtz decomposition: $\Gamma_k \coloneqq (2k+1)/(4\pi\sigma_0 k)$, *where* σ_0 *is the conductivity inside the cerebrum,* $t_k \coloneqq k$ *for all* $k \in \mathbb{N}$ *and* $\Gamma_0 = t_0 = 0$. *See Lemma 15.22 and Example 6.11.*

The results obtained for the vector continuous/star-shaped VLI kernel can also be transferred to the scalar continuous/star-shaped VLI kernel. For this purpose, we consider the vector continuous/star-shaped VLI kernel for the case $\iota = 1$. By applying the $\boldsymbol{o}_{\hat{\boldsymbol{x}}}^{(1)}$-operator, which is only a multiplication operator, we immediately obtain

$$\begin{aligned}
\boldsymbol{o}_{\hat{\boldsymbol{x}}}^{(1)} \cdot \boldsymbol{k}^{(1)}(\boldsymbol{x},\boldsymbol{y}) &= \sum_{k=0}^{\infty} \gamma_k(y) x^{t_k} \left(\boldsymbol{o}_{\hat{\boldsymbol{x}}}^{(1)} \cdot \boldsymbol{p}_k^{(1)}(\hat{\boldsymbol{x}},\hat{\boldsymbol{y}}) \right) \\
&= \sum_{k=0}^{\infty} \gamma_k(y) x^{t_k} \left(\mu_k^{(1)} \right)^{-1/2} P_k(\hat{\boldsymbol{x}} \cdot \hat{\boldsymbol{y}}) \\
&= K(\boldsymbol{x},\boldsymbol{y}), \qquad (14.2a) \\
\boldsymbol{o}_{\hat{\boldsymbol{x}}}^{(1)} K(\boldsymbol{x},\boldsymbol{y}) &= \boldsymbol{k}^{(1)}(\boldsymbol{x},\boldsymbol{y}). \qquad (14.2b)
\end{aligned}$$

Thus, the scalar-valued integral kernel is linked to $\boldsymbol{k}^{(1)}$ via the multiplication with $\hat{\boldsymbol{x}}$. This connection immediately yields the following result.

Theorem 14.5. *The following results hold true:*

i) The scalar continuous VLI kernel is bounded and the occurring series converges absolutely and uniformly in $\mathbb{G}_{\text{in}} \times \mathbb{G}_{\text{out}}$.

ii) The series from the scalar star-shaped VLI kernel converges absolutely and pointwise in $(\mathbb{G}_{\text{star}} \setminus \{\mathbf{0}\}) \times \mathbb{G}_{\text{out}}$.

iii) The scalar continuous/star-shaped VLI kernel is continuous in $\mathbb{G}_{\text{in}} \times \mathbb{G}_{\text{out}}$ *or* $(\mathbb{G}_{\text{star}} \setminus \{\mathbf{0}\}) \times \mathbb{G}_{\text{out}}$, *respectively.*

iv) The scalar continuous/star-shaped VLI kernel is an $\mathrm{L}_2(\mathbb{G}_{\text{in}} \times \mathbb{G}_{\text{out}})$*-function, or an* $\mathrm{L}_2(\mathbb{G}_{\text{star}} \times \mathbb{G}_{\text{out}})$*-function, respectively.*

v) The differential operators from Theorems 6.17 and 6.18 can be interchanged with the occurring series if the assumptions on $\{t_k\}_{k\in\mathbb{N}_0}$, $\{\gamma_k\}_{k\in\mathbb{N}_0}$ *stated therein are satisfied.*

Proof. See Lemmas 6.5, 6.7, and 6.16, Corollary 6.12, and Theorems 6.6 and 6.17 to 6.18 combined with Eq. (14.2) for the proofs. □

A scalar-valued counterpart to the continuous/star-shaped VLI operator can easily be obtained.

Lemma 14.6. *Let $\mathbb{G} \in \{\mathbb{G}_{\mathrm{in}}, \mathbb{G}_{\mathrm{star}}\}$, the scalar density $F \in \mathrm{L}_2(\mathbb{G})$, and the scalar continuous/star-shaped VLI kernel K be given. We define the corresponding scalar continuous/star-shaped VLI operator $\mathcal{S}\colon \mathrm{L}_2(\mathbb{G}) \to \mathrm{L}_2(\mathbb{G}_{\mathrm{out}})$ by*

$$(\mathcal{S}F)(\boldsymbol{y}) \coloneqq \int_{\mathbb{G}} F(\boldsymbol{x})K(\boldsymbol{x},\boldsymbol{y})\,\mathrm{d}\boldsymbol{x}, \qquad \boldsymbol{y} \in \mathbb{G}_{\mathrm{out}}.$$

Moreover, we consider the vector-valued analogue, that is $\boldsymbol{k}^{(1)}(\boldsymbol{x},\boldsymbol{y}) = \boldsymbol{o}^{(1)}_{\hat{\boldsymbol{x}}} K(\boldsymbol{x},\boldsymbol{y})$, which is a vector continuous/star-shaped VLI kernel, and we define $\boldsymbol{f}(\boldsymbol{x}) \coloneqq \boldsymbol{o}^{(1)}_{\hat{\boldsymbol{x}}} F(\boldsymbol{x})$. The relation between the scalar-valued and the vector-valued integral equation is given by

$$(\mathcal{S}F)(\boldsymbol{y}) = (\mathcal{T}\boldsymbol{f})(\boldsymbol{y}).$$

Proof. The function $\boldsymbol{f}$ satisfies $\boldsymbol{f} \in \mathbf{L}_2(\mathbb{G})$ if and only if $F \in \mathrm{L}_2(\mathbb{G})$, since

$$\begin{aligned}
\|\boldsymbol{f}\|^2_{\mathbf{L}_2(\mathbb{G})} &= \int_{\mathbb{G}} \boldsymbol{f}(\boldsymbol{x}) \cdot \boldsymbol{f}(\boldsymbol{x})\,\mathrm{d}\boldsymbol{x} \\
&= \int_{\mathbb{G}} (\hat{\boldsymbol{x}}F(\boldsymbol{x})) \cdot (\hat{\boldsymbol{x}}F(\boldsymbol{x}))\,\mathrm{d}\boldsymbol{x} \\
&= \int_{\mathbb{G}} F(\boldsymbol{x})F(\boldsymbol{x})\,\mathrm{d}\boldsymbol{x} \\
&= \|F\|^2_{\mathrm{L}_2(\mathbb{G})}.
\end{aligned}$$

Thus, we are able to apply the operator $\mathcal{T}$ in the case of $\iota = 1$ from Definition 7.1 or Definition 7.2 to $\boldsymbol{f}$. We get

$$\begin{aligned}
(\mathcal{T}\boldsymbol{f})(\boldsymbol{y}) &= \int_{\mathbb{G}} \boldsymbol{f}(\boldsymbol{x}) \cdot \boldsymbol{k}^{(1)}(\boldsymbol{x},\boldsymbol{y})\,\mathrm{d}\boldsymbol{x} \\
&= \int_{\mathbb{G}} \boldsymbol{o}^{(1)}_{\hat{\boldsymbol{x}}} F(\boldsymbol{x}) \cdot \boldsymbol{o}^{(1)}_{\hat{\boldsymbol{x}}} K(\boldsymbol{x},\boldsymbol{y})\,\mathrm{d}\boldsymbol{x} \\
&= \int_{\mathbb{G}} F(\boldsymbol{x})K(\boldsymbol{x},\boldsymbol{y})\,\mathrm{d}\boldsymbol{x} \\
&= (\mathcal{S}F)(\boldsymbol{y})
\end{aligned}$$

and the range of the operator $\mathcal{S}$ coincides with the range of the operator $\mathcal{T}$. □

Due to the connection between the operator $\mathcal{S}$ corresponding to the scalar-valued case and the operator $\mathcal{T}$ of the vector-valued case, we can transfer properties from one pair of potential and density to the other.

Corollary 14.7. *Let $\mathbb{G} \in \{\mathbb{G}_{\mathrm{in}}, \mathbb{G}_{\mathrm{star}}\}$ and let the scalar continuous/star-shaped VLI operator $\mathcal{S}$ be given as defined in Lemma 14.6. Then*

i) the operator $\mathcal{S}$ maps from $\mathrm{L}_2(\mathbb{G})$ to $\mathrm{L}_2(\mathbb{G}_{\mathrm{out}})$;

ii) the operator $\mathcal{S}$ maps from $\mathrm{L}_2(\mathbb{G})$ to $\mathrm{C}(\mathbb{G}_{\mathrm{out}})$;

iii) $\mathcal{S}\colon \mathrm{L}_2(\mathbb{G}) \to \mathrm{L}_2(\mathbb{G}_{\mathrm{out}})$ is a bounded and compact operator.

Proof. By means of $\operatorname{ran}\mathcal{S} = \operatorname{ran}\mathcal{T}$, see Lemma 14.6, combined with Corollary 7.3 and Theorems 7.8 and 12.1, we obtain most of the desired result. In order to prove that $\operatorname{ran}\mathcal{S} \subset \mathrm{C}(\mathbb{G}_{\mathrm{out}})$ in the case of the star-shaped VLI, we use the uniform convergence of the series representation of $\mathcal{T}\boldsymbol{f}$ from Theorem 7.26 and the fact that each summand is continuous in $\mathbb{G}_{\mathrm{out}}$. □

Next, we assume that the inner domain is given by the ball $\mathbb{B}_R$ with radius R. Then a function $F \in \mathrm{L}_2(\mathbb{B}_\mathbb{R})$ can be represented by a Fourier series, that is

$$\begin{aligned} F(\boldsymbol{x}) &= \sum_{m=0}^{\infty} \sum_{n=0}^{\infty} \sum_{j=1}^{2n+1} F^\wedge(m,n,j) G_{m,n,j}(R;\boldsymbol{x}) \\ &= \sum_{n=0}^{\infty} \sum_{j=1}^{2n+1} F_{n,j}(x) Y_{n,j}(\hat{\boldsymbol{x}}) \end{aligned} \tag{14.3}$$

with the abbreviations

$$F^\wedge(m,n,j) \coloneqq \int_{\mathbb{B}_R} F(\boldsymbol{x}) G_{m,n,j}(R;\boldsymbol{x}) \,\mathrm{d}\boldsymbol{x}, \tag{14.4a}$$

$$F_{n,j}(x) \coloneqq \int_{\mathbb{S}} F(\boldsymbol{x}) Y_{n,j}(\boldsymbol{x}) \,\mathrm{d}\omega(\hat{\boldsymbol{x}}). \tag{14.4b}$$

For a definition of the used basis functions see Definitions 2.22 and 5.35. The stated Fourier series can be used for the potential obtained by the operator $\mathcal{S}$. The next corollary is a generalization of a former result stated in [162]. In the case of the inverse gravimetric problem, this result is also stated in [79, 85, 154, 155].

Corollary 14.8. *Let $F \in \mathrm{L}_2(\mathbb{B}_R)$, then $\mathcal{S}F$ is given by*

$$\begin{aligned} (\mathcal{S}F)(\boldsymbol{y}) &= 4\pi \sum_{n=0}^{\infty} \sum_{j=1}^{2n+1} \frac{1}{2n+1} \left(\int_0^R F_{n,j}(x) x^{t_n+2} \,\mathrm{d}x \right) \gamma_n(y) Y_{n,j}(\hat{\boldsymbol{y}}) \\ &= 4\pi \sum_{n=0}^{\infty} \sum_{j=1}^{2n+1} \frac{R^{t_n+3/2}}{(2n+1)\sqrt{2t_n+3}} F^\wedge(0,n,j) \gamma_n(y) Y_{n,j}(\hat{\boldsymbol{y}}) \end{aligned}$$

for all $\boldsymbol{y} \in \mathbb{G}_{\mathrm{out}}$. The series converges absolutely and uniformly on $\mathbb{G}_{\mathrm{out}}$ and in the sense of $\mathrm{L}_2(\mathbb{G}_{\mathrm{out}})$. The series converges in the $\mathrm{L}_2(\mathbb{S}_R)$-sense on $\mathbb{S}_R$ if the following additional conditions are fulfilled:

i) The sequence of functions $\{\gamma_n\}_{n\in\mathbb{N}_0}$ is evaluable for $y = R$ and

ii) these functions fulfil the additional condition

$$|\gamma_n(R)| \leq \Gamma_n R^{-(n+1+\delta_{n,0})}$$

where

$$\Gamma_n \leq c\sqrt{(2n+1)^2(2t_n+3)}$$

for all $n \in \mathbb{N}_0$ with a fixed $c \in \mathbb{R}_0^+$.

Proof. Corollary 7.17 provides us with the expansion

$$(\mathcal{T}\boldsymbol{f})(\boldsymbol{y}) = 4\pi \sum_{n=0}^{\infty} \sum_{j=1}^{2n+1} \frac{1}{2n+1} \left(\int_0^R f_{n,j}^{(1)}(x) x^{t_n+2} \,\mathrm{d}x \right) \gamma_n(y) Y_{n,j}(\hat{\boldsymbol{y}})$$

for the operator $\mathcal{T}$. Note that the vector-valued function $\boldsymbol{f}$ and the scalar function F are related by $\boldsymbol{f}(\boldsymbol{x}) \coloneqq \boldsymbol{o}_{\hat{\boldsymbol{x}}}^{(1)} F(\boldsymbol{x})$. This implies the case $\iota = 1$. The functions $f_{n,j}^{(1)}$ are given by

$$\begin{aligned}
f_{n,j}^{(1)}(x) &= \sum_{m=0}^{\infty} f^{\wedge}(1,m,n,j) Q_m^{(t_n+1/2)}(R;x) \\
&= \sum_{m=0}^{\infty} \left\langle \boldsymbol{f}, \boldsymbol{g}_{m,n,j}^{(1)}(R;\cdot) \right\rangle_{\mathbf{L}_2(\mathbb{B}_R)} Q_m^{(t_n+1/2)}(R;x) \\
&= \sum_{m=0}^{\infty} \int_{\mathbb{B}_R} \boldsymbol{f}(\boldsymbol{x}) \cdot \boldsymbol{g}_{m,n,j}^{(1)}(R;\boldsymbol{x}) \,\mathrm{d}\boldsymbol{x}\, Q_m^{(t_n+1/2)}(R;x) \\
&= \sum_{m=0}^{\infty} \int_{\mathbb{B}_R} F(\boldsymbol{x}) G_{m,n,j}(R;\boldsymbol{x}) \,\mathrm{d}\boldsymbol{x}\, Q_m^{(t_n+1/2)}(R;x) \\
&= \sum_{m=0}^{\infty} \langle F, G_{m,n,j}(R;\cdot) \rangle_{\mathrm{L}_2(\mathbb{B}_R)} Q_m^{(t_n+1/2)}(R;x) \\
&= \sum_{m=0}^{\infty} F^{\wedge}(m,n,j) Q_m^{(t_n+1/2)}(R;x) \\
&= \int_{\mathbb{S}} F(\boldsymbol{x}) Y_{n,j}(\boldsymbol{x}) \,\mathrm{d}\omega(\hat{\boldsymbol{x}}) \\
&= F_{n,j}(x)
\end{aligned}$$

for all $n \in \mathbb{N}_0$, $j = 1, \ldots, 2n+1$. And, hence, $f^{\wedge}(1,m,n,j) = F^{\wedge}(m,n,j)$ for all m, $n \in \mathbb{N}_0$, $j = 1, \ldots, 2n+1$. Thus, the last identity of the corollary is obtained by Lemma 7.24 and properties of the scalar basis functions on the ball. The statements concerning the convergence are proved in Theorems 7.20 and 7.26. □

For the characterization of the ill-posedness of the scalar-valued problem, we start with the uniqueness of the density reconstruction and the null space of the integral operator, respectively.

Lemma 14.9. *Let $\mathcal{S}\colon \mathrm{L}_2(\mathbb{B}_R) \to \mathrm{L}_2(\mathbb{G}_{\mathrm{out}})$ be the scalar continuous/star-shaped VLI operator, then*

$$(\ker \mathcal{S})^{\perp} = \overline{\operatorname{span}\left\{ G_{0,n,j}(R;\cdot) \mid n \in \left\{ n' \in \mathbb{N}_0 \mid \gamma_{n'} \not\equiv 0 \right\}, j = 1, \ldots, 2n+1 \right\}}. \tag{14.5}$$

Consequently, $\mathcal{S}$ is not injective.

Proof. Lemma 12.2 provides us with a separation of the $\mathbf{L}_2(\mathbb{B}_R)$-orthonormal basis functions belonging to the null space of $\mathcal{T}$ and its complement. Due to the construction of $\mathcal{S}$, we conclude that $G_{m,n,j}(R;\cdot) \in \ker \mathcal{S}$ if and only if $\boldsymbol{g}_{m,n,j}^{(1)}(R;\cdot) \in \ker \mathcal{T}$. □

So far, the operator null space has been characterized by means of the orthonormal basis used in the SVD. However, from certain applications, such as the inverse gravimetric problem, the null space of such an integral operator can be characterized by means of a differential operator. Now, we want to transfer this result to the scalar continuous/star-shaped VLI operator in order to achieve an alternative characterization of the null space. For this purpose, we consider a particular case of the scalar continuous VLI operator. For the scalar case considered here, this result has already been published by the author in [147, 162].

Corollary 14.10. *Let $\gamma_n(y) \coloneqq \Gamma_n y^{-(n+1)}$ with $\Gamma_n \neq 0$ and let $t_n \coloneqq n + \kappa$ for all $n \in \mathbb{N}_0$ with arbitrary $\kappa \in [-1, \infty)$. We define the differential operator $\diamondsuit$ by*

$$\diamondsuit_{\boldsymbol{x}} F(\boldsymbol{x}) \coloneqq \left(\frac{\partial^2}{\partial x^2} + \frac{2}{x} \frac{\partial}{\partial x} + \frac{1}{x^2} \Delta^*_{\hat{\boldsymbol{x}}} \right) \left(x^{-\kappa} F(\boldsymbol{x}) \right).$$

Then the orthogonal complement of the null space of the scalar continuous VLI operator is equivalent to

$$(\ker \mathcal{S})^{\perp} = \overline{\{F \in \mathrm{C}^2(\mathbb{B}_R) \mid \diamondsuit F = 0\}}^{\mathrm{L}_2(\mathbb{B}_R)}.$$

Proof. Let $F \in \mathrm{C}^2(\mathbb{B}_R) \subset \mathrm{L}_2(\mathbb{B}_R)$ be given. Then, we get the relation

$$\diamondsuit_{\boldsymbol{x}} F(\boldsymbol{x}) = \left(\frac{\partial^2}{\partial x^2} + \frac{2}{x} \frac{\partial}{\partial x} + \frac{1}{x^2} \Delta^*_{\hat{\boldsymbol{x}}} \right) \left(x^{-\kappa} F(\boldsymbol{x}) \right).$$

Thus, we obtain for all $F \in \mathrm{C}^2(\mathbb{B}_R)$ with Theorem 2.14 the equivalence relation

$$\diamondsuit_{\boldsymbol{x}} F(\boldsymbol{x}) = 0 \qquad \Leftrightarrow \qquad \Delta_{\boldsymbol{x}} \left(x^{-\kappa} F(\boldsymbol{x}) \right) = 0.$$

Recall that a scalar-valued orthonormal system of $\mathrm{L}_2(\mathbb{B}_R)$ is stated in Definition 5.33. However, we first use the system $\{G_{m,n,j}\}_{m,n \in \mathbb{N}_0, j=1,\ldots,2n+1}$ defined in Definition 5.35 with $t_n \coloneqq n + \kappa$ for $n \in \mathbb{N}_0$. It is easy to verify with an appropriate normalization factor c_n that

$$\begin{aligned} \diamondsuit_{\boldsymbol{x}} G_{0,n,j}(\boldsymbol{x}) &= c_n \diamondsuit_{\boldsymbol{x}} \left(\left(\frac{x}{R} \right)^{n+\kappa} Y_{n,j}(\hat{\boldsymbol{x}}) \right) \\ &= c_n \Delta_{\boldsymbol{x}} \left(\left(\frac{x}{R} \right)^{n} Y_{n,j}(\hat{\boldsymbol{x}}) \right) \\ &= 0 \end{aligned}$$

for all $n \in \mathbb{N}_0$, $j = 1, \ldots, 2n+1$. In the last step, the harmonic property of the inner harmonics is used, see Corollary 2.29. In addition, the functions $\{G^{\mathrm{I}}_{0,n,j}(R; \cdot)\}_{n \in \mathbb{N}_0, j=1,\ldots,2n+1}$ form a basis of the space of all harmonic functions on $\mathbb{B}_R$. This is, for example, stated in [79, Rem. 3.68], where the unique solution of the interior Dirichlet problem can be represented by a Fourier series expansion in terms of inner harmonics. Then, the following equivalence relation holds true, which has already been published by the author in [162],

$$\begin{aligned} & 0 = \Delta_{\boldsymbol{x}} \left(x^{-\kappa} F(\boldsymbol{x}) \right) \qquad \text{for all } \boldsymbol{x} \in \mathbb{B}_R \\ \Leftrightarrow \quad & \left(\boldsymbol{x} \mapsto x^{-\kappa} F(\boldsymbol{x}) \right) \in \operatorname{span} \left\{ G^{\mathrm{I}}_{0,n,j}(R; \cdot) \right\}_{n \in \mathbb{N}_0, j=1,\ldots,2n+1} \\ \Leftrightarrow \quad & \left(\boldsymbol{x} \mapsto x^{-\kappa} F(\boldsymbol{x}) \right) \in \operatorname{span} \left\{ \boldsymbol{x} \mapsto \frac{x^n}{R^n} Y_{n,j}(\hat{\boldsymbol{x}}) \right\}_{n \in \mathbb{N}_0, j=1,\ldots,2n+1} \\ \Leftrightarrow \quad & \left(\boldsymbol{x} \mapsto F(\boldsymbol{x}) \right) \in \operatorname{span} \left\{ \boldsymbol{x} \mapsto \frac{x^{n+\kappa}}{R^n} Y_{n,j}(\hat{\boldsymbol{x}}) \right\}_{n \in \mathbb{N}_0, j=1,\ldots,2n+1} \\ \Leftrightarrow \quad & F(\boldsymbol{x}) \in \operatorname{span} \left\{ G_{0,n,j}(R; \cdot) \right\}_{n \in \mathbb{N}_0, j=1,\ldots,2n+1}. \end{aligned}$$

Thus, we conclude via the the fact that $\Gamma_n \neq 0$ for all $n \in \mathbb{N}_0$ and the representation of the operator null space from Eq. (14.5) the stated result, that is

$$(\ker \mathcal{T})^{\perp} = \overline{\{F \in \mathrm{C}^2(\mathbb{B}_R) \mid \diamondsuit F = 0\}}. \qquad \square$$

Note that we obtain $\diamondsuit = \Delta$ for $\kappa = 0$. This case is related to the inverse gravimetric problem, see Example 14.15. Further interesting differential operators can be obtained by setting $\kappa = -1$, where

$$\diamondsuit F(\boldsymbol{x}) = \left(x \frac{\partial^2}{\partial x^2} + 4 \frac{\partial}{\partial x} + \frac{2}{x} + \frac{1}{x} \Delta^*_{\hat{\boldsymbol{x}}} \right) F(\boldsymbol{x}),$$

and $\kappa = 1$, where

$$\diamondsuit F(\boldsymbol{x}) = \left(\frac{1}{x} \frac{\partial^2}{\partial x^2} + \frac{1}{x^3} \Delta^*_{\hat{\boldsymbol{x}}} \right) F(\boldsymbol{x}).$$

For the restriction of the operator $\mathcal{S}$ onto a sphere $\mathbb{S}_r$ with fixed $r > R$, we directly obtain an SVD of $\mathcal{S}|_{\mathbb{S}_r}$ by means of Theorem 12.4 combined with Lemma 14.6.

Theorem 14.11. *Let $\mathcal{S}|_{\mathbb{S}_r} \colon \mathrm{L}_2(\mathbb{B}_R) \to \mathrm{L}_2(\mathbb{S}_r)$ be the operator $\mathcal{S}$ with range restricted to $\mathrm{L}_2(\mathbb{S}_r)$. Then*

i) the set $\{G_{0,n,j}(R;\cdot)\}_{n \in \{n' \in \mathbb{N}_0 | \gamma_{n'}(r) \neq 0\}, j=1,\dots,2n+1}$ builds an orthonormal basis for the orthogonal complement of the null space, that is $(\ker \mathcal{S}|_{\mathbb{S}_r})^\perp \subset \mathrm{L}_2(\mathbb{B}_R)$,

ii) an orthonormal basis for $\mathrm{L}_2(\mathbb{S}_r)$ is given by $\{r^{-1} Y_{n,j}\}_{n \in \mathbb{N}_0, j=1,\dots,2n+1}$, and

iii) the singular values of $\mathcal{S}|_{\mathbb{S}_r}$ are given for all $n \in \{n' \in \mathbb{N}_0 \mid \gamma_{n'}(r) \neq 0\}$ independent of j by

$$\lambda_n \coloneqq 4\pi r \sqrt{\frac{R^3}{2t_n + 3}} \frac{R^{t_n}}{2n+1} \gamma_n(r).$$

Eventually, we obtain an SVD of $\mathcal{S}|_{\mathbb{S}_r}$, that is

$$\mathcal{S}|_{\mathbb{S}_r} F = \sum_{n=0}^{\infty} \sum_{j=1}^{2n+1} \lambda_n \langle F, G_{0,n,j}(R;\cdot) \rangle_{\mathrm{L}_2(\mathbb{B}_R)} \frac{1}{r} Y_{n,j}.$$

In addition, via the relation $\boldsymbol{f}(\boldsymbol{x}) = \boldsymbol{o}^{(1)}_{\hat{\boldsymbol{x}}} F(\boldsymbol{x})$, we observe for all $n \in \mathbb{N}_0$ and $j = 1, \dots, 2n+1$ that

$$\begin{aligned} \int_0^R f^{(1)}_{n,j}(x) x^{t_n+2} \,\mathrm{d}x &= \int_0^R F_{n,j}(x) x^{t_n+2} \,\mathrm{d}x, \\ \left\langle \boldsymbol{f}, \boldsymbol{g}^{(1)}_{0,n,j}(R;\cdot) \right\rangle_{\mathbf{L}_2(\mathbb{B}_R)} &= \langle F, G_{0,n,j}(R;\cdot) \rangle_{\mathrm{L}_2(\mathbb{B}_R)}. \end{aligned}$$

Via Lemma 7.24, we eventually get

$$\int_0^R F_{n,j}(x) x^{t_n+2} \,\mathrm{d}x = F^\wedge(0,n,j) \sqrt{\frac{R^{2t_n+3}}{2t_n+3}}$$

for all $n \in \mathbb{N}_0$ and $j = 1, \dots, 2n+1$. Thus, the Fourier coefficients of the potential $V = \mathcal{S}|_{\mathbb{S}_r} F$ are given by

$$\begin{aligned} V^\wedge(n,j) &= \left\langle \mathcal{S}|_{\mathbb{S}_r} F, \frac{1}{r} Y_{n,j} \right\rangle_{\mathrm{L}_2(\mathbb{S}_r)} \\ &= 4\pi r \sqrt{\frac{R^3}{2t_n+3}} \frac{R^{t_n}}{2n+1} \gamma_n(r) \langle F, G_{0,n,j}(R;\cdot) \rangle_{\mathrm{L}_2(\mathbb{B}_R)} \\ &= \frac{4\pi}{2n+1} \gamma_n(r) r \int_0^R F_{n,j}(x) x^{t_n+2} \,\mathrm{d}x. \end{aligned} \tag{14.6}$$

The latter formula has already been stated in [147] for the particular case of $\gamma_n = \Gamma_n y^{-(n+1)}$ for all $n \in \mathbb{N}_0$. In analogy to the previous theorem, Theorem 12.9 combined with Lemma 14.6 provides us with the next theorem.

Theorem 14.12. *Let* $(\mathrm{Harm}(\overline{\mathbb{B}_r^{\mathrm{ext}}}), \langle\cdot,\cdot\rangle_{\mathrm{L}_2(\overline{\mathbb{B}_r^{\mathrm{ext}}})})$ *be defined in Lemma 12.8. Let the operator* $\mathcal{S}$ *be given by*

$$\mathcal{S} \colon F \mapsto \int_{\mathbb{B}_R} F(\boldsymbol{x}) K(\boldsymbol{x}, \cdot) \,\mathrm{d}\boldsymbol{x}$$

with the scalar continuous/star-shaped VLI kernel K*. In addition, let* $\gamma_k \coloneqq \Gamma_k y^{-(k+1)}$ *with* $\Gamma_k \in \mathbb{R}$ *for all* $k \in \mathbb{N}$ *and* $\gamma_0 \equiv 0$*. Then*

i) $\mathcal{S} \colon \mathrm{L}_2(\mathbb{B}_R) \to (\mathrm{Harm}(\overline{\mathbb{B}_r^{\mathrm{ext}}}), \langle\cdot,\cdot\rangle_{\mathrm{L}_2(\overline{\mathbb{B}_r^{\mathrm{ext}}})})$,

ii) an orthonormal basis for the orthogonal complement of the null space is given by $\{G_{0,n,j}(R;\cdot)\}_{n \in \{n' \in \mathbb{N} \mid \Gamma_{n'} \neq 0\}, j=1,\dots,2n+1}$,

iii) an orthonormal basis for $(\mathrm{Harm}(\overline{\mathbb{B}_r^{\mathrm{ext}}}), \langle\cdot,\cdot\rangle_{\mathrm{L}_2(\overline{\mathbb{B}_r^{\mathrm{ext}}})})$ *is given by means of the basis from Lemma 12.8, that is* $\{S_{n,j}(r;\cdot)\}_{n \in \mathbb{N}, j=1,\dots,2n+1}$,

iv) the singular values of $\mathcal{S}$ *are given for all* $n \in \{n' \in \mathbb{N} \mid \Gamma_{n'} \neq 0\}$ *by*

$$\lambda_n \coloneqq 4\pi \frac{\Gamma_n}{(2n+1)\sqrt{(2t_n+3)(2n-1)}} \frac{R^{t_n+3/2}}{r^{n-1/2}},$$

and

v) the closure of the range is given by

$$\overline{\operatorname{ran} \mathcal{S}} = \overline{\operatorname{ran} \mathcal{T}} = \overline{\operatorname{span} \{S_{n,j}(r;\cdot) \mid n \in \{n' \in \mathbb{N} \mid \Gamma_{n'} \neq 0\}, j = 1, \dots, 2n+1\}}.$$

Eventually, we obtain the SVD of the scalar continuous VLI operator $\mathcal{S}$*, that is*

$$\mathcal{S}F = \sum_{\substack{n=1 \\ \Gamma_n \neq 0}}^{\infty} \sum_{j=1}^{2n+1} \lambda_n \langle F, G_{0,n,j}(R;\cdot) \rangle_{\mathrm{L}_2(\mathbb{B}_R)} S_{n,j}(r;\cdot).$$

The Fourier series of the unique best-approximate solution F^+ *of* $\mathcal{S}F = V$ *is given by*

$$F^+ = \sum_{\substack{n=1 \\ \Gamma_n \neq 0}}^{\infty} \sum_{j=1}^{2n+1} \lambda_n^{-1} \langle V, S_{n,j}(r;\cdot) \rangle_{\mathrm{L}_2(\overline{\mathbb{B}_r^{\mathrm{ext}}})} G_{0,n,j}(R;\cdot).$$

In Section 12.3, we consider additional uniqueness constraints for the vector-valued equation. Now, we want to transfer these constraints to the scalar-valued case. The additional radial uniqueness constraints for certain scalar integral equations have already been published by the author in [147, 162]. The results are summed up in the next corollary. For this purpose, we restrict ourselves to a similar setting as in Section 12.3, where we state conditions for the existence of a solution in Assumption 12.15. Now, let these assumptions also hold true for the scalar continuous/star-shaped VLI equation. With the same argumentation as in Section 12.3, we assume that $\mathbb{G}_{\text{out}} \coloneqq \overline{\mathbb{B}_r^{\text{ext}}}$ and $\gamma_n(y) \coloneqq \Gamma_n y^{-(n+1)}$ for all $n \in \mathbb{N}_0$, where the sequence has to fulfil the polynomial growth condition $(n \mapsto |\Gamma_n|) \in \mathcal{O}(n^M)$ for fixed $M \in \mathbb{N}_0$. Note that Corollary 14.8 is used for this argumentation. In addition, the next result is an immediate consequence of Corollary 14.8 for this particular setting.

Corollary 14.13. *Let $\mathcal{S}$ be a scalar continuous/star-shaped VLI operator. Let, in addition, $\mathbb{G}_{\text{out}} \coloneqq \overline{\mathbb{B}_r^{\text{ext}}}$ and $\gamma_n(y) \coloneqq \Gamma_n y^{-(n+1)}$ for all $n \in \mathbb{N}_0$ be given, where the sequence $\{\Gamma_n\}_{n\in\mathbb{N}_0}$ has to fulfil the polynomial growth condition. Then, for the potential $V = \mathcal{S}F$, the following holds true:*

$$V^\wedge(n,j) = 4\pi \frac{\Gamma_n}{(2n+1)\sqrt{2t_n+3}} \frac{R^{t_n+3/2}}{r^n} F^\wedge(0,n,j),$$
$$V^\wedge(n,j) = 4\pi \frac{\Gamma_n}{2n+1} \frac{1}{r^n} \int_0^R F_{n,j}(x) x^{t_n+2} \,\mathrm{d}x$$

for all $n \in \mathbb{N}_0$, $j = 1, \dots, 2n+1$, where the density $F \in \mathrm{L}_2(\mathbb{B}_R)$ satisfies

$$F(\boldsymbol{x}) \overset{\mathrm{L}_2(\mathbb{B}_R)}{=} \sum_{n=0}^{\infty} \sum_{j=1}^{2n+1} F_{n,j}(x) Y_{n,j}(\hat{\boldsymbol{x}}) \tag{14.7a}$$
$$\overset{\mathrm{L}_2(\mathbb{B}_R)}{=} \sum_{m=0}^{\infty} \sum_{n=0}^{\infty} \sum_{j=1}^{2n+1} F^\wedge(m,n,j) G_{m,n,j}(R;\cdot). \tag{14.7b}$$

If $\Gamma_n \neq 0$ for all $n \in \mathbb{N}_0$, only additional radial constraints are necessary for the scalar-valued case. If certain degrees are vanishing in the latter expansion of F and if $\Gamma_n = 0$ for particular values of $n \in \mathbb{N}_0$, then also angular constraints can be required.

In this chapter, we only consider radial uniqueness constraints, which are meaningful in the scalar-valued case as well as in the vector-valued case. For this purpose, we consider the auxiliary function $D_{n,j}$ defined in Eq. (12.11) and add another case to it, that is

$$D_{n,j} \coloneqq \begin{cases} F_{n,j} & \text{in the scalar-valued case for all } n \in \mathbb{N}_0,\ j = 1, \dots, 2n+1, \\ f_{n,j}^{(\iota)} & \text{in the vector-valued case for all } n \in \mathbb{N}_{0_i},\ j = 1, \dots, 2n+1, \\ 0 & \text{in the vector-valued case for all } i = 2,\ 3, \text{ and } (n,j) = (0,1). \end{cases}$$

With this abbreviation and the observation that the result in Corollary 14.13 is similar to the one in Eq. (12.9), Lemma 12.16 immediately holds true for the scalar-valued case.

Finally, we can analyze the problems of Example 14.4 more precisely. We are mainly interested in the two medical imaging examples because they correspond to the main problem of magneto-electroencephalography.

Example 14.14. *By means of the results achieved in this chapter, we can solve the two examples directly. Here, the radius of the ball modelling the cerebrum is given by ϱ_0 and the potentials are measured on $\mathbb{S}_{\varrho_L}$.*

i) The inverse MEG problem by means of the Hodge decomposition yields an integral equation, see Theorem 15.3, that fits into our general setting. Here, $\gamma_n(y) \coloneqq n/(4\pi)y^{-(n+1)}$ *and* $t_n \coloneqq n-1$ *for all* $n \in \mathbb{N}_0$*. The magnetic potential* V *is expandable into outer harmonics since it is the unique solution of the EDP. Thus, we obtain with Eq.* (14.6) *the relation*

$$\begin{aligned} V^\wedge(n,j) &= \frac{n}{2n+1}\frac{1}{\varrho_L^n}\int_0^{\varrho_0} x^{n+1}F_{n,j}(x)\,\mathrm{d}x \\ &= n\sqrt{\frac{\varrho_0}{(2n+1)^3}}\left(\frac{\varrho_0}{\varrho_L}\right)^n F^\wedge(0,n,j). \end{aligned}$$

ii) The homogeneous inverse EEG problem restricted onto the sphere $\mathbb{S}_{\varrho_L}$ *by means of the Helmholtz decomposition, see Lemma 15.22 and Example 6.11, can also be solved with this approach. In this case,* $\gamma_n(y) \coloneqq (2n+1)/(4\pi\sigma_0 n)y^{-(n+1)}$ *and* $t_n \coloneqq n$ *for all* $n \in \mathbb{N}$*,* $\Gamma_0 = t_0 = 0$*, and* $D \coloneqq \Delta\Psi$*. Thus, we calculate the Fourier coefficients of the electric potential* u_L *for all* $n \in \mathbb{N}$ *and* $j = 1,\dots,2n+1$ *as*

$$u_L^\wedge(n,j) = \frac{1}{n\sigma_0}\sqrt{\frac{\varrho_0^3}{2n+3}}\left(\frac{\varrho_0}{\varrho_L}\right)^n D^\wedge(0,n,j)$$

and $u_L^\wedge(0,1) = 0$*. Of course, in this particular case, we expand the potential in outer harmonics with respect to the surface* $\mathbb{S}_{\varrho_L}$*. This yields the additional damping factor* $(\varrho_0/\varrho_L)^n$ *for all* $n \in \mathbb{N}$*. Thus, we obtain a relation between the coefficients of* u_L *and* D*. However, we are interested in a relation between the electric potential and the function* Ψ*. For this purpose, Poisson's equation* $D \coloneqq \Delta\Psi$ *with adequate boundary conditions remains to be solved. In order to avoid this, another approach for the solution of the (homogeneous) inverse EEG problem is presented in [71, Prop. 4.1] and will be repeated in Theorem 15.23.*

Finally, the famous inverse gravimetric problem discussed in detail in [161] and summarized in [160] is also covered by this approach. We include these results in our setting and collect them in the next example.

Example 14.15 (Inverse Gravimetric Problem – Part II). *The problem consists in finding the mass density distribution* ϱ *inside the Earth given the gravitational potential* V *via the integral equation*

$$V(\boldsymbol{y}) = (\mathcal{S}|_{\mathbb{S}_r}F)(\boldsymbol{y}) = \gamma\int_{\mathbb{G}_{\mathrm{in}}}\frac{\varrho(\boldsymbol{x})}{|\boldsymbol{x}-\boldsymbol{y}|}\,\mathrm{d}\boldsymbol{x}, \qquad \boldsymbol{y} \in \mathbb{S}_r,$$

see Example 14.3. The gravitational potential V *is a harmonic function in* $\mathbb{G}_{\mathrm{out}}$ *that is regular at infinity, see Lemma 8.9. The formula for the Fourier coefficients of* V *is given by*

$$\begin{aligned} V^\wedge(n,j) &= \gamma\sqrt{\frac{R^3}{2n+3}}\frac{4\pi}{2n+1}\left(\frac{R}{r}\right)^n\langle F, G_{0,n,j}(R;\cdot)\rangle_{\mathrm{L}_2(\mathbb{B}_R)} \\ &= \frac{4\pi\gamma}{2n+1}\frac{1}{r^n}\int_0^R F_{n,j}(x)x^{n+2}\,\mathrm{d}x, \end{aligned}$$

see also [23, 24, 147, 154, 160–162, 168, 189, 196]. Sometimes, the coefficients $V^\wedge(n,j)$ *are called Stoke's coefficients, see, for instance, [26, 30] and the references therein. Obviously,*

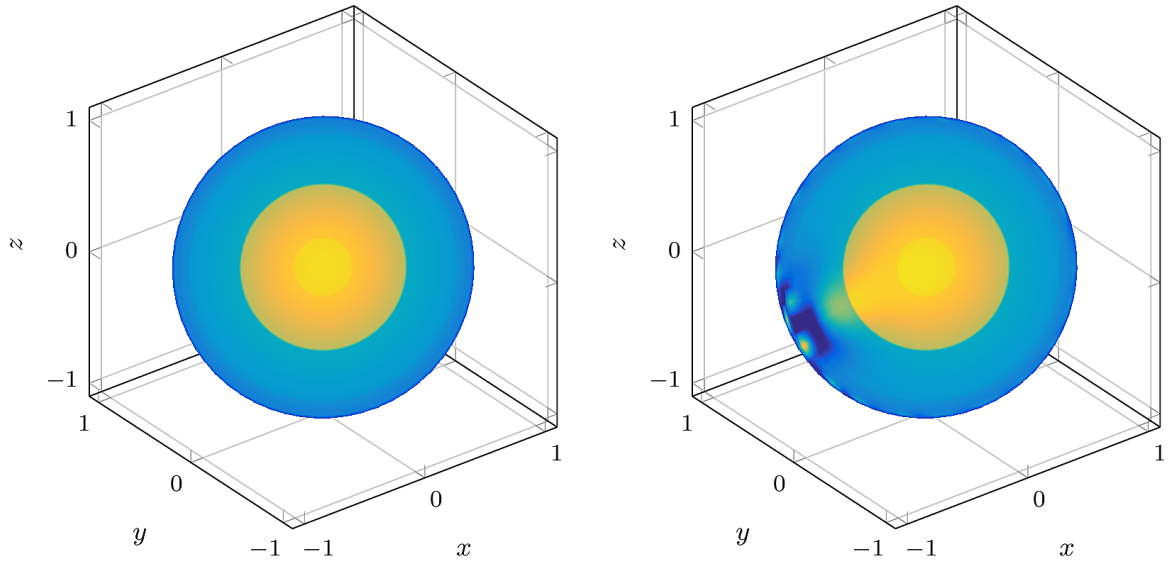

(a) PREM density *(b) PREM density disturbed by F_{dist}*

FIGURE 14.1: *The PREM model and its disturbance generate the same gravitational potential $\mathcal{S}|_{\mathbb{S}_r}(F_{\text{PREM}})$ since F_{dist} is contained in the null space of $\mathcal{S}|_{\mathbb{S}_r}$. Both are plotted on a plane inside the Earth, see also [147].*

the corresponding singular values of the operator $\mathcal{S}|_{\mathbb{S}_r}$ are exponentially decreasing, which implies the severe (exponential) ill-posedness of the inverse problem. This damping factor is often associated with the downward continuation of the satellite data onto the Earth's surface. The null space of the operator is given by

$$\ker \mathcal{S}|_{\mathbb{S}_r} = \overline{\operatorname{span}\left\{G_{m,n,j}(R;\cdot) \mid m \in \mathbb{N}, n \in \mathbb{N}_0, j = 1, \dots, 2n+1\right\}}.$$

Only the functions

$$G_{0,n,j}(R;\boldsymbol{x}) = Q_0^{(n+1/2)}(R;x)Y_{n,j}(\hat{\boldsymbol{x}}) = G^{\text{I}}_{0,n,j}(R;\boldsymbol{x}) = \sqrt{\frac{2n+3}{R^3}}\left(\frac{x}{R}\right)^n Y_{n,j}(\hat{\boldsymbol{x}}),$$

which are harmonic, are not in the null space of the operator

$$\ker \mathcal{S}|_{\mathbb{S}_r} = \left\{F \in \mathrm{C}^2(\mathbb{B}_R) \;\middle|\; \Delta F = 0\right\}^{\perp},$$

see Corollary 14.10. Thus, the inverse problem does not have a unique solution or density, respectively. The non-uniqueness of the density is comprehensively discussed in the literature, see [13, 14, 16, 154, 161, 188, 204, 206]. For example, let F_{PREM} be the Earth's density obtained by the PREM model, see [60], plotted in Fig. 14.1. Let the disturbance F_{dist} be a linear combination of orthonormal basis functions $G_{m,n,j}(R;\cdot)$ with $m \in \mathbb{N}$, $n \in \mathbb{N}_0$, $j = 1, \dots, 2n+1$ and arbitrary mounting points $\boldsymbol{z}_l \in \mathbb{B}_R$ for all $l = 1, 2, 3$, more precisely

$$F_{\text{dist}}(\boldsymbol{x}) := \sum_{l=1}^{3}\sum_{n=0}^{100}\sum_{j=1}^{2n+1}(0.95)^{1+n}G_{1,n,j}(R;\boldsymbol{x})G_{1,n,j}(R;\boldsymbol{z}_l), \qquad \boldsymbol{x} \in \mathbb{B}_R.$$

Then the potential generated by F_{PREM} coincides with $\mathcal{S}|_{\mathbb{S}_r}(F_{\text{PREM}} + F_{\text{dist}})$.

By means of the best-approximate solution F^+, we immediately obtain that the harmonic solution of the inverse gravimetric problem is the best-approximate solution, that is

$$F^+(\boldsymbol{y}) = \frac{1}{4\pi\gamma} \sum_{n=0}^{\infty} \sum_{j=1}^{2n+1} \sqrt{\frac{2n+3}{R^3}} (2n+1) \left(\frac{r}{R}\right)^n V^\wedge(n,j) G_{0,n,j}(R;\boldsymbol{y})$$

provided that Picard's criterion is fulfilled. Due to Kaula's (empirical) rule of thumb

$$\sum_{j=1}^{2n+1} V^\wedge(n,j)^2 \in \mathcal{O}(q^{n+1} n^{-3}) \qquad (as\ n \to \infty)$$

for a constant $q \in (0,1]$ related to the Bjerhammar sphere, Picard's criterion is satisfied, see [134, 199]. Hence, the harmonic solution coincides with the minimum norm solution. Certain satellite missions using satellite-to-satellite tracking like CHAMP and GRACE [132], or SGG yield data from which derivatives can be derived, such as the negative first radial derivative of the gravitational potential. The gradient of the gravitational potential is given via Eq. (5.15)*, Theorem 7.26, and Lemma 14.6 by*

$$\boldsymbol{\nabla}_{\boldsymbol{y}}((\mathcal{S}F)(\boldsymbol{y})) = -4\pi\gamma \sum_{n=0}^{\infty} \sum_{j=1}^{2n+1} \sqrt{\frac{(n+1)R^3}{(2n+1)(2n+3)}} F^\wedge(0,n,j) \frac{R^n}{y^{n+2}} \tilde{\boldsymbol{y}}^{(1)}_{n,j}(\boldsymbol{y}).$$

This result is also stated in [156], where a linear combination of the Morse-Feshbach vector spherical harmonics is used instead of the Edmonds vector spherical harmonics. A similar result concerning $\hat{\boldsymbol{y}} \cdot \boldsymbol{\nabla}_{\boldsymbol{y}}((\mathcal{S}F)(\boldsymbol{y}))$ can also be found in [155].

Chapter 15.

Previous Scalar Approaches for the Magneto-encephalography Problem

In this chapter, we present other decomposition approaches for the MEG and EEG problem that have been extensively discussed in the literature, see, for instance, [47, 48, 50, 71–75]. We compare these approaches with the Edmonds approach pursued in this thesis in order to give a broad overview of the magneto-electroencephalography problem. We also discuss the advantages and disadvantages of the Edmonds ansatz in comparison to the other approaches.

Almost all of these approaches lead to scalar continuous/star-shaped VLI equations, such that the previous chapter will help us to handle these integral equations.

15.1. Hodge Decomposition

In many other works considering the magnetoencephalography problem, the Hodge decomposition of the current $\boldsymbol{J}^{\mathrm{P}}$ is used instead of the Edmonds expansion, see, for example, [47, 71–75]. It is given by

$$\boldsymbol{J}^{\mathrm{P}}(\boldsymbol{x}) = J^r(\boldsymbol{x})\hat{\boldsymbol{x}} + \frac{1}{x}\left(\boldsymbol{\nabla}^*_{\hat{\boldsymbol{x}}} G(\boldsymbol{x}) + \boldsymbol{L}^*_{\hat{\boldsymbol{x}}} F(\boldsymbol{x})\right), \qquad \boldsymbol{x} \in \mathbb{B}_{\varrho_0} \setminus \{\boldsymbol{0}\}. \tag{15.1}$$

Here, J^r, G, $F\colon \mathbb{B}_{\varrho_0} \to \mathbb{R}$ are scalar-valued functions on the ball. The Hodge decomposition is unique, up to additional constants for G and F, see [75], and is named after W.V.D. Hodge, because the Hodge star operator is used for its derivation. Sometimes, this spherical decomposition is named after Hansen because the idea is based on the classical Hansen decomposition, see [111, 112, 205]. Here, we stick to the mainly used nomenclature and call the decomposition in Eq. (15.1) the Hodge decomposition. In order to solve the magneto-electroencephalography problem, we need some assumptions on the scalar-valued functions. These are in fact stronger conditions on the neuronal current than those required for the Edmonds approach, which is a disadvantage of the Hodge decomposition.

Assumption 15.1. *Let J^r, G, $F\colon \mathbb{B}_{\varrho_0} \to \mathbb{R}$ be scalar-valued functions with $J^r \in \mathrm{L}_2(\mathbb{B}_{\varrho_0})$ and G, $F \in \mathrm{C}^1(\mathbb{B}_{\varrho_0})$. In addition, let a similar normalization assumption as in Theorem 5.19 be fulfilled, that is*

$$\int_{\mathbb{S}} G(\boldsymbol{x})\,\mathrm{d}\omega(\hat{\boldsymbol{x}}) = \int_{\mathbb{S}} F(\boldsymbol{x})\,\mathrm{d}\omega(\hat{\boldsymbol{x}}) = 0.$$

Since $\mathbb{B}_{\varrho_0} \subset \mathbb{R}^3$ is compact, we immediately conclude that the neuronal current is an $\mathbf{L}_2(\mathbb{B}_R)$-function. The possible singularity at the origin occurring in Eq. (15.1) vanishes by means of the Jacobian determinant for spherical coordinates. Due to the normalization

assumption, we indeed obtain a unique Hodge decomposition. For the angular functions G and F, we obtain with the abbreviation $H \in \{F, G\}$ the expansion

$$H(\boldsymbol{x}) \overset{\mathrm{L}_2(\mathbb{B}_{\varrho_0})}{=} \sum_{n=0}^{\infty} \sum_{j=1}^{2n+1} H_{n,j}(x) Y_{n,j}(\hat{\boldsymbol{x}}).$$

In addition, with Eq. (2.11), we obtain for almost all $x \in [0, \varrho_0]$ the identity

$$\begin{aligned} 0 &= \int_{\mathbb{S}} H(\boldsymbol{x}) \, \mathrm{d}\omega(\hat{\boldsymbol{x}}) \\ &= \sqrt{4\pi} \int_{\mathbb{S}} \sum_{n=0}^{\infty} \sum_{j=1}^{2n+1} H_{n,j}(x) Y_{n,j}(\hat{\boldsymbol{x}}) Y_{0,1}(\hat{\boldsymbol{x}}) \, \mathrm{d}\omega(\hat{\boldsymbol{x}}) \\ &= \sqrt{4\pi} H_{0,1}(x). \end{aligned}$$

15.1.1. Hodge Decomposition for MEG

Especially for the MEG problem, the Hodge decomposition has some advantages. Here, we use the Hodge decomposition in combination with the multiple-shell model, whereas it is used in [47, 71–75] for the three-shell model. Inserting the Hodge decomposition presented in Eq. (15.1) into the formula for the magnetic potential U, see Problem 9.1, we get for all $\boldsymbol{y} \in \overline{\mathbb{B}_{\varrho_L}^{\mathrm{ext}}}$ the identity

$$U(\boldsymbol{y}) = \int_{\mathbb{B}_{\varrho_0}} \left(J^r(\boldsymbol{x}) \hat{\boldsymbol{x}} + \frac{1}{x} \left(\boldsymbol{\nabla}_{\hat{\boldsymbol{x}}}^* G(\boldsymbol{x}) + \boldsymbol{L}_{\hat{\boldsymbol{x}}}^* F(\boldsymbol{x}) \right) \right) \cdot \boldsymbol{k}_{\mathrm{M}}(\boldsymbol{x}, \boldsymbol{y}) \, \mathrm{d}\boldsymbol{x}. \tag{15.2}$$

Due to Eq. (2.6a), the summand depending on J^r vanishes. Applying Eq. (2.9a) to the first summand and, vice versa, applying Eq. (2.9b) to the second summand, we obtain

$$\begin{aligned} U(\boldsymbol{y}) = &- \int_{\mathbb{B}_{\varrho_0}} \frac{1}{x} G(\boldsymbol{x}) \boldsymbol{\nabla}_{\hat{\boldsymbol{x}}}^* \cdot \boldsymbol{k}_{\mathrm{M}}(\boldsymbol{x}, \boldsymbol{y}) \, \mathrm{d}\boldsymbol{x} \\ &- \frac{1}{4\pi} \int_{\mathbb{B}_{\varrho_0}} \left(\boldsymbol{L}_{\hat{\boldsymbol{x}}}^* \cdot \boldsymbol{L}_{\hat{\boldsymbol{x}}}^* \left(\frac{1}{x} F(\boldsymbol{x}) \right) \right) \left(\sum_{k=1}^{\infty} \frac{x^k}{(k+1) y^{k+1}} P_k(\hat{\boldsymbol{x}} \cdot \hat{\boldsymbol{y}}) \right) \mathrm{d}\boldsymbol{x}. \end{aligned} \tag{15.3}$$

Note that the integral kernel is sufficiently smooth, which is proved in Theorem 6.22. From this theorem, we also obtain that the first integral vanishes. Obviously, Assumption 15.1 is not sufficient for this calculation. This is the reason why we need to assume a higher order of smoothness, that is $F \in \mathrm{C}^2(\mathbb{B}_{\varrho_0})$. Now, we apply Theorem 2.16 to the integrand and eventually obtain for all $\boldsymbol{y} \in \overline{\mathbb{B}_{\varrho_L}^{\mathrm{ext}}}$ the magnetic potential

$$U(\boldsymbol{y}) = -\frac{1}{4\pi} \int_{\mathbb{B}_{\varrho_0}} (\Delta_{\hat{\boldsymbol{x}}}^* F(\boldsymbol{x})) \sum_{k=1}^{\infty} \frac{x^{k-1}}{(k+1) y^{k+1}} P_k(\hat{\boldsymbol{x}} \cdot \hat{\boldsymbol{y}}) \, \mathrm{d}\boldsymbol{x}. \tag{15.4}$$

This is a slight improvement of the results in [73] because we prove that the zeroth summand of the kernel does not contribute to the magnetic potential, and, hence, we can neglect the singularity of the integral kernel at the origin that occurs otherwise.

An advantage of this approach, in the case of the inverse MEG problem, is the reduction of the vector-valued problem into a scalar-valued one, see Eq. (15.4), which may significantly

reduce the computational costs. In addition, we can immediately see that the parts of the current depending on J^r and G are invisible to the magnetoencephalograph. Hence, only the function F contributes to the magnetic field and potential. A similar result is also obtained by [72, Eq. (7)], [73], and [162]. It is restated in the next lemma.

Lemma 15.2 (Hodge Decomposition for MEG, [73, Thm. 2.1]). *Let the functions of the Hodge decomposition in Eq.* (15.1) *fulfil Assumption 15.1. In addition, let the function* $F \in \mathrm{C}^2(\mathbb{B}_{\varrho_0})$ *be given by the* $\mathrm{L}_2(\mathbb{B}_{\varrho_0})$*-convergent series*

$$F(\boldsymbol{x}) \overset{\mathrm{L}_2(\mathbb{B}_{\varrho_0})}{=} \sum_{n=0}^{\infty} \sum_{j=1}^{2n+1} F_{n,j}(x) Y_{n,j}(\hat{\boldsymbol{x}}), \tag{15.5}$$

where the summability condition

$$\sum_{n=0}^{\infty} \sum_{j=1}^{2n+1} |F_{n,j}(x)|\, n^{3+\varepsilon} < \infty$$

for some $\varepsilon > 0$ *and for all* $x \in [0, \varrho_0]$ *is satisfied. Then for* $\boldsymbol{y} \in \overline{\mathbb{B}_{\varrho_L}^{\mathrm{ext}}}$ *the magnetic potential is given by*

$$U(\boldsymbol{y}) = -\frac{1}{4\pi} \int_{\mathbb{B}_{\varrho_0}} (\Delta_{\hat{\boldsymbol{x}}}^* F(\boldsymbol{x})) \sum_{k=1}^{\infty} \frac{x^{k-1}}{(k+1) y^{k+1}} P_k(\hat{\boldsymbol{x}} \cdot \hat{\boldsymbol{y}})\, \mathrm{d}\boldsymbol{x}.$$

In addition, if the magnetic potential is represented by

$$U(\boldsymbol{y}) \overset{\mathrm{L}_2(\overline{\mathbb{B}_{\varrho_L}^{\mathrm{ext}}})}{=} \sum_{n=0}^{\infty} \sum_{j=1}^{2n+1} V^{\wedge}(n,j) \frac{1}{y^{n+1}} Y_{n,j}(\hat{\boldsymbol{y}}),$$

then for all $n \in \mathbb{N}$, $j = 1, \ldots, 2n+1$ *the following relations hold true:*

$$(2n+1) V^{\wedge}(n,j) = n \int_0^{\varrho_0} F_{n,j}(x) x^{n+1}\, \mathrm{d}x \tag{15.6}$$

and $V^{\wedge}(0,1) = 0$.

The summability condition implies Picard's criterion, but we later see that the summability condition is unnecessarily strong. The assumption $F \in \mathrm{C}^2(\mathbb{B}_{\varrho_0})$ obviously implies $F \in \mathrm{L}_2(\mathbb{B}_{\varrho_0})$. By means of the proof in Theorem 7.26, we immediately obtain the stated spherical harmonics expansion of F. Recall that this smoothness condition is required in order to derive Eq. (15.4).

We are able to get rid of this strong smoothness condition by using a novel derivation of the solution via the Hodge decomposition. We also start with Eq. (15.2) and apply the same integral theorem stated in Eq. (2.9b) but switch the roles of the function $\boldsymbol{L}^* F$ and the integral kernel. Thus, for all $\boldsymbol{y} \in \overline{\mathbb{B}_{\varrho_L}^{\mathrm{ext}}}$ we get

$$\begin{aligned} U(\boldsymbol{y}) &= -\frac{1}{4\pi} \int_{\mathbb{B}_{\varrho_0}} \frac{1}{x} F(\boldsymbol{x}) \left(\boldsymbol{L}_{\hat{\boldsymbol{x}}}^* \cdot \boldsymbol{L}_{\hat{\boldsymbol{x}}}^* \sum_{k=1}^{\infty} \frac{x^k}{y^{k+1}(k+1)} P_k(\hat{\boldsymbol{x}} \cdot \hat{\boldsymbol{y}}) \right) \mathrm{d}\boldsymbol{x} \\ &= -\frac{1}{4\pi} \int_{\mathbb{B}_{\varrho_0}} \frac{1}{x} F(\boldsymbol{x}) \left(\Delta_{\hat{\boldsymbol{x}}}^* \sum_{k=1}^{\infty} \frac{x^k}{(k+1) y^{k+1}} P_k(\hat{\boldsymbol{x}} \cdot \hat{\boldsymbol{y}}) \right) \mathrm{d}\boldsymbol{x}. \end{aligned} \tag{15.7}$$

The smoothness of the integral kernel is sufficient and has already been proved in Theorem 6.22. In addition, this theorem provides us with the possibility to interchange the series with respect to k and the Beltrami operator. The Beltrami operator applied to the Legendre polynomials is calculated in Eq. (2.14). Combining these thoughts, we get

$$U(\boldsymbol{y}) = \frac{1}{4\pi} \int_{\mathbb{B}_{\varrho_0}} F(\boldsymbol{x}) \left(\sum_{k=1}^{\infty} \frac{k x^{k-1}}{y^{k+1}} P_k(\hat{\boldsymbol{x}} \cdot \hat{\boldsymbol{y}}) \right) \mathrm{d}\boldsymbol{x}, \qquad \boldsymbol{y} \in \overline{\mathbb{B}_{\varrho_L}^{\mathrm{ext}}}. \tag{15.8}$$

The problem stated in Eq. (15.8) yields the same solution as given in Lemma 15.2. We eventually obtain by means of the scalar continuous VLI operator, see Corollary 14.8, an outer harmonic expansion of U, that is

$$U(\boldsymbol{y}) = \sum_{n=0}^{\infty} \sum_{j=1}^{2n+1} \frac{n}{2n+1} \left(\int_0^{\varrho_0} F_{n,j}(x) x^{n+1} \, \mathrm{d}x \right) \frac{1}{y^{n+1}} Y_{n,j}(\hat{\boldsymbol{y}}).$$

This is exactly the same result as in Lemma 15.2. Note that this series converges uniformly in $\overline{\mathbb{B}_{\varrho_L}^{\mathrm{ext}}}$. This novel proof provides us with two advantages. First, a lower order of smoothness of the function F is required. Second, we can weaken the summability condition. Accordingly, we can lessen the requirements of Lemma 15.2 and reformulate the statement.

Theorem 15.3. *Let the functions of the Hodge decomposition in Eq.* (15.1) *fulfil Assumption 15.1. Then, for* $\boldsymbol{y} \in \overline{\mathbb{B}_{\varrho_L}^{\mathrm{ext}}}$*, the magnetic potential is given by*

$$\begin{aligned} U(\boldsymbol{y}) &= -\frac{1}{4\pi} \int_{\mathbb{B}_{\varrho_0}} F(\boldsymbol{x}) \frac{\partial}{\partial x} \frac{1}{|\boldsymbol{x} - \boldsymbol{y}|} \, \mathrm{d}\boldsymbol{x} \\ &= -\frac{1}{4\pi} \int_{\mathbb{B}_{\varrho_0}} F(\boldsymbol{x}) \sum_{k=1}^{\infty} \frac{k x^{k-1}}{y^{k+1}} P_k(\hat{\boldsymbol{x}} \cdot \hat{\boldsymbol{y}}) \, \mathrm{d}\boldsymbol{x}. \end{aligned}$$

In addition, if the magnetic potential is represented by

$$U(\boldsymbol{y}) \overset{\mathrm{L}_2(\overline{\mathbb{B}_{\varrho_L}^{\mathrm{ext}}})}{=} \sum_{n=1}^{\infty} \sum_{j=1}^{2n+1} V^{\wedge}(n,j) \frac{1}{y^{n+1}} Y_{n,j}(\hat{\boldsymbol{y}}),$$

then for all $n \in \mathbb{N}$, $j = 1, \ldots, 2n+1$ *the following relation holds true:*

$$(2n+1) V^{\wedge}(n,j) = n \int_0^{\varrho_0} F_{n,j}(x) x^{n+1} \, \mathrm{d}x. \tag{15.9}$$

The problem of finding a solution F *for given magnetic potential* U *has a solution if*

$$\sum_{n=0}^{\infty} \sum_{j=1}^{2n+1} n^2 \sup_{x \in [0,R]} |F_{n,j}(x)|^2 < \infty \tag{15.10}$$

Proof. We have already derived the integral equation containing the series representation of the integral kernel in Eq. (15.8). The closed representation of the integral kernel via the Newtonian kernel is given by the term-by-term derivative of Eq. (2.2) and Theorem 6.22.

The range of the operator is contained in $\mathrm{L}_2(\overline{\mathbb{B}^{\mathrm{ext}}_{\varrho_L}})$ for which an orthonormal basis is stated in Lemma 12.8. Thus, for all $n \in \mathbb{N}$ and $j = 1, \ldots, 2n+1$ we need to calculate the inner product, which is straightforward and not presented here in detail, and obtain

$$\begin{aligned}\langle U, S_{n,j}(\varrho_L;\cdot)\rangle_{\mathrm{L}_2(\overline{\mathbb{B}^{\mathrm{ext}}_{\varrho_L}})} &= \sqrt{2n-1}V^{\wedge}(n,j)\varrho_L^{n-1/2}\int_{\varrho_L}^{\infty}\frac{1}{y^{2n}}\,\mathrm{d}y\\ &= \frac{1}{\sqrt{2n-1}}V^{\wedge}(n,j)\varrho_L^{-n+1/2}.\end{aligned}$$

Inserting this combined with Eq. (15.9) into Picard's criterion, see Tables 13.1 and 13.2, we get the condition

$$\begin{aligned}&\sum_{n=1}^{\infty}\sum_{j=1}^{2n+1}\frac{(n+1)(2n+1)^2(2n+3)(2n-1)}{n\varrho_0^3\varrho_L}\left(\frac{\varrho_L}{\varrho_0}\right)^{2n}\langle U, S_{n,j}(\varrho_L;\cdot)\rangle^2_{\mathrm{L}_2(\overline{\mathbb{B}^{\mathrm{ext}}_{\varrho_L}})}\\ &= \sum_{n=1}^{\infty}\sum_{j=1}^{2n+1}\frac{(n+1)(2n+1)^2(2n+3)}{n}\varrho_0^{-2n-3}(V^{\wedge}(n,j))^2\\ &= \sum_{n=1}^{\infty}\sum_{j=1}^{2n+1}n(n+1)(2n+3)\varrho_0^{-2n-3}\left(\int_0^{\varrho_0}F_{n,j}(x)x^{n+1}\,\mathrm{d}x\right)^2 < \infty.\end{aligned}$$

Via the estimate

$$\begin{aligned}\left(\int_0^{\varrho_0}F_{n,j}(x)x^{n+1}\,\mathrm{d}x\right)^2 &\leq \int_0^{\varrho_0}\left(F_{n,j}(x)\right)^2\,\mathrm{d}x\int_0^{\varrho_0}x^{2n+2}\,\mathrm{d}x\\ &\leq \frac{1}{2n+3}\sup_{x\in[0,R]}|F_{n,j}(x)|^2\,\varrho_0^{2n+4},\end{aligned}$$

Picard's criterion is satisfied if the summability condition in Eq. (15.10) is valid. □

Now, we prove that the results in Lemma 15.2 or Theorem 15.3, respectively, coincide with our result from the previous section, which is stated in Theorem 9.4.

Corollary 15.4. *With the requirements from Assumption 15.1, we get*

$$\begin{aligned}&(2n+1)V^{\wedge}(n,j) = n\int_0^{\varrho_0}F_{n,j}(x)x^{n+1}\,\mathrm{d}x,\\ \Leftrightarrow\qquad &U_{\varrho_L}{}^{\wedge}(n,j) = \frac{\sqrt{n}}{\sqrt{n+1}(2n+1)\varrho_L^n}\int_0^{\varrho_0}x^{n+2}J^{(3),\sim}_{n,j}(x)\,\mathrm{d}x\end{aligned}\tag{15.11}$$

for all $n \in \mathbb{N}$, $j = 1, \ldots, 2n+1$.

Proof. First, we calculate $J^{(3),\sim}_{n,j}$ for all $n \in \mathbb{N}$, $j = 1, \ldots, 2n+1$ and for almost all $x \in (0, \varrho_0]$ by means of the Hodge decomposition in Eq. (15.1), that is

$$\begin{aligned}J^{(3),\sim}_{n,j}(x) &= \left\langle \boldsymbol{J}^{\mathrm{P}}(x\cdot), \tilde{\boldsymbol{y}}^{(3)}_{n,j}\right\rangle_{\mathbf{L}_2(\mathbb{S})}\\ &= -\frac{1}{x}\frac{1}{\sqrt{n(n+1)}}\int_{\mathbb{S}}F(\boldsymbol{x})\Delta^*_{\hat{\boldsymbol{x}}}Y_{n,j}(\hat{\boldsymbol{x}})\,\mathrm{d}\omega(\hat{\boldsymbol{x}})\\ &= \frac{\sqrt{n(n+1)}}{x}F_{n,j}(x).\end{aligned}\tag{15.12}$$

Here, we used Eq. (2.6a) and Corollary 2.21 in the first step and Lemma 2.23 and the definition of $F_{n,j}$ for all $n \in \mathbb{N}$, $j = 1, \dots, 2n+1$ in the last step. Since we use a slightly different expansion for the magnetic potential than in [72], we need to transform the related coefficients. The corresponding representation of the magnetic potential is given by

$$U(\boldsymbol{y}) \overset{\mathrm{L}_2(\overline{\mathbb{B}_{\varrho_L}^{\mathrm{ext}}})}{=} \sum_{n=1}^{\infty} \sum_{j=1}^{2n+1} V^{\wedge}(n,j) \frac{1}{\varrho_L^n} \frac{\varrho_L^n}{y^{n+1}} Y_{n,j}(\hat{\boldsymbol{y}}).$$

Comparing this formula with the outer harmonic expansion from Theorem 9.4, we get $U_{\varrho_L}^{\wedge}(n,j) = V^{\wedge}(n,j)\varrho_L^{-n}$. Inserting the representations of $V^{\wedge}(n,j)$ and $F_{n,j}$ for all $n \in \mathbb{N}$, $j = 1, \dots, 2n+1$ into Eq. (15.6), we get the desired result. □

Note that with Eq. (15.12) a one-to-one relation between $J_{n,j}^{(3),\sim}$ and $F_{n,j}$ is given for almost all $x \in (0, \varrho_0]$ and all $n \in \mathbb{N}$, $j = 1, \dots, 2n+1$.

For the sake of completeness, we state the relation between the vector outer harmonics coefficients of type 1 of the magnetic field $\boldsymbol{B}$ and the spherical harmonics coefficients of the function F.

Corollary 15.5. *Let the magnetic field $\boldsymbol{B}$ be given as in Theorem 9.4. Let Assumption 15.1 be fulfilled. Then*

$$B_{\varrho_L}^{\wedge}(n,j) = \frac{-\mu_0 n}{\varrho_L^{n+1}} \sqrt{\frac{n+1}{2n+1}} \int_0^{\varrho_0} F_{n,j}(x) x^{n+1} \,\mathrm{d}x \tag{15.13}$$

holds true for all $n \in \mathbb{N}$, $j = 1, \dots, 2n+1$ and $B_{\varrho_L}^{\wedge}(0,1) = 0$.

Proof. The identity can easily be seen by inserting Eq. (15.12) into the representation from Theorem 9.4. □

We directly see that the Hodge decomposition is as good as the Edmonds approach in the context of uniqueness results. In both cases, there exist infinitely many choices for the integrands $x \mapsto F_{n,j}(x)x^{n+1}$ and $x \mapsto J_{n,j}^{(3),\sim}(x)x^{n+2}$, respectively, in order to satisfy Eq. (15.13) if the coefficients $B_{\varrho_L}^{\wedge}(n,j)$ are given for all $n \in \mathbb{N}$, $j = 1, \dots, 2n+1$.

15.1.2. Hodge Decomposition for EEG

To the knowledge of the author, the Hodge decomposition has not been used for solving the inverse EEG problem so far. One possible reason is that the electric potential u_L on the scalp would then depend on a linear combination of J^r and G.

From Eq. (10.1), a continuous/star-shaped VLI equation of the electric potential is known. Therein, we insert the Hodge decomposition of the neuronal current from Eq. (15.1). For the next calculation, we use an appropriate representation of the integral kernel from Eq. (6.5). We split the gradient by means of spherical coordinates, see Theorem 2.14, and use the orthogonality results in Eq. (2.6) in order to simplify the formula. The integral identity in Eq. (2.9) combined with properties of the Legendre polynomials in Eq. (2.14) yields for all

$\boldsymbol{y} \in \mathbb{S}_{[\varrho_{L-1},\varrho_L]}$ the result

$$\begin{aligned} u_L(\boldsymbol{y}) &= \int_{\mathbb{B}_{\varrho_0}} \left(J^r(\boldsymbol{x})\hat{\boldsymbol{x}} + \frac{1}{x}\left(\boldsymbol{\nabla}^*_{\hat{\boldsymbol{x}}} G(\boldsymbol{x}) + \boldsymbol{L}^*_{\hat{\boldsymbol{x}}} F(\boldsymbol{x})\right)\right) \cdot \boldsymbol{k}_{\mathrm{E}}(\boldsymbol{x},\boldsymbol{y})\,\mathrm{d}\boldsymbol{x} \\ &= \frac{1}{4\pi}\int_{\mathbb{B}_{\varrho_0}} J^r(\boldsymbol{x}) \frac{\partial}{\partial x}\left(\sum_{k=1}^{\infty}(2k+1)H_k(y)x^k P_k(\hat{\boldsymbol{x}}\cdot\hat{\boldsymbol{y}})\right)\mathrm{d}\boldsymbol{x} \\ &\quad + \frac{1}{4\pi}\int_{\mathbb{B}_{\varrho_0}} \frac{1}{x^2}\boldsymbol{\nabla}^*_{\hat{\boldsymbol{x}}} G(\boldsymbol{x}) \cdot \boldsymbol{\nabla}^*_{\hat{\boldsymbol{x}}}\left(\sum_{k=1}^{\infty}(2k+1)H_k(y)x^k P_k(\hat{\boldsymbol{x}}\cdot\hat{\boldsymbol{y}})\right)\mathrm{d}\boldsymbol{x} \\ &= \frac{1}{4\pi}\int_{\mathbb{B}_{\varrho_0}} J^r(\boldsymbol{x})\left(\sum_{k=1}^{\infty}(2k+1)kH_k(y)x^{k-1}P_k(\hat{\boldsymbol{x}}\cdot\hat{\boldsymbol{y}})\right)\mathrm{d}\boldsymbol{x} \\ &\quad + \frac{1}{4\pi}\int_{\mathbb{B}_{\varrho_0}} G(\boldsymbol{x})\left(\sum_{k=1}^{\infty}(2k+1)k(k+1)H_k(y)x^{k-2}P_k(\hat{\boldsymbol{x}}\cdot\hat{\boldsymbol{y}})\right)\mathrm{d}\boldsymbol{x}. \end{aligned} \tag{15.14}$$

In analogy to the MEG case, the integrand reduces to a scalar-valued one. In contrast, we obtain two different scalar star-shaped VLI kernels depending on different components of the neuronal current. Thus, we cannot separate the parts of the electric potential generated by J^r from the parts generated by G. A result that is similar to the next is stated in [52] for the homogeneous spherical head model.

Theorem 15.6. *Let $\boldsymbol{J}^{\mathrm{P}}$ fulfil Assumption 15.1 and be represented by means of the Hodge decomposition. In addition, let the electric potential u_L be represented by the in $\mathbb{S}_{[\varrho_{L-1},\varrho_L]}$ uniformly convergent series*

$$u_L(\boldsymbol{y}) = \sum_{n=0}^{\infty}\sum_{j=1}^{2n+1} u_L^{\wedge}(n,j)\left(\frac{n+1}{2n+1}\left(\frac{y}{\varrho_L}\right)^{2n+1} + \frac{n}{2n+1}\right)\left(\frac{\varrho_L}{y}\right)^n \frac{1}{y} Y_{n,j}(\hat{\boldsymbol{y}}). \tag{15.15}$$

Then the relation between the outer harmonics coefficients of the electric potential and the current is given by $u_L^{\wedge}(0,1) = 0$ and for all $n \in \mathbb{N}$, $j = 1,\ldots,2n+1$ by

$$u_L^{\wedge}(n,j) = \left(\int_0^{\varrho_0}\left(xJ^r_{n,j}(x) + (n+1)G_{n,j}(x)\right)x^n\,\mathrm{d}x\right)\frac{(2n+1)\beta_n^{(L)}}{\varrho_L^n}. \tag{15.16}$$

Proof. We start with Eq. (15.14). We define $\gamma_n(y) \coloneqq \frac{1}{4\pi}(2n+1)nH_n(y)$ and $t_n \coloneqq n-1$ for all $n \in \mathbb{N}$. Furthermore, we set $\gamma_0 \equiv 0$. Consequently, the zeroth summand vanishes and the sequence of exponents fulfils $\inf_{n\in\mathbb{N},\gamma_n\not\equiv 0} t_n \geq -1$. Then, Corollary 14.8 yields for the first integral the expression

$$\sum_{n=1}^{\infty}\sum_{j=1}^{2n+1}\left(\int_0^{\varrho_0} J^r_{n,j}(x)x^{n+1}\,\mathrm{d}x\right)nH_n(y)Y_{n,j}(\hat{\boldsymbol{y}}).$$

For the second integral, we analogously define $\gamma_0 \equiv 0$, $\gamma_n(y) \coloneqq \frac{1}{4\pi}(2n+1)n(n+1)H_n(y)$ and $t_n \coloneqq n-2$. We obtain $\inf_{n\in\mathbb{N},\gamma_n\not\equiv 0} t_n \geq -1$ and

$$\sum_{n=1}^{\infty}\sum_{j=1}^{2n+1}\left(\int_0^{\varrho_0} G_{n,j}(x)x^n\,\mathrm{d}x\right)n(n+1)H_n(y)Y_{n,j}(\hat{\boldsymbol{y}}).$$

Combining these results, we get

$$u_L(\boldsymbol{y}) = \sum_{n=1}^{\infty} \sum_{j=1}^{2n+1} \left(\int_0^{\varrho_0} \left(x J_{n,j}^r(x) + (n+1) G_{n,j}(x) \right) x^n \, \mathrm{d}x \right) n H_n(y) Y_{n,j}(\hat{\boldsymbol{y}}).$$

Together with $u_L^\wedge(n,j) = \langle u_L|_{\mathbb{S}_{\varrho_L}}, \frac{1}{\varrho_L} Y_{n,j} \rangle_{\mathbb{Z}}$ and the representation of the functions H_n in Eq. (4.20), we arrive at the desired result. □

Theorem 15.7. *Let $\boldsymbol{J}^{\mathrm{P}}$ decomposed by means of the Hodge decomposition fulfil Assumption 15.1. Then the representation of the electric potential from Theorem 15.6 coincides with the one obtained by the Edmonds approach presented in Theorem 10.4.*

Proof. From Theorem 10.4, we obtain

$$u_L^\wedge(n,j) = \frac{1}{\varrho_L^n} \sqrt{\frac{(2n+1)^3}{n}} \beta_n^{(L)} \int_0^{\varrho_0} J_{n,j}^{(2),\sim}(x) x^{n+1} \, \mathrm{d}x.$$

First, we calculate $J_{n,j}^{(2),\sim}$ by means of the Hodge decomposition. For almost all $x \in (0, \varrho_0]$ and all $n \in \mathbb{N}$ and $j = 1, \ldots, 2n+1$, we get the expression

$$J_{n,j}^{(2),\sim}(x) = \int_{\mathbb{S}} \left(J^r(\boldsymbol{x}) \hat{\boldsymbol{x}} + \frac{1}{x} \left(\boldsymbol{\nabla}_{\hat{\boldsymbol{x}}}^* G(\boldsymbol{x}) + \boldsymbol{L}_{\hat{\boldsymbol{x}}}^* F(\boldsymbol{x}) \right) \right) \cdot \tilde{\boldsymbol{y}}_{n,j}^{(2)}(\hat{\boldsymbol{x}}) \, \mathrm{d}\omega(\hat{\boldsymbol{x}}).$$

Note that for all $n \in \mathbb{N}$, $j = 1, \ldots, 2n+1$ the Edmonds vector spherical harmonics of type 2 are defined by

$$\tilde{\boldsymbol{y}}_{n,j}^{(2)} \coloneqq \sqrt{\frac{n}{2n+1}} \boldsymbol{y}_{n,j}^{(1)} + \sqrt{\frac{n+1}{2n+1}} \boldsymbol{y}_{n,j}^{(2)},$$

see Eq. (5.4b). Hence, we split the integral into two parts. For calculating both integrals, we use the orthogonality relations from Eq. (2.6) and Corollary 2.21. The first part is given by

$$\begin{aligned}
&\int_{\mathbb{S}} \left(J^r(\boldsymbol{x}) \hat{\boldsymbol{x}} + \frac{1}{x} \left(\boldsymbol{\nabla}_{\hat{\boldsymbol{x}}}^* G(\boldsymbol{x}) + \boldsymbol{L}_{\hat{\boldsymbol{x}}}^* F(\boldsymbol{x}) \right) \right) \cdot \boldsymbol{y}_{n,j}^{(1)}(\hat{\boldsymbol{x}}) \, \mathrm{d}\omega(\hat{\boldsymbol{x}}) \\
&= \int_{\mathbb{S}} J^r(\boldsymbol{x}) \hat{\boldsymbol{x}} \cdot \hat{\boldsymbol{x}} Y_{n,j}(\hat{\boldsymbol{x}}) \, \mathrm{d}\omega(\hat{\boldsymbol{x}}) \\
&= J_{n,j}^r(x).
\end{aligned}$$

For the second part, we get with Theorem 2.16 and Lemma 2.23 the identity

$$\begin{aligned}
&\int_{\mathbb{S}} \left(J^r(\boldsymbol{x}) \hat{\boldsymbol{x}} + \frac{1}{x} \left(\boldsymbol{\nabla}_{\hat{\boldsymbol{x}}}^* G(\boldsymbol{x}) + \boldsymbol{L}_{\hat{\boldsymbol{x}}}^* F(\boldsymbol{x}) \right) \right) \cdot \boldsymbol{y}_{n,j}^{(2)}(\hat{\boldsymbol{x}}) \, \mathrm{d}\omega(\hat{\boldsymbol{x}}) \\
&= \frac{1}{x\sqrt{n(n+1)}} \int_{\mathbb{S}} \left(\boldsymbol{\nabla}_{\hat{\boldsymbol{x}}}^* G(\boldsymbol{x}) \right) \cdot \boldsymbol{\nabla}_{\hat{\boldsymbol{x}}}^* Y_{n,j}(\hat{\boldsymbol{x}}) \, \mathrm{d}\omega(\hat{\boldsymbol{x}}) \\
&= \frac{\sqrt{n(n+1)}}{x} \int_{\mathbb{S}} G(\boldsymbol{x}) Y_{n,j}(\hat{\boldsymbol{x}}) \, \mathrm{d}\omega(\hat{\boldsymbol{x}}) \\
&= \frac{1}{x} \sqrt{n(n+1)} G_{n,j}(x).
\end{aligned}$$

Combining these results, we get for all $n \in \mathbb{N}$, $j = 1, \dots, 2n+1$ the relation

$$J_{n,j}^{(2),\sim}(x) = \sqrt{\frac{n}{2n+1}} \left(J_{n,j}^{r}(x) + \frac{n+1}{x} G_{n,j}(x) \right) \qquad \text{for almost all } x \in (0, \varrho_0].$$

Inserting this into the previously stated representation of $u_L^{\wedge}(n,j)$, we get the same representation as in Theorem 15.6, that is

$$u_L^{\wedge}(n,j) = \frac{1}{\varrho_L^n} (2n+1) \beta_n^{(L)} \int_0^{\varrho_0} \left(J_{n,j}^{r}(x) + \frac{n+1}{x} G_{n,j}(x) \right) x^{n+1} \, \mathrm{d}x. \qquad \square$$

Thus, if the functions $J_{n,j}^{r}$ and $G_{n,j}$ are given, we can uniquely determine the functions $J_{n,j}^{(2),\sim}$ for all $n \in \mathbb{N}$, $j = 1, \dots, 2n+1$ but not vice versa.

Now, we summarize the results obtained by the Hodge decomposition. We see that the use of this decomposition for the magneto-electroencephalography problem has some advantages and disadvantages. In both cases, the vector-valued integral operators reduce to scalar-valued problems, see Lemma 15.2 and Eq. (15.14). This has an advantage in numerical calculations.

In the case of the MEG problem, we are able to weaken the existing assumptions for this decomposition, which is advantageous since the real smoothness of the neuronal current is unknown so far. By means of this improvement, this approach yields a result that is comparable to the result obtained by the Edmonds approach in the context of the uniqueness considerations. However, for the Edmonds approach we still need less smoothness than required for the Hodge decomposition.

In the case of the EEG problem, we see that the Hodge decomposition is not as suitable as the Edmonds approach. The outer harmonics coefficients of the electric potential u_L depend on the spherical harmonics coefficients of J^r and G. Hence, infinitely many different combinations of these two functions can generate the same electric potential. Accordingly, the Hodge decomposition is not the first choice decomposition for solving the inverse EEG problem.

15.2. Morse-Feshbach Vector Approach

The aim of the inverse MEG and EEG problem is a vector-valued reconstruction of the neuronal current. Hence, only a decomposition of the neuronal current by means of vector-valued functions yields a direct reconstruction of the current without additional computations. A possible decomposition is provided by the Morse-Feshbach expansion, which is introduced in Assumption 7.14. In this setting, the current $\boldsymbol{J}^{\mathrm{P}} \in \mathbf{L}_2(\mathbb{B}_{\varrho_0})$ has the unique Morse-Feshbach expansion

$$\boldsymbol{J}^{\mathrm{P}}(\boldsymbol{x}) \overset{\mathrm{L}_2(\mathbb{B}_{\varrho_0})}{=} \sum_{i=1}^{3} \sum_{n=0_i}^{\infty} \sum_{j=1}^{2n+1} J_{n,j}^{(i)}(x) \boldsymbol{y}_{n,j}^{(i)}(\hat{\boldsymbol{x}}), \tag{15.17}$$

see Theorem 5.15. A similar decomposition is used in [47, 48] for the reconstruction of the neuronal current from given values of the magnetic and electric potential. Therein, complex scalar-valued spherical harmonics are used as a foundation for the Morse-Feshbach vector spherical harmonics. Based on the definition of the (Edmonds vector) spherical harmonics, see Definitions 2.22 and 5.9, we can use the real as well as the complex spherical harmonics for the Edmonds approach. However, in the case of complex spherical harmonics, the used

$\mathbb{R}^3$-inner products must be replaced by $\mathbb{C}^3$-inner products. Since the neuronal current is a real and not a complex current, we stick to the real version of the Morse-Feshbach vector spherical harmonics.

For the sake of comparability, we need to mention that in [48] a non-normalized version of the vector spherical harmonics is used. The factor occurring therein (i.e. $4\pi(n+j)!/((2n+1)(n-j)!)$ with $n \in \mathbb{N}_0$, $j = 1, \ldots, 2n+1$) draws through to their result for the Fourier coefficients.

15.2.1. Morse-Feshbach Approach for MEG

In Chapter 9, we derive a relation between the magnetic field and the neuronal current by means of the Edmonds approach. We know that only the direction of the neuronal current belonging to type $i = 3$ of the Edmonds vector spherical harmonics is not silent for the magnetoencephalograph, see Theorem 13.1. Due to the definition of the Morse-Feshbach and Edmonds vector spherical harmonics, see Definitions 5.8 and 5.9, we also know that the type $i = 3$ functions of both systems coincide. Eventually, the Edmonds and the Morse-Feshbach approach are the same for the MEG problem. This has already been mentioned in Remark 9.3. Both results are comparable with the one in [47, 48] keeping the different normalization factor in mind.

15.2.2. Morse-Feshbach Approach for EEG

In [48], the complex Morse-Feshbach vector spherical harmonics are also used for the EEG problem, but only for the homogeneous case. This special case is discussed in Examples 6.11 and 13.4. Keep in mind that in this case the coefficients $\beta_n^{(L)}$ are given by $\beta_0^{(L)} = 0$ and for all $n \in \mathbb{N}$ by

$$\beta_n^{(L)} = \frac{1}{\sigma_0(2n+1)}. \tag{15.18}$$

In addition, in [48] the scalp is only modelled by the sphere $\mathbb{S}_{\varrho_L}$. Note that in this reference a slightly different expansion of the electric potential is used. Their result is summarized in the next theorem.

Theorem 15.8 ([48, Ch. 5]). *Let Assumption 3.2 be fulfilled with constant conductivity σ_0 on each region, that is the homogeneous case. Let the electric potential on the scalp be given by the $\mathrm{L}_2(\mathbb{S})$-convergent series*

$$u_L(\varrho_L \hat{\boldsymbol{y}}) \overset{\mathrm{L}_2(\mathbb{S})}{=} \sum_{n=1}^{\infty} \sum_{j=1}^{2n+1} v^{\wedge}(n,j) \frac{1}{\sigma_0 \varrho_L^{n+1}} Y_{n,j}(\hat{\boldsymbol{y}}).$$

Then for all $n \in \mathbb{N}$, $j = 1, \ldots, 2n+1$ we get

$$v^{\wedge}(n,j) = \int_0^{\varrho_0} \left(J_{n,j}^{(1)}(x) + \sqrt{\frac{n+1}{n}} J_{n,j}^{(2)}(x) \right) x^{n+1} \, \mathrm{d}x.$$

Now, we can formulate a generalization of this statement. For this purpose, we consider our case of the multiple-shell model with different constant conductivities on each shell, that is the inhomogeneous case. Furthermore, we do not restrict the electric potential onto $\mathbb{S}_{\varrho_L}$.

Theorem 15.9. *Let Assumption 3.2 with $L \geq 2$ be satisfied and let the electric potential on the scalp be given by means of the Fourier expansion with respect to the orthonormal basis from Lemma 13.2, that is*

$$u_L = \sum_{n=0}^{\infty} \sum_{j=1}^{2n+1} u_L^{\wedge}(n,j) Z_{n,j}.$$

For all $n \in \mathbb{N}$, $j = 1, \ldots, 2n+1$ the following relations hold true:

$$u_L^{\wedge}(n,j) = \frac{1}{\varrho_L^n}(2n+1)\beta_n^{(L)} \int_0^{\varrho_0} \left(J_{n,j}^{(1)}(x) + \sqrt{\frac{n+1}{n}} J_{n,j}^{(2)}(x) \right) x^{n+1} \, \mathrm{d}x \tag{15.19}$$

and $u_L^{\wedge}(0,1) = 0$.

Proof. Due to the assumption on $\boldsymbol{J}^{\mathrm{P}}$, the current can be expanded as in Eq. (15.17). From Theorem 10.4, $u_L^{\wedge}(0,1) = 0$ and a relation between the coefficients $u_L^{\wedge}(n,j)$ and the Edmonds coefficients $J_{n,j}^{(2),\sim}$ is known for all $n \in \mathbb{N}$, $j = 1, \ldots, 2n+1$. Thus, we calculate $J_{n,j}^{(2),\sim}$ in terms of the Morse-Feshbach coefficients $J_{n,j}^{(1)}$ and $J_{n,j}^{(2)}$. We directly obtain for all $n \in \mathbb{N}$, $j = 1, \ldots, 2n+1$ the relation

$$\begin{aligned} J_{n,j}^{(2),\sim}(x) &= \int_{\mathbb{S}} \boldsymbol{J}^{\mathrm{P}}(\boldsymbol{x}) \cdot \tilde{\boldsymbol{y}}_{n,j}^{(2)}(\hat{\boldsymbol{x}}) \, \mathrm{d}\omega(\hat{\boldsymbol{x}}) \\ &= \sum_{i=1}^{3} \sum_{k=0_i}^{\infty} \sum_{l=1}^{2k+1} J_{k,l}^{(i)}(x) \int_{\mathbb{S}} \boldsymbol{y}_{k,l}^{(i)}(\hat{\boldsymbol{x}}) \cdot \left(\sqrt{\frac{n}{2n+1}} \boldsymbol{y}_{n,j}^{(1)}(\hat{\boldsymbol{x}}) + \sqrt{\frac{n+1}{2n+1}} \boldsymbol{y}_{n,j}^{(2)}(\hat{\boldsymbol{x}}) \right) \mathrm{d}\omega(\hat{\boldsymbol{x}}) \\ &= \sqrt{\frac{n}{2n+1}} J_{n,j}^{(1)}(x) + \sqrt{\frac{n+1}{2n+1}} J_{n,j}^{(2)}(x). \end{aligned} \tag{15.20}$$

The interchanging of the series and the integration is allowed due to the strong convergence of the series in Eq. (15.17). Inserting this into Theorem 10.4, we arrive for all $n \in \mathbb{N}$, $j = 1, \ldots, 2n+1$ at

$$u_L^{\wedge}(n,j) = \frac{1}{\varrho_L^n} \frac{2n+1}{\sqrt{n}} \beta_n^{(L)} \int_0^{\varrho_0} \left(\sqrt{n} J_{n,j}^{(1)}(x) + \sqrt{n+1} J_{n,j}^{(2)}(x) \right) x^{n+1} \, \mathrm{d}x. \qquad \square$$

We continue by restricting our result from Theorem 15.9 to the sphere $\mathbb{S}_{\varrho_L}$ in order to obtain a comparable solution. We immediately gain the following corollary.

Corollary 15.10. *The result from Theorem 15.9 coincides in the homogeneous case with the result in [48] repeated in Theorem 15.8.*

Proof. The restriction of the electric potential onto the sphere $\mathbb{S}_{\varrho_L}$ yields, by means of Theorem 10.4, for all $n \in \mathbb{N}$, $j = 1, \ldots, 2n+1$ the expansion

$$u_L(\varrho_L \hat{\boldsymbol{y}}) = \sum_{n=1}^{\infty} \sum_{j=1}^{2n+1} u_L^{\wedge}(n,j) \frac{1}{\varrho_L} Y_{n,j}(\hat{\boldsymbol{y}}), \qquad \hat{\boldsymbol{y}} \in \mathbb{S}.$$

In addition, Theorem 15.9 provides us with

$$u_L^{\wedge}(n,j) = \frac{1}{\varrho_L^n}(2n+1)\beta_n^{(L)} \int_0^{\varrho_0} \left(J_{n,j}^{(1)}(x) + \sqrt{\frac{n+1}{n}} J_{n,j}^{(2)}(x) \right) x^{n+1} \, \mathrm{d}x$$

and $u_L^\wedge(0,1) = 0$. Since we consider the homogeneous case, we obtain with Eq. (15.18) the relation

$$u_L^\wedge(n,j) = \frac{1}{\sigma_0 \varrho_L^n} \int_0^{\varrho_0} \left(J_{n,j}^{(1)}(x) + \sqrt{\frac{n+1}{n}} J_{n,j}^{(2)}(x) \right) x^{n+1} \, \mathrm{d}x. \tag{15.21}$$

With our notation, we get $u_L^\wedge(n,j) = v^\wedge(n,j)\sigma_0^{-1}\varrho_L^{-n}$. Accordingly,

$$v^\wedge(n,j) = \int_0^{\varrho_0} \left(J_{n,j}^{(1)}(x) + \sqrt{\frac{n+1}{n}} J_{n,j}^{(2)}(x) \right) x^{n+1} \, \mathrm{d}x.$$

Eventually, the result in Theorem 15.8 coincides with the one in Theorem 15.9. □

Thus, we come to the conclusion that the Morse-Feshbach approach is as good as the Edmonds approach in the case of the MEG problem. Both provide us with the same appropriate decomposition because they separate the reconstructable direction of the neuronal current from the directions in the null space of $\mathcal{T}_{\mathrm{M}}$.

In contrast, the Morse-Feshbach approach is as inappropriate as the Hodge decomposition for the inverse EEG problem. The Morse-Feshbach coefficients of the electric potential u_L depend on two radial functions of the neuronal current decomposition. Thus, the part of the neuronal current reconstructable from electric potential data is in the subspace spanned by $\{H_{m,n,j}^{(1)}(R;\cdot)\boldsymbol{y}_{n,j}^{(1)}\}_{m,n\in\mathbb{N}_0,\, j=1,\ldots,2n+1} \cup \{H_{m,n,j}^{(2)}(R;\cdot)\boldsymbol{y}_{n,j}^{(2)}\}_{m\in\mathbb{N}_0, n\in\mathbb{N},\, j=1,\ldots,2n+1}$, where the set $\{H_{m,n,j}^{(i)}(R;\cdot)\}_{m\in N_0, n\in\mathbb{N}_{0_i}, j=1,\ldots,2n+1}$ is a suitable basis for the radial part. The considerable advantage of the Edmonds approach is a precise characterization of this subspace.

15.3. Helmholtz Representation

Inspired by classical electromagnetism, the Helmholtz decomposition is often used for the analysis of the inverse EEG problem, see, for instance, [47, 50, 71, 73, 74]. The Helmholtz decomposition of the current $\boldsymbol{J}^{\mathrm{P}} \in \mathbf{C}^1(\mathbb{B}_{\varrho_0})$ is given by

$$\boldsymbol{J}^{\mathrm{P}} = \boldsymbol{\nabla}\Psi + \boldsymbol{\nabla} \wedge \boldsymbol{A}. \tag{15.22}$$

The scalar potential $\Psi \in \mathrm{C}^2(\mathbb{B}_{\varrho_0})$ is unique up to an additive constant. The induced part $\boldsymbol{\nabla}\Psi$ is called the irrotational part. The solenoidal part of the current is given by $\boldsymbol{\nabla} \wedge \boldsymbol{A}$ with the vector potential $\boldsymbol{A} \in \mathbf{C}^2(\mathbb{B}_{\varrho_0})$. If $\boldsymbol{\nabla} \cdot \boldsymbol{A} = 0$ and $\boldsymbol{J}^{\mathrm{P}}(\boldsymbol{x}) \in \mathcal{O}(x^{-2})$ as $x \to \infty$, then the function $\boldsymbol{A}$ is also unique up to an additive constant, see, for instance, [4, 8]. The adjustment $\boldsymbol{\nabla} \cdot \boldsymbol{A} = 0$ is sometimes called the *Coulomb gauge*.

In order to compare this approach with the former ones, we decompose the irrotational and solenoidal part of the current by means of the $\boldsymbol{o}^{(i)}$-operators for $i = 1, 2, 3$. For the irrotational part, we obtain with Theorem 2.14 the equation

$$\boldsymbol{\nabla}_{\boldsymbol{x}}\Psi(\boldsymbol{x}) = \boldsymbol{o}_{\hat{\boldsymbol{x}}}^{(1)} \frac{\partial}{\partial x}\Psi(\boldsymbol{x}) + \frac{1}{x}\boldsymbol{o}_{\hat{\boldsymbol{x}}}^{(2)}\Psi(\boldsymbol{x}).$$

For the splitting of the solenoidal part, a few more easy but technical calculations are needed.

Theorem 15.11. *Let the vector potential* $\boldsymbol{A} \in \mathbf{C}^2(\mathbb{B}_{\varrho_0})$ *be represented by*

$$\boldsymbol{A}(\boldsymbol{x}) = \sum_{i=1}^{3} \boldsymbol{o}_{\hat{\boldsymbol{x}}}^{(i)} A^{(i)}(\boldsymbol{x}), \tag{15.23}$$

see Theorem 5.19, then the solenoidal part has the alternative representation

$$\begin{aligned}\boldsymbol{\nabla}_{\boldsymbol{x}} \wedge \boldsymbol{A}(\boldsymbol{x}) = \frac{1}{x}\boldsymbol{o}_{\hat{\boldsymbol{x}}}^{(1)} \Delta_{\hat{\boldsymbol{x}}}^{*} A^{(3)}(\boldsymbol{x}) - \boldsymbol{o}_{\hat{\boldsymbol{x}}}^{(2)} \left(\frac{\partial}{\partial x} + \frac{1}{x}\right) A^{(3)}(\boldsymbol{x}) \\ + \boldsymbol{o}_{\hat{\boldsymbol{x}}}^{(3)} \left(-\frac{1}{x} A^{(1)}(\boldsymbol{x}) + \left(\frac{\partial}{\partial x} + \frac{1}{x}\right) A^{(2)}(\boldsymbol{x})\right).\end{aligned}$$

Proof. For this result, we need to calculate the curl of the vector potential in Eq. (15.23). Note that this expansion is unique if $A^{(2)}$ and $A^{(3)}$ have no constant parts, see Theorem 5.19. We start with the first summand. With Lemma 2.18 and $\boldsymbol{x} \wedge \boldsymbol{x} = \mathbf{0}$, we get for all $\boldsymbol{x} \in \mathbb{R}^3 \setminus \{\mathbf{0}\}$ the identity

$$\boldsymbol{\nabla}_{\boldsymbol{x}} \wedge \left(\boldsymbol{o}_{\hat{\boldsymbol{x}}}^{(1)} A^{(1)}(\boldsymbol{x})\right) = -\frac{1}{x}\boldsymbol{o}_{\hat{\boldsymbol{x}}}^{(3)} A^{(1)}(\boldsymbol{x}).$$

For the second summand, using the definition of the surface curl gradient and Lemma 2.17, we obtain

$$\begin{aligned}\boldsymbol{\nabla}_{\boldsymbol{x}} \wedge \left(\boldsymbol{o}_{\hat{\boldsymbol{x}}}^{(2)} A^{(2)}(\boldsymbol{x})\right) &= \boldsymbol{o}_{\hat{\boldsymbol{x}}}^{(3)} \frac{\partial}{\partial x} A^{(2)}(\boldsymbol{x}) + \frac{1}{x}\boldsymbol{\nabla}_{\hat{\boldsymbol{x}}}^{*} \wedge (\boldsymbol{\nabla}_{\hat{\boldsymbol{x}}}^{*} A^{(2)}(\boldsymbol{x})) \\ &= \boldsymbol{L}_{\hat{\boldsymbol{x}}}^{*} \left(\frac{\partial}{\partial x} + \frac{1}{x}\right) A^{(2)}(\boldsymbol{x}).\end{aligned}$$

And lastly, for the third summand, we obtain by means of Lemma 2.19 and Eq. (2.5) the equation

$$\boldsymbol{\nabla}_{\boldsymbol{x}} \wedge \boldsymbol{o}_{\hat{\boldsymbol{x}}}^{(3)} A^{(3)}(\boldsymbol{x}) = \frac{1}{x}\hat{\boldsymbol{x}} \Delta_{\hat{\boldsymbol{x}}}^{*} A^{(3)}(\boldsymbol{x}) - \boldsymbol{\nabla}_{\hat{\boldsymbol{x}}}^{*} \left(\frac{1}{x} + \frac{\partial}{\partial x}\right) A^{(3)}(\boldsymbol{x}).$$

Inserting these calculations into the curl of the vector potential, we obtain the desired result. □

An immediate consequence of Theorem 15.11 is the following representation of the neuronal current for all $\boldsymbol{x} \in \mathbb{B}_{\varrho_0} \setminus \{\mathbf{0}\}$:

$$\begin{aligned}\boldsymbol{J}^{\mathrm{P}}(\boldsymbol{x}) = \boldsymbol{o}_{\hat{\boldsymbol{x}}}^{(1)} \left(\frac{\partial}{\partial x}\Psi(\boldsymbol{x}) + \frac{1}{x}\Delta_{\hat{\boldsymbol{x}}}^{*} A^{(3)}(\boldsymbol{x})\right) + \boldsymbol{o}_{\hat{\boldsymbol{x}}}^{(2)} \left(\frac{1}{x}\Psi(\boldsymbol{x}) - \left(\frac{\partial}{\partial x} + \frac{1}{x}\right) A^{(3)}(\boldsymbol{x})\right) \\ + \boldsymbol{o}_{\hat{\boldsymbol{x}}}^{(3)} \left(-\frac{1}{x} A^{(1)}(\boldsymbol{x}) + \left(\frac{\partial}{\partial x} + \frac{1}{x}\right) A^{(2)}(\boldsymbol{x})\right).\end{aligned} \tag{15.24}$$

Now, we further decompose the (scalar-valued) parts of the current into $\mathrm{L}_2(\mathbb{B}_{\varrho_0})$-convergent spherical harmonics series.

Assumption 15.12. *Let the neuronal current be decomposed by means of the Helmholtz decomposition, see also Eq.* (15.24)*. In addition, let all parts of the scalar and vector potential be twice continuously differentiable, that is* $\Psi \in \mathrm{C}^2(\mathbb{B}_{\varrho_0}) \subset \mathrm{L}_2(\mathbb{B}_{\varrho_0})$, $A^{(i)} \in \mathrm{C}^2(\mathbb{B}_{\varrho_0}) \subset \mathrm{L}_2(\mathbb{B}_{\varrho_0})$ *for* $i = 1, 2, 3$.

Due to the square integrability of the particular functions, we can expand them into spherical harmonics, where we stick to the notation from Eq. (14.3).

Corollary 15.13. *Let Assumption 15.12 be satisfied. For all $n \in \mathbb{N}$, $j = 1, \dots, 2n+1$, and $x \in (0, R]$, the identities*

$$\begin{aligned}
J_{n,j}^{(1)}(x) &= \frac{\mathrm{d}}{\mathrm{d}x}\Psi_{n,j}(x) - \frac{n(n+1)}{x}A_{n,j}^{(3)}(x),\\
J_{n,j}^{(2)}(x) &= \sqrt{n(n+1)}\left(\frac{1}{x}\left(\Psi_{n,j}(x) - A_{n,j}^{(3)}(x)\right) - \frac{\mathrm{d}}{\mathrm{d}x}A_{n,j}^{(3)}(x)\right),\\
J_{n,j}^{(3)}(x) &= \sqrt{n(n+1)}\left(\frac{1}{x}\left(A_{n,j}^{(2)}(x) - A_{n,j}^{(1)}(x)\right) + \frac{\mathrm{d}}{\mathrm{d}x}A_{n,j}^{(2)}(x)\right)
\end{aligned}$$

hold true. Furthermore, $J_{0,1}^{(1)} = \Psi_{n,j}'$.

Proof. For all $n \in \mathbb{N}_0$, $j = 1, \dots, 2n+1$, the Morse-Feshbach coefficients of type 1 on the sphere with radius $x \in [0, \varrho_0]$ can be calculated with Eq. (2.6) by

$$\begin{aligned}
J_{n,j}^{(1)}(x) &= \int_{\mathbb{S}} \boldsymbol{J}^{\mathrm{P}}(\boldsymbol{x}) \cdot \boldsymbol{y}_{n,j}^{(1)}(\hat{\boldsymbol{x}})\,\mathrm{d}\omega(\hat{\boldsymbol{x}})\\
&= \int_{\mathbb{S}} \left(\frac{\partial}{\partial x}\Psi(\boldsymbol{x}) + \frac{1}{x}\Delta_{\hat{\boldsymbol{x}}}^{*}A^{(3)}(\boldsymbol{x})\right) Y_{n,j}(\hat{\boldsymbol{x}})\,\mathrm{d}\omega(\hat{\boldsymbol{x}})\\
&= \int_{\mathbb{S}} \frac{\partial}{\partial x}\Psi(\boldsymbol{x}) Y_{n,j}(\hat{\boldsymbol{x}})\,\mathrm{d}\omega(\hat{\boldsymbol{x}}) + \frac{1}{x}\int_{\mathbb{S}} A^{(3)}(\boldsymbol{x})\Delta_{\hat{\boldsymbol{x}}}^{*}Y_{n,j}(\hat{\boldsymbol{x}})\,\mathrm{d}\omega(\hat{\boldsymbol{x}}).
\end{aligned}$$

In the last step, Green's second surface identity for the whole sphere is used, see Theorem 2.20. In order to calculate the first integral, we interchange the integration and the derivative with respect to x. The theorem of differentiation under the integral sign, see [19, Cor. 16.3], provides us with the required tool. The assumptions of this theorem are automatically fulfilled by Assumption 15.12 and Fubini's Theorem for Lebesgue-integrals. Thus,

$$\begin{aligned}
J_{n,j}^{(1)}(x) &= \frac{\partial}{\partial x}\int_{\mathbb{S}} \Psi(\boldsymbol{x}) Y_{n,j}(\hat{\boldsymbol{x}})\,\mathrm{d}\omega(\hat{\boldsymbol{x}}) - \frac{n(n+1)}{x}\int_{\mathbb{S}} A^{(3)}(\boldsymbol{x}) Y_{n,j}(\hat{\boldsymbol{x}})\,\mathrm{d}\omega(\hat{\boldsymbol{x}})\\
&= \frac{\mathrm{d}}{\mathrm{d}x}\Psi_{n,j}(x) - \frac{n(n+1)}{x}A_{n,j}^{(3)}(x).
\end{aligned}$$

For the Morse-Feshbach coefficient of type 2, we obtain for all $n \in \mathbb{N}$, $j = 1, \dots, 2n+1$ by means of Eqs. (2.6) and (2.9) and Corollary 2.21 the identity

$$\begin{aligned}
J_{n,j}^{(2)}(x) &= \int_{\mathbb{S}} \boldsymbol{J}^{\mathrm{P}}(\boldsymbol{x}) \cdot \boldsymbol{y}_{n,j}^{(2)}(\hat{\boldsymbol{x}})\,\mathrm{d}\omega(\hat{\boldsymbol{x}})\\
&= \int_{\mathbb{S}} \boldsymbol{o}_{\hat{\boldsymbol{x}}}^{(2)}\left(\frac{1}{x}\Psi(\boldsymbol{x}) - \left(\frac{\partial}{\partial x} + \frac{1}{x}\right)A^{(3)}(\boldsymbol{x})\right) \cdot \boldsymbol{y}_{n,j}^{(2)}(\hat{\boldsymbol{x}})\,\mathrm{d}\omega(\hat{\boldsymbol{x}})\\
&= -\frac{1}{\sqrt{n(n+1)}}\int_{\mathbb{S}} \left(\frac{1}{x}\Psi(\boldsymbol{x}) - \left(\frac{\partial}{\partial x} + \frac{1}{x}\right)A^{(3)}(\boldsymbol{x})\right)\Delta_{\hat{\boldsymbol{x}}}^{*}Y_{n,j}(\hat{\boldsymbol{x}})\,\mathrm{d}\omega(\hat{\boldsymbol{x}})\\
&= \sqrt{n(n+1)}\left(\frac{1}{x}\Psi_{n,j}(x) - \left(\frac{\mathrm{d}}{\mathrm{d}x} + \frac{1}{x}\right)A_{n,j}^{(3)}(x)\right).
\end{aligned}$$

The interchanging of the derivative and the integration is valid due to the theorem of differentiation under the integral sign and the argumentation above. With analogous calculations and the fact that $\boldsymbol{o}^{(3)}Y_{n,j} = \sqrt{n(n+1)}\boldsymbol{y}_{n,j}^{(3)}$, we obtain the desired result in the remaining case. □

Since the Helmholtz decomposition is unique by means of the Coulomb gauge, we proceed by analyzing the gauge condition.

Corollary 15.14. *Let Assumption 15.12 hold true. Then the Coulomb gauge* $\boldsymbol{\nabla} \cdot \boldsymbol{A} = 0$ *implies*

$$\Delta^*_{\hat{\boldsymbol{x}}} A^{(2)}(\boldsymbol{x}) = -\left(x \frac{\partial}{\partial x} + 2\right) A^{(1)}(\boldsymbol{x}), \qquad \boldsymbol{x} \in \mathbb{B}_{\varrho_0} \setminus \{\mathbf{0}\}\,. \tag{15.25}$$

Consequently, it yields for all $n \in \mathbb{N}$, $j = 1, \ldots, 2n+1$ *the identity*

$$A^{(2)}_{n,j}(x) = \frac{x}{n(n+1)} \frac{\mathrm{d}}{\mathrm{d}x} A^{(1)}_{n,j}(x) + \frac{2}{n(n+1)} A^{(1)}_{n,j}(x).$$

Proof. With Eqs. (2.4), (2.6), and (2.8), we immediately obtain for all $\boldsymbol{x} \in \mathbb{B}_{\varrho_0} \setminus \{\mathbf{0}\}$ the relation

$$\begin{aligned}
\boldsymbol{\nabla}_{\boldsymbol{x}} \cdot \boldsymbol{A}(\boldsymbol{x}) &= \left(\hat{\boldsymbol{x}} \frac{\partial}{\partial x} + \frac{1}{x} \boldsymbol{\nabla}^*_{\hat{\boldsymbol{x}}}\right) \cdot \left(\boldsymbol{o}^{(1)}_{\hat{\boldsymbol{x}}} A^{(1)}(\boldsymbol{x}) + \boldsymbol{o}^{(2)}_{\hat{\boldsymbol{x}}} A^{(2)}(\boldsymbol{x}) + \boldsymbol{o}^{(3)}_{\hat{\boldsymbol{x}}} A^{(3)}(\boldsymbol{x})\right) \\
&= \frac{\partial}{\partial x} A^{(1)}(\boldsymbol{x}) + \frac{1}{x} \left(\boldsymbol{\nabla}^*_{\hat{\boldsymbol{x}}} \cdot \left(\hat{\boldsymbol{x}} A^{(1)}(\boldsymbol{x}) + \boldsymbol{\nabla}^*_{\hat{\boldsymbol{x}}} A^{(2)}(\boldsymbol{x})\right)\right) \\
&= \frac{\partial}{\partial x} A^{(1)}(\boldsymbol{x}) + \frac{1}{x} \left(2A^{(1)}(\boldsymbol{x}) + \Delta^*_{\hat{\boldsymbol{x}}} A^{(2)}(\boldsymbol{x})\right) = 0.
\end{aligned}$$

This is equivalent to the first statement of this corollary. Furthermore, we get with the same argumentation as in the proof of Corollary 15.13 that

$$\begin{aligned}
\int_{\mathbb{S}} \frac{1}{x} A^{(2)}(\boldsymbol{x}) \Delta^*_{\hat{\boldsymbol{x}}} Y_{n,j}(\hat{\boldsymbol{x}}) \,\mathrm{d}\omega(\hat{\boldsymbol{x}}) &= -\frac{\partial}{\partial x} \int_{\mathbb{S}} A^{(1)}(\boldsymbol{x}) Y_{n,j}(\hat{\boldsymbol{x}}) \,\mathrm{d}\omega(\hat{\boldsymbol{x}}) \\
&\quad - \frac{2}{x} \int_{\mathbb{S}} A^{(1)}(\boldsymbol{x}) Y_{n,j}(\hat{\boldsymbol{x}}) \,\mathrm{d}\omega(\hat{\boldsymbol{x}}) \\
\Rightarrow \qquad -\frac{n(n+1)}{x} A^{(2)}_{n,j}(x) &= -\frac{\mathrm{d}}{\mathrm{d}x} A^{(1)}_{n,j}(x) - \frac{2}{x} A^{(1)}_{n,j}(x)
\end{aligned}$$

for all $n \in \mathbb{N}$, $j = 1, \ldots, 2n+1$. Solving the equation for $A^{(2)}_{n,j}$, we obtain the final result. □

Thus, due to the fact that $\boldsymbol{A}$ is assumed to be divergence free, we immediately obtain that $\Delta^* A^{(2)} \in \mathrm{C}^1(\mathbb{B}_{\varrho_0})$ if $A^{(1)} \in \mathrm{C}^2(\mathbb{B}_{\varrho_0})$.

As the previous corollary shows, the Coulomb gauge affects only the parts of type 1 and 2 of the vector potential. Combining this result with the one from Corollary 15.13, we see that the adjustment only affects the MEG reconstructable part of the current $\boldsymbol{J}^{\mathrm{P}}$, see Theorem 9.4. Hence, for the EEG problem this adjustment is dispensable.

15.3.1. Helmholtz Decomposition for MEG

The Helmholtz decomposition is first used in [50] for the MEG problem and a characterization of the Fourier coefficients of the magnetic field is given in [71]. By using the adjustment $\boldsymbol{\nabla} \cdot \boldsymbol{A} = 0$, one can only achieve a relation between the radial component of the vector potential $\boldsymbol{A}$ of the neuronal current and the magnetic field or magnetic potential, respectively, see Theorem 15.15.

First, we present a simplified integral equation for the MEG problem using the Helmholtz decomposition. The advantage of this decomposition is then easy to see. The MEG problem, that is the reconstruction of the neuronal current from given values of the normal component of the magnetic field, reduces to a scalar-valued problem. The normal component of the magnetic field only depends on the radial component of the solenoidal part of the neuronal current. Note that, in this particular case, we observe the radial component $\boldsymbol{y} \cdot \boldsymbol{B}(\boldsymbol{y})$ with respect to the magnetic field at the sensor position $\boldsymbol{y}$, not the normal component $\boldsymbol{\nu} \cdot \boldsymbol{B}$ with respect to the sensor surface of the magnetoencephalograph, which is actually measured. Thus, this approach does not fit as well to the multiple-shell model as the previous decompositions.

Theorem 15.15. *Let the current $\boldsymbol{J}^{\mathrm{P}}$ be decomposed by means of Eq.* (15.22) *under the Coulomb gauge and let Assumption 15.12 be fulfilled. Then the radial component of the magnetic field has the representation*

$$\boldsymbol{y} \cdot \boldsymbol{B}(\boldsymbol{y}) = -\frac{\mu_0}{4\pi} \int_{\mathbb{B}_{\varrho_0}} \left(\Delta_{\boldsymbol{x}} \left(x A^{(1)}(\boldsymbol{x})\right)\right) \frac{1}{|\boldsymbol{x} - \boldsymbol{y}|} \,\mathrm{d}\boldsymbol{x}, \qquad \boldsymbol{y} \in \mathbb{B}^{\mathrm{ext}}_{\varrho_L}.$$

Proof. We introduce an abbreviation for the integral kernel by

$$K_{\mathrm{M}}(\boldsymbol{x}, \boldsymbol{y}) \coloneqq \frac{1}{4\pi} \sum_{k=1}^{\infty} \frac{x^k}{y^{k+1}(k+1)} P_k(\hat{\boldsymbol{x}} \cdot \hat{\boldsymbol{y}}), \qquad (\boldsymbol{x}, \boldsymbol{y}) \in \mathbb{B}_{\varrho_0} \times \mathbb{B}^{\mathrm{ext}}_{\varrho_L}.$$

Using the alternative representations of the integral kernel from Eq. (3.4), for the magnetic potential we get the integral equation

$$U(\boldsymbol{y}) = \int_{\mathbb{B}_{\varrho_0}} \boldsymbol{J}^{\mathrm{P}}(\boldsymbol{x}) \cdot \boldsymbol{L}^*_{\hat{\boldsymbol{x}}} K_{\mathrm{M}}(\boldsymbol{x}, \boldsymbol{y}) \,\mathrm{d}\boldsymbol{x}.$$

We insert the representation from Eq. (15.24) into the integrand. Using the orthogonality relations in Corollary 2.21, Eq. (2.9b) in the first step, and Theorem 2.16 in the second step, we arrive at the representation

$$\begin{aligned} U(\boldsymbol{y}) &= -\int_{\mathbb{B}_{\varrho_0}} \left(\boldsymbol{L}^*_{\hat{\boldsymbol{x}}} \cdot \left(\boldsymbol{o}^{(3)}_{\hat{\boldsymbol{x}}} \left(-\frac{1}{x} A^{(1)}(\boldsymbol{x}) + \left(\frac{\partial}{\partial x} + \frac{1}{x}\right) A^{(2)}(\boldsymbol{x})\right)\right)\right) K_{\mathrm{M}}(\boldsymbol{x}, \boldsymbol{y}) \,\mathrm{d}\boldsymbol{x} \qquad (15.26) \\ &= -\int_{\mathbb{B}_{\varrho_0}} \Delta^*_{\hat{\boldsymbol{x}}} \left(-\frac{1}{x} A^{(1)}(\boldsymbol{x}) + \left(\frac{\partial}{\partial x} + \frac{1}{x}\right) A^{(2)}(\boldsymbol{x})\right) K_{\mathrm{M}}(\boldsymbol{x}, \boldsymbol{y}) \,\mathrm{d}\boldsymbol{x}. \end{aligned}$$

Note that, theoretically, we need a higher order of smoothness of $A^{(2)}$ in this case. This is in fact satisfied with the assumed Coulomb gauge, see Eq. (15.25). In this case, $\Delta^* A^{(2)} \in \mathrm{C}^1(\mathbb{B}_{\varrho_0})$ if $A^{(1)} \in \mathrm{C}^1(\mathbb{B}_{\varrho_0})$. Inserting this into the previous calculations and using Theorem 2.14, we obtain for the magnetic potential the expression

$$\begin{aligned} U(\boldsymbol{y}) &= \int_{\mathbb{B}_{\varrho_0}} \left(\frac{1}{x} \Delta^*_{\hat{\boldsymbol{x}}} + \left(\frac{\partial}{\partial x} + \frac{1}{x}\right)\left(x \frac{\partial}{\partial x} + 2\right)\right) A^{(1)}(\boldsymbol{x}) K_{\mathrm{M}}(\boldsymbol{x}, \boldsymbol{y}) \,\mathrm{d}\boldsymbol{x} \\ &= \int_{\mathbb{B}_{\varrho_0}} \left(\frac{1}{x} \Delta^*_{\hat{\boldsymbol{x}}} + x \frac{\partial^2}{\partial x^2} + 4 \frac{\partial}{\partial x} + \frac{2}{x}\right) A^{(1)}(\boldsymbol{x}) K_{\mathrm{M}}(\boldsymbol{x}, \boldsymbol{y}) \,\mathrm{d}\boldsymbol{x} \\ &= \int_{\mathbb{B}_{\varrho_0}} \left(\Delta_{\boldsymbol{x}} \left(x A^{(1)}(\boldsymbol{x})\right)\right) K_{\mathrm{M}}(\boldsymbol{x}, \boldsymbol{y}) \,\mathrm{d}\boldsymbol{x}. \qquad (15.27) \end{aligned}$$

For the radial component of the magnetic field, we need to interchange a differential operator with the integration. This is valid due to Theorem 7.11 combined with Lemma 14.6. Afterwards, we interchange this differential operator with the series of the integral kernel due to Theorem 14.5. It follows that

$$\begin{aligned}\boldsymbol{y}\cdot\boldsymbol{B}(\boldsymbol{y}) &= \mu_0 y\frac{\partial}{\partial y}U(\boldsymbol{y})\\ &= -\frac{\mu_0}{4\pi}\int_{\mathbb{B}_{\varrho_0}}\left(\Delta_{\boldsymbol{x}}\left(xA^{(1)}(\boldsymbol{x})\right)\right)\sum_{k=1}^{\infty}\frac{x^k}{y^{k+1}}P_k(\hat{\boldsymbol{x}}\cdot\hat{\boldsymbol{y}})\,\mathrm{d}\boldsymbol{x}.\end{aligned}$$

Due to Eq. (2.10), the identity in Eq. (15.26) also holds true if the summation of the kernel K_{M} is started by zero. All further calculations in order to achieve the latter representation for $\boldsymbol{y}\cdot\boldsymbol{B}(\boldsymbol{y})$ are independent of K_{M}. Thus, it holds also true if the summation is started by $k=0$. With the closed representation from Eq. (2.2) of the last series, we obtain the desired result. □

The operator derived in Theorem 15.15 is the one used in [71], where another derivation is presented. An enhancement of this integral equation for the case that the brain is modelled by a bounded domain with sufficiently smooth boundary is also stated in [47] but not solved. In addition, A.S. Fokas proves the following result in [71].

Theorem 15.16 ([71, Prop. 4.1]). *Let the current $\boldsymbol{J}^{\mathrm{P}}$ be given by the Helmholtz decomposition in Eq.* (15.22) *and let Assumption 15.12 be fulfilled. Then the radial component of the magnetic field has the representation*

$$\boldsymbol{y}\cdot\boldsymbol{B}(\boldsymbol{y}) = -\mu_0\sum_{n=1}^{\infty}\sum_{j=1}^{2n+1}\frac{\varrho_0^{n+2}}{2n+1}\left(\varrho_0\frac{\mathrm{d}A_{n,j}^{(1)}}{\mathrm{d}x}(\varrho_0)-(n-1)A_{n,j}^{(1)}(\varrho_0)\right)\frac{Y_{n,j}(\hat{\boldsymbol{y}})}{y^{n+1}},$$

where the series is $\mathrm{L}_2(\overline{\mathbb{B}_{\varrho_L}^{\mathrm{ext}}})$-convergent.

In order to prove that this result coincides with the previous one, we need to calculate the integral occurring in Theorem 9.4. Differentiating the last identity in Corollary 15.14 with respect to x, we get

$$\frac{\mathrm{d}}{\mathrm{d}x}A_{n,j}^{(2)}(x) = \frac{3}{n(n+1)}\frac{\mathrm{d}}{\mathrm{d}x}A_{n,j}^{(1)}(x)+\frac{x}{n(n+1)}\frac{\mathrm{d}^2}{\mathrm{d}x^2}A_{n,j}^{(1)}(x).$$

Inserting these representations into the expression for $J_{n,j}^{(3)}(x)x^{n+2}$ from Corollary 15.13, we obtain the identities

$$\begin{aligned}J_{n,j}^{(3)}(x)x^{n+2} &= \sqrt{n(n+1)}\left(\frac{1}{x}\left(A_{n,j}^{(2)}(x)-A_{n,j}^{(1)}(x)\right)+\frac{\mathrm{d}}{\mathrm{d}x}A_{n,j}^{(2)}(x)\right)x^{n+2}\\ &= \frac{x^{n+2}}{\sqrt{n(n+1)}}\left(\frac{1}{x}(2-n(n+1))A_{n,j}^{(1)}(x)+4\frac{\mathrm{d}}{\mathrm{d}x}A_{n,j}^{(1)}(x)+x\frac{\mathrm{d}^2}{\mathrm{d}x^2}A_{n,j}^{(1)}(x)\right)\\ &= \frac{1}{\sqrt{n(n+1)}}\left(\frac{\mathrm{d}^2}{\mathrm{d}x^2}\left(A_{n,j}^{(1)}(x)x^{n+3}\right)-2(n+1)\frac{\mathrm{d}}{\mathrm{d}x}\left(A_{n,j}^{(1)}(x)x^{n+2}\right)\right)\end{aligned}$$

for all $n \in \mathbb{N}$, $j = 1, \ldots, 2n+1$. Regarding the complete integral, we obtain

$$\begin{aligned}
&\int_0^{\varrho_0} J_{n,j}^{(3)}(x) x^{n+2} \,\mathrm{d}x \\
=&\frac{1}{\sqrt{n(n+1)}} \int_0^{\varrho_0} \frac{\mathrm{d}^2}{\mathrm{d}x^2} \left(A_{n,j}^{(1)}(x) x^{n+3} \right) - 2(n+1) \frac{\mathrm{d}}{\mathrm{d}x} \left(A_{n,j}^{(1)}(x) x^{n+2} \right) \mathrm{d}x \\
=&\frac{1}{\sqrt{n(n+1)}} \left(\frac{\mathrm{d}}{\mathrm{d}x} \left(A_{n,j}^{(1)}(x) x^{n+3} \right) - 2(n+1) \left(A_{n,j}^{(1)}(x) x^{n+2} \right) \right) \Bigg|_{x=0}^{\varrho_0} \\
=&\frac{1}{\sqrt{n(n+1)}} \left(\frac{\mathrm{d}A_{n,j}^{(1)}}{\mathrm{d}x}(x) x^{n+3} - (n-1) A_{n,j}^{(1)}(x) x^{n+2} \right) \Bigg|_{x=0}^{\varrho_0} \\
=&\frac{1}{\sqrt{n(n+1)}} \left(\frac{\mathrm{d}A_{n,j}^{(1)}}{\mathrm{d}x}(\varrho_0) \varrho_0 - (n-1) A_{n,j}^{(1)}(\varrho_0) \right) \varrho_0^{n+2}.
\end{aligned} \tag{15.28}$$

Corollary 15.17. *If Assumption 15.12 is satisfied, then the solution of the inverse MEG problem obtained by the Edmonds approach stated in Theorem 9.4 coincides with the one in [71], which is repeated in Theorem 15.16.*

Proof. From Theorem 9.4, a representation of $B_{\varrho_L}^{\wedge}(n,j)$ given by the vector outer harmonics expansion is known, that is

$$B_{\varrho_L}^{\wedge}(n,j) = \frac{-\mu_0}{\varrho_L^{n+1}} \sqrt{\frac{n}{2n+1}} \int_0^{\varrho_0} J_{n,j}^{(3)}(x) x^{n+2} \,\mathrm{d}x.$$

With the results from Eq. (15.28), we get

$$B_{\varrho_L}^{\wedge}(n,j) = -\mu_0 \varrho_0 \sqrt{\frac{1}{(2n+1)(n+1)}} \left(\frac{\mathrm{d}A_{n,j}^{(1)}}{\mathrm{d}x}(\varrho_0) \varrho_0 - (n-1) A_{n,j}^{(1)}(\varrho_0) \right) \left(\frac{\varrho_0}{\varrho_L} \right)^{n+1}. \tag{15.29}$$

Hence,

$$\begin{aligned}
\boldsymbol{y} \cdot \boldsymbol{B}(\boldsymbol{y}) &= \sum_{n=1}^{\infty} \sum_{j=1}^{2n+1} B_{\varrho_L}^{\wedge}(n,j) \boldsymbol{y} \cdot \boldsymbol{h}_{n,j}^{(1)}(\varrho_L; \boldsymbol{y}) \\
&= \sum_{n=1}^{\infty} \sum_{j=1}^{2n+1} B_{\varrho_L}^{\wedge}(n,j) \boldsymbol{y} \cdot \frac{1}{\varrho_L} \left(\frac{\varrho_L}{y} \right)^{n+2} \tilde{\boldsymbol{y}}_{n,j}^{(1)}(\hat{\boldsymbol{y}}) \\
&= \sum_{n=1}^{\infty} \sum_{j=1}^{2n+1} B_{\varrho_L}^{\wedge}(n,j) \frac{1}{\varrho_L} \left(\frac{\varrho_L}{y} \right)^{n+2} \boldsymbol{y} \cdot \left(\sqrt{\frac{n+1}{2n+1}} \boldsymbol{y}_{n,j}^{(1)}(\hat{\boldsymbol{y}}) - \sqrt{\frac{n}{2n+1}} \boldsymbol{y}_{n,j}^{(2)}(\hat{\boldsymbol{y}}) \right) \\
&= \sum_{n=1}^{\infty} \sum_{j=1}^{2n+1} B_{\varrho_L}^{\wedge}(n,j) \sqrt{\frac{n+1}{2n+1}} \frac{\varrho_L^{n+1}}{y^{n+1}} Y_{n,j}(\hat{\boldsymbol{y}})
\end{aligned}$$

and with Eq. (15.29) we eventually arrive at

$$\boldsymbol{y} \cdot \boldsymbol{B}(\boldsymbol{y}) = -\mu_0 \sum_{n=1}^{\infty} \sum_{j=1}^{2n+1} \frac{1}{2n+1} \left(\frac{\mathrm{d}A_{n,j}^{(1)}}{\mathrm{d}x}(\varrho_0) \varrho_0 - (n-1) A_{n,j}^{(1)}(\varrho_0) \right) \frac{\varrho_0^{n+2}}{y^{n+1}} Y_{n,j}(\hat{\boldsymbol{y}}). \qquad \square$$

For the sake of completeness, we summarize the result for the magnetic potential obtained via Eq. (9.7), that is

$$U_{\varrho_L}^{\wedge}(n,j) = \frac{\varrho_0^2}{(n+1)(2n+1)} \left(\frac{\mathrm{d}A_{n,j}^{(1)}}{\mathrm{d}x}(\varrho_0)\varrho_0 - (n-1)A_{n,j}^{(1)}(\varrho_0) \right) \left(\frac{\varrho_0}{\varrho_L} \right)^n \tag{15.30}$$

for all $n \in \mathbb{N}$, $j = 1, \ldots, 2n+1$.

Now, we are able to generalize this result. We analyze the normal component of the magnetic field with respect to the sensor surface, that is $\boldsymbol{\nu} \cdot \boldsymbol{B}$, with the aid of the results from the Edmonds approach. Starting with Eq. (15.29), we immediately obtain

$$\begin{aligned} \boldsymbol{\nu}(\boldsymbol{y}) \cdot \boldsymbol{B}(\boldsymbol{y}) &= \sum_{n=1}^{\infty} \sum_{j=1}^{2n+1} B_{\varrho_L}^{\wedge}(n,j) \boldsymbol{\nu}(\boldsymbol{y}) \cdot \boldsymbol{h}_{n,j}^{(1)}(\varrho_L; \boldsymbol{y}) \\ &= -\mu_0 \varrho_0 \sum_{n=1}^{\infty} \sum_{j=1}^{2n+1} \sqrt{\frac{1}{(2n+1)(n+1)}} \left(\frac{\mathrm{d}A_{n,j}^{(1)}}{\mathrm{d}x}(\varrho_0)\varrho_0 - (n-1)A_{n,j}^{(1)}(\varrho_0) \right) \left(\frac{\varrho_0}{\varrho_L} \right)^{n+1} \\ &\qquad \times \boldsymbol{\nu}(\boldsymbol{y}) \cdot \boldsymbol{h}_{n,j}^{(1)}(\varrho_L; \boldsymbol{y}). \end{aligned} \tag{15.31}$$

As a generalization, we can choose to neglect the Coulomb gauge. This allows to combine the Helmholtz decomposition with alternative gauges, such as the Lorentz gauge, the Weyl gauge, or the multipolar gauge, in order to solve the inverse MEG problem. Unfortunately, this generalization has one disadvantage. The (vector) spherical harmonics coefficients depend on two components of the solenoidal part, the functions $A^{(1)}$ and $A^{(2)}$. However, this may be fixed by another gauge. For instance, the multipolar gauge, sometimes called the *Poincaré gauge*, that is $\boldsymbol{x} \cdot \boldsymbol{A}(\boldsymbol{x}) = 0$ for all $\boldsymbol{x} \in \mathbb{B}_{\varrho_0}$, implies $A^{(1)} \equiv 0$.

Theorem 15.18. *Let Assumption 15.12 be fulfilled. Then the (vector) outer harmonics coefficients of the magnetic potential and field, respectively, have for all $n \in \mathbb{N}_0$, $j = 1, \ldots, 2n+1$ the representations*

$$\begin{aligned} U_{\varrho_L}^{\wedge}(n,j) &= \frac{n}{\varrho_L^n (2n+1)} \left(- \int_0^{\varrho_0} \left(A_{n,j}^{(1)}(x) + (n+1)A_{n,j}^{(2)}(x) \right) x^{n+1} \, \mathrm{d}x + A_{n,j}^{(2)}(\varrho_0)\varrho_0^{n+2} \right), \\ B_{\varrho_L}^{\wedge}(n,j) &= \frac{\mu_0 n}{\varrho_L^{n+1}} \sqrt{\frac{n+1}{2n+1}} \left(\int_0^{\varrho_0} \left(A_{n,j}^{(1)}(x) + (n+1)A_{n,j}^{(2)}(x) \right) x^{n+1} \, \mathrm{d}x - A_{n,j}^{(2)}(\varrho_0)\varrho_0^{n+2} \right). \end{aligned}$$

Proof. Theorem 9.4 implies $U_{\varrho_L}^{\wedge}(0,1) = B_{\varrho_L}^{\wedge}(0,1) = 0$. For all $n \in \mathbb{N}$ and $j = 1, \ldots, 2n+1$, the insertion of Corollary 15.13 into the integrands in Theorem 9.4 yields

$$\frac{1}{\sqrt{n(n+1)}} \int_0^{\varrho_0} J_{n,j}^{(3),\sim}(x) x^{n+2} \, \mathrm{d}x = \int_0^{\varrho_0} \left(\frac{1}{x} \left(A_{n,j}^{(2)}(x) - A_{n,j}^{(1)}(x) \right) + \frac{\mathrm{d}}{\mathrm{d}x} A_{n,j}^{(2)}(x) \right) x^{n+2} \, \mathrm{d}x.$$

In addition, it holds true that

$$\frac{\mathrm{d}}{\mathrm{d}x} \left(A_{n,j}^{(2)}(x) x^{n+2} \right) = \left(\frac{\mathrm{d}}{\mathrm{d}x} A_{n,j}^{(2)}(x) + \frac{n+2}{x} A_{n,j}^{(2)}(x) \right) x^{n+2}.$$

Thus,

$$\begin{aligned}
&\int_0^{\varrho_0} \left(\frac{1}{x} \left(A_{n,j}^{(2)}(x) - A_{n,j}^{(1)}(x) \right) + \frac{\mathrm{d}}{\mathrm{d}x} A_{n,j}^{(2)}(x) \right) x^{n+2} \,\mathrm{d}x \\
&= -\int_0^{\varrho_0} \left(A_{n,j}^{(1)}(x) + (n+1) A_{n,j}^{(2)}(x) \right) x^{n+1} \,\mathrm{d}x \\
&\quad + \int_0^{\varrho_0} \left(\frac{n+2}{x} A_{n,j}^{(2)}(x) + \frac{\mathrm{d}}{\mathrm{d}x} A_{n,j}^{(2)}(x) \right) x^{n+2} \,\mathrm{d}x \\
&= -\int_0^{\varrho_0} \left(A_{n,j}^{(1)}(x) + (n+1) A_{n,j}^{(2)}(x) \right) x^{n+1} \,\mathrm{d}x + \int_0^{\varrho_0} \frac{\mathrm{d}}{\mathrm{d}x} \left(A_{n,j}^{(2)}(x) x^{n+2} \right) \,\mathrm{d}x \\
&= -\int_0^{\varrho_0} \left(A_{n,j}^{(1)}(x) + (n+1) A_{n,j}^{(2)}(x) \right) x^{n+1} \,\mathrm{d}x + A_{n,j}^{(2)}(\varrho_0) \varrho_0^{n+2}.
\end{aligned}$$

Inserting this into the formula for the coefficients from Theorem 9.4, we obtain the desired result. □

An immediate consequence of this general result is a relation of the Fourier coefficients in the case of the Poincaré gauge.

Corollary 15.19. *Let Assumption 15.12 and the Poincaré gauge, that is $\boldsymbol{x} \cdot \boldsymbol{A}(\boldsymbol{x}) = 0$ for all $\boldsymbol{x} \in \mathbb{B}_{\varrho_0}$, be fulfilled. Then the (vector) outer harmonics coefficients of the magnetic potential and field, respectively, have for all $n \in \mathbb{N}_0$, $j = 1, \ldots, 2n+1$ the representations*

$$\begin{aligned}
U_{\varrho_L}^{\wedge}(n,j) &= \frac{n}{\varrho_L^n (2n+1)} \left(-(n+1) \int_0^{\varrho_0} A_{n,j}^{(2)}(x) x^{n+1} \,\mathrm{d}x + A_{n,j}^{(2)}(\varrho_0) \varrho_0^{n+2} \right), \\
B_{\varrho_L}^{\wedge}(n,j) &= \frac{\mu_0 n}{\varrho_L^{n+1}} \sqrt{\frac{n+1}{2n+1}} \left((n+1) \int_0^{\varrho_0} A_{n,j}^{(2)}(x) x^{n+1} \,\mathrm{d}x - A_{n,j}^{(2)}(\varrho_0) \varrho_0^{n+2} \right).
\end{aligned}$$

We saw before that a unique reconstruction of the neuronal current can be obtained if $\boldsymbol{J}^{\mathrm{P}} \in (\ker \mathcal{T}_{\mathrm{M}})^{\perp}$. Now, we analyze the behaviour of the functions occurring in the Helmholtz decomposition under this assumption.

Theorem 15.20. *Let the neuronal current $\boldsymbol{J}^{\mathrm{P}}$ be decomposed by the Helmholtz decomposition, see Eq.* (15.22)*, and let Assumption 15.12 be fulfilled. In addition, let the neuronal current fulfil $\boldsymbol{J}^{\mathrm{P}} \in (\ker \mathcal{T}_{\mathrm{M}})^{\perp}$. Then the neuronal current is given by*

$$\boldsymbol{J}^{\mathrm{P}}(\boldsymbol{x}) \overset{\mathbf{L}_2(\mathbb{B}_{\varrho_0})}{=} \sum_{n=1}^{\infty} \sum_{j=1}^{2n+1} c_{n,j} \sqrt{\frac{\varrho_0^3}{2n+3}} \boldsymbol{g}_{0,n,j}^{(3)}(\varrho_0; \boldsymbol{x}).$$

Coulomb Gauge: *A one-to-one relation between the coefficients $\{c_{n,j}\}_{n \in \mathbb{N}, j=1,\ldots,2n+1}$ and the magnetic potential coefficients is given for all $n \in \mathbb{N}$, $j = 1, \ldots, 2n+1$ by*

$$U_{\varrho_L}^{\wedge}(n,j) = \frac{\varrho_0^3 \sqrt{n(n+1)} c_{n,j}}{(n+1)(2n+1)(2n+3)} \left(\frac{\varrho_0}{\varrho_L} \right)^n.$$

The radial components of the scalar and vector potential of the Helmholtz decomposition are given for all $n \in \mathbb{N}$, $j = 1, \ldots, 2n+1$ by $\Psi_{n,j}(x) = \psi_{n,j} x^n$, $A_{n,j}^{(3)}(x) = \psi_{n,j} x^n/(n+1)$, and

$$A_{n,j}^{(1)}(x) = a_{n,j} \left(\frac{x}{\varrho_0} \right)^{n-1} + \frac{\sqrt{n(n+1)} c_{n,j} \varrho_0}{2(2n+3)} \left(\frac{x}{\varrho_0} \right)^{n+1}. \tag{15.32}$$

The coefficients $\{\psi_{n,j}\}_{n \in \mathbb{N}, j=1,\ldots,2n+1}$ and $\{a_{n,j}\}_{n \in \mathbb{N}, j=1,\ldots,2n+1}$ remain to be determined. Due to the chosen gauge, $A_{n,j}^{(2)}$ is given via Corollary 15.14.

Poincaré Gauge: *A relation between the coefficients* $\{c_{n,j}\}_{n\in\mathbb{N},j=1,\dots,2n+1}$ *and the magnetic potential coefficients is given by*

$$U_{\varrho_L}^{\wedge}(n,j) = c_{n,j}\frac{\sqrt{n(n+1)}}{(n+1)(2n+1)(2n+3)}\frac{\varrho_0^{n+3}}{\varrho_L^n}.$$

The radial components of the scalar and vector potential of the Helmholtz decomposition are given for all $n \in \mathbb{N}$, $j = 1,\dots,2n+1$ *by* $\Psi_{n,j}(x) = \psi_{n,j}x^n$, $A^{(1)}_{n,j} \equiv 0$, $A^{(3)}_{n,j}(x) = \psi_{n,j}x^n/(n+1)$, *and*

$$A^{(2)}_{n,j}(x) = \frac{c_{n,j}\varrho_0}{\sqrt{n(n+1)}}\frac{1}{n+2}\left(\left(\frac{x}{\varrho_0}\right)^{n+1} - \frac{\varrho_0}{x}\right) + \frac{\varrho_0}{x}a_{n,j}.$$

The coefficients $\{\psi_{n,j}\}_{n\in\mathbb{N},j=1,\dots,2n+1}$ *and* $\{a_{n,j}\}_{n\in\mathbb{N},j=1,\dots,2n+1}$ *remain to be determined.*

Corresponding to the solution of $A^{(1)}$ achieved by the Helmholtz decomposition for the MEG problem, we can always find functions Ψ, $A^{(2)}$, and $A^{(3)}$ such that the resulting neuronal current satisfies the condition $\boldsymbol{J}^{\mathrm{P}} \in (\ker \mathcal{T}_{\mathrm{M}})^{\perp}$.

Proof. Due to Theorem 13.1, the condition $\boldsymbol{J}^{\mathrm{P}} \in (\ker \mathcal{T}_{\mathrm{M}})^{\perp}$ can be split into the three conditions $J^{(1)}_{n,j} = J^{(2)}_{n,j} \equiv 0$ and $J^{(3)}_{n,j}(x) = c_{n,j}(x/\varrho_0)^n$ for all $n \in \mathbb{N}$, $j = 1,\dots,2n+1$, and $x \in [0,\varrho_0]$. From the requirements on $J^{(1)}_{n,j}$ and Corollary 15.13, we immediately get for all $n \in \mathbb{N}$, $j = 1,\dots,2n+1$ the relation

$$A^{(3)}_{n,j}(x) = \frac{x}{n(n+1)}\frac{\mathrm{d}}{\mathrm{d}x}\Psi_{n,j}(x).$$

Inserting this into the condition for the function $J^{(2)}_{n,j}$, we obtain the Euler-Cauchy differential equation

$$\begin{aligned} 0 &= \frac{1}{x}\Psi_{n,j}(x) - \frac{1}{n(n+1)}\frac{\mathrm{d}}{\mathrm{d}x}\Psi_{n,j}(x) - \frac{1}{n(n+1)}\frac{\mathrm{d}}{\mathrm{d}x}\Psi_{n,j}(x) - \frac{x}{n(n+1)}\frac{\mathrm{d}^2}{\mathrm{d}x^2}\Psi_{n,j}(x), \\ \Leftrightarrow\quad 0 &= x^2\frac{\mathrm{d}^2}{\mathrm{d}x^2}\Psi_{n,j}(x) + 2x\frac{\mathrm{d}}{\mathrm{d}x}\Psi_{n,j}(x) - n(n+1)\Psi_{n,j}(x). \end{aligned}$$

The fundamental system of this second-order homogeneous linear ordinary differential equation with variable coefficients is given by $\Psi_{n,j}(x) = \psi_{n,j}x^n + \bar{\psi}_{n,j}x^{-(n+1)}$, see [11, Thm. 5.18]. Via Assumption 15.12, we obtain $\bar{\psi}_{n,j} = 0$ for all $n \in \mathbb{N}$, $j = 1,\dots,2n+1$. Thus, $\Psi_{n,j}(x) = \psi_{n,j}x^n$ and $A^{(3)}_{n,j}(x) = \psi_{n,j}x^n/(n+1)$ for all $n \in \mathbb{N}$, $j = 1,\dots,2n+1$.

From the third condition, which affects the function $J^{(3)}_{n,j}$, we get

$$\sqrt{n(n+1)}\left(\frac{1}{x}\left(A^{(2)}_{n,j}(x) - A^{(1)}_{n,j}(x)\right) + \frac{\mathrm{d}}{\mathrm{d}x}A^{(2)}_{n,j}(x)\right) = c_{n,j}\left(\frac{x}{\varrho_0}\right)^n. \tag{15.33}$$

i) By means of the Coulomb gauge and Corollary 15.14, the left-hand side of this identity reduces to

$$\begin{aligned}
&\frac{c_{n,j}}{\sqrt{n(n+1)}}\left(\frac{x}{\varrho_0}\right)^n \\
&= \frac{1}{x}\left(\frac{x}{n(n+1)}\frac{\mathrm{d}}{\mathrm{d}x}A_{n,j}^{(1)}(x) + \frac{2-n(n+1)}{n(n+1)}A_{n,j}^{(1)}(x)\right) \\
&\quad + \frac{\mathrm{d}}{\mathrm{d}x}\left(\frac{x}{n(n+1)}\frac{\mathrm{d}}{\mathrm{d}x}A_{n,j}^{(1)}(x) + \frac{2}{n(n+1)}A_{n,j}^{(1)}(x)\right) \\
&= \frac{4}{n(n+1)}\frac{\mathrm{d}}{\mathrm{d}x}A_{n,j}^{(1)}(x) + \frac{2-n(n+1)}{n(n+1)x}A_{n,j}^{(1)}(x) + \frac{x}{n(n+1)}\frac{\mathrm{d}^2}{\mathrm{d}x^2}A_{n,j}^{(1)}(x).
\end{aligned}$$

Eventually, Eq. (15.33) is equivalent to

$$x^2\frac{\mathrm{d}^2}{\mathrm{d}x^2}A_{n,j}^{(1)}(x) + 4x\frac{\mathrm{d}}{\mathrm{d}x}A_{n,j}^{(1)}(x) + (2-n(n+1))A_{n,j}^{(1)}(x) = c_{n,j}\sqrt{n(n+1)}\frac{x^{n+1}}{\varrho_0^n},$$

which is a second-order inhomogeneous linear ordinary differential equation with variable coefficients. According to [11, Thm. 5.18], we solve this Euler-Cauchy equation trough change of variables. Thus, the characteristic polynomial corresponding to the homogeneous Euler-Cauchy equation has two distinct real roots, which are $n-1$ and $-(n+2)$. A particular solution of the inhomogeneous differential equation is given by $\sqrt{n(n+1)}c_{n,j}/(2(2n+3)\varrho_0^n)x^{n+1}$. Eventually, we have

$$A_{n,j}^{(1)}(x) = a_{n,j}\left(\frac{x}{\varrho_0}\right)^{n-1} + \bar{a}_{n,j}\left(\frac{x}{\varrho_0}\right)^{-(n+2)} + \frac{\sqrt{n(n+1)}c_{n,j}\varrho_0}{2(2n+3)}\left(\frac{x}{\varrho_0}\right)^{n+1}.$$

For the spherical harmonics expansion of the scalar-valued functions $A^{(i)}$ based on Eq. (14.3), it is necessary that $A^{(i)} \in \mathrm{L}_2(\mathbb{B}_{\varrho_0})$ for $i = 1, 2, 3$. This implies $\bar{a}_{n,j} = 0$ for all $n \in \mathbb{N}$, $j = 1, \ldots, 2n+1$. Thus, we obtain

$$A_{n,j}^{(1)}(x) = a_{n,j}\left(\frac{x}{\varrho_0}\right)^{n-1} + \frac{\sqrt{n(n+1)}c_{n,j}\varrho_0}{2(2n+3)}\left(\frac{x}{\varrho_0}\right)^{n+1}.$$

According to Eq. (15.30), the corresponding magnetic potential coefficients for all $n \in \mathbb{N}$, $j = 1, \ldots, 2n+1$ have the form

$$\begin{aligned}
U_{\varrho_L}^{\wedge}(n,j) &= \frac{\varrho_0^2}{(n+1)(2n+1)}\left(\frac{\mathrm{d}A_{n,j}^{(1)}}{\mathrm{d}x}(\varrho_0)\varrho_0 - (n-1)A_{n,j}^{(1)}(\varrho_0)\right)\left(\frac{\varrho_0}{\varrho_L}\right)^n \\
&= \frac{\varrho_0^2}{(n+1)(2n+1)}\left(\frac{\varrho_0}{\varrho_L}\right)^n \\
&\quad \times \left(a_{n,j}(n-1) + \frac{\sqrt{n(n+1)^3}c_{n,j}\varrho_0}{2(2n+3)} - (n-1)\left(a_{n,j} + \frac{\sqrt{n(n+1)}c_{n,j}\varrho_0}{2(2n+3)}\right)\right) \\
&= \frac{\varrho_0^3\sqrt{n(n+1)}c_{n,j}}{(n+1)(2n+1)(2n+3)}\left(\frac{\varrho_0}{\varrho_L}\right)^n.
\end{aligned}$$

ii) By means of the Poincaré gauge, that is $0 = \boldsymbol{x}\cdot\boldsymbol{A}(\boldsymbol{x}) = A^{(1)}(\boldsymbol{x})$ for all $\boldsymbol{x} \in \mathbb{B}_{\varrho_0}$, the identity in Eq. (15.33) reduces to

$$\sqrt{n(n+1)}\left(\frac{1}{x}A_{n,j}^{(2)}(x) + \frac{\mathrm{d}}{\mathrm{d}x}A_{n,j}^{(2)}(x)\right) = c_{n,j}\left(\frac{x}{\varrho_0}\right)^n.$$

A formula for the solution of a first-order inhomogeneous linear differential equation with some boundary conditions is stated in [29, Sec. 10.3.3]. With the arbitrary boundary condition $A^{(2)}_{n,j}(\varrho_0) = a_{n,j}$ for all $n \in \mathbb{N}$, $j = 1, \dots, 2n+1$, we get in our particular case the solution

$$\begin{aligned} A^{(2)}_{n,j}(x) &= \exp\left(-\int_{\varrho_0}^{x} \frac{1}{t}\,\mathrm{d}t\right)\left(\int_{\varrho_0}^{x} \frac{c_{n,j}}{\sqrt{n(n+1)}}\left(\frac{t}{\varrho_0}\right)^n \exp\left(\int_{\varrho_0}^{t}\frac{1}{s}\,\mathrm{d}s\right)\mathrm{d}t + a_{n,j}\right) \\ &= \frac{\varrho_0}{x}\left(\frac{c_{n,j}}{\sqrt{n(n+1)}}\int_{\varrho_0}^{x}\left(\frac{t}{\varrho_0}\right)^{n+1}\mathrm{d}t + a_{n,j}\right) \\ &= \frac{\varrho_0}{x}\left(\frac{c_{n,j}}{\sqrt{n(n+1)}}\frac{1}{n+2}\left(\frac{x^{n+2}}{\varrho_0^{n+1}} - \varrho_0\right) + a_{n,j}\right) \\ &= \frac{c_{n,j}\varrho_0}{\sqrt{n(n+1)}}\frac{1}{n+2}\left(\left(\frac{x}{\varrho_0}\right)^{n+1} - \frac{\varrho_0}{x}\right) + a_{n,j}\frac{\varrho_0}{x}. \end{aligned}$$

Now, we calculate the auxiliary integral

$$\begin{aligned} \int_0^{\varrho_0} A^{(2)}_{n,j}(x)x^{n+1}\,\mathrm{d}x &= \int_0^{\varrho_0}\left(\frac{c_{n,j}\varrho_0}{\sqrt{n(n+1)}}\frac{1}{n+2}\left(\left(\frac{x}{\varrho_0}\right)^{n+1} - \frac{\varrho_0}{x}\right) + a_{n,j}\frac{\varrho_0}{x}\right)x^{n+1}\,\mathrm{d}x \\ &= \int_0^{\varrho_0}\frac{c_{n,j}\varrho_0}{\sqrt{n(n+1)}}\frac{1}{n+2}\left(\frac{x^{2n+2}}{\varrho_0^{n+1}} - \varrho_0 x^n\right) + a_{n,j}\varrho_0 x^n\,\mathrm{d}x \\ &= \left(\frac{c_{n,j}\varrho_0}{\sqrt{n(n+1)}}\frac{1}{n+2}\left(\frac{1}{2n+3} - \frac{1}{n+1}\right) + \frac{a_{n,j}}{n+1}\right)\varrho_0^{n+2} \\ &= \left(-\frac{c_{n,j}\varrho_0}{\sqrt{n(n+1)^3}}\frac{1}{2n+3} + \frac{a_{n,j}}{n+1}\right)\varrho_0^{n+2}. \end{aligned}$$

Via Corollary 15.19, we get the identity

$$\begin{aligned} U_{\varrho_L}{}^{\wedge}(n,j) &= \frac{n}{\varrho_L^n(2n+1)}\left(-(n+1)\int_0^{\varrho_0} A^{(2)}_{n,j}(x)x^{n+1}\,\mathrm{d}x + A^{(2)}_{n,j}(\varrho_0)\varrho_0^{n+2}\right) \\ &= \frac{n}{\varrho_L^n(2n+1)}\sqrt{\frac{n+1}{n}}\frac{c_{n,j}\varrho_0}{(2n+3)(n+1)}\varrho_0^{n+2}. \end{aligned}$$

The representation of the neuronal current follows immediately with Definition 5.37. □

The essential statement of the foregoing theorem is the following: if the magnetic potential is completely known, then under the assumption that $\boldsymbol{J}^{\mathrm{P}} \in (\ker \mathcal{T}_{\mathrm{M}})^{\perp}$ the neuronal current can be completely reconstructed, see also Theorem 13.6, but the measurable components of the Helmholtz decomposition cannot be determined uniquely without additional assumptions. This can be seen in Eq. (15.32), where the coefficients $\{a_{n,j}\}_{n\in\mathbb{N},j=1,\dots,2n+1}$ cannot be determined by the data. To the opinion of the author, this is a disadvantage of the Helmholtz decomposition. Note that the same statement can be made if the magnetic field is known completely, due to the relation in Eq. (9.7).

Via the Helmholtz decomposition, we are able to decompose the neuronal current into parts belonging to a scalar and a vector potential, where only the vector potential contributes to the magnetic potential or field, respectively. This approach is often used in the literature, see, for instance, [71] and the references therein, since the direct problem reduces to a scalar-valued

problem, see Theorem 15.15. In addition, for the direct problem an integral-free relation between the spherical harmonics coefficients of the magnetic field and the reconstructable part of the neuronal current, see Eq. (15.29) and Theorem 15.16, can be achieved. The integral-free representation reveals the non-uniqueness of the solution, since only values of $A^{(1)}$ and its derivative at the boundary of the cerebrum influence the magnetic field. This problem could be solved by additionally assuming that $A^{(1)}$ is a harmonic function, but this assumption has no physical or medical indication. Eventually, the Helmholtz decomposition only allows a reconstruction of scalar-valued parts of the vector potential. If a reconstruction of the whole vector-valued current is desired, a (numerical) differentiation is required afterwards. However, for the Helmholtz decomposition of vector fields and for the derivation of the scalar MEG forward operator in this case, a higher order of smoothness for the neuronal current, see Assumption 15.12, is required than for the Edmonds approach, where $\boldsymbol{J}^{\mathrm{P}} \in \mathbf{L}_2(\mathbb{B}_{\varrho_0})$ is sufficient.

In addition, we generalize the existing results of [47, 71] in two aspects. First, we can transfer the existing results for the function $\boldsymbol{y} \cdot \boldsymbol{B}(\boldsymbol{y})$ to the magnetic flux density $\boldsymbol{\nu} \cdot \boldsymbol{B}$, which fits better to the multiple-shell model. Second, in [47, 71] the Coulomb gauge is used. Now, we are able to state a more general relation between the (vector) outer harmonics coefficients of the magnetic field or potential, respectively, and parts of the vector potential $\boldsymbol{A}$. This relation is derived by means of a gauge-free ansatz. This enables us to choose a gauge, which is required for a unique Helmholtz decomposition, afterwards. An example of another gauge is given in Corollary 15.19, where the Poincaré gauge is applied. Note that the reconstructable part depends on the chosen gauge.

15.3.2. Helmholtz Decomposition for EEG

The Helmholtz decomposition is often used in the analysis of the EEG problem. In order to compare our calculations with the ones in [47, 50, 71, 73, 74], we need to consider the same assumptions as therein. The authors in the previous references use Gauß's Theorem, see [219], in order to obtain an integral equation for the electric potential. To get rid of the occurring boundary term, they make the following assumption.

Assumption 15.21. *In addition to Assumption 15.12, we assume that*

$$\frac{\partial}{\partial x}\Psi(\boldsymbol{x}) + \frac{1}{x}\Delta^*_{\hat{\boldsymbol{x}}} A^{(3)}(\boldsymbol{x}) = 0 \qquad \text{for all } \boldsymbol{x} \in \mathbb{S}_{\varrho_0}.$$

Lemma 15.22. *If Assumption 15.21 holds true, then the EEG integral equation for the electric potential from Eq.* (10.1) *can be written as*

$$u_L(\boldsymbol{y}) = -\frac{1}{4\pi}\int_{\mathbb{B}_{\varrho_0}} (\Delta_{\boldsymbol{x}}\Psi(\boldsymbol{x})) \sum_{k=1}^{\infty} (2k+1) H_k(y) x^k P_k(\hat{\boldsymbol{x}} \cdot \hat{\boldsymbol{y}}) \,\mathrm{d}\boldsymbol{x}, \qquad \boldsymbol{y} \in \mathbb{S}_{[\varrho_{L-1},\varrho_L]}.$$

Proof. Using Gauß's Theorem for the integral in Eq. (10.1), we get for all $\boldsymbol{y} \in \mathbb{S}_{[\varrho_{L-1},\varrho_L]}$ the

representation

$$\begin{aligned} u_L(\boldsymbol{y}) &= \int_{\mathbb{B}_{\varrho_0}} \boldsymbol{J}^{\mathrm{P}}(\boldsymbol{x}) \cdot \boldsymbol{\nabla}_{\boldsymbol{x}} \sum_{k=1}^{\infty} \frac{2k+1}{4\pi} H_k(y) x^k P_k(\hat{\boldsymbol{x}} \cdot \hat{\boldsymbol{y}}) \, \mathrm{d}\boldsymbol{x} \\ &= -\frac{1}{4\pi} \int_{\mathbb{B}_{\varrho_0}} \left(\boldsymbol{\nabla}_{\boldsymbol{x}} \cdot \boldsymbol{J}^{\mathrm{P}}(\boldsymbol{x}) \right) \sum_{k=1}^{\infty} H_k(y)(2k+1) x^k P_k(\hat{\boldsymbol{x}} \cdot \hat{\boldsymbol{y}}) \, \mathrm{d}\boldsymbol{x} \\ &\quad + \frac{1}{4\pi} \int_{\mathbb{S}_{\varrho_0}} \left(\hat{\boldsymbol{x}} \cdot \boldsymbol{J}^{\mathrm{P}}(\boldsymbol{x}) \right) \sum_{k=1}^{\infty} H_k(y)(2k+1) x^k P_k(\hat{\boldsymbol{x}} \cdot \hat{\boldsymbol{y}}) \, \mathrm{d}\omega(\hat{\boldsymbol{x}}). \end{aligned}$$

The divergence of the current is given by $\boldsymbol{\nabla} \cdot \boldsymbol{J}^{\mathrm{P}} = \Delta\Psi$, see Eq. (15.22). Using Eq. (15.24), the expression $\hat{\boldsymbol{x}} \cdot \boldsymbol{J}^{\mathrm{P}}(\boldsymbol{x})$ reduces for all $\boldsymbol{x} \in \mathbb{B}_{\varrho_0}$ to

$$\hat{\boldsymbol{x}} \cdot \boldsymbol{J}^{\mathrm{P}}(\boldsymbol{x}) = \frac{\partial}{\partial x} \Psi(\boldsymbol{x}) + \frac{1}{x} \Delta^*_{\hat{\boldsymbol{x}}} A^{(3)}(\boldsymbol{x}).$$

The restriction of this identity onto the sphere $\mathbb{S}_{\varrho_0}$ and Assumption 15.21 provide us with the desired result. □

Note that with the abbreviation $s_n \coloneqq (2n+1) H_n(\varrho_L)$ for all $n \in \mathbb{N}$ the integral equation in Lemma 15.22 coincides with the one in [71]. Therein, the following result is stated.

Theorem 15.23. *[71, Prop. 4.1] If Assumption 15.21 holds true, then the electric potential on the sphere $\mathbb{S}_{\varrho_L}$ has the representation*

$$u_L(\varrho_L \hat{\boldsymbol{y}}) = -\sum_{n=1}^{\infty} \sum_{j=1}^{2n+1} \frac{s_n}{2n+1} \varrho_0^{n+1} \left(\varrho_0 \frac{\mathrm{d}\Psi_{n,j}}{\mathrm{d}x}(\varrho_0) - n \Psi_{n,j}(\varrho_0) \right) Y_{n,j}(\hat{\boldsymbol{y}}), \qquad \hat{\boldsymbol{y}} \in \mathbb{S}.$$

Eventually, we obtain for the EEG problem combined with the Helmholtz decomposition the following result.

Theorem 15.24. *Let Assumption 15.21 be fulfilled. Then the result in Theorem 15.23 from [71] coincides with the result obtained by the Edmonds approach restricted to the sphere $\mathbb{S}_{\varrho_L}$. The corresponding spherical harmonics coefficients of the electric potential have the representation*

$$u_L^{\wedge}(n,j) = \frac{2n+1}{n} \beta_n^{(L)} \left(n \Psi_{n,j}(\varrho_0) - \varrho_0 \frac{\mathrm{d}\Psi_{n,j}}{\mathrm{d}x}(\varrho_0) \right) \frac{\varrho_0^{n+1}}{\varrho_L^n} \tag{15.34}$$

for all $n \in \mathbb{N}$, $j = 1, \ldots, 2n+1$ and $u_L^{\wedge}(0,1) = 0$.

Proof. This result can also be proved by using the Edmonds approach. We calculate the

integral from Theorem 10.4 by means of Eq. (15.20) and Corollary 15.13:

$$\begin{aligned}
&\int_0^{\varrho_0} J_{n,j}^{(2),\sim}(x) x^{n+1}\,\mathrm{d}x \\
=&\int_0^{\varrho_0} \left(\sqrt{\frac{n}{2n+1}} J_{n,j}^{(1)}(x) + \sqrt{\frac{n+1}{2n+1}} J_{n,j}^{(2)}(x) \right) x^{n+1}\,\mathrm{d}x \\
=&\sqrt{\frac{1}{n(2n+1)}} \int_0^{\varrho_0} \left[n \left(\frac{\mathrm{d}}{\mathrm{d}x} \Psi_{n,j}(x) - n(n+1) \frac{1}{x} A_{n,j}^{(3)}(x) \right) \right. \\
&\qquad \left. + n(n+1) \left(\frac{1}{x} \Psi_{n,j}(x) - \left(\frac{1}{x} + \frac{\mathrm{d}}{\mathrm{d}x} \right) A_{n,j}^{(3)}(x) \right) \right] x^{n+1}\,\mathrm{d}x \\
=&\sqrt{\frac{1}{n(2n+1)}} \int_0^{\varrho_0} n \frac{\mathrm{d}}{\mathrm{d}x} \left(\Psi_{n,j}(x) x^{n+1} \right) - n(n+1) \frac{\mathrm{d}}{\mathrm{d}x} \left(A_{n,j}^{(3)}(x) x^{n+1} \right) \mathrm{d}x \\
=&\sqrt{\frac{1}{n(2n+1)}} \left(n \Psi_{n,j}(\varrho_0) - n(n+1) A_{n,j}^{(3)}(\varrho_0) \right) \varrho_0^{n+1}.
\end{aligned} \tag{15.35}$$

For the next step, we use Assumption 15.21 and get for all points on the sphere with radius ϱ_0, that is $\boldsymbol{x} \in \mathbb{S}_{\varrho_0}$, the relation

$$\begin{aligned}
0 &= \frac{\partial}{\partial x} \Psi(\boldsymbol{x}) + \frac{1}{x} \Delta_{\hat{\boldsymbol{x}}}^* A^{(3)}(\boldsymbol{x}) \\
&= \sum_{n=0}^{\infty} \sum_{j=1}^{2n+1} \left(\frac{\mathrm{d}\Psi_{n,j}}{\mathrm{d}x}(\varrho_0) + \frac{1}{\varrho_0} A_{n,j}^{(3)}(\varrho_0) \Delta_{\hat{\boldsymbol{x}}}^* \right) Y_{n,j}(\hat{\boldsymbol{x}}).
\end{aligned}$$

Thus, we get for all $n \in \mathbb{N}$, $j = 1, \ldots, 2n+1$ the equation

$$0 = \frac{\mathrm{d}\Psi_{n,j}}{\mathrm{d}x}(\varrho_0) - \frac{n(n+1)}{\varrho_0} A_{n,j}^{(3)}(\varrho_0). \tag{15.36}$$

Inserting this identity into Eq. (15.35), we eventually obtain for the coefficients from Theorem 10.4 the relation

$$u_L^{\wedge}(n,j) = \frac{2n+1}{n} \beta_n^{(L)} \left(n \Psi_{n,j}(\varrho_0) - \varrho_0 \frac{\mathrm{d}\Psi_{n,j}}{\mathrm{d}x}(\varrho_0) \right) \frac{\varrho_0^{n+1}}{\varrho_L^n}.$$

This result coincides with the one in Theorem 15.23 if the potential u_L is restricted onto the sphere $\mathbb{S}_{\varrho_L}$ using the fact that

$$s_n = (2n+1) H_n(\varrho_L) = \frac{(2n+1)^2}{n} \beta_n^{(L)} \frac{1}{\varrho_L^{n+1}} \tag{15.37}$$

for all $n \in \mathbb{N}$, where the formula for H_n can be found in Eq. (4.21). □

We already know that the inverse EEG problem is not uniquely solvable, see Theorem 13.1, and that the minimum norm assumption on the neuronal current $\boldsymbol{J}^{\mathrm{P}}$ is a quite natural condition in order to obtain uniqueness, see Theorem 13.6. Therefore, we analyze whether the minimum norm assumption is consistent with the result obtained by the Helmholtz decomposition.

Theorem 15.25. *Let the neuronal current $\boldsymbol{J}^{\mathrm{P}}$ be given by the Helmholtz decomposition from Eq. (15.22). In addition, let the neuronal current, the scalar potential Ψ, and the vector potential $\boldsymbol{A}$ fulfil the following conditions:*

i) The neuronal current fulfils $\boldsymbol{J}^{\mathrm{P}} \in (\ker \mathcal{T}_{\mathrm{E}})^{\perp}$;

ii) the conditions of Lemma 15.22 are fulfilled, that is the neuronal current is sufficiently smooth such that Gauß's Theorem can be applied and the boundary condition

$$\frac{\partial}{\partial x}\Psi(\boldsymbol{x}) + \frac{1}{x}\Delta^{*}_{\hat{\boldsymbol{x}}} A^{(3)}(\boldsymbol{x}) = 0 \qquad \text{for all } \boldsymbol{x} \in \mathbb{S}_{\varrho_0}$$

is satisfied.

Then $\boldsymbol{J}^{\mathrm{P}} \equiv 0$.

Proof. Recall that we can expand the neuronal current in terms of our orthonormal basis system such that

$$\boldsymbol{J}^{\mathrm{P}}(\boldsymbol{x}) \overset{\mathbf{L}_2(\mathbb{B}_{\varrho_0})}{=} \sum_{i=1}^{3} \sum_{n=0_i}^{\infty} \sum_{j=1}^{2n+1} J_{n,j}^{(i),\sim}(x) \tilde{\boldsymbol{y}}_{n,j}^{(i)}(\hat{\boldsymbol{x}}).$$

Now, we start with the condition $\boldsymbol{J}^{\mathrm{P}} \in (\ker \mathcal{T}_{\mathrm{E}})^{\perp}$ from Item i). Based on Theorem 13.1, this condition can be subdivided as follows:

i.a) $J_{n,j}^{(1),\sim} = 0$,

i.b) $J_{n,j}^{(3),\sim} = 0$, and

i.c) $J_{n,j}^{(2),\sim}(x) = c_{n,j}(x/\varrho_0)^{n-1}$ with some constants $c_{n,j} \in \mathbb{R}$ for all $n \in \mathbb{N}$, $j = 1, \ldots, 2n+1$.

From Corollary 15.13, we obtained a relation for all $n \in \mathbb{N}_{0_i}$, $j = 1, \ldots, 2n+1$ between the function $J_{n,j}^{(i)}$ and the functions $\Psi_{n,j}$ and $A_{n,j}^{(i)}$ for $i = 1, 2, 3$.

Note that $J_{n,j}^{(3),\sim} = J_{n,j}^{(3)}$. Thus, we immediately obtain via Item *i.b)* a constraint for the functions $A_{n,j}^{(1)}$ and $A_{n,j}^{(2)}$. Note that these functions only affect $J_{n,j}^{(i),\sim}$ for $i = 3$. Thus, without impact on the other directions, we can choose $A_{n,j}^{(1)} = A_{n,j}^{(2)} \equiv 0$ in order to fulfil Item *i.b)*. However, other choices for $A_{n,j}^{(1)}$ and $A_{n,j}^{(2)}$ are also valid as long as they satisfy the differential equation

$$\sqrt{n(n+1)}\left(\frac{1}{x}\left(A_{n,j}^{(2)}(x) - A_{n,j}^{(1)}(x)\right) + \frac{\mathrm{d}}{\mathrm{d}x}A_{n,j}^{(2)}(x)\right) = 0.$$

For the condition in Item *i.a)*, we use the relation stated in Eq. (7.16) and obtain the equivalent condition

$$J_{n,j}^{(1)}(x) = \sqrt{\frac{n}{n+1}} J_{n,j}^{(2)}(x)$$

for almost all $x \in [0, \varrho_0]$ and all $n \in \mathbb{N}_0$, $j = 1, \dots, 2n+1$. Inserting Corollary 15.13 into this equation, we get for almost all $x \in (0, \varrho_0]$ the differential equation

$$\begin{aligned} &\frac{\mathrm{d}}{\mathrm{d}x}\Psi_{n,j}(x) - \frac{n(n+1)}{x}A^{(3)}_{n,j}(x) = n\left(\frac{1}{x}\left(\Psi_{n,j}(x) - A^{(3)}_{n,j}(x)\right) - \frac{\mathrm{d}}{\mathrm{d}x}A^{(3)}_{n,j}(x)\right), \\ \Leftrightarrow \qquad &\frac{\mathrm{d}}{\mathrm{d}x}\Psi_{n,j}(x) - \frac{n}{x}\Psi_{n,j}(x) = \frac{n^2}{x}A^{(3)}_{n,j}(x) - n\frac{\mathrm{d}}{\mathrm{d}x}A^{(3)}_{n,j}(x). \end{aligned}$$

This equation can be transformed into two first-order inhomogeneous ordinary differential equations with variable coefficients. Hence, we formulate for all $n \in \mathbb{N}$, $j = 1, \dots, 2n+1$, and some $F_{n,j} \in \mathrm{C}((0, \varrho_0])$ the conditions

$$\frac{\mathrm{d}}{\mathrm{d}x}\Psi_{n,j}(x) = \frac{n}{x}\Psi_{n,j}(x) + F_{n,j}(x), \tag{15.38a}$$

$$\frac{\mathrm{d}}{\mathrm{d}x}A^{(3)}_{n,j}(x) = \frac{n}{x}A^{(3)}_{n,j}(x) - \frac{1}{n}F_{n,j}(x). \tag{15.38b}$$

The solution of these differential equations is uniquely determined under the boundary conditions $\Psi_{n,j}(\varrho_0) = \psi_{n,j} \in \mathbb{R}$ and $A^{(3)}_{n,j}(\varrho_0) = a_{n,j} \in \mathbb{R}$ for all $n \in \mathbb{N}$, $j = 1, \dots, 2n+1$. According to [29, Sec. 10.3.3], it is given by

$$\begin{aligned} \Psi_{n,j}(x) &= \exp\left(\int_{\varrho_0}^{x} \frac{n}{t}\,\mathrm{d}t\right)\left(\int_{\varrho_0}^{x} F_{n,j}(t)\exp\left(-\int_{\varrho_0}^{t}\frac{n}{s}\,\mathrm{d}s\right)\,\mathrm{d}t + \psi_{n,j}\right) \\ &= \left(\frac{x}{\varrho_0}\right)^n\left(\int_{\varrho_0}^{x} F_{n,j}(t)\left(\frac{\varrho_0}{t}\right)^n\,\mathrm{d}t + \psi_{n,j}\right), \end{aligned} \tag{15.39a}$$

$$\begin{aligned} A^{(3)}_{n,j}(x) &= \exp\left(\int_{\varrho_0}^{x} \frac{n}{t}\,\mathrm{d}t\right)\left(-\int_{\varrho_0}^{x}\frac{1}{n}F_{n,j}(t)\exp\left(-\int_{\varrho_0}^{t}\frac{n}{s}\,\mathrm{d}s\right)\,\mathrm{d}t + a_{n,j}\right) \\ &= \left(\frac{x}{\varrho_0}\right)^n\left(-\frac{1}{n}\int_{\varrho_0}^{x} F_{n,j}(t)\left(\frac{\varrho_0}{t}\right)^n\,\mathrm{d}t + a_{n,j}\right). \end{aligned} \tag{15.39b}$$

If $\Psi_{n,j}$ and $A^{(3)}_{n,j}$ are chosen according to Eq. (15.39), then Item *i.a*) is fulfilled. Consequently, using Eq. (15.20) we get for the remaining function $J^{(2),\sim}_{n,j}$ the identity

$$\begin{aligned} \sqrt{\frac{2n+1}{n}}J^{(2),\sim}_{n,j}(x) &= J^{(1)}_{n,j}(x) + \sqrt{\frac{n+1}{n}}J^{(2)}_{n,j}(x) \\ &= \frac{\mathrm{d}}{\mathrm{d}x}\Psi_{n,j}(x) + \frac{n+1}{x}\Psi_{n,j}(x) - \frac{(n+1)^2}{x}A^{(3)}_{n,j}(x) - (n+1)\frac{\mathrm{d}}{\mathrm{d}x}A^{(3)}_{n,j}(x) \\ &= \frac{2n+1}{x}\Psi_{n,j}(x) - \frac{(n+1)(2n+1)}{x}A^{(3)}_{n,j}(x) + \frac{2n+1}{n}F_{n,j}(x) \\ &= \frac{2n+1}{x}\left(\frac{x}{\varrho_0}\right)^n\left(\int_{\varrho_0}^{x} F_{n,j}(t)\left(\frac{\varrho_0}{t}\right)^n\,\mathrm{d}t + \psi_{n,j}\right) + \frac{2n+1}{n}F_{n,j}(x) \\ &\quad - \frac{(n+1)(2n+1)}{x}\left(\frac{x}{\varrho_0}\right)^n\left(-\frac{1}{n}\int_{\varrho_0}^{x} F_{n,j}(t)\left(\frac{\varrho_0}{t}\right)^n\,\mathrm{d}t + a_{n,j}\right) \\ &= \frac{2n+1}{nx}\left((2n+1)\left(\frac{x}{\varrho_0}\right)^n\left(\int_{\varrho_0}^{x} F_{n,j}(t)\left(\frac{\varrho_0}{t}\right)^n\,\mathrm{d}t\right)\right. \\ &\quad \left. + \left(\frac{x}{\varrho_0}\right)^n(n\psi_{n,j} - n(n+1)a_{n,j}) + xF_{n,j}(x)\right). \end{aligned}$$

In the first step, we used the relation between $J_{n,j}^{(2),\sim}$ and $J_{n,j}^{(1)}$ and $J_{n,j}^{(2)}$. In the second step, we used Corollary 15.13 and replaced the occurring derivatives in the third step via the relations in Eq. (15.38). In the last step, we used the solution of the ordinary differential equation from Eq. (15.39). According to Item *i.c*), we have the requirement $J_{n,j}^{(2),\sim}(x) = \tilde{c}_{n,j}(x/\varrho_0)^{n-1}$ with some constants $\tilde{c}_{n,j} \in \mathbb{R}$ for all $n \in \mathbb{N}$, $j = 1, \ldots, 2n+1$. Thus, with $\tilde{c}_{n,j} = \sqrt{n/(2n+1)}c_{n,j}$, we get

$$\begin{aligned} c_{n,j}\left(\frac{x}{\varrho_0}\right)^{n-1} = \frac{2n+1}{nx}\Bigg((2n+1)\left(\frac{x}{\varrho_0}\right)^n\left(\int_{\varrho_0}^x F_{n,j}(t)\left(\frac{\varrho_0}{t}\right)^n \mathrm{d}t\right) \\ + \left(\frac{x}{\varrho_0}\right)^n (n\psi_{n,j} - n(n+1)a_{n,j}) + xF_{n,j}(x)\Bigg). \end{aligned}$$

This is equivalent for all $x \in (0, \varrho_0]$ to

$$(2n+1)\left(\int_{\varrho_0}^x F_{n,j}(t)\left(\frac{\varrho_0}{t}\right)^n \mathrm{d}t\right) + (n\psi_{n,j} - n(n+1)a_{n,j}) + \frac{\varrho_0^n}{x^{n-1}}F_{n,j}(x) = \frac{nc_{n,j}\varrho_0}{2n+1}.$$

This equation can also be transformed into a first-order linear ordinary differential equation with variable coefficients:

$$(n+2)\frac{\varrho_0^n}{x^n}F_{n,j}(x) + \frac{\varrho_0^n}{x^{n-1}}F_{n,j}'(x) = 0, \qquad x \in (0, \varrho_0].$$

The solution of this homogeneous differential equation is given by

$$F_{n,j}(x) = f_{n,j}\left(\frac{\varrho_0}{x}\right)^{n+2}, \tag{15.40}$$

where the coefficients $\{f_{n,j}\}_{n\in\mathbb{N},j1,\ldots,2n+1} \subset \mathbb{R}$ remain to be determined by additional conditions. In order to insert Eq. (15.40) into the representation of $J_{n,j}^{(2),\sim}$, we first calculate the integral

$$\int_{\varrho_0}^x F_{n,j}(t)\left(\frac{\varrho_0}{t}\right)^n \mathrm{d}t = f_{n,j}\int_{\varrho_0}^x \left(\frac{\varrho_0}{t}\right)^{2n+2} \mathrm{d}t = -\frac{f_{n,j}\varrho_0}{2n+1}\left(\left(\frac{\varrho_0}{x}\right)^{2n+1} - 1\right). \tag{15.41}$$

Consequently, we have

$$\begin{aligned} J_{n,j}^{(2),\sim}(x) &= \sqrt{\frac{2n+1}{n}}\Bigg(-f_{n,j}\left(\left(\frac{\varrho_0}{x}\right)^{n+2} - \left(\frac{x}{\varrho_0}\right)^{n-1}\right) \\ &\quad + \frac{1}{x}\left(\frac{x}{\varrho_0}\right)^n (n\psi_{n,j} - n(n+1)a_{n,j}) + f_{n,j}\left(\frac{\varrho_0}{x}\right)^{n+2}\Bigg) \\ &= \sqrt{\frac{2n+1}{n}}\left(\frac{x}{\varrho_0}\right)^{n-1}\left(f_{n,j} + \frac{n\psi_{n,j} - n(n+1)a_{n,j}}{\varrho_0}\right). \end{aligned}$$

Eventually, the condition in Item i) is satisfied and the neuronal current has the representation

$$\boldsymbol{J}^{\mathrm{P}}(\boldsymbol{x}) \overset{\mathbf{L}_2(\mathbb{B}_{\varrho_0})}{=} \sum_{n=1}^{\infty}\sum_{j=1}^{2n+1}\sqrt{\frac{\varrho_0^3}{n}}\left(f_{n,j} + \frac{n\psi_{n,j} - n(n+1)a_{n,j}}{\varrho_0}\right)\tilde{\boldsymbol{g}}_{0,n,j}^{(2)}(\varrho_0;\boldsymbol{x}). \tag{15.42}$$

Now, we need to determine the constants $f_{n,j}$, $\psi_{n,j}$, and $a_{n,j}$ for all $n \in \mathbb{N}$, $j = 1, \dots, 2n+1$. To this end, we analyze Item ii). For the boundary condition, we need a representation of $\Psi_{n,j}$, which according to Eqs. (15.39) to (15.41) is given by

$$\begin{aligned}\Psi_{n,j}(x) &= \left(\frac{x}{\varrho_0}\right)^n \left(\int_{\varrho_0}^{x} F_{n,j}(t) \left(\frac{\varrho_0}{t}\right)^n \mathrm{d}t + \psi_{n,j}\right) \\ &= -\frac{f_{n,j}\varrho_0}{2n+1}\left(\left(\frac{\varrho_0}{x}\right)^{n+1} - \left(\frac{x}{\varrho_0}\right)^n\right) + \psi_{n,j}\left(\frac{x}{\varrho_0}\right)^n. \end{aligned} \tag{15.43}$$

In the proof of Theorem 15.24, more precisely Eq. (15.36), it is shown that the boundary condition reduces for all $n \in \mathbb{N}$, $j = 1, \dots, 2n+1$ to

$$0 = \frac{\mathrm{d}\Psi_{n,j}}{\mathrm{d}x}(\varrho_0) - \frac{n(n+1)}{\varrho_0} A^{(3)}_{n,j}(\varrho_0). \tag{15.44}$$

Thus, the derivative of $\Psi_{n,j}$ is required, which is given by

$$\begin{aligned}\frac{\mathrm{d}}{\mathrm{d}x}\Psi_{n,j}(x) &= \frac{f_{n,j}\varrho_0}{2n+1}\left((n+1)\frac{1}{\varrho_0}\left(\frac{\varrho_0}{x}\right)^{n+2} + \frac{n}{\varrho_0}\left(\frac{x}{\varrho_0}\right)^{n-1}\right) + \frac{n\psi_{n,j}}{\varrho_0}\left(\frac{x}{\varrho_0}\right)^{n-1} \\ &= \frac{f_{n,j}}{2n+1}\left((n+1)\left(\frac{\varrho_0}{x}\right)^{n+2} + n\left(\frac{x}{\varrho_0}\right)^{n-1}\right) + \frac{n\psi_{n,j}}{\varrho_0}\left(\frac{x}{\varrho_0}\right)^{n-1}. \end{aligned}$$

We insert this representation into Eq. (15.44) and use the fact that $A^{(3)}_{n,j}(\varrho_0) = a_{n,j}$ for all $n \in \mathbb{N}$, $j = 1, \dots, 2n+1$ to obtain

$$0 = f_{n,j} + \frac{n\psi_{n,j} - n(n+1)a_{n,j}}{\varrho_0}.$$

Inserting this into Eq. (15.42), we eventually obtain $\boldsymbol{J}^{\mathrm{P}} \equiv 0$. □

The essential result of Theorem 15.25 is that an almost everywhere non-vanishing neuronal current obtained by the Helmholtz decomposition cannot fulfil the minimum norm condition. In other words, every neuronal current $\boldsymbol{J}^{\mathrm{P}}$ obtained via the Helmholtz decomposition under the model assumptions of Theorem 15.24, or [71, Prop. 4.1] repeated in Theorem 15.23, has parts in the null space of $\mathcal{T}_{\mathrm{E}}$. In the opinion of the author, this is a profound disadvantage of this method.

As in the MEG case, the EEG direct problem reduces to a scalar-valued integral equation of the first kind by means of the Helmholtz decomposition, see Lemma 15.22. For the derivation of this integral equation, however, a higher order of smoothness of the neuronal current is required than by the Edmonds approach. Furthermore, an additional boundary condition is required for this derivation. The electric potential is only affected by the scalar potential of the Helmholtz decomposition. Therefore, the result can be obtained independently of the chosen gauge. Similar to the MEG case, there is an integral-free representation of the direct problem available, see Theorem 15.23. Note that, in this section, we generalized the representation of the electric potential derived in [71] from the sphere $\mathbb{S}_{\varrho_L}$ to the scalp shell $\mathbb{S}_{[\varrho_{L-1},\varrho_L]}$.

Part V.

Regularization

Chapter 16.

Preliminaries

In Chapter 13, we analyze the ill-posedness of the electroencephalography and the magnetoencephalography problem in detail. We discusse the non-uniqueness of the solution of both problems as well as their instability. Due to the exponential decay of the corresponding singular values, small variations of the measured data have a major influence on the reconstructed current. In Items (E) and (F) on page 174, we mentione that the data obtained by the magnetoencephalograph and the electroencephalograph is noisy due to several reasons. For ill-posed problems, the best-approximate solution obtained from the noisy data is not suitable for the reconstruction, since the Moore-Penrose generalized inverse is unbounded if it exists, see [63, Ch. 3.1] or Corollary 11.9. In particular, numerical algorithms for the inversion become unstable if the solution does not continuously depend on the data, see Definition 11.1. This can be handled by regularization methods, see the monographs [63, 102, 148, 194], and [192] for a short overview including the references therein.

Before we give a broad overview of regularization methods in Section 16.2, we introduce vector-valued Sobolev spaces over the ball in Section 16.1. The concept of Sobolev spaces is required for an aspect of regularization methods presented in Section 16.2. In Section 16.2, we see that regularization parameters play an important role in the context of regularization methods. Thus, the choice of these parameters is momentous. Therefore, we present several parameter choice methods in Section 16.3.

16.1. Sobolev Spaces on the Ball

In Chapter 5, we introduce several orthonormal bases for a variety of Lebesgue spaces. Formal orthogonal expansions converge only in the according strong sense. However, by means of Sobolev's Embedding Theorem, certain formal orthogonal expansions converge uniformly to a function in the ordinary sense. This can be characterized by means of certain Sobolev and reproducing kernel Hilbert spaces (RKHS). Scalar, vectorial, and tensorial Sobolev spaces on the sphere are analyzed in detail in [81]. Scalar Sobolev spaces are generally introduced in [6]. Scalar Sobolev spaces for functions on the ball are also considered in [3, 158]. This is adapted by the author to the basis functions from Definition 5.35 in [162]. Here, we are mainly interested in vector Sobolev spaces on the ball. Therefore, we construct a Hilbert space $\mathfrak{H}(\mathbb{B}_R)$ as a subspace of $\mathbf{L}_2(\mathbb{B}_R)$, where the topology on $\mathfrak{H}(\mathbb{B}_R)$ affects the decay of the Fourier coefficients. In Definition 5.37, two possible basis systems for the construction of Sobolev spaces are presented. Here, we use the Morse-Feshbach vector spherical harmonics since this system is more common. However, the construction by means of the Edmonds counterpart is straightforward.

16.1.1. Definition and Basic Properties

The idea of vector Sobolev spaces on the ball presented in this thesis is based on vector Sobolev spaces on the sphere, see [80], and scalar ones on the ball, see [3, 6, 158], or more adapted to our particular setting [162]. Based on [81, Ch. 12.4], we split the space of all vector-valued arbitrarily often continuously differentiable functions on the ball, that is $\mathbf{C}^\infty(\mathbb{B}_R) = \oplus_{i=1}^3 \mathbf{C}^{(1),\infty}(\mathbb{B}_R)$, into three (orthogonal) subspaces. In this context, orthogonal is meant with respect to the $\langle\cdot,\cdot\rangle_{\mathbf{L}_2(\mathbb{B}_R)}$-inner product. To this end, based on Eq. (2.3) and Corollary 5.6, we define the spaces

$$\begin{aligned}\mathbf{C}^{(1),\infty}(\mathbb{B}_R) &\coloneqq \{\boldsymbol{f} \in \mathbf{C}^\infty(\mathbb{B}_R) \mid \mathcal{P}_{\tan}\boldsymbol{f} = \mathbf{0}\},\\ \mathbf{C}^{(i),\infty}(\mathbb{B}_R) &\coloneqq \left\{\boldsymbol{f} \in \mathbf{C}^\infty(\mathbb{B}_R) \;\middle|\; O_{\hat{\boldsymbol{x}}}^{(j)}\boldsymbol{f}(\boldsymbol{x}) = 0 \;\text{ if } i \neq j\right\}, \qquad i = 2,\ 3.\end{aligned}$$

The idea behind this decomposition is the spherical Helmholtz decomposition, see Theorem 5.19.

Definition 16.1 (Sobolev Space). *Let $R > 0$ be a given radius, $i \in \{1,2,3\}$ be fixed, and let $a \coloneqq \{a_{m,n}^{(i)}\}_{m\in\mathbb{N}_0, n\in\mathbb{N}_{0_i}}$ be a given real sequence. We define a functional $\mathcal{E}\colon \mathbf{C}^{(i),\infty}(\mathbb{B}_R) \to \mathbb{R}$ by*

$$\mathcal{E}(\boldsymbol{f}) \coloneqq \sum_{\substack{(m,n)\in\mathbb{N}_0\times\mathbb{N}_{0_i}\\ a_{m,n}^{(i)}\neq 0}} \sum_{j=1}^{2n+1} \left(a_{m,n}^{(i)}\right)^2 \left\langle \boldsymbol{f}, \boldsymbol{g}_{m,n,j}^{(i)}(R;\cdot)\right\rangle_{\mathbf{L}_2(\mathbb{B}_R)}^2$$

and, consequently, the space $\boldsymbol{\mathcal{E}}^{(i)}(a,\mathbb{B}_R)$ is given by

$$\boldsymbol{\mathcal{E}}^{(i)}(a,\mathbb{B}_R) \coloneqq \left\{\boldsymbol{f} \in \mathbf{C}^{(i),\infty}(\mathbb{B}_R) \;\middle|\; \left\langle \boldsymbol{f}, \boldsymbol{g}_{m,n,j}^{(i)}(R;\cdot)\right\rangle_{\mathbf{L}_2(\mathbb{B}_R)} = 0,\ \text{if } a_{m,n}^{(i)} = 0,\ \text{and } \mathcal{E}(\boldsymbol{f}) < \infty\right\}.$$

The space is equipped with the inner product defined for all $\boldsymbol{f}$, $\boldsymbol{h} \in \boldsymbol{\mathcal{E}}^{(i)}(a,\mathbb{B}_R)$ by

$$\langle \boldsymbol{f}, \boldsymbol{h}\rangle_{\boldsymbol{\mathcal{H}}^{(i)}} \coloneqq \sum_{\substack{(m,n)\in\mathbb{N}_0\times\mathbb{N}_{0_i}\\ a_{m,n}^{(i)}\neq 0}} \sum_{j=1}^{2n+1} \left(a_{m,n}^{(i)}\right)^2 \left\langle \boldsymbol{f}, \boldsymbol{g}_{m,n,j}^{(i)}(R;\cdot)\right\rangle_{\mathbf{L}_2(\mathbb{B}_R)} \left\langle \boldsymbol{h}, \boldsymbol{g}_{m,n,j}^{(i)}(R;\cdot)\right\rangle_{\mathbf{L}_2(\mathbb{B}_R)}.$$

We call the completion of $\boldsymbol{\mathcal{E}}^{(i)}(a,\mathbb{B}_R)$ with respect to $\|\cdot\|_{\boldsymbol{\mathcal{H}}^{(i)}}$ the Sobolev space $\boldsymbol{\mathcal{H}}^{(i)}(a,\mathbb{B}_R)$, *that is*

$$\boldsymbol{\mathcal{H}}^{(i)}(a,\mathbb{B}_R) \coloneqq \overline{\boldsymbol{\mathcal{E}}^{(i)}(a,\mathbb{B}_R)}^{\|\cdot\|_{\boldsymbol{\mathcal{H}}^{(i)}}}.$$

In addition, we define

$$\boldsymbol{\mathcal{H}}(a,\mathbb{B}_R) \coloneqq \bigoplus_{i=1}^3 \boldsymbol{\mathcal{H}}^{(i)}(a,\mathbb{B}_R).$$

The double series in the definition of the space $\boldsymbol{\mathcal{E}}^{(i)}(a,\mathbb{B}_R)$ has to converge absolutely, which is fulfilled automatically if the series converges. Thus, by means of Cauchy's theorem of double series, the two corresponding iterated series also converge absolutely.

Lemma 16.2 (Cauchy's Theorem of Double Series, [120, Thm. 45.2]). *Let the sequence $\{a_{m,n}\}_{m,n\in\mathbb{N}_0}$ be a double sequence. If one of the iterated series*

$$\sum_{m=0}^{\infty}\left(\sum_{n=0}^{\infty} a_{m,n}\right), \quad \sum_{n=0}^{\infty}\left(\sum_{m=0}^{\infty} a_{m,n}\right)$$

converges absolutely, then the other iterated series and the double series

$$\sum_{(m,n)\in\mathbb{N}_0\times\mathbb{N}_0} a_{m,n}$$

also converge absolutely. In addition, it holds true that

$$\sum_{(m,n)\in\mathbb{N}_0\times\mathbb{N}_0} a_{m,n} = \sum_{m=0}^{\infty}\left(\sum_{n=0}^{\infty} a_{m,n}\right) = \sum_{n=0}^{\infty}\left(\sum_{m=0}^{\infty} a_{m,n}\right).$$

In other words, the double series can be split into an iterated series and the summation order can be interchanged. Note that in the general setting of scalar Sobolev spaces on the sphere the occurring sequence is allowed to depend on the order j. However, in this thesis the singular values of all considered operators are independent of the order j. Thus, the restriction to sequences independent of j is sufficient for our requirements.

With the same ansatz, scalar-valued Sobolev spaces on the ball can be defined, where the basis functions $G_{m,n,j}(R;\cdot)$ from Definition 5.35 are used. More details on these scalar-valued Sobolev spaces are stated by the author in [162].

Remark 16.3. *A second set of vector-valued Sobolev spaces on the ball called $\tilde{\mathfrak{H}}^{(i)}(a,\mathbb{B}_R)$ is based on the Edmonds vector spherical harmonics $\tilde{\boldsymbol{g}}^{(i)}_{m,n,j}$ and can be defined analogously to $\mathfrak{H}^{(i)}(a,\mathbb{B}_R)$:*

$$\tilde{\mathfrak{H}}\left(a,\mathbb{B}_R\right) = \bigoplus_{i=1}^{3} \tilde{\mathfrak{H}}^{(i)}\left(a,\mathbb{B}_R\right).$$

If the sequence a is independent of i, then $\tilde{\mathfrak{H}}\left(a,\mathbb{B}_R\right) = \mathfrak{H}\left(a,\mathbb{B}_R\right)$.

An already known Sobolev space is obtained if each element of the sequence a equals one, that is $a^{(i)}_{m,n} = 1$ for all $i = 1,\ 2,\ 3$, $m \in \mathbb{N}_0$, and $n \in \mathbb{N}_{0_i}$. In this case, we get the identity $\mathfrak{H}\left(\{1\}\ ,\mathbb{B}_R\right) = \mathbf{L}_2(\mathbb{B}_R)$.

The next corollary transfers a relation between two sequences to their induced Sobolev spaces. It can be proved by estimating one norm with the other.

Corollary 16.4. *Let $i = 1,\ 2,\ 3$ be arbitrary. Let $a \coloneqq \{a^{(i)}_{m,n}\}$ and $b \coloneqq \{b^{(i)}_{m,n}\}$ be two real sequences with $a^{(i)}_{m,n} \leq b^{(i)}_{m,n}$ and $a^{(i)}_{m,n} \neq 0 \neq b^{(i)}_{m,n}$ for all $m \in \mathbb{N}_0$ and $n \in \mathbb{N}_{0_i}$. Then*

$$\mathfrak{H}^{(i)}\left(b,\mathbb{B}_R\right) \subset \mathfrak{H}^{(i)}\left(a,\mathbb{B}_R\right).$$

For the construction of reproducing kernel Hilbert spaces later, we need to classify whether a sequence is summable in an appropriate sense or not. Therefore, we lean on the definition of summable sequences from [81]. However, we need to adapt this definition since we consider vector-valued Sobolev spaces on the ball. For all $i = 1,2,3$, $m \in \mathbb{N}_0$, $n \in \mathbb{N}_{0_i}$, and $j = 1,\ldots,2n+1$, the function $\boldsymbol{g}^{(i)}_{m,n,j}(R;\cdot)$ depends on an arbitrary real sequence $\{t^{(i)}_n\}_{n\in\mathbb{N}_{0_i}}$ with $\inf_{n\in\mathbb{N}_{0_i}} t^{(i)}_n > -3/2$, which is reflected in the next definition.

Definition 16.5. *Let $a \coloneqq \{a_{m,n}^{(i)}\}_{m\in\mathbb{N}_0,n\in\mathbb{N}_{0_i}}$ and $b \coloneqq \{b_{m,n}^{(i)}\}_{m\in\mathbb{N}_0,n\in\mathbb{N}_{0_i}}$ be two given real sequences. The sequence a is said to be* b-summable *with respect to $\{t_n^{(i)}\}_{n\in\mathbb{N}_{0_i}}$ if*

$$\sum_{\substack{(m,n)\in\mathbb{N}_0\times\mathbb{N}_{0_i}\\ a_{m,n}^{(i)}\neq 0}} \left(\frac{b_{m,n}^{(i)}}{a_{m,n}^{(i)}}\right)^2 \frac{(2n+1)\left(m+t_n^{(i)}+\frac{1}{2}\right)^{2m+1}}{(m!)^2} < \infty.$$

In the case $b_{m,n}^{(i)} = 1$ for all $m \in \mathbb{N}_0$, $n \in \mathbb{N}_{0_i}$, and $j = 1,\dots,2n+1$, we also say a is summable with respect to $\{t_n^{(i)}\}_{n\in\mathbb{N}_{0_i}}$.

A comparable definition of summability for scalar-valued Sobolev spaces on the ball is stated by the author in [162].

Now, we prove Sobolev's Embedding Theorem for the vector-valued Sobolev spaces on the ball. The proof is based on its scalar-valued counterpart on the sphere, see [81, Lem. 5.2.2].

Theorem 16.6. *Let the sequence a be b-summable with respect to $\{t_n^{(i)}\}_{n\in\mathbb{N}_{0_i}}$ for each $i = 1$, 2, 3. In addition, let $b_{m,n}^{(i)} \neq 0$ for all $(m,n) \in \mathbb{N}_0 \times \mathbb{N}_{0_i}$, $t_n^{(i)} > 0$ for all $n \in \mathbb{N}_{0_i}$, and $t_0^{(1)} \geq 0$. Then each function $\boldsymbol{f} \in \mathcal{H}(a/b, \mathbb{B}_R)$ is also continuous.*

In this context, the quotient a/b is understood as the elementwise division of the sequences a and b, that is $a/b \coloneqq \{a_{m,n}^{(i)}/b_{m,n}^{(i)}\}_{m\in\mathbb{N}_0,n\in\mathbb{N}_{0_i}}$.

Proof. Each function $\boldsymbol{f} \in \mathcal{H}(a/b, \mathbb{B}_R)$ can be represented by a Fourier series converging with respect to the $\|\cdot\|_{\mathcal{H}}$-norm. Recall that this norm is given by

$$\|\boldsymbol{f}\|_{\mathcal{H}}^2 = \sum_{i=1}^{3} \sum_{\substack{(m,n)\in\mathbb{N}_0\times\mathbb{N}_{0_i}\\ a_{m,n}^{(i)}\neq 0}} \sum_{j=1}^{2n+1} \left(\frac{a_{m,n}^{(i)}}{b_{m,n}^{(i)}}\right)^2 \left\langle \boldsymbol{f}, \boldsymbol{g}_{m,n,j}^{(i)} \right\rangle_{\mathbf{L}_2(\mathbb{B}_R)}^2 < \infty.$$

The next estimate proves that the iterated Fourier series also converges uniformly, due to the Cauchy-Schwarz inequality for series, a corollary of the Addition Theorem, see Corollary 5.25, and properties of the radial part of the orthonormal basis functions, see Lemma 5.3. Thus, the following estimate holds true for each $i = 1$, 2, 3 and all $\boldsymbol{x} \in \mathbb{B}_R$:

$$\begin{aligned}
&\left| \sum_{\substack{m=M\\ a_{m,n}^{(i)}\neq 0}}^{\infty} \sum_{n=0_i}^{\infty} \sum_{j=1}^{2n+1} \left\langle \boldsymbol{f}, \boldsymbol{g}_{m,n,j}^{(i)} \right\rangle_{\mathbf{L}_2(\mathbb{B}_R)} \boldsymbol{g}_{m,n,j}^{(i)}(R;\boldsymbol{x}) \right|^2 \\
&\leq \left(\sum_{\substack{m=M\\ a_{m,n}^{(i)}\neq 0}}^{\infty} \sum_{n=0_i}^{\infty} \sum_{j=1}^{2n+1} \left(\frac{a_{m,n}^{(i)}}{b_{m,n}^{(i)}}\right)^2 \left\langle \boldsymbol{f}, \boldsymbol{g}_{m,n,j}^{(i)} \right\rangle_{\mathbf{L}_2(\mathbb{B}_R)}^2 \right) \\
&\quad \times \left(\sum_{\substack{m=M\\ a_{m,n}^{(i)}\neq 0}}^{\infty} \sum_{n=0_i}^{\infty} \sum_{j=1}^{2n+1} \left(\frac{b_{m,n}^{(i)}}{a_{m,n}^{(i)}}\right)^2 \left| \boldsymbol{g}_{m,n,j}^{(i)}(R;\boldsymbol{x}) \right|^2 \right)
\end{aligned}$$

$$\leq \|\boldsymbol{f}\|_{\mathfrak{H}}^2 \left(\sum_{\substack{m=M \\ a_{m,n}^{(i)} \neq 0}}^{\infty} \sum_{n=0_i}^{\infty} \frac{2n+1}{4\pi} \left(\frac{b_{m,n}^{(i)}}{a_{m,n}^{(i)}} \right)^2 \left(Q_m^{(t_n^{(i)}+1/2)}(R;x) \right)^2 \right)$$

$$\leq \|\boldsymbol{f}\|_{\mathfrak{H}}^2 \left(\frac{6}{R^3} \sum_{\substack{m=M \\ a_{m,n}^{(i)} \neq 0}}^{\infty} \sum_{n=0_i}^{\infty} \frac{2n+1}{4\pi} \left(\frac{b_{m,n}^{(i)}}{a_{m,n}^{(i)}} \right)^2 \frac{\left(m + t_n^{(i)} + 1/2\right)^{2m+1}}{(m!)^2} \right).$$

The right-hand side converges to zero as $M \to \infty$ due to the summability condition. Hence, this iterated series converges uniformly and each summand is continuous in $\mathbb{B}_R$ as a composition of continuous functions. This implies the continuity of the limit function. This estimate also implies the absolute convergence of the iterated series. Due to Cauchy's theorem of double series, the absolute convergence of the iterated series suffices for the absolute convergence of the double series, see Lemma 16.2, and their limits coincide. This implies the continuity of $\boldsymbol{f}$. □

16.1.2. Reproducing Kernel Hilbert Spaces on the Ball

A particular case of these Sobolev spaces are the RKHSs, which are widely discussed in the literature, see, for instance, [9, 57]. For an introduction to scalar reproducing kernels and scalar reproducing kernel Hilbert spaces on the ball, see [6, 7].

Besides the pointwise evaluability of functions in such reproducing kernel Hilbert spaces, the RKHSs have another valuable property. They provide us with the existence of reproducing kernels. The classical definition of a reproducing kernel is as follows, see [9]. Let $\mathcal{X}(\mathbb{G})$ be a scalar-valued Hilbert space over a region $\mathbb{G} \subset \mathbb{R}^d$, then a kernel $K \colon \mathbb{G} \times \mathbb{G} \to \mathbb{R}$ is a reproducing kernel if $K(\boldsymbol{x}, \cdot) \in \mathcal{X}(\mathbb{G})$ for all $\boldsymbol{x} \in \mathbb{G}$ and $\langle K(\boldsymbol{x}, \cdot), F \rangle_{\mathcal{X}} = F(\boldsymbol{x})$ for all $\boldsymbol{x} \in \mathbb{G}$ and $F \in \mathcal{X}$. In this case, the Hilbert space $\mathcal{X}(\mathbb{G})$ is called an RKHS. If $\{G_k\}_{k \in \mathbb{N}_0}$ is a complete orthonormal system in $\mathcal{X}$ fulfilling a summability condition, then the reproducing kernel is given for all $\boldsymbol{x}$, $\boldsymbol{y} \in \mathbb{G}$ by Mercer's expansion, that is $K(\boldsymbol{x}, \boldsymbol{y}) = \sum_{k=0}^{\infty} K^{\wedge}(k) G_k(\boldsymbol{x}) G_k(\boldsymbol{y})$, see [158, Thm. 6.2].

In vector-valued Hilbert spaces, this definition leads to a problem. If a kernel $\boldsymbol{k}(\boldsymbol{x}, \cdot)$ is a function of this Hilbert space, then the inner product of $\boldsymbol{k}(\boldsymbol{x}, \cdot)$ with another function of the Hilbert space yields a scalar-valued quantity. Therefore, the definition of reproducing kernels needs to be adapted for vector-valued Hilbert spaces. Scalar-valued RKHSs on the sphere are, for instance, presented in [81] and generalized to vector-valued RKHSs. Therein, the reproducing kernel $\boldsymbol{k}$ is constructed by the tensor product of Morse-Feshbach vector spherical harmonics. Then by means of the adjoint operators in Corollary 5.6, a reproducing property is formulated.

However, we want to use the reproducing kernels in the numerical implementation. More precisely, the reproducing kernels are used as trial functions for a reconstruction. For this purpose, we want to avoid tensor-valued kernels and work with vector-valued ones. The construction of vector-valued RKHSs presented here is based on the vector kernels in [20, 21, 25].

Definition 16.7 (Reproducing Kernel). *Let $i = 1, 2, 3$ be fixed. A function $\boldsymbol{k}_{\mathcal{H}^{(i)}} : \mathbb{B}_R \times \mathbb{B}_R \to \mathbb{R}^3$ is called a* reproducing kernel *of $\mathcal{H}^{(i)}(a, \mathbb{B}_R)$ if*

i) the kernel is an element of the Hilbert space for every fixed $\boldsymbol{y} \in \mathbb{B}_R$, that is $\boldsymbol{k}_{\mathcal{H}^{(i)}}(\cdot, \boldsymbol{y}) \in \mathcal{H}^{(i)}(a, \mathbb{B}_R)$, and

ii) the reproducing property

$$O^{(i)}_{\hat{\boldsymbol{y}}} \boldsymbol{f}(\boldsymbol{y}) = \left\langle \boldsymbol{k}_{\mathcal{H}^{(i)}}(\cdot, \boldsymbol{y}), \boldsymbol{f} \right\rangle_{\mathcal{H}^{(i)}}$$

holds for all $\boldsymbol{y} \in \mathbb{B}_R$ and every $\boldsymbol{f} \in \mathcal{H}^{(i)}(a, \mathbb{B}_R)$.

If such a kernel exists, the space $\mathcal{H}^{(i)}(a, \mathbb{B}_R)$ is called a reproducing kernel Hilbert space.

Note that, in the context of the reproducing property for scalar-valued reproducing kernels, the reproducing kernel is often placed in the second argument of the inner product. However, due to the symmetry of the real-valued inner product, the arguments of the inner product can be switched. In contrast to scalar-valued reproducing kernels, where the kernel is symmetric, that is $K(\boldsymbol{x}, \boldsymbol{y}) = K(\boldsymbol{y}, \boldsymbol{x})$ for all $\boldsymbol{x}$, $\boldsymbol{y} \in \mathbb{G}$, the order of the arguments of the vector-valued reproducing kernels has a major effect. Thus, we need to distinguish between the first and second argument of the reproducing kernel. An analogon of the symmetry property is found in the next corollary.

Corollary 16.8 (Symmetry). *Let $i = 1, 2, 3$ be fixed and let $\boldsymbol{k}_{\mathcal{H}^{(i)}}$ be a reproducing kernel according to Definition 16.7. Then $\boldsymbol{k}_{\mathcal{H}^{(i)}}$ is symmetric in the sense that $O^{(i)}_{\hat{\boldsymbol{x}}} \boldsymbol{k}_{\mathcal{H}^{(i)}}(\boldsymbol{x}, \boldsymbol{y}) = O^{(i)}_{\hat{\boldsymbol{y}}} \boldsymbol{k}_{\mathcal{H}^{(i)}}(\boldsymbol{y}, \boldsymbol{x})$ for all $\boldsymbol{x}$, $\boldsymbol{y} \in \mathbb{B}_R$.*

Proof. Due to the first condition for reproducing kernels, we have $\boldsymbol{k}_{\mathcal{H}^{(i)}}(\cdot, \boldsymbol{x}) \in \mathcal{H}^{(i)}(a, \mathbb{B}_R)$ for all $\boldsymbol{x} \in \mathbb{B}_R$. Thus, due to the symmetry of the inner product and the reproducing property, we get for all $\boldsymbol{x}$, $\boldsymbol{y} \in \mathbb{B}_R$ the identity

$$\begin{aligned} O^{(i)}_{\hat{\boldsymbol{y}}} \boldsymbol{k}_{\mathcal{H}^{(i)}}(\boldsymbol{y}, \boldsymbol{x}) &= \left\langle \boldsymbol{k}_{\mathcal{H}^{(i)}}(\cdot, \boldsymbol{y}), \boldsymbol{k}_{\mathcal{H}^{(i)}}(\cdot, \boldsymbol{x}) \right\rangle_{\mathcal{H}^{(i)}} \\ &= \left\langle \boldsymbol{k}_{\mathcal{H}^{(i)}}(\cdot, \boldsymbol{x}), \boldsymbol{k}_{\mathcal{H}^{(i)}}(\cdot, \boldsymbol{y}) \right\rangle_{\mathcal{H}^{(i)}} \\ &= O^{(i)}_{\hat{\boldsymbol{x}}} \boldsymbol{k}_{\mathcal{H}^{(i)}}(\boldsymbol{x}, \boldsymbol{y}). \end{aligned}$$

□

Lemma 16.9. *If $\mathcal{H}^{(i)}(a, \mathbb{B}_R)$ is an RKHS, then the reproducing kernel is unique.*

Proof. For the classical scalar reproducing kernel, this statement is proved in [9, Ch. I.2]. However, it is an immediate consequence of the reproducing property and can directly be applied in this context. Let $\boldsymbol{k}_{\mathcal{H}^{(i)}}$ and $\boldsymbol{h}_{\mathcal{H}^{(i)}}$ be two different reproducing kernels of the same Hilbert space $\mathcal{H}^{(i)}(a, \mathbb{B}_R)$. With $\boldsymbol{y} \in \mathbb{B}_R$, we arrive at a contradiction by

$$\begin{aligned} 0 &< \left\| \boldsymbol{k}_{\mathcal{H}^{(i)}}(\cdot, \boldsymbol{y}) - \boldsymbol{h}_{\mathcal{H}^{(i)}}(\cdot, \boldsymbol{y}) \right\|^2_{\mathcal{H}^{(i)}} \\ &= \left\langle \boldsymbol{k}_{\mathcal{H}^{(i)}}(\cdot, \boldsymbol{y}) - \boldsymbol{h}_{\mathcal{H}^{(i)}}(\cdot, \boldsymbol{y}), \boldsymbol{k}_{\mathcal{H}^{(i)}}(\cdot, \boldsymbol{y}) - \boldsymbol{h}_{\mathcal{H}^{(i)}}(\cdot, \boldsymbol{y}) \right\rangle_{\mathcal{H}^{(i)}} \\ &= \left\langle \boldsymbol{k}_{\mathcal{H}^{(i)}}(\cdot, \boldsymbol{y}), \boldsymbol{k}_{\mathcal{H}^{(i)}}(\cdot, \boldsymbol{y}) - \boldsymbol{h}_{\mathcal{H}^{(i)}}(\cdot, \boldsymbol{y}) \right\rangle_{\mathcal{H}^{(i)}} - \left\langle \boldsymbol{h}_{\mathcal{H}^{(i)}}(\cdot, \boldsymbol{y}), \boldsymbol{k}_{\mathcal{H}^{(i)}}(\cdot, \boldsymbol{y}) - \boldsymbol{h}_{\mathcal{H}^{(i)}}(\cdot, \boldsymbol{y}) \right\rangle_{\mathcal{H}^{(i)}} \\ &= O^{(i)}_{\hat{\boldsymbol{y}}} \left(\boldsymbol{k}_{\mathcal{H}^{(i)}}(\boldsymbol{y}, \boldsymbol{y}) - \boldsymbol{h}_{\mathcal{H}^{(i)}}(\boldsymbol{y}, \boldsymbol{y}) \right) - O^{(i)}_{\hat{\boldsymbol{y}}} \left(\boldsymbol{k}_{\mathcal{H}^{(i)}}(\boldsymbol{y}, \boldsymbol{y}) - \boldsymbol{h}_{\mathcal{H}^{(i)}}(\boldsymbol{y}, \boldsymbol{y}) \right) = 0. \end{aligned}$$

□

For classical scalar-valued reproducing kernel Hilbert spaces, Aronszajn's Theorem is well-known. In this context, a scalar-valued Hilbert space is an RKHS if and only if the evaluation functional is continuous, see [9]. Now, we adapt this result to the vector-valued case.

Theorem 16.10 (Vector-valued Aronszajn's Theorem). *For fixed $i = 1, 2, 3$, let the space $\mathfrak{H}^{(i)}(a, \mathbb{B}_R)$ be a Sobolev space from Definition 16.1. Then $\mathfrak{H}^{(i)}(a, \mathbb{B}_R)$ is an RKHS if and only if the evaluation at all positions $\boldsymbol{x} \in \mathbb{B}_R$ of the $O^{(i)}$-operator applied to an element of the Sobolev space, that is*

$$\mathcal{L}_{\boldsymbol{x}} \colon \mathfrak{H}^{(i)}(a, \mathbb{B}_R) \to \mathbb{R}, \qquad \mathcal{L}_{\boldsymbol{x}} \boldsymbol{f} \coloneqq \left(O^{(i)}_{\hat{\boldsymbol{y}}} \boldsymbol{f}(\boldsymbol{y}) \right)_{\boldsymbol{y}=\boldsymbol{x}},$$

is continuous.

Proof. The proof is similar to the proof in the scalar-valued case, see [9, Item I.2.(2)]. We start with the first direction of the proof, that is we assume that $\mathfrak{H}^{(i)}(a, \mathbb{B}_R)$ is an RKHS and prove that $\mathcal{L}_{\boldsymbol{x}}$ is continuous. Due to the construction of the $O^{(i)}$ operator, $\mathcal{L}_{\boldsymbol{x}}$ is linear. Thus, via

$$\begin{aligned} \sup_{\substack{\boldsymbol{f} \in \mathfrak{H}^{(i)} \\ \boldsymbol{f} \neq \boldsymbol{0}}} \frac{|\mathcal{L}_{\boldsymbol{x}} \boldsymbol{f}|}{\|\boldsymbol{f}\|_{\mathfrak{H}^{(i)}}} &= \sup_{\substack{\boldsymbol{f} \in \mathfrak{H}^{(i)} \\ \boldsymbol{f} \neq \boldsymbol{0}}} \frac{|\langle \boldsymbol{k}_{\mathfrak{H}^{(i)}}(\cdot, \boldsymbol{x}), \boldsymbol{f} \rangle_{\mathfrak{H}^{(i)}}|}{\|\boldsymbol{f}\|_{\mathfrak{H}^{(i)}}} \\ &\leq \|\boldsymbol{k}_{\mathfrak{H}^{(i)}}(\cdot, \boldsymbol{x})\|_{\mathfrak{H}^{(i)}} = \left(O^{(i)}_{\hat{\boldsymbol{y}}} \boldsymbol{k}_{\mathfrak{H}^{(i)}}(\boldsymbol{y}, \boldsymbol{x}) \right)_{\boldsymbol{y}=\boldsymbol{x}} < \infty \end{aligned}$$

we obtain the boundedness of $\mathcal{L}_{\boldsymbol{x}}$ and, hence, its continuity.

Vice versa, let $\mathcal{L}_{\boldsymbol{x}}$ be continuous. Then $\mathcal{L}_{\boldsymbol{x}} \colon \mathfrak{H}^{(i)}(a, \mathbb{B}_R) \to \mathbb{R}$ is an element of the dual space of $\mathfrak{H}^{(i)}(a, \mathbb{B}_R)$ since it is a linear and continuous functional. Due to Riesz' representation theorem, see [225, Ch. III.6], there exists, for each $\boldsymbol{x} \in \mathbb{B}_R$, an element $\boldsymbol{g}_{\boldsymbol{x}} \in \mathfrak{H}^{(i)}(a, \mathbb{B}_R)$ such that

$$\left(O^{(i)}_{\hat{\boldsymbol{y}}} \boldsymbol{f}(\boldsymbol{y}) \right)_{\boldsymbol{y}=\boldsymbol{x}} = \mathcal{L}_{\boldsymbol{x}} \boldsymbol{f} = \langle \boldsymbol{f}, \boldsymbol{g}_{\boldsymbol{x}} \rangle_{\mathfrak{H}^{(i)}}.$$

We define $\boldsymbol{k}_{\mathfrak{H}^{(i)}}(\cdot, \boldsymbol{x}) \coloneqq \boldsymbol{g}_{\boldsymbol{x}}$ and the latter property of $\boldsymbol{g}_{\boldsymbol{x}}$ yields the two conditions required for $\boldsymbol{k}_{\mathfrak{H}^{(i)}}$ being a reproducing kernel, see Definition 16.7. □

Lemma 16.11. *For fixed $i = 1, 2, 3$, let the sequence a be $\{(\mu_n^{(i)})^{1/2}\}$-summable with respect to $\{t_n^{(i)}\}_{n \in \mathbb{N}_{0_i}}$, where $\inf_{n \in \mathbb{N}_{0_i}} t_n^{(i)} \geq 0$, and let $a_{m,n}^{(i)} \geq 1$ for all $m \in \mathbb{N}_0$, $n \in \mathbb{N}_{0_i}$. Then the space $\mathfrak{H}^{(i)}(a, \mathbb{B}_R)$ is an RKHS and the (unique) reproducing kernel is given for all $\boldsymbol{x}$, $\boldsymbol{y} \in \mathbb{B}_R$ by*

$$\boldsymbol{k}_{\mathfrak{H}^{(i)}}(\boldsymbol{x}, \boldsymbol{y}) = \sum_{\substack{(m,n) \in \mathbb{N}_0 \times \mathbb{N}_{0_i} \\ a_{m,n}^{(i)} \neq 0}} \sum_{j=1}^{2n+1} \left(a_{m,n}^{(i)} \right)^{-2} \sqrt{\mu_n^{(i)}} \boldsymbol{g}_{m,n,j}^{(i)}(R; \boldsymbol{x}) G_{m,n,j}(R; \boldsymbol{y}), \tag{16.1}$$

where both types of basis functions are defined with respect to the same sequence of exponents $\{t_n^{(i)}\}_{n \in \mathbb{N}_{0_i}}$, see Definitions 5.35 and 5.37.

In [150, 152] so-called vector-product kernels are defined by the series over a symbol of the vector product kernel and the multiplication with a scalar- and a vector-valued orthonormal basis system. However, these vector-product kernels are used for the construction of vector scaling functions and vector wavelets.

Proof. We only need to verify that the kernel stated in Eq. (16.1) fulfils the properties of Definition 16.7.

i) First, we calculate the $\mathbf{L}_2(\mathbb{B}_R)$-inner product of the kernel and an orthonormal basis function via Eq. (16.1) for all $\boldsymbol{y} \in \mathbb{B}_R$, that is

$$\left\langle \boldsymbol{k}_{\mathcal{H}^{(i)}}(\cdot,\boldsymbol{y}), \boldsymbol{g}^{(i)}_{m,n,j}(R;\cdot)\right\rangle_{\mathbf{L}_2(\mathbb{B}_R)} = \left(a^{(i)}_{m,n}\right)^{-2}\sqrt{\mu^{(i)}_n}G_{m,n,j}(R;\boldsymbol{y}).$$

Thus, with Definition 16.1, Theorem 2.25, and Lemma 5.3, we get for all $\boldsymbol{y} \in \mathbb{B}_R$ the estimate

$$\begin{aligned}
\left\|\boldsymbol{k}_{\mathcal{H}^{(i)}}(\cdot,\boldsymbol{y})\right\|^2_{\mathcal{H}^{(i)}} &= \sum_{\substack{(m,n)\in\mathbb{N}_0\times\mathbb{N}_{0_i}\\ a^{(i)}_{m,n}\neq 0}} \sum_{j=1}^{2n+1} \left(a^{(i)}_{m,n}\right)^2 \left\langle \boldsymbol{k}_{\mathcal{H}^{(i)}}(\cdot,\boldsymbol{y}), \boldsymbol{g}^{(i)}_{m,n,j}(R;\cdot)\right\rangle^2_{\mathbf{L}_2(\mathbb{B}_R)} \\
&= \sum_{\substack{(m,n)\in\mathbb{N}_0\times\mathbb{N}_{0_i}\\ a^{(i)}_{m,n}\neq 0}} \sum_{j=1}^{2n+1} \left(a^{(i)}_{m,n}\right)^{-2} \mu^{(i)}_n \left(G_{m,n,j}(R;\boldsymbol{y})\right)^2 \\
&= \sum_{\substack{(m,n)\in\mathbb{N}_0\times\mathbb{N}_{0_i}\\ a^{(i)}_{m,n}\neq 0}} \left(a^{(i)}_{m,n}\right)^{-2} \mu^{(i)}_n \frac{2n+1}{4\pi}\left(Q^{(t^{(i)}_n+1/2)}_m(R;y)\right)^2 \\
&\leq \frac{3}{2\pi R^3} \sum_{\substack{(m,n)\in\mathbb{N}_0\times\mathbb{N}_{0_i}\\ a^{(i)}_{m,n}\neq 0}} \mu^{(i)}_n (2n+1)\frac{(m+t^{(i)}_n+1/2)^{2m+1}}{\left(a^{(i)}_{m,n}\right)^2 (m!)^2} < \infty
\end{aligned}$$

since $\{a^{(i)}_{m,n}\}$ is $\{(\mu^{(i)}_n)^{1/2}\}$-summable with respect to $\{t^{(i)}_n\}_{n\in\mathbb{N}_{0_i}}$.

ii) The reproducing property remains to be proved. Each element $a^{(i)}_{m,n}$ is greater than one. Thus, every function $\boldsymbol{f} \in \mathcal{H}^{(i)}(a,\mathbb{B}_R) \subset \mathbf{L}_2(\mathbb{B}_R)$ can be represented by

$$\boldsymbol{f} = \sum_{\substack{(m,n)\in\mathbb{N}_0\times\mathbb{N}_{0_i}\\ a^{(i)}_{m,n}\neq 0}} \sum_{j=1}^{2n+1} f^{\wedge}(i,m,n,j)\boldsymbol{g}^{(i)}_{m,n,j}(R;\cdot), \tag{16.2}$$

where the Fourier coefficient is meant with respect to the $\mathbf{L}_2(\mathbb{B}_R)$-inner product. The series converges uniformly due to $a^{(i)}_{m,n} \geq a^{(i)}_{m,n}(\mu^{(i)}_n)^{-1/2}$, the embedding of the Sobolev spaces $\mathcal{H}^{(i)}(a,\mathbb{B}_R) \subset \mathcal{H}^{(i)}(\{a^{(i)}_{m,n}(\mu^{(i)}_n)^{-1/2}\},\mathbb{B}_R)$, see also Corollary 16.4, the $\{(\mu^{(i)}_n)^{1/2}\}$-summability of the sequence a, and Theorem 16.6. In addition, the identity

$$O^{(i)}_{\hat{\boldsymbol{x}}}\boldsymbol{g}^{(i)}_{m,n,j}(R;\boldsymbol{x}) = \sqrt{\mu^{(i)}_n}G_{m,n,j}(R;\boldsymbol{x}), \qquad m\in\mathbb{N}_0,\ n\in\mathbb{N}_{0_i},\ j=1,\ldots,2n+1$$

holds true for all $\boldsymbol{x} \in \mathbb{B}_R$, see Lemma 5.7 and Definitions 5.35 and 5.37. For all $\boldsymbol{x} \in \mathbb{B}_R$, we obtain the absolute convergence of the series via the estimate

$$\begin{aligned}
&\left|\sum_{\substack{(m,n)\in\mathbb{N}_0\times\mathbb{N}_{0_i}\\ a^{(i)}_{m,n}\neq 0}} \sum_{j=1}^{2n+1} f^{\wedge}(i,m,n,j) O^{(i)}_{\hat{\boldsymbol{x}}}\boldsymbol{g}^{(i)}_{m,n,j}(R;\boldsymbol{x})\right| \\
&\leq \frac{3}{2\pi R^3}\left\|\boldsymbol{f}\right\|_{\mathcal{H}^{(i)}} \sum_{\substack{(m,n)\in\mathbb{N}_0\times\mathbb{N}_{0_i}\\ a^{(i)}_{m,n}\neq 0}} \mu^{(i)}_n \frac{(2n+1)\,(m+t^{(i)}_n+1/2)^{2m+1}}{\left(a^{(i)}_{m,n}\right)^2 (m!)^2} < \infty.
\end{aligned}$$

Here, the $\{(\mu_n^{(i)})^{1/2}\}$-summability and Lemma 5.3 are used. Hence, for all $\boldsymbol{x} \in \mathbb{B}_R$ the $O_{\hat{\boldsymbol{x}}}^{(i)}$-operator and the series in Eq. (16.2) can be interchanged. Eventually, we get the relation

$$\begin{aligned}
&\left\langle \boldsymbol{k}_{\mathcal{H}^{(i)}}(\cdot, \boldsymbol{y}), \boldsymbol{f} \right\rangle_{\mathcal{H}^{(i)}} \\
&= \sum_{\substack{(m,n) \in \mathbb{N}_0 \times \mathbb{N}_{0_i} \\ a_{m,n}^{(i)} \neq 0}} \sum_{j=1}^{2n+1} \left(a_{m,n}^{(i)}\right)^2 \left\langle \boldsymbol{k}_{\mathcal{H}^{(i)}}(\cdot, \boldsymbol{y}), \boldsymbol{g}_{m,n,j}^{(i)}(R;\cdot) \right\rangle_{\mathbf{L}_2(\mathbb{B}_R)} \left\langle \boldsymbol{f}, \boldsymbol{g}_{m,n,j}^{(i)}(R;\cdot) \right\rangle_{\mathbf{L}_2(\mathbb{B}_R)} \\
&= \sum_{\substack{(m,n) \in \mathbb{N}_0 \times \mathbb{N}_{0_i} \\ a_{m,n}^{(i)} \neq 0}} \sum_{j=1}^{2n+1} f^{\wedge}(i,m,n,j) \sqrt{\mu_n^{(i)}} G_{m,n,j}(R;\boldsymbol{y}) \\
&= \sum_{\substack{(m,n) \in \mathbb{N}_0 \times \mathbb{N}_{0_i} \\ a_{m,n}^{(i)} \neq 0}} \sum_{j=1}^{2n+1} f^{\wedge}(i,m,n,j) O_{\hat{\boldsymbol{y}}}^{(i)} \boldsymbol{g}_{m,n,j}^{(i)}(R;\boldsymbol{y}) \\
&= O_{\hat{\boldsymbol{y}}}^{(i)} \boldsymbol{f}(\boldsymbol{y}).
\end{aligned}$$

□

Examples of reproducing kernels on $\mathbb{B}_R \times \mathbb{B}_R$ with $R = 0.71$ are depicted in Fig. 16.1. Therein, we chose $i = 3$, $t_n^{(3)} \coloneqq n$ for all $n \in \mathbb{N}$, and $a_{m,n}^{(3)} \coloneqq (n(n+1))^{1/4} h^{-n/2} \delta_{m,0}$ for all $(m,n) \in \mathbb{N}_0 \times \mathbb{N}$ and $h \in (0,1)$. The sequence is $\{(n(n+1))^{1/2}\}$-summable due to properties of the power series and

$$\sum_{\substack{(m,n) \in \mathbb{N}_0 \times \mathbb{N} \\ a_{m,n}^{(3)} \neq 0}} \mu_n^{(3)} (2n+1) \frac{\left(m + t_n^{(3)} + 1/2\right)^{2m+1}}{\left(a_{m,n}^{(3)}\right)^2 (m!)^2} = \frac{1}{2} \sum_{n=1}^{\infty} h^n (2n+1)^2 \sqrt{n(n+1)} < \infty. \quad (16.3)$$

In Fig. 16.1, the absolute values of the reproducing kernels are plotted and the directions of the functions at several points are illustrated. This reveals that these reproducing kernels are solenoidal. In addition, the parameter h can be understood to control localization, since the kernel gets more and more localized if h increases. The functions are plotted on a sphere with radius $0.95R$. More examples of reproducing kernels can be found in Chapter 19.

16.2. Basics of Regularization Methods

In order to handle this situation, we make the following considerations, see [63, Ch. 3.1]. Let $\mathcal{A}\colon \mathcal{X} \to \mathcal{Y}$ be a bounded linear operator between two arbitrary Hilbert spaces $\mathcal{X}$ and $\mathcal{Y}$. Let the problem $(\mathcal{A}, \mathcal{X}, \mathcal{Y})$ be ill-posed according to Nashed, see Definition 11.6, that is the range of $\mathcal{A}$ is not closed. The exact data $g \in \mathcal{Y}$ is unknown. In contrast, we can observe the approximation g^δ with

$$\left\| g^\delta - g \right\|_{\mathcal{Y}} \leq \delta$$

for a noise level $\delta > 0$. We call g^δ the noisy data. Due to Theorem 11.5, the Moore-Penrose inverse is unbounded, which is why even small changes in the data can substantially affect the reconstruction. Therefore, we want to replace the Moore-Penrose inverse by an

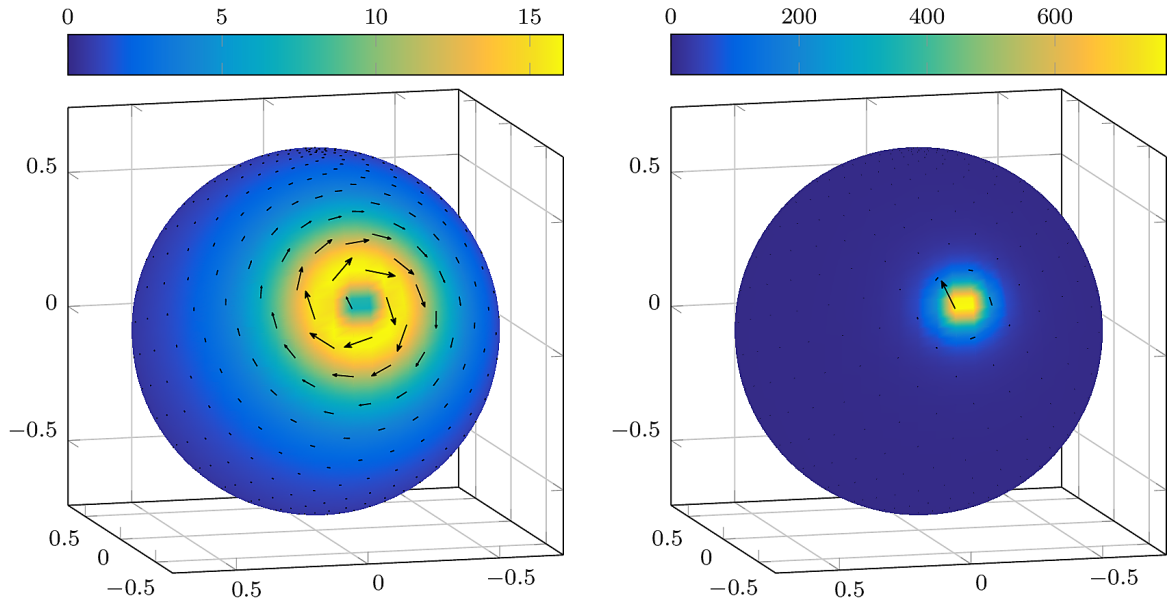

FIGURE 16.1: *Reproducing kernels* $\boldsymbol{k}_{\mathfrak{H}^{(3)}}(\cdot, \boldsymbol{z})$ *on* $\mathbb{B}_R \times \mathbb{B}_R$ *to the sequence* $a^{(3)}_{m,n} \coloneqq (n(n+1))^{1/4}\, h^{-n/2}\delta_{m,0}$ *with centre* $\boldsymbol{z} = R(-0.9511, 0, 0.3090)^{\mathrm{T}}$ *and parameter* $h = 0.7$ *(left) and* $h = 0.95$ *(right) are plotted on* $\mathbb{S}_{0.95R}$

appropriate bounded operator. As a regularization of the unbounded Moore-Penrose operator we understand a family $\{\mathcal{R}_\tau\}_\tau$ of continuous operators converging to $\mathcal{A}^+$ pointwise, see [192].

Definition 16.12 ([63, Def. 3.1]). *Let* $\mathcal{A}\colon \mathcal{X} \to \mathcal{Y}$ *be a bounded linear operator between two Hilbert spaces, and let* $\tau_0 \in \mathbb{R}^+$ *be fixed. For every* $\tau \in (0, \tau_0)$ *let*

$$\mathcal{R}_\tau\colon \mathcal{Y} \to \mathcal{X}$$

be a continuous (not necessarily linear) operator. The family $\{\mathcal{R}_\tau\}_\tau$ *is called a* regularization *for* $\mathcal{A}^+$ *if for all* $g \in \operatorname{dom}\mathcal{A}^+$ *there exists a parameter choice rule* $\tau\colon \mathbb{R}^+ \times \mathcal{Y} \to (0, \tau_0)$ *such that the limit*

$$\lim_{\delta\to 0} \sup\left\{ \left\| \mathcal{R}_{\tau(\delta,g^\delta)} g^\delta - \mathcal{A}^+ g \right\|_{\mathcal{Y}} \;\middle|\; g^\delta \in \mathcal{Y},\ \left\| g^\delta - g \right\|_{\mathcal{Y}} \le \delta \right\} = 0 \tag{16.4}$$

holds true. Furthermore, we require that

$$\lim_{\delta\to 0} \sup\left\{ \tau\left(\delta, g^\delta\right) \;\middle|\; g^\delta \in \mathcal{Y},\ \left\| g^\delta - g \right\|_{\mathcal{Y}} \le \delta \right\} = 0. \tag{16.5}$$

The parameter τ *is called a* regularization parameter. *For a specific* $g \in \operatorname{dom}\mathcal{A}^+$*, a pair* $(\mathcal{R}_\tau, \tau)$ *is called a (convergent) regularization method (for solving* $\mathcal{A}f = g$*) if Eqs.* (16.4) *and* (16.5) *hold true.*

If τ is independent of g^δ, then we call τ an a-priori parameter choice rule and write $\tau = \tau(\delta)$. Otherwise, we call τ an a-posteriori parameter choice rule, see [63, Def. 3.2]. If a function is obtained via a regularization method corresponding to the data g^δ, we will often use the notation $f^\delta_{\tau(\delta,g^\delta)} \coloneqq \mathcal{R}_{\tau(\delta,g^\delta)} g^\delta$.

Lemma 16.13 ([63, Prop. 3.4]). *Let the (possibly nonlinear) operators $\mathcal{R}_\tau$ be continuous for all $\tau > 0$. Then the family $\{\mathcal{R}_\tau\}_\tau$ is a regularization for $\mathcal{A}^+$ if $\mathcal{R}_\tau$ converges pointwise on $\operatorname{dom}\mathcal{A}^+$ to $\mathcal{A}^+$ as τ converges to zero. In this case, there exists for every $g \in \operatorname{dom}\mathcal{A}^+$ an a-priori parameter choice rule τ such that $(\mathcal{R}_\tau, \tau)$ is a convergent regularization method for solving $\mathcal{A}f = g$.*

We can characterize all linear convergent regularizations by two limit conditions.

Lemma 16.14 ([63, Prop. 3.7]). *Let $\{\mathcal{R}_\tau\}_\tau$ be a linear regularization. Let $\tau\colon \mathbb{R}^+ \to \mathbb{R}^+$ be an a-priori parameter choice rule for every $g \in \operatorname{dom}\mathcal{A}^+$. Then $(\mathcal{R}_\tau, \tau)$ is a convergent regularization method if and only if*

$$\lim_{\delta\to 0} \tau(\delta) = 0 \quad \text{and} \quad \lim_{\delta\to 0} \delta \left\|\mathcal{R}_{\tau(\delta)}\right\|_{\mathcal{L}(\mathcal{Y},\mathcal{X})} = 0.$$

Naturally, the speed of convergence of the regularization method is of interest, since a regularization method can converge arbitrarily slowly, see [192]. For this purpose, a smoothness condition is introduced.

Definition 16.15 ([63, Ch. 8.5]). *If the best-approximate solution f^+ is an element of* $\operatorname{ran}((\mathcal{A}^*\mathcal{A})^\nu)$ *for some $\nu > 0$, then f^+ fulfils the* Hölder-type source condition*.*

If the Hölder-type source condition is fulfilled, then a regularization method is called *order optimal* if for a given parameter choice rule $\tau = \tau(\delta, g^\delta)$ the relation

$$\left\|f^+ - f^\delta_{\tau(\delta,g^\delta)}\right\|_{\mathcal{X}} \in \mathcal{O}\left(\delta^{2\nu/(2\nu+1)}\right) \quad (\text{as } \delta \to 0) \tag{16.6}$$

holds true for $\|g^\delta - g\|_{\mathcal{Y}} \le \delta$ and there exists a fixed $H \in \mathbb{R}^+$ such that

$$f^+ \in \{f \in \mathcal{X} \mid f = (\mathcal{A}^*\mathcal{A})^\nu h \text{ and } \|h\|_{\mathcal{X}} \le H\},$$

see [63, 192, 194].

As seen before, a particular class of operators causing ill-posed problems are the compact operators, which possess an SVD, see Theorem 11.10. For these operators, a particular class of regularization methods exists.

Definition 16.16 ([148, Def. 3.3.2]). *Let $\mathcal{A}\colon \mathcal{X} \to \mathcal{Y}$ be a compact operator with the singular values $\{\lambda_k\}_{k\in\mathbb{N}}$ and let $\mathcal{A}^+$ be the generalized Moore-Penrose inverse. A function $\upsilon_\tau\colon \mathbb{R} \to \mathbb{R}$ is called a* regularizing filter *for $\mathcal{A}^+$ if there exists a constant $c \in \mathbb{R}^+$ such that for all $k \in \mathbb{N}$ and all $\tau > 0$ the following relation holds true:*

$$\sup_{k\in\mathbb{N}} \left|\lambda_k^{-1}\upsilon_\tau(\lambda_k)\right| < \infty, \qquad |\upsilon_\tau(\lambda_k)| \le c, \qquad \lim_{\tau\to 0} \upsilon_\tau(\lambda_k) = 1.$$

Theorem 16.17 ([148, Thm. 3.3.3]). *Let $\mathcal{A}\colon \mathcal{X} \to \mathcal{Y}$ be a compact operator with the singular system $\{f_k, g_k; \lambda_k\}_{k\in\mathbb{N}}$ and let υ_τ be a regularizing filter for $\tau > 0$. Let the family of operators $\{\mathcal{R}_\tau\}_\tau$ be defined by*

$$\mathcal{R}_\tau g^\delta := \sum_{k=1}^{\infty} \lambda_k^{-1}\upsilon_\tau(\lambda_k)\left\langle g^\delta, g_k\right\rangle_{\mathcal{Y}} f_k, \qquad g^\delta \in \mathcal{Y}.$$

Then $\{\mathcal{R}_\tau\}_\tau$ is a regularization of $\mathcal{A}^+$.

Several regularizing filters exist in the literature, see, for example, [148, 194]. Now, we consider some particular regularizing filters in detail.

Example 16.18 (Truncated Singular Value Decomposition, [148, Ch. 4.1]). *Let $\mathcal{A}\colon \mathcal{X} \to \mathcal{Y}$ be a compact operator with the singular system $\{f_k, g_k; \lambda_k\}_{k\in\mathbb{N}}$. Let $\tau > 0$ and let the regularizing filter be defined by*

$$\upsilon_\tau(\lambda) \coloneqq \begin{cases} 1 & \text{if } \lambda \geq \tau, \\ 0 & \text{if } \lambda < \tau. \end{cases}$$

In Theorem 11.10, we assumed that the singular values are sorted descending. Then there exists $K \coloneqq \max\{k \in \mathbb{N} \mid \lambda_k \geq \tau\}$ and for all $g^\delta \in \mathcal{Y}$ a regularization of $\mathcal{A}^+$ is given by

$$\mathcal{R}_\tau g^\delta \coloneqq \sum_{k=1}^{K} \lambda_k^{-1} \left\langle g^\delta, g_k \right\rangle_{\mathcal{Y}} f_k.$$

This series is often called the truncated singular value decomposition (TSVD) of $\mathcal{A}^+$.

Remark 16.19. *The TSVD from Example 16.18 can be interpreted as a projection onto a finite-dimensional subspace of $\mathcal{Y}$ that is spanned by a finite number of orthonormal basis functions g_k, see [63, Sec. 3.3, Exam. 4.8]. Alternatively, we can apply the projection onto a subspace $\mathcal{V}_m \subset \mathcal{X}$ with dimension $m \in \mathbb{N}$ in the preimage space $\mathcal{X}$. This is equivalent to replacing $\mathcal{A}$ with a finite rank approximation $\mathcal{A}_m$ that is a restriction of $\mathcal{A}$ onto the finite-dimensional subspace $\mathcal{V}_m$ for all $m \in \mathbb{N}$, which means $\mathcal{A}_m \coloneqq \mathcal{A}|_{\mathcal{V}_m}$.*

Suppose that $\mathcal{V}_m \coloneqq \operatorname{span}\{f_k\}_{k=1,\dots,m}$, then the sequence of finite-dimensional subspaces $\{\mathcal{V}_m\}_{m\in\mathbb{N}}$ increases and their union is dense in $\mathcal{X}$, that is $\overline{\cup_{m=1}^{\infty} \mathcal{V}_m} = \mathcal{X}$. It is easy to see that a regularization is given by

$$\mathcal{R}_{1/m} g^\delta \coloneqq \mathcal{A}_m^+ g^\delta = \sum_{k=1}^{m} \lambda_k^{-1} \left\langle g^\delta, g_k \right\rangle_{\mathcal{Y}} f_k$$

with the regularizing filter

$$\upsilon_{1/m}(\lambda) \coloneqq \begin{cases} 1 & \text{if } \lambda \geq \lambda_m, \\ 0 & \text{if } \lambda < \lambda_m. \end{cases}$$

Under certain conditions, it can be proved that $(\mathcal{R}_{1/m}, m)$ is a convergent regularization method for $m \to \infty$, see [102, Thm. 4.1.1]. In this context, note that $g \in \operatorname{dom} \mathcal{A}^+$ is always an element of $\operatorname{dom} \mathcal{A}_m^+$ since $\mathcal{A}_m$ is a finite rank operator.

Concluding, we see that this approach also leads to the TSVD, see [63, Sec. 3.3, Exam. 4.8].

Another class of regularizing filters can be constructed similarly to wavelets and scaling functions, which are used for multi-scale approximations, see [82], for instance. Note that we restrict ourselves to scalar-valued Hilbert spaces in the next example. However, this method is also presented for vector- and tensor-valued Hilbert spaces in [155].

Example 16.20 (Scaling Functions, [155]). *Let $\mathcal{A}\colon \mathcal{X} \to \mathcal{Y}$ be a linear and continuous operator between two scalar-valued Hilbert spaces $\mathcal{X} \coloneqq \mathcal{X}(\mathbb{G})$ with $\mathbb{G} \subset \mathbb{R}^d$, $d \in \mathbb{N}$, and $\mathcal{Y}$.*

Suppose its (possibly unbounded) inverse operator exists and let the singular system of $\mathcal{A}$ be given by $\{f_k, g_k; \lambda_k\}_{k\in\mathbb{N}}$. Now, we can define a regularizing filter by

$$v_{1/J}(\lambda_k) \coloneqq \lambda_k \Phi_J^\wedge(k), \qquad J \in \mathbb{Z},\ k \in \mathbb{N},$$

where the used symbols $\{\Phi_J^\wedge(k)\}_{J\in\mathbb{Z}}$ of the product kernel $\Phi_J\colon \mathbb{G}\times\mathbb{G}\to\mathbb{R}$ have to satisfy the following conditions:

i) $\{\Phi_J^\wedge(k)\}_{J\in\mathbb{Z}}$ is monotonically increasing for every $k\in\mathbb{N}$,

ii) $\lim_{J\to\infty}\Phi_J^\wedge(k) = \lambda_k^{-1}$ for every $k\in\mathbb{N}$,

iii) $\lim_{J\to-\infty}\Phi_J^\wedge(k) = 0$ for every $k\in\mathbb{N}$, and

iv) for each $J\in\mathbb{Z}$ the sequence $\{\Phi_J^\wedge(k)\}_{k\in\mathbb{N}}$ is square-summable.

Then the family of corresponding product kernels $\{\Phi_J\}_{J\in\mathbb{Z}}$ is called (scale discrete) scaling functions (with respect to the operator $\mathcal{A}$). Note that the product kernel and its symbols are related by

$$\Phi_J(\boldsymbol{x},\boldsymbol{y}) = \sum_{k=1}^{\infty}\Phi_J^\wedge(k) f_k(\boldsymbol{x}) f_k(\boldsymbol{y}), \qquad \boldsymbol{x},\ \boldsymbol{y}\in\mathbb{G}.$$

For all $g\in\mathcal{Y}$ and $J\in\mathbb{Z}$, we define an operator

$$\mathcal{R}_{1/J} g \coloneqq \Phi_J * g \coloneqq \sum_{k=1}^{\infty}\Phi_J^\wedge(k)\langle g, g_k\rangle_{\mathcal{Y}} f_k.$$

Then, according to [155, Thm. 2.4.5], the pair $(\mathcal{R}_{1/J}, 1/J)$ satisfies

$$\lim_{J\to\infty}\left\|\mathcal{R}_{1/J} g - \mathcal{A}^+ g\right\| = 0, \qquad g\in\operatorname{ran}\mathcal{A}.$$

In addition, see [155, Thm. 2.4.12], the operator $\mathcal{R}_{1/J}\colon \operatorname{ran}\mathcal{A}\to\mathcal{X}$ is continuous.

In the literature, there exist a variety of different scaling functions, see, for instance, [82, 155] and the references therein. Examples are the Shannon, the de la Vallé-Poussin, the cubic polynomial, and the Abel-Poisson scaling function. Note that the Shannon scaling function is closely related to the TSVD.

The next filter considered in this thesis is the Tikhonov-regularization, which is a widely used and analyzed tool for solving inverse problems such as integral equations of the first kind, see, for instance, [63, 102, 136, 148, 178, 192] and the references therein.

Example 16.21 (Tikhonov-Philips Regularization, [148, Ch. 4.2]). *First, we introduce for given data $g^\delta\in\mathcal{Y}$ and for the regularization parameter $\tau>0$ the Tikhonov-Philips functional*

$$\mathcal{J}_\tau(f) = \left\|\mathcal{A}f - g^\delta\right\|_{\mathcal{Y}}^2 + \tau\varpi(f)^2,$$

where the penalty term is defined by a strongly convex function $\varpi\colon\mathcal{X}\to\mathbb{R}^+$. Note that for the classical Tikhonov regularization [213], the penalty term coincides with the norm in $\mathcal{X}$, and with the norm of the second-order derivative of f in the case of the classical Philips

regularization, see [187]. In addition, the penalty term can be induced by an appropriate densely defined pseudodifferential operator $\mathcal{B}\colon (\ker \mathcal{A})^{\perp} \to \mathcal{X}$*, that is*

$$\mathcal{J}_\tau(f) = \left\| \mathcal{A}f - g^\delta \right\|_{\mathcal{Y}}^2 + \tau \left\| \mathcal{B}f \right\|_{\mathcal{X}}^2 . \tag{16.7}$$

Then the unique minimizer of the Tikhonov-Philips functional is given by $f_\tau^\delta := \mathcal{R}_\tau g^\delta$*, where the regularization operator* $\mathcal{R}_\tau$ *has the representation*

$$\mathcal{R}_\tau = (\mathcal{A}^*\mathcal{A} + \tau \mathcal{B}^*\mathcal{B})^{-1}\mathcal{A}^*.$$

Let $\mathcal{A}\colon \mathcal{X} \to \mathcal{Y}$ *be a compact operator with the singular system* $\{f_k, g_k; \lambda_k\}_{k\in\mathbb{N}}$*. If there exists* $\beta > 0$ *such that* $\|\mathcal{B}f\|_{\mathcal{X}} \geq \beta \|f\|_{\mathcal{X}}$ *for all* $f \in (\ker \mathcal{A})^{\perp}$ *and if there are coefficients* $\{\beta_k\}_{k\in\mathbb{N}}$ *such that*

$$\mathcal{B}^*\mathcal{B}f = \sum_{k=1}^{\infty} \beta_k^2 \langle f, f_k\rangle_{\mathcal{Y}} f_k,$$

then the operator $(\mathcal{B}^*\mathcal{B})^{-1}\colon (\ker \mathcal{A})^{\perp} \to \mathcal{X}$ *is bounded. In this case, we get*

$$\|\mathcal{B}f\|_{\mathcal{X}}^2 = \sum_{k=1}^{\infty} \beta_k^2 \langle f, f_k\rangle_{\mathcal{Y}}^2.$$

Thus, the domain of the operator is given by

$$\operatorname{dom} \mathcal{B} = \left\{ f \in \mathcal{X} \;\middle|\; \sum_{k=1}^{\infty} \beta_k^2 \langle f, f_k\rangle_{\mathcal{Y}}^2 < \infty \right\},$$

which is dense in $\mathcal{X}$*.*

Let the non-negative real sequence $\{\beta_k\}_{k\in\mathbb{N}}$ *fulfil* $\beta_k^2 \geq c\lambda_k$ *with a constant* $c > 0$*. Then a regularization* $\mathcal{R}_\tau$ *is given by Theorem 16.17 and* $f_\tau^\delta := \mathcal{R}_\tau g^\delta$ *is the unique minimizer of the Tikhonov functional from Eq.* (16.7)*, see also [193].*

In Section 16.1, we have already seen spaces like $\operatorname{dom} \mathcal{B}$ given in the previous example if $\mathcal{X} = \mathbf{L}_2(\mathbb{B}_R)$. In this context the domain of $\mathcal{B}$ coincides with the the pre-Hilbert space $\oplus_{i=1}^3 \mathcal{E}^{(i)}(\{\beta_k\}_{k\in\mathbb{N}}, \mathbb{B}_R)$.

Theorem 16.22 ([136, Thm. 2.11]). *Let* $\mathcal{A}\colon \mathcal{X} \to \mathcal{Y}$ *be a linear and bounded operator between two Hilbert spaces, let* $g^\delta \in \mathcal{Y}$ *and* $\tau > 0$*. Then the classical Tikhonov functional* $\mathcal{J}_\tau$ *has a unique minimizer* $f_\tau \in \mathcal{X}$ *that is the unique solution of the so-called Tikhonov-regularized normal equation, that is*

$$(\mathcal{A}^*\mathcal{A} + \tau\mathcal{I})f_\tau = \mathcal{A}^* g^\delta.$$

Consequently, for all $\tau > 0$ *the following identity holds true:*

$$f_\tau = (\mathcal{A}^*\mathcal{A} + \tau\mathcal{I})^{-1}\mathcal{A}^* g^\delta.$$

Now, we can combine the Tikhonov regularization with the projection onto a finite-dimensional subspace. The resulting method is called the *regularized Ritz method* and goes back to [195]. For more details on the method and its theoretical properties, see [176, Sec. 5.2], [101–103], for example.

Example 16.23 (Regularized Ritz Method, [102, Ch. 4.2]). *Let an expanding sequence of finite-dimensional subspaces $\mathcal{V}_m$ with $m \in \mathbb{N}$ of $\mathcal{X}$ be given as in Remark 16.19. Now, we are interested in finding a minimizer $f_{1/m,\tau}$ of the classical Tikhonov functional, that is*

$$\mathcal{J}_\tau(f) = \left\| \mathcal{A}f - g^\delta \right\|_{\mathcal{Y}}^2 + \tau \left\| f \right\|_{\mathcal{X}}^2,$$

over the finite-dimensional subspace $\mathcal{V}_m$. Then, according to Theorem 16.22, this minimizer can be represented by

$$f_{1/m,\tau} = (\mathcal{A}_m^* \mathcal{A}_m + \tau \mathcal{I}_m)^{-1} \mathcal{A}_m^* g^\delta,$$

where $\mathcal{I}_m$ is the identity operator on $\mathcal{V}_m$ and $\mathcal{A}_m \coloneqq \mathcal{A}|_{\mathcal{V}_m}$ for all $m \in \mathbb{N}$.

The next statement can be proved, see [102, Thm. 4.2.17]: let the finite space dimension $m = m(\delta)$ and the regularization parameter $\tau = \tau(m(\delta))$ satisfy a certain dependency on the noise level δ. If $f^+ \in \operatorname{ran}(\mathcal{A}^*)$, then the regularized Ritz method is a convergent regularization method with $\|f_{1/m,\tau}^\delta - f^+\|_{\mathcal{X}} \in \mathcal{O}(\delta^{1/2})$ as $\delta \to 0$.

More details on regularization methods, parameter choice rules, and order optimality can be found, for instance, in [63, 136, 148, 192–194] and the references therein.

16.3. Parameter Choice Methods

As we have already seen in Lemma 16.14, every regularization method requires an appropriate parameter choice method for its convergence. A result with respect to the Tikhonov regularization has already been known.

Lemma 16.24 ([193, Prop. 2.14, 2.18]). *The Tikhonov regularization combined with a parameter choice rule that either satisfies*

i) $\tau(\delta, g^\delta) \to 0$ and $\delta^2/\tau(\delta, g^\delta) \to 0$ as $\delta \to 0$, or

ii) $\tau(\delta, g^\delta)$ chosen such that $\|g^\delta - \mathcal{A}f_\tau^\delta\|_{\mathcal{Y}} = m\delta$ for fixed $m > 1$ (discrepancy principle)

is a regularization method. In addition, the Tikhonov regularization together with the discrepancy principle is order optimal for some $0 < \nu \leq 0.5$ (see [192, p. 1235]) occurring in the Hölder-type source condition, see Definition 16.15.

Based on the forthcoming regularization method, we are interested in the particular case of a Hölder-type source condition with $\nu = 1$. However, for this source condition, it is verified in [194, p. 75f.] that the discrepancy principle is not appropriate for the Tikhonov regularization, since it does not result in an order optimal convergence rate. The discrepancy principle requires exact knowledge (and control) of the uncertainty δ in the measurements. For real data obtained from real measurements, this information is not available exactly and control of the measurement noise is impossible. Therefore, we proceed by presenting selected parameter choice methods that are suitable in the context of our application and the algorithms applied in this thesis, which are closely related to Tikhonov regularization.

In [17, 18], the parameter choice methods presented in the following and other additional methods are tested for Tikhonov regularization as well as TSVD with both white and coloured stochastic noise. In [17], the methods are tested for the downward continuation occurring in

many geoscientific applications, such as the inverse gravimetric problem, see Example 14.15. However, the downward continuation problem is also a part of the inverse MEG and EEG problem as we have already seen in Section 13.2. In [105], these methods are tested for the downward continuation problem solved by an algorithm called the regularized functional matching pursuit algorithm (RFMP) as well as the regularized orthogonal functional matching pursuit algorithm (ROFMP), which we will also use to solve the inverse MEG and EEG problem numerically, see Chapter 17.

For two Hilbert spaces $\mathcal{X}$ and $\mathcal{Y}$, let the inverse problem $(\mathcal{A}, \mathcal{X}, \mathcal{Y})$ be given, where the data $g^\delta \in \mathcal{Y}$ can also be noisy and $f^\delta_{\tau_j}$ is obtained via the regularization method, that is $f^\delta_{\tau_j} = \mathcal{R}_{\tau_j} g^\delta$. For example, the applied regularization method can be Tikhonov regularization, TSVD, or the RFMP. Furthermore, let us assume that an SVD of $\mathcal{A}$ with the singular values $\{\lambda_k\}_k$ is available. Here, depending on the problem, k can either be an element of a countably infinite index set or of a finite index set. First, we define a finite monotonically decreasing sequence of regularization parameters $\{\tau_j\}_j$. The range of the regularization parameter depends on the underlying problem and the regularization term. According to [105], we calculate the variance propagation factor of the Tikhonov solution in the case of white noise by

$$\varrho^2(j) = \sum_k \frac{\lambda_k^2}{(\lambda_k^2 + \tau_j)^2},$$

where $\{\lambda_k\}_k$ are the singular values of the considered operator $\mathcal{A}\colon \mathcal{X} \to \mathcal{Y}$. The restriction to white noise is reasonable since we will use white noise in the synthetic test cases and in the real data situation the technical noise is also assumed to be white, see Item (E) on page 174. Note that most of the considered parameter choice methods need $\mathcal{Y} = \mathbb{R}^\ell$. Before applying the parameter choice method, we remove the regularization parameters causing high variances by limiting the index set of $\{\tau_j\}_j$ to the upper bound J given by

$$J \coloneqq \max\left\{ j \;\middle|\; \varrho(j) < 0.5 \left(\max_n \varrho(n) \right) \right\}.$$

Based on the results of [105], we consider the following parameter choice methods:

L-curve Method (LC) The relative residual is plotted against the $\mathcal{X}$-norm of the approximation. The resulting parametric log-log plot is called the L-curve, since the plot is often L-shaped. Then, the regularization parameter τ_{j_*} that corresponds to the point near the corner of the L-curve is chosen. Thus, a parameter is sought that keeps the relative residual small as well as the norm of the approximation, see [63, p. 108f.]. A disadvantage of this method is that the parameter τ_{j_*} has to be chosen manually. We also call this method the manual L-curve method (LCM). In contrast, a variation that can be calculated automatically (LCA) is known in the literature and also stated in [105], that is

$$j_* = \operatorname*{arg\,min}_{j \le J} \left\{ \left\| \mathcal{A} f^\delta_{\tau_j} - g^\delta \right\|_{\mathbb{R}^\ell} \left\| f^\delta_{\tau_j} \right\|_{\mathcal{X}} \right\}.$$

There exist first rigorous optimality results for the L-curve method, see [17, 149].

Generalized Cross Validation (GCV) According to [17], the GCV is best suited to stochastic white noise and discrete data, which will be used in the forthcoming synthetic

test cases. However, according to [105], the best results can be obtained with a regularly distributed data grid, which is not given in our application. Here, the selection criterion for the regularization parameter is given by

$$j_* = \underset{j \leq J}{\arg\min} \left\{ \frac{\|\mathcal{A} f_{\tau_j}^{\delta} - g^{\delta}\|_{\mathbb{R}^\ell}^2}{\left(\ell^{-1} \operatorname{tr}(\mathcal{I} - \mathcal{A}\bar{\mathcal{R}}_{\tau_j})\right)^2} \right\},$$

where the linear regularization operator $\bar{\mathcal{R}}_{\tau_j} \colon \mathbb{R}^\ell \to \mathcal{X}$ is defined by

$$\bar{\mathcal{R}}_{\tau_j} \coloneqq (\mathcal{A}^*\mathcal{A} + \tau_j \mathcal{I})^{-1} \mathcal{A}^*. \tag{16.8}$$

The trace $\operatorname{tr}(\mathcal{I} - \mathcal{A}\bar{\mathcal{R}}_{\tau_j})$ can be calculated by

$$\operatorname{tr}(\mathcal{I} - \mathcal{A}\bar{\mathcal{R}}_{\tau_j}) = \sum_k \left(1 - \frac{\lambda_k^2}{\lambda_k^2 + \tau_j}\right),$$

see [142, Ch. 30.3]. According to [63, p. 106], it is a disadvantage of this method that detailed information about the singular values of $\mathcal{A}$ are required for the analytical calculation of the trace term expression. However, in our application we will use a numerical approximation of these singular values.

Robust GCV (RGCV) The RGCV method is a further development of the GCV in order to overcome the instability of the GCV, see [17]. To this end, a robustness parameter $\gamma \in (0, 1)$ is introduced. In the case of $\gamma = 1$, the RGCV coincides with the GCV. Using the regularization operator from Eq. (16.8), the selection criterion is given by

$$j_* = \underset{j \leq J}{\arg\min} \left\{ \frac{\|\mathcal{A} f_{\tau_j}^{\delta} - g^{\delta}\|_{\mathbb{R}^\ell}^2}{\left(\ell^{-1} \operatorname{tr}(\mathcal{I} - \mathcal{A}\bar{\mathcal{R}}_{\tau_j})\right)^2} \left(\gamma + (1-\gamma)\ell^{-1} \operatorname{tr}\left(\left(\mathcal{A}\bar{\mathcal{R}}_{\tau_j}\right)^2\right)\right) \right\}. \tag{16.9}$$

We will choose $\gamma = 0.1$ for the RGCV. The RGCV yields good results for Tikhonov regularization with solutions of lowest smoothness, see [17]. The remaining trace can be calculated by

$$\operatorname{tr}\left(\left(\mathcal{A}\bar{\mathcal{R}}_{\tau_j}\right)^2\right) = \sum_k \left(\frac{\lambda_k^2}{\lambda_k^2 + \tau_j}\right)^2.$$

Strong RGCV (SRGCV) The SRGCV is a particular case of the RGCV, where the robustness parameter is chosen near to one. We use $\gamma = 0.95$ in Eq. (16.9).

Modified GCV (MGCV) Another modification of the GCV is given by the MGCV, which is designed to stabilize the GCV. Here, the selection criterion for the regularization index is given by

$$j_* = \underset{j \leq J}{\arg\min} \left\{ \frac{\|\mathcal{A} f_{\tau_j}^{\delta} - g^{\delta}\|_{\mathbb{R}^\ell}^2}{\left(\ell^{-1} \operatorname{tr}\left(\mathcal{I} - c\mathcal{A}\bar{\mathcal{R}}_{\tau_j}\right)\right)^2} \right\},$$

where the regularization operator is given as in Eq. (16.8) and the stabilization parameter $c > 1$ needs to be chosen. We choose $c = 3$ for our calculations.

Residual Method (RM) The aim of the RM is to minimize a weighted form of the $\mathbb{R}^\ell$-norm of the residuals. The weighting should penalize under-smoothing parameter values, see [17]. The parameter choice rule is given by

$$j_* = \operatorname*{arg\,min}_{j \leq J} \left\{ \frac{\|\mathcal{A} f_{\tau_j}^\delta - g^\delta\|_{\mathbb{R}^\ell}}{\left(\operatorname{tr}(\mathcal{B}_{\tau_j}^* \mathcal{B}_{\tau_j})\right)^{1/4}} \right\},$$

where the occurring operator $\mathcal{B}_{\tau_j} \colon \mathcal{X} \to \mathbb{R}^\ell$ is defined with the regularization operator $\bar{\mathcal{R}}_{\tau_j}$ from Eq. (16.8) by

$$\mathcal{B}_{\tau_j} \coloneqq \mathcal{A}\left(\mathcal{I} - \bar{\mathcal{R}}_{\tau_j} \mathcal{A}\right).$$

The corresponding trace is given by

$$\operatorname{tr}(\mathcal{B}_{\tau_j}^* \mathcal{B}_{\tau_j}) = \sum_k \left(\lambda_k \left(1 - \frac{\lambda_k^2}{\lambda_k^2 + \tau_j} \right) \right)^2.$$

For several parameter choice methods, such as the (strong) RGCV and the MGCV, additional parameters need to be determined. In these cases, we chose the same parameters as in [105].

More information on the different parameter choice methods and their advantages and disadvantages can be found in [17, 18, 105] and the references therein.

Chapter 17.

Regularized Functional Matching Pursuit Algorithm

17.1. Algorithm and Properties

In this chapter, we present an algorithm for solving (ill-posed) inverse problems that is called the regularized functional matching pursuit algorithm (RFMP). The RFMP was originally invented for the inversion of gravitational data and normal mode anomalies, see [66]. Especially for the inversion of gravitational data, several different approaches with different function systems and bases exist, for instance, spherical harmonics, wavelets, Slepian functions, and splines. Since each of these systems has advantages but also disadvantages, an algorithm was sought that enables the possibility to combine several different function types. This leads to a dictionary that may contain linearly dependent functions and may be redundant. The aim of this method is to acquire all the advantages of the different systems and to reduce the disadvantages.

Several variants of the RFMP are presented in the literature starting from [23] and are applied to several ill-posed inverse problems in the geosciences, see [66–69, 86, 159, 165, 166]. They are based on a greedy algorithm introduced in [151] and enhanced in [218] which is called the matching pursuit algorithm. This algorithm is an approximation method. In [66, 67], the functional matching pursuit algorithm was developed, which is used for the reconstruction of functions. Due to the additional regularization, see also [159], the RFMP is applicable to ill-posed inverse problems. In [66], convergence results of the RFMP are stated for the first time. In the setting used in [66], only operators mapping from $\mathrm{L}_2(\mathbb{G})$ to $\mathbb{R}^\ell$ are considered, where $\mathbb{G} \subset \mathbb{R}^d$ is a compact region. The convergence results of the RFMP consist of two statements: the sequence of approximations produced by the RFMP converges and the RFMP is a convergent regularization method. The convergence result was transferred to an arbitrary separable Hilbert space as the domain of the operator in [163, 210]. In this context, the statement concerning the convergence of the sequence of approximations produced by the RFMP was improved by the author in [163]. In [137, 138], the RFMP was considered as a particular case of the so-called regularized weak functional matching pursuit (RWFMP).

Therein, the RFMP for operators between two (infinite-dimensional) Hilbert spaces was considered for the first time. This approach yields a characterization of the convergence order of the regularization induced by the RFMP. However, the convergence result follows as a corollary since the RFMP is a particular case of the RWFMP. Here, we present an alternative approach to achieve this convergence result without the technique required for the RWFMP. The transition to the infinite-dimensional setting in the operator range requires only a small adjustment of the proof stated in [163]. We consider the following setting, which perfectly fits to the inverse magneto-electroencephalography problem.

Problem 17.1. *Let $\mathcal{X}$ and $\mathcal{Y}$ be two (infinite-dimensional) Hilbert spaces. Let $g \in \mathcal{Y}$ be the given data (function) and $\mathcal{A}\colon \mathcal{X} \to \mathcal{Y}$ be a given linear and continuous operator. The task is to find a solution $f \in \mathcal{X}$ such that*

$$\mathcal{A}f = g.$$

We proceed by considering the RFMP iteration in detail, which constructs a sequence $\{f_k\}_{k\in\mathbb{N}} \subset \mathcal{X}$ of approximations to the (unknown) solution f. The elements f_k are linear combinations of elements from a so-called dictionary $\mathcal{D}$, which is a subset of $\mathcal{X}$ containing possibly useful trial functions. Thus, in the kth step we have already calculated the approximation f_k and we are searching for a tuple $(\alpha_{k+1}, d_{k+1}) \in \mathbb{R} \times \mathcal{D}$ containing the best-fitting next dictionary element and its coefficient. In this context, best-fitting element is meant as the minimizer of the resulting regularized Tikhonov-functional, that is

$$\begin{aligned}(\alpha_{k+1}, d_{k+1}) &= \operatorname*{arg\,min}_{(\alpha,d)\in\mathbb{R}\times\mathcal{D}} \mathcal{J}_\tau(g, f_k, d, \alpha),\\ \mathcal{J}_\tau(g, f, d, \alpha) &\coloneqq \|g - \mathcal{A}(f + \alpha d)\|_{\mathcal{Y}}^2 + \tau \|f + \alpha d\|_{\mathcal{X}}^2 .\end{aligned}$$

Assume that the next chosen dictionary element d_{k+1} has already been known. Then the optimal coefficient α_{k+1} can be calculated as the root of the derivative with respect to α of this regularized Tikhonov-functional, see [66]. In addition, the second derivative with respect to α of the regularized Tikhonov-functional is non-negative, that is

$$\frac{\partial^2}{\partial\alpha^2}\left(\|g - \mathcal{A}(f_k + \alpha d_{k+1})\|_{\mathcal{Y}}^2 + \tau \|f_k + \alpha d_{k+1}\|_{\mathcal{X}}^2\right) = 2\|\mathcal{A}d_{k+1}\|_{\mathcal{Y}}^2 + 2\tau\|d_{k+1}\|_{\mathcal{X}}^2 \geq 0.$$

Thus, the regularized Tikhonov-function is convex as a function in α and the optimal coefficient α_{k+1} is unique. This greedy procedure leads to the next algorithm.

Algorithm 17.2 (RFMP, [163, Algo. 2]). *Let $\mathcal{A}$ and g be given as in Problem 17.1. Choose a dictionary $\mathcal{D} \subset \mathcal{X} \setminus \{0\}$, an initial approximation $f_0 \in \mathcal{X}$, for example $f_0 = 0$, and a regularization parameter $\tau \in \mathbb{R}_0^+$.*

i) Initialize the step counter to $k \coloneqq 0$, define the residual $r_0 \coloneqq g - \mathcal{A}f_0$, and choose a stopping criterion.

ii) Find

$$d_{k+1} \coloneqq \operatorname*{arg\,max}_{d\in\mathcal{D}} \frac{\left(\langle r_k, \mathcal{A}d\rangle_{\mathcal{Y}} - \tau\langle f_k, d\rangle_{\mathcal{X}}\right)^2}{\|\mathcal{A}d\|_{\mathcal{Y}}^2 + \tau\|d\|_{\mathcal{X}}^2} \tag{17.1}$$

and set

$$\alpha_{k+1} \coloneqq \frac{\langle r_k, \mathcal{A}d_{k+1}\rangle_{\mathcal{Y}} - \tau\langle f_k, d_{k+1}\rangle_{\mathcal{X}}}{\|\mathcal{A}d_{k+1}\|_{\mathcal{Y}}^2 + \tau\|d_{k+1}\|_{\mathcal{X}}^2} \tag{17.2}$$

as well as $f_{k+1} \coloneqq f_k + \alpha_{k+1}d_{k+1}$ and $r_{k+1} \coloneqq g - \mathcal{A}f_{k+1} = r_k - \alpha_{k+1}\mathcal{A}d_{k+1}$.

iii) If the stopping criterion is fulfilled, then f_{k+1} is the output. Otherwise, increase k by 1 and go to step ii).

Several properties required for the convergence theorem of the RFMP are analyzed in [66, 159] and summarized in this thesis. In order to accelerate the algorithm, several quantities can be calculated in a preprocessing step, such as the inner products between the dictionary elements or the forward operator action $\mathcal{A}d$ for all dictionary elements $d \in \mathcal{D}$.

In practice, the algorithm will be stopped when some stopping criterion is satisfied, see, for example, [159]. The stopping criterion can, for instance, be a (relative) bound for the residual or an upper bound for the number of iterations. However, we neglect the stopping criterion for the analysis of the convergence of the sequence produced by the algorithm.

Lemma 17.3 ([163, Lem. 3]). *The sequences $\{f_k\}_{k\in\mathbb{N}} \subset \mathcal{X}$ and $\{r_k\}_{k\in\mathbb{N}} \subset \mathcal{Y}$ of the RFMP satisfy*

$$\|r_k\|_{\mathcal{Y}}^2 + \tau \|f_k\|_{\mathcal{X}}^2 = \|r_{k-1}\|_{\mathcal{Y}}^2 + \tau \|f_{k-1}\|_{\mathcal{X}}^2 - \frac{\left(\langle r_{k-1}, \mathcal{A}d_k\rangle_{\mathcal{Y}} - \tau\langle f_{k-1}, d_k\rangle_{\mathcal{X}}\right)^2}{\|\mathcal{A}d_k\|_{\mathcal{Y}}^2 + \tau\|d_k\|_{\mathcal{X}}^2} \tag{17.3}$$

for all $k \in \mathbb{N}$. Hence, the sequence $\{\|r_k\|_{\mathcal{Y}}^2 + \tau\|f_k\|_{\mathcal{X}}^2\}_{k\in\mathbb{N}}$ is monotonically decreasing, bounded from below by zero, and convergent.

The next lemmas are parts of [163, Thm. 4], which are separated here for the sake of structure. Note that the condition of the next lemma implies $0 \notin \mathcal{D}$ in the regularized case and $\ker \mathcal{A} \cap \mathcal{D} = \emptyset$ in the non-regularized case.

Lemma 17.4 ([163, Thm. 4]). *If the dictionary fulfils*

$$c_1 \coloneqq \inf_{d\in\mathcal{D}} (\|\mathcal{A}d\|_{\mathcal{Y}}^2 + \tau \|d\|_{\mathcal{X}}^2) > 0,$$

then the sequence $\{\alpha_k\}_{k\in\mathbb{N}}$ produced by the RFMP is square summable and, consequently, a null sequence.

In Problem 17.1, the considered operator $\mathcal{A}$ is assumed to be continuous, which means that the operator norm $\|\mathcal{A}\|_{\mathcal{L}} \coloneqq \sup_{f\in\mathcal{X}, f\neq 0} \|\mathcal{A}f\|_{\mathcal{Y}}/\|f\|_{\mathcal{X}}$ is finite. We make use of this continuity in combination with Eq. (17.1) in the next lemma.

Lemma 17.5 ([163, Thm. 4]). *If the dictionary is bounded (i.e. $c_2 \coloneqq \sup_{d\in\mathcal{D}} \|d\|_{\mathcal{X}} < \infty$), then the sequence of coefficients $\{\alpha_k\}_{k\in\mathbb{N}}$ produced by the RFMP fulfils for all $k \in \mathbb{N}$ and all $d \in \mathcal{D}$ the estimate*

$$\begin{aligned}
\alpha_{k+1}^2 &\geq \frac{1}{(\|\mathcal{A}\|_{\mathcal{L}}^2 + \tau)\|d_{k+1}\|_{\mathcal{X}}^2} \frac{\left(\langle r_k, \mathcal{A}d_{k+1}\rangle_{\mathcal{Y}} - \tau\langle f_k, d_{k+1}\rangle_{\mathcal{X}}\right)^2}{\|\mathcal{A}d_{k+1}\|_{\mathcal{Y}}^2 + \tau\|d_{k+1}\|_{\mathcal{X}}^2} \\
&\geq \frac{1}{(\|\mathcal{A}\|_{\mathcal{L}}^2 + \tau)c_2^2} \frac{\left(\langle r_k, \mathcal{A}d\rangle_{\mathcal{Y}} - \tau\langle f_k, d\rangle_{\mathcal{X}}\right)^2}{\|\mathcal{A}d\|_{\mathcal{Y}}^2 + \tau\|d\|_{\mathcal{X}}^2}.
\end{aligned}$$

The convergence theorem presented in this thesis requires a semi-frame condition for the dictionary, which is stated below.

Assumption 17.6 (Semi-frame Condition). *There exists a constant $c_3 > 0$ and an integer $M \in \mathbb{N}$ such that for all expansions $h = \sum_{k=1}^{\infty} \beta_k d_k$ with $\beta_k \in \mathbb{R}$ and $d_k \in \mathcal{D}$, where the d_k are not necessarily pairwise distinct but $|\{j \in \mathbb{N} \mid d_j = d_k\}| \leq M$ for each $k \in \mathbb{N}$, the following inequality is valid:*

$$c_3 \|h\|_{\mathcal{X}}^2 \leq \sum_{k=1}^{\infty} \beta_k^2.$$

The following theorems published by the author in [163] improve the results from [66, Thm. 3.5], [67, Thm. 4.5], [159, Thm. 2], and [165, Thm. 6.3]. In [163], the result is formulated for the case of a finite-dimensional Hilbert space $\mathcal{Y}$. However, the proof of this result is in fact independent of the structure of the operator range and the space $\mathcal{Y}$. Thus, the next theorem is also valid in the context of infinite-dimensional Hilbert spaces $\mathcal{Y}$.

Theorem 17.7 (Convergence Theorem, [163, Thm. 4]). *Let the setting of Problem 17.1 and an arbitrary regularization parameter $\tau \in \mathbb{R}_0^+$ be given. Let the dictionary $\mathcal{D} \subseteq \mathcal{X}$ satisfy the semi-frame condition from Assumption 17.6 and the conditions of Lemmas 17.4 and 17.5.*

If the sequence $\{f_k\}_{k\in\mathbb{N}}$ is produced by the RFMP and no dictionary element is chosen more than M times, then $\{f_k\}_{k\in\mathbb{N}}$ converges in $\mathcal{X}$ to $f_\infty \coloneqq f_0 + \sum_{k=1}^{\infty} \alpha_k d_k \in \mathcal{X}$ and the sequence of residuals $\{r_k\}_{k\in\mathbb{N}}$ converges in $\mathcal{Y}$.

Proof. We can define $f_\infty \coloneqq f_0 + \sum_{n=1}^{\infty} \alpha_n d_n$, which is an element of $\mathcal{X}$ due to the semi-frame condition and Lemma 17.4. These two properties also reveal that the sequence $\{f_k\}_{k\in\mathbb{N}}$ converges to f_∞ in the strong sense, that is

$$\lim_{k\to\infty} \|f_\infty - f_k\|_{\mathcal{X}}^2 = \lim_{k\to\infty} \left\| \sum_{n=k+1}^{\infty} \alpha_n d_n \right\|_{\mathcal{X}}^2 \leq \frac{1}{c_3} \lim_{k\to\infty} \sum_{n=k+1}^{\infty} \alpha_n^2 = 0.$$

Since $\mathcal{A}$ is continuous, $\{r_k\}_{k\in\mathbb{N}} = \{g - \mathcal{A}f_k\}_{k\in\mathbb{N}}$ must converge (strongly) in $\mathcal{Y}$. □

The semi-frame condition is not easy to handle. It is hard to verify that a chosen dictionary fulfils this condition. In [137], a first step is taken in order to get rid of this semi-frame condition. Therein, the convergence of the residuals $\{r_k\}_{k\in\mathbb{N}}$ could be proved without using the semi-frame condition. In addition, there exist first considerations by M. Kontak in order to get rid of the semi-frame condition also for the convergence in the domain.

Theorem 17.8 ([163, Thm. 4]). *Let the conditions of Theorem 17.7 be satisfied and let the span of the dictionary be dense in $\mathcal{X}$. Then for all $g^\delta \in \mathcal{Y}$ the function f_∞ obtained by the RFMP solves the Tikhonov-regularized normal equation*

$$(\mathcal{A}^*\mathcal{A} + \tau\mathcal{I}) f_\infty = \mathcal{A}^* g^\delta, \tag{17.4}$$

where $\mathcal{A}^*$ is the adjoint operator of $\mathcal{A}$ and $\mathcal{I}$ is the identity operator on $\mathcal{X}$.

Proof. Since $\mathcal{A}$ is continuous, the sequences $\{\mathcal{A}f_k\}_{k\in\mathbb{N}}$, $\{r_k\}_{k\in\mathbb{N}}$, and $\{\mathcal{A}^*r_k\}_{k\in\mathbb{N}}$ must converge (strongly), too. Due to Lemma 17.4, $\lim_{k\to\infty} \alpha_k = 0$. An immediate consequence of the estimate in Lemma 17.5 is the relation

$$\langle r_k, \mathcal{A}d\rangle_{\mathcal{Y}} - \tau\langle f_k, d\rangle_{\mathcal{X}} = \langle \mathcal{A}^* r_k - \tau f_k, d\rangle_{\mathcal{X}} \to 0 \quad (\text{as } k \to \infty) \tag{17.5}$$

for all $d \in \mathcal{D}$. Due to the bilinearity of the inner product and the algebraic limit theorem, we also have

$$\langle \mathcal{A}^* r_k - \tau f_k, d\rangle_{\mathcal{X}} \to 0 \quad (\text{as } k \to \infty)$$

for all $d \in \operatorname{span} \mathcal{D}$. As we derived above, $\{\mathcal{A}^* r_k - \tau f_k\}_{k\in\mathbb{N}}$ is a strongly convergent and, thus, bounded sequence.

Now, let $h \in \mathcal{X}$ be arbitrary. Since the span of the dictionary is dense in $\mathcal{X}$, there exists a sequence $\{h_m\}_{m\in\mathbb{N}} \subset \operatorname{span}\mathcal{D}$ such that $\|h_m - h\|_{\mathcal{X}} \to 0$ as $m \to \infty$. Then the Cauchy-Schwarz inequality yields

$$\begin{aligned}|\langle \mathcal{A}^* r_k - \tau f_k, h_m - h\rangle_{\mathcal{X}}| &\le \|\mathcal{A}^* r_k - \tau f_k\|_{\mathcal{X}} \, \|h_m - h\|_{\mathcal{X}} \\ &\le \left(\sup_{k\in\mathbb{N}_0} \|\mathcal{A}^* r_k - \tau f_k\|_{\mathcal{X}}\right) \|h_m - h\|_{\mathcal{X}} \\ &\to 0 \qquad (\text{as } m \to \infty).\end{aligned}$$

Since this convergence for m to infinity is uniform with respect to k, we get, by applying the Moore-Osgood double limit theorem, for all $h \in \mathcal{X}$ the identity

$$\begin{aligned}\lim_{k\to\infty} \langle \mathcal{A}^* r_k - \tau f_k, h\rangle_{\mathcal{X}} &= \lim_{k\to\infty} \lim_{m\to\infty} \langle \mathcal{A}^* r_k - \tau f_k, h_m\rangle_{\mathcal{X}} \\ &= \lim_{m\to\infty} \lim_{k\to\infty} \langle \mathcal{A}^* r_k - \tau f_k, h_m\rangle_{\mathcal{X}} \\ &= 0.\end{aligned}$$

This shows that the sequence $\{\mathcal{A}^* r_k\}_{k\in\mathbb{N}}$ weakly converges to τf_∞ in $\mathcal{X}$ (and, due to the considerations above, also strongly). Consequently, using the identity $\mathcal{A}^* r_k = \mathcal{A}^* g^\delta - \mathcal{A}^*\mathcal{A} f_k$ and again the continuity of $\mathcal{A}$, we obtain that

$$\mathcal{A}^* g^\delta - \mathcal{A}^*\mathcal{A} f_\infty = \tau f_\infty,$$

which is equivalent to the Tikhonov-regularized normal equation, see Theorem 16.22. □

It is a basic result of Tikhonov regularization, see Example 16.21, that every solution of Eq. (17.4) minimizes the regularized Tikhonov-Philips functional. If $\tau > 0$, then this minimizer and the solution of the Tikhonov-regularized normal equation are both uniquely determined by

$$f_\infty = (\mathcal{A}^*\mathcal{A} + \tau\mathcal{I})^{-1}\mathcal{A}^* g^\delta, \qquad g^\delta \in \mathcal{Y}.$$

The next result is stated in [210] in the case of $\mathcal{Y} = \mathbb{R}^\ell$. However, the proof is based on Eq. (16.7) and can be applied one-to-one to the case of an infinite-dimensional operator range.

Lemma 17.9 ([210, Lem. 4.2.5]). *Under the assumptions of Theorem 17.7, the function f_∞ produced by the RFMP is contained in the orthogonal complement of the operator null space, that is $f_\infty \in (\ker\mathcal{A})^\perp$.*

Due to this result, the denseness of the span of the dictionary $\mathcal{D}$ in $\mathcal{X}$ in the convergence theorem is an unnecessarily strong condition. We are able to weaken this condition in the next corollary.

Corollary 17.10. *Let the conditions of Theorem 17.7 be fulfilled except that the span of the dictionary $\mathcal{D}$ only has to be dense in $(\ker\mathcal{A})^\perp$. Then f_∞ obtained by the RFMP solves the Tikhonov-regularized normal equation*

$$(\mathcal{A}^*\mathcal{A} + \tau\mathcal{I})\, f_\infty = \mathcal{A}^* g^\delta, \qquad g^\delta \in \mathcal{Y}.$$

Proof. This proof is based on the one of Theorem 17.8. Since $(\ker \mathcal{A})^\perp$ is a closed subspace of the Hilbert space $\mathcal{X}$, the space $((\ker \mathcal{A})^\perp, \langle\cdot,\cdot\rangle_\mathcal{X})$ is a (complete) Hilbert space. We define the operators

$$\begin{aligned}\mathcal{A}_{(\ker \mathcal{A})^\perp} &\coloneqq \mathcal{A}\mathcal{P}_{(\ker \mathcal{A})^\perp} \colon \mathcal{X} \to \mathcal{Y},\\ \mathcal{A}^*_{(\ker \mathcal{A})^\perp} &= \left(\mathcal{A}\mathcal{P}_{(\ker \mathcal{A})^\perp}\right)^* = \mathcal{P}_{(\ker \mathcal{A})^\perp}\mathcal{A}^* = \mathcal{A}^*,\end{aligned}$$

where the last equation is due to $\overline{\operatorname{ran} \mathcal{A}^*} = (\ker \mathcal{A})^\perp$, see Eq. (11.2). Let $f_{\infty,(\ker \mathcal{A})^\perp} \in (\ker \mathcal{A})^\perp$ solve the Tikhonov-regularized normal equation in $((\ker \mathcal{A})^\perp, \langle\cdot,\cdot\rangle_\mathcal{X})$, that is

$$\left(\mathcal{A}^*\mathcal{A}_{(\ker \mathcal{A})^\perp} + \tau \mathcal{I}_{(\ker \mathcal{A})^\perp}\right) f_{\infty,(\ker \mathcal{A})^\perp} = \mathcal{A}^* g^\delta.$$

In addition, we have $\mathcal{A}f = \mathcal{A}_{(\ker \mathcal{A})^\perp} f$ for all $f \in \mathcal{X}$. Thus, we arrive at

$$\left(\mathcal{A}^*\mathcal{A} + \tau \mathcal{I}_{(\ker \mathcal{A})^\perp}\right) f_{\infty,(\ker \mathcal{A})^\perp} = \mathcal{A}^* g^\delta.$$

Via Lemma 17.9, we obtain that the solutions of the Tikhonov-regularized normal equations in $((\ker \mathcal{A})^\perp, \langle\cdot,\cdot\rangle_\mathcal{X})$ and in $\mathcal{X}$ coincide. □

If the smoothness of the function f is unknown, it can be necessary to regularize with certain different norms that are generated by a pseudodifferential operator, see Example 16.21. By means of the pseudodifferential operators, we are able to define a function space similar to the Sobolev spaces on the ball defined in Definition 16.1.

Definition 17.11. *Let $\mathcal{B}\colon (\ker \mathcal{A})^\perp \to \mathcal{X}$ be a densely defined pseudodifferential operator with $\|\mathcal{B}f\|_\mathcal{X} \geq \beta \|f\|_\mathcal{X}$ for a $\beta > 0$ and all $f \in \operatorname{dom} \mathcal{B}$. Furthermore, let its singular system $(f_k, g_k; \beta_k)$ be given such that*

$$\mathcal{B}^*\mathcal{B}f = \sum_{k=1}^\infty \beta_k^2 \langle f, f_k\rangle_\mathcal{X} f_k.$$

With the definition

$$\mathcal{E} \coloneqq \left\{ f \in (\ker \mathcal{A})^\perp \;\middle|\; \sum_{k=1}^\infty \beta_k^2 \langle f, f_k\rangle_\mathcal{X}^2 < \infty \right\}$$

we get $\operatorname{dom} \mathcal{B} = \mathcal{E}$, which is dense in $\mathcal{X}$ with respect to the $\mathcal{X}$-norm. In addition, with the inner product

$$\langle f, h\rangle_\mathcal{H} \coloneqq \sum_{k=1}^\infty \beta_k^2 \langle f, f_k\rangle_\mathcal{X} \langle h, f_k\rangle_\mathcal{X} = \langle \mathcal{B}f, \mathcal{B}h\rangle_\mathcal{X},$$

the space $\mathcal{H} \coloneqq \overline{\mathcal{E}}^{\|\cdot\|_\mathcal{H}}$ is a Hilbert space, see also Example 16.21.

Theorem 17.12. *Let $(\mathcal{A}, \mathcal{X}, \mathcal{Y})$ be given as in Problem 17.1, let $\mathcal{H} \subset \mathcal{X}$ as in Definition 17.11, and let $g^\delta \in \mathcal{Y}$. Then the solution of the RFMP with respect to the Tikhonov-functional*

$$\mathcal{J}_\tau(f) = \left\|\mathcal{A}f - g^\delta\right\|_\mathcal{Y}^2 + \tau \|f\|_\mathcal{H}^2$$

converges to $f_\infty \in \mathcal{H}$ fulfilling

$$(\mathcal{P}_\mathcal{H}\mathcal{A}^*\mathcal{A} + \tau\mathcal{B}^*\mathcal{B})f_\infty = \mathcal{P}_\mathcal{H}\mathcal{A}^* g^\delta$$

if the conditions of Theorem 17.7 with respect to the topology in $\mathcal{H}$ are fulfilled. Note that $\mathcal{B}^*$ is the adjoint operator of $\mathcal{B}$ with respect to the topology in $\mathcal{X}$.

Proof. In order to apply Theorem 17.7 to the problem $(\mathcal{A}_\mathcal{H}, \mathcal{H}, \mathcal{Y})$ with $\mathcal{A}_\mathcal{H} \coloneqq \mathcal{A}|_\mathcal{H}$, we need the continuity of $\mathcal{A}_\mathcal{H}$, which is given by

$$\begin{aligned}\|\mathcal{A}_\mathcal{H}\|_{\mathcal{L}(\mathcal{H},\mathcal{Y})} &= \sup_{f\in\mathcal{H}, f\neq 0} \frac{\|\mathcal{A}_\mathcal{H} f\|_\mathcal{Y}}{\|f\|_\mathcal{H}} = \sup_{f\in\mathcal{H}, f\neq 0} \frac{\|\mathcal{A} f\|_\mathcal{Y}}{\|f\|_\mathcal{H}} \\ &\leq \sup_{f\in\mathcal{H}, f\neq 0} \frac{\|\mathcal{A}\|_{\mathcal{L}(\mathcal{X},\mathcal{Y})}\|f\|_\mathcal{X}}{\|f\|_\mathcal{H}} \leq \frac{1}{\beta}\|\mathcal{A}\|_{\mathcal{L}(\mathcal{X},\mathcal{Y})} < \infty.\end{aligned}$$

Here, we used that $\mathcal{A}\colon \mathcal{X} \to \mathcal{Y}$ is a bounded linear operator and $\|f\|_\mathcal{H} \geq \beta\|f\|_\mathcal{X}$ for a $\beta > 0$. Thus, the sequence produced by the RFMP converges to $f_\infty \in \mathcal{H}$, which fulfills

$$(\mathcal{A}_\mathcal{H}^*\mathcal{A}_\mathcal{H} + \tau\mathcal{I}_\mathcal{H})f_\infty = \mathcal{A}_\mathcal{H}^* g^\delta, \tag{17.6}$$

see Theorem 17.7. Note that the adjoint operator $\mathcal{A}_\mathcal{H}^*$ of $\mathcal{A}_\mathcal{H}$ is subject to the $\mathcal{H}$-inner product. For all $f \in \mathcal{H}$, $g^\delta \in \mathcal{Y}$, we also get the relations

$$\begin{aligned}\left\langle f, \mathcal{A}_\mathcal{H}^* g^\delta \right\rangle_\mathcal{H} &= \left\langle \mathcal{A}_\mathcal{H} f, g^\delta \right\rangle_\mathcal{Y} = \left\langle \mathcal{A} f, g^\delta \right\rangle_\mathcal{Y} = \left\langle f, \mathcal{A}^* g^\delta \right\rangle_\mathcal{X}, \\ \left\langle f, \mathcal{A}_\mathcal{H}^* g^\delta \right\rangle_\mathcal{H} &= \left\langle \mathcal{B} f, \mathcal{B}\mathcal{A}_\mathcal{H}^* g^\delta \right\rangle_\mathcal{X} = \left\langle f, \mathcal{B}^*\mathcal{B}\mathcal{A}_\mathcal{H}^* g^\delta \right\rangle_\mathcal{X}.\end{aligned}$$

Thus,

$$\left\langle f, \mathcal{B}^*\mathcal{B}\mathcal{A}_\mathcal{H}^* g^\delta - \mathcal{A}^* g^\delta \right\rangle_\mathcal{X} = 0 \qquad \text{for all } f \in \mathcal{H},$$

which implies $\mathcal{B}^*\mathcal{B}\mathcal{A}_\mathcal{H}^* - \mathcal{P}_\mathcal{H}\mathcal{A}^* \in \mathcal{H}^\perp = \{0\}$ since $\mathcal{H}$ is dense in $\mathcal{X}$ and $\operatorname{ran}\mathcal{B}^* = (\ker\mathcal{B})^\perp = \operatorname{dom}\mathcal{B} \subset \mathcal{H}$. Accordingly, we get $\mathcal{B}^*\mathcal{B}\mathcal{A}_\mathcal{H}^* = \mathcal{P}_\mathcal{H}\mathcal{A}^*$. Due to Example 16.21, the operator $\mathcal{B}^*\mathcal{B}$ has a bounded inverse. Thus, for the adjoint operator $\mathcal{A}_\mathcal{H}^*$, the identity $\mathcal{A}_\mathcal{H}^* = (\mathcal{B}^*\mathcal{B})^{-1}\mathcal{P}_\mathcal{H}\mathcal{A}^*$ holds true. Inserting this into Eq. (17.6), we immediately get

$$\begin{aligned}&((\mathcal{B}^*\mathcal{B})^{-1}\mathcal{P}_\mathcal{H}\mathcal{A}^*\mathcal{A}_\mathcal{H} + \tau\mathcal{I}_\mathcal{H})f_\infty = (\mathcal{B}^*\mathcal{B})^{-1}\mathcal{P}_\mathcal{H}\mathcal{A}^* g^\delta, \\ \Leftrightarrow\quad &(\mathcal{P}_\mathcal{H}\mathcal{A}^*\mathcal{A} + \tau\mathcal{B}^*\mathcal{B})f_\infty = \mathcal{P}_\mathcal{H}\mathcal{A}^* g^\delta.\end{aligned}$$

□

If more knowledge on the operator $\mathcal{A}$ is available, for instance an SVD $\{f_k, g_k; \lambda_k\}_{k\in\mathbb{N}}$, then the spanning condition for the dictionary in Theorem 17.8 can be weakened.

Theorem 17.13 ([163, Thm. 6]). *Let $g^\delta \in \mathcal{Y}$ and $\mathcal{A}$ be given as in Problem 17.1 where additionally $\mathcal{A}$ is assumed to be a compact operator with singular system $\{f_k, g_k; \lambda_k\}_{k\in\mathbb{N}}$. Let the conditions of Theorem 17.8 be fulfilled, except that the dictionary is only a spanning set for $\mathcal{V} \coloneqq \overline{\operatorname{span}\{f_k\}_{k\in\mathbb{J}}}$, where $\mathbb{J} \subset \mathbb{N}$ is a countable index set.*

Then the solution $f_{\infty,\mathcal{V}} \in \mathcal{V}$ produced by the RFMP and the unique solution of the Tikhonov-regularized normal equation $f_\infty \in \mathcal{X}$ satisfy

$$(\mathcal{A}^*\mathcal{A} + \tau\mathcal{I})f_{\infty,\mathcal{V}} = (\mathcal{A}^*\mathcal{A} + \tau\mathcal{I})\mathcal{P}_\mathcal{V} f_\infty.$$

If $\tau > 0$, then the operator $\mathcal{A}^*\mathcal{A} + \tau\mathcal{I}$ is one-to-one and we obtain $f_{\infty,\mathcal{V}} = \mathcal{P}_\mathcal{V} f_\infty$.

Proof. $(\mathcal{V}, \langle\cdot,\cdot\rangle_\mathcal{X})$ is a Hilbert space since $\mathcal{V} \subset \mathcal{X}$ is closed. The operator $\mathcal{A}_\mathcal{V} \coloneqq \mathcal{A}\mathcal{P}_\mathcal{V}$ is a bounded operator $\mathcal{A}_\mathcal{V}\colon \mathcal{X} \to \mathbb{R}^\ell$ and, hence, its restriction $\mathcal{A}_\mathcal{V}|_\mathcal{V}\colon \mathcal{V} \to \mathbb{R}^\ell$ is also bounded, where $\mathcal{A}_\mathcal{V}|_\mathcal{V} = \mathcal{A}|_\mathcal{V}$. We can apply Theorem 17.7 to this setting and obtain the solution $f_{\infty,\mathcal{V}} \in \mathcal{V}$ produced by the RFMP, which due to Theorem 17.8 solves the Tikhonov-regularized normal equation in $\mathcal{V}$, that is

$$(\mathcal{A}_\mathcal{V}^*\mathcal{A}_\mathcal{V} + \tau\mathcal{I}_\mathcal{V})f_{\infty,\mathcal{V}} = \mathcal{A}_\mathcal{V}^* g^\delta.$$

In order to prove that $f_{\infty,\mathcal{V}}$ is the best approximation of f_∞ in $\mathcal{V}$, it remains to show that $f_{\infty,\mathcal{V}} = \mathcal{P}_\mathcal{V} f_\infty$. For this purpose, we study the singular system $\{f_k, g_k; \lambda_k\}_{k\in\mathbb{N}}$ of $\mathcal{A}$, which exists because of the compactness of $\mathcal{A}$. Due to the construction of $\mathcal{V}$, we obtain for each $k \in \mathbb{N}$ that f_k is either in $\mathcal{V}$ or in $\mathcal{V}^\perp$. Hence, $\mathcal{A}^*\mathcal{A}$ and $\mathcal{P}_\mathcal{V}$ commute, that is

$$\mathcal{P}_\mathcal{V}\mathcal{A}^*\mathcal{A}f = \sum_{\substack{k=1\\ f_k\in\mathcal{V}}}^{\infty} \lambda_k^2 \langle f, f_k\rangle_\mathcal{X} f_k = \mathcal{A}^*\mathcal{A}\mathcal{P}_\mathcal{V} f \qquad \text{for all } f \in \mathcal{X}.$$

Due to $\mathcal{A}_\mathcal{V} = \mathcal{A}\mathcal{P}_\mathcal{V}$, see also [102, p. 79], we immediately obtain $\mathcal{A}_\mathcal{V}^* = \mathcal{P}_\mathcal{V}\mathcal{A}^*$. For $f_{\infty,\mathcal{V}}$, we get

$$\begin{aligned}(\mathcal{A}^*\mathcal{A} + \tau\mathcal{I})\, f_{\infty,\mathcal{V}} &= \left(\mathcal{A}^*\mathcal{A}\mathcal{P}_\mathcal{V}^2 + \tau\mathcal{P}_\mathcal{V}\right) f_{\infty,\mathcal{V}} = (\mathcal{P}_\mathcal{V}\mathcal{A}^*\mathcal{A}\mathcal{P}_\mathcal{V} + \tau\mathcal{P}_\mathcal{V})\, f_{\infty,\mathcal{V}}\\ &= (\mathcal{A}_\mathcal{V}^*\mathcal{A}_\mathcal{V} + \tau\mathcal{P}_\mathcal{V})\, f_{\infty,\mathcal{V}} = \mathcal{A}_\mathcal{V}^* g^\delta = \mathcal{P}_\mathcal{V}\mathcal{A}^* g^\delta\\ &= \mathcal{P}_\mathcal{V}\left((\mathcal{A}^*\mathcal{A} + \tau\mathcal{I})\, f_\infty\right) = (\mathcal{A}^*\mathcal{A} + \tau\mathcal{I})\, \mathcal{P}_\mathcal{V} f_\infty.\end{aligned}$$

Via Theorem 16.22, the last statement can be proved by applying the inverse operator $(\mathcal{A}^*\mathcal{A} + \tau\mathcal{I})^{-1}$ to the last equation. □

Besides the presented convergence statements in the regularized case, we are also able to achieve a result in the unregularized case, that is $\tau = 0$. The next theorem is a generalization to the infinite-dimensional Hilbert space $\mathcal{Y}$ of the result presented by the author in [163, Cor. 5].

Theorem 17.14. *Let the conditions of Theorem 17.7 be satisfied with $\tau = 0$ (no regularization) and let $\mathcal{W} \coloneqq \operatorname{span}\{\mathcal{A}d \mid d \in \mathcal{D}\}$. Then f_∞ obtained by the RFMP solves $\mathcal{A}f_\infty = \mathcal{P}_{\overline{\mathcal{W}}} g^\delta$, where $\mathcal{P}_{\overline{\mathcal{W}}}$ is the orthogonal projection onto the closed space $\overline{\mathcal{W}}$ and $g^\delta \in \mathcal{Y}$.*

Proof. Due to the continuity of $\mathcal{A}$, the sequence $\{r_k\}_{k\in\mathbb{N}}$ converges strongly, that is $r_\infty = \lim_{k\to\infty} r_k = \lim_{k\to\infty}(g - \mathcal{A}f_k)$. This is inferred from Theorem 17.7, which also holds true for $\tau = 0$. We recall the estimate of Lemma 17.5 with $\tau = 0$, that is

$$0 \le \frac{1}{c_2^2\|\mathcal{A}\|_\mathcal{L}^2} \frac{\langle r_k, \mathcal{A}d\rangle_\mathcal{Y}^2}{\|\mathcal{A}d\|_\mathcal{Y}^2} \le \alpha_{k+1}^2 \to 0 \quad (\text{as } k \to \infty).$$

With the Squeeze Theorem, we directly obtain $\lim_{k\to\infty}\langle r_k, \mathcal{A}d\rangle_\mathcal{Y} = 0$ for all $d \in \mathcal{D}$. Consequently, due to the bilinearity of the inner product and the algebraic limit theorem, we obtain $\lim_{k\to\infty}\langle r_k, h\rangle_\mathcal{Y} = 0$ for all $h \in \mathcal{W}$. Since $\mathcal{A}\mathcal{D}$ is dense in the closed space $\overline{\mathcal{W}}$, there exists for all $h \in \overline{\mathcal{W}}$ a strongly convergent sequence $\{h_m\}_{m\in\mathbb{N}} \subset \mathcal{A}\mathcal{D}$ with $\lim_{m\to\infty}\|h_m - h\|_\mathcal{Y} = 0$. With Lemma 17.3, we conclude that

$$0 \le |\langle r_k, h_m - h\rangle_\mathcal{Y}| \le \|r_k\|_\mathcal{Y}\, \|h_m - h\|_\mathcal{Y} \le \|r_0\|_\mathcal{Y}\, \|h_m - h\|_\mathcal{Y} \to 0 \quad (\text{as } m \to \infty),$$

where the convergence in m is uniform with respect to k. Thus, using the Moore-Osgood double limit theorem, we obtain for all $h \in \overline{\mathcal{W}}$ the limit

$$\lim_{k\to\infty} \langle r_k, h\rangle_{\mathcal{Y}} = \lim_{k\to\infty} \lim_{m\to\infty} \langle r_k, h_m\rangle_{\mathcal{Y}} = \lim_{m\to\infty} \lim_{k\to\infty} \langle r_k, h_m\rangle_{\mathcal{Y}} = 0.$$

Since $\overline{\mathcal{W}}$ is closed, we can decompose $\mathcal{Y} = \overline{\mathcal{W}} \oplus \overline{\mathcal{W}}^{\perp}$. The residual has the unique representation $r_k = \mathcal{P}_{\overline{\mathcal{W}}} r_k + \mathcal{P}_{\overline{\mathcal{W}}^{\perp}} r_k$, where $\langle \mathcal{P}_{\overline{\mathcal{W}}^{\perp}} r_k, h\rangle_{\mathcal{Y}} = 0$ for all $h \in \overline{\mathcal{W}}$. Thus,

$$0 = \lim_{k\to\infty} \langle r_k, h\rangle_{\mathcal{Y}} = \lim_{k\to\infty} \langle \mathcal{P}_{\overline{\mathcal{W}}} r_k, h\rangle_{\mathcal{Y}} = \langle \mathcal{P}_{\overline{\mathcal{W}}} r_\infty, h\rangle_{\mathcal{Y}},$$

where we used the continuity of the orthogonal projection $\mathcal{P}_{\overline{\mathcal{W}}}$. Concluding, $\{\mathcal{P}_{\overline{\mathcal{W}}} r_k\}_{k\in\mathbb{N}}$ weakly converges to zero in $\overline{\mathcal{W}}$. Due to the uniqueness of the limit, we obtain $\mathcal{P}_{\overline{\mathcal{W}}} r_\infty = 0$. Eventually, we conclude

$$0 = \mathcal{P}_{\overline{\mathcal{W}}} r_\infty = \mathcal{P}_{\overline{\mathcal{W}}} \left(g^\delta - \mathcal{A} f_\infty \right) = \mathcal{P}_{\overline{\mathcal{W}}} g^\delta - \mathcal{A} f_\infty. \qquad \square$$

If the dictionary fulfils $\mathbb{R}^\ell = \operatorname{span}\{\mathcal{A}d \mid d \in \mathcal{D}\}$ for a surjective operator $\mathcal{A}$ with finite-dimensional range, then the previous theorem coincides with the results in [66, Thm. 3.5], [67, Thm. 4.5], [159, Thm. 2], and [165, Thm. 6.3].

For a fixed regularization parameter $\tau > 0$, we have already seen that the limit of the sequence $\{f_k\}_{k\in\mathbb{N}}$ of approximations obtained by the RFMP converges to f_∞, which is the unique minimizer of the Tikhonov-Philips functional. This is an indicator for the RFMP inducing a regularization in the sense of Definition 16.12.

In [210, Thm. 4.2.7], this is proved for the case of a finite range operator without a convergence order. In [137], this is generalized to the setting of Problem 17.1 under appropriate assumptions. In addition, the statement in [137] takes into account that the RFMP stops after a finite number of iterations K.

Theorem 17.15 ([137, Thm. 9.35]). *Let $\{f^\delta_{\tau,k}\}_{k\in\mathbb{N}_0}$ be the sequence of iterations of the RFMP to the inverse problem $\mathcal{A}f = g^\delta$ with $g^\delta \in \mathcal{Y}$ fulfilling $\|g - g^\delta\|_{\mathcal{Y}} \leq \delta$ using the regularization parameter $\tau > 0$. We assume that*

- *the dictionary is normalized in the sense that $\|\mathcal{A}d\|^2_{\mathcal{Y}} + \|d\|^2_{\mathcal{X}} = 1$ for all $d \in \mathcal{D}$,*
- *the best-approximate solution f^+ fulfils a Hölder-type source condition for $\nu = 1$, see also Definition 16.15,*
- *the function $|f^\delta_{\tau,k}|_{\mathcal{D}}$ is uniformly bounded with respect to τ, where $|\cdot|_{\mathcal{D}}$ is a certain measure for the sparsity, see [137, Lem. 9.30], and*
- *there exist constants m_1, $m_2 > 0$ such that $\tau(\delta) = m_1\delta^{2/3}$ and $K(\delta) = m_2\delta^{-6}$.*

Then there exists a constant $C > 0$ such that

$$\left\| f^\delta_{\tau,K(\delta)} - f^+ \right\|_{\mathcal{X}} \leq C\delta^{2/3}.$$

Eventually, this theorem shows that the RFMP has a convergence rate of $\delta^{2/3}$ for $\delta \to 0+$ and that this rate can even be retained when only a finite number of iterations is used, see [137, p. 160].

This convergence rate is not surprising, since the order of convergence of the Tikhonov regularization is also $\delta^{2/3}$. This order of convergence is optimal with respect to the source condition, see Eq. (16.6).

17.2. Regularized Functional Matching Pursuit Algorithm for Simultaneous Inversion

The RFMP can be used for a simultaneous joint inversion of several data types. This can be reasonable if a source induces several physical quantities that can be measured. Then a joint inversion of these quantities can yield more information about the source than the single inversion of each data set. For example, the RFMP has been used before for a joint inversion of gravitational data and normal mode anomalies in order to reconstruct the mass density inside the Earth, see [66]. Hence, the question arises whether a joint inversion of MEG and EEG data also exhibits this advantage when reconstructing the neuronal current. Due to the structure of the MEG and EEG null spaces, we are able to prove in this section that a joint inversion cannot yield more details of the neuronal current than independent single inversions.

For this purpose, we define for each $i = 1, 2, 3$ the Hilbert space

$$\tilde{\mathbf{L}}_2^{(i)}(\mathbb{B}_{\varrho_0}) \coloneqq \overline{\left\{ \boldsymbol{x} \mapsto \tilde{\boldsymbol{o}}_{\hat{\boldsymbol{x}}}^{(i)} F(\boldsymbol{x}) \;\middle|\; F \in \mathrm{C}^\infty(\mathbb{B}_{\varrho_0}) \right\}}^{\|\cdot\|_{\mathbf{L}_2(\mathbb{B}_{\varrho_0})}},$$

which is a similar construction to the vector-valued Hilbert space on the sphere from Eq. (5.10). Recall that more details of the inverse MEG and EEG problem can be found in Problems 9.1 and 10.2.

Problem 17.16 (Joint Inversion of MEG and EEG Data). *In all three cases, we want to solve Problem 17.1 by means of the RFMP, where the occurring quantities are determined in the following. In addition, we choose the same regularization parameter $\tau > 0$ for the RFMP in all three cases.*

MEG: Let $\mathcal{X}_{\mathrm{M}} \coloneqq \left(\tilde{\mathbf{L}}_2^{(3)}(\mathbb{B}_{\varrho_0}), \langle\cdot,\cdot\rangle_{\mathbf{L}_2(\mathbb{B}_{\varrho_0})}\right)$ *and let* $\mathcal{Y}_{\mathrm{M}} \coloneqq \mathbb{R}^{\ell_{\mathrm{M}}}$ *with an* $\ell_{\mathrm{M}} \in \mathbb{N}$. *Let the data vector* $\boldsymbol{g}_{\mathrm{M}} \in \mathbb{R}^{\ell_{\mathrm{M}}}$ *be given. Then the forward operator is given by*

$$\mathcal{A}_{\mathrm{M}} \colon \mathcal{X}_{\mathrm{M}} \to \mathbb{R}^{\ell_{\mathrm{M}}}, \qquad \mathcal{A}_{\mathrm{M}} \boldsymbol{J}^{\mathrm{P}} \coloneqq \sum_{\ell=1}^{\ell_{\mathrm{M}}} \left(\boldsymbol{\nu}(\boldsymbol{y}_\ell) \cdot \left(\mathcal{T}_{\mathrm{M}} \boldsymbol{J}^{\mathrm{P}} \right)(\boldsymbol{y}_\ell) \right) \boldsymbol{\varepsilon}^\ell,$$

where $\boldsymbol{\varepsilon}^\ell$ *is the* ℓ*th canonical unit vector. In addition, let the span of the dictionary* $\mathcal{D}_{\mathrm{M}}$ *be dense in* $(\ker \mathcal{A}_{\mathrm{M}})^\perp$, *bounded, and satisfy the semi-frame condition in* $\mathcal{X}_{\mathrm{M}}$ *as well as the condition in Lemma 17.4.*

EEG: Let $\mathcal{X}_{\mathrm{E}} \coloneqq \left(\tilde{\mathbf{L}}_2^{(2)}(\mathbb{B}_{\varrho_0}), \langle\cdot,\cdot\rangle_{\mathbf{L}_2(\mathbb{B}_{\varrho_0})}\right)$ *and let* $\mathcal{Y}_{\mathrm{E}} \coloneqq \mathbb{R}^{\ell_{\mathrm{E}}}$ *with an* $\ell_{\mathrm{E}} \in \mathbb{N}$. *Let the data vector* $\boldsymbol{g}_{\mathrm{E}} \in \mathbb{R}^{\ell_{\mathrm{E}}}$ *be given. Then the forward operator is given by*

$$\mathcal{A}_{\mathrm{E}} \colon \mathcal{X}_{\mathrm{E}} \to \mathbb{R}^{\ell_{\mathrm{E}}}, \qquad \mathcal{A}_{\mathrm{E}} \boldsymbol{J}^{\mathrm{P}} \coloneqq \sum_{\ell=1}^{\ell_{\mathrm{E}}} \left(\mathcal{T}_{\mathrm{E}} \boldsymbol{J}^{\mathrm{P}} \right)(\boldsymbol{y}_{\ell_{\mathrm{M}}+\ell}) \boldsymbol{\varepsilon}^\ell.$$

In addition, let the span of the dictionary $\mathcal{D}_{\mathrm{E}}$ *be dense in* $(\ker \mathcal{A}_{\mathrm{E}})^\perp$, *bounded, and satisfy the semi-frame condition in* $\mathcal{X}_{\mathrm{E}}$ *as well as the condition in Lemma 17.4.*

Joint: Let $\mathcal{X}$ *be defined by the internal direct sum, that is* $\mathcal{X} \coloneqq \mathcal{X}_{\mathrm{M}} \oplus \mathcal{X}_{\mathrm{E}}$, *let* $\mathcal{Y} \coloneqq \mathbb{R}^{\ell_\Sigma}$ *with* $\ell_\Sigma \coloneqq \ell_{\mathrm{M}} + \ell_{\mathrm{E}}$, *let the data be given by* $\boldsymbol{g}^{\mathrm{T}} \coloneqq (\boldsymbol{g}_{\mathrm{M}}^{\mathrm{T}}, \boldsymbol{g}_{\mathrm{E}}^{\mathrm{T}}) \in \mathbb{R}^{\ell_\Sigma}$, *and let the operator*

$\mathcal{A}\colon \mathcal{X} \to \mathbb{R}^{\ell_\Sigma}$ *for the RFMP be given by*

$$\mathcal{A}\boldsymbol{J}^{\mathrm{P}} \coloneqq \left(\left(\mathcal{A}_{\mathrm{M}} \left(\mathcal{P}_{\mathcal{X}_{\mathrm{M}}} \boldsymbol{J}^{\mathrm{P}} \right) \right)^{\mathrm{T}}, \left(\mathcal{A}_{\mathrm{E}} \left(\mathcal{P}_{\mathcal{X}_{\mathrm{E}}} \boldsymbol{J}^{\mathrm{P}} \right) \right)^{\mathrm{T}} \right)^{\mathrm{T}}. \tag{17.7}$$

For the dictionary, we choose $\mathcal{D} = \mathcal{D}_{\mathrm{M}} \cup \mathcal{D}_{\mathrm{E}}$.

In this setting, we can prove that no more information can be obtained by a simultaneous joint inversion based on the RFMP than by the independent inversion of both data sets. Note that the precise representation of $\mathcal{A}_{\mathrm{M}}$ and $\mathcal{A}_{\mathrm{E}}$ is not necessary for the proof.

Theorem 17.17. *Let the setting of Problem 17.16 be given, let a fixed regularization parameter* $\tau > 0$ *be chosen for all three cases. Then the RFMP solution of the joint case* $\boldsymbol{f}_\infty$ *coincides with the sum of the solutions independently obtained by the RFMP in the MEG and EEG case, that is* $\boldsymbol{f}_\infty = \boldsymbol{f}_{\mathrm{M},\infty} + \boldsymbol{f}_{\mathrm{E},\infty}$.

Proof. Note that Problem 17.16 implies all conditions of Theorem 17.8. Thus, we immediately obtain that the two solutions of the independent cases fulfil

$$(\mathcal{A}_{\mathrm{M}}^* \mathcal{A}_{\mathrm{M}} + \tau \mathcal{I}_{\mathcal{X}_{\mathrm{M}}}) \boldsymbol{f}_{\mathrm{M},\infty} = \mathcal{A}_{\mathrm{M}}^* g_{\mathrm{M}}, \qquad \text{in } \mathcal{X}_{\mathrm{M}}, \tag{17.8a}$$

$$(\mathcal{A}_{\mathrm{E}}^* \mathcal{A}_{\mathrm{E}} + \tau \mathcal{I}_{\mathcal{X}_{\mathrm{E}}}) \boldsymbol{f}_{\mathrm{E},\infty} = \mathcal{A}_{\mathrm{E}}^* g_{\mathrm{E}}, \qquad \text{in } \mathcal{X}_{\mathrm{E}}. \tag{17.8b}$$

In the joint case, we also obtain a Tikhonov-regularized normal equation in $\mathcal{X}$. In addition, $\overline{\operatorname{ran} \mathcal{A}_{\mathrm{M}}^*} = (\ker \mathcal{A}_{\mathrm{M}})^\perp \subset \mathcal{X}_{\mathrm{M}} \perp \mathcal{X}_{\mathrm{E}} \supset (\ker \mathcal{A}_{\mathrm{E}})^\perp = \overline{\operatorname{ran} \mathcal{A}_{\mathrm{E}}^*}$, see also Eq. (11.2). This complementarity of the orthogonal complements of the operator null spaces is essential for this proof. In order to prove the statement, we first calculate the adjoint operator $\mathcal{A}^*$ of the joint operator $\mathcal{A}$ in $\mathcal{X}$. It has to fulfil $\langle \mathcal{A}^* \boldsymbol{h}, \boldsymbol{f} \rangle_{\mathcal{X}} = \langle \boldsymbol{h}, \mathcal{A}\boldsymbol{f} \rangle_{\mathbb{R}^{\ell_\Sigma}}$ for all $\boldsymbol{f} \in \mathcal{X}$, $\boldsymbol{h} \in \mathbb{R}^{\ell_\Sigma}$. The vector $\boldsymbol{h}$ can be decomposed into $\boldsymbol{h}^{\mathrm{T}} = (\boldsymbol{h}_{\mathrm{M}}^{\mathrm{T}}, \boldsymbol{h}_{\mathrm{E}}^{\mathrm{T}})$ with $\boldsymbol{h}_{\mathrm{M}} \coloneqq \sum_{\ell=1}^{\ell_{\mathrm{M}}} (\boldsymbol{h})_\ell \boldsymbol{\varepsilon}^\ell$ and $\boldsymbol{h}_{\mathrm{E}} \coloneqq \sum_{\ell=1}^{\ell_{\mathrm{E}}} (\boldsymbol{h})_{\ell_{\mathrm{M}}+\ell} \boldsymbol{\varepsilon}^\ell$. Thus, via Eq. (17.7) we get

$$\begin{aligned}
\langle \boldsymbol{h}, \mathcal{A}\boldsymbol{f} \rangle_{\mathbb{R}^{\ell_\Sigma}} &= \langle \boldsymbol{h}_{\mathrm{M}}, \mathcal{A}_{\mathrm{M}} \mathcal{P}_{\mathcal{X}_{\mathrm{M}}} \boldsymbol{f} \rangle_{\mathbb{R}^{\ell_{\mathrm{M}}}} + \langle \boldsymbol{h}_{\mathrm{E}}, \mathcal{A}_{\mathrm{E}} \mathcal{P}_{\mathcal{X}_{\mathrm{E}}} \boldsymbol{f} \rangle_{\mathbb{R}^{\ell_{\mathrm{E}}}} \\
&= \langle \mathcal{A}_{\mathrm{M}}^* \boldsymbol{h}_{\mathrm{M}}, \mathcal{P}_{\mathcal{X}_{\mathrm{M}}} \boldsymbol{f} \rangle_{\mathcal{X}_{\mathrm{M}}} + \langle \mathcal{A}_{\mathrm{E}}^* \boldsymbol{h}_{\mathrm{E}}, \mathcal{P}_{\mathcal{X}_{\mathrm{E}}} \boldsymbol{f} \rangle_{\mathcal{X}_{\mathrm{E}}} \\
&= \langle \mathcal{A}_{\mathrm{M}}^* \boldsymbol{h}_{\mathrm{M}}, \mathcal{P}_{\mathcal{X}_{\mathrm{M}}} \boldsymbol{f} \rangle_{\mathcal{X}} + \langle \mathcal{A}_{\mathrm{E}}^* \boldsymbol{h}_{\mathrm{E}}, \mathcal{P}_{\mathcal{X}_{\mathrm{E}}} \boldsymbol{f} \rangle_{\mathcal{X}} \\
&= \langle \mathcal{A}_{\mathrm{M}}^* \boldsymbol{h}_{\mathrm{M}}, \boldsymbol{f} \rangle_{\mathcal{X}} + \langle \mathcal{A}_{\mathrm{E}}^* \boldsymbol{h}_{\mathrm{E}}, \boldsymbol{f} \rangle_{\mathcal{X}} \\
&= \langle \mathcal{A}_{\mathrm{M}}^* \boldsymbol{h}_{\mathrm{M}} + \mathcal{A}_{\mathrm{E}}^* \boldsymbol{h}_{\mathrm{E}}, \boldsymbol{f} \rangle_{\mathcal{X}}.
\end{aligned}$$

The last step is valid due to the orthogonality and structure of the occurring spaces. Eventually, we obtain $\mathcal{A}^* \boldsymbol{h} = \mathcal{A}_{\mathrm{M}}^* \boldsymbol{h}_{\mathrm{M}} + \mathcal{A}_{\mathrm{E}}^* \boldsymbol{h}_{\mathrm{E}}$ for all $\boldsymbol{h} \in \mathbb{R}^{\ell_\Sigma}$, in particular for $\boldsymbol{h} = \boldsymbol{g}$. Setting $\boldsymbol{h} = \mathcal{A}\boldsymbol{f}_\infty$, we immediately arrive at

$$\mathcal{A}^* \mathcal{A} \boldsymbol{f}_\infty = \mathcal{A}_{\mathrm{M}}^* \mathcal{A}_{\mathrm{M}} \mathcal{P}_{\mathcal{X}_{\mathrm{M}}} \boldsymbol{f}_\infty + \mathcal{A}_{\mathrm{E}}^* \mathcal{A}_{\mathrm{E}} \mathcal{P}_{\mathcal{X}_{\mathrm{E}}} \boldsymbol{f}_\infty.$$

Thus, for the Tikhonov-regularized normal equation in $\mathcal{X}$, we obtain the identity

$$\begin{aligned}
\mathcal{A}_{\mathrm{M}}^* \boldsymbol{g}_{\mathrm{M}} + \mathcal{A}_{\mathrm{E}}^* \boldsymbol{g}_{\mathrm{E}} &= \mathcal{A}^* \boldsymbol{g} = (\mathcal{A}^* \mathcal{A} + \tau \mathcal{I})\, \boldsymbol{f}_\infty \\
&= (\mathcal{A}_{\mathrm{M}}^* \mathcal{A}_{\mathrm{M}} + \tau \mathcal{I}_{\mathcal{X}_{\mathrm{M}}})\, \mathcal{P}_{\mathcal{X}_{\mathrm{M}}} \boldsymbol{f}_\infty + (\mathcal{A}_{\mathrm{E}}^* \mathcal{A}_{\mathrm{E}} + \tau \mathcal{I}_{\mathcal{X}_{\mathrm{E}}})\, \mathcal{P}_{\mathcal{X}_{\mathrm{E}}} \boldsymbol{f}_\infty.
\end{aligned}$$

The complementarity of the adjoint operator ranges allows to split the last equation into a system of two equations, that is

$$\begin{aligned} \mathcal{A}_{\mathrm{M}}^{*}\boldsymbol{g}_{\mathrm{M}} &= (\mathcal{A}_{\mathrm{M}}^{*}\mathcal{A}_{\mathrm{M}} + \tau\mathcal{I}_{\mathcal{X}_{\mathrm{M}}})\,\mathcal{P}_{\mathcal{X}_{\mathrm{M}}}\boldsymbol{f}_{\infty}, && \text{in } \mathcal{X}_{\mathrm{M}}, \\ \mathcal{A}_{\mathrm{E}}^{*}\boldsymbol{g}_{\mathrm{E}} &= (\mathcal{A}_{\mathrm{E}}^{*}\mathcal{A}_{\mathrm{E}} + \tau\mathcal{I}_{\mathcal{X}_{\mathrm{E}}})\,\mathcal{P}_{\mathcal{X}_{\mathrm{E}}}\boldsymbol{f}_{\infty}, && \text{in } \mathcal{X}_{\mathrm{E}}. \end{aligned}$$

With Eq. (17.8), we get

$$\begin{aligned} (\mathcal{A}_{\mathrm{M}}^{*}\mathcal{A}_{\mathrm{M}} + \tau\mathcal{I}_{\mathcal{X}_{\mathrm{M}}})\boldsymbol{f}_{\mathrm{M},\infty} &= (\mathcal{A}_{\mathrm{M}}^{*}\mathcal{A}_{\mathrm{M}} + \tau\mathcal{I}_{\mathcal{X}_{\mathrm{M}}})\,\mathcal{P}_{\mathcal{X}_{\mathrm{M}}}\boldsymbol{f}_{\infty}, \\ (\mathcal{A}_{\mathrm{E}}^{*}\mathcal{A}_{\mathrm{E}} + \tau\mathcal{I}_{\mathcal{X}_{\mathrm{E}}})\boldsymbol{f}_{\mathrm{E},\infty} &= (\mathcal{A}_{\mathrm{E}}^{*}\mathcal{A}_{\mathrm{E}} + \tau\mathcal{I}_{\mathcal{X}_{\mathrm{E}}})\,\mathcal{P}_{\mathcal{X}_{\mathrm{E}}}\boldsymbol{f}_{\infty}. \end{aligned}$$

The two occurring operators are one-to-one since $\tau > 0$, see Theorem 16.22. Thus, $\boldsymbol{f}_{\mathrm{M},\infty} = \mathcal{P}_{\mathcal{X}_{\mathrm{M}}}\boldsymbol{f}_{\infty}$ and $\boldsymbol{f}_{\mathrm{E},\infty} = \mathcal{P}_{\mathcal{X}_{\mathrm{E}}}\boldsymbol{f}_{\infty}$. □

Note that this property holds true in a more general setting.

Remark 17.18. *The statement of theorem is achieved without particular properties of the RFMP. If the three solutions $\boldsymbol{f}_{\infty}$, $\boldsymbol{f}_{\mathrm{M},\infty}$, and $\boldsymbol{f}_{\mathrm{E},\infty}$ are just the unique solutions of the respective Tikhonov-regularized normal equations corresponding to the setting of Problem 17.16, then $\boldsymbol{f}_{\infty} = \boldsymbol{f}_{\mathrm{M},\infty} + \boldsymbol{f}_{\mathrm{E},\infty}$.*

Since the solution obtained by the simultaneous inversion of both data sets equals the sum of the solutions obtained by the independent inversion of each single data set, no additional information is gained.

Furthermore, the separated inversion is more efficient than the simultaneous one for the following reasons. For the RFMP, the inner products between all dictionary elements are required, see Eq. (17.1). Thus, finding the maximum in Eq. (17.1) can be accelerated by splitting the inversion since the memory capacity requirement for storing these inner products grows quadratically with the amount of dictionary elements. Another problem in the simultaneous inversion of two different data sets emerges if the magnitude of the data differs, see [66]. Therein, the data sets have to be weighted in order to obtain a good reconstruction. This is unnecessary in the case of a split inversion. Additionally, a split inversion provides us with the possibility to fit the regularization parameter to the particular problems without a modification of the RFMP algorithm and its implementation. This statement holds true for all problems where the operator $\mathcal{A}$ consists of a finite amount of operators $\mathcal{A}_i$ with $(\ker \mathcal{A}_i)^{\perp} \perp (\ker \mathcal{A}_j)^{\perp}$ for $i \neq j$.

17.3. Regularized Orthogonal Functional Matching Pursuit Algorithm

A problem of the RFMP occurring in numerical tests is that certain dictionary elements may be chosen repeatedly. This can be understood as a correction for some previously chosen coefficients $\alpha_1, \ldots, \alpha_k$. A reason for this phenomenon is that the residual r_k is not orthogonal to the image of the span of the previously chosen dictionary elements, that is span $\{\mathcal{A}d_1, \ldots, \mathcal{A}d_k\}$. In order to get rid of this unwanted effect, an enhancement of the RFMP is developed in [210]. Therein, an orthogonalization step based on the idea of [186, 218] is introduced. The final algorithm is called the regularized orthogonal functional

matching pursuit algorithm (ROFMP) and is stated in [166, 210]. A short overview of the ROFMP can also be found in [86].

Unfortunately, at the state of art the ROFMP is only analyzed in the case of a finite-dimensional space $\mathcal{Y}$. Therefore, $\mathcal{Y}$ coincides with the $\mathbb{R}^\ell$ for an $\ell \in \mathbb{N}$. According to our notation, elements of this space are denoted by bold letters. However, for a consistent notation to Algorithm 17.2 we use non-bold letters in this Section 17.3.

Algorithm 17.19 (ROFMP, [86, Algo. 8]). *Let $\mathcal{A}$ and g be given as in Problem 17.1 with $\mathcal{Y} \coloneqq \mathbb{R}^\ell$ and $\ell \in \mathbb{N}$. Choose a stopping criterion, a dictionary $\mathcal{D} \subset \mathcal{X}$, an initial approximation $f_0 \in \mathcal{X}$, and a regularization parameter $\tau \in \mathbb{R}_0^+$.*

i) Initialize the step counter to $k \coloneqq 0$, define the residual $r_0 \coloneqq g - \mathcal{A}f_0$, set $\mathcal{V}_0 \coloneqq \emptyset$, $\mathcal{W}_0 \coloneqq \mathcal{V}_0^\perp$, and $\mathcal{B}_0(d) \coloneqq \mathcal{I}_\mathcal{X}$.

ii) Find

$$d_{k+1} \coloneqq \operatorname*{arg\,max}_{d\in\mathcal{D}} \frac{\left(\langle r_k, \mathcal{P}_{\mathcal{W}_k}(\mathcal{A}d)\rangle_{\mathbb{R}^\ell} + \tau\langle f_k, \mathcal{B}_k(d) - d\rangle_\mathcal{X}\right)^2}{\|\mathcal{P}_{\mathcal{W}_k}(\mathcal{A}d)\|_{\mathbb{R}^\ell}^2 + \tau\|\mathcal{B}_k(d) - d\|_\mathcal{X}^2} \tag{17.9}$$

and set

$$\alpha_{k+1} \coloneqq \frac{\langle r_k, \mathcal{P}_{\mathcal{W}_k}(\mathcal{A}d_{k+1})\rangle_{\mathbb{R}^\ell} + \tau\langle f_k, \mathcal{B}_k(d_{k+1}) - d_{k+1}\rangle_\mathcal{X}}{\|\mathcal{P}_{\mathcal{W}_k}(\mathcal{A}d_{k+1})\|_{\mathbb{R}^\ell}^2 + \tau\|\mathcal{B}_{k+1}(d_{k+1}) - d_{k+1}\|_\mathcal{X}^2}. \tag{17.10}$$

iii) For all $d \in \mathcal{D}$, define the mappings

$$\begin{aligned}
\beta_k^{(k)}(d) &\coloneqq \frac{\langle \mathcal{A}d, \mathcal{P}_{\mathcal{W}_{k-1}}\mathcal{A}d_k\rangle_{\mathbb{R}^\ell}}{\|\mathcal{P}_{\mathcal{W}_{k-1}}\mathcal{A}d_k\|_{\mathbb{R}^\ell}^2},\\
\beta_i^{(k)}(d) &= \beta_i^{(k-1)}(d) - \beta_k^{(k)}(d)\beta_i^{(k-1)}(d_k) \qquad \text{for } i = 1, \dots, k-1,\\
\mathcal{B}_k(d) &\coloneqq \sum_{i=1}^k \beta_i^{(k)}(d) d_i.
\end{aligned}$$

iv) Update the coefficients as follows:

$$\begin{aligned}
\alpha_i^{(k+1)} &= \alpha_i^{(k)} - \alpha_{k+1}\beta_i^{(k)}(d_{k+1}) \qquad \text{for } i = 1, \dots, k,\\
\alpha_{k+1}^{(k+1)} &= \alpha_{k+1}
\end{aligned}$$

and set $f_{k+1} \coloneqq \sum_{i=1}^{k+1} \alpha_i^{(k+1)} d_i$ as well as $r_{k+1} \coloneqq g - \mathcal{A}f_{k+1}$. Update the spaces such that

$$\mathcal{V}_{k+1} \coloneqq \operatorname{span}\{\mathcal{A}d_1, \dots, \mathcal{A}d_{k+1}\}, \qquad \mathcal{W}_{k+1} = \mathcal{V}_{k+1}^\perp.$$

v) If the stopping criterion is satisfied, then use f_{k+1} as an approximate solution to $\mathcal{A}f = g$. Otherwise, increase k by 1 and go to step ii).

The functionals $\beta_i^{(k)}$ are used for the projection of $\mathcal{A}d$ onto $\mathcal{V}_k$, since the images of the dictionary elements under $\mathcal{A}$ are not necessarily orthogonal, that is

$$\mathcal{A}f_{k+1} = \sum_{i=1}^k \left(\alpha_i^{(k)} - \alpha_{k+1}\beta_i^{(k)}(d_{k+1})\right)\mathcal{A}d_i + \alpha_{k+1}\mathcal{A}d_{k+1}.$$

These functionals are used to correct the dictionary elements by means of the operator $\mathcal{B}_k$. This correction is sometimes called backfitting.

Theorem 17.20 ([210, Thm. 4.3.6]). *Let* $\operatorname{span}\{\mathcal{A}d \mid d \in \mathcal{D}\} = \mathbb{R}^\ell$ *and* $\tau = 0$. *Then* $\mathcal{V}_\ell = \mathbb{R}^\ell$ *and there exists a number* $L \in \{1, \dots, \ell\}$ *such that* $\mathcal{A}(\sum_{i=1}^{L} \alpha_i^L d_i) = g$ *and, consequently,* $r_L = 0$.

However, this result cannot be transferred to the regularized case. Indeed, the sequence of residuals obtained by the ROFMP stagnates starting from a specific step.

Theorem 17.21 ([210, Thm. 4.3.9]). *Let* ℓ *be the dimension of the data space. Moreover, let functions from* $\mathcal{D}$ *and corresponding coefficients be chosen according to Algorithm 17.19. Then there exists a number* $K \coloneqq K(\tau) \geq \ell$ *such that*

$$r_k = r_K \qquad \text{for all } k \geq K.$$

In order to obtain convergence of the ROFMP, an iterative refinement is necessary. In this case, after a certain number of steps $K \in \mathbb{N}$ the algorithm is restarted with $g - \mathcal{A}f_K$ as the new data vector. It may be useful to keep the previous approximation in the penalty term, see [86, 210].

Theorem 17.22 (Convergence of the Iterated ROFMP, [210, Thm. 4.3.13]). *Let* $\mathcal{A}$ *and* g *be given as in Problem 17.1 with* $\mathcal{Y} \coloneqq \mathbb{R}^\ell$ *and* $\ell > 0$. *Furthermore, let* $0 < K < \infty$ *be a fixed integer and let*

- *the span of the dictionary be dense in* $\mathcal{X}$,
- *there be a constant* $c_1 \in \mathbb{R}^+$ *such that for every* $0 < n < K$ *and every choice of dictionary elements* $d_1, \dots, d_n \in \mathcal{D}$, *we have* $\operatorname{dist}(d, \operatorname{span}\{d_1, \dots, d_n\}) \geq c_1$ *for all* $d \in \mathcal{D} \setminus \{d_1, \dots, d_n\}$, *where* $\operatorname{dist}(d, \mathcal{V}) \coloneqq \inf_{f \in \mathcal{V}} \|d - f\|_{\mathcal{H}}$,
- *the dictionary fulfil* $c_2 \coloneqq \sup_{d \in \mathcal{D}} \|\mathcal{A}d\|_{\mathbb{R}^\ell} < \infty$,
- *the dictionary fulfil, for a constant* $c_3 > 0$, *the condition* $c_3^2 \sum_{i=1}^{K} \gamma_i^2 \leq \|\sum_{i=1}^{K} \gamma_i \mathcal{A}d_i\|_{\mathbb{R}^\ell}^2$ *for all finite linear combinations with* $\gamma_i \in \mathbb{R}$, *and*
- *the dictionary fulfil the semi-frame condition 17.6.*

Then the sequence $\{f_k\}_{k \in \mathbb{N}}$ *produced by the iterated ROFMP converges to* $f_\infty \in \mathcal{X}$.

Part VI.

Numerical Solution of the MEG and EEG Problem

In this part, the regularization method called the RFMP and its enhancement, the ROFMP, will be tested for the inverse MEG and EEG problem. In addition, the results of these algorithms will be compared to existing methods, such as a spline approach or a regularized Ritz method. For a fair comparison of these methods, a synthetic test case, where the exact solution is known, is constructed in Chapter 18. Afterwards, some foundations for the implementation with focus on the RFMP are presented in Chapter 19. However, some of these foundations are also required for the other reconstruction methods. Parts of the theoretical background of these further reconstruction methods are presented in Chapter 20. Having the implementation at hand, the RFMP, the ROFMP, the regularized Ritz method, and some spline methods are used for the reconstruction of the neuronal current from non-noisy and noisy synthetic data in Chapter 21. Therein, the results achieved via the different reconstruction methods are also compared in Section 21.5. Finally, the ROFMP is used for the inversion of real data, see Section 21.6.

All computations in this part are performed on a single node of the HorUS cluster of the University of Siegen. Each node is equipped with 48 GiB memory and two Intel Xeon X5650 CPUs running at 2.66 GHz having a total of 12 (physical) CPU cores. Due to the memory requirements of the methods, we do not share the compute node with other users of the cluster during our computations.

The reconstruction methods considered in this thesis are implemented in Matlab [212] using highly vectorized and parallelized code. In order to accelerate the preprocessing, the inner products of the reproducing kernels in the RFMP preprocessing are calculated by a C++ code, see [207], using OpenMP, see [185]. Matlab code for the evaluation of fully normalized Morse-Feshbach vector spherical harmonics was kindly provided by C. Gerhards, see [92], and Matlab code for the generation of a modified Reuter grid on the ball was kindly provided by A. Ishtiaq, see [128]. In addition, sensor positions of the electro-magnetoencephalography device and real data were provided by O. Hauk, see [116].

Chapter 18.

Synthetic Test Case

In order to validate the results obtained by the reconstruction methods, we construct a synthetic test case similar to the one in [73]. We construct synthetic test currents for the MEG as well as the EEG case separately since both problems are solved independent of each other. In each case, the corresponding synthetic test current is assumed to be in the orthogonal complement of the operator null space in order to handle the non-uniqueness of the ill-posed problems. In order to gain information about the instability of the problems, we generate non-noisy and noisy data from the synthetic test case.

18.1. Synthetic Test Current

First, we need to determine the synthetic test current that we want to reconstruct. We avoid the current to have parts in the null spaces of the forward operators $\mathcal{T}_{\mathrm{M}}$ or $\mathcal{T}_{\mathrm{E}}$, respectively, in order to get a unique reconstruction. Thus, the synthetic current is assumed to fulfil the assumptions of Theorem 13.7. This implies that the synthetic current is harmonic and solenoidal. The current is based on the classical Abel-Poisson kernel, which is also used in [73] for building an appropriate test case. However, it needs to be adapted in order to obtain a vector-valued current. The classical Abel-Poisson kernel is given by the next theorem.

Theorem 18.1 ([81, Lem. 3.2.5]). *For all $h \in (-1,1)$ and all $t \in [-1,1]$, the so-called Abel-Poisson kernel is given by the following Legendre series with closed representation:*

$$\frac{1}{4\pi}\frac{1-h^2}{(1+h^2-2ht)^{3/2}} = \sum_{n=0}^{\infty}\frac{2n+1}{4\pi}h^n P_n(t).$$

Now, we assume that the neuronal current is given as a (linear combination of some) vectorial generalization of the Abel-Poisson kernel. In the case of the inverse MEG problem, we generate this vectorial kernel by means of the $\boldsymbol{L}^*$ operator since the test current is supposed not to lie in the null space of the MEG operator. In analogy, in the case of the inverse EEG problem, the test current is supposed to be generated by the gradient. Thus, the synthetic currents are of the following form.

Definition 18.2. *Let $h \in [0,1)$ be fixed and $\boldsymbol{z} \in \mathbb{B}_{\varrho_0}$ be given. Then the synthetic MEG current $\boldsymbol{I}_{\mathrm{M}}$ and the synthetic EEG current $\boldsymbol{I}_{\mathrm{E}}$ are for all $\boldsymbol{x} \in \mathbb{B}_{\varrho_0}$ defined by*

$$\boldsymbol{I}_{\mathrm{M}}(\boldsymbol{x};h,\boldsymbol{z}) \coloneqq \boldsymbol{L}^*_{\hat{\boldsymbol{x}}}\left(\sum_{n=1}^{\infty}\frac{2n+1}{4\pi}\left(\frac{hxz}{\varrho_0^2}\right)^n P_n(\hat{\boldsymbol{x}}\cdot\hat{\boldsymbol{z}})\right),$$

$$\boldsymbol{I}_{\mathrm{E}}(\boldsymbol{x};h,\boldsymbol{z}) \coloneqq \boldsymbol{\nabla}_{\boldsymbol{x}}\left(\sum_{n=1}^{\infty}\frac{2n+1}{4\pi}\left(\left(\frac{hxz}{\varrho_0^2}\right)^n P_n(\hat{\boldsymbol{x}}\cdot\hat{\boldsymbol{z}})\right)\right).$$

In a first step, we need to verify that the synthetic currents do not have parts in the null spaces of the respective forward operators.

Theorem 18.3. *Let the synthetic currents be defined as in Definition 18.2. Then for all* $h \in [0,1)$ *and all* $\boldsymbol{z} \in \mathbb{B}_{\varrho_0}$ *we have* $\boldsymbol{I}_{\mathrm{M}}(\cdot;h,\boldsymbol{z}) \in (\ker \mathcal{T}_{\mathrm{M}})^{\perp}$ *and* $\boldsymbol{I}_{\mathrm{E}}(\cdot;h,\boldsymbol{z}) \in (\ker \mathcal{T}_{\mathrm{E}})^{\perp}$.

Proof. Since the Legendre polynomials are bounded, see Theorem 2.7, and since $(hxz)/\varrho_0^2 < 1$, the series occurring in the synthetic currents can be estimated by convergent power series. Thus, the series and its derivatives converge uniformly and we are able to interchange the gradient and the $\boldsymbol{L}^*$ operator with the respective series.

Now, we start with the MEG case. We interchange the differential operator with the series, use the definition of the Morse-Feshbach vector Legendre polynomials, and Theorem 5.24. Hence, for all $\boldsymbol{x} \in \mathbb{B}_{\varrho_0}$ we get the identity

$$\begin{aligned}
\boldsymbol{I}_{\mathrm{M}}(\boldsymbol{x};h,\boldsymbol{z}) &= \sum_{n=1}^{\infty} \frac{2n+1}{4\pi} \left(\frac{hxz}{\varrho_0^2}\right)^n \boldsymbol{L}_{\hat{\boldsymbol{x}}}^* P_n(\hat{\boldsymbol{x}} \cdot \hat{\boldsymbol{z}}) \\
&= \sum_{n=1}^{\infty} \frac{2n+1}{4\pi} \sqrt{\mu_n^{(3)}} \left(\frac{hxz}{\varrho_0^2}\right)^n \boldsymbol{p}_n^{(3)}(\hat{\boldsymbol{x}};\hat{\boldsymbol{z}}) \\
&= \sum_{n=1}^{\infty} \sum_{j=1}^{2n+1} \left(\frac{hxz}{\varrho_0^2}\right)^n \sqrt{\mu_n^{(3)}} \boldsymbol{y}_{n,j}^{(3)}(\hat{\boldsymbol{x}}) Y_{n,j}(\hat{\boldsymbol{z}}) \\
&= \varrho_0^3 \sum_{n=1}^{\infty} \sum_{j=1}^{2n+1} h^n \frac{\sqrt{n(n+1)}}{2n+3} \boldsymbol{g}_{0,n,j}^{(3)}(\varrho_0;\boldsymbol{x}) G_{0,n,j}(\varrho_0;\boldsymbol{z}).
\end{aligned}$$

In the last step, we used Definition 5.35 for the scalar basis functions with $m = 0$, $t_n = n$ and Definition 5.37 for the vectorial basis functions with $m = 0$, $t_n^{(3)} = n$.

In the EEG case, we analogously obtain with Eq. (5.6) and Definitions 5.21 and 5.35, but for $m = 0$ and $t_n^{(2)} = n-1$ in the vector-valued basis functions and $t_n = n$ in the scalar-valued basis functions, for all $\boldsymbol{x} \in \mathbb{B}_{\varrho_0}$ the representation

$$\begin{aligned}
\boldsymbol{I}_{\mathrm{E}}(\boldsymbol{x};h,\boldsymbol{z}) &= \sum_{n=1}^{\infty} \frac{2n+1}{4\pi} \boldsymbol{\nabla}_{\boldsymbol{x}} \left(\left(\frac{hxz}{\varrho_0^2}\right)^n P_n(\hat{\boldsymbol{x}} \cdot \hat{\boldsymbol{z}}) \right) \\
&= \sum_{n=1}^{\infty} \frac{2n+1}{4\pi} \sqrt{\tilde{\mu}_n^{(2)}} \left(\frac{hz}{\varrho_0^2}\right)^n x^{n-1} \tilde{\boldsymbol{p}}_n^{(2)}(\hat{\boldsymbol{x}};\hat{\boldsymbol{z}}) \\
&= \varrho_0^2 \sum_{n=1}^{\infty} \sum_{j=1}^{2n+1} h^n Q_0^{(n+1/2)}(\varrho_0;z) Q_0^{(n-1/2)}(\varrho_0;x) \sqrt{\frac{n}{2n+3}} \tilde{\boldsymbol{y}}_{n,j}^{(2)}(\hat{\boldsymbol{x}}) Y_{n,j}(\hat{\boldsymbol{z}}) \\
&= \varrho_0^2 \sum_{n=1}^{\infty} \sum_{j=1}^{2n+1} h^n \sqrt{\frac{n}{2n+3}} \tilde{\boldsymbol{g}}_{0,n,j}^{(2)}(\varrho_0;\boldsymbol{x}) G_{0,n,j}(\varrho_0;\boldsymbol{z}).
\end{aligned}$$

Eventually, Theorem 13.1 provides us with the desired result. □

For the implementation of the synthetic current, the series representation is not appropriate since a required truncation of the series will always result in approximation errors. In order to avoid these additional errors, we calculate the closed representations of the synthetic currents.

Lemma 18.4. *Let the synthetic current $\boldsymbol{I}_{\mathrm{M}}$ be defined as in Definition 18.2 and $q \coloneqq (hxz)/\varrho_0^2$ for all $h \in [0,1)$ and $\boldsymbol{z} \in \mathbb{B}_{\varrho_0}$. Then*

$$\boldsymbol{I}_{\mathrm{M}}(\boldsymbol{x}; h, \boldsymbol{z}) = \frac{3}{4\pi} \frac{(1-q^2)\, q}{(1+q^2-2q(\hat{\boldsymbol{x}} \cdot \hat{\boldsymbol{z}}))^{5/2}} (\hat{\boldsymbol{x}} \wedge \hat{\boldsymbol{z}}), \qquad \boldsymbol{x} \in \mathbb{B}_{\varrho_0}.$$

Proof. We start with the definition of the synthetic current from Definition 18.2, use the closed representation of the Abel-Poisson kernel from Theorem 18.1, and use the fact that $\boldsymbol{L}^* 1 = \boldsymbol{0}$. Thus, with $q \coloneqq (hxz)/\varrho_0^2$ we get for all $h \in [0,1)$ and $\boldsymbol{z} \in \mathbb{B}_{\varrho_0}$ the identity

$$\begin{aligned} \boldsymbol{I}_{\mathrm{M}}(\boldsymbol{x}; h, \boldsymbol{z}) &= \frac{1}{4\pi} \boldsymbol{L}^*_{\hat{\boldsymbol{x}}} \left(\sum_{n=0}^{\infty} (2n+1) q^n P_n(\hat{\boldsymbol{x}} \cdot \hat{\boldsymbol{z}}) - 1 \right) \\ &= \frac{1}{4\pi} \boldsymbol{L}^*_{\hat{\boldsymbol{x}}} \frac{1-q^2}{(1+q^2-2q(\hat{\boldsymbol{x}} \cdot \hat{\boldsymbol{z}}))^{3/2}}. \end{aligned}$$

The variable q is independent of the angular part of $\boldsymbol{x}$. We obtain with Theorem 2.15 and the quotient rule the desired representation. □

Lemma 18.5. *Let the synthetic current $\boldsymbol{I}_{\mathrm{E}}$ be defined as in Definition 18.2 and let abbreviations be given by $r \coloneqq \hat{\boldsymbol{x}} \cdot \hat{\boldsymbol{z}}$ and $q \coloneqq q(x) \coloneqq (hxz)/\varrho_0^2$ for all $h \in [0,1)$ and $\boldsymbol{z} \in \mathbb{B}_{\varrho_0}$. Then*

$$\boldsymbol{I}_{\mathrm{E}}(\boldsymbol{x}; h, \boldsymbol{z}) = \frac{q^2 \left(-5+q^2+4qr\right) \hat{\boldsymbol{x}} + 3\left(1-q^2\right) q \hat{\boldsymbol{z}}}{x \left(1+q^2-2qr\right)^{5/2}}, \qquad \boldsymbol{x} \in \mathbb{B}_{\varrho_0}.$$

Proof. We start with the same considerations as in Lemma 18.4 and immediately get

$$\boldsymbol{I}_{\mathrm{E}}(\boldsymbol{x}; h, \boldsymbol{z}) = \frac{1}{4\pi} \boldsymbol{\nabla}_{\boldsymbol{x}} \frac{1-q(x)^2}{(1+q(x)^2-2q(x)(\hat{\boldsymbol{x}} \cdot \hat{\boldsymbol{z}}))^{3/2}}.$$

Due to Theorem 2.14, the gradient can be split into a radial and an angular derivative. Then we obtain with Theorem 2.15 and the quotient rule the representation

$$\begin{aligned} 4\pi \boldsymbol{I}_{\mathrm{E}}(\boldsymbol{x}; h, \boldsymbol{z}) &= \left(\hat{\boldsymbol{x}} \frac{\partial}{\partial x} + \frac{1}{x} \boldsymbol{\nabla}^*_{\hat{\boldsymbol{x}}} \right) \frac{1-q(x)^2}{(1+q(x)^2-2q(x)(\hat{\boldsymbol{x}} \cdot \hat{\boldsymbol{z}}))^{3/2}} \\ &= \hat{\boldsymbol{x}} \frac{\partial}{\partial x} \frac{1-q(x)^2}{(1+q(x)^2-2q(x)(\hat{\boldsymbol{x}} \cdot \hat{\boldsymbol{z}}))^{3/2}} + \frac{3}{x} \frac{(1-q(x)^2)\, q(x)}{(1+q(x)^2-2q(x)(\hat{\boldsymbol{x}} \cdot \hat{\boldsymbol{z}}))^{5/2}} \left(\hat{\boldsymbol{z}} - (\hat{\boldsymbol{x}} \cdot \hat{\boldsymbol{z}}) \hat{\boldsymbol{x}} \right). \end{aligned}$$

In addition, again with the quotient rule, $q'(x) = q(x)/x$, and the abbreviation for r, we get

$$\begin{aligned} \frac{\partial}{\partial x} \frac{1-q(x)^2}{(1+q(x)^2-2q(x)r)^{3/2}} &= \frac{q(x)}{x} \frac{-2q(x)\left(1+q(x)^2-2q(x)r\right) - 3(1-q(x)^2)\left(q(x)-r\right)}{(1+q(x)^2-2q(x)r)^{5/2}} \\ &= \frac{q(x)}{x} \frac{-5q(x)+q(x)^3+q(x)^2 r+3r}{(1+q(x)^2-2q(x)r)^{5/2}}. \end{aligned}$$

Inserting this into the formula for the synthetic current, we get with $q \coloneqq q(x)$ the stated result, that is

$$\begin{aligned}\boldsymbol{I}_{\mathrm{E}}(\boldsymbol{x}; h, \boldsymbol{z}) &= \frac{q^2\left(-5+q^2+qr\right)+3qr}{x\left(1+q^2-2qr\right)^{5/2}}\hat{\boldsymbol{x}} + \frac{3\left(1-q^2\right)q}{x\left(1+q^2-2qr\right)^{5/2}}\left(\hat{\boldsymbol{z}} - r\hat{\boldsymbol{x}}\right)\\ &= \frac{q^2\left(-5+q^2+qr\right)+3qr-3qr+3q^3r}{x\left(1+q^2-2qr\right)^{5/2}}\hat{\boldsymbol{x}} + \frac{3\left(1-q^2\right)q}{x\left(1+q^2-2qr\right)^{5/2}}\hat{\boldsymbol{z}}\\ &= \frac{q^2\left(-5+q^2+4qr\right)\hat{\boldsymbol{x}} + 3\left(1-q^2\right)q\hat{\boldsymbol{z}}}{x\left(1+q^2-2qr\right)^{5/2}}.\end{aligned}$$

□

An example of a linear combination of these synthetic currents for the inverse MEG as well as for the inverse EEG problem is shown in Figs. 18.1 and 18.2. Therein, we choose

$$\boldsymbol{J}_{\mathrm{M}} \coloneqq \sum_{l=1}^{2} \kappa_l \boldsymbol{I}_{\mathrm{M}}(\cdot; h_l, \boldsymbol{z}_l), \qquad \boldsymbol{J}_{\mathrm{E}} \coloneqq \sum_{l=1}^{2} \kappa_l \boldsymbol{I}_{\mathrm{E}}(\cdot; h_l, \boldsymbol{z}_l). \tag{18.1}$$

In addition, the radius of the cerebrum is given as in Eq. (19.2), that is $\varrho_0 = 0.071\,\mathrm{m}$. In both cases, the occurring parameters are chosen according to Table 18.1. In Section 21.6, we use some real data for the ROFMP for which the visual cortex of the human brain is supposed to be active. A visualization of human brain lobes is also given in Fig. 21.36 in Section 21.6. The visual cortex is an area of the brain which is located near the boundary of the brain, thus, we locate our synthetic tests current also near the boundary. Note that in Figs. 18.1 and 18.2 and in the following plots, the unit of the axes is given in dm.

l	κ_l	h_l	z_l	$\hat{\boldsymbol{z}}_l$
1	1	0.9	$0.85\varrho_0$	$(0,-2,1)^{\mathrm{T}}/\sqrt{5}$
2	1.5	0.8	$0.9\varrho_0$	$(-1,1,1)^{\mathrm{T}}/\sqrt{3}$

TABLE 18.1: *Chosen parameters for the synthetic test current from Eq.* (18.1) *for the inverse MEG and EEG problem*

18.2. Synthetic Data

Now, we generate the synthetic data induced by the synthetic test current from Eq. (18.1), which will be used within our numerical tests. For this purpose, we need to apply the MEG and EEG operator introduced in Problem 17.16, which are repeated below, to the synthetic currents from Eq. (18.1). The action of the operators on the synthetic test currents are given by

$$\mathcal{A}_{\mathrm{M}}\boldsymbol{J}_{\mathrm{M}} = \sum_{\ell=1}^{\ell_{\mathrm{M}}} \left(\boldsymbol{\nu}(\boldsymbol{y}_\ell) \cdot \left(\sum_{l=1}^{2} \kappa_l \mathcal{T}_{\mathrm{M}}\left(\boldsymbol{I}_{\mathrm{M}}(\cdot; h_l, \boldsymbol{z}_l)\right)(\boldsymbol{y}_\ell) \right) \right) \varepsilon^\ell, \tag{18.2}$$

$$\mathcal{A}_{\mathrm{E}}\boldsymbol{J}^{\mathrm{P}} = \sum_{l=1}^{2} \kappa_l \sum_{\ell=1}^{\ell_{\mathrm{E}}} \left(\mathcal{T}_{\mathrm{E}}\left(\boldsymbol{I}_{\mathrm{E}}(\cdot; h_l, \boldsymbol{z}_l)\right)\right)(\boldsymbol{y}_{\ell_{\mathrm{M}}+\ell})\varepsilon^\ell, \tag{18.3}$$

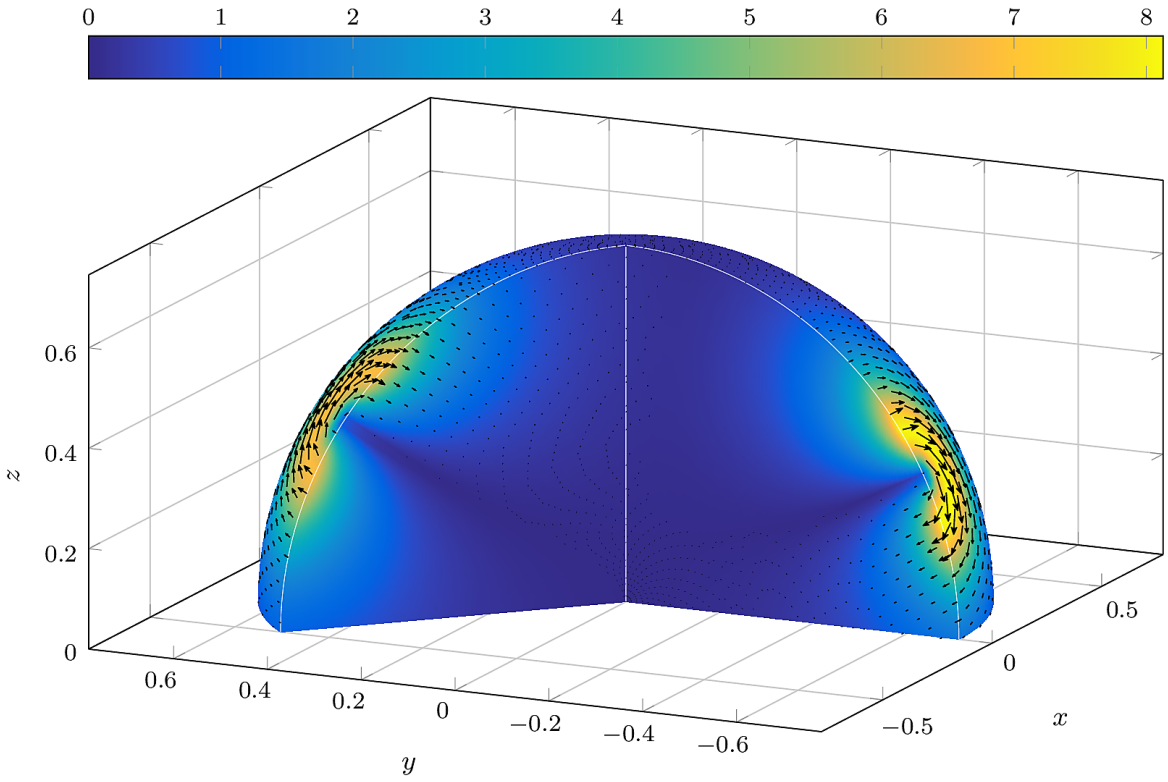

(a) MEG synthetic test current

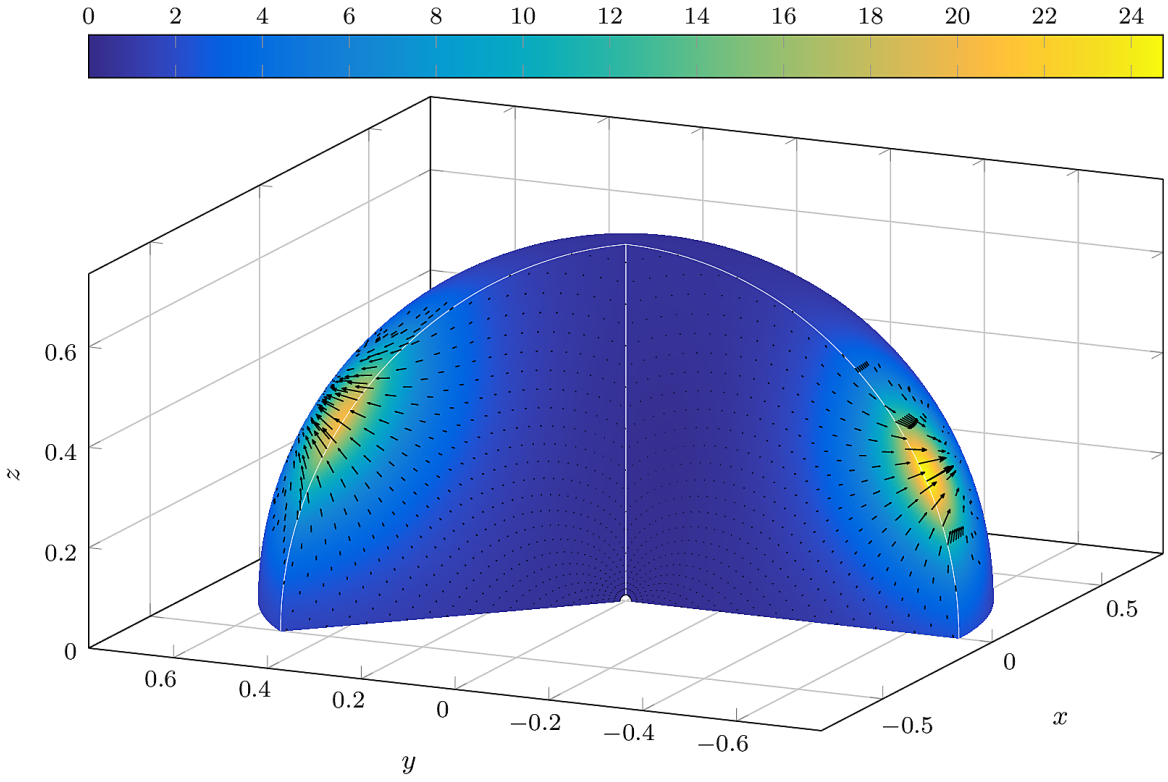

(b) EEG synthetic test current

FIGURE 18.1: *The absolute value of the synthetic currents given in Eq.* (18.1) *with parameters from Table 18.1 for the inverse MEG (top) and EEG (bottom) plotted on a cutout of the ball* $\mathbb{B}_{\varrho_0}$ *with directions of the current superimposed*

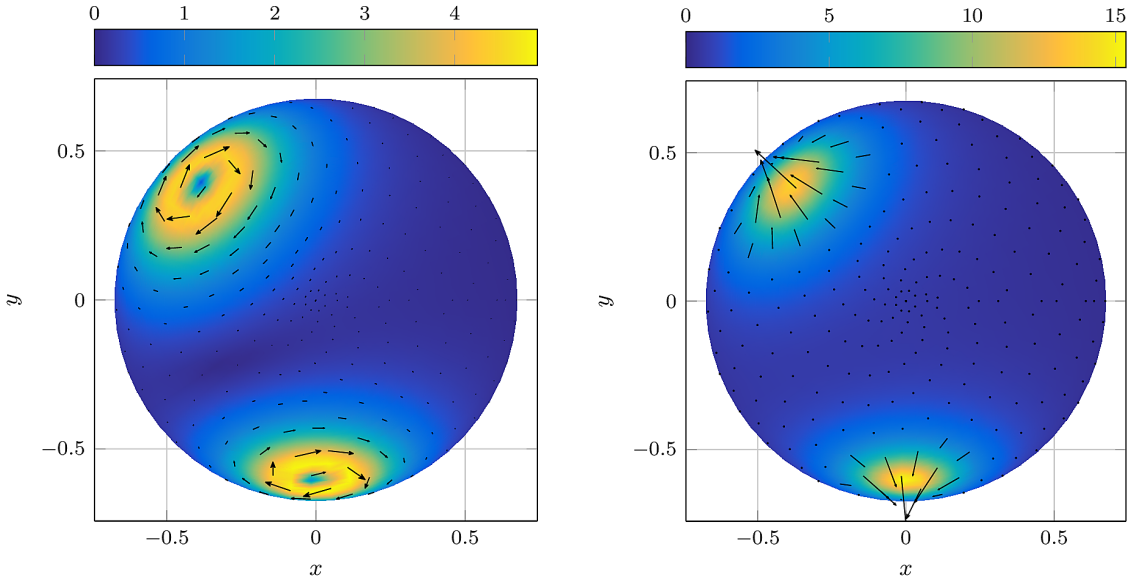

FIGURE 18.2: *The absolute value of the synthetic currents given in Eq.* (18.1) *with parameters from Table 18.1 for the inverse MEG (left) and EEG (right) plotted on the sphere with radius* $0.95\varrho_0$ *with directions of the current superimposed*

where the occurring parameters κ_l, h_l, and $\boldsymbol{z}_l$ for $l = 1, 2$ will be given according to Table 18.1 in the numerical tests. For this purpose, the two forward operators $\mathcal{T}_{\mathrm{M}}$ and $\mathcal{T}_{\mathrm{E}}$ need to be applied onto the synthetic test currents. This result will be stated in the next theorem.

Theorem 18.6. *Let* $\boldsymbol{y} \in \overline{\mathbb{B}_{\varrho_L}^{\mathrm{ext}}}$ *in the MEG case and let* $\boldsymbol{y} \in \mathbb{S}_{[\varrho_{L-1},\varrho_L]}$ *in the EEG case. Then we get*

$$\left(\mathcal{T}_{\mathrm{M}}\boldsymbol{J}_{\mathrm{M}}\right)(\boldsymbol{y}) = -\frac{\mu_0}{4\pi}\varrho_0^3 \sum_{l=1}^{2} \kappa_l \sum_{n=1}^{\infty} \sqrt{\frac{n^2(n+1)(2n+1)}{(2n+3)^2}} \frac{(h_l z_l)^n}{y^{n+2}} \tilde{\boldsymbol{p}}_n^{(1)}(\hat{\boldsymbol{y}}; \hat{\boldsymbol{z}}_l),$$

$$\left(\mathcal{T}_{\mathrm{E}}\boldsymbol{J}_{\mathrm{E}}\right)(\boldsymbol{y}) = \frac{\varrho_0}{4\pi} \sum_{l=1}^{2} \kappa_l \sum_{n=1}^{\infty} \beta_n^{(L)} \frac{(h_l z_l)^n}{y^{n+1}} (2n+1) \left((n+1) \left(\frac{y}{\varrho_L} \right)^{2n+1} + n \right) P_n(\hat{\boldsymbol{z}}_l \cdot \hat{\boldsymbol{y}})$$

with $\kappa_l \in \mathbb{R}$, $h_l \in [0, 1)$, *and* $\boldsymbol{z}_l \in \mathbb{B}_{\varrho_0}$ *for* $l = 1, 2$.

Proof. Via Theorem 9.4 in the MEG case and Table 13.1 in the EEG case, which holds true on the assumed domains, we get

$$\mathcal{T}_{\mathrm{M}}\boldsymbol{J}_{\mathrm{M}} = -\mu_0 \sum_{n=1}^{\infty} \sum_{j=1}^{2n+1} \sqrt{\frac{n\varrho_0}{(2n+1)(2n+3)}} \left(\frac{\varrho_0}{\varrho_L} \right)^{n+1} J_{\mathrm{M}}{}^{\wedge}[3, 0, n, j] \boldsymbol{h}_{n,j}^{(1)}(\varrho_L; \cdot),$$

$$\mathcal{T}_{\mathrm{E}}\boldsymbol{J}_{\mathrm{E}} = \sum_{n=1}^{\infty} \sum_{j=1}^{2n+1} (2n+1) \sqrt{\frac{\varrho_0}{n}} \beta_n^{(L)} \left(\frac{\varrho_0}{\varrho_L} \right)^{n} J_{\mathrm{E}}{}^{\wedge}[2, 0, n, j] Z_{n,j}.$$

Only the calculation of the Fourier coefficients remains to be done. Since $\boldsymbol{J}_{\mathrm{M}}$ and $\boldsymbol{J}_{\mathrm{E}}$ are linear combinations of $\boldsymbol{I}_{\mathrm{M}}(\cdot, h, \boldsymbol{z})$ or $\boldsymbol{I}_{\mathrm{E}}(\cdot, h, \boldsymbol{z})$, respectively, with some parameters $h \in [0, 1)$ and $\boldsymbol{z} \in \mathbb{B}_{\varrho_0}$, we calculate the Fourier coefficients for these functions and then use the linearity

of $\mathcal{T}_{\mathrm{M}}$ and $\mathcal{T}_{\mathrm{E}}$ in order to obtain the result for $\boldsymbol{J}_{\mathrm{M}}$ and $\boldsymbol{J}_{\mathrm{E}}$, respectively. By means of the representation of the synthetic current from the proof of Theorem 18.3 for $h \in [0,1)$, $\boldsymbol{z} \in \mathbb{B}_{\varrho_0}$, and $t_n = n$, we obtain for all $n \in \mathbb{N}$, $j = 1, \dots, 2n+1$ the identities

$$\begin{aligned} \boldsymbol{I}_{\mathrm{M}}{}^{\wedge}[3,0,n,j] &= \varrho_0^3 h^n \frac{\sqrt{n(n+1)}}{2n+3} G_{0,n,j}(\varrho_0;\boldsymbol{z}), & t_n^{(3)} &= n, \\ \boldsymbol{I}_{\mathrm{E}}{}^{\wedge}[2,0,n,j] &= \varrho_0^2 h^n \sqrt{\frac{n}{2n+3}} G_{0,n,j}(\varrho_0;\boldsymbol{z}), & t_n^{(2)} &= n-1. \end{aligned}$$

In the MEG case, we then obtain with $h \in [0,1)$ and $\boldsymbol{z} \in \mathbb{B}_{\varrho_0}$ that

$$\mathcal{T}_{\mathrm{M}}\left(\boldsymbol{I}_{\mathrm{M}}(\cdot;h,\boldsymbol{z})\right) = -\mu_0 \sum_{n=1}^{\infty} \sum_{j=1}^{2n+1} \sqrt{\frac{n^2(n+1)\varrho_0}{(2n+1)(2n+3)^3}} \left(\frac{\varrho_0}{\varrho_L}\right)^{n+1} \varrho_0^3 h^n G_{0,n,j}(\varrho_0;\boldsymbol{z}) \boldsymbol{h}_{n,j}^{(1)}(\varrho_L;\cdot).$$

Using Definitions 5.27 and 5.35 and Theorem 5.24, we obtain for $h \in [0,1)$, $\boldsymbol{z} \in \mathbb{B}_{\varrho_0}$, and all $\boldsymbol{y} \in \overline{\mathbb{B}_{\varrho_L}^{\mathrm{ext}}}$ the relation

$$\begin{aligned} \mathcal{T}_{\mathrm{M}}\left(\boldsymbol{I}_{\mathrm{M}}(\cdot;h,\boldsymbol{z})\right)(\boldsymbol{y}) &= -\mu_0 \varrho_0^3 \sum_{n=1}^{\infty} \sum_{j=1}^{2n+1} \sqrt{\frac{n^2(n+1)}{(2n+1)(2n+3)^2}} \frac{(hz)^n}{y^{n+2}} Y_{n,j}(\hat{\boldsymbol{z}}) \tilde{\boldsymbol{y}}_{n,j}^{(1)}(\hat{\boldsymbol{y}}) \\ &= -\frac{\mu_0}{4\pi} \varrho_0^3 \sum_{n=1}^{\infty} \sqrt{\frac{n^2(n+1)(2n+1)}{(2n+3)^2}} \frac{(hz)^n}{y^{n+2}} \tilde{\boldsymbol{p}}_n^{(1)}(\hat{\boldsymbol{y}};\hat{\boldsymbol{z}}). \end{aligned}$$

In the EEG case, we obtain with Lemma 13.2 for all $\boldsymbol{y} \in \mathbb{S}_{[\varrho_{L-1},\varrho_L]}$ the result

$$\begin{aligned} \left(\mathcal{T}_{\mathrm{E}} \boldsymbol{I}_{\mathrm{E}}(\cdot;h,\boldsymbol{z})\right)(\boldsymbol{y}) &= \sum_{n=1}^{\infty} \sum_{j=1}^{2n+1} \beta_n^{(L)} \frac{\varrho_0^{n+5/2}}{\varrho_L^n} h^n \sqrt{\frac{(2n+1)^2}{2n+3}} G_{0,n,j}(\varrho_0;\boldsymbol{z}) Z_{n,j}(\boldsymbol{y}) \\ &= \frac{\varrho_0}{4\pi} \sum_{n=1}^{\infty} \beta_n^{(L)} \frac{h^n z^n}{y^{n+1}} (2n+1) \left((n+1)\left(\frac{y}{\varrho_L}\right)^{2n+1} + n\right) P_n(\hat{\boldsymbol{z}} \cdot \hat{\boldsymbol{y}}). \end{aligned}$$

□

Unfortunately, we are neither able to find a closed representation of $\mathcal{T}_{\mathrm{M}}\left(\boldsymbol{I}_{\mathrm{M}}(\cdot;h,\boldsymbol{z})\right)$ nor of $\left(\mathcal{T}_{\mathrm{E}} \boldsymbol{I}_{\mathrm{E}}(\cdot;h,\boldsymbol{z})\right)$. Therefore, we need to truncate the series for the computation of the synthetic data. Thus, we are interested in a bound for the truncation error.

Lemma 18.7. *For all $h \in [0,1)$, $\boldsymbol{z} \in \mathbb{B}_{\varrho_0}$, $\boldsymbol{y} \in \overline{\mathbb{B}_{\varrho_L}^{\mathrm{ext}}}$, and $N \in \mathbb{N}$, the following estimate holds true:*

$$\varrho_0^3 \left| \sum_{n=N+1}^{\infty} \sqrt{\frac{n^2(n+1)(2n+1)}{(2n+3)^2}} \frac{(hz)^n}{y^{n+2}} \tilde{\boldsymbol{p}}_n^{(1)}(\hat{\boldsymbol{y}};\hat{\boldsymbol{z}}) \right| \leq \frac{\varrho_0^3}{\varrho_L^2} \frac{\left(\frac{h\varrho_0}{\varrho_L}\right)^{N+1} (N+2)^2}{(1-\frac{h\varrho_0}{\varrho_L})^3}.$$

In addition, for all $h \in [0,1)$, $\boldsymbol{z} \in \mathbb{B}_{\varrho_0}$, $\boldsymbol{y} \in \mathbb{S}_{[\varrho_{L-1},\varrho_L]}$, and $N \in \mathbb{N}$, we get

$$\begin{aligned} &\varrho_0 \left| \sum_{n=N+1}^{\infty} \beta_n^{(L)} \frac{h^n z^n}{y^{n+1}} (2n+1) \left((n+1)\left(\frac{y}{\varrho_L}\right)^{2n+1} + n\right) P_n(\hat{\boldsymbol{z}} \cdot \hat{\boldsymbol{y}}) \right| \\ &\leq \frac{9\varrho_0}{2\sigma_L \varrho_{L-1} C^{(L)}} \frac{\left(\frac{h\varrho_0}{\varrho_{L-1}}\right)^{N+1} (N+1)}{\left(1-\frac{h\varrho_0}{\varrho_{L-1}}\right)^2}, \end{aligned}$$

where $C^{(L)}$ is given in Corollary 4.3 if $\{n\beta_n^{(L)}\}_{n\in\mathbb{N}}$ is monotonically increasing.

Note that the condition on $\{n\beta_n^{(L)}\}_{n\in\mathbb{N}}$ is fulfilled in our particular numerical setting, see Eq. (19.2).

Proof. From Theorem 18.6, Lemma 5.22, and Definition 5.21, we get for the truncation error

$$\frac{\mu_0}{4\pi}\varrho_0^3\left|\sum_{n=N+1}^{\infty}\sqrt{\frac{n^2(n+1)(2n+1)}{(2n+3)^2}}\frac{(hz)^n}{y^{n+2}}\tilde{\boldsymbol{p}}_n^{(1)}(\hat{\boldsymbol{y}};\hat{\boldsymbol{z}})\right| \leq \frac{\mu_0}{4\pi}\frac{\varrho_0^3}{\varrho_L^2}\sum_{n=N+1}^{\infty} n(n+1)\left(\frac{h\varrho_0}{\varrho_L}\right)^n.$$

We define $q \coloneqq h\varrho_0/\varrho_L \in [0,1)$ and obtain with the closed representation of the power series and some lengthy calculations, the estimate

$$\begin{aligned}
\sum_{n=N+1}^{\infty} n(n+1)\left(\frac{h\varrho_0}{\varrho_L}\right)^n &= \frac{q^{N+1}\left(-q^2N^2+2qN^2-N^2-q^2N+4qN-3N-2\right)}{(q-1)^3}\\
&= \frac{q^{N+1}\left(-(q-1)N((q-1)N+q-3)-2\right)}{(q-1)^3}\\
&= \frac{q^{N+1}\left((1-q)N((1-q)N-q+3)+2\right)}{(1-q)^3}\\
&\leq \frac{q^{N+1}\left((1-q)N(N+3)+2\right)}{(1-q)^3}\\
&\leq \frac{q^{N+1}(N+2)(N+1)}{(1-q)^3},
\end{aligned}$$

where $N \in \mathbb{N}$. Vice versa from Theorem 18.6 with Corollary 4.3, the abbreviation $q \coloneqq h\varrho_0/\varrho_{L-1} \in [0,1)$, and the inequality $(2n+1)^2 \leq 9n^2$ for all $n \in \mathbb{N}$, we similarly obtain for all $N \in \mathbb{N}$ the estimate

$$\begin{aligned}
&\frac{\varrho_0}{4\pi}\left|\sum_{n=N+1}^{\infty}\beta_n^{(L)}\frac{h^n z^n}{y^{n+1}}(2n+1)\left((n+1)\left(\frac{y}{\varrho_L}\right)^{2n+1}+n\right)P_n(\hat{\boldsymbol{z}}\cdot\hat{\boldsymbol{y}})\right|\\
&\leq \frac{\varrho_0}{4\pi}\sum_{n=N+1}^{\infty}\left|\beta_n^{(L)}\right|\frac{h^n\varrho_0^n}{\varrho_{L-1}^{n+1}}(2n+1)^2\\
&\leq \frac{9\varrho_0}{8\pi\sigma_L\varrho_{L-1}C^{(L)}}\sum_{n=N+1}^{\infty} nq^n\\
&= \frac{9\varrho_0}{8\pi\sigma_L\varrho_{L-1}C^{(L)}}\frac{q^{N+1}\left((1-q)N+1\right)}{(1-q)^2}\\
&\leq \frac{9\varrho_0}{8\pi\sigma_L\varrho_{L-1}C^{(L)}}\frac{q^{N+1}(N+1)}{(1-q)^2}.
\end{aligned}$$

□

If a maximal truncation error, for example the machine precision, is desired, then the results stated in Table 18.2 yields the required number of summands depending on the parameter h. According to the results from Table 18.2, which were also obtained via Mathematica [223], we choose $N_{\mathrm{M}} = 177$ and $N_{\mathrm{E}} = 237$.

In addition, numerical summation always implies a numerical error due to the finite precision of the floating point numbers. In order to reduce the truncation and round-off error incurred by the summation, we use the Kahan summation algorithm, see [121], for the MEG forward operator. From the results stated in Table 18.2, we can deduce that $N_{\mathrm{M}}\mathrm{eps} \leq 1$,

where eps is the machine precision. Thus, the error of compensated summation is effectively $\mathcal{O}(\text{eps})$, which is independent of N, see [121]. For the calculation of the electric potential, we use the Clenshaw algorithm for the summation of Legendre polynomials, see [31] or [158, p. 48].

error	h	N_{M}	N_{E}
10^{-4}	0.8	48	62
10^{-4}	0.9	74	103
10^{-5}	0.8	54	69
10^{-5}	0.9	83	114
10^{-16}	0.8	121	149
10^{-16}	0.9	**177**	**237**

TABLE 18.2: *Number of summands N_{M} for the truncated series in Theorem 18.6 and N_{E} for the series in Theorem 18.6 depending on h for a given maximal truncation error. The shell radii and conductivities are chosen according to Eq.* (19.2)*, which implies $C^{(L)} \approx 4.6495$, see Corollary 4.3.*

Besides non-noisy data, we want to generate noisy data for the synthetic tests. For this purpose, we use additive white Gaussian noise. In this case, let $\{y_i\}_{1 \le i \le N}$ be the data. Then the additive noise for each component y_i of the data vector is normally distributed with zero mean and standard deviation $\delta |y_i|$, where $\delta \in [0, 0.1]$ is the (relative) noise level.

Chapter 19.

Foundation for Implementation

For the implementation of the RFMP and ROFMP algorithm, several quantities are necessary, see Algorithms 17.2 and 17.19, such as the forward operators, appropriate Hilbert spaces, a penalty term, a dictionary, and an initial approximation. In Problem 17.16, the forward operators considered for the implementation are stated:

$$\mathcal{A}_{\mathrm{M}}\boldsymbol{J}^{\mathrm{P}} = \sum_{\ell=1}^{\ell_{\mathrm{M}}} \left(\boldsymbol{\nu}(\boldsymbol{y}_\ell) \cdot \left(\mathcal{T}_{\mathrm{M}}\boldsymbol{J}^{\mathrm{P}}\right)(\boldsymbol{y}_\ell)\right)\boldsymbol{\varepsilon}^\ell, \qquad \mathcal{A}_{\mathrm{E}}\boldsymbol{J}^{\mathrm{P}} = \sum_{\ell=1}^{\ell_{\mathrm{E}}} \left(\mathcal{T}_{\mathrm{E}}\boldsymbol{J}^{\mathrm{P}}\right)(\boldsymbol{y}_{\ell_{\mathrm{M}}+\ell})\boldsymbol{\varepsilon}^\ell. \tag{19.1}$$

For the implementation, we need to consider a particular instance of the multiple-shell model. We assume that $L = 3$, that is the three-shell model, with the following radii and conductivities:

$$\varrho_0 = 0.071\,\mathrm{m}, \qquad \varrho_1 = 0.072\,\mathrm{m}, \qquad \varrho_2 = 0.079\,\mathrm{m}, \qquad \varrho_3 = 0.085\,\mathrm{m}, \tag{19.2a}$$

$$\sigma_0 = 0.330\,\mathrm{S\,m^{-1}}, \quad \sigma_1 = 1.000\,\mathrm{S\,m^{-1}}, \quad \sigma_2 = 0.042\,\mathrm{S\,m^{-1}}, \quad \sigma_3 = 0.330\,\mathrm{S\,m^{-1}}. \tag{19.2b}$$

Note that this model coincides with the one in [73] and is partially based on results stated in [117, Ch. 9.3]. In our implementation, we calculated in fact in dm. Note that the values of the conductivities for the brain, the skull, and the scalp shell correspond to the one chosen in [32] for their forward model. For the sensor positions of the magnetoencephalography device and the electroencephalography cap, we have

$$\|\boldsymbol{y}_\ell\|_{\mathbb{R}^3} \in [1.4978\varrho_L, 2.0522\varrho_L] \qquad \text{for all } \ell = 1, \dots, \ell_{\mathrm{M}}, \tag{19.3}$$

$$\|\boldsymbol{y}_\ell\|_{\mathbb{R}^3} \in [\varrho_{L-1}, \varrho_L] \qquad \text{for all } \ell = \ell_{\mathrm{M}}+1, \dots, \ell_{\mathrm{M}}+\ell_{\mathrm{E}}. \tag{19.4}$$

The precise positions of the sensors in our synthetic test case as well as in the real data situation is visualized in Fig. 19.1 and provided by [116]. In this case, we have $\ell_{\mathrm{M}} = 102$ and $\ell_{\mathrm{E}} = 70$.

As we can see in Fig. 19.1, both sets of positions are irregularly distributed with major gaps, for example in the region of the face.

In Problem 17.16, the Hilbert spaces for domain and range of the operators have already been defined. For the domain, we choose vectorial Lebesgue spaces with $p = 2$ on the ball, where we only need to consider the directions that are not in the null space of the respective operator, that is $\tilde{\mathbf{L}}_2^{(i)}(\mathbb{B}_{\varrho_0})$ with $i = 2$ for EEG and $i = 3$ for MEG. Based on the results of Theorem 17.12, we can use a variety of norms for the penalty term. Here, we choose several Sobolev norms for the penalty term based on Definition 16.1 with the sequence depending on a parameter $s \in \mathbb{R}_0^+$, that is

$$a_{m,n}^{(i)} \coloneqq a_n^{(i)}\delta_{m,0} = \begin{cases} \left(n+\frac{1}{2}\right)^s \left(n+\frac{1}{2}\right)^s \delta_{m,0} & \text{if } i = 2, \\ \left(n+\frac{1}{2}\right)^s \left(n+\frac{3}{2}\right)^s \delta_{m,0} & \text{if } i = 3. \end{cases} \tag{19.5}$$

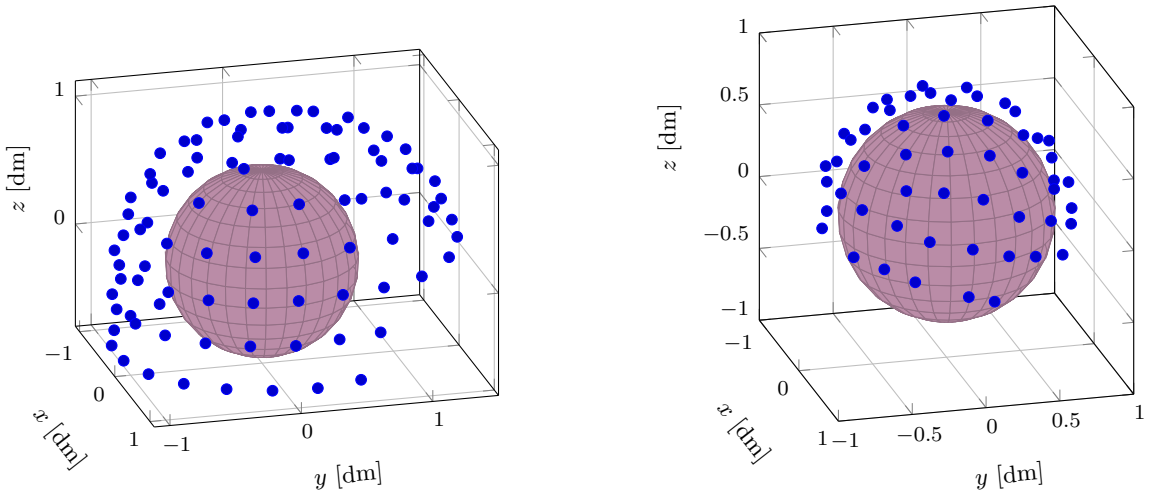

FIGURE 19.1: *Position of the MEG (left) and EEG (right) sensors around a ball with radius ϱ_0 modelling the cerebrum*

The corresponding Sobolev space will be denoted by $\tilde{\mathcal{H}}_s^{(i)}(\mathbb{B}_{\varrho_0})$. For the parameter s, we choose $s \in \{0, 1, 2\}$ within our numerical tests.

In [162], we construct scalar-valued Sobolev spaces $\mathcal{H}_s(\mathbb{B}_{\varrho_0})$ on the ball. The scalar-valued Sobolev space belonging to the sequence chosen above is a particular case of these spaces. In addition, using this sequence we construct a second order differential operator ${}^{**}\Delta$. The scalar orthonormal basis functions defined in Definition 5.35 are eigenfunctions of this differential operator, such that $\|{}^{**}\Delta F\|_{\mathcal{H}_{s-2}(\mathbb{B}_{\varrho_0})} = \|F\|_{\mathcal{H}_s(\mathbb{B}_{\varrho_0})}$. Thus, the $\mathcal{H}_s(\mathbb{B}_{\varrho_0})$-norm seems to be a measure for the smoothness of a function with respect to the differential operator ${}^{**}\Delta$. In some first numerical tests with the ROFMP, which are not shown here, we considered the scalar problem that arises from the Helmholtz decomposition of the inverse MEG problem from Theorem 15.3. In this setting, a penalty term corresponding to $\mathcal{H}_s(\mathbb{B}_{\varrho_0})$ yielded good numerical results. Based on these results, we also use this sequence for the construction of the vector-valued Sobolev spaces on the ball, even though we have not found a closed representation of the corresponding operator in this case.

Now, we introduce the abbreviation $\bullet \in \{\mathrm{M}, \mathrm{E}\}$ that will be used if a quantity can either be used for the MEG or the EEG case. Based on Algorithm 17.2, an initial approximation has to be chosen before starting the algorithm. Since we do not have a-priori knowledge of the neuronal current at hand, we chose the zero-function to be the initial approximation. Recall that in each step of the RFMP we are searching for the maximizer of

$$\boldsymbol{d}_{k+1} := \operatorname*{arg\,max}_{\boldsymbol{d} \in \mathcal{D}_\bullet} \frac{\left(\langle \boldsymbol{r}_k, \mathcal{A}_\bullet \boldsymbol{d} \rangle_{\mathbb{R}^{\ell_\bullet}} - \tau \langle \boldsymbol{f}_k, \boldsymbol{d} \rangle_{\mathcal{X}_\bullet}\right)^2}{\|\mathcal{A}_\bullet \boldsymbol{d}\|^2_{\mathbb{R}^{\ell_\bullet}} + \tau \|\boldsymbol{d}\|^2_{\mathcal{X}_\bullet}}, \tag{19.6}$$

where the given data comes into play in the form of $\boldsymbol{r}_0 := \boldsymbol{g}^{\delta_\bullet}$. Here, we have $\mathcal{X}_\bullet = \tilde{\mathcal{H}}_s^{(i)}(\mathbb{B}_{\varrho_0})$ with $i \in \{2, 3\}$ according to the respective problem and parameter s. Thus, some more quantities need to be determined further.

19.1. The Dictionaries

We start with the construction of the dictionaries $\mathcal{D}_\bullet$. The elements of the dictionary have to be chosen in such a way that they are not in the null space of the forward operators $\mathcal{T}_\mathrm{M}$ and $\mathcal{T}_\mathrm{E}$. For $N_\bullet$, $I_\bullet$, $L_\bullet \in \mathbb{N}$ with $I_\bullet \coloneqq \{\boldsymbol{z}_l \in \mathbb{B}_{\varrho_0} \mid l = 1, \dots, L_\bullet\}$ and a discrete set $H_\bullet \subset [0, 1)$, we choose the dictionary

$$\mathcal{D}_\bullet(N_\bullet, H_\bullet, I_\bullet) = \left\{\tilde{\boldsymbol{g}}^{(i)}_{0,n,j}(\varrho_0; \cdot)\right\}_{n=1,\dots,N_\bullet, j=1,\dots,2n+1} \cup \left\{\tilde{\boldsymbol{k}}^{(i)}_h(\cdot, \boldsymbol{z}_l)\right\}_{h\in H_\bullet, l=1,\dots,L_\bullet}, \tag{19.7}$$

where $i = 2$, 3 depending on the particular problem. Here, the global orthonormal basis functions are given as in Eqs. (13.2) and (13.3). Besides these functions, we use localized reproducing kernels from Lemma 16.11. The kernels are of the form

$$\tilde{\boldsymbol{k}}^{(i)}_h(\boldsymbol{x}, \boldsymbol{z}) \coloneqq \sum_{\substack{(m,n)\in\mathbb{N}_0\times\mathbb{N}_{0_i}\\ k^{(i)}_{m,n}\neq 0}} \sum_{j=1}^{2n+1} \left(k^{(i)}_{m,n}\right)^{-2} \sqrt{\tilde{\mu}^{(i)}_n}\, \tilde{\boldsymbol{g}}^{(i)}_{m,n,j}(\varrho_0; \boldsymbol{x}) G_{m,n,j}(\varrho_0; \boldsymbol{z})$$

with $\boldsymbol{x}$, $\boldsymbol{z} \in \mathbb{B}_{\varrho_0}$. The sequence $\{k^{(i)}_{m,n}\}_{(m,n)\in\mathbb{N}_0\times\mathbb{N}_{0_i}}$ is defined by

$$k^{(i)}_{m,n} \coloneqq h^{-n/2} \left(\tilde{\mu}^{(i)}_n\right)^{1/4} \delta_{m,0}, \qquad h \in (0, 1),$$

and vanishes for all $m \neq 0$. Note that the radial part of the function $G_{m,n,j}$ depends on a sequence $\{t_n\}_{n\in\mathbb{N}_{0_i}}$ that was originally defined independent of $i = 1$, 2, 3. However, for the construction of reproducing kernels, it is necessary that this sequence coincides with the sequence $\{t^{(i)}_n\}_{n\in\mathbb{N}_{0_i}}$ from the vector-valued orthonormal basis. Thus, the kernel reduces for all $\boldsymbol{x}$, $\boldsymbol{z} \in \mathbb{B}_{\varrho_0}$ and $i \neq 1$ to

$$\begin{aligned}
\tilde{\boldsymbol{k}}^{(i)}_h(\boldsymbol{x}, \boldsymbol{z}) &\coloneqq \frac{1}{4\pi} \sum_{n=1}^{\infty} (2n+1) h^n Q_0^{(t^{(i)}_n + 1/2)}(\varrho_0; x) Q_0^{(t^{(i)}_n + 1/2)}(\varrho_0; z) \tilde{\boldsymbol{p}}^{(i)}_n(\hat{\boldsymbol{x}}, \hat{\boldsymbol{z}}) \\
&= \frac{1}{4\pi\varrho_0^3} \begin{cases} \sum_{n=1}^{\infty} (2n+1)^2 h^n \left(\frac{xz}{\varrho_0^2}\right)^{n-1} \tilde{\boldsymbol{p}}^{(2)}_n(\hat{\boldsymbol{x}}, \hat{\boldsymbol{z}}) & \text{if } i = 2, \\ \sum_{n=1}^{\infty} (2n+3)(2n+1) h^n \left(\frac{xz}{\varrho_0^2}\right)^{n} \tilde{\boldsymbol{p}}^{(3)}_n(\hat{\boldsymbol{x}}, \hat{\boldsymbol{z}}) & \text{if } i = 3. \end{cases}
\end{aligned}$$

Note that the sequence of the kernel $\{k^{(i)}_{m,n}\}_{(m,n)\in\mathbb{N}_0\times\mathbb{N}_{0_i}}$ does not need to coincide with the sequence of the Sobolev space $\tilde{\mathcal{H}}^{(i)}_s(\mathbb{B}_{\varrho_0})$. Thus, within our dictionary we can use reproducing kernels based on several different sequences. This is an advantage in comparison to a spline approach, where for an interpolation or approximation only one fixed sequence can be used.

In order to use the theoretical convergence result of the ROFMP from Theorem 17.7, the conditions of this statement need to be verified. This involves two estimates. The first one is given by

$$c_1 \coloneqq \inf_{d\in\mathcal{D}_\bullet} \left(\|\mathcal{A}_\bullet d\|^2_{\mathbb{R}^{\ell_\bullet}} + \tau \|d\|^2_{\tilde{\mathcal{H}}^{(i)}_s}\right) > 0,$$

which is immediately fulfilled since the dictionary elements are contained in $(\ker \mathcal{A}_\bullet)^\perp$ and non-zero. The second estimate, that is the boundedness of the dictionary, is naturally fulfilled, since the finite dictionary is contained in the Hilbert space, that is $\mathcal{D}_\bullet \subset \tilde{\mathcal{H}}^{(i)}_s$. The latter statement becomes more clear with Theorem 19.2 from the next section. The semi-frame

h	MEG		EEG	
	error $\tilde{\boldsymbol{k}}_h^{(3)}$	error $\mathcal{T}_{\mathrm{M}}\tilde{\boldsymbol{k}}_h^{(3)}$	error $\tilde{\boldsymbol{k}}_h^{(2)}$	error $\mathcal{T}_{\mathrm{E}}\tilde{\boldsymbol{k}}_h^{(2)}$
0.80	$1.9104 \cdot 10^{-25}$	$1.3107 \cdot 10^{-36}$	$8.6759 \cdot 10^{-26}$	$1.0741 \cdot 10^{-28}$
0.90	$1.8955 \cdot 10^{-13}$	$1.1575 \cdot 10^{-24}$	$8.6079 \cdot 10^{-14}$	$1.1719 \cdot 10^{-16}$
0.95	$6.7759 \cdot 10^{-8}$	$3.7216 \cdot 10^{-19}$	$3.0769 \cdot 10^{-8}$	$4.3234 \cdot 10^{-11}$
0.99	$1.2855 \cdot 10^{-3}$	$6.1445 \cdot 10^{-15}$	$5.8372 \cdot 10^{-4}$	$8.2779 \cdot 10^{-7}$

TABLE 19.1: *A maximal upper bound for the truncation error of the reproducing kernels and their forward solutions depending on the parameter $h \in (0,1)$ after $N = 230$ summands*

condition for this particular dictionary needs to be verified. However, this is not done in this thesis. Since there exist first unpublished results of M. Kontak and V. Michel to prove the convergence theorem of the RFMP without this condition, this is not crucial to the opinion of the author. For the proof of Theorem 17.8, we need another assumption, which is violated in our particular case: the implemented dictionary is only a finite set of functions, thus its span cannot be dense in $\tilde{\mathcal{H}}_s^{(i)}$. The numerical results suggest that in this setting the solution obtained by the RFMP still converges to the unique minimizer of the Tikhonov-regularized normal equation, but the proof of this statement is still an open question. On the other hand, the conditions of Theorem 17.15, which states that the RFMP is a regularization method, are not verified for our particular setting and its verification would exceed the scope of this part. One crucial problem is to verify that the best-approximate solution satisfies the Hölder-source condition, since in our application the operator $\mathcal{A}_\bullet^*$ and hence $\mathrm{ran}(\mathcal{A}_\bullet^*\mathcal{A}_\bullet)$ is unknown.

For the implementation of the kernels, we need to truncate the occurring series. Based on the results of Table 18.2, where the truncation error of the series expansion of the synthetic test current is listed, we decided to truncate all further implemented series after 230 summands. Some estimates for the corresponding maximal truncation errors depending on the parameter $h \in (0,1)$ are listed in Table 19.1. The truncation error of $\tilde{\boldsymbol{k}}_h^{(3)}$ for $h = 0.99$ seems to be high, but the actual value of this quantity is around $3.5 \cdot 10^3$, which implies a relative error in the order of 10^{-6}. Therefore, the truncation error is still acceptable. The same holds true for the kernel $\tilde{\boldsymbol{k}}_h^{(2)}$.

From Lemmas 5.40 and 5.41 and the summability condition verified in Eq. (16.3), we immediately obtain that all dictionary elements are harmonic and solenoidal. Thus, the additional uniqueness constraints are not violated by our dictionary. In addition, we need to fix the centres of the kernels. For this purpose, we need a suitably distributed grid on the ball. Here, we use a modified Reuter grid on the ball presented in [129, 130] with a parameter P. The grid corresponding to $P = 8$, which yields 289 different grid points, is plotted in Fig. 19.2.

In some first numerical tests of the RFMP, a third type of dictionary elements was used. These functions were vector-valued radially invariant functions similar to the scalar-valued radially invariant functions used in [73] in order to solve the scalar inverse MEG problem discussed in Lemma 15.2. For $0 < a \leq x \leq b < \varrho_0$, the functions were of the form

$$\boldsymbol{f}_{n,j}^{(i)}(\boldsymbol{x}) \coloneqq \chi_{[a,b]}(x)\tilde{\boldsymbol{y}}_{n,j}^{(i)}(\hat{\boldsymbol{x}}), \qquad n \in \mathbb{N}_{0_i},\ j = 1, \ldots, 2n+1.$$

However, no dictionary element of this type was chosen in any numerical test. In Theorem 13.7, we showed that the harmonicity constraint in combination with the solenoidal condition is

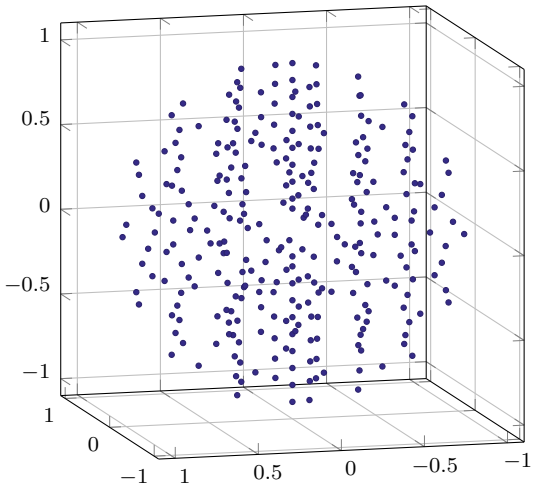

FIGURE 19.2: *Modified Reuter grid on the ball for $P = 8$*

sufficient for a unique solution of the inverse problem. This unique solution coincides with the best-approximate solution stated in Theorem 13.6. In addition, the sequence obtained by the RFMP converges under certain conditions to the best-approximate solution of the inverse problem, see Theorem 17.8. Based on the definition of the radially invariant functions, the harmonicity constraint $\Delta \boldsymbol{f}_{n,j}^{(i)} = \mathbf{0}$ inside the entire ball $\mathbb{B}_{\varrho_0}$ is never fulfilled. This can be a possible reason for the RFMP not to choose these radially invariant functions.

19.2. The Preprocessing

In the case of the R(O)FMP, the preprocessing is an excellent way to accelerate the algorithm, especially if a single dictionary is used for several R(O)FMP runs. Quantities that are frequently used within the algorithm, such as inner products of the dictionary elements and the application of the forward operator to the dictionary elements, are calculated for all dictionary elements in advance. Then, for a fixed regularization parameter, due to the linearity of the inner product and the update of the approximation, all quantities occurring in Eq. (19.6) are known. Thus, searching the maximizer of Eq. (19.6) among all dictionary items reduces to finding the maximal entry of a vector whose length equals the amount of dictionary elements. This search can easily be parallelized. The same holds true for the ROFMP, since the additional backfitting consists of linear combinations of inner products of the dictionary elements.

In addition, parts of this preprocessing can also be used for the implementation of other reconstruction methods, which will be presented in Chapter 20.

For the preprocessing of the R(O)FMP, we start with the calculation of the application of the operators $\mathcal{A}_{\mathrm{M}}$ and $\mathcal{A}_{\mathrm{E}}$, respectively, to the corresponding dictionary elements. For this purpose, we state the next theorem.

Theorem 19.1. *Let $\mathcal{T}_{\mathrm{M}}$ and $\mathcal{T}_{\mathrm{E}}$ be given as in Problems 9.1 and 10.2. Then the forward operator maps the orthogonal basis functions to*

$$\left(\mathcal{T}_{\mathrm{M}}\tilde{\boldsymbol{g}}_{0,n,j}^{(3)}(\varrho_0;\cdot)\right)(\boldsymbol{y}) = -\mu_0\sqrt{\frac{n\varrho_0}{(2n+1)(2n+3)}}\left(\frac{\varrho_0}{\varrho_L}\right)^{n+1}\boldsymbol{h}_{n,j}^{(1)}(\varrho_L;\boldsymbol{y}),$$
$$\left(\mathcal{T}_{\mathrm{E}}\tilde{\boldsymbol{g}}_{0,n,j}^{(2)}(\varrho_0;\cdot)\right)(\boldsymbol{y}) = \frac{1}{\sqrt{n\varrho_0}}\beta_n^{(L)}\left((n+1)\left(\frac{y}{\varrho_L}\right)^{2n+1}+n\right)\left(\frac{\varrho_0}{y}\right)^{n+1}Y_{n,j}(\hat{\boldsymbol{y}}),$$

where $n \in \mathbb{N}$, $j = 1,\dots,2n+1$. For the reproducing kernels, we get for all $h \in (0,1)$, $\boldsymbol{z}_l \in \mathbb{B}_{\varrho_0}$, and with the abbreviation $t_l := \hat{\boldsymbol{y}}\cdot\hat{\boldsymbol{z}}_l$ for all $l = 1,\dots,L_\bullet$ the identities

$$\left(\mathcal{T}_{\mathrm{M}}\tilde{\boldsymbol{k}}_h^{(3)}(\cdot,\boldsymbol{z}_l)\right)(\boldsymbol{y}) = -\frac{\mu_0}{4\pi}\sum_{n=1}^{\infty}\sqrt{\frac{n}{n+1}}\frac{(hz_l)^n}{y^{n+2}}\left((n+1)\hat{\boldsymbol{y}}P_n(t_l)-(\hat{\boldsymbol{z}}_l-t_l\hat{\boldsymbol{y}})P_n'(t_l)\right),$$
$$\left(\mathcal{T}_{\mathrm{E}}\tilde{\boldsymbol{k}}_h^{(2)}(\cdot,\boldsymbol{z}_l)\right)(\boldsymbol{y}) = \frac{1}{4\pi}\sum_{n=1}^{\infty}h^n\sqrt{\frac{(2n+1)^3}{n}}\beta_n^{(L)}\left((n+1)\left(\frac{y}{\varrho_L}\right)^{2n+1}+n\right)\frac{z_l^{n-1}}{y^{n+1}}P_n(t_l).$$

Proof. The first two identities concerning the orthonormal basis functions $\tilde{\boldsymbol{g}}_{0,n,j}^{(i)}(\varrho_0;\cdot)$ for $i = 2$, 3 and for all $n \in \mathbb{N}$, $j = 1,\dots,2n+1$ are based on the results of the SVD of $\mathcal{T}_{\mathrm{M}}$ and $\mathcal{T}_{\mathrm{E}}$ summarized in Table 13.1. Note that a relation between the orthonormal basis $\{\boldsymbol{s}_{n,j}(\varrho_L;\cdot)\}_{n\in\mathbb{N},j=1,\dots,2n+1}$ stated in Table 13.1 and the vector outer harmonics is given in Definition 12.12. In addition, we insert the definition of the orthonormal basis functions $Z_{n,j}$ for all $n \in \mathbb{N}$, $j = 1,\dots,2n+1$ from Lemma 13.2 for $i = 2$.

With the representation of the kernel $\tilde{\boldsymbol{k}}_h^{(3)}$ and the results from Eqs. (5.12a) and (5.14) and Definitions 5.1 and 5.27, we obtain for all $h \in (0,1)$, $l = 1,\dots,l_{\mathrm{M}}$, $t_n = n$, and $\boldsymbol{z}_l \in \mathbb{B}_{\varrho_0}$ the identity

$$\begin{aligned}
\left(\mathcal{T}_{\mathrm{M}}\tilde{\boldsymbol{k}}_h^{(3)}(\cdot,\boldsymbol{z}_l)\right)(\boldsymbol{y}) &= -\mu_0\sum_{n=1}^{\infty}\sum_{j=1}^{2n+1}h^n\sqrt{\frac{n\varrho_0}{(2n+1)(2n+3)}}\left(\frac{\varrho_0}{\varrho_L}\right)^{n+1}\boldsymbol{h}_{n,j}^{(1)}(\varrho_L;\boldsymbol{y})G_{0,n,j}(\varrho_0;\boldsymbol{z}_l)\\
&= -\mu_0\sum_{n=1}^{\infty}\sum_{j=1}^{2n+1}h^n\sqrt{\frac{n\varrho_0}{(2n+1)(2n+3)}}\frac{\varrho_0^{n+1}}{y^{n+2}}Q_0^{(n+1/2)}(\varrho_0;z_l)Y_{n,j}(\hat{\boldsymbol{z}}_l)\tilde{\boldsymbol{y}}_{n,j}^{(1)}(\hat{\boldsymbol{y}})\\
&= -\frac{\mu_0}{4\pi}\sum_{n=1}^{\infty}h^n\sqrt{n(2n+1)}\frac{z_l^n}{y^{n+2}}\tilde{\boldsymbol{p}}_n^{(1)}(\hat{\boldsymbol{y}},\hat{\boldsymbol{z}}_l)\\
&= -\frac{\mu_0}{4\pi}\sum_{n=1}^{\infty}h^n\frac{z_l^n}{y^{n+2}}\left(\sqrt{n(n+1)}\boldsymbol{p}_n^{(1)}(\hat{\boldsymbol{y}},\hat{\boldsymbol{z}}_l)-n\boldsymbol{p}_n^{(2)}(\hat{\boldsymbol{y}},\hat{\boldsymbol{z}}_l)\right).
\end{aligned}$$

For the implementation, we can also insert Definition 5.21 and Theorem 2.15 and obtain for all $n \in \mathbb{N}$ and $\hat{\boldsymbol{y}}$, $\hat{\boldsymbol{z}}_l \in \mathbb{S}$ with $l = 1,\dots,l_{\mathrm{M}}$ the identities

$$\boldsymbol{p}_n^{(1)}(\hat{\boldsymbol{y}},\hat{\boldsymbol{z}}_l) = \hat{\boldsymbol{y}}P_n(\hat{\boldsymbol{y}}\cdot\hat{\boldsymbol{z}}_l), \qquad \boldsymbol{p}_n^{(2)}(\hat{\boldsymbol{y}},\hat{\boldsymbol{z}}_l) = \frac{1}{\sqrt{n(n+1)}}(\hat{\boldsymbol{z}}_l-(\hat{\boldsymbol{y}}\cdot\hat{\boldsymbol{z}}_l)\hat{\boldsymbol{y}})P_n'(\hat{\boldsymbol{y}}\cdot\hat{\boldsymbol{z}}_l).$$

Similarly, we use Eqs. (5.17) and (13.3), Theorem 2.25, and Lemma 13.2 and get for the

kernel $\tilde{\boldsymbol{k}}_h^{(2)}$ the identity

$$\begin{aligned}
&\left(\mathcal{T}_{\mathrm{E}}\tilde{\boldsymbol{k}}_h^{(2)}(\cdot,\boldsymbol{z}_l)\right)(\boldsymbol{y}) \\
&= \sum_{n=1}^{\infty}\sum_{j=1}^{2n+1} h^n(2n+1)\sqrt{\frac{\varrho_0}{n}}\beta_n^{(L)}\left(\frac{\varrho_0}{\varrho_L}\right)^n Z_{n,j}(\boldsymbol{y})G_{0,n,j}(\varrho_0;\boldsymbol{z}_l) \\
&= \frac{1}{4\pi}\sum_{n=1}^{\infty} h^n\sqrt{\frac{(2n+1)^3}{n}}\beta_n^{(L)}\left((n+1)\left(\frac{y}{\varrho_L}\right)^{2n+1}+n\right)\frac{z_l^{n-1}}{y^{n+1}}P_n(\hat{\boldsymbol{y}}\cdot\hat{\boldsymbol{z}}_l)
\end{aligned}$$

for all $h\in(0,1)$, $l=1,\dots,l_{\mathrm{E}}$, and $\boldsymbol{z}_l\in\mathbb{B}_{\varrho_0}$. Note that in this case the sequence $\{t_n\}_{n\in\mathbb{N}}$ occurring in the functions $G_{0,n,j}(\varrho_0;\cdot)$ is given by $t_n\coloneqq n-1$ for all $n\in\mathbb{N}$. □

Examples of orthonormal basis functions and their induced magnetic fields or electric potentials are plotted in Figs. 19.3 and 19.5 for both problems. The same is shown for reproducing kernels in Figs. 19.4 and 19.6.

In the MEG case, we observe that vortices of the current generate sources and sinks of the magnetic field, see Figs. 19.3 and 19.4. In the EEG case, we can see that outbound currents generate a positive electric potential whereas inbound currents generate a negative electric potential, see Fig. 19.5. In Figs. 19.4 and 19.6, the influence of the damping factor of the singular values can be seen, since reproducing kernels with strongly varying amplitudes generate magnetic fields or electric potentials of the same order of magnitude. The damping factors are based on the quotients $\varrho_0/\varrho_L=0.8353$ for the MEG and $\varrho_0/\varrho_{L-1}=0.8987$ for the EEG, respectively.

Besides the application of the forward operators to the dictionary elements, we can calculate the inner products of the dictionary elements with each other in the preprocessing and store them in the computer. Recall that the inverse MEG and EEG problem are solved separately. Thus, we only need to calculate the inner products between all dictionary elements belonging to the same type i.

Theorem 19.2. *Let $i\in\{2,3\}$ be fixed. Then we get for all n, $\bar{n}\in\mathbb{N}$, $j=1,\dots,2n+1$, $\bar{j}=1,\dots,2\bar{n}+1$, h, $h'\in(0,1)$, and $\boldsymbol{z}_l$, $\boldsymbol{z}_k\in\mathbb{B}_{\varrho_0}$ with l, $k=1,\dots,L_\bullet$ the following inner products between two dictionary functions:*

$$\begin{aligned}
\left\langle\tilde{\boldsymbol{g}}_{0,n,j}^{(i)}(\varrho_0;\cdot),\tilde{\boldsymbol{g}}_{0,\bar{n},\bar{j}}^{(i)}(\varrho_0;\cdot)\right\rangle_{\tilde{\mathfrak{H}}_s^{(i)}} &= \left(a_n^{(i)}\right)^2\delta_{n,\bar{n}}\delta_{j,\bar{j}}, \\
\left\langle\tilde{\boldsymbol{k}}_h^{(i)}(\cdot,\boldsymbol{z}_l),\tilde{\boldsymbol{g}}_{0,n,j}^{(i)}(\varrho_0;\cdot)\right\rangle_{\tilde{\mathfrak{H}}_s^{(i)}} &= \sqrt{\frac{2t_n^{(i)}+3}{\varrho_0^3}}\left(a_n^{(i)}\right)^2 h^n\left(\frac{z_l}{\varrho_0}\right)^{t_n^{(i)}}Y_{n,j}(\hat{\boldsymbol{z}}_l), \\
\left\langle\tilde{\boldsymbol{k}}_h^{(i)}(\cdot,\boldsymbol{z}_l),\tilde{\boldsymbol{k}}_{h'}^{(i)}(\cdot,\boldsymbol{z}_k)\right\rangle_{\tilde{\mathfrak{H}}_s^{(i)}} &= \frac{1}{4\pi\varrho_0^3}\sum_{\substack{n\in\mathbb{N}\\ a_n^{(i)}\neq 0}}\left(a_n^{(i)}\right)^2(hh')^n(2n+1)(2t_n^{(i)}+3)\left(\frac{z_lz_k}{\varrho_0^2}\right)^{t_n^{(i)}}P_n(t),
\end{aligned}$$

where $t\coloneqq\hat{\boldsymbol{z}}_l\cdot\hat{\boldsymbol{z}}_k\in[-1,1]$. Recall that the Sobolev space $\tilde{\mathfrak{H}}_s^{(i)}$ is defined with respect to the sequence $\{a_{m,n}^{(i)}\}_{m\in\mathbb{N}_0,n\in\mathbb{N}_{0_i}}$ in Eq. (19.5).

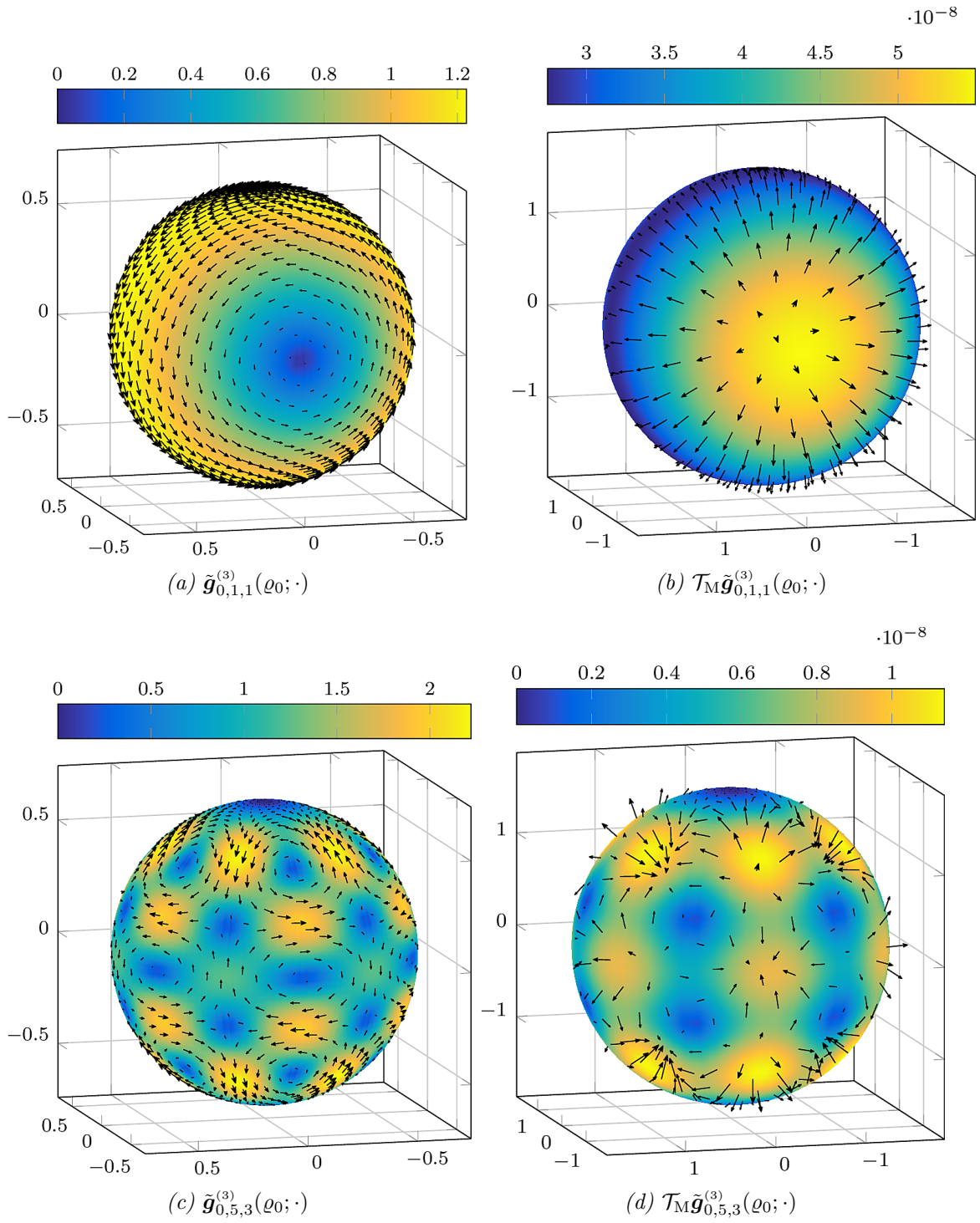

(a) $\tilde{\boldsymbol{g}}^{(3)}_{0,1,1}(\varrho_0;\cdot)$ *(b)* $\mathcal{T}_{\mathrm{M}}\tilde{\boldsymbol{g}}^{(3)}_{0,1,1}(\varrho_0;\cdot)$

(c) $\tilde{\boldsymbol{g}}^{(3)}_{0,5,3}(\varrho_0;\cdot)$ *(d)* $\mathcal{T}_{\mathrm{M}}\tilde{\boldsymbol{g}}^{(3)}_{0,5,3}(\varrho_0;\cdot)$

FIGURE 19.3: *The absolute value and the directions of some (vector-valued) orthonormal basis functions* $\tilde{\boldsymbol{g}}^{(3)}_{m,n,j}(\varrho_0;\cdot)$ *plotted on the sphere* $\mathbb{S}_{0.95\varrho_0}$ *(left) and the absolute value and the directions of their generated magnetic field plotted on the sphere* $\mathbb{S}_{1.7\varrho_L}$ *(right)*

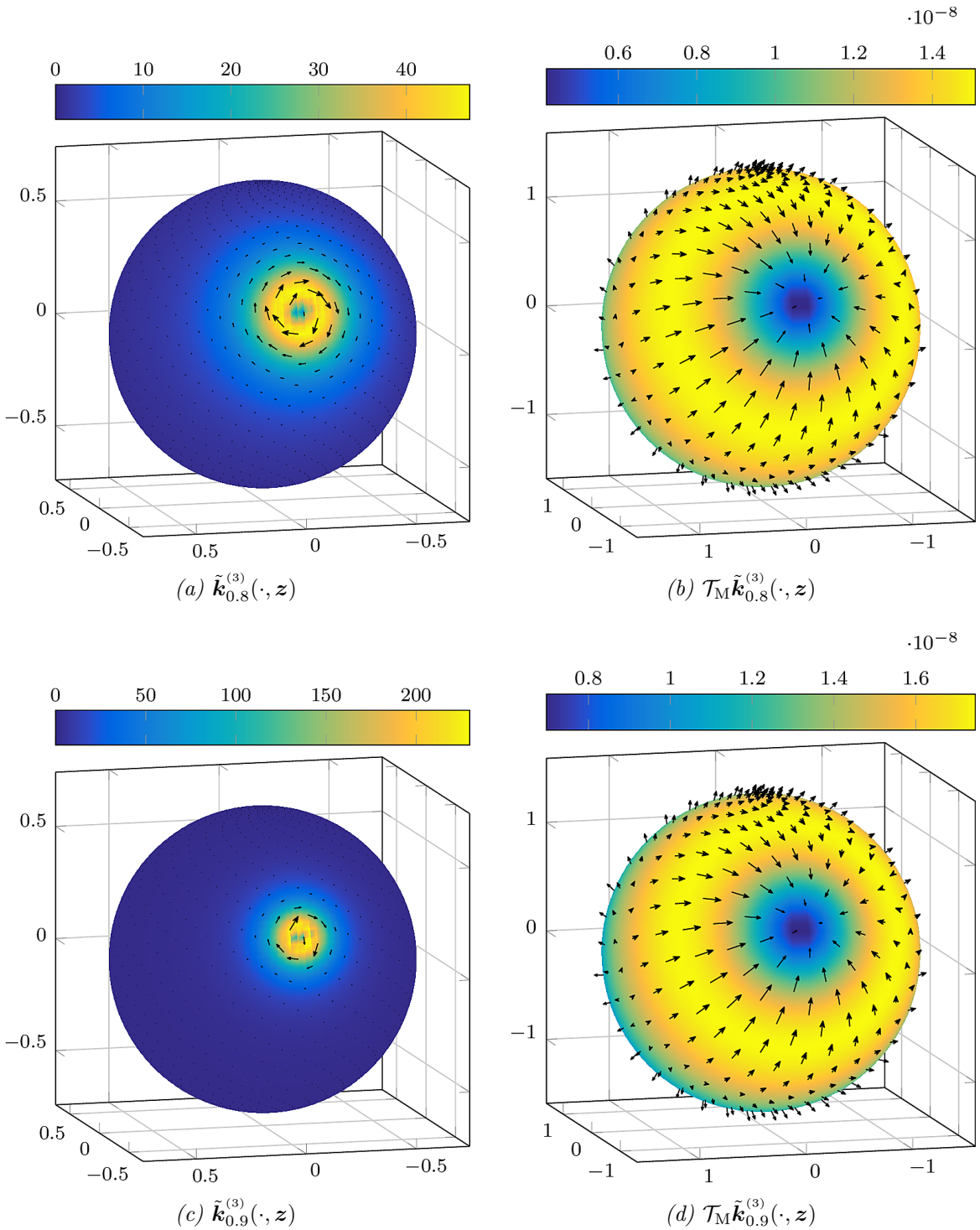

(a) $\tilde{\boldsymbol{k}}_{0.8}^{(3)}(\cdot, \boldsymbol{z})$ (b) $\mathcal{T}_{\mathrm{M}}\tilde{\boldsymbol{k}}_{0.8}^{(3)}(\cdot, \boldsymbol{z})$

(c) $\tilde{\boldsymbol{k}}_{0.9}^{(3)}(\cdot, \boldsymbol{z})$ (d) $\mathcal{T}_{\mathrm{M}}\tilde{\boldsymbol{k}}_{0.9}^{(3)}(\cdot, \boldsymbol{z})$

FIGURE 19.4: *The absolute value and the directions of some (vector-valued) reproducing kernels* $\tilde{\boldsymbol{k}}_h^{(3)}(\cdot, \boldsymbol{z})$ *localized in* $\boldsymbol{z} = \varrho_0(-0.9511, 0, 0.3090)^{\mathrm{T}}$ *plotted on the sphere* $\mathbb{S}_{0.95\varrho_0}$ *(left) and the absolute value and the directions of their generated magnetic field plotted on the sphere* $\mathbb{S}_{1.7\varrho_L}$ *(right)*

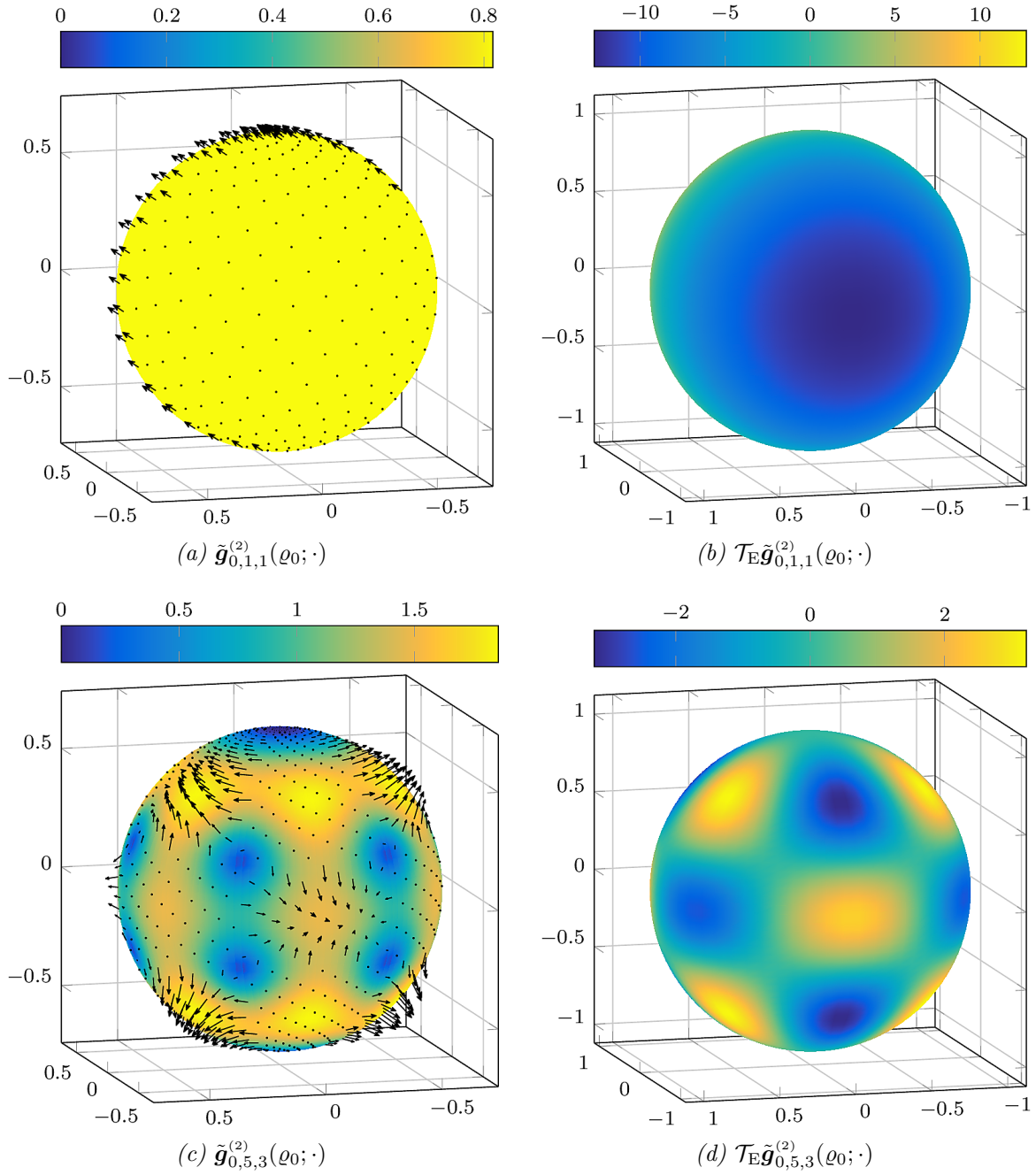

(a) $\tilde{\boldsymbol{g}}^{(2)}_{0,1,1}(\varrho_0;\cdot)$ (b) $\mathcal{T}_{\mathrm{E}}\tilde{\boldsymbol{g}}^{(2)}_{0,1,1}(\varrho_0;\cdot)$

(c) $\tilde{\boldsymbol{g}}^{(2)}_{0,5,3}(\varrho_0;\cdot)$ (d) $\mathcal{T}_{\mathrm{E}}\tilde{\boldsymbol{g}}^{(2)}_{0,5,3}(\varrho_0;\cdot)$

FIGURE 19.5: *The absolute value and the directions of some (vector-valued) orthonormal basis functions* $\tilde{\boldsymbol{g}}^{(2)}_{m,n,j}(\varrho_0;\cdot)$ *plotted on the sphere* $\mathbb{S}_{0.95\varrho_0}$ *(left) and their generated electric potential plotted on the sphere* $\mathbb{S}_{\varrho_L}$ *(right)*

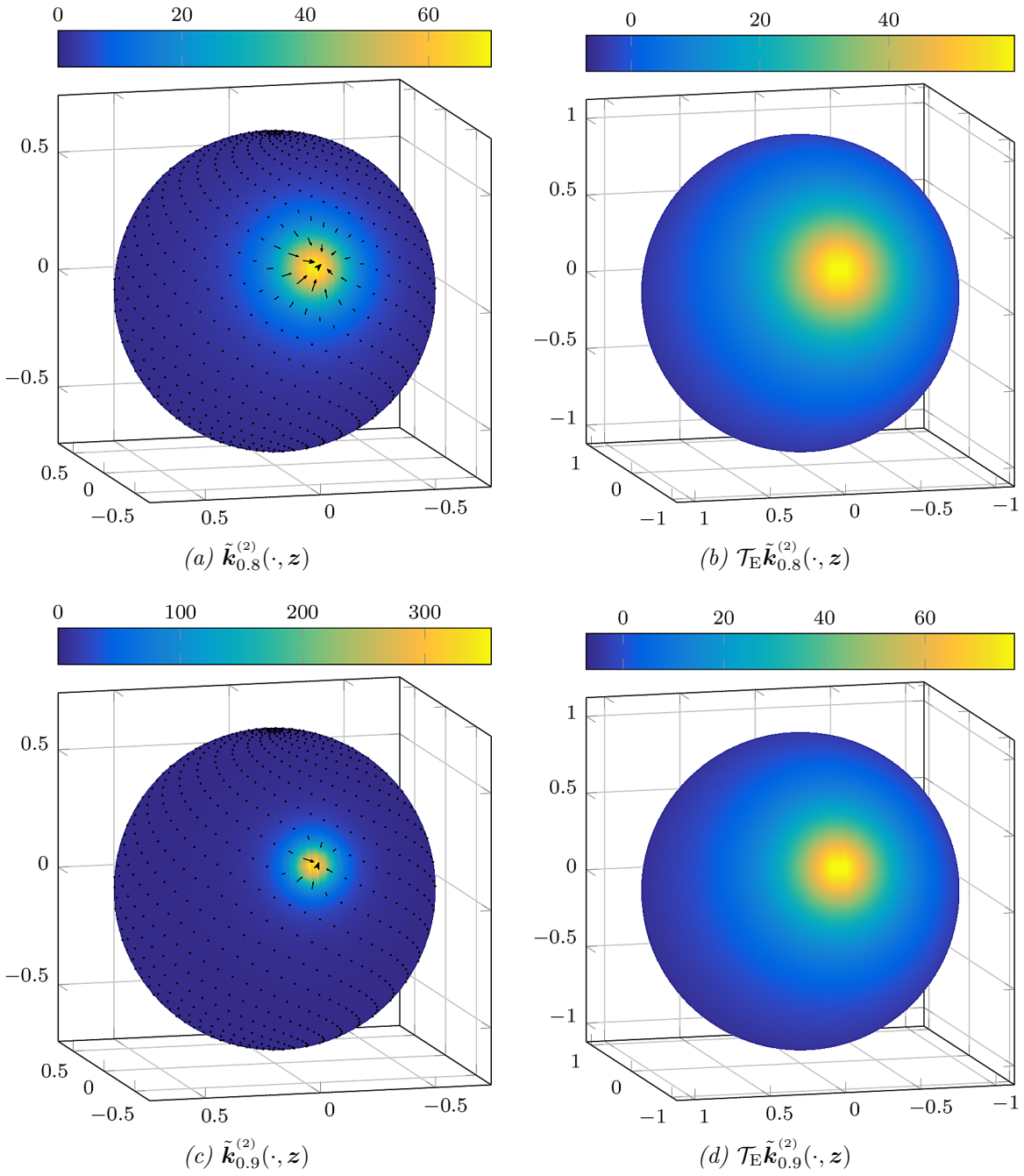

(a) $\tilde{\boldsymbol{k}}_{0.8}^{(2)}(\cdot, \boldsymbol{z})$ *(b)* $\mathcal{T}_{\mathrm{E}}\tilde{\boldsymbol{k}}_{0.8}^{(2)}(\cdot, \boldsymbol{z})$

(c) $\tilde{\boldsymbol{k}}_{0.9}^{(2)}(\cdot, \boldsymbol{z})$ *(d)* $\mathcal{T}_{\mathrm{E}}\tilde{\boldsymbol{k}}_{0.9}^{(2)}(\cdot, \boldsymbol{z})$

FIGURE 19.6: *The absolute value and the directions of some (vector-valued) reproducing kernels* $\tilde{\boldsymbol{k}}_h^{(2)}(\cdot, \boldsymbol{z})$ *localized in* $\boldsymbol{z} = \varrho_0(-0.9511, 0, 0.3090)^{\mathrm{T}}$ *plotted on the sphere* $\mathbb{S}_{0.95\varrho_0}$ *(left) and their generated electric potential plotted on the sphere* $\mathbb{S}_{\varrho_L}$ *(right)*

Proof. For the orthonormal basis functions, we get for all $n,\, \bar{n} \in \mathbb{N}$, $j = 1, \ldots, 2n+1$, and $\bar{j} = 1, \ldots, 2\bar{n}+1$ via Parseval's identity and Eq. (19.5) the relation

$$\begin{aligned}
&\left\langle \tilde{\boldsymbol{g}}_{0,n,j}^{(i)}(\varrho_0;\cdot), \tilde{\boldsymbol{g}}_{0,\bar{n},\bar{j}}^{(i)}(\varrho_0;\cdot) \right\rangle_{\tilde{\mathfrak{H}}_s^{(i)}} \\
&= \sum_{\substack{(m',n')\in\mathbb{N}_0\times\mathbb{N} \\ a_{m',n'}^{(i)}\neq 0}} \sum_{j'=1}^{2n'+1} \left(a_{m',n'}^{(i)}\right)^2 \left\langle \tilde{\boldsymbol{g}}_{0,n,j}^{(i)}(\varrho_0;\cdot), \tilde{\boldsymbol{g}}_{m',n',j'(\varrho_0;\cdot)}^{(i)}(\varrho_0;\cdot) \right\rangle_{\mathbf{L}_2(\mathbb{B}_{\varrho_0})} \\
&\quad \times \left\langle \tilde{\boldsymbol{g}}_{0,\bar{n},\bar{j}}^{(i)}(\varrho_0;\cdot), \tilde{\boldsymbol{g}}_{m',n',j'}^{(i)}(\varrho_0;\cdot) \right\rangle_{\mathbf{L}_2(\mathbb{B}_{\varrho_0})} \\
&= \left(a_n^{(i)}\right)^2 \left\langle \tilde{\boldsymbol{g}}_{0,\bar{n},\bar{j}}^{(i)}(\varrho_0;\cdot), \tilde{\boldsymbol{g}}_{0,n,j}^{(i)}(\varrho_0;\cdot) \right\rangle_{\mathbf{L}_2(\mathbb{B}_{\varrho_0})} = \left(a_n^{(i)}\right)^2 \delta_{n,\bar{n}}\delta_{j,\bar{j}}.
\end{aligned}$$

In order to calculate the $\tilde{\mathfrak{H}}_s^{(i)}(a, \mathbb{B}_{\varrho_0})$-inner product of reproducing kernels localized in $\boldsymbol{z}_l \in \mathbb{B}_{\varrho_0}$ for $l = 1, \ldots, L_\bullet$ with other dictionary elements, we compute an auxiliary inner product. For all $n \in \mathbb{N}$, $j = 1, \ldots, 2n+1$, and $h \in (0,1)$, we have

$$\begin{aligned}
&\left\langle \tilde{\boldsymbol{k}}_h^{(i)}(\cdot, \boldsymbol{z}_l), \tilde{\boldsymbol{g}}_{0,n,j}^{(i)}(\varrho_0;\cdot) \right\rangle_{\mathbf{L}_2(\mathbb{B}_{\varrho_0})} \\
&= \left\langle \sum_{n'=1}^{\infty} \sum_{j'=1}^{2n'+1} h^{n'} G_{0,n',j'}(\varrho_0; \boldsymbol{z}_l) \tilde{\boldsymbol{g}}_{0,n',j'}^{(i)}(\varrho_0;\cdot), \tilde{\boldsymbol{g}}_{0,n,j}^{(i)}(\varrho_0;\cdot) \right\rangle_{\mathbf{L}_2(\mathbb{B}_{\varrho_0})} \\
&= h^n G_{0,n,j}(\varrho_0; \boldsymbol{z}_l).
\end{aligned}$$

Eventually, we obtain via Parseval's identity and Definition 5.35 for all $\boldsymbol{z}_l \in \mathbb{B}_{\varrho_0}$, $l = 1, \ldots, L_\bullet$, $h \in (0,1)$, $n \in \mathbb{N}$, and $j = 1, \ldots, 2n+1$ the relation

$$\begin{aligned}
&\left\langle \tilde{\boldsymbol{k}}_h^{(i)}(\cdot, \boldsymbol{z}_l), \tilde{\boldsymbol{g}}_{0,n,j}^{(i)}(\varrho_0;\cdot) \right\rangle_{\tilde{\mathfrak{H}}_s^{(i)}} \\
&= \sum_{\substack{(m',n')\in\mathbb{N}_0\times\mathbb{N} \\ a_{m',n'}^{(i)}\neq 0}} \sum_{j'=1}^{2n'+1} \left(a_{m',n'}^{(i)}\right)^2 \left\langle \tilde{\boldsymbol{k}}_h^{(i)}(\cdot, \boldsymbol{z}_l), \boldsymbol{g}_{m',n',j'}^{(i)}(\varrho_0;\cdot) \right\rangle_{\mathbf{L}_2(\mathbb{B}_{\varrho_0})} \delta_{m',0}\delta_{n',n}\delta_{j',j} \\
&= \left(a_n^{(i)}\right)^2 \left\langle \tilde{\boldsymbol{k}}_h^{(i)}(\cdot, \boldsymbol{z}_l), \boldsymbol{g}_{0,n,j}^{(i)}(\varrho_0;\cdot) \right\rangle_{\mathbf{L}_2(\mathbb{B}_{\varrho_0})} \\
&= \left(a_n^{(i)}\right)^2 h^n G_{0,n,j}(\varrho_0; \boldsymbol{z}_l) \\
&= \sqrt{\frac{2t_n^{(i)}+3}{\varrho_0^3}} \left(a_n^{(i)}\right)^2 h^n \left(\frac{z_l}{\varrho_0}\right)^{t_n^{(i)}} Y_{n,j}(\hat{\boldsymbol{z}}_l).
\end{aligned}$$

Finally, for two kernel functions with centres $\boldsymbol{z}_l,\, \boldsymbol{z}_k \in \mathbb{B}_{\varrho_0}$ where $l,\ k \in \{1, \ldots, L_\bullet\}$ and parameters $h,\, h' \in (0,1)$, we get with Eq. (5.17) the result

$$\begin{aligned}
&\left\langle \tilde{\boldsymbol{k}}_h^{(i)}(\cdot, \boldsymbol{z}_l), \tilde{\boldsymbol{k}}_{h'}^{(i)}(\cdot, \boldsymbol{z}_k) \right\rangle_{\tilde{\mathfrak{H}}_s^{(i)}} \\
&= \sum_{\substack{(m,n)\in\mathbb{N}_0\times\mathbb{N} \\ a_{m,n}^{(i)}\neq 0}} \sum_{j=1}^{2n+1} \left(a_{m,n}^{(i)}\right)^2 \left\langle \tilde{\boldsymbol{k}}_h^{(i)}(\cdot, \boldsymbol{z}_l), \tilde{\boldsymbol{g}}_{m,n,j}^{(i)}(\varrho_0;\cdot) \right\rangle_{\mathbf{L}_2(\mathbb{B}_{\varrho_0})} \left\langle \tilde{\boldsymbol{k}}_{h'}^{(i)}(\cdot, \boldsymbol{z}_k), \tilde{\boldsymbol{g}}_{m,n,j}^{(i)}(\varrho_0;\cdot) \right\rangle_{\mathbf{L}_2(\mathbb{B}_{\varrho_0})}
\end{aligned}$$

$$= \sum_{\substack{n\in\mathbb{N}\\ a_n^{(i)}\neq 0}} \sum_{j=1}^{2n+1} \left(a_n^{(i)}\right)^2 (hh')^n G_{0,n,j}(\varrho_0;\boldsymbol{z}_l) G_{0,n,j}(\varrho_0;\boldsymbol{z}_k)$$

$$= \sum_{\substack{n\in\mathbb{N}\\ a_n^{(i)}\neq 0}} \left(a_n^{(i)}\right)^2 (hh')^n \frac{2n+1}{4\pi} Q_0^{(t_n^{(i)}+1/2)}(\varrho_0;z_l) Q_0^{(t_n^{(i)}+1/2)}(\varrho_0;z_k) P_n(\hat{\boldsymbol{z}}_l\cdot\hat{\boldsymbol{z}}_k)$$

$$= \frac{1}{4\pi\varrho_0^3} \sum_{\substack{n\in\mathbb{N}\\ a_n^{(i)}\neq 0}} \left(a_n^{(i)}\right)^2 (hh')^n (2n+1)(2t_n^{(i)}+3) \left(\frac{z_l z_k}{\varrho_0^2}\right)^{t_n^{(i)}} P_n(\hat{\boldsymbol{z}}_l\cdot\hat{\boldsymbol{z}}_k). \qquad \square$$

The inner products between all dictionary elements can be stored in a (large) matrix. For the sake of memory reduction, we only save a linearization of the lower diagonal matrix in a vector, which is sufficient because of the symmetry of the matrix.

19.3. The Visualization

For a visualization of the numerical results, the approximations are plotted on a spherical point grid within the cerebrum $\mathbb{B}_{\varrho_0}$. The radius of this sphere is typically chosen as $0.95\varrho_0$. More precisely, we use the equiangular Driscoll-Healy grid introduced in [58], see also [158, Exam. 5.35]. For t, $s\in\mathbb{N}$ with $1\le s,t\le 60$, it is given by

$$\varphi_t = \frac{2\pi}{60}t, \qquad \vartheta_s = \frac{2\pi}{60}s, \tag{19.8a}$$

$$x_{t,s} = 0.95\varrho_0 \sin(\vartheta_s)\cos(\varphi_t), \qquad y_{t,s} = 0.95\varrho_0 \sin(\vartheta_s)\sin(\varphi_t), \tag{19.8b}$$

$$z_{t,s} = 0.95\varrho_0 \cos(\vartheta_s). \tag{19.8c}$$

The resulting grid with 3600 points is plotted in Fig. 19.7.

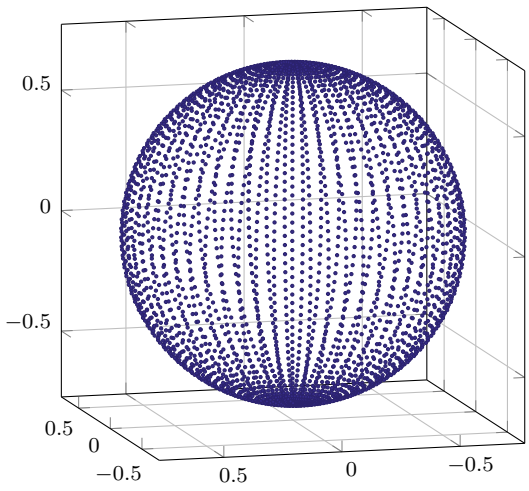

FIGURE 19.7: *Driscoll-Healy grid with* 3600 *points from Eq.* (19.8)

Chapter 20.

Other Reconstruction Methods

20.1. Regularized Ritz Method

As we saw in Remark 16.19 and Example 16.23, the idea behind this method is to minimize the Tikhonov-Philips functional on a finite-dimensional subspace. In Example 16.23, a representation of the resulting minimizer is stated. For this representation, we need to calculate the restriction of $\mathcal{A}_\bullet$ with $\bullet \in \{\mathrm{M}, \mathrm{E}\}$ onto this finite-dimensional subspace. Recall that the operators are stated in Eq. (19.1). Then each restricted operator, as a mapping between two finite-dimensional spaces, can be represented by a matrix. In order to do so, we assume that the finite-dimensional subspace is spanned for fixed $i \in \{2, 3\}$ by the orthonormal basis functions $\tilde{\boldsymbol{g}}^{(i)}_{0,n,j}(\varrho_0;\cdot)$ up to degree $N_\bullet \in \mathbb{N}$. More precisely, we choose $N \coloneqq N_\bullet \coloneqq 100$ within our numerical tests. The corresponding finite-dimensional subspace in the domain of the operator is for $i = 2$, 3 given by

$$\mathcal{V}_{N_\bullet(N_\bullet+2)} \coloneqq \operatorname{span}\left\{ \tilde{\boldsymbol{g}}^{(i)}_{0,n,j}(\varrho_0;\cdot) \;\middle|\; 1 \le n \le N_\bullet,\ j = 1, \dots, 2n+1 \right\}.$$

The dimension of this space is $N_\bullet(N_\bullet + 2)$. For the next identities, we set $i = 3$ in the case of the inverse MEG problem and $i = 2$ in the case of the inverse EEG problem.

In the finite-dimensional subspace $\mathcal{V}_{N_\bullet(N_\bullet+2)}$, the current is given by

$$\boldsymbol{J}_{N_\bullet} = \sum_{n=1}^{N_\bullet} \sum_{j=1}^{2n+1} J^\bullet_{n,j} \tilde{\boldsymbol{g}}^{(i)}_{0,n,j}(\varrho_0;\cdot), \tag{20.1}$$

which coincides with the orthogonal projection of $\boldsymbol{J}^{\mathrm{P}}$ onto $\mathcal{V}_{N_\bullet(N_\bullet+2)}$ if the coefficients $J^\bullet_{n,j}$ are chosen accordingly. The restricted linear mapping

$$\mathcal{A}_\bullet|_{\mathcal{V}_{N_\bullet(N_\bullet+2)}} \colon \mathcal{V}_{N_\bullet(N_\bullet+2)} \to \mathbb{R}^{\ell_\bullet}, \qquad \mathcal{A}_\bullet|_{\mathcal{V}_{N_\bullet(N_\bullet+2)}} \boldsymbol{f} = \mathcal{A}_\bullet \boldsymbol{f} \qquad \text{for all } \boldsymbol{f} \in \mathcal{V}_{N_\bullet(N_\bullet+2)}$$

can be represented by an $\ell_\bullet \times N_\bullet(N_\bullet + 2)$-matrix. We denote the corresponding matrix by $\mathfrak{A}^\bullet = (\mathfrak{A}^\bullet_{k,l})_{k,l}$ and the vector containing the coefficients $J^\bullet_{n,j}$ by $\boldsymbol{f}_\bullet$. For constructing this matrix, we define a mapping of the basis function index tuple (n, j) with degree n and order j onto a single index $l = 1, \dots, N_\bullet(N_\bullet + 2)$ by

$$n(l) = \left\lfloor \sqrt{l} \right\rfloor, \qquad j(l) = l - (n(l))^2 + 1.$$

Then, the entries of the matrix and the vector are for all $k = 1, \dots, \ell_\bullet$ and $l = 1, \dots, N_\bullet(N_\bullet+2)$ given by

$$\mathfrak{A}^{\mathrm{M}}_{k,l} \coloneqq \left(\boldsymbol{\nu}(\boldsymbol{y}_k) \cdot \mathcal{T}_{\mathrm{M}} \tilde{\boldsymbol{g}}^{(3)}_{0,n(l),j(l)}(\varrho_0;\cdot) \right)(\boldsymbol{y}_k), \tag{20.2a}$$

$$\mathfrak{A}^{\mathrm{E}}_{k,l} \coloneqq \left(\mathcal{T}_{\mathrm{E}} \tilde{\boldsymbol{g}}^{(2)}_{0,n(l),j(l)}(\varrho_0;\cdot) \right)(\boldsymbol{y}_{\ell_{\mathrm{M}}+k}), \tag{20.2b}$$

$$\boldsymbol{f}_\bullet \coloneqq (J^\bullet_{n(l),j(l)})_{l=1,\dots,N_\bullet(N_\bullet+2)}. \tag{20.2c}$$

For the implementation of these matrices, we can use the result stated in Theorem 19.1 for the forward operator action.

According to the Ritz method, see Example 16.23, we calculate our approximation by

$$\boldsymbol{f}^{\delta_\bullet}_{N_\bullet,\tau} = \left((\mathfrak{A}^\bullet)^{\mathrm{T}}\mathfrak{A}^\bullet + \tau\mathfrak{I}_{N_\bullet}\right)^{-1}\left((\mathfrak{A}^\bullet)^{\mathrm{T}}\boldsymbol{g}^{\delta_\bullet}\right),$$

where $\mathfrak{I}_{N_\bullet}$ is the identity matrix in $\mathbb{R}^{N_\bullet(N_\bullet+2)}$. This is the unique minimizer of the Tikhonov-Philips functional, see Example 16.21, with the norm of the domain space as penalty term.

Now, we go a step further and allow different norms in the regularization term. This leads to

$$\boldsymbol{f}^{\delta_\bullet}_{N_\bullet,\tau} = \left((\mathfrak{A}^\bullet)^{\mathrm{T}}\mathfrak{A}^\bullet + \tau\mathfrak{B}^*_\bullet\mathfrak{B}_\bullet\right)^{-1}\left((\mathfrak{A}^\bullet)^{\mathrm{T}}\boldsymbol{g}^{\delta_\bullet}\right), \tag{20.3}$$

where the regularization matrix $\mathfrak{B}_\bullet$ will be a diagonal matrix containing the Sobolev sequence $a^{(i)}_{0,n(l)}$ for $l = 1,\ldots,N_\bullet(N_\bullet+2)$, see Eq. (19.5), on its diagonal.

In our numerical test, the same three sequences were used for the regularization as for the construction of the $\tilde{\mathcal{H}}^{(i)}_s$-spaces used for the regularization term of the RFMP, see Eq. (19.5), that is $s \in \{0,1,2\}$. The case $s = 0$ implies $a^{(i)}_{0,n(l)} = 1$ for all $l = 1,\ldots,N_\bullet(N_\bullet+2)$. Thus, $\mathfrak{B}_\bullet$ is the identity matrix and the regularization corresponds to the $\mathbf{L}_2(\mathbb{B}_{\varrho_0})$-regularization. Otherwise, the regularization corresponds to the $\tilde{\mathcal{H}}^{(i)}_s$-regularization due to Example 16.21. Note that $\mathfrak{B}^*_\bullet\mathfrak{B}_\bullet$ is the Gramian matrix of the inner product of this Sobolev space.

Eventually, we denote the neuronal current corresponding to the vector $\boldsymbol{f}^{\delta_\bullet}_{N_\bullet,\tau}$ by $\boldsymbol{J}^{\delta_\bullet}_{N,\tau}$, which is obtained via Eq. (20.1).

20.2. Scalar Spline Method

Scalar spline methods are widely used in approximation and inverse problems. The method and properties of the spline functions are discussed and analyzed in the literature, see [6, 7, 158, 160], for instance. In the context of medical imaging, it is used for the reconstruction of scalar parts of the neuronal current inside the cerebrum $\mathbb{B}_{\varrho_0}$ in [73].

We first give a short overview of a reproducing kernel based spline method on the ball in Section 20.2.1. Within this section a *spline method* is always meant as this reproducing kernel based spline method on the ball. Then, in Section 20.2.2, we adapt this general setting to the scalar MEG problem considered in Section 15.3. Besides solving the scalar MEG problem via this particular spline method, we are interested in comparing the spline approximation with the reconstruction of the neuronal current achieved via the R(O)FMP. Unfortunately, the particular scalar spline used in [73] does not satisfy this requirement since the resulting neuronal current has parts in the null space of the operator $\mathcal{T}_{\mathrm{M}}$ and the R(O)FMP will not reconstruct these parts. This will also be further discussed in Section 20.2.2. After constructing appropriate scalar splines for the scalar MEG problem, we will use them for the inversion of our synthetic test case from Chapter 18. In Section 20.2.3, we calculate the scalar part of the synthetic test current that will be reconstructed by the scalar spline method in order to get the exact reference solution for this test case. Eventually, in Section 20.2.4, we present a formula that allows the conversion from the scalar spline solution to the entire vector-valued neuronal current reconstruction. Lastly, we discuss some aspects of the scalar spline method for the inverse EEG problem from [73] in Section 20.2.4.

20.2.1. Scalar Splines

Let the data $\boldsymbol{g} = (g_1, \dots, g_\ell)^{\mathrm{T}} \in \mathbb{R}^\ell$ with $\ell \in \mathbb{N}$ be given. For the scalar spline approach, we split the operator $\mathcal{A}$ into its rows, that is

$$\boldsymbol{g} = \mathcal{A}F \qquad \Leftrightarrow \qquad g_k = \mathcal{A}^k F, \qquad k = 1, \dots, \ell.$$

Here, the operator $\mathcal{A}$ is defined via some auxiliary continuous linear functionals, that is $\mathcal{A} \coloneqq (\mathcal{A}^1, \dots, \mathcal{A}^\ell)^{\mathrm{T}}$, where each functional $\mathcal{A}^k$ for $k = 1, \dots, \ell$ maps from an appropriate Sobolev space $\mathcal{H} \coloneqq \mathcal{H}(\{\kappa_n\}_{n\in\mathbb{N}_0}; \mathbb{B}_{\varrho_0})$ onto $\mathbb{R}$. In this setting, the function $F \in \mathcal{H}$ is the desired quantity. Scalar Sobolev spaces on the ball are, for example, defined in [3, 158]. They can be defined similar to Definition 16.1. In this case, the vector-valued orthonormal basis needs to be replaced by the scalar-valued one from Definition 5.35. In addition, the sequence $\{\kappa_n\}_{n\in\mathbb{N}}$ of the Sobolev space is assumed to be chosen in such a way that $\mathcal{H} \subset \mathrm{L}_2(\mathbb{B}_{\varrho_0})$.

For example, in [158, Thm. 10.4], scalar reproducing kernels over the ball based on the orthonormal system from Definition 5.33 are introduced. In our application, however, these orthonormal bases are not necessarily the first choice since we do not know a-priori which of these functions are in the null space of the operator and which are not. For this purpose, we use the more general definition of the scalar reproducing kernel over the ball from [73, Eq. (40)], that is

$$K(\boldsymbol{x}, \boldsymbol{z}) = \sum_{\substack{n\in\mathbb{N}_0 \\ \kappa_n \neq 0}} \sum_{j=1}^{2n+1} \kappa_n^{-2} G_n(x) G_n(z) Y_{n,j}(\hat{\boldsymbol{x}}) Y_{n,j}(\hat{\boldsymbol{z}}), \qquad \boldsymbol{x},\ \boldsymbol{z} \in \mathbb{B}_{\varrho_0}, \tag{20.4}$$

where the functions G_n for all $n \in \mathbb{N}_0$ are normalized with respect to the $\mathrm{L}_2^w([0, \varrho_0])$-inner product corresponding to the weight function $w(x) \coloneqq x^2$ with $x \in [0, \varrho_0]$. The functions G_n can be chosen based on the problem of interest.

According to [73, Eq. (41)], the corresponding *(scalar) spline function* is of the form

$$S(\boldsymbol{x}) = \sum_{k=1}^{\ell} a_k \mathcal{A}_{\boldsymbol{z}}^k K(\boldsymbol{x}, \boldsymbol{z}) \tag{20.5a}$$

$$= \sum_{k=1}^{\ell} a_k \sum_{\substack{n\in\mathbb{N}_0 \\ \kappa_n \neq 0}} \sum_{j=1}^{2n+1} \kappa_n^{-2} G_n(x) Y_{n,j}(\hat{\boldsymbol{x}}) \mathcal{A}_{\boldsymbol{z}}^k (G_n(z) Y_{n,j}(\hat{\boldsymbol{z}})), \qquad \boldsymbol{x} \in \mathbb{B}_{\varrho_0}. \tag{20.5b}$$

The spline function and the data are for all $l = 1, \dots, \ell$ connected by

$$g_l = \mathcal{A}_{\boldsymbol{x}}^l S(\boldsymbol{x}) = \sum_{k=1}^{\ell} a_k \mathcal{A}_{\boldsymbol{x}}^l \mathcal{A}_{\boldsymbol{z}}^k K(\boldsymbol{x}, \boldsymbol{z}), \tag{20.6}$$

see [73, Eq. (42)]. It is well-known, see [6, 73, 158], that a spline function has the following properties:

i) For given data $\boldsymbol{g} \in \mathbb{R}^\ell$ and continuous linear functionals $\mathcal{A}^k$ for $k = 1, \dots, \ell$, the interpolation problem in Eq. (20.6) is uniquely solvable if and only if the functionals $\mathcal{A}^k$ are linearly independent, see [158, Thm. 10.10].

ii) Among all solutions F interpolating the data, that is $\mathcal{A}^k F = g_k$ for $k = 1, \dots, \ell$, the spline function is the solution with minimal $\mathcal{H}$-norm, see [158, Thm. 10.13].

iii) The spline function satisfies a best-approximation property, see [158, Thm. 10.14].

In addition, in the regularized case the following theorem holds true.

Theorem 20.1 (Spline Approximation, [158, Thm. 6.40]). *Let $\boldsymbol{g} \in \mathbb{R}^\ell$ and a regularization parameter $\tau > 0$ be given. If the vector $\boldsymbol{a} = (a_k)_{k=1,\dots,\ell}$ is the solution of*

$$\left(\left(\mathcal{A}^l_{\boldsymbol{x}} \mathcal{A}^k_{\boldsymbol{z}} \left(K(\boldsymbol{x}, \boldsymbol{z}) \right) \right)_{l,k=1,\dots,\ell} + \tau \mathcal{I}_{\mathbb{R}^{\ell \times \ell}} \right) \boldsymbol{a} = \boldsymbol{g}, \tag{20.7}$$

then the spline function given by Eq. (20.5b) *with Eq.* (20.6) *is the unique minimizer of the corresponding Tikhonov functional, that is*

$$S = \min_{F \in \mathcal{H}} \left(\|\boldsymbol{g} - \mathcal{A}F\|^2_{\mathbb{R}^\ell} + \tau \|F\|^2_{\mathcal{H}} \right).$$

20.2.2. Scalar Splines for the MEG Problem

In order to apply the scalar splines to the MEG problem, we need to consider an inverse problem with a scalar density. For this purpose, we use the Helmholtz decomposition of the neuronal current from Eq. (15.22) combined with the Coulomb gauge. In addition, we assume that Assumption 15.12 holds true, which implies a certain smoothness of the current and the functions of the Helmholtz decomposition. Then, according to Eq. (15.31), we get a relation between the scalar part $A^{(1)}$ of the neuronal current and the magnetic flux density. Recall that the function $A^{(1)}$ equals the radial component of the vector potential of the Helmholtz decomposition, see Eq. (15.23). For given data $\boldsymbol{g} \in \mathbb{R}^{\ell_{\mathrm{M}}}$, we consider the problem

$$\mathcal{A}^k A^{(1)} = g_k \qquad \text{for all } k = 1, \dots, \ell_{\mathrm{M}}.$$

The related functionals $\mathcal{A}^k$ are for all $k = 1, \dots, \ell_{\mathrm{M}}$ defined by

$$\begin{aligned} \mathcal{A}^k A^{(1)} \coloneqq -\mu_0 \varrho_0 \sum_{n=1}^{\infty} \sum_{j=1}^{2n+1} \sqrt{\frac{1}{(2n+1)(n+1)}} \left(\frac{\mathrm{d} A^{(1)}_{n,j}}{\mathrm{d}x}(\varrho_0)\varrho_0 - (n-1) A^{(1)}_{n,j}(\varrho_0) \right) \left(\frac{\varrho_0}{\varrho_L} \right)^{n+1} \\ \times \boldsymbol{\nu}(\boldsymbol{y}_k) \cdot \boldsymbol{h}^{(1)}_{n,j}(\varrho_L; \boldsymbol{y}_k), \end{aligned}$$

where the abbreviation $A^{(1)}_{n,j}$, firstly introduces in Eq. (14.4) for arbitrary $\mathrm{L}_2(\mathbb{B}_{\varrho_0})$-functions, is used and where $\boldsymbol{y}_k$ are the measurement positions according to Problem 9.1.

In fact, scalar splines are used in [73] for solving this particular problem. For the spline method, the functions G_n occurring in Eq. (20.4) remain to be determined for all $n \in \mathbb{N}$. Note that degree $n = 0$ is in the null space of the functional. In [73, Eq. (53)], they are chosen for all $n \in \mathbb{N}$ and a particular $r \in (0, \varrho_0)$ as

$$G_n(x) = \sqrt{\frac{3}{1 - r^3}} \chi_{[r, \varrho_0]}(x), \qquad x \in [0, \varrho_0].$$

Due to the non-uniqueness issue of the inverse MEG problem, these functions are chosen to accomplish an additional non-uniqueness constraint, namely the layer density constraint, see Table 12.1. However, from Theorem 15.20 it is known that with these functions the minimum norm assumption, which is used as the additional uniqueness constraint in the previous considerations for the R(O)FMP, cannot be fulfilled. Therefore, we need to adapt

the setting from [73] in order to achieve a comparable setting for both methods. Hence, we choose the function G_n for all $n \in \mathbb{N}_0$ to be

$$G_n(x) \coloneqq \sqrt{\frac{2n+5}{\varrho_0^3}} \left(\frac{x}{\varrho_0}\right)^{n+1}, \qquad x \in [0, \varrho_0]. \tag{20.8}$$

Thus, the considered reproducing kernel has the form

$$\begin{aligned} K(\boldsymbol{x}, \boldsymbol{z}) &= \sum_{\substack{n \in \mathbb{N}_0 \\ \kappa_n \neq 0}} \sum_{j=1}^{2n+1} \kappa_n^{-2} \frac{2n+5}{\varrho_0^3} \left(\frac{xz}{\varrho_0^2}\right)^{n+1} Y_{n,j}(\hat{\boldsymbol{x}}) Y_{n,j}(\hat{\boldsymbol{z}}) \\ &= \frac{1}{4\pi\varrho_0^3} \sum_{\substack{n \in \mathbb{N}_0 \\ \kappa_n \neq 0}} \kappa_n^{-2} (2n+5)(2n+1) \left(\frac{xz}{\varrho_0^2}\right)^{n+1} P_n(\hat{\boldsymbol{x}} \cdot \hat{\boldsymbol{z}}), \qquad \boldsymbol{x},\ \boldsymbol{z} \in \mathbb{B}_{\varrho_0}. \end{aligned}$$

Note that the Addition Theorem, see Theorem 2.25, was used in the latter step. In order to construct the scalar spline, we need to apply the functionals $\mathcal{A}^k$ for all $k = 1, \ldots, \ell_{\mathrm{M}}$ to the reproducing kernel. Eventually, we get the identity

$$\mathcal{A}_{\boldsymbol{z}}^k (G_n(z) Y_{n,j}(\hat{\boldsymbol{z}})) = -\mu_0 \boldsymbol{\nu}(\boldsymbol{y}_k) \cdot \left(\frac{G_n'(\varrho_0)\varrho_0 - (n-1)G_n(\varrho_0)}{\sqrt{(2n+1)(n+1)}} \left(\frac{\varrho_0}{y_k}\right)^{n+2} \tilde{\boldsymbol{y}}_{n,j}^{(1)}(\hat{\boldsymbol{y}}_k) \right) \delta_{n,0},$$

where we have additionally used the definition of the vector outer harmonics from Definition 5.27. The precise function G_n and its derivative have for all $n \in \mathbb{N}$ the following values at the boundary:

$$G_n(\varrho_0) = \sqrt{\frac{2n+5}{\varrho_0^3}}, \qquad G_n'(\varrho_0) = \sqrt{\frac{2n+5}{\varrho_0^3}} \frac{n+1}{\varrho_0}.$$

Hence, we get for all $n \in \mathbb{N}$ the identity

$$G_n'(\varrho_0)\varrho_0 - (n-1)G_n(\varrho_0) = 2\sqrt{\frac{2n+5}{\varrho_0^3}}. \tag{20.9}$$

Eventually, for all $k = 1, \ldots, \ell_{\mathrm{M}}$ the functional applied to the reproducing kernel has the representation

$$\begin{aligned} &\mathcal{A}_{\boldsymbol{z}}^k K(\boldsymbol{x}, \boldsymbol{z}) \\ &= -\mu_0 \boldsymbol{\nu}(\boldsymbol{y}_k) \cdot \left(\sum_{\substack{n \in \mathbb{N} \\ \kappa_n \neq 0}} \sum_{j=1}^{2n+1} \frac{G_n'(\varrho_0)\varrho_0 - (n-1)G_n(\varrho_0)}{\sqrt{(n+1)(2n+1)}} \kappa_n^{-2} G_n(x) \left(\frac{\varrho_0}{y_k}\right)^{n+2} Y_{n,j}(\hat{\boldsymbol{x}}) \tilde{\boldsymbol{y}}_{n,j}^{(1)}(\hat{\boldsymbol{y}}_k) \right) \\ &= \frac{-\mu_0}{2\pi\varrho_0^{3/2}} \boldsymbol{\nu}(\boldsymbol{y}_k) \cdot \left(\sum_{\substack{n \in \mathbb{N} \\ \kappa_n \neq 0}} \sqrt{\frac{(2n+1)(2n+5)}{n+1}} \kappa_n^{-2} G_n(x) \left(\frac{\varrho_0}{y_k}\right)^{n+2} \tilde{\boldsymbol{p}}_n^{(1)}(\hat{\boldsymbol{y}}_k, \hat{\boldsymbol{x}}) \right) \\ &= \frac{-\mu_0}{2\pi\varrho_0^2} \boldsymbol{\nu}(\boldsymbol{y}_k) \cdot \left(\sum_{\substack{n \in \mathbb{N} \\ \kappa_n \neq 0}} \sqrt{\frac{(2n+1)(2n+5)^2}{n+1}} \kappa_n^{-2} \frac{x^{n+1}}{y_k^{n+2}} \tilde{\boldsymbol{p}}_n^{(1)}(\hat{\boldsymbol{y}}_k, \hat{\boldsymbol{x}}) \right). \end{aligned} \tag{20.10}$$

In the first step, we used Eq. (20.9) and the Addition Theorem for Edmonds vector spherical harmonics, see Eq. (5.14). In the second step, we inserted Eq. (20.8). For the numerical implementation, it is necessary to further expand the Edmonds vector Legendre polynomials. Thus, we use Eq. (5.12a) and Theorem 2.15 and obtain for all $n \in \mathbb{N}$ and all $\boldsymbol{\xi}, \boldsymbol{\eta} \in \mathbb{S}$ the identity

$$\begin{aligned}\tilde{\boldsymbol{p}}_n^{(1)}(\boldsymbol{\xi}, \boldsymbol{\eta}) &= \sqrt{\frac{n+1}{2n+1}} \boldsymbol{p}_n^{(1)}(\boldsymbol{\xi}, \boldsymbol{\eta}) - \sqrt{\frac{n}{2n+1}} \boldsymbol{p}_n^{(2)}(\boldsymbol{\xi}, \boldsymbol{\eta}) \\ &= \sqrt{\frac{n+1}{2n+1}} P_n(\boldsymbol{\xi} \cdot \boldsymbol{\eta}) \boldsymbol{\xi} - \sqrt{\frac{1}{(2n+1)(n+1)}} P_n'(\boldsymbol{\xi} \cdot \boldsymbol{\eta})(\boldsymbol{\eta} - (\boldsymbol{\xi} \cdot \boldsymbol{\eta}) \boldsymbol{\xi}).\end{aligned}$$

Eventually, we obtain with the abbreviation $t_k \coloneqq \hat{\boldsymbol{y}}_k \cdot \hat{\boldsymbol{x}}$ for $k = 1, \ldots, \ell_{\mathrm{M}}$ for the spline function for all $\boldsymbol{x} \in \mathbb{B}_{\varrho_0}$ the representation

$$S(\boldsymbol{x}) = \frac{-\mu_0}{2\pi \varrho_0^2} \sum_{k=1}^{\ell_{\mathrm{M}}} a_k \boldsymbol{\nu}(\boldsymbol{y}_k) \cdot \left(\sum_{\substack{n \in \mathbb{N} \\ \kappa_n \neq 0}} \frac{2n+5}{\kappa_n^2} \frac{x^{n+1}}{y_k^{n+2}} \left(P_n(t_k) \hat{\boldsymbol{y}}_k - \frac{1}{n+1} P_n'(t_k)(\hat{\boldsymbol{x}} - t_k \hat{\boldsymbol{y}}_k) \right) \right).$$

In addition, we need to calculate the corresponding spline matrix from Eq. (20.7). Each entry of the matrix is given for all $l, k = 1, \ldots, \ell_{\mathrm{M}}$ by

$$\begin{aligned}&\mathcal{A}_{\boldsymbol{x}}^l \mathcal{A}_{\boldsymbol{z}}^k K(\boldsymbol{x}, \boldsymbol{z}) \qquad (20.11)\\ &= \frac{\mu_0^2}{\varrho_0^3} \sum_{\substack{n \in \mathbb{N} \\ \kappa_n \neq 0}} \sum_{j=1}^{2n+1} \frac{4(2n+5)}{(n+1)(2n+1)\kappa_n^2} \left(\frac{\varrho_0^2}{y_k y_l} \right)^{n+2} \left(\boldsymbol{\nu}(\boldsymbol{y}_k) \cdot \tilde{\boldsymbol{y}}_{n,j}^{(1)}(\hat{\boldsymbol{y}}_k) \right) \left(\boldsymbol{\nu}(\boldsymbol{y}_l) \cdot \tilde{\boldsymbol{y}}_{n,j}^{(1)}(\hat{\boldsymbol{y}}_l) \right).\end{aligned}$$

The expression on the right-hand side can be further expanded by using some basic mathematical techniques and the Addition Theorem for scalar- as well as vector-valued spherical harmonics, see [73, Ch. 3.5]. In the end, we arrive at an expression that essentially involves only Legendre series and series with derivatives of Legendre polynomials up to second order. Hence, variants of the Clenshaw algorithm can be used to evaluate the matrix entries. In numerical experiments conducted with Matlab [212], however, the computational time decreased when directly using Kahan summation for the expression in Eq. (20.11) instead. For the computation via the Kahan summation $5.5623 \cdot 10^3$ s of CPU time are required whereas the Clenshaw algorithms need $5.8179 \cdot 10^3$ s. The relative deviation of the two matrices in the 2-matrix norm is given by $7.2180 \cdot 10^{-13}$. Therefore, we choose to use Eq. (20.11) combined with the Kahan summation within our numerical tests and do not proceed by further expanding this expression here.

20.2.3. Scalar Synthetic Test Current

Now, we want to use the described scalar spline method for reconstructing the function $A^{(1)}$ from given values of the magnetic flux density. Due to Theorem 15.20 and the choice of the radial functions, this approach can be combined with the minimum norm condition in order to achieve uniqueness. For this purpose, we can use the data obtained within the synthetic test case from Section 18.1. However, the corresponding exact scalar solution is required for a qualification of the numerical results obtained via the scalar spline.

Thus, we need to convert the vector-valued synthetic test current to this scalar function. Using Eq. (18.1) combined with the calculations from the proof of Theorem 18.3, a representation of the synthetic test current for $\boldsymbol{x} \in \mathbb{B}_{\varrho_0}$ is given by

$$\begin{aligned}\boldsymbol{J}_{\mathrm{M}}(\boldsymbol{x}) &= \varrho_0^3 \sum_{l=1}^{2} \kappa_l \sum_{n=1}^{\infty} \sum_{j=1}^{2n+1} h_l^n \frac{\sqrt{n(n+1)}}{2n+3} \boldsymbol{g}_{0,n,j}^{(3)}(\varrho_0; \boldsymbol{x}) G_{0,n,j}(\varrho_0; \boldsymbol{z}_l) \\ &= \sum_{n=1}^{\infty} \sum_{j=1}^{2n+1} \left(\sqrt{\varrho_0^3} \sum_{l=1}^{2} \kappa_l h_l^n \sqrt{\frac{n(n+1)}{2n+3}} G_{0,n,j}(\varrho_0; \boldsymbol{z}_l) \right) \sqrt{\frac{\varrho_0^3}{2n+3}} \boldsymbol{g}_{0,n,j}^{(3)}(\varrho_0; \boldsymbol{x}),\end{aligned}$$

where the parameters $\kappa_l \in \mathbb{R}$, $h_l \in (0,1)$, $\boldsymbol{z}_l \in \mathbb{B}_{\varrho_0}$ are chosen for $l = 1,\ 2$ according to Table 18.1. Note that in this section concerning the scalar synthetic test current, κ_l for $l = 1,\ 2$ is used as the parameter for the linear combination. This should not be confused with the sequence $\{\kappa_n\}_{n\in\mathbb{N}}$ occurring in the definition of the reproducing kernel from the previous section. Using the representation of the neuronal current from Theorem 15.20, that is

$$\boldsymbol{J}^{\mathrm{P}}(\boldsymbol{x}) \overset{\mathbf{L}_2(\mathbb{B}_{\varrho_0})}{=} \sum_{n=1}^{\infty} \sum_{j=1}^{2n+1} c_{n,j} \sqrt{\frac{\varrho_0^3}{2n+3}} \boldsymbol{g}_{0,n,j}^{(3)}(\varrho_0; \boldsymbol{x}),$$

we immediately obtain in the case of the synthetic test current that

$$c_{n,j} = \sqrt{\varrho_0^3} \sum_{l=1}^{2} \kappa_l h_l^n \sqrt{\frac{n(n+1)}{2n+3}} G_{0,n,j}(\varrho_0; \boldsymbol{z}_l)$$

for all $n \in \mathbb{N}$, $j = 1, \ldots, 2n+1$. Then, Theorem 15.20 provides us for all $\boldsymbol{x} \in \mathbb{B}_{\varrho_0}$ with a representation of the radial component of the vector potential. We will denote the exact synthetic test solution by $A_{\mathrm{M}}^{(1)}$. It is given by

$$\begin{aligned}A_{\mathrm{M}}^{(1)}(\boldsymbol{x}) &\overset{\mathrm{L}_2(\mathbb{B}_{\varrho_0})}{=} \sum_{n=1}^{\infty} \sum_{j=1}^{2n+1} A_{n,j}^{(1)}(x) Y_{n,j}(\hat{\boldsymbol{x}}) \\ &= \sum_{n=1}^{\infty} \sum_{j=1}^{2n+1} \frac{\sqrt{n(n+1)} c_{n,j} \varrho_0}{2(2n+3)} \left(\frac{x}{\varrho_0} \right)^{n+1} Y_{n,j}(\hat{\boldsymbol{x}}).\end{aligned}$$

Note that a second sequence of parameters that needs to be determined originally appears in Eq. (15.32). In our test case, we chose this remaining sequence of parameters to be equal to zero since it has no effect on the neuronal current. Inserting the representation of $c_{n,j}$ for all $n \in \mathbb{N}$, $j = 1, \ldots, 2n+1$ into this equation and using Definition 5.35 with $t_n \coloneqq n$ for all $n \in \mathbb{N}$, which is determined in Theorem 18.3, we get the expansion

$$\begin{aligned}A_{\mathrm{M}}^{(1)}(\boldsymbol{x}) &\overset{\mathrm{L}_2(\mathbb{B}_{\varrho_0})}{=} \varrho_0^{5/2} \sum_{n=1}^{\infty} \sum_{j=1}^{2n+1} \frac{n(n+1)}{2(2n+3)^{3/2}} \sum_{l=1}^{2} \kappa_l h_l^n G_{0,n,j}(\varrho_0; \boldsymbol{z}_l) \left(\frac{x}{\varrho_0} \right)^{n+1} Y_{n,j}(\hat{\boldsymbol{x}}) \\ &= \sum_{n=1}^{\infty} \sum_{j=1}^{2n+1} \frac{n(n+1)}{2(2n+3)} \sum_{l=1}^{2} \kappa_l h_l^n \frac{z_l^n x^{n+1}}{\varrho_0^{2n}} Y_{n,j}(\hat{\boldsymbol{z}}_l) Y_{n,j}(\hat{\boldsymbol{x}}) \\ &= \frac{1}{8\pi} \sum_{n=1}^{\infty} \frac{n(n+1)(2n+1)}{2n+3} \sum_{l=1}^{2} \kappa_l h_l^n \frac{z_l^n x^{n+1}}{\varrho_0^{2n}} P_n(\hat{\boldsymbol{z}}_l \cdot \hat{\boldsymbol{x}}), \qquad \boldsymbol{x} \in \mathbb{B}_{\varrho_0}.\end{aligned}$$

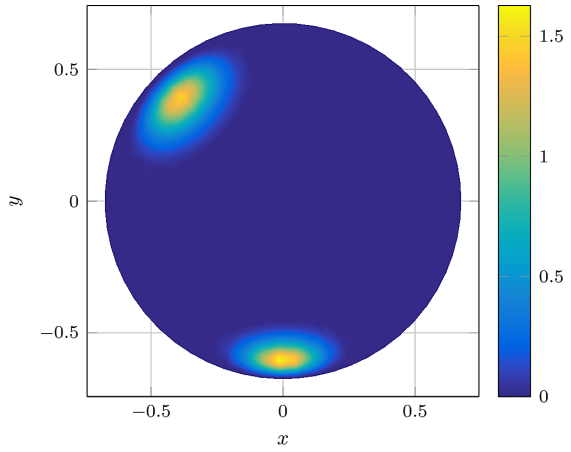

FIGURE 20.1: *Exact scalar solution* $A_{\mathrm{M}}^{(1)}$ *plotted on an upper hemisphere with radius* $0.95\varrho_0$

A visualization of the exact solution is shown in Fig. 20.1. It reveals that this scalar function has the same structure as the absolute value of the vector-valued test current concerning the active regions.

20.2.4. Corresponding Vector-Valued Neuronal Current

At this point, we have all tools required for the solution of the synthetic test case via scalar splines at hand. However, we want to compare the result obtained by this method with the reconstruction by means of the R(O)FMP. For this purpose, we need to calculate the vector-valued neuronal current corresponding to the scalar spline solution. There exist several strategies in order to obtain the neuronal current from the function $A^{(1)}$. For example, it is possible to use further assumptions on the functions Ψ, $A^{(2)}$, and $A^{(3)}$ that appear in the Helmholtz decomposition of the neuronal current. Then the gradient and the curl operator can be applied (at least numerically) to the scalar and vector potential.

However, in order to avoid additional numerical errors caused by the differentiation, we instead want to use some knowledge of the relation between the neuronal current and the function $A^{(1)}$ stated in Theorem 15.20. Therein, it is stated that if the function $A^{(1)}$ of the Helmholtz decomposition combined with the Coulomb gauge is given by

$$A_{n,j}^{(1)}(x) = \frac{\sqrt{n(n+1)}c_{n,j}\varrho_0}{2(2n+3)}\left(\frac{x}{\varrho_0}\right)^{n+1}, \qquad \boldsymbol{x} \in \mathbb{B}_{\varrho_0} \tag{20.12}$$

with a sequence of coefficients $\{c_{n,j}\}_{n\in\mathbb{N},j=1,\dots,2n+1}$, then the corresponding neuronal current has the representation

$$\boldsymbol{J}^{\mathrm{P}}(\boldsymbol{x}) \overset{\mathbf{L}_2(\mathbb{B}_{\varrho_0})}{=} \sum_{n=1}^{\infty}\sum_{j=1}^{2n+1} c_{n,j}\sqrt{\frac{\varrho_0^3}{2n+3}}\boldsymbol{g}_{0,n,j}^{(3)}(\varrho_0;\boldsymbol{x}), \qquad \boldsymbol{x} \in \mathbb{B}_{\varrho_0}. \tag{20.13}$$

Recall that, based on the calculations in Eq. (20.10), the scalar spline solution is for all

$\boldsymbol{x} \in \mathbb{B}_{\varrho_0}$ of the form

$$S(\boldsymbol{x}) = \frac{-2\mu_0}{\varrho_0^{3/2}} \sum_{\substack{n \in \mathbb{N} \\ \kappa_n \neq 0}} \sum_{j=1}^{2n+1} \left(\sqrt{\frac{2n+5}{(n+1)(2n+1)}} \kappa_n^{-2} G_n(x) \right.$$
$$\left. \times \left(\sum_{k=1}^{\ell_{\mathrm{M}}} \left(\frac{\varrho_0}{y_k} \right)^{n+2} a_k \boldsymbol{\nu}(\boldsymbol{y}_k) \cdot \tilde{\boldsymbol{y}}_{n,j}^{(1)}(\hat{\boldsymbol{y}}_k) \right) \right) Y_{n,j}(\hat{\boldsymbol{x}}).$$

Here, the sequence $\{\kappa_n\}_{n \in \mathbb{N}}$ belongs to the sequence occurring in the representation of the reproducing kernel from Eq. (20.4). Thus, we calculate the spherical harmonics coefficients depending on the radius of the spline evaluation point $x \in [0, \varrho_0]$. Using Eq. (20.8), we get for all $n \in \mathbb{N}$ with $\kappa_n \neq 0$ and $j = 1, \ldots, 2n+1$ the function

$$\begin{aligned}
&S_{n,j}(x) \\
&= \int_{\mathbb{S}} S(\boldsymbol{x}) Y_{n,j}(\hat{\boldsymbol{x}}) \, \mathrm{d}\omega(\hat{\boldsymbol{x}}) \\
&= \frac{-2\mu_0}{\varrho_0^{3/2}} \sqrt{\frac{2n+5}{(n+1)(2n+1)}} \kappa_n^{-2} \left(\sum_{k=1}^{\ell_{\mathrm{M}}} \left(\frac{\varrho_0}{y_k} \right)^{n+2} a_k \boldsymbol{\nu}(\boldsymbol{y}_k) \cdot \tilde{\boldsymbol{y}}_{n,j}^{(1)}(\hat{\boldsymbol{y}}_k) \right) G_n(x) \\
&= \frac{-2\mu_0}{\varrho_0^{3}} \frac{2n+5}{\sqrt{(n+1)(2n+1)}} \kappa_n^{-2} \left(\sum_{k=1}^{\ell_{\mathrm{M}}} \left(\frac{\varrho_0}{y_k} \right)^{n+2} a_k \boldsymbol{\nu}(\boldsymbol{y}_k) \cdot \tilde{\boldsymbol{y}}_{n,j}^{(1)}(\hat{\boldsymbol{y}}_k) \right) \left(\frac{x}{\varrho_0} \right)^{n+1}.
\end{aligned}$$

We can insert this expression into the left-hand side of Eq. (20.12) and solve the resulting equation for $c_{n,j}$ for all $n \in \mathbb{N}$, $j = 1, \ldots, 2+1$. Then we get for all $n \in \mathbb{N}$ with $\kappa_n \neq 0$ and $j = 1, \ldots, 2+1$ the identity

$$c_{n,j} = \frac{-4\mu_0}{\varrho_0^4} \frac{(2n+3)(2n+5)}{(n+1)\sqrt{n(2n+1)}} \kappa_n^{-2} \left(\sum_{k=1}^{\ell_{\mathrm{M}}} \left(\frac{\varrho_0}{y_k} \right)^{n+2} a_k \boldsymbol{\nu}(\boldsymbol{y}_k) \cdot \tilde{\boldsymbol{y}}_{n,j}^{(1)}(\hat{\boldsymbol{y}}_k) \right). \tag{20.14}$$

Eventually, using Eq. (20.13), we obtain for the neuronal current $\boldsymbol{J}_S$ corresponding to the spline S for all $\boldsymbol{x} \in \mathbb{B}_{\varrho_0}$ the identity

$$\boldsymbol{J}_S(\boldsymbol{x}) = -\frac{4\mu_0}{\varrho_0^2} \sum_{\substack{n \in \mathbb{N} \\ \kappa_n \neq 0}} \sum_{j=1}^{2n+1} \frac{(2n+3)(2n+5)}{(n+1)\sqrt{n(2n+1)}} \kappa_n^{-2} \left(\sum_{k=1}^{\ell_{\mathrm{M}}} a_k \frac{x^n}{y_k^{n+2}} \boldsymbol{\nu}(\boldsymbol{y}_k) \cdot \tilde{\boldsymbol{y}}_{n,j}^{(1)}(\hat{\boldsymbol{y}}_k) \right) \boldsymbol{y}_{n,j}^{(3)}(\hat{\boldsymbol{x}}).$$

Again, in the numerical implementation, we will use Kahan summation for the (truncated) series. Thus, we are able to directly calculate the neuronal current from the coefficients $\boldsymbol{a} = (a_k)_{k=1,\ldots,\ell_{\mathrm{M}}}$ computed by the spline method from Eq. (20.6).

20.2.5. Scalar Splines for the EEG Problem

Besides the derivation of a scalar MEG problem based on the Helmholtz decomposition, Section 15.3 also provides us with a scalar formulation of the inverse EEG problem. For this particular problem, scalar splines are also constructed in [73].

In this context, Theorem 15.23 is used in order to formulate the continuous linear functionals $\mathcal{A}^k$ for $k = 1, \ldots, \ell_{\mathrm{E}}$ mapping the scalar potential Ψ of the Helmholtz decomposition onto the electric potential on the boundary of the scalp $u_L|_{\mathbb{S}_{\varrho_L}}$, that is

$$\mathcal{A}^k \Psi := -\sum_{n=1}^{\infty} \sum_{j=1}^{2n+1} \frac{s_n}{2n+1} \varrho_0^{n+1} \left(\varrho_0 \frac{\mathrm{d}\Psi_{n,j}}{\mathrm{d}x}(\varrho_0) - n\Psi_{n,j}(\varrho_0) \right) Y_{n,j}(\hat{\boldsymbol{y}}_k). \tag{20.15}$$

Here, $\varrho_L \hat{\boldsymbol{y}}_k \in \mathbb{S}_{\varrho_L}$ are the sensor positions for $k = 1, \ldots, \ell_{\mathrm{E}}$. The occurring sequence $\{s_n\}_{n\in\mathbb{N}}$ only depends on the fixed radii of the shells from the multiple-shell model and the corresponding conductivities. This sequence has no radial dependency, hence it is independent of $y \in [\varrho_{L-1}, \varrho_L]$. We saw in Problem 10.2 that the electric potential on the entire shell $\mathbb{S}_{[\varrho_{L-1},\varrho_L]}$ depends on functions H_n with $n \in \mathbb{N}$, which indeed have a radial dependency on $y \in [\varrho_{L-1}, \varrho_L]$. A relation between the sequences $\{s_n\}_{n\in\mathbb{N}}$ and $\{H_n\}_{n\in\mathbb{N}}$ is stated in Eq. (15.37) and for all $n \in \mathbb{N}$ given by

$$s_n = (2n+1) H_n(\varrho_L).$$

The functions $\{H_n\}_{n\in\mathbb{N}}$ are stated in Eq. (4.20), that is

$$H_n(y) = \left(\frac{n+1}{n} \left(\frac{y}{\varrho_L} \right)^{2n+1} + 1 \right) \beta_n^{(L)} \frac{1}{y^{n+1}}, \qquad y \in [\varrho_{L-1}, \varrho_L]$$

with some coefficients $\{\beta_n^{(L)}\}_{n\in\mathbb{N}}$. Contradicting their own theoretical result, a radius dependent formula for the electric potential is used in [73, Eq. (55)] for the numerical considerations. This radial dependency is introduced by the additional factor $(\varrho_L/y)^n$ used in the spherical harmonics expansion from Eq. (20.15). Due to the previous considerations and the representation of the functions H_n with $n \in \mathbb{N}$, see Eq. (4.20), this formula can only hold true on the boundary $\mathbb{S}_{\varrho_L}$. However, in [73] this formula is used inside the entire shell $\mathbb{S}_{[\varrho_{L-1},\varrho_L]}$ for the computations, due to the positions of the sensors $\boldsymbol{y}_k$ for $k = 1, \ldots, \ell_{\mathrm{E}}$. This introduces some modelling error.

In addition, in [73, p. 22] the sequence occurring in the reproducing kernels from Eq. (20.4) is chosen to be $\kappa_n := h^{n(n+1)/2}$ for all $n \in \mathbb{N}$ with $h \in (0, 1)$. According to Corollary 16.4, which analogously holds true for scalar Sobolev spaces, see [158, p. 272], we get by means of the zero-sequence $\{\kappa_n\}_{n\in\mathbb{N}}$ that $\mathrm{L}_2(\mathbb{B}_{\varrho_0}) \subsetneq \mathcal{H}(\{\kappa_n\}_{n\in\mathbb{N}}, \mathbb{B}_{\varrho_0})$. This is a direct contradiction to the assumption that $\mathcal{H}(\{\kappa_n\}_{n\in\mathbb{N}}, \mathbb{B}_{\varrho_0}) \subset \mathrm{L}_2(\mathbb{B}_{\varrho_0})$, see [73, p. 11]. This particular choice of $\{\kappa_n\}_{n\in\mathbb{N}}$ leads to a divergent series representation of the underlying reproducing kernel. This would also yield divergent representations of the scalar spline in Eq. (20.5b) and of the interpolation problem in Eq. (20.6). However, this is not crucial for the numerical implementation since therein bandlimited functions are considered.

We are able to correct these errors and present the improved numerical results in Section 21.3.2. To this end, we need some preliminary calculations. We use the reproducing kernels defined in Eq. (20.4) combined with the radial ansatz functions from [73, p. 22] for all $n \in \mathbb{N}$, which are given by

$$G_n(x) = \gamma_n \left(\frac{1}{n} - \ln\left(\frac{x}{\varrho_0} \right) \right) x^n, \qquad x \in [0, R].$$

Since we assumed that the functions G_n are normalized, we have to calculate the normalization factor γ_n corresponding to G_n for all $n \in \mathbb{N}$, which can also be found in [73, p. 22]. By

solving

$$\begin{aligned}1 &= \gamma_n^2 \int_0^{\varrho_0} x^2 G_n(x)^2 \,\mathrm{d}x \\ &= \gamma_n^2 \int_0^{\varrho_0} \left(\frac{1}{n} - \ln\left(\frac{x}{\varrho_0}\right)\right)^2 x^{2n+2} \,\mathrm{d}x \\ &= \gamma_n^2 \frac{9 + 2n(9+5n)}{n^2(2n+3)^3} \varrho_0^{2n+3}\end{aligned}$$

for γ_n^2, we obtain for all $n \in \mathbb{N}$ the identity

$$\gamma_n^2 = \frac{n^2(2n+3)^3}{9 + 2n(9+5n)} \varrho_0^{-(2n+3)}.$$

The continuous linear functionals required for the construction of the splines for this particular problem are stated in Theorem 10.4 combined with Eqs. (4.20) and (15.34). Thus, for all $k = 1, \ldots, \ell_{\mathrm{E}}$ we achieve

$$\begin{aligned}\mathcal{A}^k \Psi &\coloneqq \sum_{n=0}^{\infty} \sum_{j=1}^{2n+1} \frac{n}{2n+1} (\beta_n^{(L)})^{-1} \varrho_L^n u_L^{\wedge}(n,j) Y_{n,j}(\hat{\boldsymbol{y}}_k) \\ &= \sum_{n=0}^{\infty} \sum_{j=1}^{2n+1} H_n(y_k) \left(n \Psi_{n,j}(\varrho_0) - \varrho_0 \Psi'_{n,j}(\varrho_0)\right) \varrho_0^{n+1} Y_{n,j}(\hat{\boldsymbol{y}}_k).\end{aligned}$$

The use of this forward operator allows to evaluate the potential at the given sensor positions and not only on the sphere $\mathbb{S}_{\varrho_L}$.

For the construction of the spline function, we have to calculate for all $n \in \mathbb{N}$ the expressions

$$\begin{aligned}\frac{\mathrm{d}}{\mathrm{d}x}\left(x^n \left(\frac{1}{n} - \ln\left(\frac{x}{\varrho_0}\right)\right)\right) &= n x^{n-1} \ln\left(\frac{\varrho_0}{x}\right), \\ \varrho_0 G_n'(\varrho_0) - n G_n(\varrho_0) &= -\sqrt{\frac{n^2(2n+3)^3}{9 + 2n(9+5n)}} \varrho_0^{-3/2}.\end{aligned}$$

Eventually, the scalar spline is given for $\boldsymbol{x} \in \mathbb{B}_{\varrho_0}$ by

$$\begin{aligned}S(\boldsymbol{x}) &= \sum_{k=1}^{\ell_{\mathrm{M}}} a_k \mathcal{A}_{\boldsymbol{z}}^k K(\boldsymbol{z}, \boldsymbol{x}) \\ &= \sum_{k=1}^{\ell_{\mathrm{M}}} a_k \sum_{\substack{n=1 \\ \kappa_n \neq 0}}^{\infty} \sum_{j=1}^{2n+1} \sqrt{\frac{n^2(2n+3)^3}{9 + 2n(9+5n)}} \varrho_0^{n-1/2} \kappa_n^{-2} G_n(x) Y_{n,j}(\hat{\boldsymbol{x}}) H_n(y_k) Y_{n,j}(\hat{\boldsymbol{y}}_k).\end{aligned}$$

Accordingly, we can calculate for each k, $l = 1, \ldots, \ell_{\mathrm{E}}$ the entries of the corresponding spline matrix by

$$\mathcal{A}_{\boldsymbol{x}}^l \mathcal{A}_{\boldsymbol{z}}^k K(\boldsymbol{z}, \boldsymbol{x}) = \sum_{\substack{n=1 \\ \kappa_n \neq 0}}^{\infty} \sum_{j=1}^{2n+1} \frac{n^2(2n+3)^3}{9 + 2n(9+5n)} \varrho_0^{2n-1} \kappa_n^{-2} H_n(y_l) H_n(y_k) Y_{n,j}(\hat{\boldsymbol{y}}_l) Y_{n,j}(\hat{\boldsymbol{y}}_k). \quad (20.16)$$

However, we are not able to compare results obtained with the R(O)FMP to results obtained with the scalar spline method for the EEG problem. The reason for this lack of

comparability is stated in Theorem 15.25. Therein, we proved that the neuronal current can only satisfy the conditions of Theorem 15.23, which are required for the formulation of the continuous linear functionals $\mathcal{A}^k$ for $k = 1, \ldots, \ell_{\mathrm{E}}$, simultaneously to the condition that $\boldsymbol{J}^{\mathrm{P}} \in (\ker \mathcal{T}_{\mathrm{E}})^{\perp}$, which is required for the R(O)FMP, if and only if $\boldsymbol{J}^{\mathrm{P}} \equiv 0$. Therefore, we are not able to construct a fair EEG test case that is applicable to both the R(O)FMP and the scalar spline method. To conclude, we are not able to use the scalar spline method for the inversion of the EEG synthetic test case in Chapter 18.

20.3. Vector Spline Method

In the previous section, we realized that we cannot use the scalar spline method for the inverse EEG problem if the minimum norm condition is required. However, we still want to compare our numerical results achieved by means of the R(O)FMP with a spline method. For this purpose, we construct vector-valued splines as an analogue of the scalar splines. Note that the spline method developed in this section is not limited to the EEG problem, but could be easily applied to other problems as well, such as the MEG problem.

We have already constructed reproducing kernels based on our vector-valued orthonormal basis system in Definition 16.7. In this context, we pointed out that this definition does not follow the setting of [81], since we want the reproducing kernel to be a vector-valued function in order to use it as a trial function in the dictionary. However, for a vectorial spline method we in fact need another type of reproducing kernels. For this method, the reproducing kernel is constructed via the tensor product of vector-valued orthonormal basis functions. This approach has already been used in [80, 81] for vector-valued splines on the unit sphere.

Another construction of tensor-valued reproducing kernels is stated in [22, 24]. Here, the reproducing kernels can be represented by 3×3-dimensional diagonal matrices. In this case, they only satisfy a certain reproducing property on vector-valued Sobolev spaces that are product spaces of scalar Sobolev spaces. The Sobolev space considered in our problem, that is $\tilde{\mathfrak{H}}^{(i)} \coloneqq \tilde{\mathfrak{H}}^{(i)}(\{\kappa_{m,n}^{(i)}\}_{(m,n)\in\mathbb{N}_0\times\mathbb{N}_{0_i}}, \mathbb{B}_{\varrho_0})$, does not provide us with this particular structure, see Definition 16.1 and Remark 16.3.

Following the approach of [80, 81], the reproducing kernel $\mathfrak{k}^{(i)} \colon \mathbb{B}_{\varrho_0} \times \mathbb{B}_{\varrho_0} \to \mathbb{R}^{3\times 3}$ considered in this section depends on $i = 1, 2, 3$ and is defined for all $\boldsymbol{x}, \boldsymbol{y} \in \mathbb{B}_{\varrho_0}$ by

$$\mathfrak{k}^{(i)}(\boldsymbol{x}, \boldsymbol{y}) \coloneqq \sum_{\substack{(m,n)\in\mathbb{N}_0\times\mathbb{N}_{0_i} \\ \kappa_{m,n}^{(i)}\neq 0}} \sum_{j=1}^{2n+1} \left(\kappa_{m,n}^{(i)}\right)^{-2} \tilde{\boldsymbol{g}}_{m,n,j}^{(i)}(\varrho_0; \boldsymbol{x}) \otimes \tilde{\boldsymbol{g}}_{m,n,j}^{(i)}(\varrho_0; \boldsymbol{y}). \tag{20.17}$$

Reproducing kernels of this kind are also introduced in [20, 25] and used for the construction of interpolating vector splines and vector-valued wavelets on the sphere. For more details on vector-valued reproducing kernels, such as the reproducing property, we refer to [80] since the conversion from the spherical case to the ball case is straightforward. Note that the results of this section still hold true if the employed orthonormal basis $\{\tilde{\boldsymbol{g}}_{m,n,j}^{(i)}(\varrho_0; \cdot)\}_{(m,n)\in\mathbb{N}_0\times\mathbb{N}_{0_i}, j=1,\ldots,2n+1}$ is replaced by an arbitrary orthonormal basis of $\mathbf{L}_2(\mathbb{B}_{\varrho_0})$. Furthermore, we assume that the sequence $\{\kappa_{m,n}^{(i)}\}_{(m,n)\in\mathbb{N}_0\times\mathbb{N}_{0_i}}$ is given in such a way that $\tilde{\mathfrak{H}}^{(i)} \subset \mathbf{L}_2(\mathbb{B}_{\varrho_0})$.

The spline constructed in [20, 80] is used for an interpolation problem. In contrast, we want to use the spline for approximating the solution of an inverse problem. Having the

vector-valued reproducing kernels at hand, we develop in the following a novel approach to vector-valued splines for inverse problems.

In [78], a concept for spline approximation on the sphere is presented where the data $\boldsymbol{g} = (g_1, \ldots, g_\ell) \in \mathbb{R}^\ell$ is of the form

$$\boldsymbol{g} = \mathcal{A}\boldsymbol{f} \qquad \Leftrightarrow \qquad g_k = \mathcal{A}^k \boldsymbol{f}, \qquad k = 1, \ldots, \ell$$

with the operator $\mathcal{A} \coloneqq (\mathcal{A}^1, \ldots, \mathcal{A}^\ell)^{\mathrm{T}}$, the functionals $\mathcal{A}^k \colon \tilde{\mathfrak{H}}^{(i)} \to \mathbb{R}$ for all $k = 1, \ldots, \ell$, and the (sought) quantity $\boldsymbol{f} \in \tilde{\mathfrak{H}}^{(i)}$. In [158, Ch. 6.4., Ch. 10], this method is extended to a scalar spline approximation on the ball. Thus, we call a function of the form

$$\boldsymbol{s}(\boldsymbol{x}) = \sum_{k=1}^{\ell} a_k \mathcal{A}_{\boldsymbol{z}}^k \left(\mathfrak{k}^{(i)}(\boldsymbol{z}, \boldsymbol{x}) \right), \qquad \boldsymbol{x} \in \mathbb{B}_{\varrho_0} \tag{20.18}$$

with the coefficients $\boldsymbol{a} = (a_k)_{k=1,\ldots,\ell} \in \mathbb{R}^\ell$ a *spline function in* $\tilde{\mathfrak{H}}^{(i)}$ *subject to* $\mathcal{A}$. For this definition to make sense, we need to define what we understand by applying the functional $\mathcal{A}^k$ to a tensor product of two vector-valued functions. For two functions $\boldsymbol{f}$, $\boldsymbol{h} = (h_1, h_2, h_3)^{\mathrm{T}} \colon \mathbb{B}_{\varrho_0} \to \mathbb{R}^3$, we define

$$\begin{aligned} \mathcal{A}_{\boldsymbol{z}}^k \left(\boldsymbol{f}(\boldsymbol{z}) \otimes \boldsymbol{h} \right) &= \mathcal{A}_{\boldsymbol{z}}^k \left(\boldsymbol{f}(\boldsymbol{z}) h_1, \boldsymbol{f}(\boldsymbol{z}) h_2, \boldsymbol{f}(\boldsymbol{z}) h_3 \right) \\ &\coloneqq \left(\left(\mathcal{A}_{\boldsymbol{z}}^k \boldsymbol{f}(\boldsymbol{z}) \right) h_1, \left(\mathcal{A}_{\boldsymbol{z}}^k \boldsymbol{f}(\boldsymbol{z}) \right) h_2, \left(\mathcal{A}_{\boldsymbol{z}}^k \boldsymbol{f}(\boldsymbol{z}) \right) h_3 \right)^{\mathrm{T}} \\ &= \left(\mathcal{A}_{\boldsymbol{z}}^k \boldsymbol{f}(\boldsymbol{z}) \right) \boldsymbol{h}. \end{aligned} \tag{20.19}$$

Eventually, the vector-valued spline function has the representation

$$\boldsymbol{s}(\boldsymbol{x}) = \sum_{k=1}^{\ell} a_k \sum_{\substack{(m,n) \in \mathbb{N}_0 \times \mathbb{N}_{0_i} \\ \kappa_{m,n}^{(i)} \neq 0}} \sum_{j=1}^{2n+1} \left(\kappa_{m,n}^{(i)} \right)^{-2} \tilde{\boldsymbol{g}}_{m,n,j}^{(i)}(\varrho_0; \boldsymbol{x}) \mathcal{A}_{\boldsymbol{z}}^k \tilde{\boldsymbol{g}}_{m,n,j}^{(i)}(\varrho_0; \boldsymbol{z}), \qquad \boldsymbol{x} \in \mathbb{B}_{\varrho_0}.$$

This approach is novel in two aspects. First, we define tensor-valued reproducing kernels on the ball in Eq. (20.17) as a generalization of tensor-valued reproducing kernels on the sphere from [80, 81]. Second, we combine this definition with the approach for the construction of splines used for the approximation from [158, Ch. 6.4., Ch. 10] in order to achieve the novel vector splines subject to the operator $\mathcal{A}$. These vector splines are different from the ones stated in [22, 24]. The splines from [22, 24] are only defined for particular structures of the underlying Hilbert space, where the tensor-valued reproducing kernel is given by a 3×3-diagonal matrix containing classical scalar-valued reproducing kernels in each entry.

Several useful properties of (scalar) splines (over the ball) have already been known. For example, in [158, Thm. 10.13-14], two minimum properties of scalar splines over the ball are proved. These statements also hold true in the vector-valued case, which is proved for the particular setting of $\tilde{\mathfrak{H}}^{(i)}$ being the product space of two scalar Sobolev spaces in [22, 24] using tensor-valued reproducing kernels. Now, we adapt these statements to our setting. For this purpose, three central properties need to be verified.

Lemma 20.2. *Let the reproducing kernel be given as in Eq.* (20.17)*, then*

i) a kind of reproducing property holds true for all $k = 1, \ldots, \ell$*, that is*

$$\left\langle \mathcal{A}_{\boldsymbol{x}}^{k} \left(\mathfrak{k}^{(i)}(\boldsymbol{x}, \cdot) \right), \boldsymbol{f} \right\rangle_{\tilde{\mathfrak{H}}^{(i)}} = \mathcal{A}^{k} \boldsymbol{f},$$

for all $\boldsymbol{f} \in \tilde{\mathfrak{H}}^{(i)}$*,*

ii) a vector-valued spline function $\boldsymbol{s} \in \tilde{\mathfrak{H}}^{(i)}$ *subject to* $\mathcal{A}$ *satisfies the relation*

$$\langle \boldsymbol{s}, \boldsymbol{f} \rangle_{\tilde{\mathfrak{H}}^{(i)}} = \sum_{k=1}^{\ell} a_k \mathcal{A}^{k} \boldsymbol{f} \tag{20.20}$$

for all $\boldsymbol{f} \in \tilde{\mathfrak{H}}^{(i)}$*, and*

iii) for all $k,\ l = 1, \ldots, \ell$ *the following relation holds true:*

$$\mathcal{A}_{\boldsymbol{x}}^{l} \mathcal{A}_{\boldsymbol{z}}^{k} \mathfrak{k}^{(i)}(\boldsymbol{x}, \boldsymbol{z}) = \left\langle \mathcal{A}_{\boldsymbol{x}}^{k} \mathfrak{k}^{(i)}(\cdot, \boldsymbol{x}), \mathcal{A}_{\boldsymbol{z}}^{k} \mathfrak{k}^{(i)}(\cdot, \boldsymbol{z}) \right\rangle_{\tilde{\mathfrak{H}}^{(i)}}.$$

Proof. We start with the proof of the first item. Then, we obtain with the definition of the reproducing kernel form Eq. (20.17) the identity

$$\begin{aligned}
&\left\langle \mathcal{A}_{\boldsymbol{x}}^{k} \left(\mathfrak{k}^{(i)}(\boldsymbol{x}, \cdot) \right), \boldsymbol{f} \right\rangle_{\tilde{\mathfrak{H}}^{(i)}} \\
&= \sum_{\substack{(m,n) \in \mathbb{N}_0 \times \mathbb{N}_{0_i} \\ \kappa_{m,n}^{(i)} \neq 0}} \sum_{j=1}^{2n+1} \left(\kappa_{m,n}^{(i)} \right)^{-2} \left\langle \mathcal{A}_{\boldsymbol{x}}^{k} \left(\tilde{\boldsymbol{g}}_{m,n,j}^{(i)}(\varrho_0; \boldsymbol{x}) \otimes \tilde{\boldsymbol{g}}_{m,n,j}^{(i)}(\varrho_0; \cdot) \right), \boldsymbol{f} \right\rangle_{\tilde{\mathfrak{H}}^{(i)}}.
\end{aligned}$$

Now, we use Eq. (20.19), properties of the $\tilde{\mathfrak{H}}^{(i)}$-inner product, see Definition 16.1, and the linearity and continuity of $\mathcal{A}^{k}$ and get

$$\begin{aligned}
&\left\langle \mathcal{A}_{\boldsymbol{x}}^{k} \left(\mathfrak{k}^{(i)}(\boldsymbol{x}, \cdot) \right), \boldsymbol{f} \right\rangle_{\tilde{\mathfrak{H}}^{(i)}} \\
&= \sum_{\substack{(m,n) \in \mathbb{N}_0 \times \mathbb{N}_{0_i} \\ \kappa_{m,n}^{(i)} \neq 0}} \sum_{j=1}^{2n+1} \left(\kappa_{m,n}^{(i)} \right)^{-2} \mathcal{A}_{\boldsymbol{x}}^{k} \left(\tilde{\boldsymbol{g}}_{m,n,j}^{(i)}(\varrho_0; \boldsymbol{x}) \right) \left\langle \tilde{\boldsymbol{g}}_{m,n,j}^{(i)}(\varrho_0; \cdot), \boldsymbol{f} \right\rangle_{\tilde{\mathfrak{H}}^{(i)}} \\
&= \sum_{\substack{(m,n) \in \mathbb{N}_0 \times \mathbb{N}_{0_i} \\ \kappa_{m,n}^{(i)} \neq 0}} \sum_{j=1}^{2n+1} \mathcal{A}_{\boldsymbol{x}}^{k} \left(\tilde{\boldsymbol{g}}_{m,n,j}^{(i)}(\varrho_0; \boldsymbol{x}) \right) \left\langle \tilde{\boldsymbol{g}}_{m,n,j}^{(i)}(\varrho_0; \cdot), \boldsymbol{f} \right\rangle_{\mathbf{L}_2(\mathbb{B}_{\varrho_0})} \\
&= \mathcal{A}_{\boldsymbol{x}}^{k} \left(\sum_{\substack{(m,n) \in \mathbb{N}_0 \times \mathbb{N}_{0_i} \\ \kappa_{m,n}^{(i)} \neq 0}} \sum_{j=1}^{2n+1} \tilde{\boldsymbol{g}}_{m,n,j}^{(i)}(\varrho_0; \boldsymbol{x}) \left\langle \tilde{\boldsymbol{g}}_{m,n,j}^{(i)}(\varrho_0; \cdot), \boldsymbol{f} \right\rangle_{\mathbf{L}_2(\mathbb{B}_{\varrho_0})} \right) \\
&= \mathcal{A}^{k} \boldsymbol{f}.
\end{aligned}$$

The last step is valid since $\tilde{\mathfrak{H}}^{(i)} \subset \mathbf{L}_2(\mathbb{B}_{\varrho_0})$ and, hence, $\boldsymbol{f}$ can be represented by the Fourier series.

For the proof of the second statement, we only need to use the representation of the vector-valued spline from Eq. (20.18) and the linearity of the inner-product. Eventually, the third item is a particular case of the first with $\boldsymbol{f} = \mathcal{A}_{\boldsymbol{z}}^k \mathfrak{k}^{(i)}(\cdot, \boldsymbol{z})$. □

With this preliminary work, the original proofs of the next statements are still valid in the vector-valued case.

Theorem 20.3 ([158, Thm. 10.10]). *Let $\boldsymbol{g} \in \mathbb{R}^\ell$ be the given data and the spline function $\boldsymbol{s} \in \tilde{\mathfrak{H}}^{(i)}$ be unknown. Then the spline interpolation problem $\mathcal{A}^k \boldsymbol{s} = g_k$ for all $k = 1, \ldots, \ell$ is uniquely solvable if and only if the functionals $\mathcal{A}^k$ for $k = 1, \ldots, \ell$ are linearly independent.*

An immediate consequence of Lemma 20.2 is that the matrix corresponding to the spline functions stated in the following theorem is as a Gramian matrix positive definite if the functionals $\mathcal{A}^k$ for $k = 1, \ldots, \ell$ are linearly independent.

Theorem 20.4 (Minimum Property, [158, Thm. 10.13-14]). *Let $\tilde{\mathfrak{H}}^{(i)} \subset \mathbf{L}_2(\mathbb{B}_{\varrho_0})$ be a given Sobolev space and $\mathcal{A}^k \colon \tilde{\mathfrak{H}}^{(i)} \to \mathbb{R}$ be bounded linear functionals for all $k = 1, \ldots, \ell$ that are linearly independent. Then the following properties hold true:*

i) If $\boldsymbol{g} \in \mathbb{R}^\ell$ is a given vector and the spline $\boldsymbol{s}$ is given by $\mathcal{A}^k \boldsymbol{s} = g_k$ for all $k = 1, \ldots, \ell$, then $\boldsymbol{s}$ is the unique solution of

$$\|\boldsymbol{s}\|_{\tilde{\mathfrak{H}}^{(i)}} = \min \left\{ \|\boldsymbol{f}\|_{\tilde{\mathfrak{H}}^{(i)}} \;\middle|\; \boldsymbol{f} \in \tilde{\mathfrak{H}}^{(i)} \text{ with } \mathcal{A}^k \boldsymbol{f} = g_k \text{ for all } k = 1, \ldots, \ell \right\}.$$

ii) If $\boldsymbol{f} \in \tilde{\mathfrak{H}}^{(i)}$ is a given function and the spline $\boldsymbol{s}$ is defined by $\mathcal{A}^k \boldsymbol{s} = \mathcal{A}^k \boldsymbol{f}$ for all $k = 1, \ldots, \ell$, then $\boldsymbol{s}$ is the unique solution of

$$\|\boldsymbol{f} - \boldsymbol{s}\|_{\tilde{\mathfrak{H}}^{(i)}} = \min \left\{ \|\boldsymbol{f} - \bar{\boldsymbol{s}}\|_{\tilde{\mathfrak{H}}^{(i)}} \;\middle|\; \bar{\boldsymbol{s}} \in \tilde{\mathfrak{H}}^{(i)} \text{ is a spline function s.t. } \mathcal{A} \right\}.$$

The proof of the following theorem is identical to the one in [158, Thm. 10.16], where again Eq. (20.20) comes into play.

Theorem 20.5 ([158, Thm. 10.16]). *Let $\boldsymbol{g} \in \mathbb{R}^\ell$ and a regularization parameter $\tau > 0$ be given. Let the bounded linear functionals $\mathcal{A}^k \colon \tilde{\mathfrak{H}}^{(i)} \to \mathbb{R}$, with $k = 1, \ldots, \ell$, be linearly independent. If the vector $\boldsymbol{a} = (a_k)_{k=1,\ldots,\ell}$ is the solution of*

$$\left(\left(\mathcal{A}_{\boldsymbol{x}}^l \mathcal{A}_{\boldsymbol{z}}^k \left(\mathfrak{k}^{(i)}(\boldsymbol{z}, \boldsymbol{x}) \right) \right)_{l,k=1,\ldots,\ell} + \tau \mathcal{I}_{\mathbb{R}^{\ell \times \ell}} \right) \boldsymbol{a} = \boldsymbol{g}, \tag{20.21}$$

then the spline function given by Eq. (20.18) is the unique minimizer of the corresponding Tikhonov-functional, that is

$$\boldsymbol{s} = \min_{\boldsymbol{f} \in \tilde{\mathfrak{H}}^{(i)}} \left(\|\boldsymbol{g} - \mathcal{A}\boldsymbol{f}\|_{\mathbb{R}^\ell}^2 + \tau \|\boldsymbol{f}\|_{\tilde{\mathfrak{H}}^{(i)}}^2 \right).$$

An entry of the spline matrix occurring in Eq. (20.21) has for all $\boldsymbol{x}, \boldsymbol{z} \in \mathbb{B}_{\varrho_0}$ the representation

$$\mathcal{A}_{\boldsymbol{x}}^l \mathcal{A}_{\boldsymbol{z}}^k \left(\mathfrak{k}^{(i)}(\boldsymbol{z}, \boldsymbol{x}) \right) = \sum_{\substack{(m,n) \in \mathbb{N}_0 \times \mathbb{N}_{0_i} \\ \kappa_{m,n}^{(i)} \neq 0}} \sum_{j=1}^{2n+1} (\kappa_{m,n}^{(i)})^{-2} \left(\mathcal{A}_{\boldsymbol{x}}^l \tilde{\boldsymbol{g}}_{m,n,j}^{(i)}(\varrho_0; \boldsymbol{x}) \right) \left(\mathcal{A}_{\boldsymbol{z}}^k \tilde{\boldsymbol{g}}_{m,n,j}^{(i)}(\varrho_0; \boldsymbol{z}) \right).$$

The presented vectorial spline method will be tested for the inverse EEG problem. Thus, for the numerical implementation of this spline method, we need to calculate the spline function and the corresponding matrix in this particular setting. Here, the operator $\mathcal{A}$ is given in Eq. (19.1) and we choose the sequence

$$\kappa_{m,n}^{(2)} := \kappa_n^{(2)} \delta_{m,0} \qquad \text{for all } n \in \mathbb{N},$$

which fits to the null space of the operator $\mathcal{T}_{\mathrm{E}}$. The precise orthonormal basis is stated in Eq. (13.5a), for example. Due to Theorem 19.1, the spline matrix can be assembled with the functions

$$\mathcal{A}_{\boldsymbol{z}}^k \tilde{\boldsymbol{g}}_{0,n,j}^{(2)}(\varrho_0; \boldsymbol{z}) = \frac{1}{\sqrt{n\varrho_0}} \beta_n^{(L)} \left((n+1) \left(\frac{y_k}{\varrho_L} \right)^{2n+1} + n \right) \left(\frac{\varrho_0}{y_k} \right)^{n+1} Y_{n,j}(\hat{\boldsymbol{y}}_k).$$

Recall that $\boldsymbol{y}_k$ for all $k = 1, \ldots, \ell_{\mathrm{E}}$ denotes the sensor positions of the electroencephalograph. Hence, the entries of the matrix are given for all l, $k = 1 \ldots, \ell_{\mathrm{E}}$ by

$$\begin{aligned}
\mathcal{A}_{\boldsymbol{x}}^l \mathcal{A}_{\boldsymbol{z}}^k \left(\mathfrak{k}^{(2)}(\boldsymbol{z}, \boldsymbol{x}) \right) &= \sum_{\substack{n \in \mathbb{N} \\ \kappa_n^{(2)} \neq 0}} \left(\kappa_n^{(2)} \right)^{-2} \sum_{j=1}^{2n+1} \frac{\left(\beta_n^{(L)} \right)^2}{n\varrho_0} \left(\frac{\varrho_0^2}{y_l y_k} \right)^{n+1} \left((n+1) \left(\frac{y_l}{\varrho_L} \right)^{2n+1} + n \right) \\
&\quad \times \left((n+1) \left(\frac{y_k}{\varrho_L} \right)^{2n+1} + n \right) Y_{n,j}(\hat{\boldsymbol{y}}_l) Y_{n,j}(\hat{\boldsymbol{y}}_k) \\
&= \frac{1}{4\pi} \sum_{\substack{n \in \mathbb{N} \\ \kappa_n^{(2)} \neq 0}} \left(\kappa_n^{(2)} \right)^{-2} \frac{2n+1}{n\varrho_0} \left(\beta_n^{(L)} \right)^2 \left(\frac{\varrho_0^2}{y_l y_k} \right)^{n+1} \left((n+1) \left(\frac{y_l}{\varrho_L} \right)^{2n+1} + n \right) \\
&\quad \times \left((n+1) \left(\frac{y_k}{\varrho_L} \right)^{2n+1} + n \right) P_n(\hat{\boldsymbol{y}}_l \cdot \hat{\boldsymbol{y}}_k).
\end{aligned}$$

Note that the Addition Theorem, see Theorem 2.25, is used in the last step. The Legendre series can be efficiently evaluated using the Clenshaw algorithm.

We calculate the following expression for the representation of the corresponding spline:

$$\begin{aligned}
&\mathcal{A}_{\boldsymbol{z}}^k \mathfrak{k}^{(2)}(\boldsymbol{z}, \boldsymbol{x}) \\
&= \sum_{\substack{n \in \mathbb{N} \\ \kappa_n^{(2)} \neq 0}} \sum_{j=1}^{2n+1} \left(\kappa_n^{(2)} \right)^{-2} \tilde{\boldsymbol{g}}_{0,n,j}^{(2)}(\varrho_0; \boldsymbol{x}) \mathcal{A}_{\boldsymbol{z}}^k \tilde{\boldsymbol{g}}_{0,n,j}^{(2)}(\varrho_0; \boldsymbol{z}) \\
&= \sum_{\substack{n \in \mathbb{N} \\ \kappa_n^{(2)} \neq 0}} \sum_{j=1}^{2n+1} \left(\kappa_n^{(2)} \right)^{-2} \tilde{\boldsymbol{g}}_{0,n,j}^{(2)}(\varrho_0; \boldsymbol{x}) \frac{1}{\sqrt{n\varrho_0}} \beta_n^{(L)} \left((n+1) \left(\frac{y_k}{\varrho_L} \right)^{2n+1} + n \right) \left(\frac{\varrho_0}{y_k} \right)^{n+1} Y_{n,j}(\hat{\boldsymbol{y}}_k) \\
&= \sum_{\substack{n \in \mathbb{N} \\ \kappa_n^{(2)} \neq 0}} \sum_{j=1}^{2n+1} \left(\kappa_n^{(2)} \right)^{-2} \sqrt{\frac{2n+1}{n\varrho_0^4}} \frac{x^{n-1}}{\varrho_0^{n-1}} \beta_n^{(L)} \left((n+1) \left(\frac{y_k}{\varrho_L} \right)^{2n+1} + n \right) \left(\frac{\varrho_0}{y_k} \right)^{n+1} \tilde{\boldsymbol{y}}_{n,j}^{(2)}(\hat{\boldsymbol{x}}) Y_{n,j}(\hat{\boldsymbol{y}}_k) \\
&= \sum_{\substack{n \in \mathbb{N} \\ \kappa_n^{(2)} \neq 0}} \sum_{j=1}^{2n+1} \left(\kappa_n^{(2)} \right)^{-2} \sqrt{\frac{2n+1}{n}} \frac{x^{n-1}}{y_k^{n+1}} \beta_n^{(L)} \left((n+1) \left(\frac{y_k}{\varrho_L} \right)^{2n+1} + n \right) \tilde{\boldsymbol{y}}_{n,j}^{(2)}(\hat{\boldsymbol{x}}) Y_{n,j}(\hat{\boldsymbol{y}}_k)
\end{aligned}$$

$$= \frac{1}{4\pi} \sum_{\substack{n\in\mathbb{N} \\ \kappa_n^{(2)}\neq 0}} \left(\kappa_n^{(2)}\right)^{-2} \frac{(2n+1)^{3/2}}{\sqrt{n}} \frac{x^{n-1}}{y_k^{n+1}} \beta_n^{(L)} \left((n+1) \left(\frac{y_k}{\varrho_L} \right)^{2n+1} + n \right) \tilde{\boldsymbol{p}}_n^{(2)}(\hat{\boldsymbol{x}}; \hat{\boldsymbol{y}}_k).$$

For the implementation of the spline function, we can further expand the Edmonds vector Legendre polynomial. For all $\boldsymbol{\xi}, \boldsymbol{\eta} \in \mathbb{S}$, the following identity holds true, see also Eq. (5.12a):

$$\begin{aligned} \tilde{\boldsymbol{p}}_n^{(2)}(\boldsymbol{\xi}, \boldsymbol{\eta}) &= \sqrt{\frac{n}{2n+1}} \boldsymbol{p}_n^{(1)}(\boldsymbol{\xi}, \boldsymbol{\eta}) + \sqrt{\frac{n+1}{2n+1}} \boldsymbol{p}_n^{(2)}(\boldsymbol{\xi}, \boldsymbol{\eta}) \\ &= \sqrt{\frac{n}{2n+1}} P_n(\boldsymbol{\xi} \cdot \boldsymbol{\eta}) \boldsymbol{\xi} + \sqrt{\frac{1}{(2n+1)n}} P_n'(\boldsymbol{\xi} \cdot \boldsymbol{\eta})(\boldsymbol{\eta} - (\boldsymbol{\xi} \cdot \boldsymbol{\eta}) \boldsymbol{\xi}). \end{aligned}$$

Eventually, the spline function is given by

$$\begin{aligned} \boldsymbol{s}(\boldsymbol{x}) = \frac{1}{4\pi} \sum_{k=1}^{\ell_\mathrm{E}} a_k \sum_{\substack{n\in\mathbb{N} \\ \kappa_n^{(2)}\neq 0}} \left(\kappa_n^{(2)}\right)^{-2} (2n+1) \frac{x^{n-1}}{y_k^{n+1}} \beta_n^{(L)} \left((n+1) \left(\frac{y_k}{\varrho_L} \right)^{2n+1} + n \right) \\ \times \left(P_n(\hat{\boldsymbol{x}} \cdot \hat{\boldsymbol{y}}_k) \hat{\boldsymbol{x}} + \frac{1}{n} P_n'(\hat{\boldsymbol{x}} \cdot \hat{\boldsymbol{y}}_k)(\hat{\boldsymbol{y}}_k - (\hat{\boldsymbol{x}} \cdot \hat{\boldsymbol{y}}_k) \hat{\boldsymbol{x}}) \right). \end{aligned}$$

Again, this expression can be evaluated using the Clenshaw algorithm and its variant for the first derivatives of the Legendre polynomials.

Chapter 21.

Numerical Results

21.1. Regularized (Orthogonal) Functional Matching Pursuit

We use the abbreviation R(O)FMP if a statement holds true for the RFMP as well as for the ROFMP. For the numerical solution of the synthetic test cases by means of the R(O)FMP, we used the following dictionaries:

$$\mathcal{D}_{\mathrm{M}}(5, \{0.8, 0.9, 0.95, 0.99\}, 12\,655), \qquad \mathcal{D}_{\mathrm{E}}(5, \{0.8, 0.9, 0.95, 0.99\}, 12\,655).$$

See Eq. (19.7) for the definition of $\mathcal{D}_{\mathrm{M}}$ and $\mathcal{D}_{\mathrm{E}}$. Each of these dictionaries contains 35 different orthonormal basis functions from degree 1 up to degree 5 and 50 620 reproducing kernels, which have 12 655 different centres within the ball and four different values for the parameter $h \in \{0.8, 0.9, 0.95, 0.99\}$. Hence, each dictionary consists of 50 655 dictionary elements. The choice of the dictionary has an influence on the reconstruction since we can only use a finite amount of dictionary elements in the actual computation. Thus, the choice of the dictionary can also be understood as a regularization. For example, numerical tests showed that more orthonormal basis functions with a maximal degree higher than $n = 5$ yield poorer results, since the RFMP tries to reconstruct details and delicate structures with these high-degree orthonormal basis functions instead of using the localized reproducing kernels. This contradicts former numerical experiments in the geosciences. A reason for this behaviour may be the few (up to about 100) data given in our particular problems, whereas, for example, in [210] 8500 data points where used in a synthetic downward continuation. Thus, the few data points in our particular problem can also be interpolated with these basis functions. On the other hand, for the sake of computation time we removed dictionary elements that were almost never chosen, such as reproducing kernels with a parameter h smaller than 0.8. However, these refinements are done by trial and error.

In an ongoing research, see [201], a *Learning Regularized (Orthogonal) Functional Matching Pursuit Algorithm* (LR(O)FMP) will be constructed. The aim of the LR(O)FMP is to build, based on a large initial dictionary, a smaller learned dictionary containing the best-fitting dictionary elements. The learned dictionary is not necessarily a subset of the initial dictionary. In an optimization step, it can generate new dictionary elements of existing types. First numerical tests using the RFMP showed that the learned dictionary yielded more accurate and sparser results than a manually chosen larger one. And it does so in a fraction of computational time. In this context, a reconstruction is said to be *sparser* if fewer dictionary elements are required for its representation.

Let again the parameter $\bullet \in \{\mathrm{M}, \mathrm{E}\}$ be chosen according to the considered problem. In both synthetic test cases, the R(O)FMP is tested for several noise levels, that is $\delta_\bullet \in \{0, 0.01, 0.05, 0.1\}$, and three different regularization terms. The regularization terms are given by the vectorial Sobolev spaces over the ball induced by the sequence from Eq. (19.5) for the parameters $s \in \{0, 1, 2\}$, see Definition 16.1.

For judging the quality of the reconstruction obtained by the R(O)FMP, we consider the next quantities. The R(O)FMP returns the residual of the approximation, see Algorithms 17.2 and 17.19. For the sake of comparability, we normalize the residual with respect to the data $\boldsymbol{g}^{\delta_\bullet}$. Let $\boldsymbol{J}_\tau^{\delta_\bullet}$ denote the solution obtained via the R(O)FMP from the data $\boldsymbol{g}^{\delta_\bullet} \in \mathbb{R}^{\ell_\bullet} \setminus \{\boldsymbol{0}\}$ with regularization parameter $\tau > 0$. Then the relative residual is given by

$$\text{rel. residual} \coloneqq \frac{\left\| \mathcal{A}_\bullet \boldsymbol{J}_\tau^{\delta_\bullet} - \boldsymbol{g}^{\delta_\bullet} \right\|_{\mathbb{R}^{\ell_\bullet}}}{\| \boldsymbol{g}^{\delta_\bullet} \|_{\mathbb{R}^{\ell_\bullet}}}.$$

Based on Algorithms 17.2 and 17.19, we have to define a stopping criterion for both algorithms. The RFMP is stopped after a fixed amount of 600 iterations. The maximal number of iterations for the ROFMP is 250, where the algorithm is restarted after 25 steps. However, due to the fast decrease of the relative residual in the ROFMP, we additionally stop the algorithm if the relative residual after a restart is smaller than or equal to 2 %, that is rel. residual ≤ 0.02.

The evolution of the relative residual during the R(O)FMP is shown in Fig. 21.1 for both synthetic test cases with $\delta_\bullet = 0.05$ and $s = 1$. In the EEG case, the relative residual drops below 5 % after the first few iterations, which is desired for the noise level of 5 % according to the discrepancy principle, see [18, 63, 192] and the references therein. More precisely, 5 % are reached after six iterations in the case of the RFMP and after four iterations in the case of the ROFMP. Similar observations can be made for the other noise levels and regularization terms, which are not shown here. Thus, regarding the relative residual, the RFMP works as it should. Although the curve of the relative residual in the MEG case is qualitatively similar to the curve in the EEG case, the decay is significantly slower. The RFMP needs 282 iterations and the ROFMP needs 32 iterations for the relative residual to fall below 5 %. One possible reason for this behaviour is the severe ill-posedness of the problems and the faster decay of the MEG singular values.

For a qualification of the approximation, we calculate the normalized root mean square difference from the reconstruction to the synthetic test current from Eq. (18.1) on the 3600-points Driscoll-Healy grid given in Eq. (19.8). The normalized root mean square error (NRMSE) is defined by

$$\text{RMSE} \coloneqq \sqrt{\frac{\sum_{t=1}^{60} \sum_{s=1}^{60} \left(\boldsymbol{J}_\tau^{\delta_\bullet}(x_{t,s}, y_{t,s}, z_{t,s}) - \boldsymbol{J}_\bullet(x_{t,s}, y_{t,s}, z_{t,s}) \right)^2}{3600}}, \tag{21.1}$$

$$\text{NRMSE} \coloneqq \frac{\text{RMSE}}{\max_{1 \leq t,s \leq 60} \boldsymbol{J}_\bullet(x_{t,s}, y_{t,s}, z_{t,s}) - \min_{1 \leq t,s \leq 60} \boldsymbol{J}_\bullet(x_{t,s}, y_{t,s}, z_{t,s})}. \tag{21.2}$$

According to the setting of the parameter choice methods from Section 16.3, the R(O)FMP is started with 100 to 300 different regularization parameters τ. First, we try to find the *optimal* regularization parameter τ_{k_*} that minimizes the NRMSE. Corresponding to this regularization parameter, the values of the approximation norm, the NRMSE, and the relative residual obtained via the R(O)FMP are listed for all MEG test cases in Table 21.1 and for all EEG test cases in Table 21.2.

Since the inverse MEG and EEG problems are severely ill-posed problems, it is not surprising that the approximation error, which is represented by the NRMSE, is larger than the relative residual and the noise level throughout almost all numerical tests.

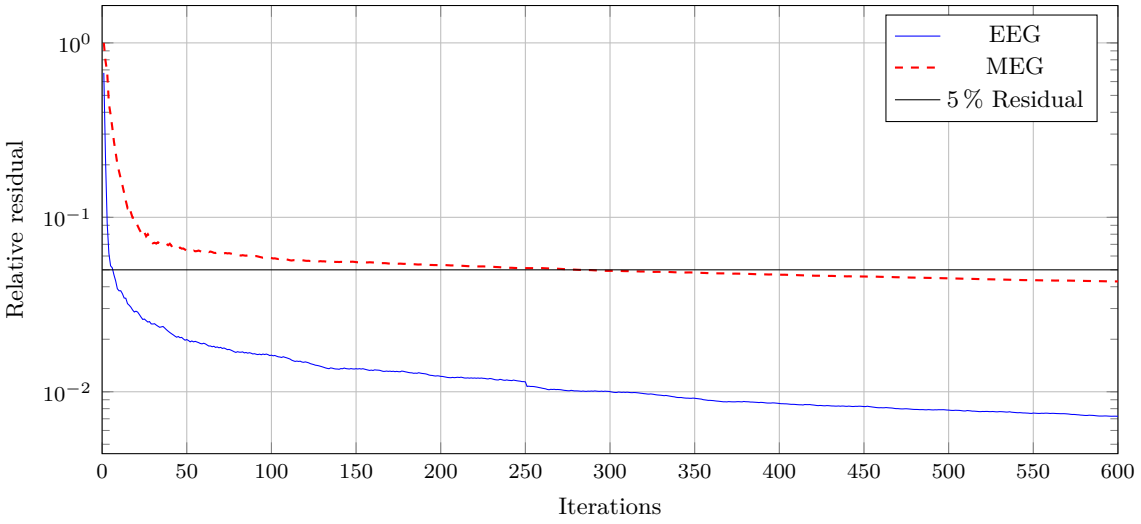

(a) RFMP

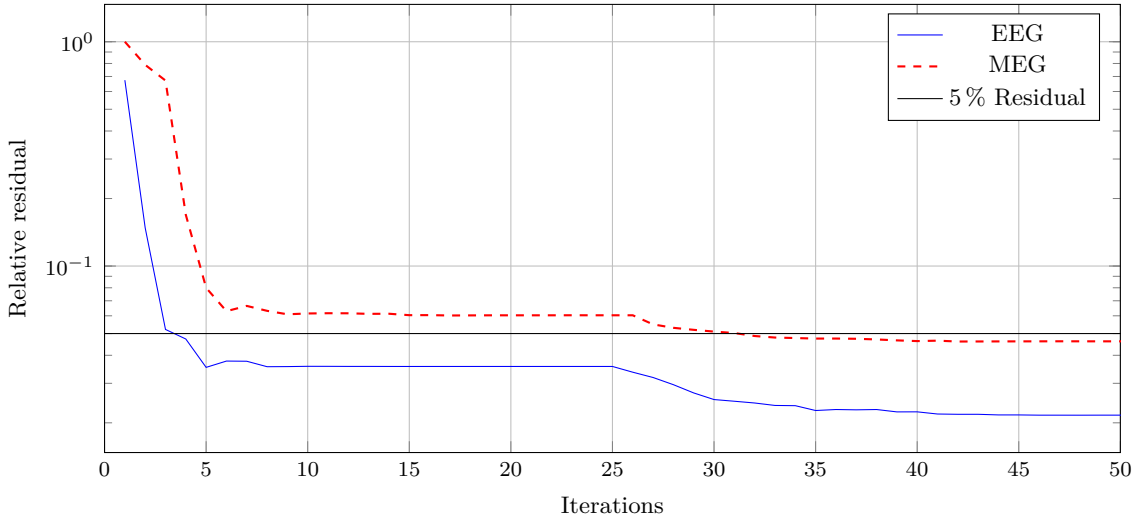

(b) ROFMP

FIGURE 21.1: *Evolution of the relative residual during the R(O)FMP iterations for* $\delta_\bullet = 0.05$ *and* $s = 1$ *for the synthetic EEG test case (solid blue) the MEG test case (dashed red) and the* 5 % *line (solid black)*

		RFMP				ROFMP			
δ_{M}	s	τ_*	$\left\|\boldsymbol{J}_{\tau_*}^{\delta_{\mathrm{M}}}\right\|^2_{\tilde{\mathcal{H}}_s^{(3)}}$	NRMSE	rel. residual	τ_*	$\left\|\boldsymbol{J}_{\tau_*}^{\delta_{\mathrm{M}}}\right\|^2_{\tilde{\mathcal{H}}_s^{(3)}}$	NRMSE	rel. residual
0.00	0	$1.8738 \cdot 10^{5}$	$8.6273 \cdot 10^{-1}$	$6.6916 \cdot 10^{-2}$	$1.7786 \cdot 10^{-2}$	$2.8480 \cdot 10^{3}$	$9.0774 \cdot 10^{-1}$	$1.4555 \cdot 10^{-2}$	$2.3038 \cdot 10^{-3}$
0.00	1	$8.6975 \cdot 10^{0}$	$5.1997 \cdot 10^{1}$	$6.4885 \cdot 10^{-2}$	$1.6521 \cdot 10^{-2}$	$1.7475 \cdot 10^{-1}$	$6.3350 \cdot 10^{1}$	$8.4138 \cdot 10^{-3}$	$3.5752 \cdot 10^{-3}$
0.00	2	$5.7224 \cdot 10^{-6}$	$5.1546 \cdot 10^{4}$	$8.5392 \cdot 10^{-2}$	$1.8046 \cdot 10^{-2}$	$8.3022 \cdot 10^{-8}$	$1.8680 \cdot 10^{4}$	$6.4770 \cdot 10^{-3}$	$3.4596 \cdot 10^{-3}$
0.01	0	$1.5557 \cdot 10^{5}$	$8.8543 \cdot 10^{-1}$	$7.4416 \cdot 10^{-2}$	$1.9521 \cdot 10^{-2}$	$1.8307 \cdot 10^{4}$	$9.1814 \cdot 10^{-1}$	$2.6388 \cdot 10^{-2}$	$8.6169 \cdot 10^{-3}$
0.01	1	$1.0476 \cdot 10^{1}$	$5.0655 \cdot 10^{1}$	$6.2324 \cdot 10^{-2}$	$1.7808 \cdot 10^{-2}$	$1.1233 \cdot 10^{0}$	$5.9932 \cdot 10^{1}$	$1.3075 \cdot 10^{-2}$	$1.5531 \cdot 10^{-2}$
0.01	2	$1.7886 \cdot 10^{-5}$	$2.1568 \cdot 10^{4}$	$7.0103 \cdot 10^{-2}$	$1.4887 \cdot 10^{-2}$	$1.1233 \cdot 10^{-6}$	$1.4212 \cdot 10^{4}$	$1.0797 \cdot 10^{-2}$	$1.2831 \cdot 10^{-2}$
0.05	0	$2.2570 \cdot 10^{5}$	$8.8230 \cdot 10^{-1}$	$8.5450 \cdot 10^{-2}$	$4.0184 \cdot 10^{-2}$	$3.5938 \cdot 10^{5}$	$8.0839 \cdot 10^{-1}$	$9.1041 \cdot 10^{-2}$	$4.0265 \cdot 10^{-2}$
0.05	1	$1.8307 \cdot 10^{1}$	$4.7801 \cdot 10^{1}$	$6.8622 \cdot 10^{-2}$	$4.2893 \cdot 10^{-2}$	$4.6416 \cdot 10^{1}$	$3.5723 \cdot 10^{1}$	$6.5536 \cdot 10^{-2}$	$4.0978 \cdot 10^{-2}$
0.05	2	$3.4305 \cdot 10^{-5}$	$2.2089 \cdot 10^{4}$	$7.5374 \cdot 10^{-2}$	$4.1140 \cdot 10^{-2}$	$2.8480 \cdot 10^{-4}$	$6.6664 \cdot 10^{3}$	$4.6956 \cdot 10^{-2}$	$3.7493 \cdot 10^{-2}$
0.10	0	$7.5646 \cdot 10^{5}$	$8.1762 \cdot 10^{-1}$	$1.0298 \cdot 10^{-1}$	$7.6666 \cdot 10^{-2}$	$6.2803 \cdot 10^{5}$	$8.0962 \cdot 10^{-1}$	$1.0720 \cdot 10^{-1}$	$6.9617 \cdot 10^{-2}$
0.10	1	$8.1113 \cdot 10^{1}$	$3.7236 \cdot 10^{1}$	$7.9808 \cdot 10^{-2}$	$7.5450 \cdot 10^{-2}$	$2.6561 \cdot 10^{1}$	$4.9232 \cdot 10^{1}$	$7.6992 \cdot 10^{-2}$	$6.0133 \cdot 10^{-2}$
0.10	2	$2.3645 \cdot 10^{-3}$	$4.5962 \cdot 10^{3}$	$6.5784 \cdot 10^{-2}$	$7.4879 \cdot 10^{-2}$	$2.0092 \cdot 10^{-3}$	$5.0435 \cdot 10^{3}$	$6.0430 \cdot 10^{-2}$	$7.6376 \cdot 10^{-2}$

TABLE 21.1: *Norm of approximation, NRMSE, and relative residual corresponding to the approximation with the smallest NRMSE, that is* $\boldsymbol{J}_{\tau_*}^{\delta_{\mathrm{M}}}$*, for different noise levels* $\delta_{\mathrm{M}} \in \{0, 0.01, 0.05, 0.1\}$ *and regularization terms* $\tilde{\mathcal{H}}_s^{(3)}$ *with* $s \in \{0, 1, 2\}$ *for the synthetic MEG test case*

		RFMP				ROFMP			
δ_{E}	s	τ_*	$\left\|\boldsymbol{J}_{\tau_*}^{\delta_{\mathrm{E}}}\right\|^2_{\mathfrak{K}_s^{(2)}}$	NRMSE	rel. residual	τ_*	$\left\|\boldsymbol{J}_{\tau_*}^{\delta_{\mathrm{E}}}\right\|^2_{\mathfrak{K}_s^{(2)}}$	NRMSE	rel. residual
0.00	0	$6.6249 \cdot 10^{1}$	$2.0107 \cdot 10^{0}$	$2.4900 \cdot 10^{-2}$	$3.0149 \cdot 10^{-3}$	$2.3485 \cdot 10^{1}$	$7.9669 \cdot 10^{-3}$	$6.3571 \cdot 10^{-3}$	$5.6546 \cdot 10^{-3}$
0.00	1	$3.1993 \cdot 10^{-2}$	$4.4766 \cdot 10^{1}$	$1.5974 \cdot 10^{-2}$	$4.9797 \cdot 10^{-3}$	$1.5923 \cdot 10^{-4}$	$5.9145 \cdot 10^{1}$	$3.6468 \cdot 10^{-3}$	$1.4721 \cdot 10^{-3}$
0.00	2	$3.0539 \cdot 10^{-7}$	$4.1788 \cdot 10^{2}$	$1.2099 \cdot 10^{-2}$	$2.3943 \cdot 10^{-3}$	$2.7826 \cdot 10^{-8}$	$5.7689 \cdot 10^{3}$	$2.4002 \cdot 10^{-3}$	$3.8910 \cdot 10^{-3}$
0.01	0	$6.1359 \cdot 10^{1}$	$2.0249 \cdot 10^{0}$	$2.6383 \cdot 10^{-2}$	$3.0369 \cdot 10^{-3}$	$1.7273 \cdot 10^{1}$	$1.0954 \cdot 10^{-2}$	$1.2517 \cdot 10^{-2}$	$7.3059 \cdot 10^{-3}$
0.01	1	$1.3849 \cdot 10^{-2}$	$6.9540 \cdot 10^{1}$	$1.6806 \cdot 10^{-2}$	$5.9435 \cdot 10^{-3}$	$6.5793 \cdot 10^{-3}$	$1.9628 \cdot 10^{1}$	$6.4557 \cdot 10^{-3}$	$9.8922 \cdot 10^{-3}$
0.01	2	$5.4623 \cdot 10^{-7}$	$9.0635 \cdot 10^{3}$	$1.2293 \cdot 10^{-2}$	$6.7286 \cdot 10^{-3}$	$1.1768 \cdot 10^{-8}$	$4.3554 \cdot 10^{2}$	$6.5172 \cdot 10^{-3}$	$4.8654 \cdot 10^{-3}$
0.05	0	$1.8307 \cdot 10^{2}$	$1.3990 \cdot 10^{0}$	$3.4130 \cdot 10^{-2}$	$9.9109 \cdot 10^{-3}$	$1.7571 \cdot 10^{2}$	$1.2326 \cdot 10^{-1}$	$2.5993 \cdot 10^{-2}$	$1.7185 \cdot 10^{-2}$
0.05	1	$1.0476 \cdot 10^{-2}$	$8.7506 \cdot 10^{1}$	$2.2983 \cdot 10^{-2}$	$1.1355 \cdot 10^{-2}$	$1.7074 \cdot 10^{-1}$	$1.4539 \cdot 10^{1}$	$1.3757 \cdot 10^{-2}$	$1.9817 \cdot 10^{-2}$
0.05	2	$1.5199 \cdot 10^{-6}$	$7.0918 \cdot 10^{3}$	$1.9738 \cdot 10^{-2}$	$1.4941 \cdot 10^{-2}$	$1.1498 \cdot 10^{-6}$	$5.9625 \cdot 10^{3}$	$1.6114 \cdot 10^{-2}$	$1.7548 \cdot 10^{-2}$
0.10	0	$9.7701 \cdot 10^{2}$	$4.2859 \cdot 10^{-1}$	$5.7522 \cdot 10^{-2}$	$4.4368 \cdot 10^{-2}$	$1.4081 \cdot 10^{2}$	$1.3825 \cdot 10^{-1}$	$7.7406 \cdot 10^{-2}$	$1.8412 \cdot 10^{-2}$
0.10	1	$3.2745 \cdot 10^{-1}$	$4.2863 \cdot 10^{1}$	$3.9270 \cdot 10^{-2}$	$6.1547 \cdot 10^{-2}$	$1.8307 \cdot 10^{-1}$	$2.0787 \cdot 10^{1}$	$4.6999 \cdot 10^{-2}$	$3.8657 \cdot 10^{-2}$
0.10	2	$2.2051 \cdot 10^{-6}$	$9.1825 \cdot 10^{3}$	$4.5781 \cdot 10^{-2}$	$4.9857 \cdot 10^{-2}$	$6.4281 \cdot 10^{-5}$	$2.0550 \cdot 10^{2}$	$4.5224 \cdot 10^{-2}$	$5.9492 \cdot 10^{-2}$

TABLE 21.2: *Norm of approximation, NRMSE, and relative residual corresponding to the approximation with the smallest NRMSE, that is* $\boldsymbol{J}_{\tau_*}^{\delta_{\mathrm{E}}}$*, for different noise levels* $\delta_{\mathrm{E}} \in \{0, 0.01, 0.05, 0.1\}$ *and regularization terms* $\mathfrak{K}_s^{(2)}$ *with* $s \in \{0, 1, 2\}$ *for the synthetic EEG test case*

Based on Tables 21.1 and 21.2, we can conclude that in the MEG and EEG synthetic tests the regularization term with $s = 0$, that is the $\mathbf{L}_2(\mathbb{B}_{\varrho_0})$-regularization, yields the highest values for the NRMSE for all noise levels and, consequently, the most inexact approximations of $\boldsymbol{J}_\bullet$. Consequently, we neglect this regularization term in the following discussion.

In the MEG case solved with the RFMP, the smallest NRMSE values are achieved via the regularization term corresponding to $s = 1$ except for $\delta_{\mathrm{M}} = 0.1$, where $s = 2$ yields a significantly better result. For all reconstructions via the ROFMP, the regularization term with $s = 2$ yields the best results concerning the NRMSE. Furthermore, throughout all noise levels and $s \in \{1, 2\}$, the ROFMP yields more accurate results than the RFMP. This may be coherent with the additional residual based stopping criterion for the ROFMP and the differing allowed maximal steps for the algorithms. For a more fair comparison of these two methods, a discrepancy based stopping rule for both algorithms could be used, which is left for future investigations. However, the difference in the NRMSE between the RFMP and the ROFMP decreases as the noise level increases. This can also be seen in Figs. 21.2 and 21.3, which shows the deviation of the reconstruction from the exact test current for the MEG. The corresponding approximations can be found in Figs. 21.4 and 21.5. Note that the colour bars in Figs. 21.2 and 21.3 have different scales and recall that the exact synthetic test current is plotted in Fig. 18.2. The maximal value of the synthetic current on the test grid is 4.9188, whereas the maximal deviation obtained with the RFMP for non-noisy data is 4.1409. However, the ROFMP is able to reduce this deviation by an order of magnitude. This effect is also observed for the other noise levels but, as pointed out before, much less pronounced as the difference between the maximal deviations of the RFMP and ROFMP shrinks with increasing noise level. In addition, the RFMP produces some artefacts in the case of higher noise levels, whereas the reconstruction via the ROFMP is more accurate. One of these artefacts can be seen in the case of 5 % noise on the data in Fig. 21.3a, where a structure resembling an isolated reproducing kernel appears on the middle of the right-hand side. We conclude that the ROFMP with $s = 2$ yields the best results among the tested cases for the reconstruction of the synthetic test current $\boldsymbol{J}_{\mathrm{M}}$.

In the EEG case, the interpretation of Table 21.2 is not as simple as in the MEG case. Both regularization terms, that is $s = 1$ and $s = 2$, yield good results. Using the RFMP, the smallest NRMSE throughout the noise levels $\delta_{\mathrm{E}} = \{0, 0.01, 0.05\}$ is obtained for $s = 2$. However, with 10 % noise on the data, the regularization term corresponding to $s = 1$ yields a slightly smaller NRMSE. If the ROFMP is used, $s = 2$ yields better results on non-noisy data and for $\delta_{\mathrm{E}} = 0.1$, whereas $s = 1$ yields smaller NRMSEs for the other noise levels. Thus, the regularization terms with $s \in \{1, 2\}$ should be preferred to $s = 0$ in the EEG case since we cannot find a clear winner. Figure 21.6 clearly shows the superior quality of the reconstructions with higher smoothness parameter s in the case of non-noisy data. Note that the colour bars of the plots of the deviation change their scale with different parameters s. For reference, recall that the exact solution of the synthetic test case is plotted in Fig. 18.2.

Figures 21.3, 21.5, and 21.7 show that the reconstruction of the synthetic MEG and EEG currents is still good even for 10 % noise. The active regions are well identifiable and the reconstruction is not too blurry, which is quite good for such a severely ill-posed problem. In the MEG case, however, the severe influence of the damping factor is visible for $\delta_{\mathrm{M}} = 0.1$, since the original order of magnitude of one kernel cannot be reconstructed and the corresponding kernel looks damped.

Eventually, for two particular cases, we also visualize the reconstruction and its difference to the exact solution on a cutout of the cerebrum modelled by the ball $\mathbb{B}_{\varrho_0}$, see Figs. 21.8

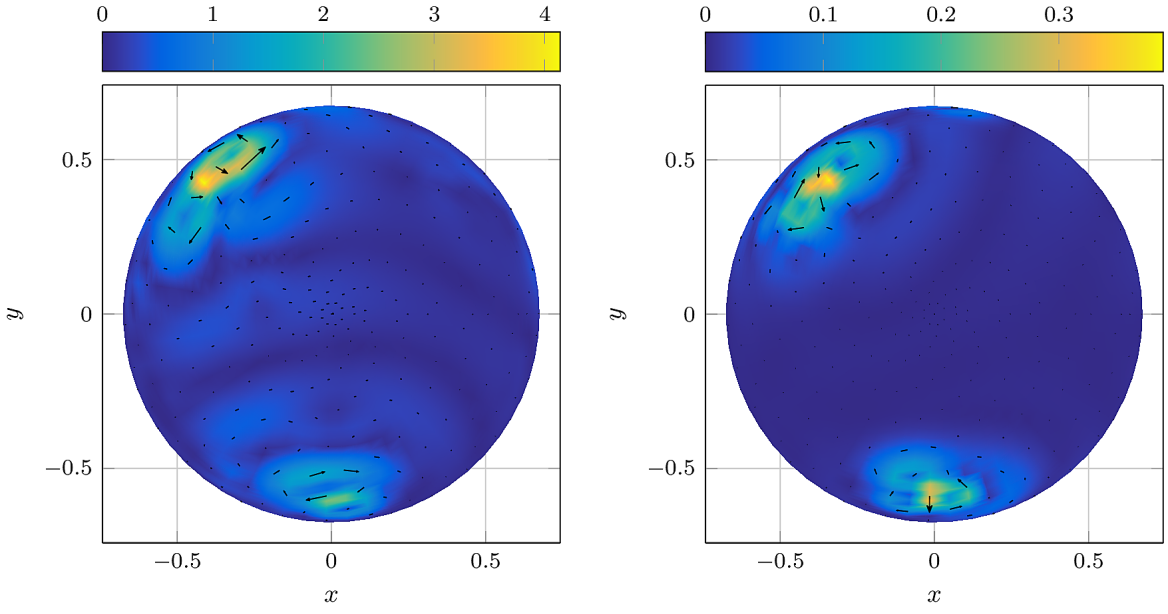

(a) *RFMP*, $\delta_{\mathrm{M}} = 0$

(b) *ROFMP*, $\delta_{\mathrm{M}} = 0$

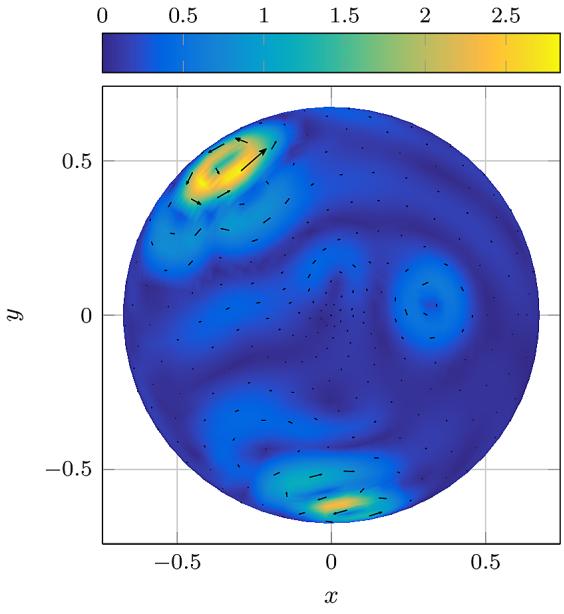

(c) *RFMP*, $\delta_{\mathrm{M}} = 0.01$

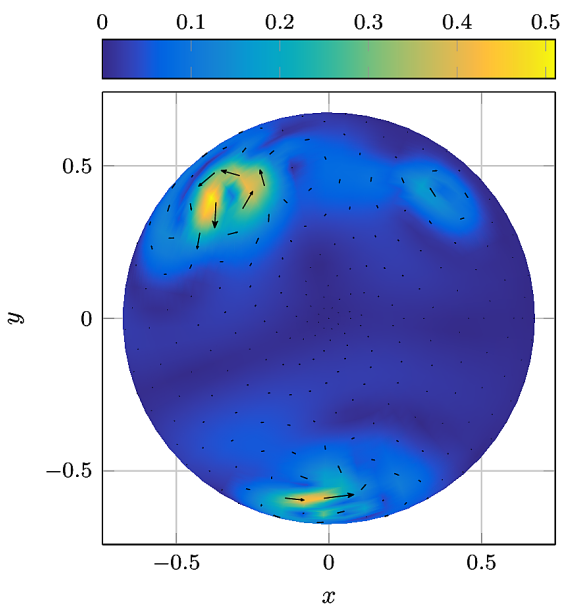

(d) *ROFMP*, $\delta_{\mathrm{M}} = 0.01$

FIGURE 21.2: *Deviation of the approximation from the exact current* $\boldsymbol{J}_{\tau_*}^{\delta_{\mathrm{M}}} - \boldsymbol{J}_{\mathrm{M}}$ *obtained from magnetic flux data with different noise levels via the RFMP (left column) and via the ROFMP (right column) for the regularization term with parameter* $s = 2$ *plotted on an upper hemisphere with radius* $0.95\varrho_0$

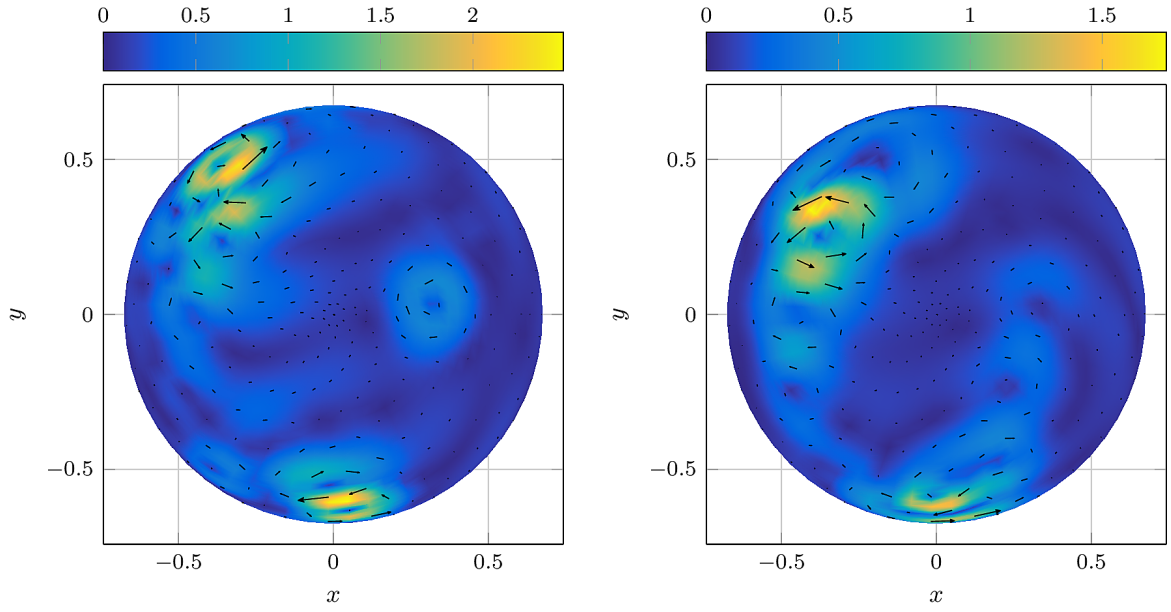

(a) *RFMP*, $\delta_{\mathrm{M}} = 0.05$

(b) *ROFMP*, $\delta_{\mathrm{M}} = 0.05$

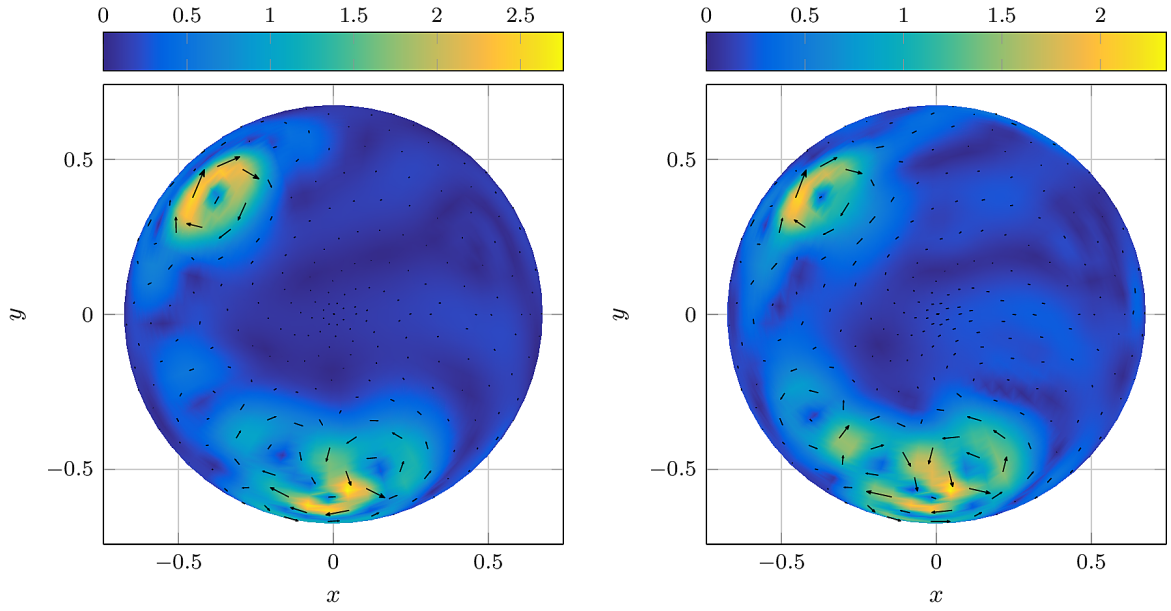

(c) *ROFMP*, $\delta_{\mathrm{M}} = 0.1$

(d) *ROFMP*, $\delta_{\mathrm{M}} = 0.1$

FIGURE 21.3: *Deviation of the approximation from the exact current* $\boldsymbol{J}_{\tau_*}^{\delta_{\mathrm{M}}} - \boldsymbol{J}_{\mathrm{M}}$ *obtained from magnetic flux data with different noise levels via the RFMP (left column) and via the ROFMP (right column) for the regularization term with parameter* $s = 2$ *plotted on an upper hemisphere with radius* $0.95\varrho_0$

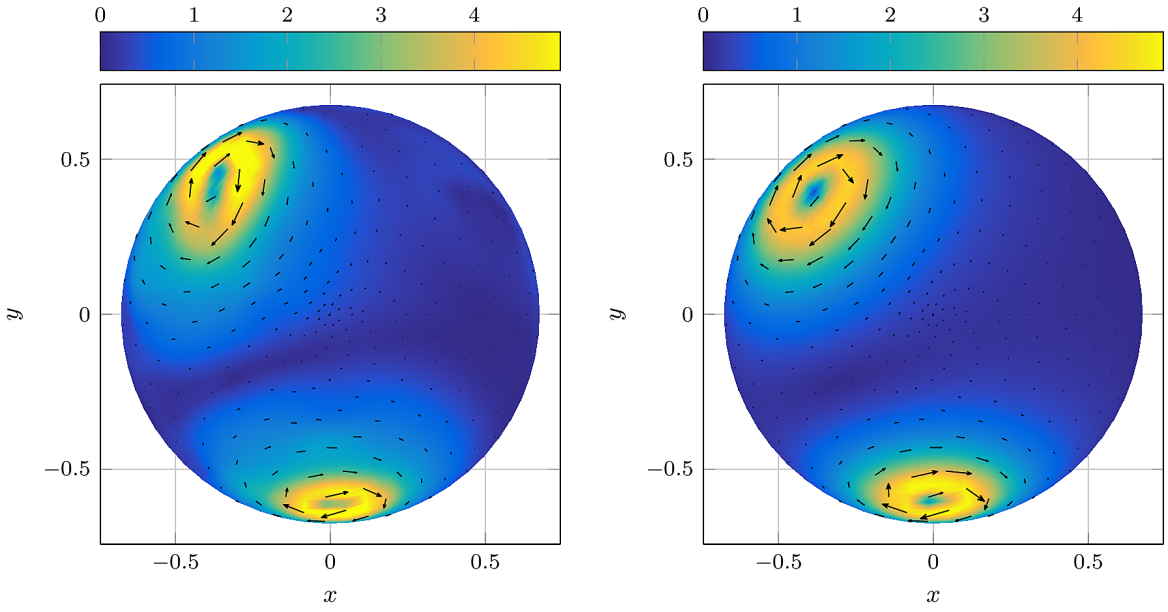

(a) *RFMP*, $\delta_{\mathrm{M}} = 0$

(b) *ROFMP*, $\delta_{\mathrm{M}} = 0$

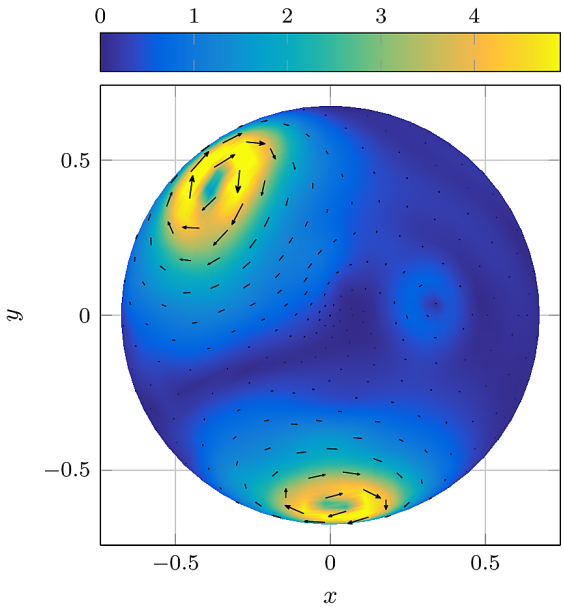

(c) *RFMP*, $\delta_{\mathrm{M}} = 0.01$

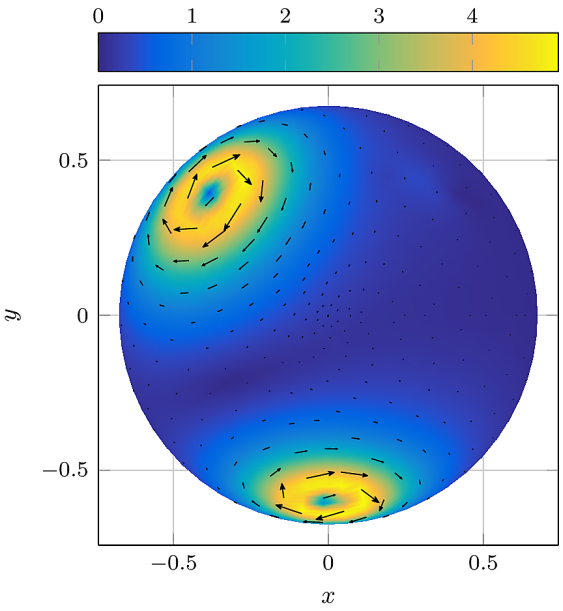

(d) *ROFMP*, $\delta_{\mathrm{M}} = 0.01$

FIGURE 21.4: *Approximation from the exact current* $\boldsymbol{J}_{\tau_*}^{\delta_{\mathrm{M}}}$ *obtained from magnetic flux data with different noise levels via the RFMP (left column) and via the ROFMP (right column) for the regularization term with parameter* $s = 2$ *plotted on an upper hemisphere with radius* $0.95\varrho_0$

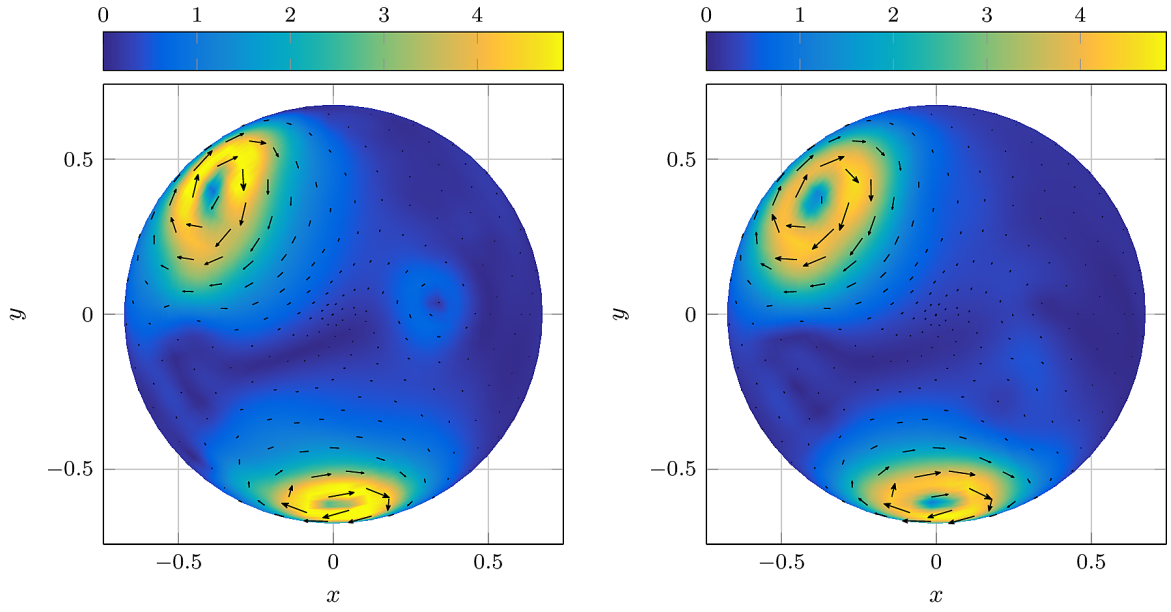

(a) RFMP, $\delta_{\mathrm{M}} = 0.05$

(b) ROFMP, $\delta_{\mathrm{M}} = 0.05$

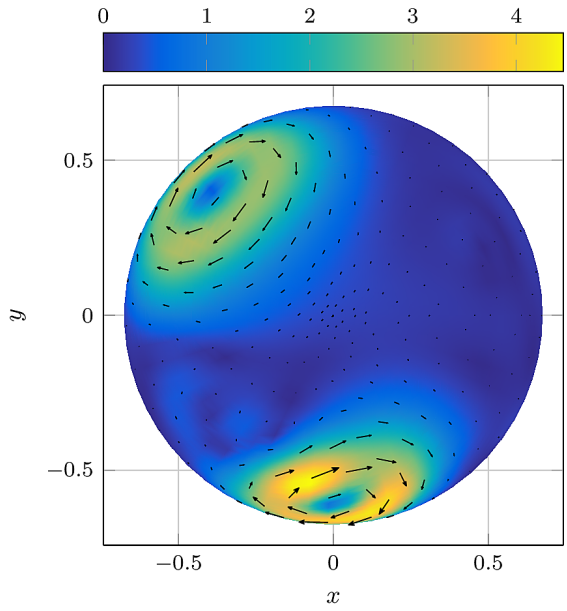

(c) RFMP, $\delta_{\mathrm{M}} = 0.1$

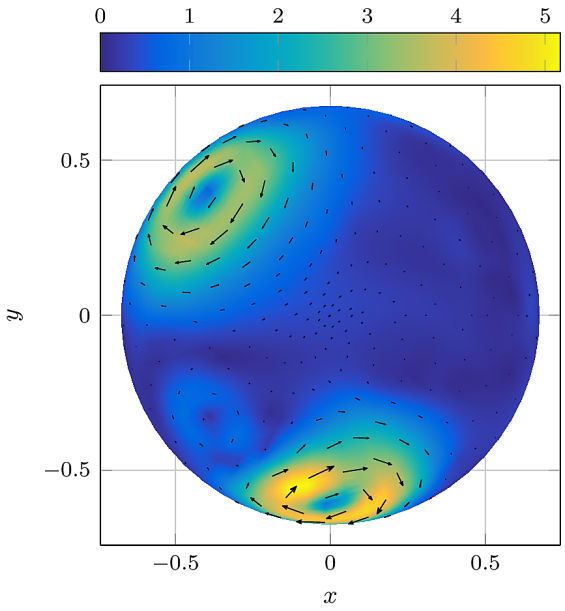

(d) ROFMP, $\delta_{\mathrm{M}} = 0.1$

FIGURE 21.5: *Approximation from the exact current* $\boldsymbol{J}_{\tau_*}^{\delta_{\mathrm{M}}}$ *obtained from magnetic flux data with different noise levels via the RFMP (left column) and via the ROFMP (right column) for the regularization term with parameter* $s = 2$ *plotted on an upper hemisphere with radius* $0.95\varrho_0$

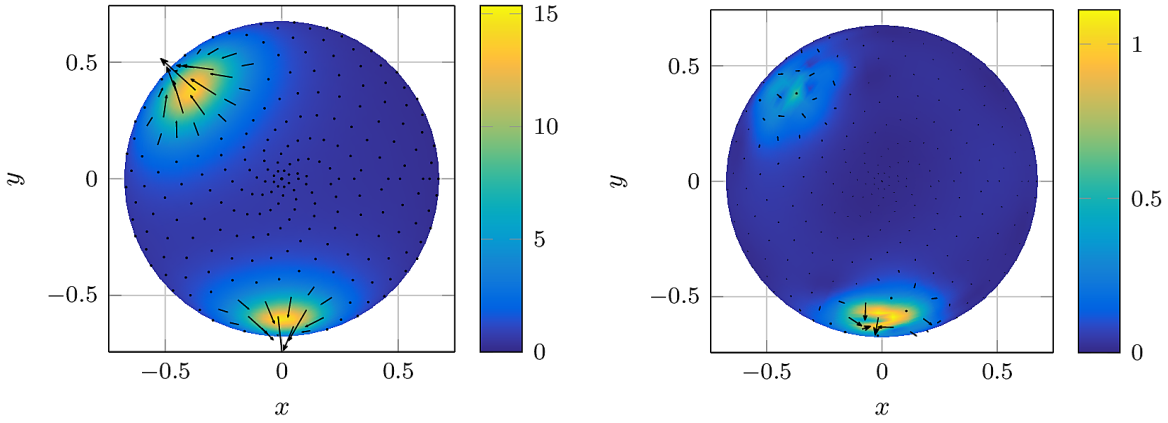

(a) *Approximation,* $s = 0$

(b) *Deviation,* $s = 0$

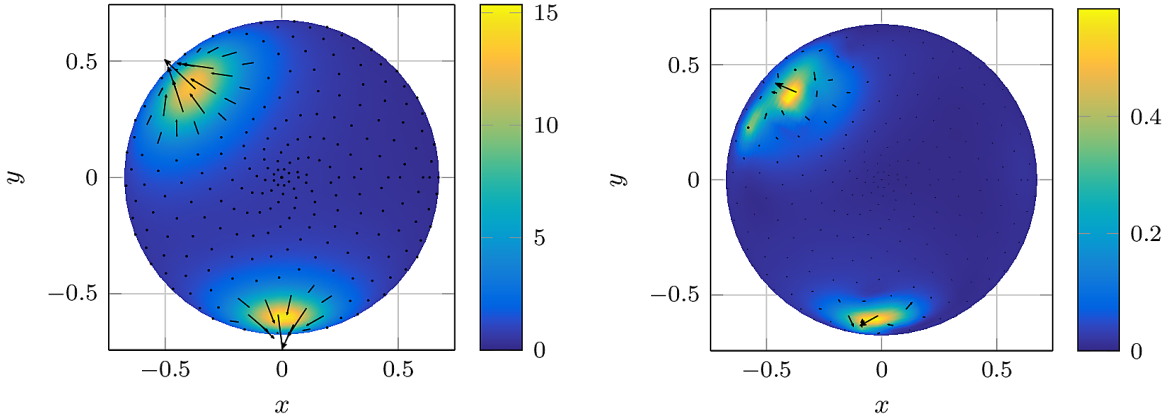

(c) *Approximation,* $s = 1$

(d) *Deviation,* $s = 1$

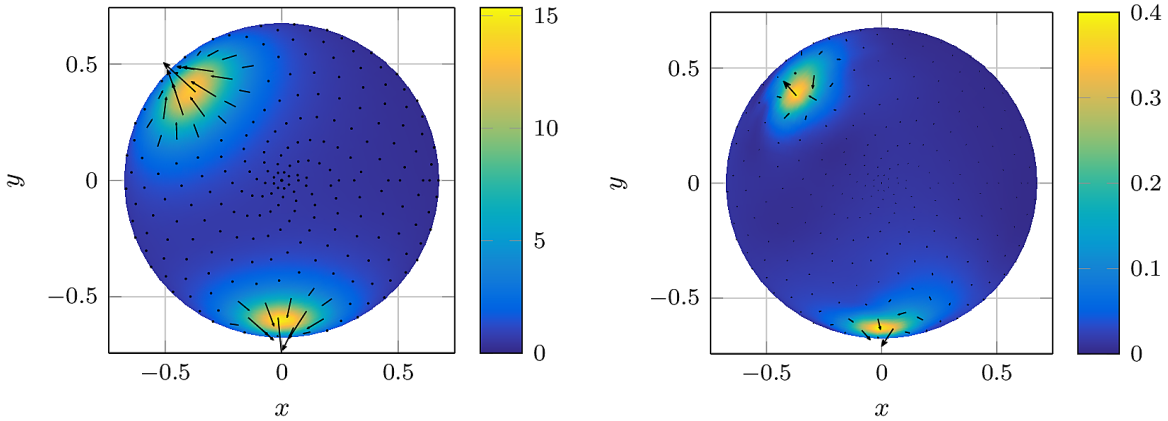

(e) *Approximation,* $s = 2$

(f) *Deviation,* $s = 2$

FIGURE 21.6: *Approximation* $\boldsymbol{J}^{\delta_{\mathrm{E}}}_{\tau_*}$ *of the neuronal current from electric potential data obtained by the ROFMP from non-noisy data for different regularization terms with parameter* s *(left column) and its deviation from the exact solution (right column), see Fig. 18.2, plotted on an upper hemisphere with radius* $0.95\varrho_0$

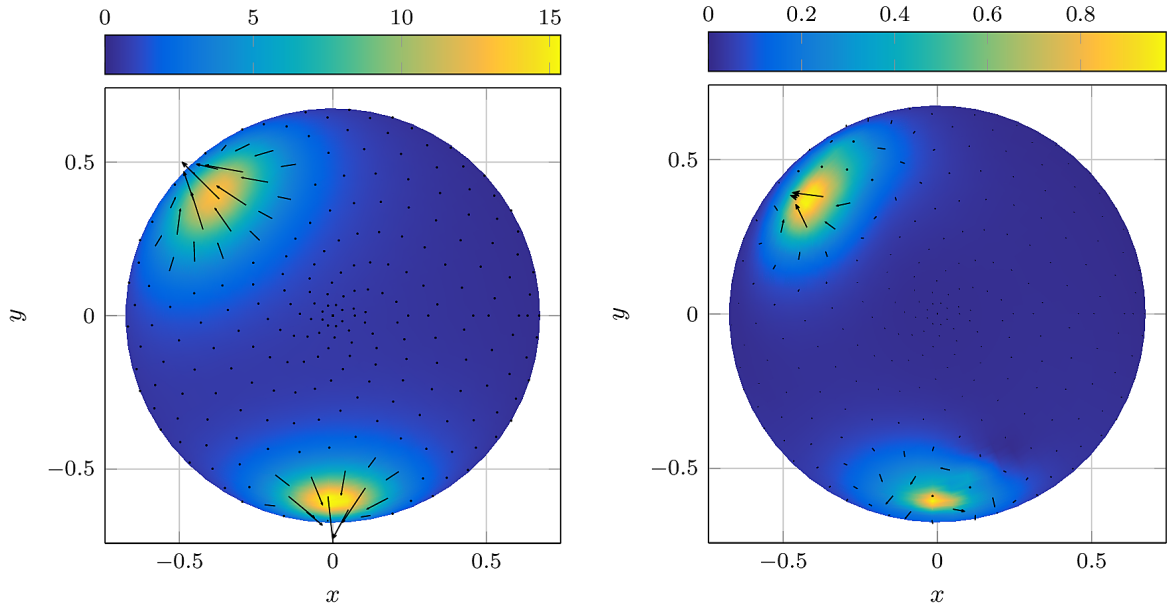

(a) *Approximation,* $\delta_{\mathrm{E}} = 0.01$

(b) *Deviation,* $\delta_{\mathrm{E}} = 0.01$

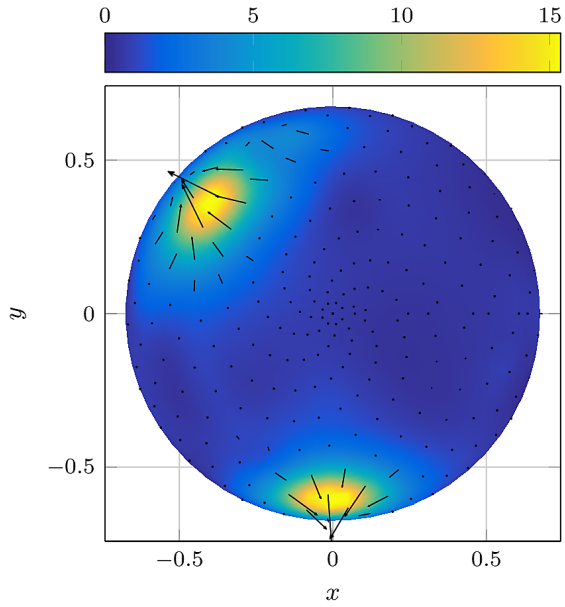

(c) *Approximation,* $\delta_{\mathrm{E}} = 0.1$

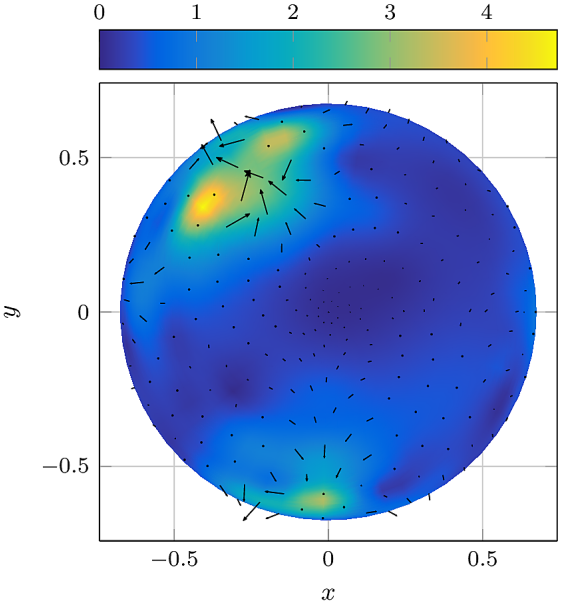

(d) *Deviation,* $\delta_{\mathrm{E}} = 0.1$

FIGURE 21.7: *Approximation* $\boldsymbol{J}_{\tau_*}^{\delta_{\mathrm{E}}}$ *of the neuronal current from electric potential data obtained by the ROFMP with parameter* $s = 1$ *for different noise levels* δ_{E} *(left column) and its deviation from the exact solution (right column), see Fig. 18.2, plotted on an upper hemisphere with radius* $0.95\varrho_0$

to 21.11. These figures reveal that the quality of the reconstruction inside the cerebrum is comparable to the quality of the reconstruction on the single sphere $\mathbb{S}_{0.95\varrho_0}$. In addition, in the region around the origin no activity is expected, which is well reconstructed within the synthetic test case. Besides, one can observe that the deviation of the approximation from the exact solution has its maximum at the boundary. This is not surprising, since the synthetic test case as well as the reconstruction of the neuronal current are harmonic functions. The harmonicity is given by the fact that these functions are elements of the orthogonal complements of the respective operator null spaces.

In addition, the NRMSE listed in Table 21.2 reveals that, independent of the regularization term, the ROFMP produces better reconstructions of the synthetic test current than the RFMP if $\delta_{\mathrm{E}} < 0.1$. For $\delta_{\mathrm{E}} = 0.1$, both algorithms yield comparable results concerning the NRMSE. However, the ROFMP has the advantage that it needs a smaller amount of dictionary elements for the reconstruction, which can be seen in Table 21.3. Thus, the solution obtained via the ROFMP is analytically sparser. Recall that the RFMP uses 600 iterations independent of noise level and regularization term.

		Iterations				Iterations	
$\delta_\bullet$	s	EEG	MEG	$\delta_\bullet$	s	EEG	MEG
0	0	25	25	0.05	0	25	250
0	1	25	25	0.05	1	75	250
0	2	25	25	0.05	2	50	250
0.01	0	25	25	0.1	0	75	250
0.01	1	25	25	0.1	1	250	250
0.01	2	25	25	0.1	2	250	250

TABLE 21.3: *Number of ROFMP iterations in the synthetic test cases depending on noise level and regularization term*

Combining all these numerical results, we conclude that the ROFMP with regularization term $s = 2$ generates good reconstructions for the synthetic MEG test case with noisy data. Therefore, we choose this regularization term for the inversion of real magnetic flux data. For the inversion of the real electric potential data, we will additionally take the regularization term $s = 1$ into account.

Now, we have a closer look at one particular RFMP and ROFMP run for each problem in order to analyze the behaviour of the algorithm. For this particular study, we choose the noise level $\delta_\bullet = 0.05$ and the regularization parameter producing the smallest NRMSE. In the MEG case, we choose the penalty term belonging to $s = 2$ and for the EEG we choose $s = 1$. According to Table 21.3, the ROFMP requires 250 iterations for the MEG problem and 75 iterations for the EEG problem. Both RFMP runs are stopped after 600 iterations. In Table 21.4, the number of chosen orthonormal basis functions and reproducing kernels is listed. In this particular experiment with the ROFMP, about 9 % to 11 % of the chosen dictionary elements are orthonormal basis function. This is also observed for the other noise levels, whose data are not shown here. On the other hand, the RFMP picks an unsteady amount of orthonormal basis functions, which is also shown in these two particular runs (remaining data not shown).

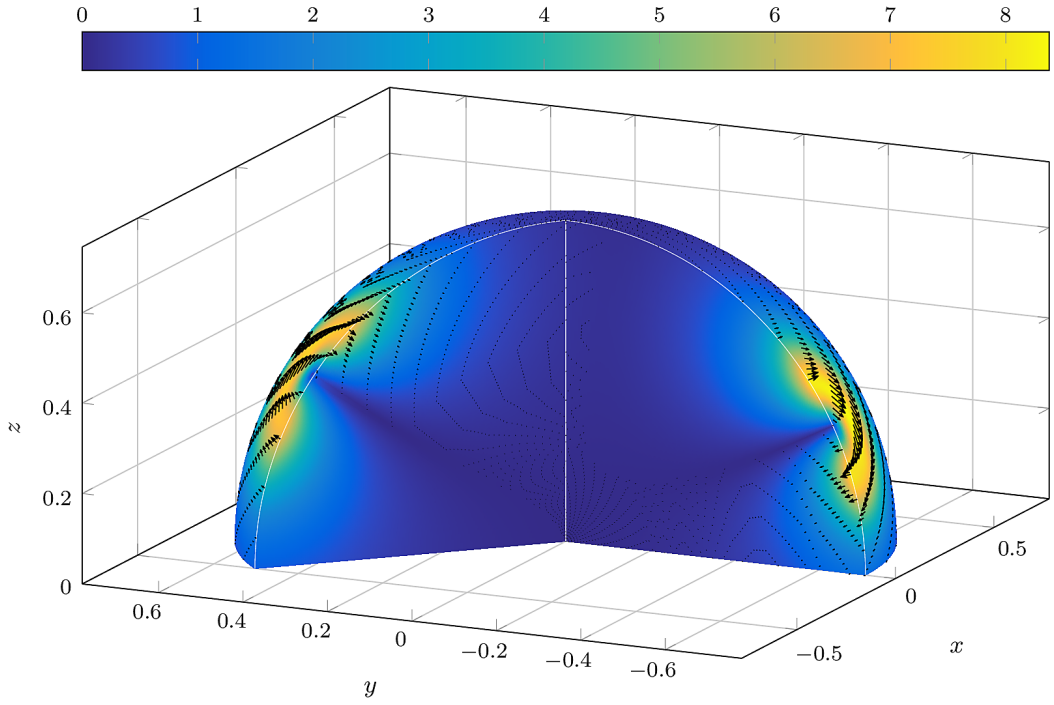

(a) Approximation

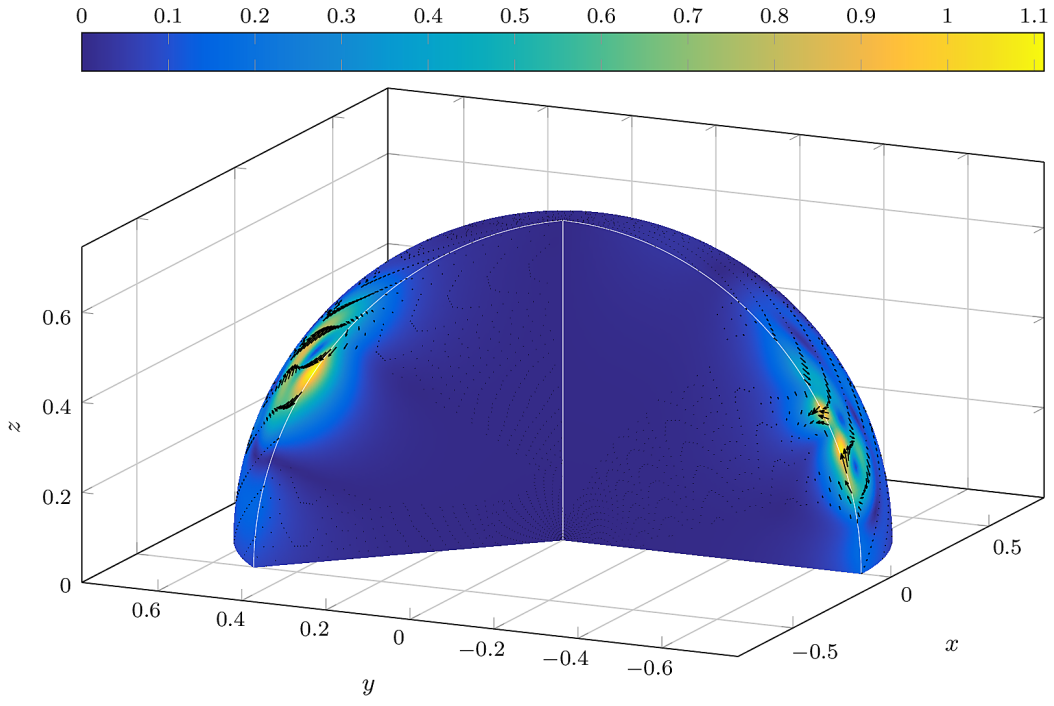

(b) Difference

FIGURE 21.8: *Reconstruction of the neuronal current* $\boldsymbol{J}^{\delta_{\mathrm{M}}}_{\tau_*}$ *(top) from synthetic magnetic flux density data with* $\delta_{\mathrm{M}} = 0.01$ *via the ROFMP with* $s = 2$ *and its deviation from the exact solution (bottom) plotted on a cutout of the ball* $\mathbb{B}_{\varrho_0}$

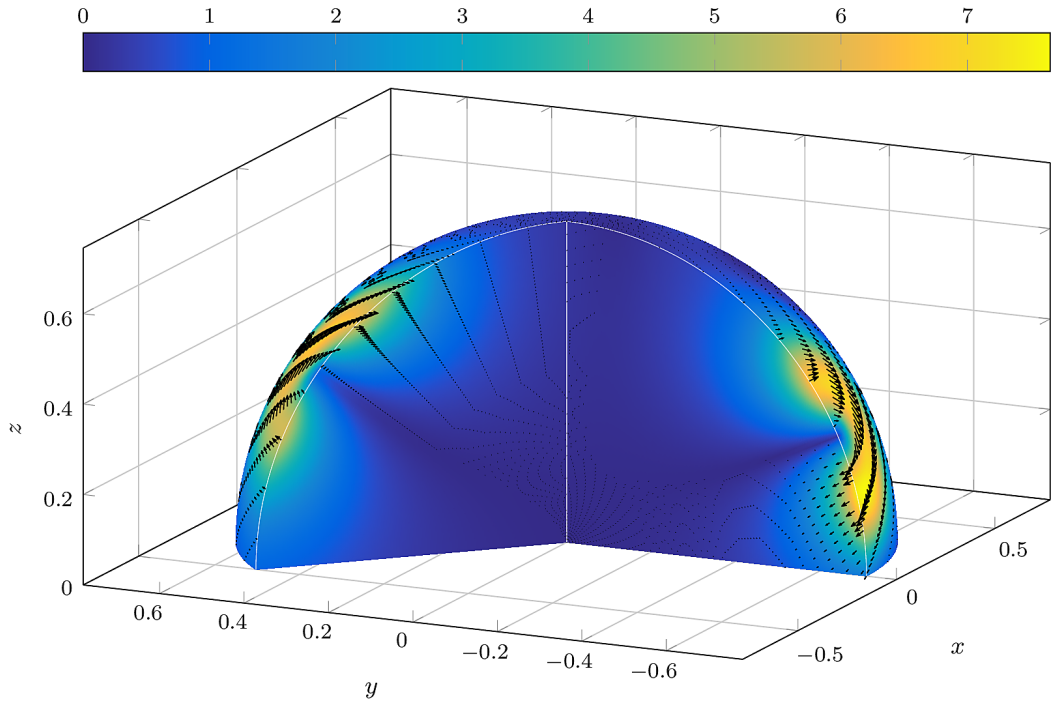

(a) Approximation

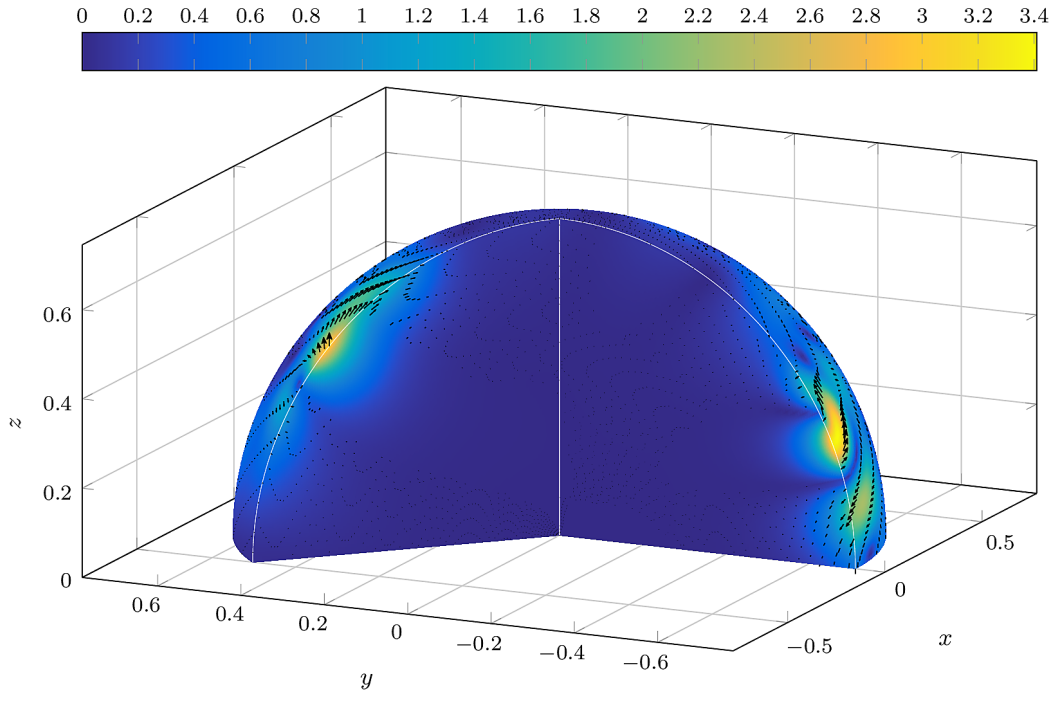

(b) Difference

FIGURE 21.9: *Reconstruction of the neuronal current* $\boldsymbol{J}^{\delta_{\mathrm{M}}}_{\tau_*}$ *(top) from synthetic magnetic flux density data with* $\delta_{\mathrm{M}} = 0.05$ *via the ROFMP with* $s = 2$ *and its deviation from the exact solution (bottom) plotted on a cutout of the ball* $\mathbb{B}_{\varrho_0}$

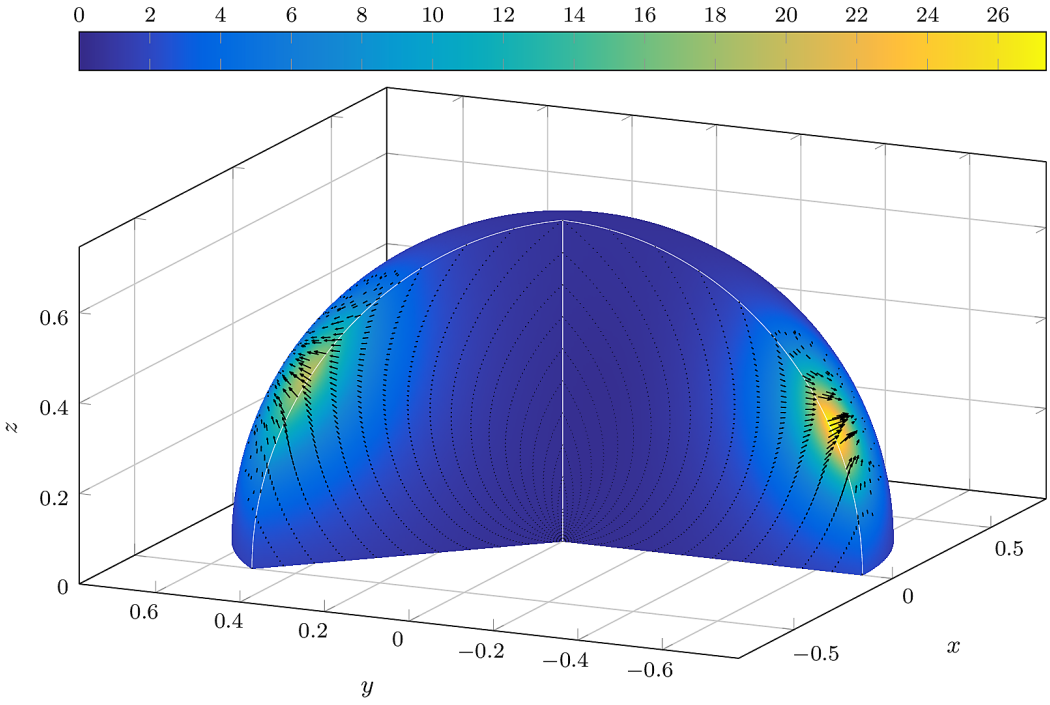

(a) Approximation

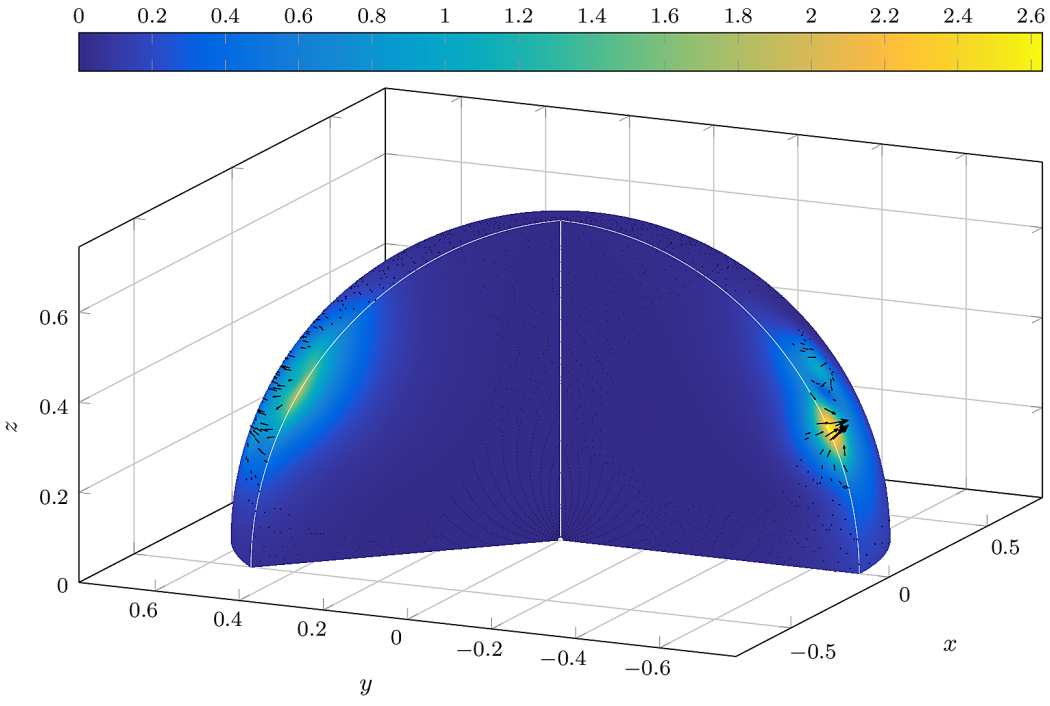

(b) Difference

FIGURE 21.10: *Reconstruction of the neuronal current* $\boldsymbol{J}^{\delta_{\mathrm{E}}}_{\tau_*}$ *(top) from synthetic electric potential data with* $\delta_{\mathrm{E}} = 0.01$ *via the ROFMP with* $s = 1$ *and its deviation from the exact solution (bottom) plotted on a cutout of the ball* $\mathbb{B}_{\varrho_0}$

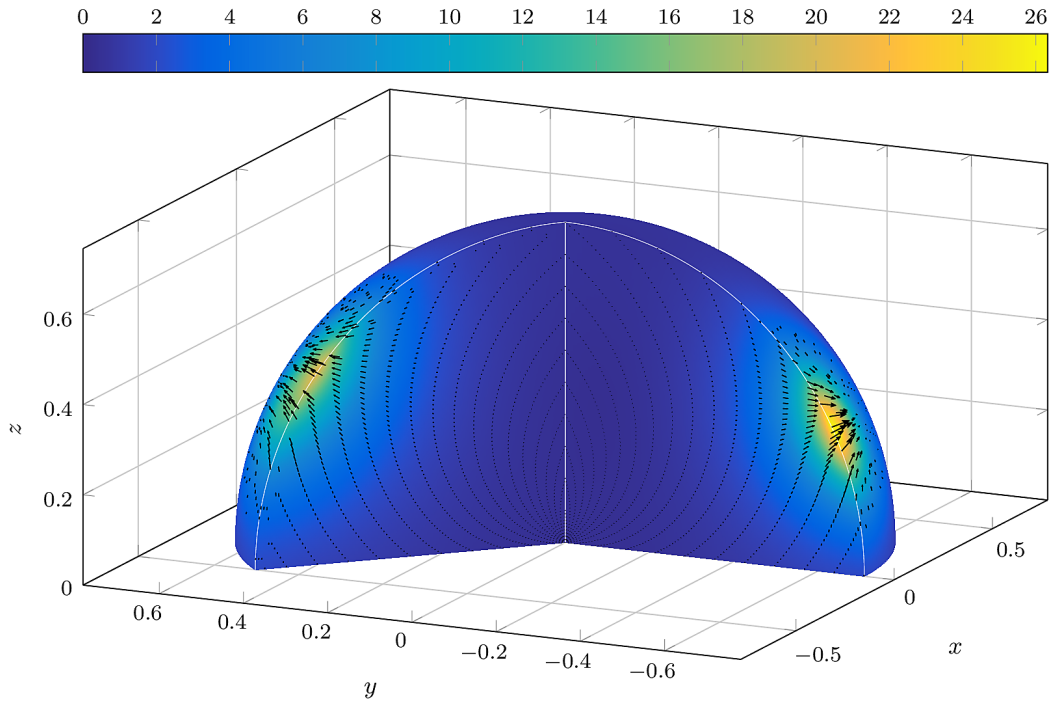

(a) Approximation

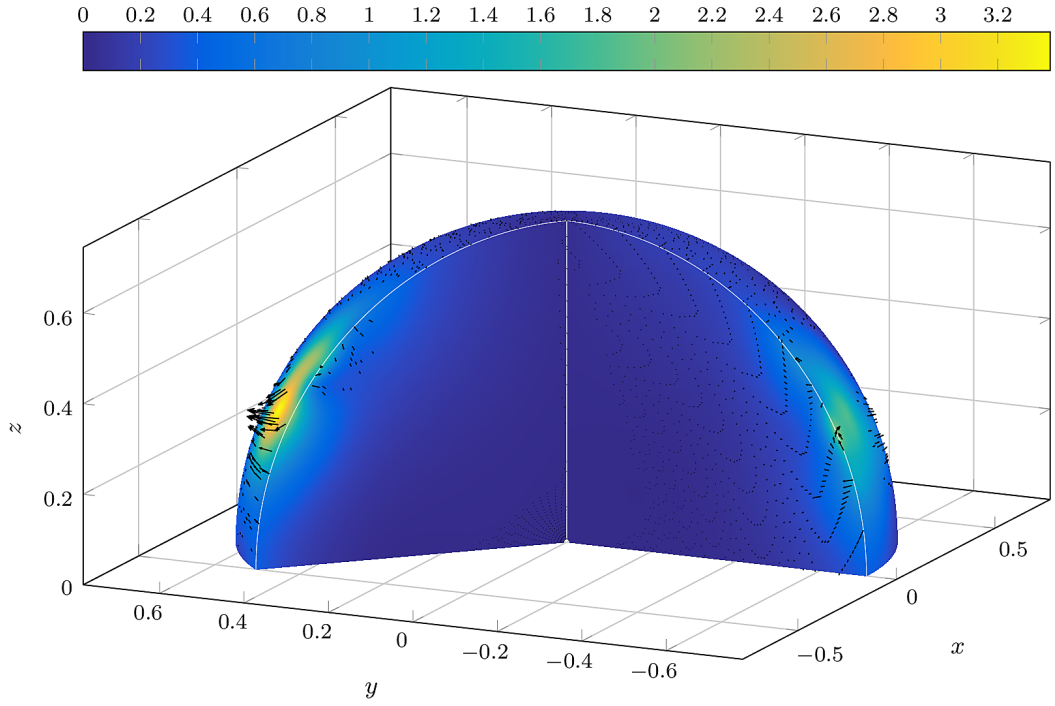

(b) Difference

FIGURE 21.11: *Reconstruction of the neuronal current* $\boldsymbol{J}^{\delta_{\mathrm{E}}}_{\tau_*}$ *(top) from synthetic electric potential data with* $\delta_{\mathrm{E}} = 0.05$ *via the ROFMP with* $s = 1$ *and its deviation from the exact solution (bottom) plotted on a cutout of the ball* $\mathbb{B}_{\varrho_0}$

	MEG		EEG	
	RFMP	ROFMP	RFMP	ROFMP
$\tilde{\boldsymbol{g}}_{0,n,j}^{(i)}(\varrho_0,\cdot)$	20	8	112	23
$\tilde{\boldsymbol{k}}_h^{(i)}(\cdot,\boldsymbol{z})$	580	67	488	227

TABLE 21.4: *Number of chosen dictionary elements for* $\delta_\bullet = 0.05$ *and* $\tilde{\mathfrak{H}}_1^{(2)}$- *or* $\tilde{\mathfrak{H}}_2^{(3)}$*-penalty term, respectively*

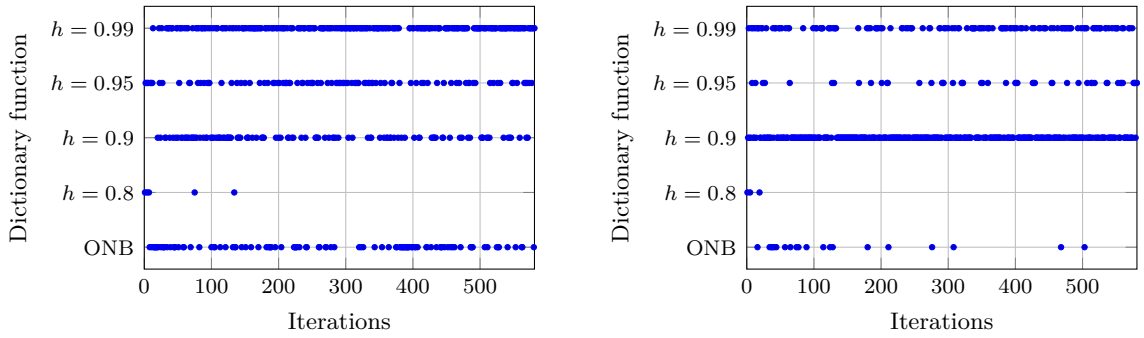

(a) MEG, $s = 2$ *(b) EEG,* $s = 1$

FIGURE 21.12: *Chosen dictionary elements by the RFMP for* $s = 2$ *in the MEG case (left) and for* $s = 1$ *in the EEG case (right) depending on the iterations*

From some applications in the geoscience, it is known that the R(O)FMP tends to first approximate coarse structures with global functions, such as the orthonormal basis functions, and afterwards it reconstructs details with the more localized trial functions, see [66, 68, 165, 210]. This trend can also be observed in the EEG test case, see Fig. 21.12. Here, orthonormal basis functions and reproducing kernels with a broader width, for instance corresponding to $h = 0.8$, are mainly only chosen at the beginning of the algorithm. The influence of the parameter $h \in [0, 1)$ on the width of the reproducing kernel, which is understood as the region significantly differing from zero, can be seen in Figs. 19.4 and 19.6. Afterwards, more localized kernels are chosen. In addition, from former tests it is also known that the R(O)FMP increasingly often chooses reproducing kernels near or in regions that are rich of structure. In the test case, the centres of the reproducing kernels are predominantly chosen close to the active regions. This is visualized in Fig. 21.13 for the RFMP and in Fig. 21.14 for the ROFMP. Especially for the ROFMP, the sparsity of the solution highlights the active regions. For a coarse image of the active regions, it is, hence, sufficient to only know the chosen centres. This can be interesting if an outline of the active regions is desired, which can also be produced in a fractional amount of time, instead of the precise structure of the neuronal current.

21.1.1. Performance Benchmark

Although the ROFMP requires much less iterations than the RFMP, it is, with few exceptions, the slower algorithm due to the required backfitting steps. The CPU time is visualized in Fig. 21.15 in the form of a boxplot. Therein, boxes are plotted for each combination

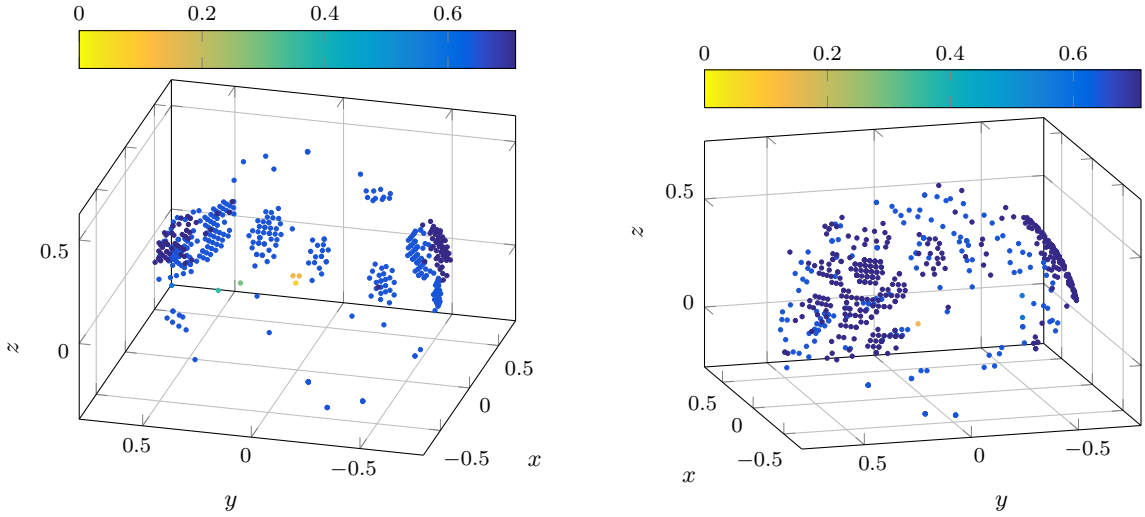

(a) MEG, $s = 2$ *(b) EEG, $s = 1$*

FIGURE 21.13: *Centres of chosen reproducing kernels by the RFMP for $s = 2$ in the MEG case (left) and $s = 1$ in the EEG case (right). The colour represents the distance of the kernel centres from the origin.*

of noise level and regularization term. For each test case and parameter combination, the R(O)FMP is started with 100 different regularization parameters and the required CPU time is recorded. The box contains the timings that are greater than 25 % and smaller than 75 % of all 100 observed values. The horizontal lines inside the boxes mark the median of the CPU times. Finally, the 'whiskers', which are the very first and last horizontal lines, represent the minimum and maximum of the measured timings. In addition, the time required for the regularization parameter with minimal NRMSE is marked with $*$. The boxes corresponding to the RFMP are significantly smaller than the ones belonging to the ROFMP. The reason for this behaviour is that the ROFMP stops depending on the relative residual, which causes inconsistent timings. In the underregularized case, for example, the ROFMP stops after less iterations due to Theorem 17.20, which accelerates the algorithm. The number of iterations for the RFMP is constant, which leads to small variations in the required computation time. In the EEG inversion, however, the ROFMP run with the actually chosen regularization parameter is sometimes faster than the corresponding RFMP run although the required computation time also varies with the regularization term for the ROFMP. However, due to the ROFMP approximations being significantly sparser than the RFMP ones, the postprocessing accelerates. For example, the time required for plotting the approximation depends almost linearly on the amount of chosen dictionary elements.

21.1.2. Evaluation of Parameter Choice Methods

In contrast to the synthetic test case, we cannot determine the *optimal* regularization parameter via the NRMSE in a real data situation as an exact reference solution is not available. Hence, we have to resort to parameter choice methods, which are presented in Section 16.3. Since the choice of the regularization parameter is essential for the quality of

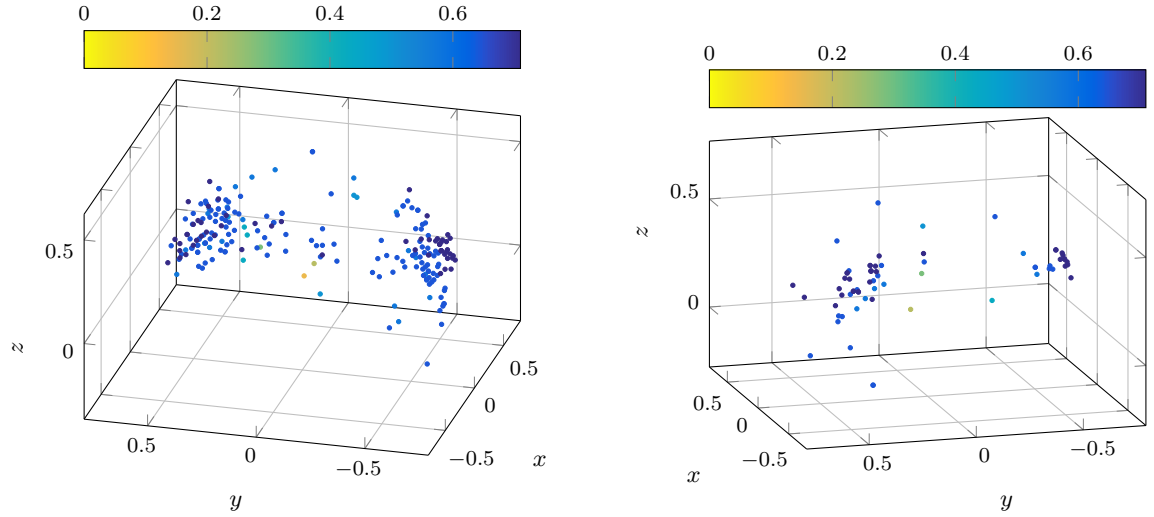

(a) MEG, $s = 2$ *(b) EEG, $s = 1$*

FIGURE 21.14: *Centres of chosen reproducing kernels by the ROFMP for $s = 2$ in the MEG case (left) and $s = 1$ in the EEG case (right). The colour represents the distance of the kernel centres from the origin.*

the result obtained by the R(O)FMP, we compare several parameter choice methods using the synthetic data in order to select suitable methods for the problem at hand.

In Section 16.3, it is specified that most parameter choice methods require the singular values of the operator $\mathcal{A}_\bullet \colon \operatorname{span} \mathcal{D}_\bullet \to \mathbb{R}^{\ell_\bullet}$. In the case of the inverse MEG and EEG problem, however, we only know the singular values of the related (continuous) operator $\mathcal{T}_\bullet \colon \mathbf{L}_2(\mathbb{B}_{\varrho_0}) \to \operatorname{ran} \mathcal{T}_\bullet$ and not of the (discrete) operator $\mathcal{A}_\bullet$. Still, we can calculate the singular values of the discrete operators numerically with the aid of Matlab, see [212]. To this end, we compute the action of the respective operator on the corresponding orthonormal basis functions up to degree $N = 230$. Since the series of the reproducing kernels are also truncated at $N = 230$, see Section 19.1, these basis functions effectively span the dictionary. We collect the actions of the operator in a rectangular matrix of size $\ell_\bullet \times 53\,360$, which represents the (discrete) operator. The singular values of this matrix are plotted in the case of the MEG operator in Fig. 21.17a and in in the case of the EEG operator in Fig. 21.17b.

Based on these singular values, we are able to calculate all quantities required for the parameter choice methods from Section 16.3. In the MEG case, the results are listed in Table 21.5. This table reveals that the modified generalized cross validation and the automatic L-curve method yield the best results for noise levels below 5 %. However, these methods fail for the inversion of 5 %-noisy data. The remaining parameter choice methods yield better but not good results for this noise level since the corresponding NRMSEs are 2 to 3 times as high as with the optimal parameter. The generalized cross validation and the (strong) robust generalized cross validation yield the smallest NRMSEs among all parameter choice methods for $\delta_{\mathrm{M}} = 0.1$, but the error is twice as high as with the optimal parameter.

The evaluation of the parameter choice methods for the EEG problem via the ROFMP with $s = 1$ are presented in Table 21.6. Here, the manual L-curve method is the parameter choice method with the best approximation error except for non-noisy data, where the modified

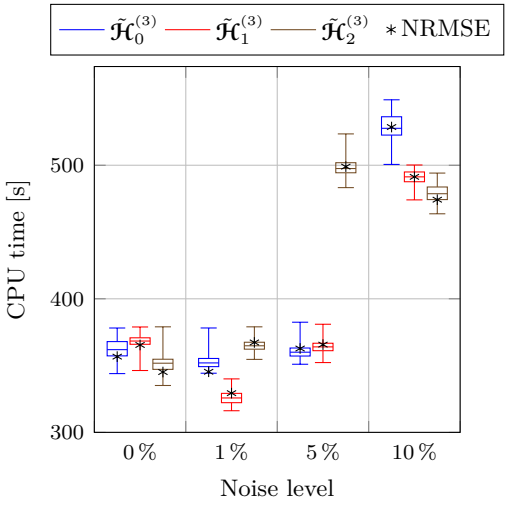

(a) *RFMP for MEG*

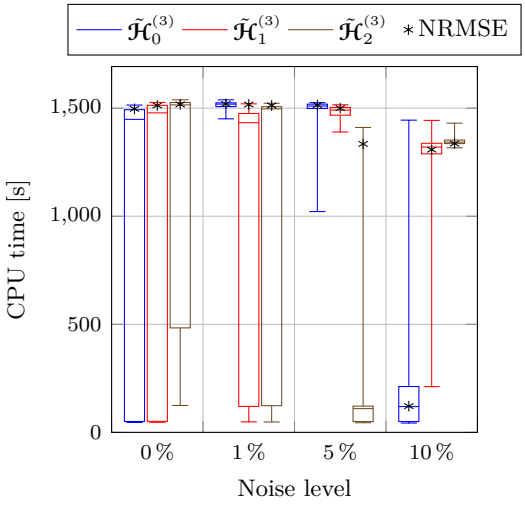

(b) *ROFMP for MEG*

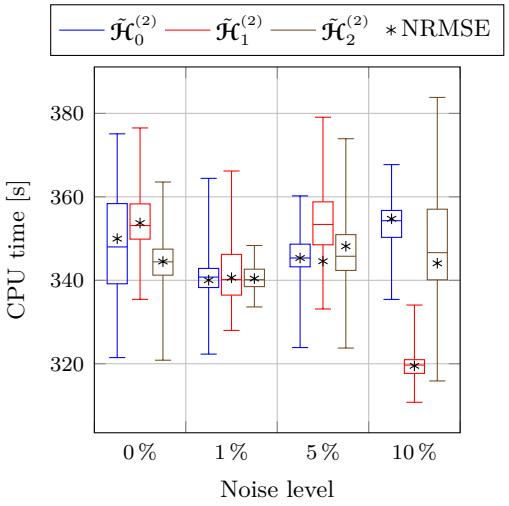

(c) *RFMP for EEG*

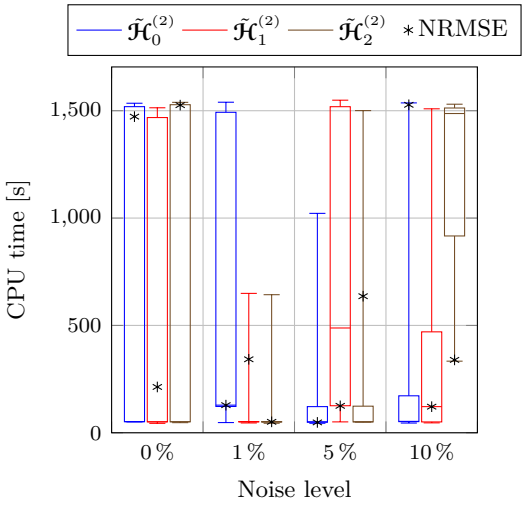

(d) *ROFMP for EEG*

FIGURE 21.15: *Boxplots of the required CPU time for the MEG (first row) and EEG (second row) with the RFMP (left column) and the ROFMP (right column) problem in seconds.*

Parameter Choice		$\delta_{\mathrm{M}} = 0$	$\delta_{\mathrm{M}} = 0.01$	$\delta_{\mathrm{M}} = 0.05$	$\delta_{\mathrm{M}} = 0.1$
NRMSE	NRMSE	0.006 47	0.010 79	0.046 95	0.060 43
	Rel. residual	0.003 45	0.012 83	0.037 49	0.076 37
GCV	NRMSE	0.111 72	0.113 77	0.110 40	**0.12078**
	Rel. residual	0.043 08	0.041 08	0.070 69	0.103 40
MGCV	NRMSE	**0.01089**	**0.03635**	0.403 17	0.427 26
	Rel. residual	0.001 36	0.005 35	0.017 78	0.026 78
RGCV	NRMSE	0.111 72	0.113 77	0.110 40	**0.12078**
	Rel. residual	0.043 08	0.041 08	0.070 69	0.103 40
SRGCV	NRMSE	0.111 72	0.113 77	0.110 40	**0.12078**
	Rel. residual	0.043 08	0.041 08	0.070 69	0.103 40
RM	NRMSE	0.111 72	0.113 77	0.110 40	**0.12078**
	Rel. residual	0.043 08	0.041 08	0.070 69	0.103 40
LCA	NRMSE	**0.01089**	**0.03635**	0.433 89	0.495 96
	Rel. residual	0.001 36	0.005 35	0.018 07	0.027 82
LCM	NRMSE	0.024 06	0.063 90	**0.07857**	0.209 37
	Rel. residual	0.006 10	0.020 12	0.031 34	0.040 74

TABLE 21.5: *NRMSE and relative residual achieved by $\boldsymbol{J}_{\tau_*}^{\delta_{\mathrm{M}}}$ (MEG) via the ROFMP with $s = 2$, where τ_* is chosen according to different parameter choice methods. Best methods are marked in bold.*

Parameter Choice		$\delta_{\mathrm{E}} = 0$	$\delta_{\mathrm{E}} = 0.01$	$\delta_{\mathrm{E}} = 0.05$	$\delta_{\mathrm{E}} = 0.1$
NRMSE	NRMSE	0.003 64	0.006 45	0.013 75	0.050 41
	Rel. residual	0.001 47	0.009 89	0.019 81	0.041 51
GCV	NRMSE	0.042 58	0.057 26	0.052 32	0.072 23
	Rel. residual	0.016 91	0.018 64	0.019 46	0.048 45
MGCV	NRMSE	**0.00596**	0.012 84	0.046 64	0.111 27
	Rel. residual	0.001 35	0.002 60	0.007 47	0.011 34
RGCV	NRMSE	0.042 58	0.057 26	0.052 32	0.072 23
	Rel. residual	0.016 91	0.018 64	0.019 46	0.048 45
SRGCV	NRMSE	0.042 58	0.057 26	0.052 32	0.072 23
	Rel. residual	0.016 91	0.018 64	0.019 46	0.048 45
RM	NRMSE	0.042 58	0.057 26	0.052 32	0.072 23
	Rel. residual	0.016 91	0.018 64	0.019 46	0.048 45
LCA	NRMSE	0.011 56	0.024 12	0.030 97	0.070 07
	Rel. residual	0.017 94	0.013 73	0.019 67	0.015 42
LCM	NRMSE	0.006 18	**0.00869**	**0.02233**	**0.05867**
	Rel. residual	0.004 51	0.004 26	0.011 69	0.033 11

TABLE 21.6: *NRMSE and relative residual achieved by $\boldsymbol{J}_{\tau_*}^{\delta_{\mathrm{E}}}$ (EEG) via the ROFMP with $s = 1$, where τ_* is chosen according to different parameter choice methods. Best methods are marked in bold.*

Parameter Choice		$\delta_{\mathrm{E}} = 0$	$\delta_{\mathrm{E}} = 0.01$	$\delta_{\mathrm{E}} = 0.05$	$\delta_{\mathrm{E}} = 0.1$
NRMSE	NRMSE	0.002 40	0.006 51	0.016 11	0.045 22
	Rel. residual	0.003 89	0.004 86	0.017 54	0.059 49
GCV	NRMSE	0.029 98	0.018 52	0.057 78	**0.05561**
	Rel. residual	0.019 48	0.017 05	0.021 34	0.087 25
MGCV	NRMSE	**0.00859**	0.011 24	**0.02610**	0.069 39
	Rel. residual	0.002 43	0.003 08	0.009 11	0.047 23
RGCV	NRMSE	0.029 98	0.018 52	0.057 78	**0.05561**
	Rel. residual	0.019 48	0.017 05	0.021 34	0.087 25
SRGCV	NRMSE	0.029 98	0.018 52	0.057 78	**0.05561**
	Rel. residual	0.019 48	0.017 05	0.021 34	0.087 25
RM	NRMSE	0.029 34	0.018 52	0.057 78	0.064 96
	Rel. residual	0.018 17	0.017 05	0.021 34	0.073 58
LCA	NRMSE	**0.00859**	0.011 24	**0.02610**	0.062 89
	Rel. residual	0.002 43	0.003 08	0.009 11	0.071 20
LCM	NRMSE	0.029 98	**0.00934**	0.039 49	0.062 41
	Rel. residual	0.019 48	0.007 07	0.024 83	0.052 02

TABLE 21.7: *NRMSE and relative residual achieved by $\boldsymbol{J}_{\tau_*}^{\delta_{\mathrm{E}}}$ (EEG) via the ROFMP with $s = 2$, where τ_* is chosen according to different parameter choice methods. Best methods are marked in bold.*

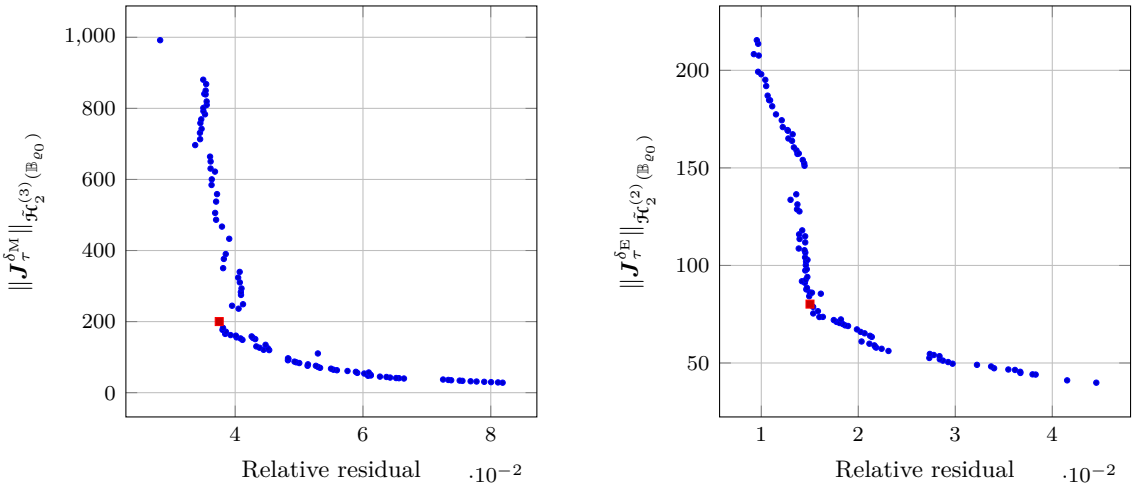

(a) MEG *(b) EEG*

FIGURE 21.16: *L-curve plot in the case of the MEG inversion (left) and the EEG inversion (right) for* $s = 2$ *and noise level* $\delta_\bullet = 0.05$ *using the RFMP with the chosen regularization parameter marked by a red square*

generalized cross validation yields a slightly smaller NRMSE. Note that the deviation in NRMSE between the optimal parameter and the chosen one is generally smaller than for the MEG problem.

Table 21.7 shows the results of the parameter choice methods for EEG in the case $s = 2$. In this scenario, the automatic/manual L-curve method as well as the MGCV yield small approximation errors, which are the closest to the optimal values within all noise levels. For $\delta_E = 0.05$ and $s = 2$, the corresponding reconstructions obtained via the ROFMP using the optimal NRMSE method and the MGCV are plotted in Fig. 21.18 and the reconstructions obtained via the LCM and the RM are plotted in Fig. 21.19. Note that the colour bar of the deviation plots changes its scale from one parameter choice method to another.

By means of each of the four parameter choice methods, the active regions can be visualized. The reconstruction is not too blurry and the round shape of the activity is reconstructed. However, especially for the LCM and the RM method, the amplitudes of the active regions cannot be reconstructed adequately, at least for the lower one. In addition, the active regions are not as well separated as for the other two methods.

The corresponding L-curve and its analogue for a magnetic flux inversion is plotted in Fig. 21.16. Especially for the MEG data, the inflexion point of the L-curve is clearly visible.

Based on the plots in Figs. 21.18 and 21.19 and the results in Tables 21.5 and 21.6, we conclude that how to find the best or even a good regularization parameter for the R(O)FMP combined with the inverse MEG and EEG problem depend on the noise level and is still an open question. Solving this problem would exceed the scope of this thesis and is left for future research.

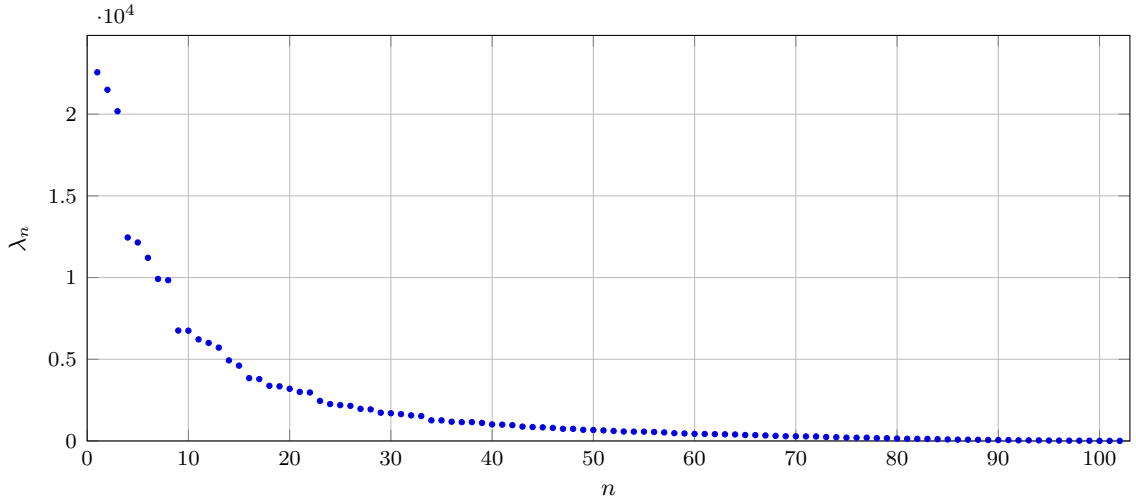

(a) All 102 singular values of the operator $\mathcal{A}_{\mathrm{M}}$

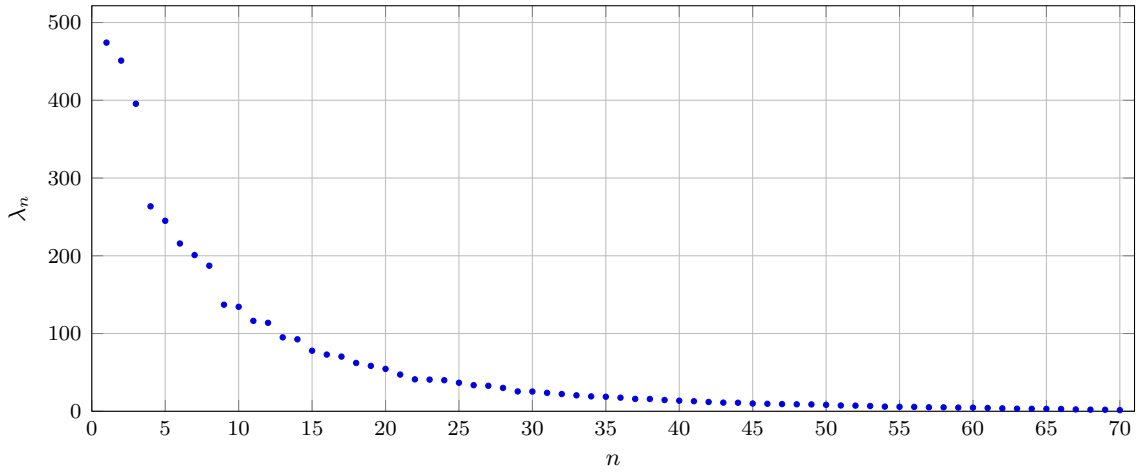

(b) All 70 singular values of the operator $\mathcal{A}_{\mathrm{E}}$

FIGURE 21.17: *Singular values of the operator $\mathcal{A}_\bullet$ restricted to a finite-dimensional subspace spanning the dictionary*

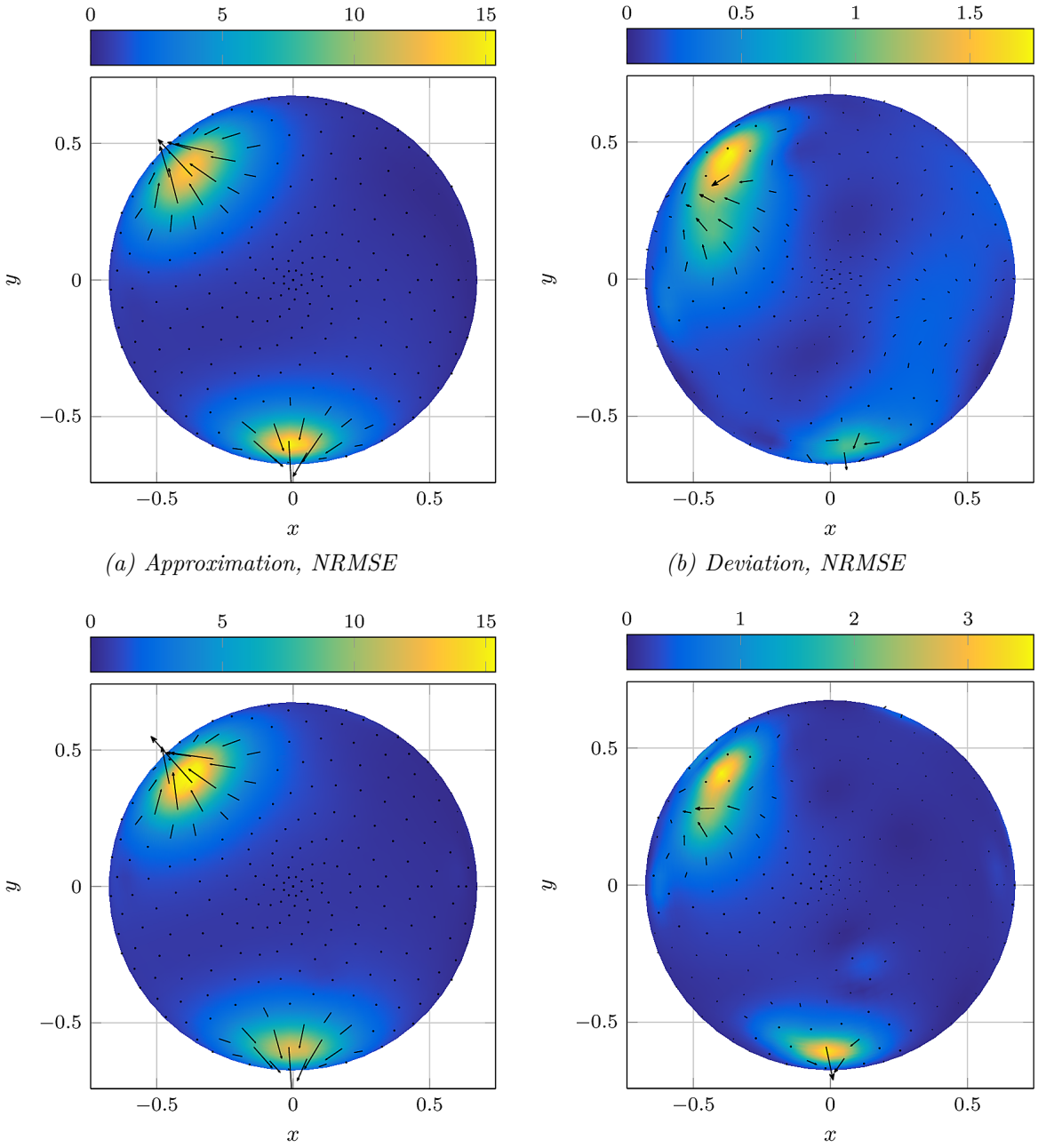

(a) Approximation, NRMSE

(b) Deviation, NRMSE

(c) Approximation, MGCV

(d) Deviation, MGCV

FIGURE 21.18: *Approximation* $\boldsymbol{J}_{\tau_*}^{\delta_{\mathrm{E}}}$ *of the neuronal current from electric potential data obtained by the ROFMP, where* τ_* *is chosen according to the respective parameter choice method, with parameter* $s = 2$ *and noise levels* $\delta_{\mathrm{E}} = 0.05$ *(left column) and its deviation from the exact solution (right column), see Fig. 18.2, plotted on an upper hemisphere with radius* $0.95\varrho_0$

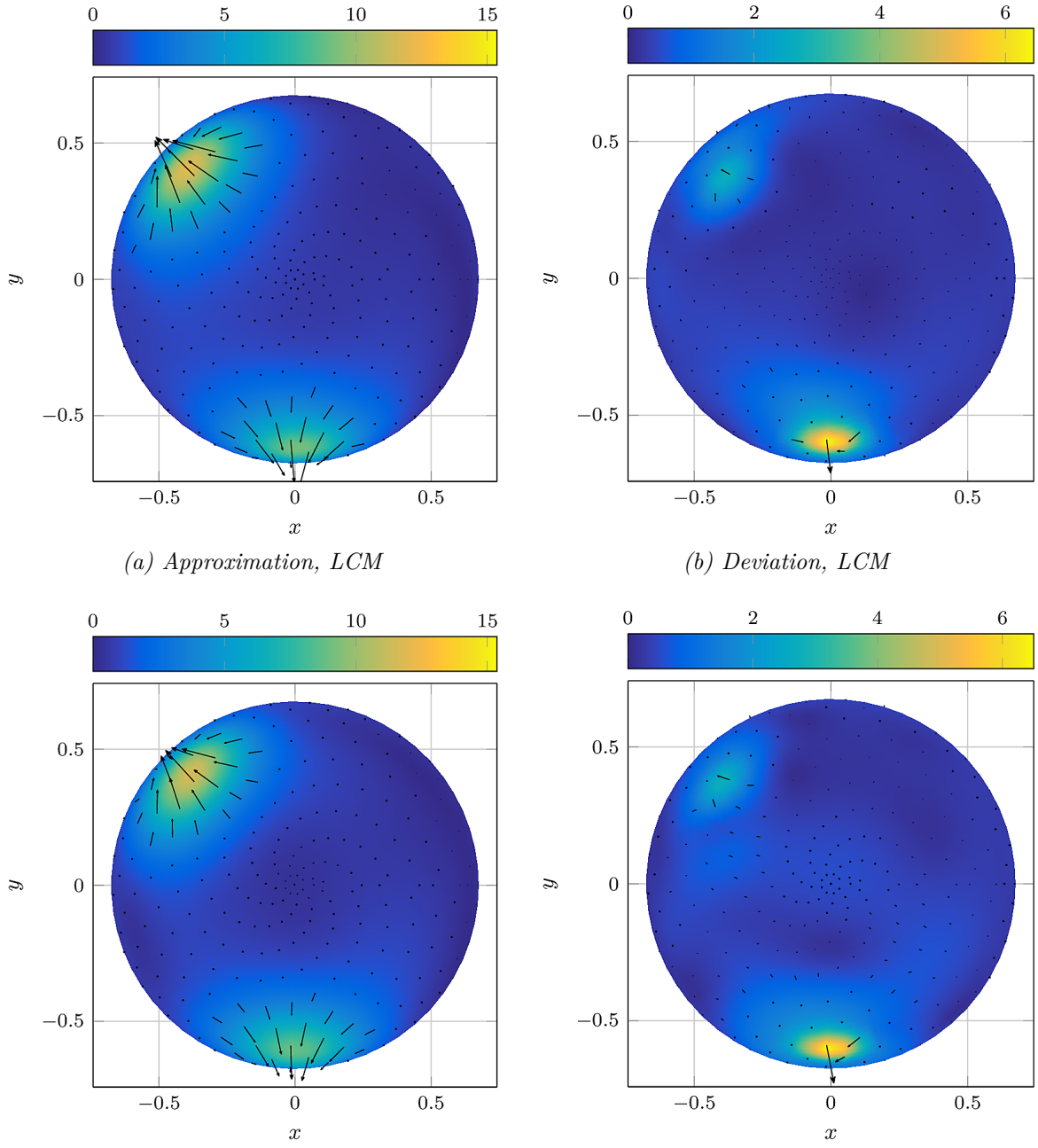

(a) Approximation, LCM

(b) Deviation, LCM

(c) Approximation, RM

(d) Deviation, RM

FIGURE 21.19: *Approximation* $\boldsymbol{J}_{\tau_*}^{\delta_{\mathrm{E}}}$ *of the neuronal current from electric potential data obtained by the ROFMP, where* τ_* *is chosen according to the respective parameter choice method, with parameter* $s = 2$ *and noise levels* $\delta_{\mathrm{E}} = 0.05$ *(left column) and its deviation from the exact solution (right column), see Fig. 18.2, plotted on an upper hemisphere with radius* $0.95\varrho_0$

21.2. Regularized Ritz Method

In Section 20.1, the regularized Ritz method is presented. Therein, we mentioned that the number of summands $N_\bullet$ in the finite Fourier series equals 100 in the MEG case as well as in the EEG case. Therewith, the matrix $\mathfrak{A}^\bullet$ defined in Eq. (20.2) is an $\ell_\bullet \times 10\,200$-matrix. Recall that $\ell_\mathrm{M} = 102$ and $\ell_\mathrm{E} = 70$. Besides using the classical Ritz method from Example 16.23 based on minimizing the classical Tikhonov-functional, we also used a variant where the Tikhonov-Philips functional is minimized instead. In this case, the regularization matrix $\mathfrak{B}_\bullet$ in Eq. (20.3) is chosen according to the $\tilde{\mathfrak{H}}_s^{(i)}$-regularization.

The system of linear equations in Eq. (20.3) is solved for each parameter $s \in \{0, 1, 2\}$ and each noise level $\delta_\bullet \in \{0, 0.01, 0.05, 0.1\}$ using 300 different regularization parameters. Then, the regularization parameter that yields the smallest NRMSE among all tested parameters is chosen. Eventually, the corresponding NRMSE and the relative residual are listed in Table 21.8 depending on the noise level and the chosen regularization sequence.

According to Table 21.8, we clearly see that the regularization with $s = 0$ yields the best results independent of the noise level for the MEG and the EEG problem. The NRMSEs for $s = 0$ are the lowest among all tested regularization norms. For all three regularization terms, the relative residual decreases with the noise level in the MEG case. In the EEG case, the relative residual is comparatively robust with respect to the noise level. Due to these observations, we fix $s = 0$ for the rest of this section.

The approximation and its deviation from the synthetic test current are plotted in Fig. 21.20 for the MEG and in Fig. 21.21 for the EEG problem. In the MEG case, the reconstruction obtained via the Ritz method is very blurry even for small noise levels. The round-shaped structure of the synthetic test current cannot be recovered. In particular, the reconstructed active regions shade into non-active regions if the noise level increases.

The same is observed in the EEG case, see Fig. 21.21. In this case, however, the fuzziness is not as strong as in the MEG case but the active regions are still not localized very well.

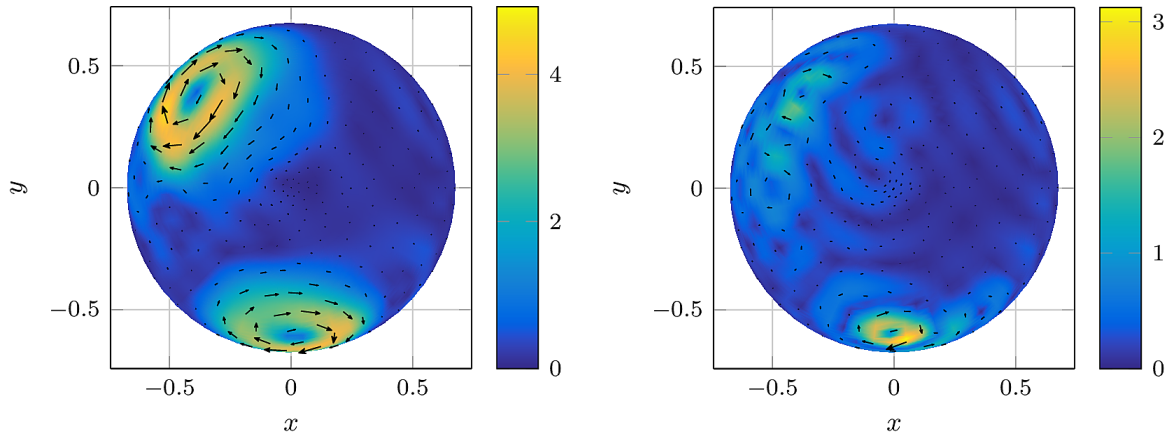

(a) *Approximation,* $\delta_{\mathrm{M}} = 0.01$

(b) *Deviation,* $\delta_{\mathrm{M}} = 0.01$

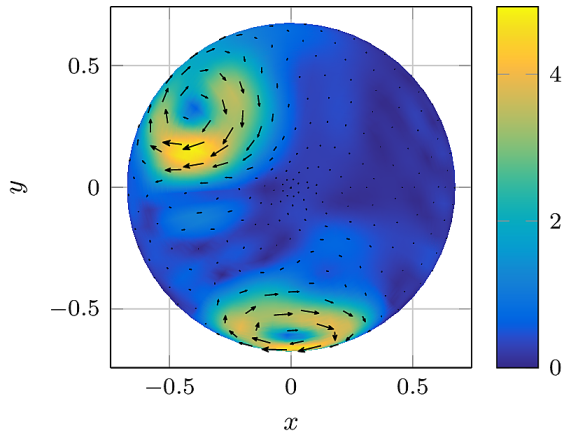

(c) *Approximation,* $\delta_{\mathrm{M}} = 0.05$

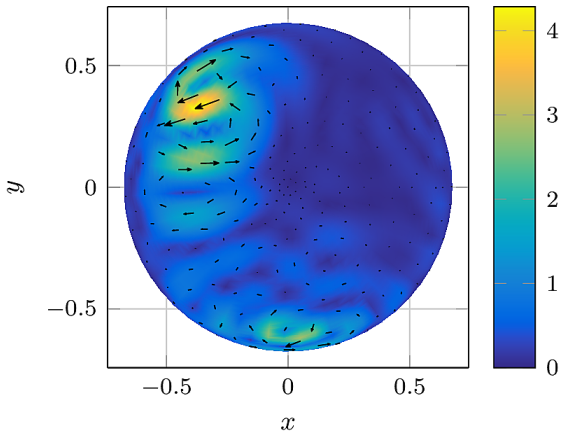

(d) *Deviation,* $\delta_{\mathrm{M}} = 0.05$

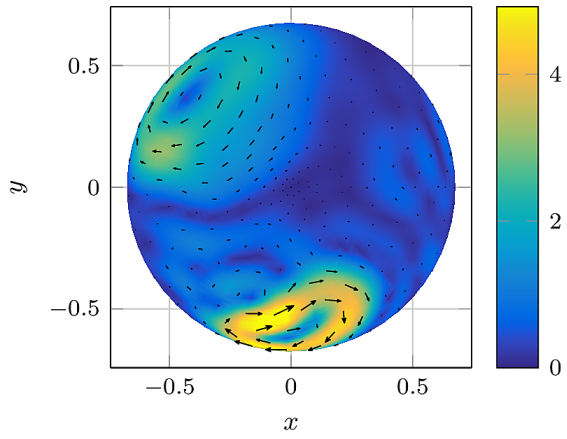

(e) *Approximation,* $\delta_{\mathrm{M}} = 0.1$

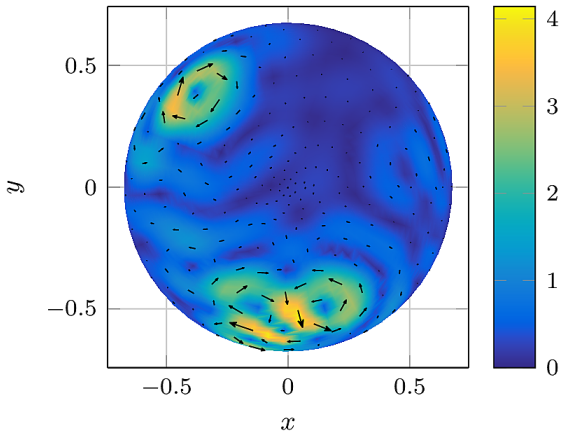

(f) *Deviation,* $\delta_{\mathrm{M}} = 0.1$

FIGURE 21.20: *Approximation* $\boldsymbol{J}^{\delta_{\mathrm{M}}}_{100,\tau_*}$ *of the neuronal current from magnetic flux data obtained by the regularized Ritz method with parameters* $s = 0$ *for different noise levels* δ_{M} *(left column) and its deviation from the exact solution (right column), see Fig. 18.2, plotted on an upper hemisphere with radius* $0.95\varrho_0$

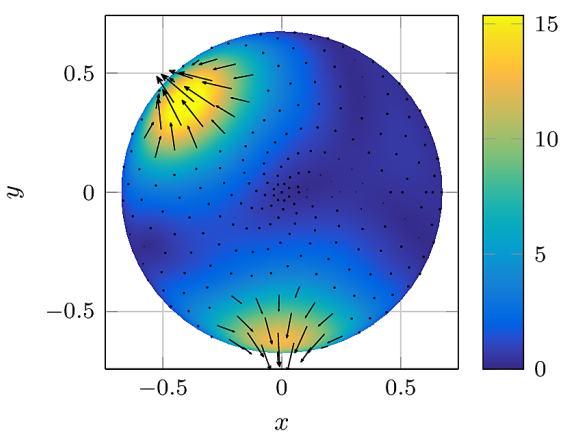

(a) *Approximation,* $\delta_{\mathrm{E}} = 0.01$

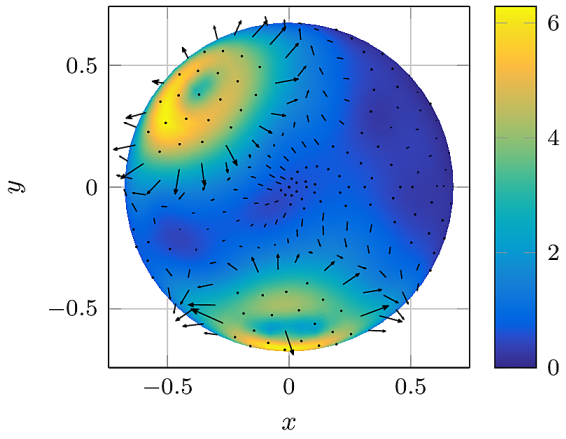

(b) *Deviation,* $\delta_{\mathrm{E}} = 0.01$

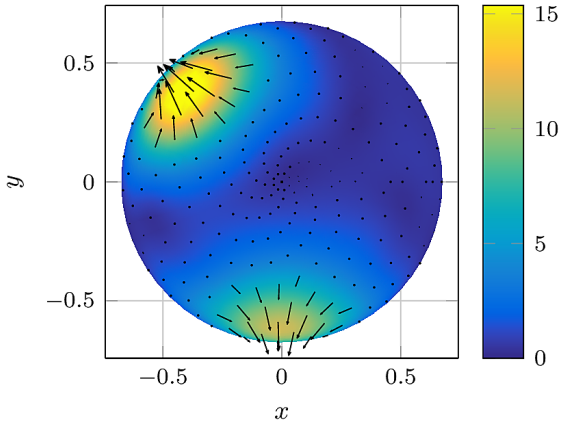

(c) *Approximation,* $\delta_{\mathrm{E}} = 0.05$

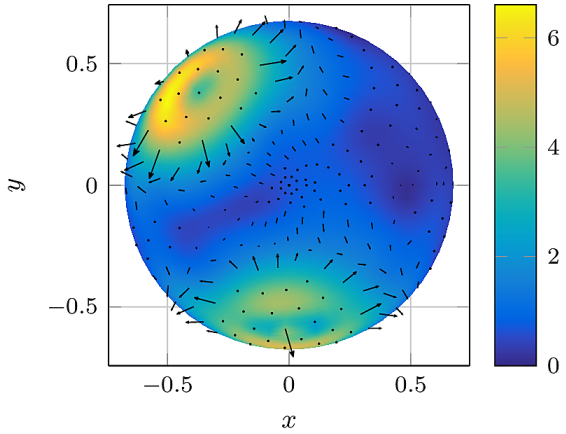

(d) *Deviation,* $\delta_{\mathrm{E}} = 0.05$

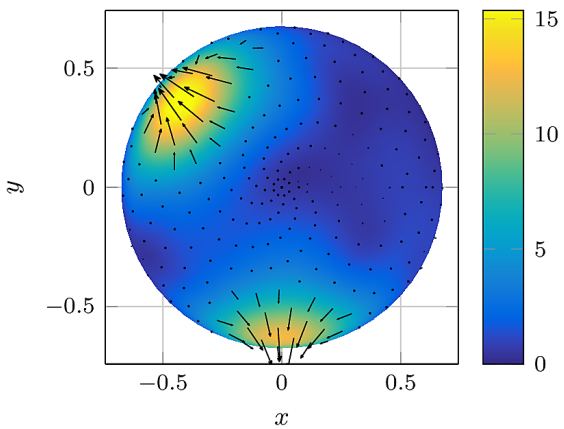

(e) *Approximation,* $\delta_{\mathrm{E}} = 0.1$

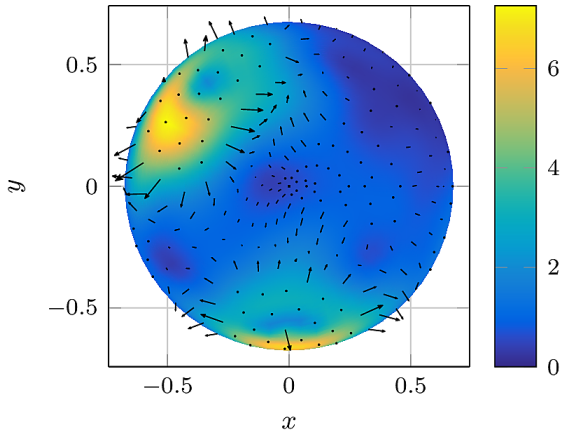

(f) *Deviation,* $\delta_{\mathrm{E}} = 0.1$

FIGURE 21.21: *Approximation* $\boldsymbol{J}^{\delta_{\mathrm{E}}}_{100,\tau_*}$ *of the neuronal current from electric potential data obtained by the regularized Ritz method with parameters* $s = 0$ *for different noise levels* δ_{E} *(left column) and its deviation from the exact solution (right column), see Fig. 18.2, plotted on an upper hemisphere with radius* $0.95\varrho_0$

		MEG		EEG	
$\delta_\bullet$	s	NRMSE	rel. residual	NRMSE	rel. residual
0.00	0	$5.7664 \cdot 10^{-2}$	$3.7803 \cdot 10^{-13}$	$9.2598 \cdot 10^{-2}$	$7.8985 \cdot 10^{-2}$
0.00	1	$6.8290 \cdot 10^{-2}$	$4.4447 \cdot 10^{-12}$	$1.2408 \cdot 10^{-1}$	$5.9080 \cdot 10^{-2}$
0.00	2	$1.1149 \cdot 10^{-1}$	$9.8826 \cdot 10^{-4}$	$1.5666 \cdot 10^{-1}$	$6.9919 \cdot 10^{-2}$
0.01	0	$7.9113 \cdot 10^{-2}$	$2.3378 \cdot 10^{-3}$	$9.3978 \cdot 10^{-2}$	$7.8122 \cdot 10^{-2}$
0.01	1	$9.0074 \cdot 10^{-2}$	$3.3097 \cdot 10^{-3}$	$1.2516 \cdot 10^{-1}$	$5.7168 \cdot 10^{-2}$
0.01	2	$1.1951 \cdot 10^{-1}$	$6.6637 \cdot 10^{-3}$	$1.5678 \cdot 10^{-1}$	$6.9657 \cdot 10^{-2}$
0.05	0	$1.1603 \cdot 10^{-1}$	$2.9661 \cdot 10^{-2}$	$8.9989 \cdot 10^{-2}$	$8.0846 \cdot 10^{-2}$
0.05	1	$1.2529 \cdot 10^{-1}$	$3.5705 \cdot 10^{-2}$	$1.1958 \cdot 10^{-1}$	$6.1897 \cdot 10^{-2}$
0.05	2	$1.5048 \cdot 10^{-1}$	$4.0998 \cdot 10^{-2}$	$1.5247 \cdot 10^{-1}$	$7.3621 \cdot 10^{-2}$
0.10	0	$1.1695 \cdot 10^{-1}$	$5.5270 \cdot 10^{-2}$	$9.9934 \cdot 10^{-2}$	$1.2196 \cdot 10^{-1}$
0.10	1	$1.2654 \cdot 10^{-1}$	$5.6537 \cdot 10^{-2}$	$1.4147 \cdot 10^{-1}$	$9.5631 \cdot 10^{-2}$
0.10	2	$1.4543 \cdot 10^{-1}$	$5.9161 \cdot 10^{-2}$	$1.7923 \cdot 10^{-1}$	$1.0279 \cdot 10^{-1}$

TABLE 21.8: *Relative residual and NRMSE of the approximation $\boldsymbol{J}^{\delta_\bullet}_{100,\tau_*}$ with the smallest NRMSE obtained by the regularized Ritz method depending on the noise level $\delta_\bullet$ and the chosen regularization sequence with parameter s*

21.3. Scalar Splines

21.3.1. Scalar Splines for MEG

We have already mentioned in Section 20.2 that in [73] a scalar spline method is used for the reconstruction of scalar-valued parts of the neuronal current. Therein, a good and stable approximation can be obtained by means of this numerical method.

However, in Section 20.2.2 we have also pointed out that the spline method used in [73] does not fit to our minimum norm assumption and, hence, we adapted the spline method to this setting. Using this adapted spline, we now reconstruct the scalar-valued part $A^{(1)}$ of the neuronal current in the case of the synthetic problem from Chapter 18 for different noise levels, that is $\delta_{\mathrm{M}} \in \{0, 0.01, 0.05, 0.1\}$.

The sequence occurring in the definition of the reproducing kernel, see Eq. (20.4), remains to be chosen. In our particular application, we choose

$$\kappa_n \coloneqq h^{-n^2/2}\sqrt{n}, \qquad n \in \mathbb{N},\ h = 0.99.$$

Among all tested sequences, this one yields the best results. In order to solve the interpolation problem from Eq. (20.6), a regularization is necessary since the corresponding scalar spline matrix is ill-conditioned with a condition number of $1.7748 \cdot 10^8$, see Theorem 20.1 for the regularized spline approximation. The matrix is visualized in Fig. 21.22.

For each noise level, we start the spline method for 1000 different regularization parameters $\tau \in [0, 10^{20}]$. Then, we choose the regularization parameter that results in the reconstruction with the smallest NRMSE. The results are presented in Table 21.9 and Fig. 21.24. Recall that the exact solution is depicted in Fig. 20.1. We conclude that a higher regularization of the problem is needed with decreasing noise level. Due to the regularization and the higher noise levels, the reconstructions become more damped.

A comparison of the scalar spline method with the regularized Ritz method and the ROFMP is given in Table 21.10. For this purpose, the corresponding vector-valued current

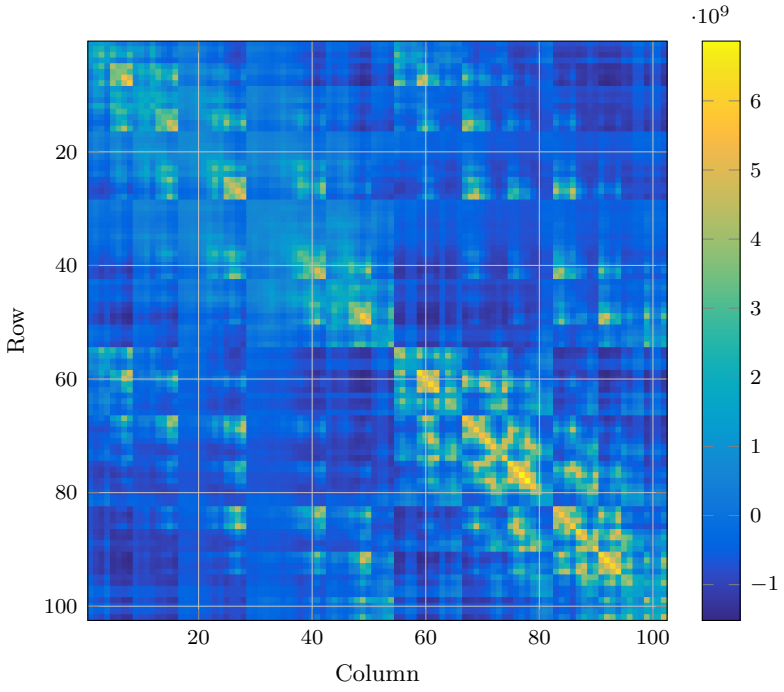

FIGURE 21.22: *Entries of the scalar spline matrix for the MEG problem*

δ_{M}	τ_*	scalar NRMSE	rel. residual	vector NRMSE
0.00	$3.8422 \cdot 10^{4}$	$2.2641 \cdot 10^{-2}$	$7.4822 \cdot 10^{-7}$	$1.2718 \cdot 10^{-1}$
0.01	$1.0448 \cdot 10^{13}$	$3.0243 \cdot 10^{-2}$	$3.4608 \cdot 10^{-3}$	$8.6959 \cdot 10^{-2}$
0.05	$8.8705 \cdot 10^{15}$	$4.0909 \cdot 10^{-2}$	$4.1975 \cdot 10^{-2}$	$1.0082 \cdot 10^{-1}$
0.10	$4.0608 \cdot 10^{16}$	$4.6126 \cdot 10^{-2}$	$8.1716 \cdot 10^{-2}$	$1.0919 \cdot 10^{-1}$

TABLE 21.9: *NRMSE for the scalar- as well as the corresponding vector-valued reconstruction and the relative residual corresponding to the approximation with the smallest NRMSE, that is* $\boldsymbol{J}_{\tau_*}^{\delta_{\mathrm{M}}}$*, for different noise levels* $\delta_{\mathrm{M}} \in \{0, 0.01, 0.05, 0.1\}$ *for the scalar synthetic MEG test case achieved via the spline method*

is calculated from the scalar part $A^{(1)}$ as described in Section 20.2.4. For the two presented scalar results in Figs. 21.23 and 21.24, the corresponding vector-valued approximation and its deviation from the vector-valued reference current is plotted in Figs. 21.25 and 21.26. These plots reveal the same result as Table 21.9: the NRMSE and the quality of the approximation are worsened by the translation from the scalar-valued solution to the vector-valued solution. One possible reason for this effect can be found in Eq. (20.14). Therein, the coefficients $c_{n,j}$ are related to the spline coefficients a_k by means of an additional damping factor $(\varrho_0/y_k)^n$ for all $n \in \mathbb{N}$, $j = 1, \ldots, 2n+1$, and $k = 1, \ldots, \ell$.

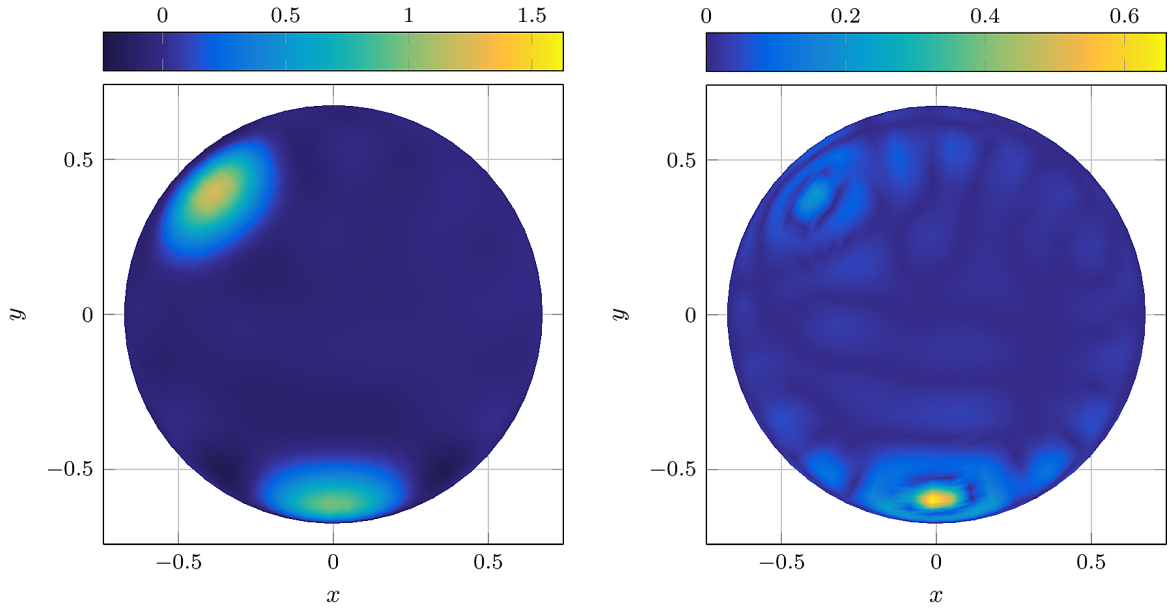

(a) Approximation, $\delta_{\mathrm{M}} = 0$

(b) Deviation, $\delta_{\mathrm{M}} = 0$

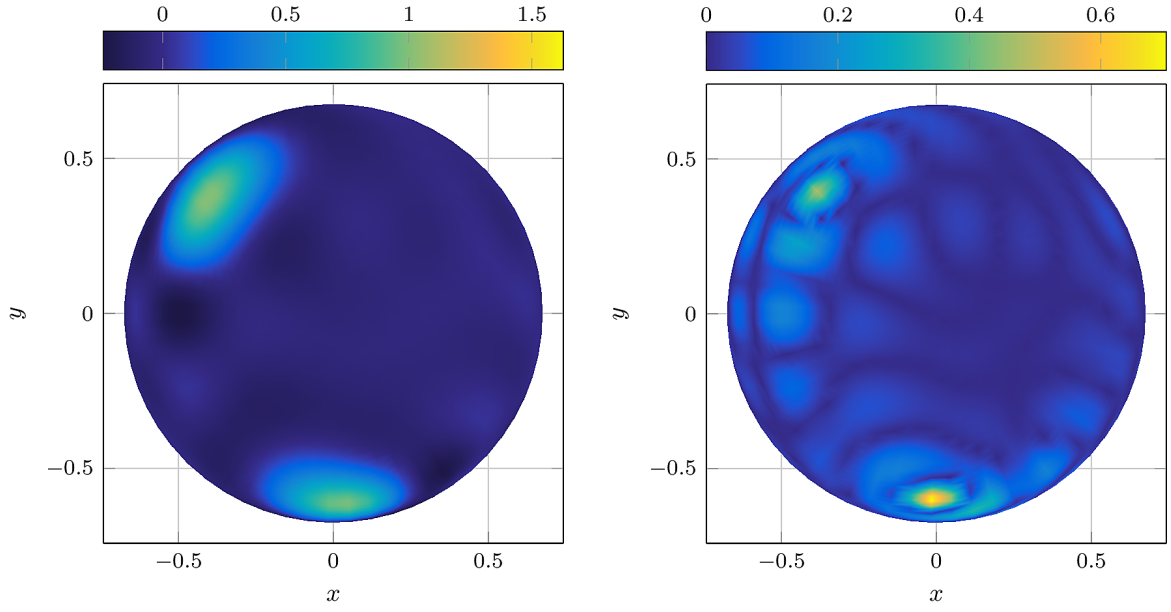

(c) Approximation, $\delta_{\mathrm{M}} = 0.01$

(d) Deviation, $\delta_{\mathrm{M}} = 0.01$

FIGURE 21.23: *Approximation of the part $A^{(1)}$ of the neuronal current (left column) and its deviation from the synthetic test solution (right column) depending on the noise level δ_{M} plotted on an upper hemisphere with radius $0.95\varrho_0$*

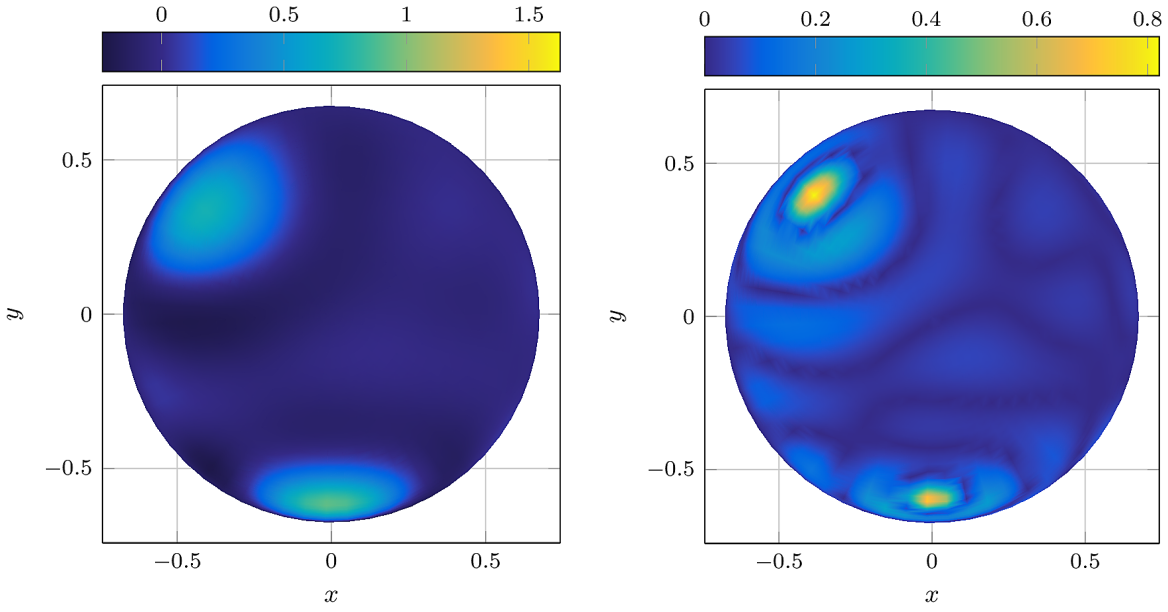

(a) *Approximation,* $\delta_{\mathrm{M}} = 0.05$

(b) *Deviation,* $\delta_{\mathrm{M}} = 0.05$

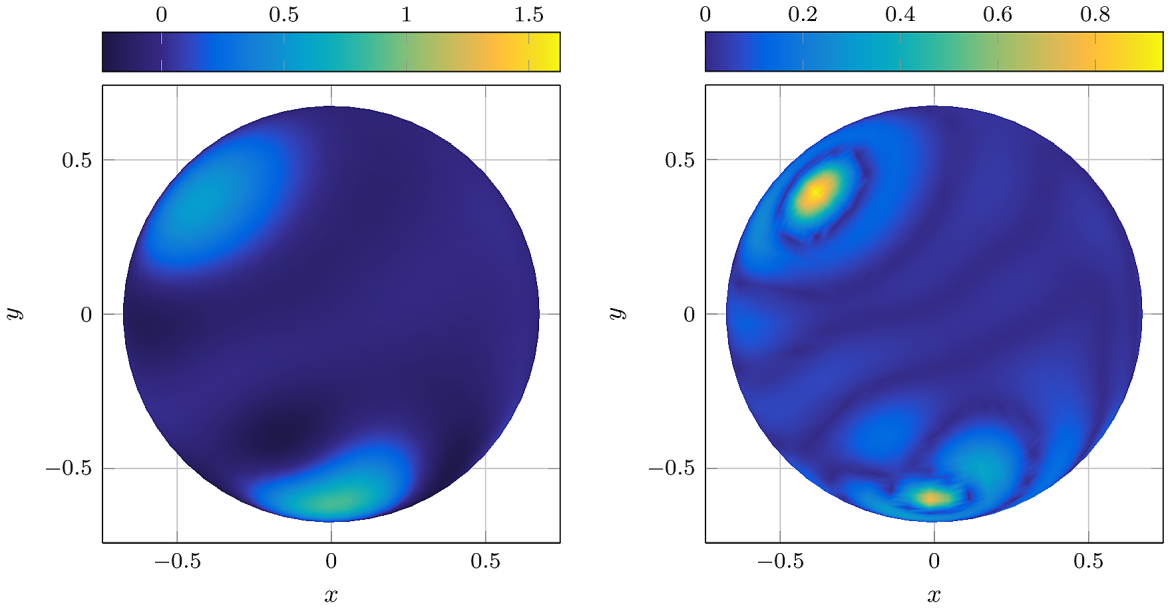

(c) *Approximation,* $\delta_{\mathrm{M}} = 0.1$

(d) *Deviation,* $\delta_{\mathrm{M}} = 0.1$

FIGURE 21.24: *Approximation of the part* $A^{(1)}$ *of the neuronal current (left column) and its deviation from the synthetic test solution (right column) depending on the noise level* δ_{M} *plotted on an upper hemisphere with radius* $0.95\varrho_0$

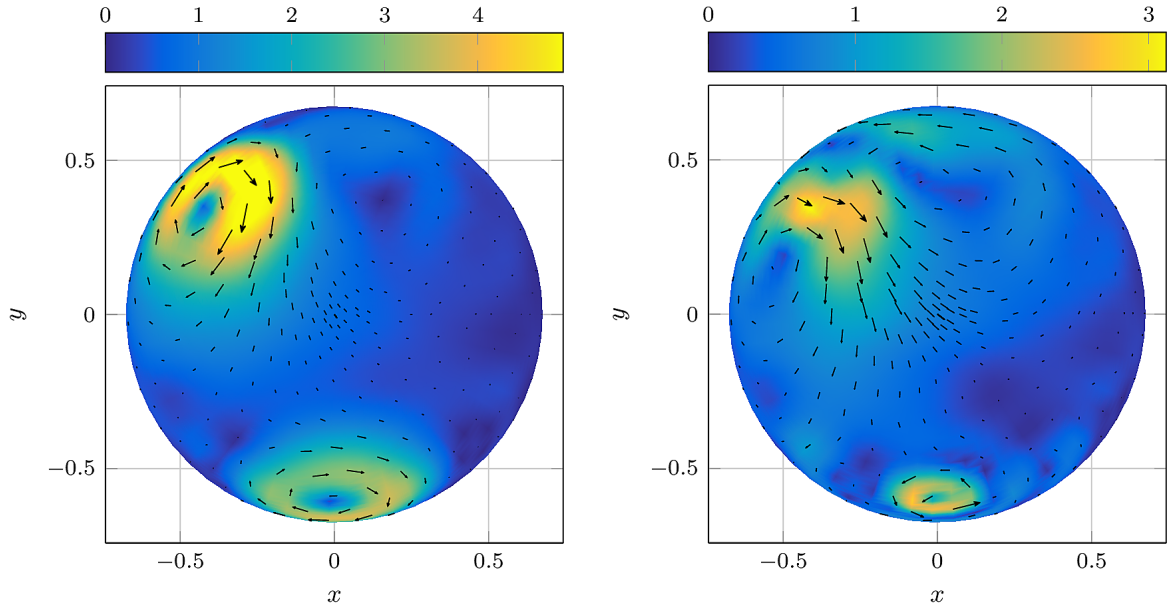

(a) *Approximation,* $\delta_{\mathrm{M}} = 0$

(b) *Deviation,* $\delta_{\mathrm{M}} = 0$

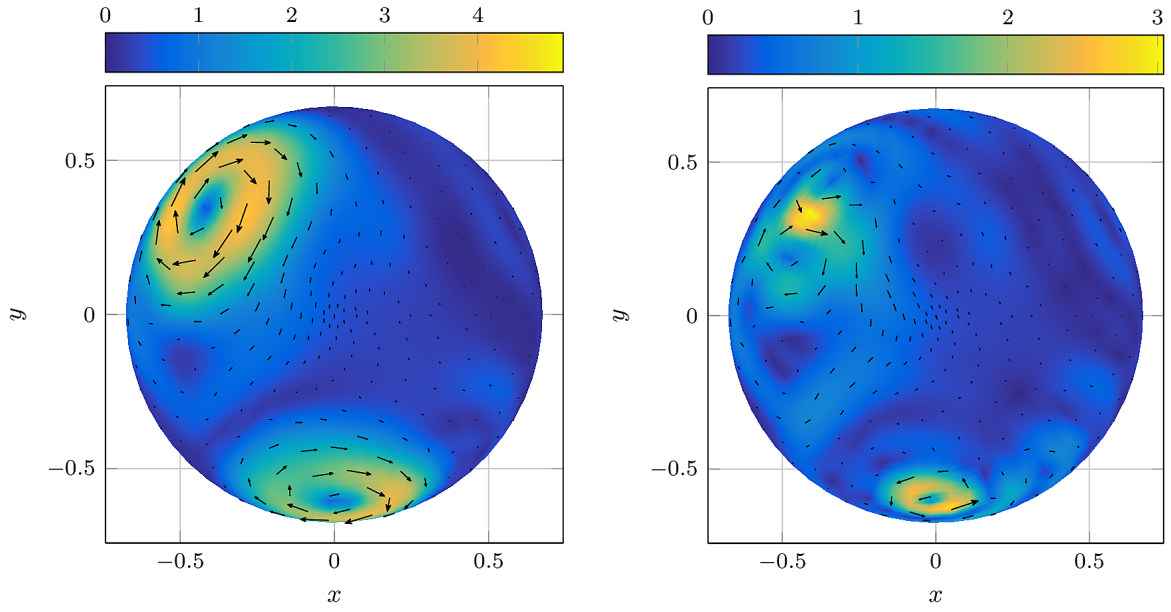

(c) *Approximation,* $\delta_{\mathrm{M}} = 0.01$

(d) *Deviation,* $\delta_{\mathrm{M}} = 0.01$

FIGURE 21.25: *Vector-valued approximation of the neuronal current achieved via approximating the scalar part* $A^{(1)}$ *(left column) and its deviation from the vectorial synthetic test current (right column) depending on the noise level* δ_{M} *plotted on an upper hemisphere with radius* $0.95\varrho_0$

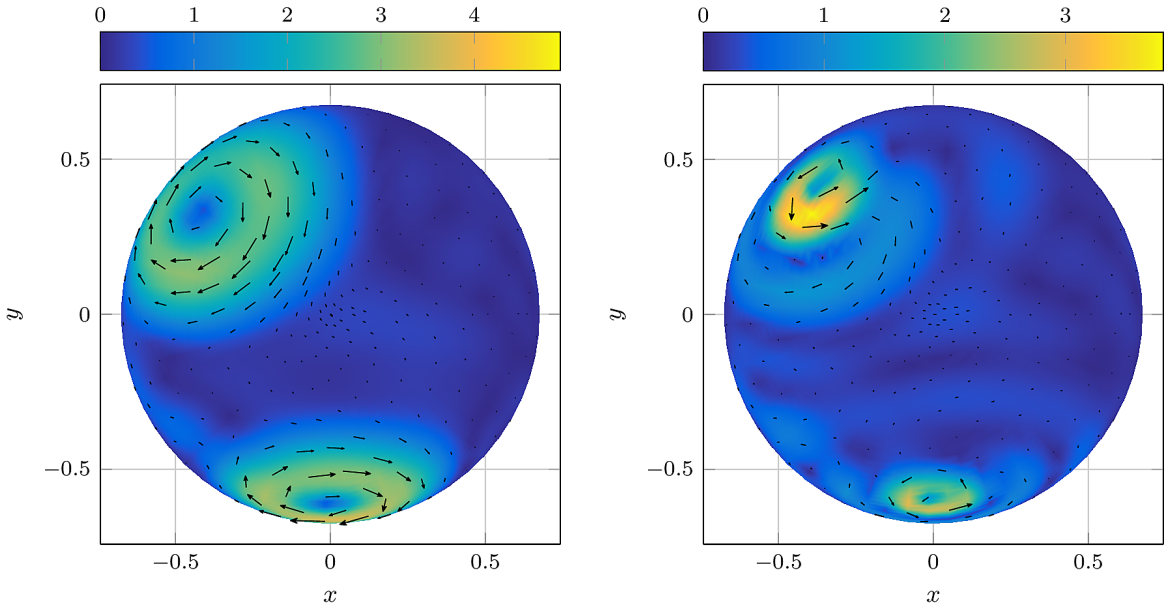

(a) *Approximation,* $\delta_{\mathrm{M}} = 0.05$

(b) *Deviation,* $\delta_{\mathrm{M}} = 0.05$

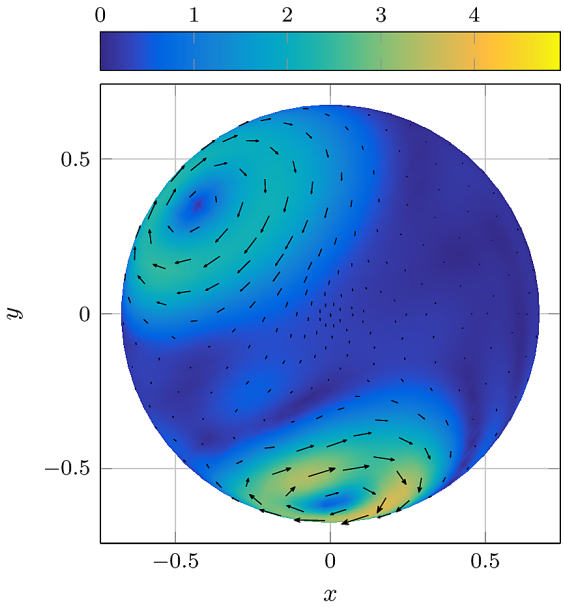

(c) *Approximation,* $\delta_{\mathrm{M}} = 0.1$

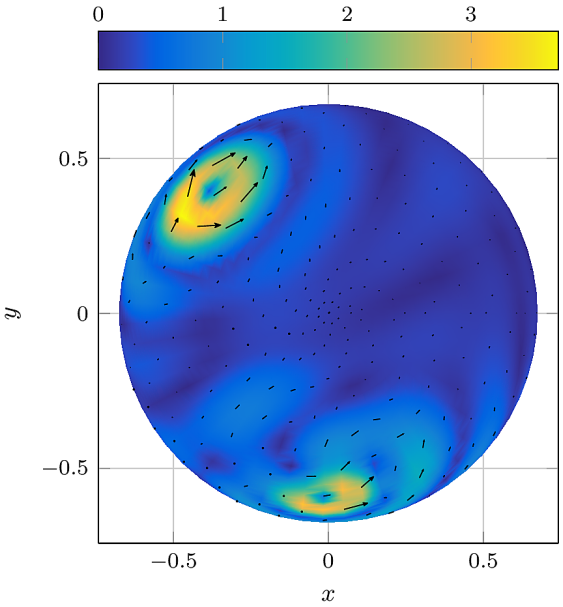

(d) *Deviation,* $\delta_{\mathrm{M}} = 0.1$

FIGURE 21.26: *Vector-valued approximation of the neuronal current achieved via approximating the scalar part* $A^{(1)}$ *(left column) and its deviation from the vectorial synthetic test current (right column) depending on the noise level* δ_{M} *plotted on an upper hemisphere with radius* $0.95\varrho_0$

21.3.2. Scalar Splines for EEG

We have already pointed out in Section 20.2.5 that the scalar spline approach is not appropriate for the inversion of the synthetic test case from Chapter 18. However, we found some errors in [73] that have a significant effect on some of their numerical results. Therefore, we present the corrected numerical results in this section.

For the implementation of all tested methods for the inversion of the EEG problem, the precise coefficients $\{\beta_n^{(L)}\}_{n\in\mathbb{N}}$ that, for example, appear in the forward operators from Theorem 19.1 are required. In Chapter 10, we discussed several methods for computing these coefficients. First, we derived for each $n \in \mathbb{N}$ a system of linear equations in Eq. (4.15). In the particular case of the three-shell model, which is used in our numerical computations, we also stated a corresponding tridiagonal matrix in Lemma 4.1 such that the inversion of this matrix reduces the computational costs. In addition, we stated a formula for the coefficients $\beta_n^{(L)}$ in Eq. (4.18), which can be achieved for each $n \in \mathbb{N}$ by recursion over the shells. For the latter method, no inversion is required. This is an advantage since the two mentioned matrices are ill-conditioned and the condition number increases as n increases. For example, the condition is about $1.4413 \cdot 10^{62}$ for $n = 200$.

The inversion of the matrix, the inversion of the tridiagonal matrix, and the recursive method all yield the same results. The maximal deviation among these methods up to degree $n = 500$ is $2.6645 \cdot 10^{-15}$, which means an agreement of about 12 digits. Note that the inversions are conducted with Matlab, see [212]. However, all three approaches have in common that the coefficients $\beta_n^{(L)}$ for $n \in \mathbb{N}$ need to be calculated for each degree n separately. Besides these approaches, we solved the system of linear equations from Eq. (4.15) symbolically via Mathematica, see [223]. The advantage of this method is that all required degrees can be calculated simultaneously, which accelerates the calculations. On the other hand, numerical tests showed that for higher degrees, that is $n \geq 220$, this symbolic method is highly unstable and yields not-a-number results. However, up to this degree this method yields the same results as the three previous described methods.

In addition, we implemented a fifth method for the calculation of these coefficients, namely the method described in [73]. This method is based on solving Eq. (4.15). Since the matrix is ill-conditioned, the authors regularize the system by adding a 'trial-and-error-value' of 10 % of the maximal absolute entry to the diagonal, see [73, p. 22]. Since by now, the methods described previously are available, the results obtained via the inversion of the regularized matrix seem unreliable. This is visualized in Fig. 21.27.

In Eq. (20.16), we have already stated a formula for the calculation of the spline matrix. Only the sequence $\{\kappa_n\}_{n\in\mathbb{N}}$ from the reproducing kernel remains to be determined. We choose

$$\kappa_n := h^{-n(n+1)/2}, \qquad h = 0.99,$$

which leads to convergent series in Eq. (20.16) as well as in the representation of the corresponding scalar spline function.

The spline matrix is visualized in Fig. 21.28 and its condition number is given by 133.3776. Thus, the inversion of this matrix is stable enough without additional regularization.

In addition, the spline approach is compared to a spherical harmonics ansatz in [73]. For this ansatz, the electric potential u_L is expanded into a finite Fourier series. In analogy to the regularized Ritz method, one achieves a system of linear equations with the potential data as the given right-hand side. This system is solved with an additional regularization.

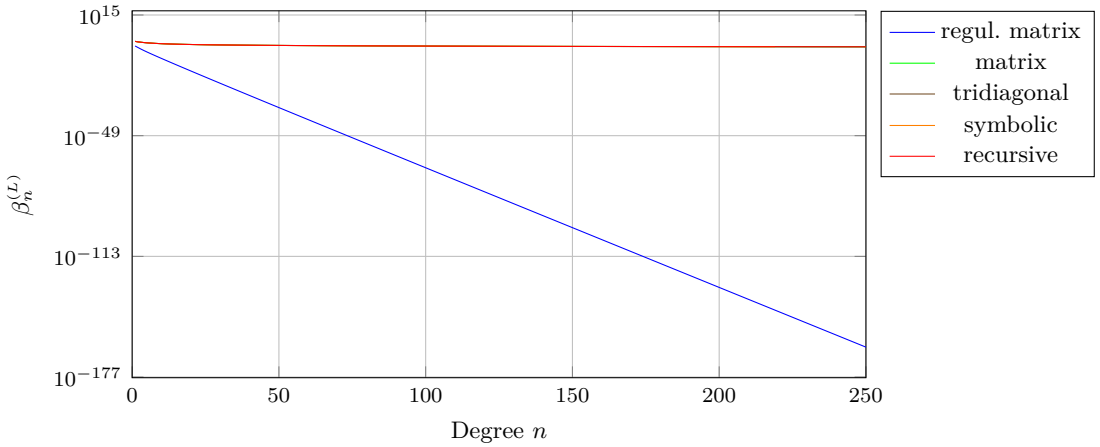

FIGURE 21.27: *The coefficients $\beta_n^{(3)}$ for the setting from Eq.* (19.2) *calculated with several methods depending on the degree $1 \leq n \leq 250$: via the inversion of the regularized matrix (blue), the unregularized matrix (green), and the tridiagonal matrix (brown), via a symbolic expression (orange), and via recursion (red)*

Afterwards, Eq. (15.34) is used in order to determine the coefficients of Ψ from the Helmholtz decomposition. In [73, Fig. 10], it is shown that this method does not provide us with a suitable result. To the opinion of the author, the reason for the failure of this method is the inaccurate calculation of the coefficients $\beta_n^{(L)}$. The results with the corrected coefficients as well as the scalar spline reconstruction are presented in Fig. 21.29. Therein, we used the synthetic test current presented in [73] and not the current constructed in Chapter 18, which is used in all other numerical tests.

Due to the adjustments of the presented methods, we are able to improve the results in [73] in the case of the scalar spline method, see Fig. 21.29. The root mean square error for the spline reduces from 0.009 573 8 to 0.000 395 6. In contrast, we were able to profoundly improve the spherical harmonics approach. In this case, the root mean square error reduces from 306.1623 to 0.003 970 8, which is about 6 orders of magnitude. However, the spline method still yields the better reconstruction, which can also be seen in Fig. 21.29.

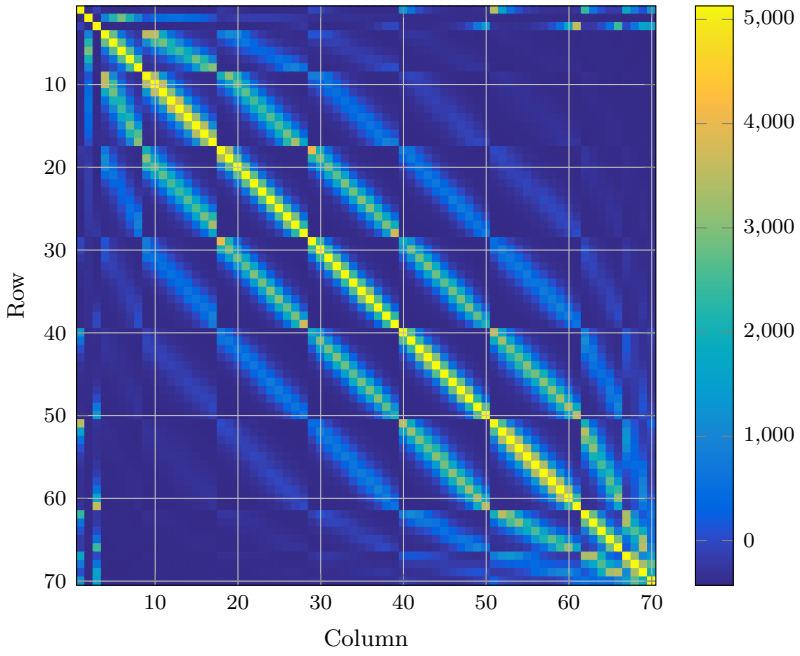

FIGURE 21.28: *Entries of the scalar spline matrix for the EEG problem*

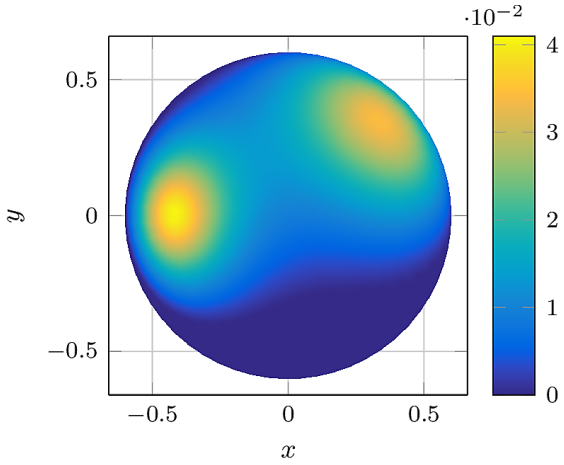

(a) *Scalar synthetic test current* Ψ

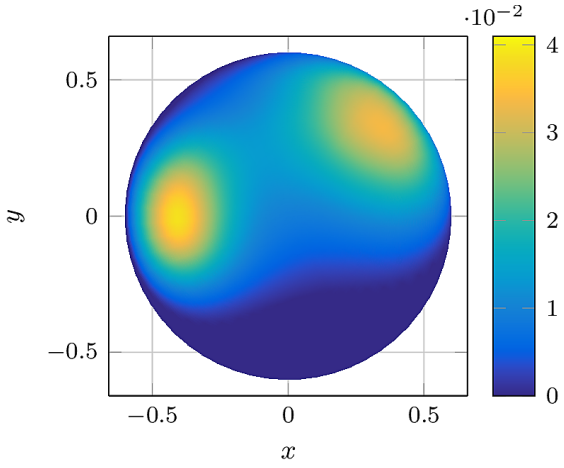

(b) *Approximation by scalar splines*

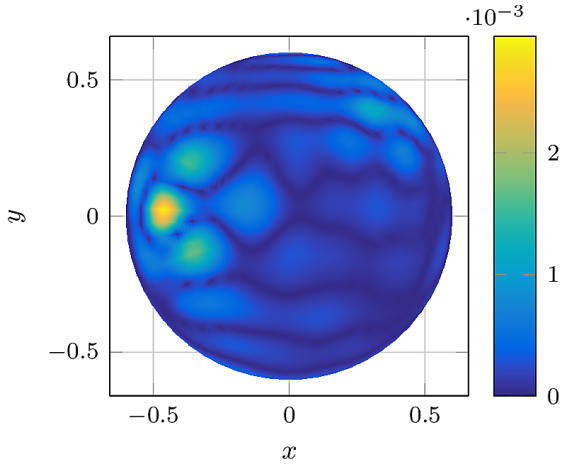

(c) *Deviation of the spline solution*

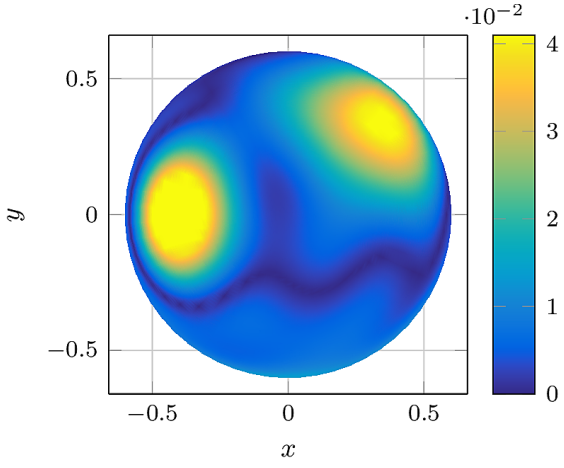

(d) *Approximation via spherical harmonics approach*

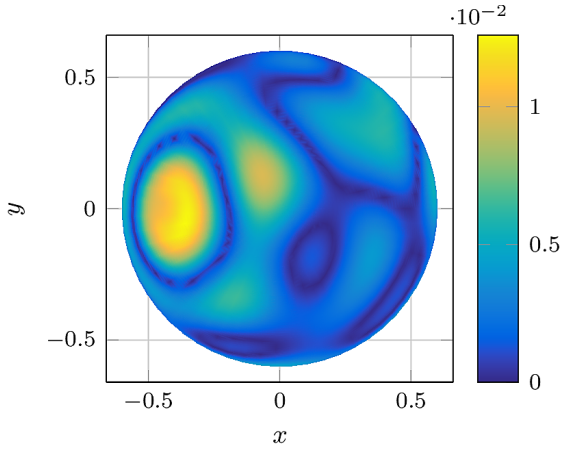

(e) *Deviation of the spherical harmonics result*

FIGURE 21.29: *Reconstructions of the scalar synthetic test function* Ψ *stated in [73, p. 23] (first row) via the scalar spline approach (second row) and a spherical harmonics ansatz (third row) from non-noisy data plotted on an upper hemisphere with radius* $0.8451\varrho_0$

21.4. Vector Splines for EEG

In Section 20.3, we introduce a vector spline method. Therein, we construct splines as vector-valued functions via tensor-product based reproducing kernels, see Eq. (20.18). In this section, we apply this method to the inverse electroencephalography problem. In contrast to the MEG case, we cannot employ a scalar spline method for the EEG problem using the Helmholtz decomposition since this would be incompatible with the minimum norm constraint. This fact has already been pointed out in Section 20.2, which motivated us to develop a vector-valued spline method. For comparison, we now apply this vector spline method to the EEG problem.

For this purpose, we set $i = 2$ and define the sequence of the reproducing kernel occurring in Eq. (20.17) as

$$\kappa_n^{(2)} := h^{-n/2} \qquad \text{for all } n \in \mathbb{N}$$

with $h = 0.9$.

Based on the calculation in Section 20.3, we calculate the EEG spline matrix. This matrix is visualized in Fig. 21.30. In this precise application with the parameters from Eq. (19.2), the condition number of the matrix is given by 1755.3073. Thus, the inversion of the matrix is stable such that additional regularization is not necessary.

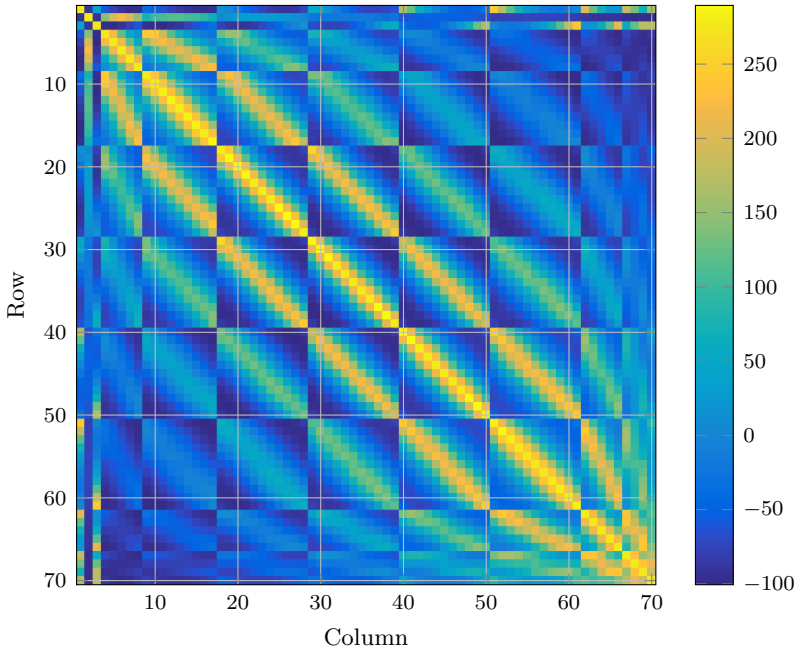

FIGURE 21.30: *Entries of the vector spline matrix for the EEG problem*

The reconstruction of the EEG synthetic test current by means of this vector-valued spline method is presented in Figs. 21.31 and 21.32 for several noise levels. Within these plots, we see that the quality of the reconstruction is relatively robust for noise levels up to $\delta_{\mathrm{E}} = 0.05$. The active regions are localized and their round-shaped structure is reconstructed. However, the amplitude of at least one activity cannot be recovered very well. This leads to high maximal deviations of the vector spline reconstruction from the exact solution. In addition,

the quality of the reconstruction is blurry for 10 % noise on the data. The fuzziness can be reduced by an additional regularization of the spline matrix inversion, as presented in Theorem 20.5. Numerical tests showed that the approximation error increases with additional smoothness of the reconstruction. Thus, we decided not to regularize in this particular case. The NRMSE of the approximations and the corresponding relative residual is listed in Table 21.11. Therein, we can also see that the approximation error is relatively constant up to the noise level of 5 %. Even though the NRMSE for 10 % noise on the data is nearly double as high as for the lower noise levels, the reconstruction is still acceptable. In addition, the relative residual of all reconstructions is very small. More precisely, it is in the range of $3 \cdot 10^{-14}$ to $8 \cdot 10^{-14}$.

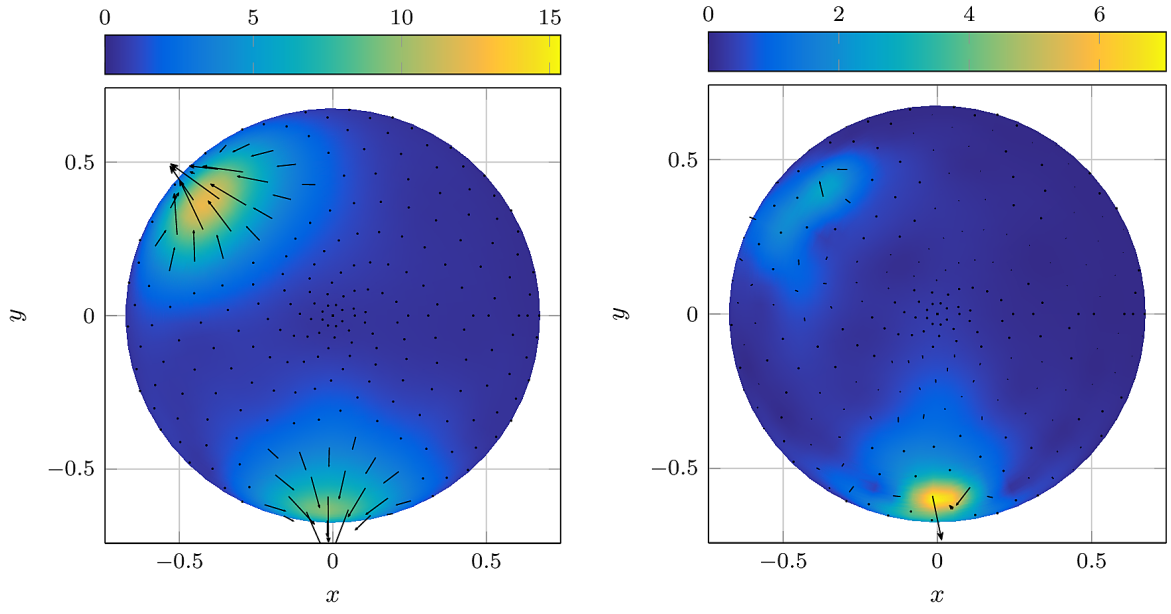

(a) *Approximation,* $\delta_{\mathrm{E}} = 0$

(b) *Deviation,* $\delta_{\mathrm{E}} = 0$

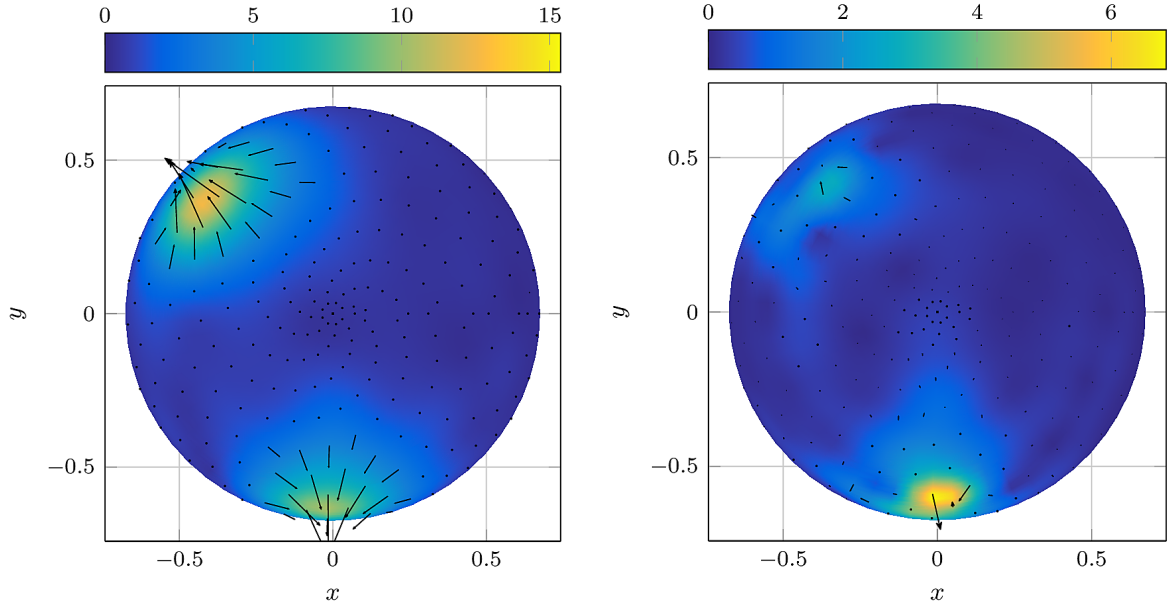

(c) *Approximation,* $\delta_{\mathrm{E}} = 0.01$

(d) *Deviation,* $\delta_{\mathrm{E}} = 0.01$

FIGURE 21.31: *Approximation* $\boldsymbol{J}_{\tau_*}^{\delta_{\mathrm{E}}}$ *of the neuronal current from electric potential data obtained by the unregularized vector spline method for different noise levels* δ_{E} *(left column) and its deviation from the exact solution (right column), see Fig. 18.2, plotted on an upper hemisphere with radius* $0.95\varrho_0$

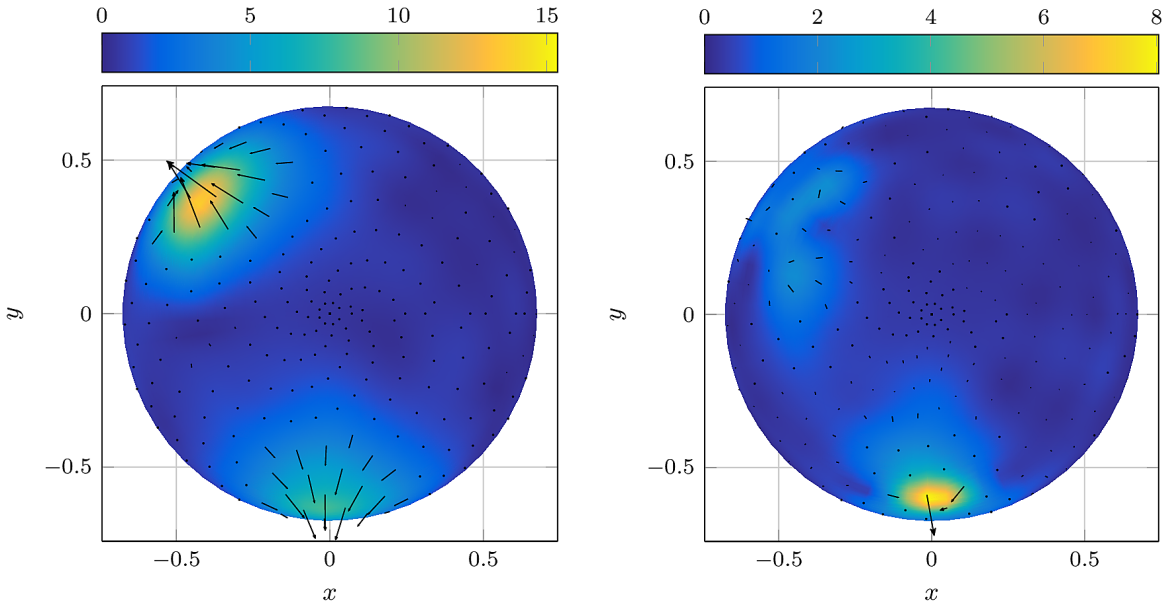

(a) *Approximation,* $\delta_{\mathrm{E}} = 0.05$

(b) *Deviation,* $\delta_{\mathrm{E}} = 0.05$

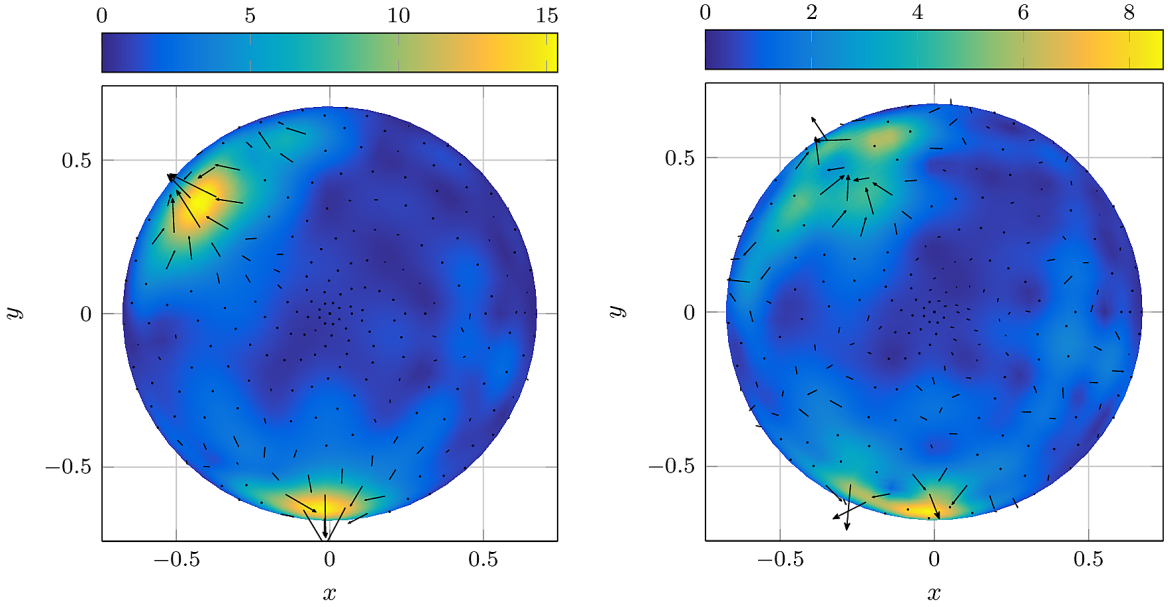

(c) *Approximation,* $\delta_{\mathrm{E}} = 0.1$

(d) *Deviation,* $\delta_{\mathrm{E}} = 0.1$

FIGURE 21.32: *Approximation* $\boldsymbol{J}_{\tau_*}^{\delta_{\mathrm{E}}}$ *of the neuronal current from electric potential data obtained by the unregularized vector spline method for different noise levels* δ_{E} *(left column) and its deviation from the exact solution (right column), see Fig. 18.2, plotted on an upper hemisphere with radius* $0.95\varrho_0$

21.5. Comparison of the Numerical Methods

After solving the inverse MEG and EEG problem with each of the three different reconstruction methods, that is the R(O)FMP, the regularized Ritz method, and the scalar or vector spline method, we now compare the results. The numerical results of each method are separately discussed in detail in the foregoing sections. If several parameters are tested for a particular regularization method, we now choose the parameter setting that yields the best results concerning the NRMSE. The particular parameters can be found in the corresponding captions of Tables 21.10 and 21.11.

First, we consider the MEG problem. A comparison of the NRMSEs and the relative residuals among the results achieved via the ROFMP, the regularized Ritz method, and the scalar spline method is given in Table 21.10. The corresponding regularization parameters are listed in Table 21.1 for the ROFMP method and in Table 21.9 for the spline method. The comparison of the three reconstruction methods reveals that the ROFMP yields the smallest NRMSE in the synthetic MEG test case for all noise levels. The Ritz method yields comparable results to the scalar spline method with respect to the NRMSE but with higher relative residuals. Thus, in the spline method we gain accuracy in the data space at the cost of accuracy in the domain when compared to the ROFMP result. However, the approximation quality of the ROFMP cannot be reached by either of these two methods.

	ROFMP		Spline		Ritz	
δ_{M}	NRMSE	rel. residual	NRMSE	rel. residual	NRMSE	rel. residual
0.00	$6.4770 \cdot 10^{-3}$	$3.5960 \cdot 10^{-3}$	$1.2718 \cdot 10^{-1}$	$7.4822 \cdot 10^{-7}$	$9.2598 \cdot 10^{-2}$	$7.8985 \cdot 10^{-2}$
0.01	$1.0797 \cdot 10^{-2}$	$1.2831 \cdot 10^{-2}$	$8.6959 \cdot 10^{-2}$	$3.4608 \cdot 10^{-3}$	$9.3978 \cdot 10^{-2}$	$7.8122 \cdot 10^{-2}$
0.05	$4.6956 \cdot 10^{-2}$	$3.7493 \cdot 10^{-2}$	$1.0082 \cdot 10^{-1}$	$4.1975 \cdot 10^{-2}$	$8.9989 \cdot 10^{-2}$	$8.0846 \cdot 10^{-2}$
0.10	$6.0430 \cdot 10^{-2}$	$7.6376 \cdot 10^{-2}$	$1.0919 \cdot 10^{-1}$	$8.1716 \cdot 10^{-2}$	$9.9934 \cdot 10^{-2}$	$1.2196 \cdot 10^{-1}$

TABLE 21.10: *NRMSE and relative residual for different noise levels* $\delta_{\mathrm{M}} \in \{0, 0.01, 0.05, 0.1\}$ *achieved by the ROFMP* ($s = 2$)*, the regularized scalar spline method, and the regularized Ritz method* ($s = 0$) *for the synthetic MEG test case*

For the inverse EEG problem, a comparison of the ROFMP, the regularized Ritz method, and the vectorial spline method is given in Table 21.11. The table reveals that the NRMSE achieved by the ROFMP has at least one order of magnitude less than the NRMSE obtained by the other two methods if the noise level is small, that is $\delta_{\mathrm{E}} \leq 0.01$. While this discrepancy reduces for higher noise levels, the NRMSE achieved by the ROFMP is still smaller than for the other methods. For small noise levels, the vector spline method and the Ritz method yield comparable results. In contrast, for higher noise levels, the vector spline method is better than the Ritz method with respect to the NRMSE. In addition, the spline method yields the smallest relative residuals among all tested methods.

Now, we conclude the results of Tables 21.10 and 21.11. The ROFMP yields the best results among all tested methods for both problems. This accuracy in the reconstruction is at the expense of computation time. In the case of the vector spline method, the time required for assembling the spline matrix is (10.5175 ± 0.2399) s. However, the spline matrix corresponding to one problem only needs to be calculated once. Afterwards, only the inversion of the (regularized) matrix is necessary. The CPU time required for the inversion is $(90.0000 \pm 3.8299) \cdot 10^{-4}$ s tested among 10 000 inversions. With a CPU time of (10.5175 ± 0.2399) s for the inversion of the EEG data throughout our numerical experiments,

the regularized Ritz method is slower than the vector spline method but still fast when compared to the ROFMP. Note that the CPU time required for inversion of the MEG data is at least as high as for the EEG, since more data is available. The computational time required for the R(O)FMP is plotted in Fig. 21.15 and is at least five times as high as the previously mentioned timings, but usually more than tenfold. That does not include the time required for the preprocessing of the dictionary, see Section 19.2, which is around 6000 s (wall clock time) for both problems using a parallelized and vectorized code on 12 CPU cores.

	ROFMP		Spline		Ritz	
δ_{E}	NRMSE	rel. residual	NRMSE	rel. residual	NRMSE	rel. residual
0.00	$3.4866 \cdot 10^{-3}$	$1.5125 \cdot 10^{-3}$	$4.1598 \cdot 10^{-2}$	$3.4573 \cdot 10^{-14}$	$5.7664 \cdot 10^{-2}$	$3.7803 \cdot 10^{-13}$
0.01	$6.4613 \cdot 10^{-3}$	$9.0329 \cdot 10^{-3}$	$4.2126 \cdot 10^{-2}$	$3.7071 \cdot 10^{-14}$	$7.9113 \cdot 10^{-2}$	$2.3378 \cdot 10^{-3}$
0.05	$1.5962 \cdot 10^{-2}$	$1.7879 \cdot 10^{-2}$	$4.6886 \cdot 10^{-2}$	$3.5985 \cdot 10^{-14}$	$1.1603 \cdot 10^{-1}$	$2.9661 \cdot 10^{-2}$
0.10	$4.6999 \cdot 10^{-2}$	$3.8657 \cdot 10^{-2}$	$8.6227 \cdot 10^{-2}$	$8.3282 \cdot 10^{-14}$	$1.1695 \cdot 10^{-1}$	$5.5270 \cdot 10^{-2}$

TABLE 21.11: *NRMSE and relative residual for different noise levels* $\delta_{\mathrm{E}} \in \{0, 0.01, 0.05, 0.1\}$ *achieved by the ROFMP* ($s = 1$)*, the vectorial spline method, and the Ritz method* ($s = 0$) *for the synthetic EEG test case*

A visualization of the comparison can also be found in Fig. 21.33 for the MEG problem. Comparing the reconstruction of the Ritz method to the ROFMP reconstruction, the active regions produced by the Ritz method are not localized anymore, which is outperformed by the results obtained with the ROFMP, see Figs. 21.4, 21.5, and 21.20. In addition, the maximal deviation of the ROFMP solution from the exact solution is only 16.8 % as high as the deviation of the spline reconstruction, see Figs. 21.2, 21.3, and 21.26. Concluding, we clearly see that structure, localization, and order of magnitude of the approximation obtained by the ROFMP are closest to the synthetic test current from Fig. 18.2 among all tested methods.

For the EEG problem, the results are shown in Fig. 21.34. In comparison to the results obtained by the ROFMP from Fig. 21.7, we observe that the amplitudes of the reconstruction via the spline method are slightly smaller than the one of the ROFMP. Particularly, for small noise levels, the maximal deviation from the exact solution is up to 6.39 times higher than with the ROFMP reconstruction, see Figs. 21.7 and 21.21. In the case of the vector spline method, we see that the amplitudes of the spline reconstruction are smaller than the one of the ROFMP and the active regions are more spread out. In addition, the maximal deviation of the vector spline method for the EEG case is up to 6.93 times higher than with the ROFMP in the case of $\delta_{\mathrm{E}} = 0.01$, see Figs. 21.7 and 21.31. This can also be seen in the NRMSE in Table 21.11. This table additionally reveals that the relative residual of the spline method is substantially smaller than the one of the ROFMP. In contrast to the spline solution, which is still localized to some extent, the Ritz method yields an even less localized reconstruction. The active regions are much larger than the exact solution and their amplitudes do not match either. Concluding, the ROFMP again provides the best reconstruction in terms of structure, localization, and order of magnitude among all tested methods.

Naturally, the question arises whether some methods yield better reconstructions than others. For the regularized Ritz method, the Tikhonov-regularized normal equation is solved over a finite-dimensional subspace. In this thesis, we use a subset of the orthonormal basis system for spanning this subspace, which means that the solution vector contains the

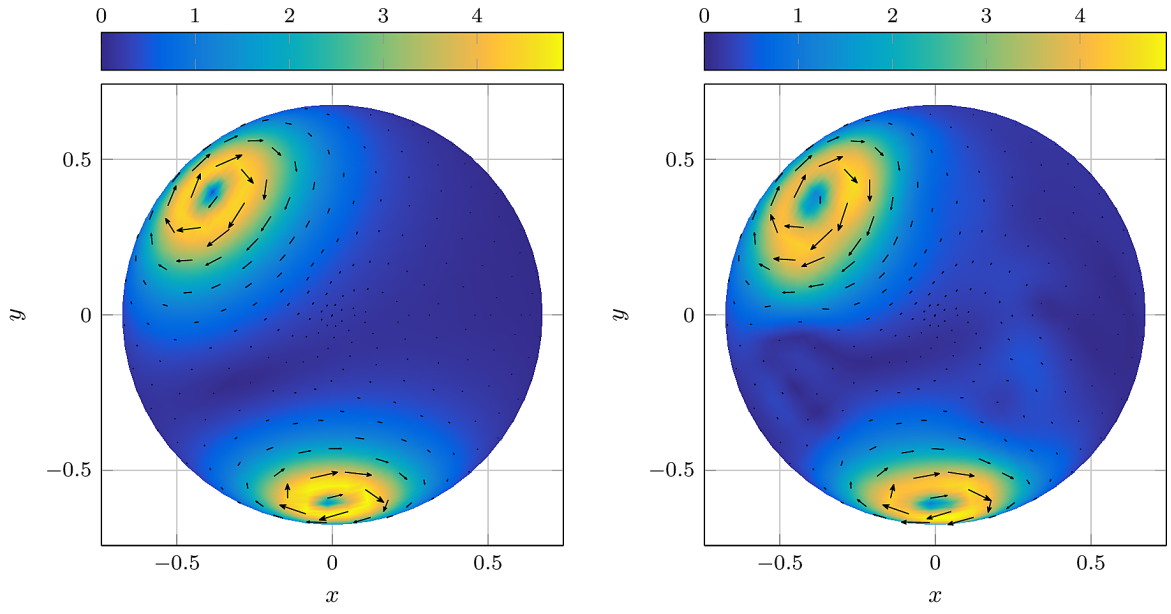

(a) Exact solution

(b) ROFMP

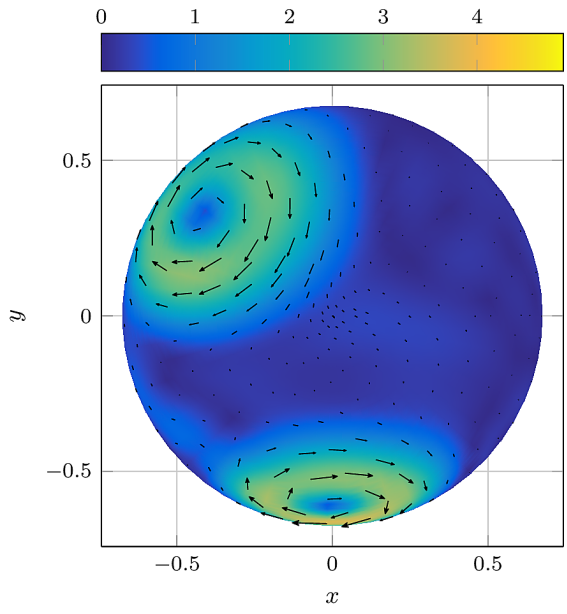

(c) Scalar spline

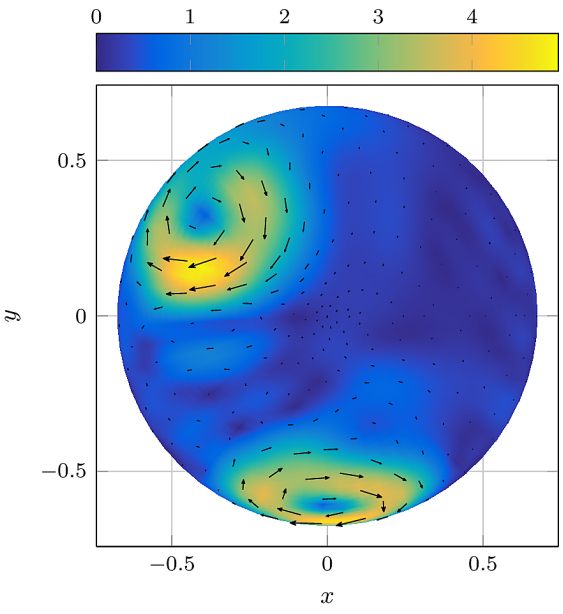

(d) Ritz method

FIGURE 21.33: *Approximation of the neuronal current from magnetic flux data with 5 % noise obtained by the ROFMP ($s = 2$), the scalar spline method, and the regularized Ritz method ($s = 0$) in comparison to the exact test current plotted on an upper hemisphere with radius* $0.95\varrho_0$

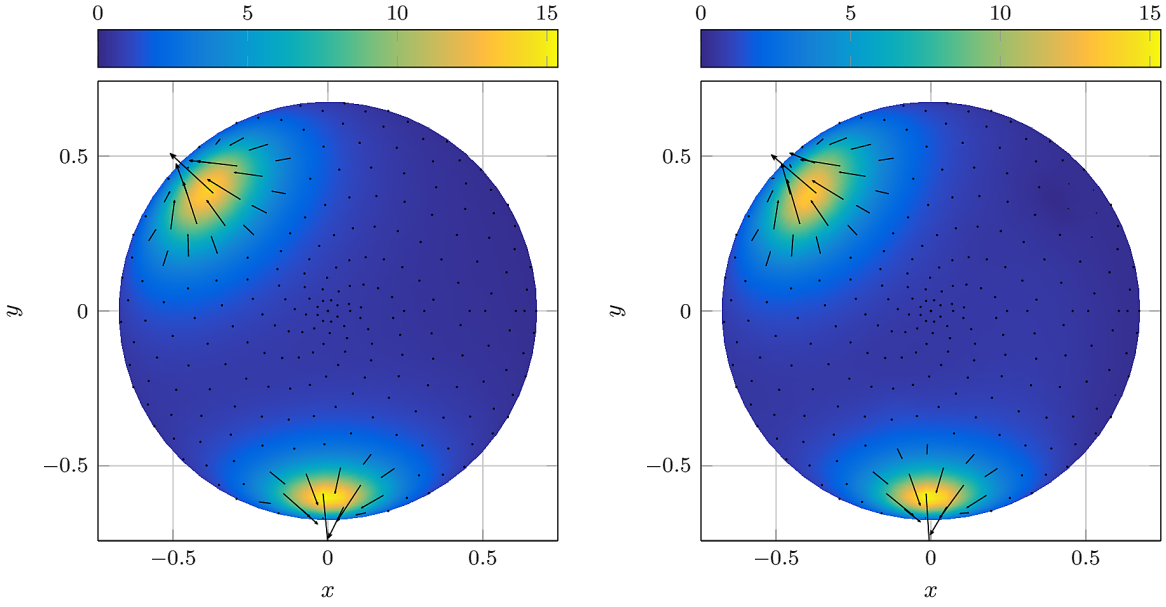

(a) Exact solution

(b) ROFMP

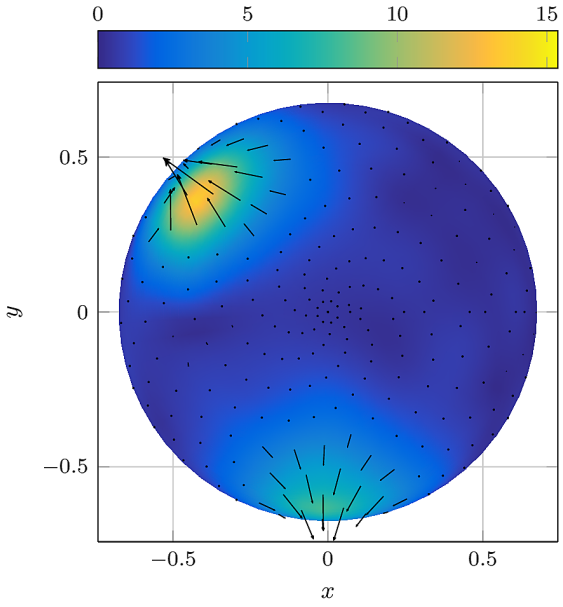

(c) Vector spline

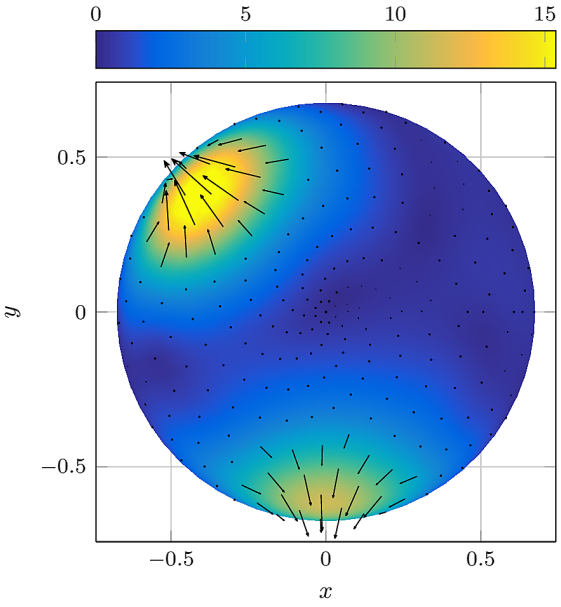

(d) Ritz method

FIGURE 21.34: *Approximation of the neuronal current from electric potential data with 5 % noise obtained by the ROFMP ($s = 1$), the vector spline method, and the regularized Ritz method ($s = 0$) in comparison to the exact test current plotted on an upper hemisphere with radius* $0.95\varrho_0$

orthonormal basis coefficients of the approximation. Thus, local effects, such as certain outliers in the data or locally higher noise levels, have a global impact on the reconstruction. This leads to a general blurriness in the reconstructions for higher noise levels even in the regions where no activity is presumed. In addition, such 'global' methods often experience difficulties with irregularly distributed data grids, which are also found in our application. This behaviour is typical for approximation methods based on orthonormal basis functions, see also the discussion in [158, Sec. 5.3].

The spline based methods are interpolation methods that satisfy a best-approximation property. In the regularized case, which is used for the MEG scalar spline method, the solution of this approach is the unique solution of the Tikhonov-regularized normal equation in a certain Sobolev space, see Theorem 20.1. The results of the scalar reconstruction in Fig. 21.23 and Section 20.2.2 suggest that this Sobolev space is chosen appropriately. However, via the transformation to the vector-valued case, structure and quality of the approximation get lost, see Fig. 21.25, which has already been discussed earlier. Thus, the lack of quality of the vector-valued reconstruction presumably originates from the Helmholtz decomposition approach. For this purpose, a direct reconstruction of the vector-valued current should be preferred. This can also be seen in the vector spline method used for the EEG. This spline method, which is stated in Section 21.4, is used without regularization. Thus, the spline is the unique solution of the interpolation problem, see Theorem 20.3. In Fig. 21.34, we see that this method works well if the activity is near the data points, which is the case for the activity in the upper left region of the plot. In contrast, the second active region lies in the middle of a sensor gap, which results in a too flat approximation even in the case of non-noisy data, see Fig. 21.31. This is a known disadvantage of interpolation based approximation methods.

However, these methods also have advantages. The reconstructions obtained via splines are robust with respect to the noise level. In addition, coarse structures can be reconstructed quickly with the regularized Ritz method, since only few basis functions are required for this purpose.

The RFMP as well as its enhancement, the ROFMP, combine the advantages of these methods. Due to the reproducing kernels in the dictionary, which are related to splines, the R(O)FMP is robust with respect to the noise level and can also handle irregularly distributed point grids. Coarse structures can be reconstructed with only few dictionary elements using the additional orthonormal basis functions. This also results in a sparse solution, especially for lower noise levels, which can be seen in Table 21.3. Using the penalty term of the R(O)FMP, the smoothness of the reconstruction can be controlled, similar to the spline methods. In contrast to the spline methods, the R(O)FMP is not an interpolation method, which results in a better handling of the lack of data. Finally, the R(O)FMP is directly used for the reconstruction of the entire vector-valued neuronal current, which is more stable than a reconstruction of scalar-valued parts that are transferred to the vector-valued current afterwards.

21.6. Inversion of Real Data

After having tested the R(O)FMP extensively within our synthetic test case, we complete this chapter by reconstructing neuronal currents from real data. For this purpose, a set of real data was given to the author by O. Hauk, see [116]. In this setting, a subject wearing an EEG sensor

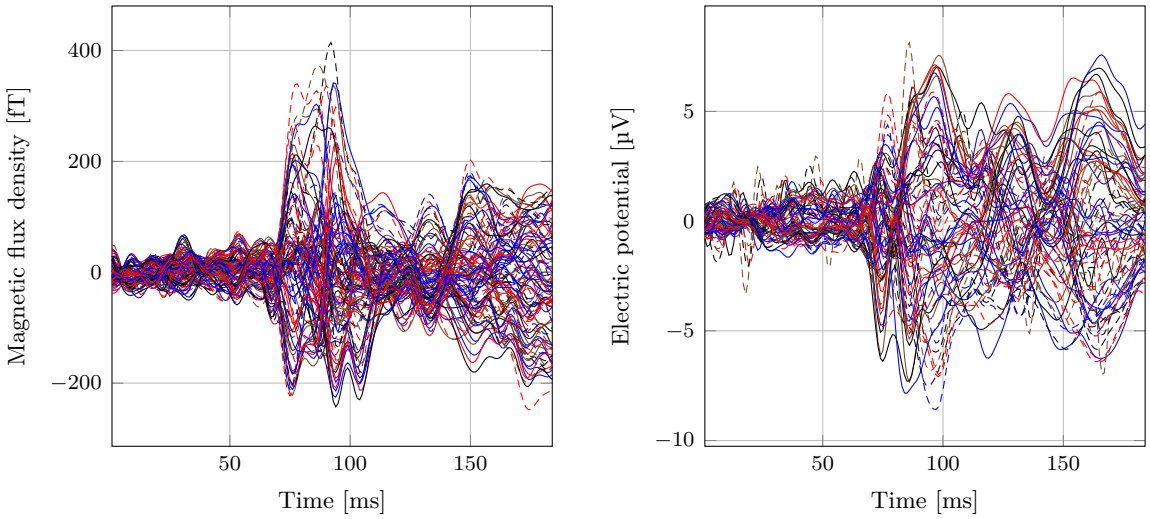

FIGURE 21.35: *Recordings of the magnetic flux density (left) and the electric potential (right) for the VR data set*

cap was placed in an MEG device. The device used for this study is installed at the MRC Cognition and Brain Sciences Unit, Cambridge, UK. It is a 306-channel Vectorview system (Elekta Neuromag®, Helsinki, Finland), see [172], which combines 204 planar gradiometers, 102 magnetometers, and 62 to 124 EEG channels providing comprehensive high-density coverage of electromagnetic brain activity. However, for the recording of the provided data set 70 EEG channels were used.

In our particular setting, a visual stimulus in form of a chequered pattern is given to the subject. For this data set, the chequered pattern is presented from the right-hand side (VR, visual right). Then, the brain activity is measured for a short time frame. The magnetic flux density and the electric potential are plotted in Fig. 21.35 for a 184 ms recording, where the time starts when the stimulus is applied. In the case of the magnetic flux density, 102 channels are plotted and in the case of the electric potential, 70 channels are visualized. After a delay of approximately 75 ms to 80 ms, the brain activity increases as well as the magnetic flux density and the electric potential. For the inversion, we choose the measurement corresponding to the point of time with the highest values of the measured quantity. In our case, we choose the data belonging to the point of time 89 ms for both inversions, which will also allow a combination of the inversions in the postprocessing.

For the inversion of the magnetic flux density as well as the electric potential, we use the same dictionary as within the synthetic test case, see Section 19.1. In both cases, we apply the ROFMP algorithm since it yielded the best approximation results within the synthetic test cases, see Figs. 21.33 and 21.34 and Tables 21.10 and 21.11. In the MEG case, we use the norm corresponding to $s = 2$ for the penalty term. In the EEG case, we test the $\tilde{\mathcal{H}}_1^{(2)}$- as well as the $\tilde{\mathcal{H}}_2^{(2)}$-norm.

In all cases, the absolute value of the neuronal current is plotted on the sphere with radius $0.95\varrho_0$. For the inversion of one data set, two images of the neuronal current are presented. One as viewed from the back of the head (always on the left column) and one from the front (right column). Note that different angles of view are chosen for the reconstructions belonging to the VR data set. Since the optical nerve fibers associated to the nasal side of

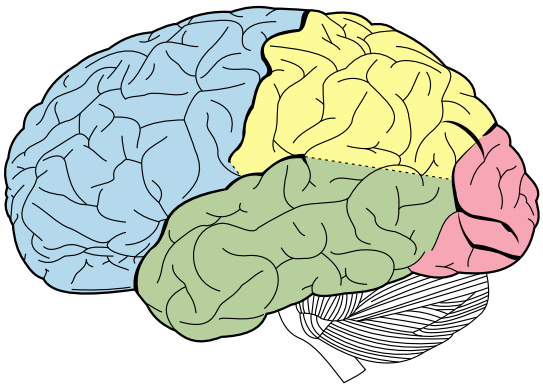

FIGURE 21.36: *Lobes of the human brain with visual cortex marked in red, figure taken from [222]*

the retinas cross each other in the optic chiasm, the brain activity should be maximal at the contralateral visual cortex, see [133]. This means that, for example, a visual right stimulus mainly induces brain activity in the left visual cortex and vice versa. The visual cortex itself is located at the back of the brain, see Fig. 21.36.

In the case of our three-shell model, the medial longitudinal fissure separating the two brain hemispheres is located in the yz-plane. On the other hand, the position of the face is reflected in the round-shaped gap in the sensor positions on the front side of the head in the direction of $(0, 1, 0)^{\mathrm{T}}$.

In order to get an impression of the quality of the reconstruction, the absolute value of the measured data is superimposed in each figure. Therefore, each plot has two different colour bars. The upper colour bar always belongs to the neuronal current, whereas the lower colour bar belongs to the measurement. In contrast to previous plots, we decide not to show the direction of the neuronal current in order not to overload the plots.

The regularization parameter is determined via the parameter choice methods presented in Section 16.3. To this end, the ROFMP is started with 500 to 750 different regularization parameter values. After applying all parameter choice methods to the results, we manually select the reconstruction that best fits the data in the following way: as realized within the test of the parameter choice methods in Section 21.1.2, these methods in some cases choose regularization parameters that yield strongly over- or underregularized solutions. Thus, we eliminate these results in a first step. Afterwards, all remaining reconstructions selected by the parameter choice methods are plotted in combination with the absolute value of the measured data. We choose the reconstruction that visually fits best to the data based on the empirical knowledge from the synthetic test case. The parameter choice method that produced the shown result is stated in the respective caption.

In the case of the real data, also the L-curve method yields a good result. The corresponding L-curve for this data set is plotted in Fig. 21.37.

In the case of the MEG recordings, numerical results are depicted in Fig. 21.38. On the back of the head, we see that activity in the contralateral left visual cortex is reconstructed, which fits to the recorded data, the experiment, and the theory. However, to the opinion of the author, some artefacts are reconstructed in the front of the brain. These artefacts are more or less pronounced depending on the chosen regularization parameter. In the case

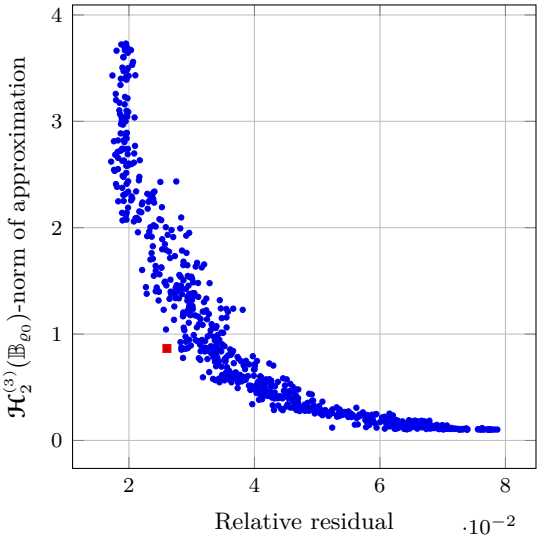

FIGURE 21.37: *Relative residual plotted against the $\mathcal{H}_2^{(3)}(\mathbb{B}_{\varrho_0})$-norm of the reconstruction for 727 regularization parameter values with the chosen parameter marked in red*

where the regularization parameter is chosen according to the LCM, we see that this artefact is located in the data gap in the area of the face.

Concluding, the MEG real data inversions yield activity in the desired regions. However, in certain cases artefacts arise, especially near the data gap, which may correspond to an insufficient regularization or an inappropriate penalty term.

According to O. Hauk [116], the brain activity should be bipolar in the case of the EEG recordings, that is a positive brain activity at the back results in a (smaller) negative brain activity at the front. Inversions of the real EEG data are visualized in Fig. 21.39. The activity of the visual cortex on the left-hand side is clearly recognizable and only small activity at the front is reconstructed. In the case of $\tilde{\mathcal{H}}_1^{(2)}$-regularization, however, no tested parameter choice method yields a suitable result such that the regularization parameter is chosen manually.

Now, we further investigate the ROFMP runs belonging to the presented parameters for the VR data set. In Fig. 21.40a, the chosen dictionary elements depending on the number of iterations is visualized. One can see a trend in the choice of the dictionary elements. In the first 75 iterations, mainly orthonormal basis functions and reproducing kernels with a larger width, that is $h = 0.8$ and sometimes $h = 0.9$, are chosen. Afterwards, smaller reproducing kernels belonging to $h \in \{0.9, 0.95\}$ are chosen primarily. In the end, the very fine reproducing kernels belonging to $h = 0.99$ are chosen increasingly. This trend is more pronounced in the real data case as in the synthetic test case, which could be attributed to the structure of the real neuronal current and the synthetic test current. In Fig. 21.40b, the centres belonging to the chosen reproducing kernels are plotted. We observe that mainly reproducing kernels located in an outer shell of the cerebrum are chosen. This corresponds to the structure of the brain and the location of the visual cortex. In addition, there are significant accumulation points of centres in the left visual cortex, which fits to the presumed active region.

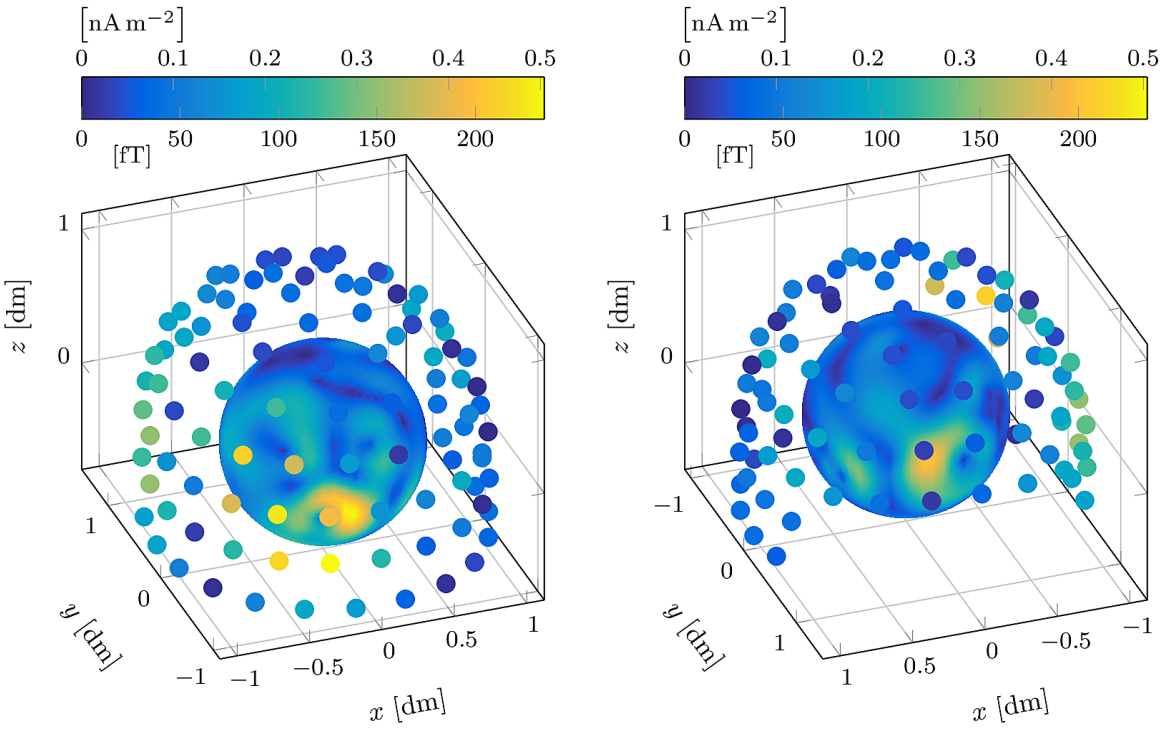

(a) Back view, $s = 2$, LCM *(b) Front view, $s = 2$, LCM*

FIGURE 21.38: *Neuronal current reconstruction from real magnetic flux density data (VR) plotted on a sphere with radius* $0.95\varrho_0$. *The result is obtained via the ROFMP for different parameter choice methods. The upper colour bar denotes magnitude of the current, whereas the lower colour bar belongs to the measurement.*

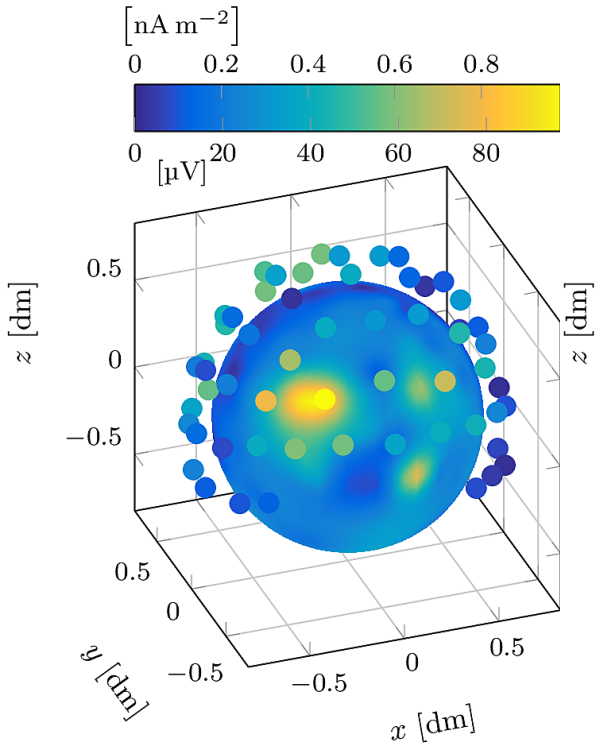

(a) *Back view, $s = 2$, MGCV*

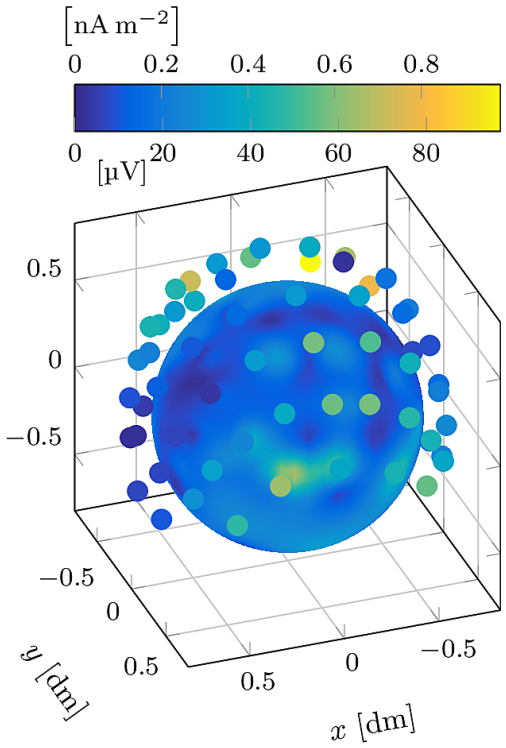

(b) *Front view, $s = 2$, MGCV*

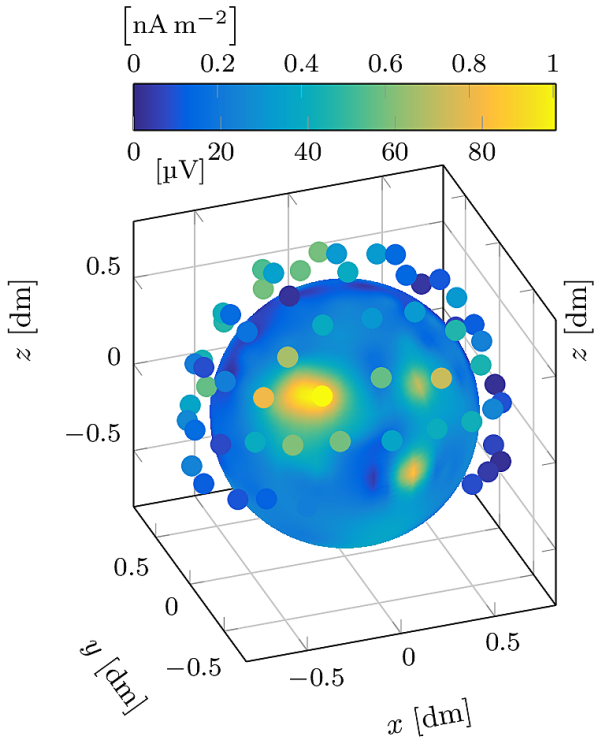

(c) *Back view, $s = 1$, Manual*

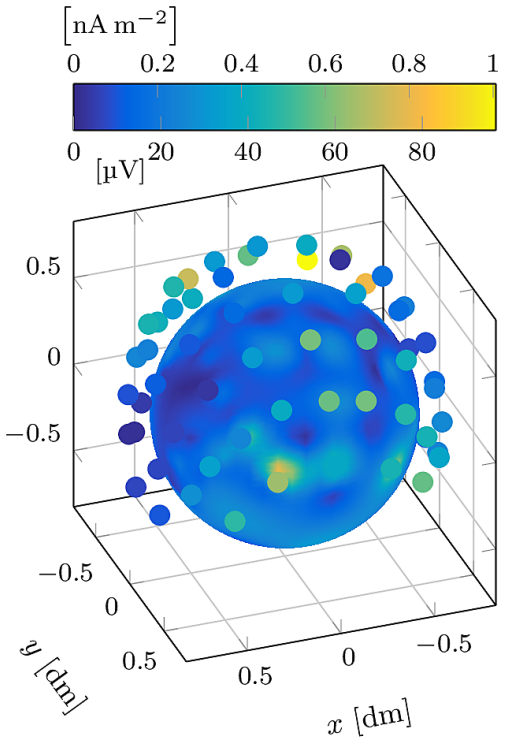

(d) *Front view, $s = 1$, Manual*

FIGURE 21.39: *Neuronal current reconstruction from real electric potential data (VR) plotted on a sphere with radius $0.95\varrho_0$. The result is obtained via the ROFMP for different penalty term parameters s and parameter choice methods. The upper colour bar denotes magnitude of the current, whereas the lower colour bar denotes the absolute value of the measurement.*

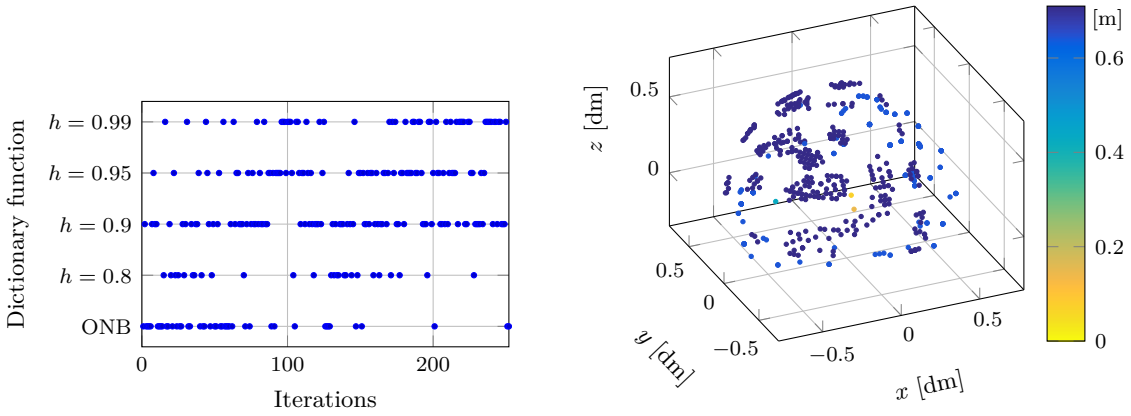

(a) MEG, $s = 2$ *(b) EEG, $s = 1$*

FIGURE 21.40: *Chosen dictionary elements and reproducing kernel centres by means of the ROFMP depending on the number of iterations. The colour in the right figure represents the distance of the kernel centres from the origin.*

For the inversion of the real electric potential data, we conclude that the ROFMP is able to reconstruct a reasonable neuronal current, which can especially be verified in Fig. 21.39. However, depending on the data set and the chosen penalty term, it is hard to find an appropriate regularization parameter. In contrast, in some tests activity is reconstructed in areas where no activity is recorded, such as in the case of Fig. 21.38. It is standing to reason that this activity is an artefact fostered by the lack of data. This could be solved, for instance, by adapting the dictionary. One could think of removing reproducing kernels from the dictionary that are located in the regions of the face, in the bottom of the ball-shaped brain model, or in parts of the brain where no activity is presumed.

We chose the same point of time for the reconstruction of both measurements, which enables us to combine the MEG and EEG reconstruction to a simultaneous inversion. For this purpose, we choose the MEG reconstruction obtained via the regularization parameter obtained by the L-curve method. For the reconstruction of the neuronal current from EEG data, we take the manually chosen regularization parameter with regularization term $s = 1$. Eventually, the joint inversion of the two separate inversion from Figs. 21.38 and 21.39 is given in Fig. 21.41. The plotted reconstruction on the sphere in Figs. 21.41b and 21.41c reveals some activity on the bottom of the cerebrum, which seems to be unreliable and can be attributed to the missing sensor positions in this area. Besides, Fig. 21.41c reveals some small activity in the frontal lobe, which is anticipated due to the bipolar behaviour of the neuronal current. The main activity of the brain is located in the visual left cortex as it should be, see Fig. 21.41b. In the visualization of the neuronal current on a cutout of the ball, one can additionally observe that most of the activity is located in the outer region of the ball, which corresponds to the structure of the visual cortex. Concluding, the ROFMP solution for this joint data set yields a plausible reconstruction of the neuronal current. The presumed active regions are clearly reconstructed and the visualization of the neuronal currents fits to the data. Artefacts, which especially occur in the MEG reconstruction, can be smoothed by the joint inversion.

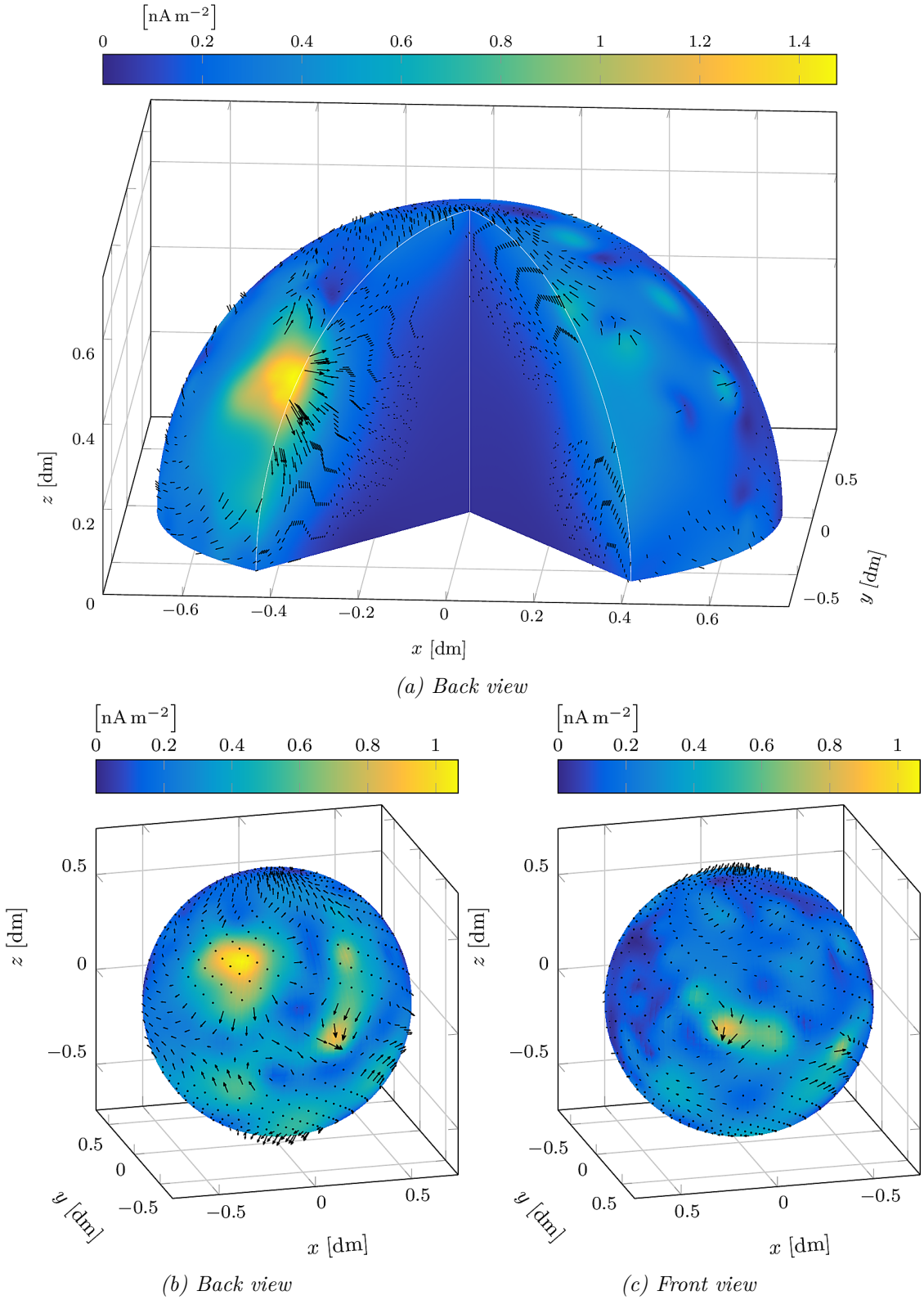

(a) Back view

(b) Back view

(c) Front view

FIGURE 21.41: *Neuronal current reconstruction from real magnetic flux density and electric potential data (VR) plotted on a cutout of the cerebrum viewed from the back (top) and on a sphere with radius* $0.95\varrho_0$ *(bottom)*

Based on the review of the executed real date inversions, the results of the ROFMP can still be optimized. This enhancement can be performed on different levels.

First, from the implementation point of view, several extensions are reasonable. The lack of data in the MEG case can be reduced by including the additional 204 gradiometer measurements into the R(O)FMP algorithm. The theoretical foundation for the implementation can be found in Appendix A. The dictionary, which is required for the ROFMP, consists of orthonormal basis functions and particular reproducing kernels in our numerical tests. Besides these two sets of trial functions, we could add more different types of functions into the dictionary. For example, wavelet-based reconstructions and multiresolution analysis yield good results in spherical applications, see, for example, [20, 25, 150, 153] for vectorial cases. The construction of appropriate wavelets as dictionary elements for the inverse MEG and EEG problem is not such challenging, since we have already found the corresponding SVDs which are required for the construction of adequate scaling functions. Note that the usage of wavelets as dictionary elements differs from the previously mentioned wavelet method for the inversion of ill-posed problems. Therefore, it is reasonable to include them as trial functions for the inverse MEG and EEG problem. Furthermore, Slepian functions, as particular linear combinations of the used vector-valued orthonormal basis functions, yield good spatial localization, see [5, 37, 140, 202, 203, 221]. Thus, Slepian functions could be constructed for particular regions of the brain, such as the real-shaped visual cortex or even smaller parts of it. A foundation for this approach is presented by V. Michel, N. Schneider and the author in [146], where vector-valued Slepian functions for certain regions on the ball are constructed. However, in the construction of these Slepian functions only a localization property with respect to the region is incorporated. In [164], an approach is presented which enables to construct Slepian functions in relation to an inverse problem. For this approach the singular values of the underlying operator are required, which is not a problem in the inverse MEG and EEG problem for the multiple-shell model.

Besides an enlargement of the dictionary, we could additionally test regularization terms that also take the time dependency of the data into account. Instead of only penalizing the approximation in a certain norm, we could additionally penalize its deviation from the one of the previous time step. By means of this approach, we can take advantage of the time dependency of the data that is not yet taken into account in the current investigations. Additionally, many more data points would become available. This idea could be taken further to a postprocessing step that penalizes the deviation from the previous and the next approximation after all single time points have been inverted independently. Of course, different Sobolev norms that have not been tested yet as penalty terms for the inverse MEG and EEG problem could also improve the results.

Second, from the algorithmic side, we could also try several enhancements of the R(O)FMP. For instance, in [137, 138], a massively accelerated variant of the algorithm called the regularized weak functional matching pursuit algorithm (RWFMP) is developed, which yielded good results in the considered numerical test cases. Due to the acceleration of the algorithm, more iterations in a shorter period of time are realizable, which is generally desirable. Moreover, in a forthcoming work, see [201], a learned-dictionary-based enhancement of the RFMP will be presented, which may improve the numerical results by adapting the used dictionary.

Third, a reason for the discrepancy between the quality of the results obtained in the synthetic test case and in the real data situation may be grounded in an insufficient modelling of the brain. In the case of the used multiple-shell model, we assume that the conductivities

are known and constant on each particular shell. Instead of setting the conductivities on each shell based on values stated in [117], novel approaches for their inference can be used, see [32]. In addition, one could allow different radial and tangential conductivities, which is considered in [174], for instance. Another reason for the inferiority of the real data results might be the multiple-shell model itself, since the real structure of the brain is inherently non-spherical. In order to overcome this model error, other geometries could be used, such as the elliptical-shell model, see [39, 54, 95]. In this case, however, more research concerning the theory of the inverse MEG and EEG problem is required. Although real-shaped brain models cannot be used to achieve theoretical knowledge of the null spaces of the operators, they may well be used in the numerics. For this purpose, the derived integral equations modelling the inverse MEG and EEG problem need to be adapted.

Lastly, an additional difficulty in the real data situation is that, besides technical noise, one has to handle supplementary human-driven noise. In order to handle this situation, additional postprocessing of the real data could be helpful according to [116]. Alternatively, the R(O)FMP could be further tested with some benchmark data sets as provided in [98].

Part VII.

Final Remarks

Chapter 22.

Conclusion and Outlook

Solving the (inverse) MEG and EEG problem for the spherical multiple-shell model from the theoretical as well as the numerical point of view was the main task of this work. For this purpose, we first derived in Part I an integral equation connecting the sought neuronal current, which we model as a continuous dipole distribution, with the measured magnetic flux density in the exterior of the head and the electric potential on the scalp. These derivations were based on the quasi-static version of Maxwell's equations and used the spherical multiple-shell model. In accordance with the literature, the EEG model includes a sequence of coefficients $\{\beta_k^{(L)}\}_{k\in\mathbb{N}}$ depending on the degree k, the radii of the various shells in the multiple-shell model, and their conductivities. The novel analysis of the asymptotic behaviour of these coefficients was crucial for the well-definedness, which implies the convergence of the integral kernel series representation of the EEG problem. In addition, for both problems, the a-priori assumptions on the neuronal current in our derivation could be substantially reduced in comparison to other derivations in the literature.

Via the extensive analysis of more general classes of integral kernels, such as the continuous, the star-shaped, and the harmonic vector Legendre-type integral (VLI) kernels, and their corresponding integral operators in Part II, results concerning the inverse MEG and EEG problem could be achieved. Besides, the different VLI operators are not limited to MEG and EEG, but also cover other problems occurring, for example, in the geosciences, such as the inverse Earth's crustal magnetization problem or the inverse gravimetric problem in the scalar case.

Based on the definition of ill-posed problems according to Hadamard [106, 107], we analyzed three aspects of the inverse MEG and EEG problem in Part III:

Non-uniqueness Even though the non-uniqueness of the inverse MEG and EEG problem is extensively discussed in the literature, see [47, 71–75, 108], there are still some open questions, which we were able to answer within this work. We expanded the neuronal current by means of a tailor-made orthonormal basis for the space $\mathbf{L}_2(\mathbb{B}_{\varrho_0})$. This basis consists of Edmonds vector spherical harmonics in the angular part. These particular basis functions allowed to characterize precisely which direction of the neuronal current can be detected by the measurement devices. The part belonging to the Edmonds type $i = 2$ functions can be measured by the electroencephalograph, whereas the part belonging to type $i = 3$ is detected by the magnetoencephalograph. In addition, the part belonging to type $i = 1$ is silent for both devices. Thus, the information that can be obtained by the two measurement methods is complementary. This improves and concretizes the results of, for instance, [47]. As a novelty, we also expanded the radial part of the neuronal current by means of an appropriate orthonormal basis on the interval. In combination with the derived singular value decomposition (SVD) of the MEG and EEG operators, we could characterize their null spaces precisely. For the joint inversion, we concluded that only the harmonic solenoidal part of the neuronal

current can be reconstructed from magneto-electroencephalography data. In addition, we stated several additional uniqueness constraints to overcome this non-uniqueness. The most natural condition seems to be the minimum-norm condition on the entire vector-valued neuronal current, due to the principle of stationary action, see [70].

Instability The instability of the inverse MEG and EEG problem is presumed in former research, see [33, 108, 117]. In this work, we provided a mathematical foundation for this instability. Based on the derived SVDs for both operators, the exponentially fast decay of the singular values to zero is proved, which implies the severe ill-posedness of the two problems, see [148, 214].

Existence of a Solution Via the SVDs of the two operators, we formulated Picard's criterion for these problems in order to guarantee the existence of a solution.

Besides this, the SVD provided us with a representation of the best-approximate solution.

In addition to the comprehensive analysis of the derived integral equation and operator, we compared our approach with former approaches from the literature. Most existing methods for continuous dipole distributions in spherical geometries further decompose the neuronal current. Preceding decompositions are the Hodge and the Helmholtz decomposition used in [47, 50, 71–75], which both yield integral equations relating some scalar-valued parts of the neuronal current to the measured quantities. These decompositions are insufficient for a precise characterization of the reconstructable parts of the neuronal current, since, for example, an orthonormal basis decomposition for the radial part of the neuronal current is missing. Furthermore, they can only be combined with additional uniqueness constraints in some cases. For instance, we proved that the Helmholtz decomposition for the EEG problem always produces parts of the neuronal current that cannot be measured by the electroencephalograph. Thus, the Helmholtz decomposition cannot be combined with the minimum-norm condition of the neuronal current. The detailed comparison among these approaches and further improvements of the existing methods were presented in Chapter 15.

In Part V, we presented the regularized functional matching pursuit (RFMP) algorithm and its enhancement, the regularized orthogonal functional matching pursuit (ROFMP) algorithm, see [66, 68, 137, 138, 159, 163, 166, 210]. We improved some of the existing convergence results on the RFMP and analyzed further properties of the solution obtained by the algorithm.

Afterwards, in Part VI, we applied these two algorithms to the inverse MEG and EEG problem in order to solve them numerically. For this purpose, we constructed a synthetic test case with known solution that satisfies the minimum-norm condition as additional uniqueness constraint. The instability of the problems was handled by the Tikhonov-regularization term occurring in the RFMP as well as the ROFMP. For appropriate penalty terms, we constructed novel vector-valued Sobolev spaces on the ball. We conducted the synthetic tests for non-noisy data as well as for noisy data with 1 % to 10 % additive white Gaussian noise. Besides difficulties attributed to the ill-posedness of the problems, we also needed to handle the lack of data. Each measurement device only provides 70 to 102 measurements per time step at irregularly distributed sensor positions. Nevertheless, the RFMP yielded good reconstruction results concerning the normalized root mean square error of the approximation as well as concerning the visual representation of the reconstruction itself. In addition, the RFMP was outperformed by the ROFMP with respect to reconstruction quality and sparsity of the solution. In order to compare these two algorithms with established methods, we also implemented the regularized Ritz method as well as two different spline methods. We used the

scalar spline method from [73] for the inverse MEG problem as well as a novel tensor-valued reproducing kernel based spline method on the ball for the inverse EEG problem. Whereas the Ritz method generally produced comparably poor results, the two spline methods yielded good numerical results, which are stable with respect to increasing noise level, but still inferior compared to the ROFMP solution. Another disadvantage of the scalar spline method is given by the transformation of the good scalar reconstruction to the vector-valued density. Within this transformation, accuracy of the scalar spline reconstruction is lost due to the additional damping term. Concluding, the ROFMP yielded the best results among all tested methods independent of the noise level and resulted in satisfactory reconstructions of the test current. Furthermore, we solved some issues from [73] concerning the scalar spline method for the EEG problem.

We completed this part with the inversion of real MEG and EEG data from a visual stimulus experiment. The results of the real data inversion, especially for the combination of the MEG and EEG inversion, were satisfying and the ROFMP worked as it should. However, some artefacts in the reconstructions were observed. This opens up directions for future research.

For further investigations, the ROFMP could be applied to more realistic benchmark problems for which the exact solution or at least an approximation of the solution is available. Such benchmarks are included in the MNE software package, for example, see [98]. In addition, the approximation power of the R(O)FMP could be enhanced by adding further types of functions to the dictionary, such as vector-valued wavelets, see [20, 25, 150, 153], or Slepian functions that can be concentrated on particular real-shaped brain regions, such as the visual cortex or even the entire human brain, see [146, 164]. Eventually, the numerical tests could be accelerated by using the regularized weak functional matching pursuit algorithm instead, see [137, 138].

Besides this, we could improve on the model itself and the constants involved. The determination of the conductivities required for the multiple-shell model could be more sophisticated. For example, the method developed in [32] could be used for the determination of the conductivities. In addition, the multiple-shell model could be extended by allowing different radial and tangential conductivities, see [174]. Of course, the same analysis that is carried out in this thesis would be required for the extended model. A further step could be the analysis of the ellipsoidal-shell model, see [39, 95], for which certain forward solutions exist. However, finding a singular system in this particular case seems challenging since the angular and the radial part of an expansion into ellipsoidal harmonics are not decoupled.

Another, more radical, possibility would be to drop the quasi-static approach and to analyze the time-dependent Maxwell's equations because the measurements are also dependent on time. In this context, novel integral or integro-differential equations need to be derived for the multiple-shell model. However, finding the corresponding operators and their singular systems seems to be very challenging. Alternatively, the time dependency could be included in the regularization of the quasi-static approach by using spatio-temporal regularizations.

Appendix

Appendix A.

Supplementary Calculations for the MEG Gradiometer

In Section 9.2, we investigate the quantity measured by the MEG gradiometers, that is a tangential derivative of the magnetic flux density. The following result is stated in Lemma 9.5 with the proof omitted. Now, we present the missing proof and some lengthy auxiliary calculations.

Lemma A.1. *The gradient of the magnetic flux density $B_{\boldsymbol{\nu}}$ is given for $\boldsymbol{y} \in \overline{\mathbb{B}_{\varrho_L}^{\mathrm{ext}}}$ by*

$$\begin{aligned}\boldsymbol{\nabla}_{\boldsymbol{y}} B_{\boldsymbol{\nu}}(\boldsymbol{y}) = \sum_{n=1}^{\infty} \sum_{j=1}^{2n+1} B_r^{\wedge}(n,j) \Bigg(&+ \sqrt{\frac{n+1}{2n+1}} \boldsymbol{\nu}(\boldsymbol{y}) Y_{n,j}(\hat{\boldsymbol{y}}) \\ &+ (\boldsymbol{\nu}(\boldsymbol{y}) \cdot \hat{\boldsymbol{y}}) \left(-(n+3) \sqrt{\frac{n+1}{2n+1}} \boldsymbol{y}_{n,j}^{(1)}(\hat{\boldsymbol{y}}) + (n+2) \sqrt{\frac{n}{2n+1}} \boldsymbol{y}_{n,j}^{(2)}(\hat{\boldsymbol{y}}) \right) \\ &+ \sqrt{\frac{n(n+1)^2}{2n+1}} \hat{\boldsymbol{y}} \left(\boldsymbol{\nu}(\boldsymbol{y}) \cdot \boldsymbol{y}_{n,j}^{(2)}(\hat{\boldsymbol{y}}) \right) - \sqrt{\frac{n}{2n+1}} (\boldsymbol{\nu}(\boldsymbol{y}) \cdot \boldsymbol{\nabla}_{\hat{\boldsymbol{y}}}^{*}) \boldsymbol{y}_{n,j}^{(2)}(\hat{\boldsymbol{y}}) \Bigg) \Bigg).\end{aligned}$$

Proof. Keep in mind within this proof that $\boldsymbol{y} \in \overline{\mathbb{B}_{\varrho_L}^{\mathrm{ext}}}$. For the gradient of the investigated quantity, we obtain

$$\boldsymbol{\nabla}_{\boldsymbol{y}} B_{\boldsymbol{\nu}}(\boldsymbol{y}) = \boldsymbol{\nabla}_{\boldsymbol{y}} \left(\boldsymbol{\nu}(\boldsymbol{y}) \cdot \boldsymbol{B}(\boldsymbol{y}) \right). \tag{A.1}$$

We use the product rule for the gradient, see [141, Sec. 22], that is the identity

$$\boldsymbol{\nabla}(\boldsymbol{f} \cdot \boldsymbol{g}) = \boldsymbol{f} \wedge (\boldsymbol{\nabla} \wedge \boldsymbol{g}) + \boldsymbol{g} \wedge (\boldsymbol{\nabla} \wedge \boldsymbol{f}) + (\boldsymbol{f} \cdot \boldsymbol{\nabla}) \boldsymbol{g} + (\boldsymbol{g} \cdot \boldsymbol{\nabla}) \boldsymbol{f}$$

for all $\boldsymbol{f}, \boldsymbol{g} \in \mathbf{C}(\mathbb{R}^3)$, in order to further expand the expression in Eq. (A.1). This leads to

$$\begin{aligned}\boldsymbol{\nabla}_{\boldsymbol{y}} \left(\boldsymbol{\nu}(\boldsymbol{y}) \cdot \boldsymbol{B}(\boldsymbol{y}) \right) = &\left(\boldsymbol{\nu}(\boldsymbol{y}) \cdot \boldsymbol{\nabla}_{\boldsymbol{y}} \right) \boldsymbol{B}(\boldsymbol{y}) + \left(\boldsymbol{B}(\boldsymbol{y}) \cdot \boldsymbol{\nabla}_{\boldsymbol{y}} \right) \boldsymbol{\nu}(\boldsymbol{y}) \\ &+ \boldsymbol{\nu}(\boldsymbol{y}) \wedge (\boldsymbol{\nabla}_{\boldsymbol{y}} \wedge \boldsymbol{B}(\boldsymbol{y})) + \boldsymbol{B}(\boldsymbol{y}) \wedge (\boldsymbol{\nabla}_{\boldsymbol{y}} \wedge \boldsymbol{\nu}(\boldsymbol{y})).\end{aligned}$$

Since the normal vector $\boldsymbol{\nu}(\boldsymbol{y}) \equiv \boldsymbol{\nu}$ is constant on each sensor surface, the second and the last summand vanish. Hence, the formula reduces to

$$\boldsymbol{\nabla}_{\boldsymbol{y}} \left(\boldsymbol{\nu} \cdot \boldsymbol{B}(\boldsymbol{y}) \right) = \left(\boldsymbol{\nu} \cdot \boldsymbol{\nabla}_{\boldsymbol{y}} \right) \boldsymbol{B}(\boldsymbol{y}) + \boldsymbol{\nu} \wedge (\boldsymbol{\nabla}_{\boldsymbol{y}} \wedge \boldsymbol{B}(\boldsymbol{y})).$$

For the last summand, we keep the derivation of the magnetic field $\boldsymbol{B}$ in mind, which is generated by the gradient of the scalar magnetic potential in the exterior of the head. Since

conservative (i.e. gradient) fields are always irrotational and $\boldsymbol{y} \in \overline{\mathbb{B}_{\varrho_L}^{\mathrm{ext}}}$, the last summand in the previous equation also vanishes. Thus, with $r \geq \varrho_L$, we get

$$\begin{aligned}\boldsymbol{\nabla}_{\boldsymbol{y}} \left(\boldsymbol{\nu} \cdot \boldsymbol{B}(\boldsymbol{y})\right) &= \left(\boldsymbol{\nu} \cdot \boldsymbol{\nabla}_{\boldsymbol{y}}\right) \boldsymbol{B}(\boldsymbol{y}) \\ &= \left(\boldsymbol{\nu} \cdot \boldsymbol{\nabla}_{\boldsymbol{y}}\right) \left(\sum_{n=1}^{\infty} \sum_{j=1}^{2n+1} B_r^{\wedge}(n,j) \boldsymbol{h}_{n,j}^{(1)}(r;\boldsymbol{y}) \right).\end{aligned}$$

The series representation of the magnetic field is valid, see Theorem 9.4. The derivative and the series of $\boldsymbol{B}$ can be interchanged due to Theorems 8.7 and 9.4 and the fact that the MEG integral kernel is a harmonic VLI kernel. Hence, using $\boldsymbol{y} = y\hat{\boldsymbol{y}}$, we can apply the derivative term-by-term. For this purpose, we use Theorem 2.14 for the representation of the gradient and obtain for all $n \in \mathbb{N}$, $j = 1, \ldots, 2n+1$ the identity

$$\begin{aligned}\left(\boldsymbol{\nu} \cdot \boldsymbol{\nabla}_{\boldsymbol{y}}\right) \boldsymbol{h}_{n,j}^{(1)}(r;\boldsymbol{y}) &= \left(\boldsymbol{\nu} \cdot \left(\hat{\boldsymbol{y}} \frac{\partial}{\partial y} + \frac{1}{y} \boldsymbol{\nabla}_{\hat{\boldsymbol{y}}}^{*}\right)\right) \boldsymbol{h}_{n,j}^{(1)}(r; y\hat{\boldsymbol{y}}) \\ &= \left(\boldsymbol{\nu} \cdot \hat{\boldsymbol{y}}\right) \frac{\partial}{\partial y} \boldsymbol{h}_{n,j}^{(1)}(r; y\hat{\boldsymbol{y}}) + \frac{1}{y} \left(\boldsymbol{\nu} \cdot \boldsymbol{\nabla}_{\hat{\boldsymbol{y}}}^{*}\right) \boldsymbol{h}_{n,j}^{(1)}(r; y\hat{\boldsymbol{y}}). \qquad \text{(A.2)}\end{aligned}$$

In order to calculate the two remaining summands of the right-hand side of Eq. (A.2), we first use Definition 5.27 to expand the vector outer harmonics into

$$\begin{aligned}\boldsymbol{h}_{n,j}^{(1)}(r;\boldsymbol{y}) &= \frac{1}{r} \left(\frac{r}{y}\right)^{n+2} \tilde{\boldsymbol{y}}_{n,j}^{(1)}(\hat{\boldsymbol{y}}) \qquad \text{(A.3a)} \\ &= \frac{1}{r} \left(\frac{r}{y}\right)^{n+2} \left(\sqrt{\frac{n+1}{2n+1}} \boldsymbol{y}_{n,j}^{(1)}(\hat{\boldsymbol{y}}) - \sqrt{\frac{n}{2n+1}} \boldsymbol{y}_{n,j}^{(2)}(\hat{\boldsymbol{y}}) \right). \qquad \text{(A.3b)}\end{aligned}$$

Hence, inserting Eq. (A.3a) into Eq. (A.2), the first summand reduces to

$$\begin{aligned}\left(\boldsymbol{\nu} \cdot \hat{\boldsymbol{y}}\right) \frac{\partial}{\partial y} \boldsymbol{h}_{n,j}^{(1)}(r; y\hat{\boldsymbol{y}}) &= \left(\boldsymbol{\nu} \cdot \hat{\boldsymbol{y}}\right) \frac{\partial}{\partial y} \frac{1}{r} \left(\frac{r}{y}\right)^{n+2} \tilde{\boldsymbol{y}}_{n,j}^{(1)}(\hat{\boldsymbol{y}}) \\ &= -(n+2) \left(\boldsymbol{\nu} \cdot \hat{\boldsymbol{y}}\right) \frac{r^{n+1}}{y^{n+3}} \tilde{\boldsymbol{y}}_{n,j}^{(1)}(\hat{\boldsymbol{y}}).\end{aligned}$$

For the second summand in Eq. (A.2), we obtain using the representation in Eq. (A.3b) the identity

$$\begin{aligned}\frac{1}{y} \left(\boldsymbol{\nu} \cdot \boldsymbol{\nabla}_{\hat{\boldsymbol{y}}}^{*}\right) \boldsymbol{h}_{n,j}^{(1)}(r; y\hat{\boldsymbol{y}}) &= \frac{r^{n+1}}{y^{n+3}} \left(\boldsymbol{\nu} \cdot \boldsymbol{\nabla}_{\hat{\boldsymbol{y}}}^{*}\right) \left(\sqrt{\frac{n+1}{2n+1}} \boldsymbol{y}_{n,j}^{(1)}(\hat{\boldsymbol{y}}) - \sqrt{\frac{n}{2n+1}} \boldsymbol{y}_{n,j}^{(2)}(\hat{\boldsymbol{y}}) \right) \\ &= \frac{r^{n+1}}{y^{n+3}} \left(\sqrt{\frac{n+1}{2n+1}} (\boldsymbol{\nu} \cdot \boldsymbol{\nabla}_{\hat{\boldsymbol{y}}}^{*}) \left(\hat{\boldsymbol{y}} Y_{n,j}(\hat{\boldsymbol{y}})\right) - \sqrt{\frac{n}{2n+1}} (\boldsymbol{\nu} \cdot \boldsymbol{\nabla}_{\hat{\boldsymbol{y}}}^{*}) \boldsymbol{y}_{n,j}^{(2)}(\hat{\boldsymbol{y}}) \right).\end{aligned}$$

We expand the first summand on the right-hand side. Recall that $\hat{\boldsymbol{y}}$ depends on the longitude φ and the polar distance t, see Definition 2.11. By means of the coordinate representation of

the surface gradient, see Theorem 2.14, we get the representation

$$\begin{aligned}
(\boldsymbol{\nu}\cdot\boldsymbol{\nabla}^*_{\hat{\boldsymbol{y}}})\,(\hat{\boldsymbol{y}}Y_{n,j}(\hat{\boldsymbol{y}})) &= Y_{n,j}(\hat{\boldsymbol{y}})(\boldsymbol{\nu}\cdot\boldsymbol{\nabla}^*_{\hat{\boldsymbol{y}}})\hat{\boldsymbol{y}} + \hat{\boldsymbol{y}}(\boldsymbol{\nu}\cdot\boldsymbol{\nabla}^*_{\hat{\boldsymbol{y}}})Y_{n,j}(\hat{\boldsymbol{y}}) \\
&= Y_{n,j}(\hat{\boldsymbol{y}})\left(\boldsymbol{\nu}\cdot\left(\boldsymbol{\varepsilon}^{\varphi}\frac{1}{\sqrt{1-t^2}}\frac{\partial}{\partial\varphi} + \boldsymbol{\varepsilon}^{t}\sqrt{1-t^2}\frac{\partial}{\partial t}\right)\right)\hat{\boldsymbol{y}} + \hat{\boldsymbol{y}}(\boldsymbol{\nu}\cdot\boldsymbol{\nabla}^*_{\hat{\boldsymbol{y}}}Y_{n,j}(\hat{\boldsymbol{y}})) \\
&= Y_{n,j}(\hat{\boldsymbol{y}})\left((\boldsymbol{\nu}\cdot\boldsymbol{\varepsilon}^{\varphi})\,\frac{1}{\sqrt{1-t^2}}\frac{\partial}{\partial\varphi}\hat{\boldsymbol{y}} + \left(\boldsymbol{\nu}\cdot\boldsymbol{\varepsilon}^{t}\right)\sqrt{1-t^2}\frac{\partial}{\partial t}\hat{\boldsymbol{y}}\right) \\
&\qquad + \sqrt{n(n+1)}\hat{\boldsymbol{y}}(\boldsymbol{\nu}\cdot\boldsymbol{y}^{(2)}_{n,j}(\hat{\boldsymbol{y}})) \\
&= Y_{n,j}(\hat{\boldsymbol{y}})\left((\boldsymbol{\nu}\cdot\boldsymbol{\varepsilon}^{\varphi})\,\boldsymbol{\varepsilon}^{\varphi} + \left(\boldsymbol{\nu}\cdot\boldsymbol{\varepsilon}^{t}\right)\boldsymbol{\varepsilon}^{t}\right) + \sqrt{n(n+1)}\hat{\boldsymbol{y}}\left(\boldsymbol{\nu}\cdot\boldsymbol{y}^{(2)}_{n,j}(\hat{\boldsymbol{y}})\right),
\end{aligned}$$

where we used the identities of Corollary 2.13 in the last step. Inserting these results into Eq. (A.2), we obtain

$$\begin{aligned}
&(\boldsymbol{\nu}\cdot\boldsymbol{\nabla}_{\boldsymbol{y}})\,\boldsymbol{h}^{(1)}_{n,j}(r;\boldsymbol{y}) \\
&= (\boldsymbol{\nu}\cdot\hat{\boldsymbol{y}})\frac{\partial}{\partial y}\boldsymbol{h}^{(1)}_{n,j}(r;y\hat{\boldsymbol{y}}) + \frac{1}{y}\left(\boldsymbol{\nu}\cdot\boldsymbol{\nabla}^*_{\hat{\boldsymbol{y}}}\right)\boldsymbol{h}^{(1)}_{n,j}(r;y\hat{\boldsymbol{y}}) \\
&= \frac{r^{n+1}}{y^{n+3}}\Bigg(-(n+2)(\boldsymbol{\nu}\cdot\hat{\boldsymbol{y}})\tilde{\boldsymbol{y}}^{(1)}_{n,j}(\hat{\boldsymbol{y}}) + \sqrt{\frac{n+1}{2n+1}}Y_{n,j}(\hat{\boldsymbol{y}})\left((\boldsymbol{\nu}\cdot\boldsymbol{\varepsilon}^{\varphi})\,\boldsymbol{\varepsilon}^{\varphi} + \left(\boldsymbol{\nu}\cdot\boldsymbol{\varepsilon}^{t}\right)\boldsymbol{\varepsilon}^{t}\right) \\
&\qquad + \sqrt{\frac{n(n+1)^2}{2n+1}}\hat{\boldsymbol{y}}\left(\boldsymbol{\nu}\cdot\boldsymbol{y}^{(2)}_{n,j}(\hat{\boldsymbol{y}})\right) - \sqrt{\frac{n}{2n+1}}(\boldsymbol{\nu}\cdot\boldsymbol{\nabla}^*_{\hat{\boldsymbol{y}}})\boldsymbol{y}^{(2)}_{n,j}(\hat{\boldsymbol{y}})\Bigg).
\end{aligned}$$

We further analyze the first two summands. Since $\boldsymbol{\nu}$ can also be represented in the local basis, that is $\boldsymbol{\nu} = (\boldsymbol{\nu}\cdot\boldsymbol{\varepsilon}^{\varphi})\boldsymbol{\varepsilon}^{\varphi} + (\boldsymbol{\nu}\cdot\boldsymbol{\varepsilon}^{t})\boldsymbol{\varepsilon}^{t} + (\boldsymbol{\nu}\cdot\hat{\boldsymbol{y}})\hat{\boldsymbol{y}}$, we use Eq. (A.3b) to obtain

$$\begin{aligned}
&-(n+2)(\boldsymbol{\nu}\cdot\hat{\boldsymbol{y}})\tilde{\boldsymbol{y}}^{(1)}_{n,j}(\hat{\boldsymbol{y}}) + \sqrt{\frac{n+1}{2n+1}}Y_{n,j}(\hat{\boldsymbol{y}})\left((\boldsymbol{\nu}\cdot\boldsymbol{\varepsilon}^{\varphi})\,\boldsymbol{\varepsilon}^{\varphi} + \left(\boldsymbol{\nu}\cdot\boldsymbol{\varepsilon}^{t}\right)\boldsymbol{\varepsilon}^{t}\right) \\
&= -(n+2)(\boldsymbol{\nu}\cdot\hat{\boldsymbol{y}})\tilde{\boldsymbol{y}}^{(1)}_{n,j}(\hat{\boldsymbol{y}}) + \sqrt{\frac{n+1}{2n+1}}Y_{n,j}(\hat{\boldsymbol{y}})\,(\boldsymbol{\nu} - (\boldsymbol{\nu}\cdot\hat{\boldsymbol{y}})\,\hat{\boldsymbol{y}}) \\
&= -(n+2)(\boldsymbol{\nu}\cdot\hat{\boldsymbol{y}})\left(\sqrt{\frac{n+1}{2n+1}}\boldsymbol{y}^{(1)}_{n,j}(\hat{\boldsymbol{y}}) - \sqrt{\frac{n}{2n+1}}\boldsymbol{y}^{(2)}_{n,j}(\hat{\boldsymbol{y}})\right) \\
&\qquad + \sqrt{\frac{n+1}{2n+1}}\left(\boldsymbol{\nu}Y_{n,j}(\hat{\boldsymbol{y}}) - (\boldsymbol{\nu}\cdot\hat{\boldsymbol{y}})\,\boldsymbol{y}^{(1)}_{n,j}(\hat{\boldsymbol{y}})\right) \\
&= (\boldsymbol{\nu}\cdot\hat{\boldsymbol{y}})\left(-(n+3)\sqrt{\frac{n+1}{2n+1}}\boldsymbol{y}^{(1)}_{n,j}(\hat{\boldsymbol{y}}) + (n+2)\sqrt{\frac{n}{2n+1}}\boldsymbol{y}^{(2)}_{n,j}(\hat{\boldsymbol{y}})\right) + \sqrt{\frac{n+1}{2n+1}}\boldsymbol{\nu}Y_{n,j}(\hat{\boldsymbol{y}}).
\end{aligned}$$

Inserting the last two results into Eq. (A.1), we obtain the desired result:

$$\begin{aligned}
\boldsymbol{\nabla}_{\boldsymbol{y}}B_{\boldsymbol{\nu}}(\boldsymbol{y}) &= (\boldsymbol{\nu}\cdot\boldsymbol{\nabla}_{\boldsymbol{y}})\left(\sum_{n=1}^{\infty}\sum_{j=1}^{2n+1}B_r^{\wedge}(n,j)\boldsymbol{h}^{(1)}_{n,j}(r;\boldsymbol{y})\right) \\
&= \sum_{n=1}^{\infty}\sum_{j=1}^{2n+1}B_r^{\wedge}(n,j)\Bigg(\frac{r^{n+1}}{y^{n+3}}\Bigg(-(n+2)(\boldsymbol{\nu}\cdot\hat{\boldsymbol{y}})\tilde{\boldsymbol{y}}^{(1)}_{n,j}(\hat{\boldsymbol{y}})
\end{aligned}$$

$$
\begin{aligned}
&+\sqrt{\frac{n+1}{2n+1}}Y_{n,j}(\hat{\boldsymbol{y}})\left((\boldsymbol{\nu}\cdot\boldsymbol{\varepsilon}^{\varphi})\,\boldsymbol{\varepsilon}^{\varphi}+\left(\boldsymbol{\nu}\cdot\boldsymbol{\varepsilon}^{t}\right)\boldsymbol{\varepsilon}^{t}\right)\\
&+\sqrt{\frac{n(n+1)^2}{2n+1}}\hat{\boldsymbol{y}}\left(\boldsymbol{\nu}\cdot\boldsymbol{y}^{(2)}_{n,j}(\hat{\boldsymbol{y}})\right)-\sqrt{\frac{n}{2n+1}}(\boldsymbol{\nu}\cdot\boldsymbol{\nabla}^{*}_{\hat{\boldsymbol{y}}})\boldsymbol{y}^{(2)}_{n,j}(\hat{\boldsymbol{y}})\Bigg)\Bigg)\\
=&\sum_{n=1}^{\infty}\sum_{j=1}^{2n+1}B_r^{\wedge}(n,j)\Bigg(+\sqrt{\frac{n+1}{2n+1}}\boldsymbol{\nu}Y_{n,j}(\hat{\boldsymbol{y}})\\
&+(\boldsymbol{\nu}\cdot\hat{\boldsymbol{y}})\left(-(n+3)\sqrt{\frac{n+1}{2n+1}}\boldsymbol{y}^{(1)}_{n,j}(\hat{\boldsymbol{y}})+(n+2)\sqrt{\frac{n}{2n+1}}\boldsymbol{y}^{(2)}_{n,j}(\hat{\boldsymbol{y}})\right)\\
&+\sqrt{\frac{n(n+1)^2}{2n+1}}\hat{\boldsymbol{y}}\left(\boldsymbol{\nu}\cdot\boldsymbol{y}^{(2)}_{n,j}(\hat{\boldsymbol{y}})\right)-\sqrt{\frac{n}{2n+1}}(\boldsymbol{\nu}\cdot\boldsymbol{\nabla}^{*}_{\hat{\boldsymbol{y}}})\boldsymbol{y}^{(2)}_{n,j}(\hat{\boldsymbol{y}})\Bigg)\Bigg).
\end{aligned}
$$

□

For numerical implementation, further calculations of the term $(\boldsymbol{\nu}\cdot\boldsymbol{\nabla}^{*})\boldsymbol{y}^{(2)}_{n,j}$ are required.

Lemma A.2. *The identity*

$$
\begin{aligned}
(\boldsymbol{\nu}\cdot\boldsymbol{\nabla}^{*}_{\hat{\boldsymbol{y}}})\boldsymbol{\nabla}^{*}_{\hat{\boldsymbol{y}}}Y_{n,j}(\hat{\boldsymbol{y}})&=(\boldsymbol{\nu}\cdot\boldsymbol{\varepsilon}^{\varphi})\frac{1}{\sqrt{1-t^2}}\left(t\boldsymbol{L}^{*}_{\hat{\boldsymbol{y}}}-\hat{\boldsymbol{y}}\frac{\partial}{\partial\varphi}+\boldsymbol{\nabla}^{*}_{\hat{\boldsymbol{y}}}\frac{\partial}{\partial\varphi}\right)Y_{n,j}(\hat{\boldsymbol{y}})\\
&+(\boldsymbol{\nu}\cdot\boldsymbol{\varepsilon}^{t})\left(\sqrt{1-t^2}\left(-\hat{\boldsymbol{y}}+\boldsymbol{\nabla}^{*}_{\hat{\boldsymbol{y}}}\right)\frac{\partial}{\partial t}-\frac{t}{\sqrt{1-t^2}}\boldsymbol{\nabla}^{*}_{\hat{\boldsymbol{y}}}+\frac{2t}{1-t^2}\boldsymbol{\varepsilon}^{\varphi}\frac{\partial}{\partial\varphi}\right)Y_{n,j}(\hat{\boldsymbol{y}})
\end{aligned}
\tag{A.4}
$$

holds true for all $n\in\mathbb{N}$, $j=1,\dots,2n+1$.

Proof. We use the product rule for the derivatives combined with Corollary 2.13 and obtain

$$
\begin{aligned}
&(\boldsymbol{\nu}\cdot\boldsymbol{\nabla}^{*}_{\hat{\boldsymbol{y}}})\boldsymbol{\nabla}^{*}_{\hat{\boldsymbol{y}}}Y_{n,j}(\hat{\boldsymbol{y}})\\
=&\left(\boldsymbol{\nu}\cdot\left(\boldsymbol{\varepsilon}^{\varphi}\frac{1}{\sqrt{1-t^2}}\frac{\partial}{\partial\varphi}+\boldsymbol{\varepsilon}^{t}\sqrt{1-t^2}\frac{\partial}{\partial t}\right)\right)\boldsymbol{\nabla}^{*}_{\hat{\boldsymbol{y}}}Y_{n,j}(\hat{\boldsymbol{y}})\\
=&(\boldsymbol{\nu}\cdot\boldsymbol{\varepsilon}^{\varphi})\frac{1}{\sqrt{1-t^2}}\frac{\partial}{\partial\varphi}\left(\boldsymbol{\varepsilon}^{\varphi}\frac{1}{\sqrt{1-t^2}}\frac{\partial}{\partial\varphi}+\boldsymbol{\varepsilon}^{t}\sqrt{1-t^2}\frac{\partial}{\partial t}\right)Y_{n,j}(\hat{\boldsymbol{y}})\\
&+(\boldsymbol{\nu}\cdot\boldsymbol{\varepsilon}^{t})\sqrt{1-t^2}\frac{\partial}{\partial t}\left(\boldsymbol{\varepsilon}^{\varphi}\frac{1}{\sqrt{1-t^2}}\frac{\partial}{\partial\varphi}+\boldsymbol{\varepsilon}^{t}\sqrt{1-t^2}\frac{\partial}{\partial t}\right)Y_{n,j}(\hat{\boldsymbol{y}})\\
=&(\boldsymbol{\nu}\cdot\boldsymbol{\varepsilon}^{\varphi})\left(\left(t\boldsymbol{\varepsilon}^{t}-\sqrt{1-t^2}\hat{\boldsymbol{y}}\right)\frac{1}{1-t^2}\frac{\partial}{\partial\varphi}+\boldsymbol{\varepsilon}^{\varphi}\frac{1}{1-t^2}\frac{\partial^2}{\partial\varphi^2}-t\boldsymbol{\varepsilon}^{\varphi}\frac{\partial}{\partial t}+\boldsymbol{\varepsilon}^{t}\frac{\partial^2}{\partial\varphi\partial t}\right)Y_{n,j}(\hat{\boldsymbol{y}})\\
&+(\boldsymbol{\nu}\cdot\boldsymbol{\varepsilon}^{t})\left(\boldsymbol{\varepsilon}^{\varphi}\frac{\partial^2}{\partial t\partial\varphi}+\boldsymbol{\varepsilon}^{\varphi}\frac{t}{1-t^2}\frac{\partial}{\partial\varphi}-\sqrt{1-t^2}\hat{\boldsymbol{y}}\frac{\partial}{\partial t}+\boldsymbol{\varepsilon}^{t}(1-t^2)\frac{\partial^2}{\partial t^2}-t\boldsymbol{\varepsilon}^{t}\frac{\partial}{\partial t}\right)Y_{n,j}(\hat{\boldsymbol{y}})\\
=&(\boldsymbol{\nu}\cdot\boldsymbol{\varepsilon}^{\varphi})\frac{1}{\sqrt{1-t^2}}\left(t\boldsymbol{L}^{*}_{\hat{\boldsymbol{y}}}-\hat{\boldsymbol{y}}\frac{\partial}{\partial\varphi}+\boldsymbol{\nabla}^{*}_{\hat{\boldsymbol{y}}}\frac{\partial}{\partial\varphi}\right)Y_{n,j}(\hat{\boldsymbol{y}})\\
&+(\boldsymbol{\nu}\cdot\boldsymbol{\varepsilon}^{t})\left(\sqrt{1-t^2}\left(-\hat{\boldsymbol{y}}+\boldsymbol{\nabla}^{*}_{\hat{\boldsymbol{y}}}\right)\frac{\partial}{\partial t}-\frac{t}{\sqrt{1-t^2}}\boldsymbol{\nabla}^{*}_{\hat{\boldsymbol{y}}}+\frac{2t}{1-t^2}\boldsymbol{\varepsilon}^{\varphi}\frac{\partial}{\partial\varphi}\right)Y_{n,j}(\hat{\boldsymbol{y}}).
\end{aligned}
$$

The last step can be verified by inserting the definition of the surface curl and the surface gradient into the equation from Theorem 2.14, which results into a lengthy calculation. □

List of Figures

List of Tables

Bibliography

[1] L.R. Abramo, P.H. Reimberg, and H.S. Xavier. CMB in a box: causal structure and the Fourier-Bessel expansion. *Phys. Rev. D* **82** (2010), 043510.

[2] M. Abramowitz and I.A. Stegun. *Handbook of Mathematical Functions with Formulas, Graphs, and Mathematical Tables*. New York: Dover Publications, Inc., 1974.

[3] M. Akram, I. Amina, and V. Michel. A study of differential operators for complete orthonormal systems on a 3D ball. *Int. J. Pure Appl. Math.* **73** (2011), 489–506.

[4] M. Akram and V. Michel. Regularisation of the Helmholtz decomposition and its application to geomagnetic field modelling. *Int. J. Geomath.* **1** (2010), 101–120.

[5] A. Albertella, F. Sansò, and N. Sneeuw. Band-limited functions on a bounded spherical domain: the Slepian problem on the sphere. *J. Geodesy* **73** (1999), 436–447.

[6] A. Amirbekyan. *The Application of Reproducing Kernel Based Spline Approximation to Seismic Surface and Body Wave Tomography: Theoretical Aspects and Numerical Results*. PhD thesis. University of Kaiserslautern, Department of Mathematics, Geomathematics Group, 2007. URL: `http://nbn-resolving.de/urn:nbn:de:hbz:386-kluedo-21039`.

[7] A. Amirbekyan and V. Michel. Splines on the three-dimensional ball and their application to seismic body wave tomography. *Inverse Probl.* **24** (2008), 015022.

[8] G.B. Arfken. *Mathematical Methods for Physicists*. 3rd ed. Orlando: Academic Press, 1985.

[9] N. Aronszajn. Theory of reproducing kernels. *T. Am. Math. Soc.* **68** (1950), 337–404.

[10] H. Aurlien, I.O. Gjerde, J.H. Aarseth, G. Eldøen, B. Karlsen, H. Skeidsvoll, and N.E. Gilhus. EEG background activity described by a large computerized database. *Clin. Neurophysiol.* **115** (2004), 665–673.

[11] J. Awrejcewicz. *Ordinary Differential Equations and Mechanical Systems*. Cham: Springer International Publishing, 2014.

[12] G. Backus, R.L. Parker, and C. Constable. *Foundations of Geomagnetism*. Cambridge: Cambridge University Press, 1996.

[13] L. Ballani, J. Engels, and E.W. Grafarend. Global base functions for the mass density in the interior of a massive body (Earth). *Manuscr. Geodaet.* **18** (1993), 99–114.

[14] L. Ballani and D. Stromeyer. *On the structure of uniqueness in linear inverse source source problems*. In: *Theory and Practice of Geophysical Data Inversion*. Proc. of the 8th Int. Math. Geophys. Seminar on Model Optimization in Exploration Geophysics 1990. (Berlin). Ed. by A. Vogel, A. Sarwar, R. Gorenflo, and O. Kounchev. Vol. 5. Theory and Practice of Applied Geophysics. Wiesbaden: Vieweg+Teubner, 1992, 85–98.

[15] L. Baratchart and C. Gerhards. On the recovery of core and crustal components of geomagnetic potential fields. *SIAM J. Appl. Math.* **77** (2017), 1756–1780.

[16] R. Barzaghi and F. Sansò. Remarks on the inverse gravimetric problem. *Geophys. J.* **92** (1988), 505–511.

[17] F. Bauer, M. Gutting, and M.A. Lukas. *Evaluation of parameter choice methods for regularization of ill-posed problems in geomathematics*. In: *Handbook of Geomathematics*. Ed. by W. Freeden, M.Z. Nashed, and T. Sonar. 2nd ed. Berlin, Heidelberg: Springer, 2015, 1713–1774.

[18] F. Bauer and M.A. Lukas. Comparing parameter choice methods for regularization of ill-posed problems. *Math. Comput. Simulat.* **81** (2011), 1795–1841.

[19] H. Bauer. *Measure and Integration Theory*. De Gruyter Studies in Mathematics. Berlin: De Gruyter, 2001.

[20] M. Bayer. *Geomagnetic Field Modelling From Satellite Data by First and Second Generation Vector Wavelets*. PhD thesis. Shaker-Verlag Aachen: University of Kaiserslautern, Department of Mathematics, Geomathematics Group, 2000.

[21] M. Bayer, S. Beth, and W. Freeden. Geophysical field modelling by multiresolution analysis. *Acta Geod. Geoph. Hung.* **33** (1998), 289–319.

[22] P. Berkel. *Multiscale Methods for the Combined Inversion of Normal Mode and Gravity Variations*. PhD thesis. Shaker-Verlag Aachen: University of Kaiserslautern, Department of Mathematics, Geomathematics Group, 2009.

[23] P. Berkel, D. Fischer, and V. Michel. Spline multiresolution and numerical results for joint gravitation and normal-mode inversion with an outlook on sparse regularisation. *Int. J. Geomath.* **1** (2010), 167–204.

[24] P. Berkel and V. Michel. On mathematical aspects of a combined inversion of gravity and normal mode variations by a spline method. *Math. Geosci.* **42** (2010), 795–816.

[25] S. Beth. *Multiscale Approximation by Vector Radial Basis Functions on the Sphere*. PhD thesis. Shaker-Verlag Aachen: University of Kaiserslautern, Department of Mathematics, Geomathematics Group, 2000.

[26] G. Beutler, M.R. Drinkwater, R. Rummel, and R. Von Steiger, eds. *Earth Gravity Field from Space – From Sensors to Earth Sciences*. Dordrecht: Springer, 2003.

[27] A. Bjerhammar. *Gravity reduction to a spherical surface of reference*. Tech. rep. Div. Geodesy. Stockholm: Royal Institute of Technology, 1962.

[28] R.J. Blakely. *Potential Theory in Gravity and Magnetic Applications*. Cambridge: Cambridge University Press, 1995.

[29] C. Canuto and A. Tabacco. *Mathematical Analysis II*. 2nd ed. Cham: Springer, 2015.

[30] B.F. Chao. On inversion for mass distribution from global (time-variable) gravity field. *J. Geodyn.* **39** (2005), 223–230.

[31] C.W. Clenshaw. A note on the summation of Chebyshev series. *Math. Comp.* **9** (1955), 118–120.

[32] M. Clerc, J. Leblond, J.-P. Marmorat, and C. Papageorgakis. Uniqueness result for an inverse conductivity recovery problem with application to EEG. *Rend. Istit. Mat. Univ. Trieste* **48** (2016), 385–406.

[33] D. Cohen and E. Halgren. *Magnetoencephalography*. In: *Encyclopedia of Neuroscience*. Ed. by L.R. Squire. Vol. 5. Oxford: Academic Press, 2009, 615–622.

[34] D. Colton and R. Kress. *Inverse Acoustic and Electromagnetic Scattering Theory.* 3rd ed. Berlin, Heidelberg: Springer, 2013.

[35] S.D. Conte and C. de Boor. *Elementary Numerical Analysis. An Algorithmic Approach.* 2nd ed. New York: McGraw-Hill, 1972.

[36] D.M. Cook. *The Theory of the Electromagnetic Field.* Mineola NY: Courier Dover Publications, 2002.

[37] F.A. Dahlen and F.J. Simons. Spectral estimation on a sphere in geophysics and cosmology. *Geophys. J. Int.* **174** (2008), 774–807.

[38] G. Dassios. What is recoverable in the inverse magnetoencephalography problem? *Contemp. Math.* **408** (2006): *Inverse Problems, Multi-Scale Analysis and Effective Medium Theory.* Ed. by H. Ammari and H. Kang, 181–200.

[39] G. Dassios. The magnetic potential for the ellipsoidal MEG problem. *J. Comp. Math.* **25** (2007), 145–156.

[40] G. Dassios. Neuronal currents and EEG-MEG fields. *Math. Med. Biol.* **25** (2008), 133–139.

[41] G. Dassios. The scalar magnetic potential in magnetoencephalography. *J. Phys.: Conf. Ser.* **124** (2008), 012020.

[42] G. Dassios. *Electric and magnetic activity of the brain in spherical and ellipsoidal geometry.* In: *Mathematical Modeling in Biomedical Imaging I.* Ed. by H. Ammari. Lecture Notes in Mathematics. Berlin, Heidelberg: Springer, 2009. Chap. 4, 133–202.

[43] G. Dassios. *Ellipsoidal Harmonics.* Cambridge: Cambridge University Press, 2009.

[44] G. Dassios and A.S. Fokas. Electro-magneto-encephalography and fundamental solutions. *Q. Appl. Math.* **67** (2009), 771–780.

[45] G. Dassios and A.S. Fokas. Electro-magneto-encephalography for a three-shell model: dipoles and beyond for the spherical geometry. *Inverse Probl.* **25** (2009), 035001.

[46] G. Dassios and A.S. Fokas. Electro-magneto-encephalography for the three-shell model: a single dipole in ellipsoidal geometry. *Math. Meth. Appl. Sci.* **35** (2012), 1415–1422.

[47] G. Dassios and A.S. Fokas. The definite non-uniqueness results for deterministic EEG and MEG data. *Inverse Probl.* **29** (2013), 065012.

[48] G. Dassios, A.S. Fokas, and D. Hadjiloizi. On the complementarity of electroencephalography and magnetoencephalography. *Inverse Probl.* **23** (2007), 2541–2549.

[49] G. Dassios, A.S. Fokas, P. Hashemzadeh, and R.M. Leahy. EEG for current with two-dimensional support. *IEEE Trans. Biomed. Eng.* **65** (2018), 2101–2108.

[50] G. Dassios, A.S. Fokas, and F. Kariotou. On the non-uniqueness of the inverse MEG problem. *Inverse Probl.* **21** (2005), L1–L5.

[51] G. Dassios, S.N. Giapalaki, A.N. Kandili, and F. Kariotou. The exterior magnetic field for the multilayer ellipsoidal model of the brain. *Q. J. Mech. Appl. Math.* **60** (2007), 1–25.

[52] G. Dassios and D. Hadjiloizi. On the non-uniqueness of the inverse problem associated with electroencephalography. *Inverse Probl.* **25** (2009), 115012.

[53] G. Dassios, D. Hadjiloizi, and F. Kariotou. The octapolic ellipsoidal term in magnetoencephalography. *J. Math. Phys.* **50** (2009), 013508.

[54] G. Dassios and F. Kariotou. Magnetoencephalography in ellipsoidal geometry. *J. Math. Phys.* **44** (2003), 220–241.

[55] G. Dassios and F. Kariotou. On the exterior magnetic field and silent sources in magnetoencephalography. *Abstr. Appl. Anal.* **2004** (2004), 307–314.

[56] G. Dassios and F. Kariotou. The direct MEG problem in the presence of an ellipsoidal shell inhomogeneity. *Q. Appl. Math.* **63** (2005), 601–618.

[57] P.J. Davis. *Interpolation and Approximation*. New York: Dover Publications, 1975.

[58] J.R. Driscoll and D.M. Healy. Computing Fourier transforms and convolutions on the 2-sphere. *Adv. Appl. Math.* **15** (1994), 202–250.

[59] H.M. Dufour. Fonctions orthogonales dans la sphère résolution théorique du problème du potential terrestre. *B. Geod.* **51** (1977), 227–237.

[60] A.M. Dziewonski and D.L. Anderson. Preliminary reference Earth model. *Phys. Earth Planet In.* **25** (1981), 297–356.

[61] A.R. Edmonds. *Angular Momentum in Quantum Mechanics*. Princeton: Princeton University Press, 1957.

[62] Elekta Neuromag. *Elekta Neuromag System Hardware Technical Manual. Revision F.* 2005. URL: `http://imaging.mrc-cbu.cam.ac.uk/meg/VectorviewDescription?action=AttachFile&do=get&target=HardwareTechnical.pdf` (visited on 29/06/2018).

[63] H.W. Engl, M. Hanke, and A. Neubauer. *Regularization of Inverse Problems*. Dordrecht: Kluwer Academic Publishers, 1996.

[64] L.C. Evans. *Partial Differential Equations*. Vol. 19. Graduate Studies in Mathematics. Providence, Rhode Island: American Mathematical Society (AMS), 1998.

[65] M.J. Fengler, D. Michel, and V. Michel. Harmonic spline-wavelets on the 3-dimensional ball and their application to the reconstruction of the Earth's density distribution from gravitational data at arbitrarily shaped satellite orbits. *J. Appl. Math. Mech.* **86** (2006), 856–873.

[66] D. Fischer. *Sparse Regularization of a Joint Inversion of Gravitational Data and Normal Mode Anomalies*. PhD thesis. Verlag Dr. Hut Munich: University of Siegen, Department of Mathematics, Geomathematics Group, 2011. URL: `http://dokumentix.ub.uni-siegen.de/opus/volltexte/2012/544/`.

[67] D. Fischer and V. Michel. Sparse regularization of inverse gravimetry – case study: spatial and temporal mass variations in South America. *Inverse Probl.* **28** (2012), 065012.

[68] D. Fischer and V. Michel. Automatic best-basis selection for geophysical tomographic inverse problems. *Geophys. J. Int.* **193** (2013), 1291–1299.

[69] D. Fischer and V. Michel. Inverting GRACE gravity data for local climate effects. *J. Geo. S.* **3** (2013), 151–162.

[70] T. Fließbach. *Mechanik*. Berlin, Heidelberg: Springer, 2015.

[71] A.S. Fokas. Electro-magneto-encephalography for a three-shell model: distributed current in arbitrary, spherical and ellipsoidal geometries. *J. R. Soc. Interface* **6** (2009), 479–488.

[72] A.S. Fokas, I.M. Gel-fand, and Y. Kurylev. Inversion method for magnetoencephalography. *Inverse Probl.* **12** (1996), L9–L11.

[73] A.S. Fokas, O. Hauk, and V. Michel. Electro-magneto-encephalography for the three-shell model: numerical implementation via splines for distributed current in spherical geometry. *Inverse Probl.* **28** (2012), 035009.

[74] A.S. Fokas and Y. Kurylev. Electro-magneto-encephalography for the three-shell model: minimal L^2-norm in spherical geometry. *Inverse Probl.* **28** (2012), 035010.

[75] A.S. Fokas, Y. Kurylev, and V. Marinakis. The unique determination of neuronal currents in the brain via magnetoencephalography. *Inverse Probl.* **20** (2004), 1067–1082.

[76] M. Fornasier and F. Pitolli. Adaptive iterative thresholding algorithms for magneto-encephalography (MEG). *J. Comput. Appl. Math.* **221** (2008), 386–395.

[77] I. Fredholm. Sur une classe d'équations fonctionnelles. *Acta Math.* **27** (1903), 365–390.

[78] W. Freeden. *Multiscale Modelling of Spaceborne Geodata.* Stuttgart: B. G. Teubner, 1999.

[79] W. Freeden and C. Gerhards. *Geomathematically Oriented Potential Theory.* Pure and Applied Mathematics. Boca Raton: Chapman and Hall/CRC, 2012.

[80] W. Freeden and T. Gervens. Vector spherical spline interpolation – basic theory and computational aspects. *Math. Methods. Appl. Sci.* **16** (1993), 151–183.

[81] W. Freeden, T. Gervens, and M. Schreiner. *Constructive Approximation on the Sphere (With Applications to Geomathematics).* Oxford: Oxford University Press, 1998.

[82] W. Freeden, O. Glockner, and R. Litzenberger. A general Hilbert space approach to wavelets and its application in geopotential determination. *Numer. Func. Anal. Opt.* **20** (1999), 853–879.

[83] W. Freeden and M. Gutting. On the completeness and closure of vector and tensor spherical harmonics. *Integ. Transf. Spec. Func.* **19** (2008), 713–734.

[84] W. Freeden and M. Gutting. *Special Functions of Mathematical (Geo-)Physics.* Basel: Birkhäuser, 2013.

[85] W. Freeden and V. Michel. *Multiscale Potential Theory.* Boston: Birkhäuser, 2004.

[86] W. Freeden, V. Michel, and F.J. Simons. *Spherical harmonics based special function systems and constructive approximation methods.* In: *Handbook of Mathematical Geodesy.* Ed. by W. Freeden and M.Z. Nashed. Basel: Birkhäuser, 2018, 753–819.

[87] W. Freeden, M.Z. Nashed, and T. Sonar, eds. *Handbook of Geomathematics.* 2nd ed. Berlin, Heidelberg: Springer, 2015.

[88] W. Freeden and M. Schreiner. *Spherical Functions of Mathematical Geosciences. A Scalar, Vectorial and Tensorial Setup.* Berlin: Springer, 2009.

[89] W. Freeden and M. Schreiner. *Special functions in mathematical geosciences: an attempt at a categorization.* In: *Handbook of Geomathematics.* Ed. by W. Freeden, M.Z. Nashed, and T. Sonar. Berlin Heidelberg: Springer, 2010, 925–948.

[90] L. Gårding. *Some Points of Analysis and Their History*. Vol. 11. University Lecture Series. Providence, Rhode Island: American Mathematical Society (AMS), 1997.

[91] C. Gerhards. *Spherical Multiscale Methods in Terms of Locally Supported Wavelets: Theory and Application to Geomagnetic Modeling*. PhD thesis. Verlag Dr. Hut Munich: University of Kaiserslautern, Department of Mathematics, Geomathematics Group, 2011.

[92] C. Gerhards. *Fully normalized Morse-Feshbach vector spherical harmonics (Matlab code)*. Personal Communication. University of Siegen, Department of Mathematics, Geomathematics Group, 2014.

[93] C. Gerhards. On the unique reconstruction of induced spherical magnetizations. *Inverse Probl.* **32** (2016), 015002.

[94] D.B. Geselowitz. On the magnetic field generated outside an inhomogeneous volume conductor by internal current sources. *IEEE Trans. Magn.* **6** (1970), 346–347.

[95] S.N. Giapalaki and F. Kariotou. The complete ellipsoidal shell-model in EEG imaging. *Abstr. Appl. Anal.* **2006** (2006), 1–18.

[96] G.H. Golub and C.F. van Loan. *Matrix Computation*. 3rd ed. Baltimore and London: The Johns Hopkins University Press, 1996.

[97] I.G. Graham and I.H. Sloan. On the compactness of certain integral operators. *J. Math. Anal. Appl.* **68** (1979), 580–594.

[98] A. Gramfort, M. Luessi, E. Larson, D.A. Engemann, D. Strohmeier, C. Brodbeck, L. Parkkonen, and M.S. Hämäläinen. MNE software for processing MEG and EEG data. *NeuroImage* **86** (2014), 446–460.

[99] R. Grech, T. Cassar, J. Muscat, K.P. Camilleri, S.G. Fabri, M. Zervakis, P. Xanthopoulos, V. Sakkalis, and B. Vanrumste. Review on solving the inverse problem in EEG source analysis. *J. Neuroeng. Rehabil.* **5** (2008), 25.

[100] C.W. Groetsch. *Generalized Inverses of Linear Operators*. New York and Basel: Marcel Dekker, 1977.

[101] C.W. Groetsch. On a regularization–Ritz method for Fredholm equations of the first kind. *J. Integral Equat.* **4** (1982), 173–182.

[102] C.W. Groetsch. *The Theory of Tikhonov Regularization for Fredholm Equations of the First Kind*. Boston: Pitman Advanced Publishing Program, 1984.

[103] C.W. Groetsch and J. Guacaneme. Regularized Ritz approximations for Fredholm equations of the first kind. *Rocky. Mt. J. Math.* **15** (1985), 33–38.

[104] J. Gross, S. Baillet, G.R. Barnes, R.N. Henson, A. Hillebrand, O. Jensen, K. Jerbi, V. Litvak, B. Maess, R. Oostenveld, L. Parkkonen, J.R. Taylor, V. van Wassenhove, M. Wibral, and J.-M. Schoffelen. Good practice for conducting and reporting MEG research. *NeuroImage* **65** (2013), 349–363.

[105] M. Gutting, B. Kretz, V. Michel, and R. Telschow. Study on parameter choice methods for the RFMP with respect to downward continuation. *Front. Appl. Math. Stat.* **3** (2017). Article 10.

[106] J. Hadamard. Sur les problèmes aux dérivés partielles et leur signification physique. *Princeton University Bulletin* **13** (1902), 49–52.

[107] J. Hadamard. *Lectures on Cauchy's Problem in Linear Partial Differential Equations*. Reprint of the original from 1923. Mineola, New York: Dover Publications, 1952.

[108] M.S. Hämäläinen, R. Hari, R.J. Ilmoniemi, J. Knuutila, and O.V. Lounasmaa. Magnetoencephalography – theory, instrumentation, and applications to noninvasive studies of the working human brain. *Rev. Mod. Phys.* **65** (1993), 413–505.

[109] M.S. Hämäläinen and R.J. Ilmoniemi. Interpreting magnetic fields of the brain: minimum norm estimates. *Med. Biol. Eng. Comput.* **32** (1994), 35–42.

[110] M.S. Hämäläinen and J. Sarvas. Feasibility of the homogeneous head model in the interpretation of neuromagnetic fields. *Phys. Med. Biol.* **32** (1987), 91–97.

[111] W.W. Hansen. A new type of expansion in radiation problems. *Phys. Rev.* **47** (1934), 139–143.

[112] W.W. Hansen and J.G. Beckerley. Radiation from an antenna over a plane earth of arbitrary characteristics. *J. Appl. Phys.* **7** (1936), 220.

[113] R. Hari and A. Puce. *MEG-EEG Primer*. New York: Oxford University Press, 2017.

[114] P. Hashemzadeh and A.S. Fokas. *BVP for EEG spherical geometry*. Personal Communication. DAMTP, 2017.

[115] O. Hauk. Keep it simple: a case for using classical minimum norm estimation in the analysis of EEG and MEG data. *NeuroImage* **21** (2004), 1612–1621.

[116] O. Hauk. *MEG and EEG measurement data*. Personal Communication. MRC Cognition and Brain Sciences Unit, Cambridge, UK, 2013.

[117] B. He, ed. *Modeling and Imaging of Bioelectrical Activity: Principles and Applications*. Bioelectric Engineering. New York: Kluwer Academic Publishers, 2005.

[118] C. Heil. *A Basis Theory Primer*. Boston: Birkhäuser, 2011.

[119] H. Helmholtz. Ueber einige Gesetze der Vertheilung elektrischer Ströme in körperlichen Leitern mit Anwendung auf die thierisch-elektrischen Versuche. *Ann. Phys. (Berlin)* **165** (1853), 211–233.

[120] H. Heuser. *Lehrbuch der Analysis Teil 1*. 12th ed. Stuttgart, Leipzig, Wiesbaden: B.G. Teubner, 1998.

[121] N.J. Higham. The accuracy of floating point summation. *SIAM J. Sci. Comput.* **14** (1993), 783–799.

[122] F.G. Hillary and J. DeLuca, eds. *Functional Neuroimaging in Clinical Populations*. New York: The Guilford Press, 2007.

[123] L. Hörmander. *The Analysis of Linear Partial Differential Operators I*. Berlin, Heidelberg: Springer, 1983.

[124] T. Hsing and R. Eubank. *Theoretical Foundations of Functional Data Analysis, with an Introduction to Linear Operators*. New York: John Wiley & Sons, 2015.

[125] M.X. Huang, J.C. Mosher, and R.M. Leahy. A sensor-weighted overlapping-sphere head model and exhaustive head model comparison for MEG. *Phys. Med. Biol.* **44** (1999), 423–440.

[126] R. Ilmoniemi, M. Hämäläinen, and J. Knuutila. *The forward and inverse problems in the spherical model*. In: *Biomagnetism: Applications and Theory*. Proc. 5th World Conf. on Biomagnetism. (Vancouver, Canada, Aug. 1984). Ed. by H. Weinberg, G. Stroink, and T. Katila. New York: Pergamon Press, 1985, 278–282.

[127] V. Isakov. *Inverse Problems for Partial Differential Equations*. 2nd ed. New York: Springer, 2006.

[128] A. Ishtiaq. *Modified Reuter grid (Matlab code)*. Personal Communication. University of Siegen, Department of Mathematics, Geomathematics Group, 2015.

[129] A. Ishtiaq. *Grid points and Generalized Discrepancies on the d-dimensional Ball*. PhD thesis. University of Siegen, Department of Mathematics, Geomathematics Group, 2018. URL: `http://dokumentix.ub.uni-siegen.de/opus/volltexte/2018/1373/`.

[130] A. Ishtiaq and V. Michel. Pseudo-differential operators, cubature and equidistribution on the 3D ball: an approach based on orthonormal basis systems. *Numer. Func. Anal. Opt.* **38** (2017), 891–910.

[131] L. Jantscher. *Distributionen*. Berlin: Walter de Gruyter, 1971.

[132] Jet Propulsion Laboratory. *GRACE*. 2002. URL: `https://grace.jpl.nasa.gov` (visited on 18/05/2018).

[133] E.R. Kandel, J.H. Schwartz, T.M. Jessell, S.A. Siegelbaum, and A.J. Hudspeth. *Principles of Neural Science*. 5th ed. New York: McGraw-Hill Medical, 2013.

[134] W.M. Kaula. Statistical and harmonic analysis of gravity. *J. Geophys. Res.* **64** (1959), 2401–2421.

[135] O.D. Kellogg. *Foundations of Potential Theory*. Berlin, Heidelberg: Springer, 1967.

[136] A. Kirsch. *An Introduction to the Mathematical Theory of Inverse Problems*. 2nd ed. Vol. 120. Applied Mathematical Sciences. New York: Springer, 2011.

[137] M. Kontak. *Novel Algorithms of Greedy-type for Probability Density Estimation as well as Linear and Nonlinear Inverse Problems*. PhD thesis. University of Siegen, Department of Mathematics, Geomathematics Group, 2018. URL: `http://dokumentix.ub.uni-siegen.de/opus/volltexte/2018/1316/`.

[138] M. Kontak and V. Michel. The regularized weak functional matching pursuit for linear inverse problems. *J. Inverse Ill-Posed Probl.* (2018). Pre-published.

[139] E. Landau. *Handbuch der Lehre von der Verteilung der Primzahlen*. Leipzig: B. G. Teubner, 1909.

[140] H.J. Landau and H.O. Pollak. Prolate Spheroidal Wave Functions, Fourier Analysis and Uncertainty - II. *Bell Syst. Tech. J.* **40** (1961), 65–84.

[141] H. Lass. *Vector and Tensor Analysis*. New York: McGraw Hill, 1950.

[142] P.D. Lax. *Functional Analysis*. New York: John Wiley & Sons, 2002.

[143] J.M. Lee. *Manifolds and Differential Geometry*. Providence: American Mathematical Society, 2009.

[144] B. Leistedt and J.D. McEwen. Exact wavelets on the ball. *IEEE Trans. Signal. Process.* **60** (2012), 6257–6269.

[145] S. Leweke. *TikZ picture of EEG and MEG setting*. Personal Communication. 2015.

[146] S. Leweke, V. Michel, and N. Schneider. Vectorial Slepian functions on the ball. *Numer. Func. Anal. Opt.* **39** (2018), 1120–1152.

[147] S. Leweke, V. Michel, and R. Telschow. *On the non-uniqueness of gravitational and magnetic field data inversion (survey article)*. In: *Handbook of Mathematical Geodesy*. Ed. by W. Freeden and M.Z. Nashed. Basel: Birkhäuser, 2018, 883–919.

[148] A.K. Louis. *Inverse und schlecht gestellte Probleme*. Stuttgart: B.G. Teubner, 1989.

[149] S. Lu and P. Mathé. Heuristic parameter selection based on functional minimization: optimality and model function approach. *Math. Comput.* **82** (2013), 1609–1630.

[150] T. Maier. *Multiscale Geomagnetic Field Modelling from Satellite Data: Theoretical Aspects and Numerical Application*. PhD thesis. University of Kaiserslautern, Department of Mathematics, Geomathematics Group, 2003. URL: `http://nbn-resolving.de/urn:nbn:de:bsz:386-kluedo-15533`.

[151] S.G. Mallat and Z. Zhang. Matching pursuits with time-frequency dictionaries. *IEEE Trans. Signal. Process.* **41** (1993), 3397–3415.

[152] C. Mayer. *Wavelet Modelling of Ionospheric Currents and Induced Magnetic Fields from Satellite Data*. PhD thesis. University of Kaiserslautern, Department of Mathematics, Geomathematics Group, 2003. URL: `http://nbn-resolving.de/urn:nbn:de:bsz:386-kluedo-16236`.

[153] C. Mayer. Wavelet decomposition of spherical vector fields with respect to sources. *J. Fourier Anal. Appl.* **12** (2006).

[154] V. Michel. *A Multiscale Method for the Gravimetry Problem*. PhD thesis. Shaker-Verlag Aachen: University of Kaiserslautern, Department of Mathematics, Geomathematics Group, 1999.

[155] V. Michel. *A Multiscale Approximation for Operator Equations in Separable Hilbert Spaces – Case Study: Reconstruction and Description of the Earth's Interior*. Habilitation thesis. Shaker-Verlag Aachen: University of Kaiserslautern, Department of Mathematics, Geomathematics Group, 2002.

[156] V. Michel. Regularized wavelet-based multiresolution recovery of the harmonic mass density distribution from data of the Earth's gravitational field at satellite height. *Inverse Probl.* **21** (2005), 997–1025.

[157] V. Michel. Wavelets on the 3-dimensional ball. *Proc. Appl. Math. Mech.* **5** (2005), 775–776.

[158] V. Michel. *Lectures on Constructive Approximation. Fourier, Spline, and Wavelet Methods on the Real Line, the Sphere, and the Ball*. New York: Birkhäuser, 2013.

[159] V. Michel. *RFMP: an iterative best basis algorithm for inverse problems in the geosciences*. In: *Handbook of Geomathematics*. Ed. by W. Freeden, M.Z. Nashed, and T. Sonar. 2nd ed. Berlin, Heidelberg: Springer, 2015, 2121–2147.

[160] V. Michel. *Tomography: problems and multiscale solutions*. In: *Handbook of Geomathematics*. Ed. by W. Freeden, M.Z. Nashed, and T. Sonar. 2nd ed. Berlin, Heidelberg: Springer, 2015, 2087–2119.

[161] V. Michel and A.S. Fokas. A unified approach to various techniques for the non-uniqueness of the inverse gravimetric problem and wavelet-based methods. *Inverse Probl.* **24** (2008), 045019.

[162] V. Michel and S. Orzlowski. On the null space of a class of Fredholm integral equations of the first kind. *J. Inverse Ill-Posed Probl.* **24** (2016), 687–710.

[163] V. Michel and S. Orzlowski. On the convergence theorem for the regularized functional matching pursuit (RFMP) algorithm. *Int. J. Geomath.* **8** (2017), 183–190.

[164] V. Michel and F.J. Simons. A general approach to regularizing inverse problems with regional data using Slepian wavelets. *Inverse Probl.* **33** (2017), 125016.

[165] V. Michel and R. Telschow. A non-linear approximation method on the sphere. *Int. J. Geomath.* **5** (2014), 195–224.

[166] V. Michel and R. Telschow. The regularized orthogonal functional matching pursuit for ill-posed inverse problems. *SIAM J. Numer. Anal.* **54** (2016), 262–287.

[167] V. Michel and K. Wolf. Numerical aspects of a spline-based multiresolution recovery of the harmonic mass density out of gravity functionals. *Geophys. J. Int.* **173** (2008), 1–16.

[168] H. Moritz. *The Figure of the Earth. Theoretical Geodesy and the Earth's Interior*. Karlsruhe: Wichmann Verlag, 1990.

[169] P.M. Morse and H. Feshbach. *Methods of Theoretical Physics*. Vol. 1. New York: McGraw-Hill, 1953.

[170] P.M. Morse and H. Feshbach. *Methods of Theoretical Physics*. Vol. 2. New York: McGraw-Hill, 1953.

[171] J.C. Mosher, R.M. Leahy, and P.S. Lewis. EEG and MEG: forward solutions for inverse methods. *IEEE Trans. Biomed. Eng.* **46** (1999), 245–259.

[172] MRC Cognition and Brain Sciences Unit. *The Elekta Neuromag Vectorview System*. 2013. URL: `http://imaging.mrc-cbu.cam.ac.uk/meg/VectorviewDescription` (visited on 19/05/2018).

[173] C. Müller. *Spherical Harmonics*. Lecture Notes in Mathematics. Berlin, Heidelberg: Springer, 1966.

[174] J.C. de Munck. The potential distribution in a layered anisotropic spheroidal volume conductor. *J. Appl. Phys.* **64** (1988), 464–470.

[175] J.C. de Munck and M.J. Peters. A fast method to compute the potential in the multisphere model (EEG application). *IEEE Trans. Biomed. Eng.* **40** (1993), 1166–1174.

[176] M.T. Nair. *Linear Operator Equations – Approximation and Regularization*. Singapore: World Scientific Publishing Co. Pte. Ltd., 2009.

[177] M.Z. Nashed. *A new approach to classification and regularization of ill-posed operator equations*. In: *Inverse and Ill-Posed Problems*. Ed. by H.W. Engl and C.W. Groetsch. Notes and Reports in Mathematics in Science and Engineering. Orlando: Academic Press, 1987.

[178] A. Neubauer. Tikhonov-regularization of ill-posed linear operator equations on closed convex sets. *J. Approx. Theory* **53** (1988), 304–320.

[179] A.F. Nikiforov and V.B. Uvarov. *Special Functions of Mathematical Physics. A Unified Introduction with Applications*. Basel: Birkhäuser, 1988.

[180] G. Nolte. The magnetic lead field theorem in the quasi-static approximation and its use for magnetoencephalography forward calculation in realistic volume conductors. *Phys. Med. Biol.* **48** (2003), 3637–3652.

[181] G. Nolte and G. Dassios. Analytic expansion of the EEG lead field for realistic volume conductors. *Phys. Med. Biol.* **50** (2005), 3807–3823.

[182] G. Nolte, T. Fieseler, and G. Curio. Perturbative analytical solutions of the magnetic forward problem for realistic volume conductors. *J. Appl. Phys.* **89** (2001), 2360–2369.

[183] P. Novikoff. Sur le problème inverse du potentiel. *C.R. Acad. Sci. U.R.S.S.* **18** (1938), 165–168.

[184] H. Nutz. *A Unified Setup of Gravitational Field Observables*. PhD thesis. Shaker-Verlag Aachen: University of Kaiserslautern, Department of Mathematics, Geomathematics Group, 2002.

[185] OpenMP Architecture Review Board. *OpenMP Application Program Interface*. Version 4.0. 2013. URL: `https://www.openmp.org/wp-content/uploads/OpenMP4.0.0.pdf` (visited on 27/06/2018).

[186] Y.C. Pati, R. Rezaiifar, and P.S. Krishnaprasad. *Orthogonal matching pursuit: recursive function approximation with applications to wavelet decomposition*. In: *Proceedings of 27th Asilomar Conference on Signals, Systems and Computers*. (Pacific Grove, CA, USA, 1st–3rd Nov. 1993). Vol. 1. Washington, DC: IEEE Comput. Soc. Press, 1993, 40–44.

[187] D.L. Phillips. A technique for the numerical solution of certain integral equations of the first kind. *Journal of the ACM* **9** (1962), 84–97.

[188] P. Pizzetti. Corpi equivalenti rispetto alla attrazione Newtoniana esterna. *Acc. L. Rend.* **18** (1909), 211–215.

[189] P. Pizzetti. Intorno alle possibili distribuzioni della massa nell'interno della terra. *Ann. Mat. Milano* **17** (1910), 225–258.

[190] R. Plonsey. *Biomagnetic Phenomena*. New York: McGraw-Hill, 1969.

[191] R. Plonsey and D.B. Heppner. Considerations of quasi-stationarity in electrophysiological systems. *Bull. Math. Biophys.* **29** (1967), 657–664.

[192] R. Ramlau and H.W. Engl. *Regularization of inverse problems*. In: *Encyclopedia of Applied and Computational Mathematics*. Ed. by B. Engquist. Berlin, Heidelberg: Springer, 2015, 1233–1241.

[193] R. Ramlau and G. Teschke. *Sparse recovery in inverse problems*. In: *Theoretical Foundations and Numerical Methods for Sparse Recovery*. Ed. by M. Fornasier. Radon Series on Computational and Applied Mathematics. Berlin: De Gruyter, 2010, 201–263.

[194] A. Rieder. *Keine Probleme mit Inversen Problemen*. Wiesbaden: Vieweg+Teubner Verlag, 2003.

[195] W. Ritz. Über eine neue Methode zur Lösung gewisser Variationsprobleme der mathematischen Physik. *J. Reine Angew. Math.* **135** (1909), 1–61.

[196] D.P. Rubincam. Gravitational potential energy of the Earth: a spherical harmonic approach. *J. Geophys. Res-Sol. Ea.* **84** (1979), 6219–6225.

[197] W. Rudin. *Principles of Mathematical Analysis*. 3rd ed. International Series in Pure and Applied Mathematics. New York: McGraw-Hill, 1976.

[198] W. Rudin. *Functional Analysis*. 2nd ed. New York: McGraw-Hill, 1991.

[199] F. Sansò and R. Rummel, eds. *Geodetic Boundary Value Problems in View of the One Centimeter Geoid*. Vol. 65. Lect. Notes Earth Sci. Berlin, Heidelberg: Springer, 1997.

[200] J. Sarvas. Basic mathematical and electromagnetic concepts of the biomagnetic inverse problem. *Phys. Med. Biol.* **32** (1987), 11–22.

[201] N. Schneider. PhD thesis. University of Siegen, Department of Mathematics, Geomathematics Group, 2019. In preparation.

[202] F.J. Simons. *Slepian functions and their use in signal estimation and spectral analysis*. In: *Handbook of Geomathematics*. Ed. by W. Freeden, M.Z. Nashed, and T. Sonar. Berlin Heidelberg: Springer, 2010, 891–923.

[203] F.J. Simons, F.A. Dahlen, and M.A. Wieczorek. Spatiospectral concentration on a sphere. *SIAM Rev.* **48** (2006), 504–536.

[204] G.G. Stokes. On the internal distribution of matter which shall produce a given potential at the surface of a gravitating mass. *Proc. Royal Soc.* **15** (1867), 482–486.

[205] J.A. Stratton. *Electromagnetic Theory*. New York: McGraw-Hill, 1941.

[206] D. Stromeyer and L. Ballani. Uniqueness of the inverse gravimetric problem for point mass models. *Manuscr. Geodaet.* **9** (1984), 125–136.

[207] B. Stroustrup. *The C++ Programming Language*. 4th ed. 2nd printing. Upper Saddle River: Pearson Education, 2013.

[208] S. Supek and C.J. Aine, eds. *Magnetoencephalography*. Berlin, Heidelberg: Springer, 2014.

[209] G. Szegö. *Orthogonal Polynomials*. 4th ed. Providence, Rhode Island: American Mathematical Society, 1975.

[210] R. Telschow. *An Orthogonal Matching Pursuit for the Regularization of Spherical Inverse Problems*. PhD thesis. Verlag Dr. Hut Munich: University of Siegen, Department of Mathematics, Geomathematics Group, 2014.

[211] The Human Brain Project. *Short Overview of the Human Brain Project*. 2017. URL: `https://www.humanbrainproject.eu/en/about/overview/` (visited on 28/06/2018).

[212] The MathWorks Inc. *MATLAB*. Version 9.2 (R2017a). Natick, Massachusetts, 2017.

[213] A.N. Tikhonov. Solution of incorrectly formulated problems and the regularization method. *Soviet Math. Dokl.* **4** (1963), 1035–1038.

[214] A.N. Tikhonov and V.Y. Arsenin. *Solutions of Ill-Posed Problems*. Washington D.C.: V. H. Winston & Sons, 1977.

[215] C.C. Tscherning. Isotropic reproducing kernels for the inner of a sphere or spherical shell and their use as density covariance functions. *Math. Geol.* **28** (1996), 161–168.

[216] C. Uhl, ed. *Analysis of Neurophysiological Brain Functioning*. Berlin, Heidelberg: Springer, 1999.

[217] F. Vatta, F. Meneghini, F. Esposito, S. Mininel, and F. di Salle. Realistic and spherical head modeling for EEG forward problem solution: a comparative cortex-based analysis. *Comput. Intell. Neurosci.* **2010** (2010). Article ID 972060, 1–11.

[218] P. Vincent and Y. Bengio. Kernel matching pursuit. *Mach. Learn.* **48** (2002), 165–187.

[219] W. Walter. *Analysis 2*. 4th ed. Berlin, Heidelberg: Springer, 1995.

[220] N. Weck. Inverse Probleme der Potentialtheorie. *Appl. Anal.* **2** (1972), 195–204.

[221] M.A. Wieczorek and F.J. Simons. Localized spectral analysis on the sphere. *Geophys. J. Int.* **162** (2005), 655–675.

[222] Wikimedia Commons. *Principal fissures and lobes of the cerebrum viewed laterally.* Public Domain. 2010. URL: `https://commons.wikimedia.org/w/index.php?title=File:Lobes_of_the_brain_NL.svg&oldid=284464984` (visited on 26/05/2018). Based on an illustration by V. H. Carter in *Gray's Anatomy* (Fig. 728) from 1918.

[223] Wolfram Research, Inc. *Mathematica*. Version 10.0. Champaign, Illinois, 2014.

[224] K. Yosida. *Lectures on Differential and Integral Equations*. New York: John Wiley & Sons, 1960.

[225] K. Yosida. *Functional Analysis*. 6th ed. Berlin, Heidelberg, New York: Springer, 1980.

[226] Z. Zhang. A fast method to compute surface potentials generated by dipoles within multilayer anisotropic spheres. *Phys. Med. Biol.* **40** (1995), 335–349.

[227] Z. Zhang and D.L. Jewett. Insidious errors in dipole localization parameters at a single time-point due to model misspecification of number of shells. *Electroen. Clin. Neuro.* **88** (1993), 1–11.